7-17-2009

Sizing Up the Stars

Tabetha Suzanne Boyajian

Sizing Up the Stars

by

Tabetha S. Boyajian

Under the Direction of Harold McAlister

Abstract

For the main part of this dissertation, I have executed a survey of nearby, main sequence A, F, and G-type stars with the CHARA Array, successfully measuring the angular diameters of forty-four stars to better than 4% accuracy. The results of these observations also yield empirical determinations of stellar linear radii and effective temperatures for the stars observed. In addition, these CHARA-determined temperatures, radii, and luminosities are fit to Yonsei-Yale isochrones to constrain the masses and ages of the stars. These quantities are compared to the results found in Allende Prieto & Lambert (1999), Holmberg et al. (2007), and Takeda (2007), who indirectly determine these same properties by fitting models to observed photometry. I find that for most cases, the models underestimate the radius of the star by $\sim 12\%$, while in turn they overestimate the effective temperature by $\sim 1.5 - 4\%$, when compared to my directly measured values, with no apparent correlation to the star's metallicity or color index. These overestimated temperatures and underestimated radii in

these works appear to cause an additional offset in the star's surface gravity measurements, which consequently yield higher masses and younger ages, in particular for stars with masses greater than $\sim 1.3\ M_{\odot}$. Alternatively, these quantities I measure are also compared to direct measurements from a large sample of eclipsing binary stars in Andersen (1991), and excellent agreement is seen within both data sets. Finally, a multi-parameter solution is found to fit color-temperature-metallicity values of the stars in this sample to provide a new calibration of the effective temperature scale for these types of stars.

Published work in the field of stellar interferometry and optical spectroscopy of early-type stars are presented in Appendix D and E, respectively.

INDEX WORDS: Interferometry, Infrared, Stellar Astronomy, Fundamental Properties, Effective Temperatures, Stellar Radii

Sizing Up the Stars

by

Tabetha S. Boyajian

A Dissertation Presented in Partial Fulfillment of Requirements for the Degree of

Doctor of Philosophy

in the College of Arts and Sciences

Georgia State University

2009

Sizing Up the Stars

by

Tabetha S. Boyajian

Major Professor:	Harold McAlister
Committee:	Nikolaus Dietz
	Douglas Gies
	Todd Henry
	Gerard van Belle
	Russel White
	Paul Wiita

Electronic Version Approved:

Office of Graduate Studies
College of Arts & Sciences
Georgia State University
August 2009

To Alex. Je t'm!

Acknowledgments

A big, warm, and fuzzy hug to my family, friends, and colleagues. Alex, I know it has not been easy to deal with our *growing* family, with my head buried in the books and my eyes glued to the laptop. The magnitude of patience that you have to deal with a pregnant wife (and now a young child) can only be attributed to true love, and I am the luckiest person on Earth to have you as my husband and father of our son Jude. I also feel a need to thank Jude. Although he is only a few months old at the time of this writing, about 90% of his life has been spent staring at my bookshelf of old Physics and Astronomy books, notebooks, and papers. You deserve more attention than that of my left foot, which I used to rock you to sleep while I work at my desk. To my dear Kepler, I apologize for discovering a clever method of playing Frisbee with you (up our steep driveway), devised only to tire you out quickly so I could get back to work. Sincerest thanks to every member of my family that has had to miss my presence due my urgency in working to meet deadlines. Thank you for being so very understanding, for your never-ending support, and for your interest in my studies.

I would also like to thank the people at the CHARA Array who work so hard so that everything runs smoothly for the scientists. I apologize that you may only hear of our problems when observing, you deserve to be acknowledged for the invaluable improvements that you make on a daily basis to make our work easier! To the night operators, thank you for dealing with us graduate students running the CHARA Array remotely from AROC.

Special thanks to all of my committee members for spending your valuable time reviewing my progress reports and documents. In particular, to my dissertation advisor, Hal McAlister,

thank you for making the time to teach me all about interferometry, review my work in such a speedy manner, and encourage me to pursue any stray idea that came to mind. To Doug Gies, my masters advisor, thank you for allowing the opportunity to work with you researching the properties of massive stars.

Thank you to all of the graduate students that have helped me along the way. Thank you Ginny McSwain, for your continuous encouragement to be an independent researcher, for inviting me to be a collaborator in your work, and for taking me observing with you and your team. Thank you Deepak Raghavan, David O'Brien, Yamina Touhami, and Noel Richardson for your support with CHARA observations and research. Thank you Ellyn Baines for teaching me how to drive the Array in the graduate winter observing sessions of 2007; I have (hopefully) succeeded in passing this experience onto other graduate students since then. Thank you Alvin Das, for making a dissertation template for future PhD students. Thank you Rajesh Deo and Justin Cantrell for your technical support.

Finally, I would like to thank all the folks at the College of Charleston for encouraging me to pursue a career in Astronomy.

Table of Contents

Acknowledgments v

List of Tables xii

List of Figures xv

Abbreviations and Acronyms xxvii

1 Introduction 1

1.1 Motivation 1

1.1.1 Stellar Radii 1

1.1.2 Stellar Effective Temperatures 2

1.1.3 Angular Diameters of Main Sequence Stars 5

1.2 Interferometry 6

1.3 The CHARA Array 7

1.3.1 Description of the Instrument 7

1.3.2 Observing and Data Reduction 10

2 The Sample of A, F, and G Dwarfs 13

2.1 Selection Criteria 13

2.1.1 Resolution Limits 13

2.1.2 Instrumental Limits 14

2.2 The *HIPPARCOS* Catalogue Query 16

2.2.1 *RECONS* Stars 20

3 Interferometric Calibrators 26

3.1 The Calibrator 26

3.1.1 Calibrator Selection 26

3.2 Calibrating Interferometric Data 28

3.3 Observing Techniques . . . 30
3.3.1 When Is a Good Time to Align NIRO? . . . 31
3.3.2 Classic Observing: 1×1 Versus 2×2 Pixels . . . 31
3.3.3 Night-to-Night Repeatability . . . 33
3.3.4 Object/Calibrator Brightness Offsets and Calibration . . . 35
3.3.5 Observing with Two Calibrators . . . 38
3.3.6 Signs of a Bad Calibrator . . . 40
3.4 Miscellaneous . . . 41
3.4.1 The Baseline Test . . . 41
3.4.2 Lab Vibrations . . . 42

4 Observations . . . 49

5 Stellar Diameters . . . 59

5.1 Diameter Fit to a Single Star . . . 59
5.2 CHARA Versus Palomar Testbed Interferometer Diameters . . . 63
5.3 Systematics of CHARA Versus Other OLBI Diameters . . . 66

6 Luminosities and Temperatures . . . 71

6.1 Luminosities and Temperatures . . . 71
6.2 Discussion of the CHARA Determined Fundamental Parameters . . . 73

7 Analysis . . . 84

7.1 Comparative Analysis of Linear Radii . . . 84
7.2 Comparative Analysis of Effective Temperatures . . . 86
7.2.1 CHARA Versus Allende Prieto & Lambert (1999) . . . 87
7.2.2 CHARA Versus Holmberg et al. (2007) . . . 91
7.2.3 CHARA Versus Takeda (2007) . . . 92
7.3 Model Mass and Age Relations to Measured CHARA Data . . . 94
7.4 CHARA Masses . . . 107
7.5 Comparative Analysis to Eclipsing Binaries . . . 109

8 Yonsei-Yale Models 124

8.1 Introduction 124

8.2 Discussion 125

8.3 Comparative Analysis to Results from Other Works 128

9 Effective Temperature Calibrations 137

10 Summary and Future Work 144

References **151**

Appendices 156

A Appendix A 157

B Appendix B 198

C Appendix C 230

C.1 HD 4614 230

C.2 HD 5015 233

C.3 HD 6582 236

C.4 HD 10780 239

C.5 HD 16895 242

C.6 HD 19373 245

C.7 HD 20630 248

C.8 HD 22484 251

C.9 HD 30652 254

C.10 HD 34411 257

C.11 HD 39587 260

C.12 HD 48682 263

C.13 HD 48737 266

C.14 HD 56537 269

C.15 HD 58946 272
C.16 HD 81937 275
C.17 HD 82328 278
C.18 HD 82885 281
C.19 HD 86728 284
C.20 HD 90839 287
C.21 HD 97603 290
C.22 HD 101501 293
C.23 HD 102870 296
C.24 HD 103095 299
C.25 HD 109358 302
C.26 HD 114710 305
C.27 HD 118098 308
C.28 HD 126660 311
C.29 HD 128167 314
C.30 HD 131156 317
C.31 HD 141795 320
C.32 HD 142860 323
C.33 HD 146233 326
C.34 HD 162003 329
C.35 HD 164259 332
C.36 HD 173667 335
C.37 HD 177724 338
C.38 HD 182572 341
C.39 HD 185144 344
C.40 HD 185395 347

C.41 HD 210418 350
C.42 HD 213558 353
C.43 HD 215648 356
C.44 HD 222368 359

D Appendix D: Published Work in the Field of Stellar Interferometry . 362

E Appendix E: Published Work in the Field of Optical Spectroscopy . . 377

List of Tables

1.1 CHARA Baseline Configurations 12

2.1 Sample Criteria 22
2.2 The Sample of A, F, and G Dwarfs 22
2.3 Magnitudes and Colors of the Sample 23

3.1 Calibrators Observed 45
3.2 Calibrator SED Diameters 46
3.3 Bad Calibrators 48

4.1 Observations of A, F, and G Dwarfs 52
4.2 Problem Stars 58

5.1 Angular Diameters 68
5.2 CHARA Versus PTI Angular Diameters 69
5.3 CHARA Versus PTI Calibrators 70

6.1 Bolometric Fluxes 81
6.2 Luminosities and Temperatures 82

8.1 Y^2 Model Isochrone Results 135

C.1 HD 4614 Visibilities 230
C.2 HD 5015 Visibilities 233
C.3 HD 6582 Visibilities 236
C.4 HD 10780 Visibilities 239
C.5 HD 16895 Visibilities 242

C.6 HD 19373 Visibilities 245
C.7 HD 20630 Visibilities 248
C.8 HD 22484 Visibilities 251
C.9 HD 30652 Visibilities 254
C.10 HD 34411 Visibilities 257
C.11 HD 39587 Visibilities 260
C.12 HD 48682 Visibilities 263
C.13 HD 48737 Visibilities 266
C.14 HD 56537 Visibilities 269
C.15 HD 59846 Visibilities 272
C.16 HD 81937 Visibilities 275
C.17 HD 82328 Visibilities 278
C.18 HD 82885 Visibilities 281
C.19 HD 86728 Visibilities 284
C.20 HD 90839 Visibilities 287
C.21 HD 97603 Visibilities 290
C.22 HD 101501 Visibilities 293
C.23 HD 102870 Visibilities 296
C.24 HD 103095 Visibilities 299
C.25 HD 109358 Visibilities 302
C.26 HD 114710 Visibilities 305
C.27 HD 118098 Visibilities 308
C.28 HD 126660 Visibilities 311
C.29 HD 128167 Visibilities 314
C.30 HD 131156 Visibilities 317
C.31 HD 141795 Visibilities 320

C.32 HD 142860 Visibilities 323
C.33 HD 146233 Visibilities 326
C.34 HD 162003 Visibilities 329
C.35 HD 164259 Visibilities 332
C.36 HD 173667 Visibilities 335
C.37 HD 177724 Visibilities 338
C.38 HD 182572 Visibilities 341
C.39 HD 185144 Visibilities 344
C.40 HD 185395 Visibilities 347
C.41 HD 210418 Visibilities 350
C.42 HD 213558 Visibilities 353
C.43 HD 215648 Visibilities 356
C.44 HD 222368 Visibilities 359

List of Figures

1.1 The Two-Telescope Interferometer 8
1.2 Mount Wilson Observatory 9
1.3 Layout of the CHARA Array Facilities 10

2.1 Angular Size Versus Distance 15
2.2 Angular Diameter as a Function of Temperature and Magnitude 17
2.3 Color Magnitude Diagram of Sample 21

3.1 The Calibrator's Diameter 30
3.2 Bad NIRO Alignment Effects 32
3.3 Bad NIRO Alignment Effects 33
3.4 NIRO 1×1 Versus 2×2 Pixels 34
3.5 NIRO 1×1 Versus 2×2 Pixels 35
3.6 Night-to-Night Repeatability 36
3.7 Night-to-Night Repeatability 37
3.8 Two Calibrator Diameter Fit 39
3.9 Binary Calibrator Brackets 41
3.10 Lab Vibrations 44
3.11 Lab Vibrations 44

5.1 SED Versus LD Diameters with Respect to $(B-V)$ Color 61
5.2 Comparison of SED to LD Diameters with Respect to $(B-V)$ Color . . . 62
5.3 CHARA Versus PTI Diameters 64
5.4 Offsets in Various OLBI Data Sets 68

6.1 CHARA Luminosity Versus Temperature 75
6.2 CHARA Luminosity Versus Temperature and Radius 75
6.3 CHARA Luminosity Versus Temperature and Metallicity 76
6.4 CHARA Luminosity Versus $(B-V)$ 77
6.5 CHARA Luminosity Versus $(B-V)$ and Radius 77
6.6 CHARA Luminosity Versus $(B-V)$ and Metallicity 78
6.7 CHARA Temperature Versus Radius 78
6.8 CHARA Radius Versus $(B-V)$ 79
6.9 CHARA Luminosity Versus Radius 79
6.10 CHARA Temperature Versus $(B-V)$ and Metallicity 80

7.1 Measured Versus Model Radii 85
7.2 Effects of Metallicity on Radii Offsets 86
7.3 Empirical Versus Model Effective Temperatures 87
7.4 Empirical Versus Model Effective Temperatures 88
7.5 Effects of Metallicity on Temperature Offsets 89
7.6 Effects of $(b-y)$ on Temperature Offsets 90
7.7 Empirical Versus Model Effective Temperatures 92
7.8 Empirical Versus Model Effective Temperatures 93
7.9 Effects of Metallicity on Temperature Offsets 94
7.10 Effects of $(b-y)$ on Temperature Offsets 95
7.11 Empirical Versus Model Effective Temperatures 96
7.12 Empirical Versus Model Effective Temperatures 97
7.13 Effects of Metallicity on Temperature Offsets 98
7.14 Effects of $(b-y)$ on Temperature Offsets 99
7.15 Radius-Temperature-Mass 100
7.16 Radius-Temperature-Mass 101

7.17 Radius-Temperature-Mass 102
7.18 Radius-Temperature-Age 103
7.19 Radius-Temperature-Age 104
7.20 Radius-Age 106
7.21 Radius-Age 107
7.22 Radius-Mass 108
7.23 Radius-Mass-Metallicity 109
7.24 Radius-Mass 110
7.25 Radius-Mass-Metallicity 111
7.26 Radius-Mass 112
7.27 Radius-Mass-Metallicity 113
7.28 Temperature-Mass 114
7.29 Temperature-Mass 115
7.30 Temperature-Mass 116
7.31 CHARA Masses Versus Model Masses 117
7.32 CHARA Masses Versus Model Masses 118
7.33 Eclipsing Binary and CHARA Radii Versus (B-V) 119
7.34 Eclipsing Binary and CHARA Masses Versus Radius 120
7.35 Eclipsing Binary and CHARA Luminosities Versus Radii 121
7.36 Eclipsing Binary and CHARA Mass Versus $(B-V)$ 122
7.37 Eclipsing Binary and CHARA Mass Versus Luminosity 123

8.1 Y^2 Model Ages Versus Ages from Holmberg et al. (2007) and Takeda (2007) 129
8.2 Y^2 Model Ages Versus Metallicity 130
8.3 Y^2 Model Masses Versus Masses from Allende Prieto & Lambert (1999), Holmberg et al. (2007), and Takeda (2007) 131
8.4 Y^2 Model Masses Versus Masses Derived from $\log g$ 132

8.5 Mass Versus Color Index 133
8.6 Mass Versus Luminosity 134

9.1 Color-Temperature-Metallicity 139
9.2 Comparing Color-Temperature-Metallicity Relations 141
9.3 Residuals of Color-Temperature-Metallicity Relations 143

A.1 SED plot for HD 166 158
A.2 SED plot for HD 4614 158
A.3 SED plot for HD 5015 159
A.4 SED plot for HD 6582 159
A.5 SED plot for HD 10780 160
A.6 SED plot for HD 16895 160
A.7 SED plot for HD 19373 161
A.8 SED plot for HD 20630 161
A.9 SED plot for HD 22484 162
A.10 SED plot for HD 25457 162
A.11 SED plot for HD 27045 163
A.12 SED plot for HD 30652 163
A.13 SED plot for HD 33564 164
A.14 SED plot for HD 34411 164
A.15 SED plot for HD 35296 165
A.16 SED plot for HD 38858 165
A.17 SED plot for HD 39587 166
A.18 SED plot for HD 43042 166
A.19 SED plot for HD 43386 167
A.20 SED plot for HD 46588 167
A.21 SED plot for HD 48682 168

A.22 SED plot for HD 48737 168
A.23 SED plot for HD 50692 169
A.24 SED plot for HD 55575 169
A.25 SED plot for HD 56537 170
A.26 SED plot for HD 58855 170
A.27 SED plot for HD 58946 171
A.28 SED plot for HD 69897 171
A.29 SED plot for HD 78154 172
A.30 SED plot for HD 78209 172
A.31 SED plot for HD 81937 173
A.32 SED plot for HD 82328 173
A.33 SED plot for HD 82885 174
A.34 SED plot for HD 86728 174
A.35 SED plot for HD 87696 175
A.36 SED plot for HD 90089 175
A.37 SED plot for HD 90839 176
A.38 SED plot for HD 95418 176
A.39 SED plot for HD 97603 177
A.40 SED plot for HD 101501 177
A.41 SED plot for HD 102870 178
A.42 SED plot for HD 103095 178
A.43 SED plot for HD 103287 179
A.44 SED plot for HD 106591 179
A.45 SED plot for HD 109358 180
A.46 SED plot for HD 110897 180
A.47 SED plot for HD 114710 181

A.48 SED plot for HD 116842 181
A.49 SED plot for HD 118098 182
A.50 SED plot for HD 126660 182
A.51 SED plot for HD 126868 183
A.52 SED plot for HD 128167 183
A.53 SED plot for HD 131156 184
A.54 SED plot for HD 134083 184
A.55 SED plot for HD 140538 185
A.56 SED plot for HD 141795 185
A.57 SED plot for HD 142860 186
A.58 SED plot for HD 146233 186
A.59 SED plot for HD 157214 187
A.60 SED plot for HD 161868 187
A.61 SED plot for HD 162003 188
A.62 SED plot for HD 164259 188
A.63 SED plot for HD 165777 189
A.64 SED plot for HD 168151 189
A.65 SED plot for HD 173667 190
A.66 SED plot for HD 177724 190
A.67 SED plot for HD 182572 191
A.68 SED plot for HD 185144 191
A.69 SED plot for HD 185395 192
A.70 SED plot for HD 187013 192
A.71 SED plot for HD 187691 193
A.72 SED plot for HD 195564 193
A.73 SED plot for HD 201091 194

A.74 SED plot for HD 201092 194
A.75 SED plot for HD 210418 195
A.76 SED plot for HD 211336 195
A.77 SED plot for HD 213558 196
A.78 SED plot for HD 215648 196
A.79 SED plot for HD 222368 197

B.1 SED plot for HD 71 199
B.2 SED plot for HD 6210 199
B.3 SED plot for HD 9407 200
B.4 SED plot for HD 20675 200
B.5 SED plot for HD 21790 201
B.6 SED plot for HD 22879 201
B.7 SED plot for HD 28355 202
B.8 SED plot for HD 30739 202
B.9 SED plot for HD 31295 203
B.10 SED plot for HD 34904 203
B.11 SED plot for HD 38558 204
B.12 SED plot for HD 42807 204
B.13 SED plot for HD 43042 205
B.14 SED plot for HD 43795 205
B.15 SED plot for HD 50277 206
B.16 SED plot for HD 58551 206
B.17 SED plot for HD 59037 207
B.18 SED plot for HD 65583 207
B.19 SED plot for HD 83951 208
B.20 SED plot for HD 87141 208

B.21 SED plot for HD 88986 209
B.22 SED plot for HD 89389 209
B.23 SED plot for HD 91480 210
B.24 SED plot for HD 99285 210
B.25 SED plot for HD 99984 211
B.26 SED plot for HD 102124 211
B.27 SED plot for HD 102634 212
B.28 SED plot for HD 103799 212
B.29 SED plot for HD 110897 213
B.30 SED plot for HD 114093 213
B.31 SED plot for HD 120066 214
B.32 SED plot for HD 128093 214
B.33 SED plot for HD 129153 215
B.34 SED plot for HD 132254 215
B.35 SED plot for HD 135101 216
B.36 SED plot for HD 139225 216
B.37 SED plot for HD 140775 217
B.38 SED plot for HD 145607 217
B.39 SED plot for HD 150177 218
B.40 SED plot for HD 154099 218
B.41 SED plot for HD 158352 219
B.42 SED plot for HD 158633 219
B.43 SED plot for HD 162004 220
B.44 SED plot for HD 167564 220
B.45 SED plot for HD 174897 221
B.46 SED plot for HD 176303 221

B.47 SED plot for HD 180317 222
B.48 SED plot for HD 183534 222
B.49 SED plot for HD 184499 223
B.50 SED plot for HD 189395 223
B.51 SED plot for HD 191195 224
B.52 SED plot for HD 193555 224
B.53 SED plot for HD 193664 225
B.54 SED plot for HD 195838 225
B.55 SED plot for HD 204485 226
B.56 SED plot for HD 210715 226
B.57 SED plot for HD 211976 227
B.58 SED plot for HD 214923 227
B.59 SED plot for HD 216735 228
B.60 SED plot for HD 218470 228
B.61 SED plot for HD 222603 229
B.62 SED plot for HD 225003 229

C.1 Diameter fit for HD 4614 231
C.2 Y^2 Model Isochrones for HD 4614 232
C.3 Diameter fit for HD 5015 234
C.4 Y^2 Model Isochrones for HD 5015 235
C.5 Diameter fit for HD 6582 237
C.6 Y^2 Model Isochrones for HD 6582 238
C.7 Diameter fit for HD 10780 240
C.8 Y^2 Model Isochrones for HD 10780 241
C.9 Diameter fit for HD 16895 243
C.10 Y^2 Model Isochrones for HD 16895 244

C.11 Diameter fit for HD 19373 246
C.12 Y^2 Model Isochrones for HD 19373 247
C.13 Diameter fit for HD 20630 249
C.14 Y^2 Model Isochrones for HD 20630 250
C.15 Diameter fit for HD 22484 252
C.16 Y^2 Model Isochrones for HD 22484 253
C.17 Diameter fit for HD 30652 255
C.18 Y^2 Model Isochrones for HD 30652 256
C.19 Diameter fit for HD 34411 258
C.20 Y^2 Model Isochrones for HD 34411 259
C.21 Diameter fit for HD 39587 261
C.22 Y^2 Model Isochrones for HD 39587 262
C.23 Diameter fit for HD 48682 264
C.24 Y^2 Model Isochrones for HD 48682 265
C.25 Diameter fit for HD 48737 267
C.26 Y^2 Model Isochrones for HD 48737 268
C.27 Diameter fit for HD 56537 270
C.28 Y^2 Model Isochrones for HD 56537 271
C.29 Diameter fit for HD 58946 273
C.30 Y^2 Model Isochrones for HD 58946 274
C.31 Diameter fit for HD 81937 276
C.32 Y^2 Model Isochrones for HD 81937 277
C.33 Diameter fit for HD 82328 279
C.34 Y^2 Model Isochrones for HD 82328 280
C.35 Diameter fit for HD 82885 282
C.36 Y^2 Model Isochrones for HD 82885 283

C.37 Diameter fit for HD 86728 285
C.38 Y^2 Model Isochrones for HD 86728 286
C.39 Diameter fit for HD 90839 288
C.40 Y^2 Model Isochrones for HD 90839 289
C.41 Diameter fit for HD 97603 291
C.42 Y^2 Model Isochrones for HD 97603 292
C.43 Diameter fit for HD 101501 294
C.44 Y^2 Model Isochrones for HD 101501 295
C.45 Diameter fit for HD 102870 297
C.46 Y^2 Model Isochrones for HD 102870 298
C.47 Diameter fit for HD 103095 300
C.48 Y^2 Model Isochrones for HD 103095 301
C.49 Diameter fit for HD 109358 303
C.50 Y^2 Model Isochrones for HD 109358 304
C.51 Diameter fit for HD 114710 306
C.52 Y^2 Model Isochrones for HD 114710 307
C.53 Diameter fit for HD 118098 309
C.54 Y^2 Model Isochrones for HD 118098 310
C.55 Diameter fit for HD 126660 312
C.56 Y^2 Model Isochrones for HD 126660 313
C.57 Diameter fit for HD 128167 315
C.58 Y^2 Model Isochrones for HD 128167 316
C.59 Diameter fit for HD 131156 318
C.60 Y^2 Model Isochrones for HD 131156 319
C.61 Diameter fit for HD 141795 321
C.62 Y^2 Model Isochrones for HD 141795 322

C.63 Diameter fit for HD 142860 324
C.64 Y^2 Model Isochrones for HD 142860 325
C.65 Diameter fit for HD 146233 327
C.66 Y^2 Model Isochrones for HD 146233 328
C.67 Diameter fit for HD 162003 330
C.68 Y^2 Model Isochrones for HD 162003 331
C.69 Diameter fit for HD 164259 333
C.70 Y^2 Model Isochrones for HD 164259 334
C.71 Diameter fit for HD 173667 336
C.72 Y^2 Model Isochrones for HD 173667 337
C.73 Diameter fit for HD 177724 339
C.74 Y^2 Model Isochrones for HD 177724 340
C.75 Diameter fit for HD 182572 342
C.76 Y^2 Model Isochrones for HD 182572 343
C.77 Diameter fit for HD 185144 345
C.78 Y^2 Model Isochrones for HD 185144 346
C.79 Diameter fit for HD 185395 348
C.80 Y^2 Model Isochrones for HD 185395 349
C.81 Diameter fit for HD 210418 351
C.82 Y^2 Model Isochrones for HD 210418 352
C.83 Diameter fit for HD 213558 354
C.84 Y^2 Model Isochrones for HD 213558 355
C.85 Diameter fit for HD 215648 357
C.86 Y^2 Model Isochrones for HD 215648 358
C.87 Diameter fit for HD 222368 360
C.88 Y^2 Model Isochrones for HD 222368 361

Abbreviations and Acronyms

AROC	Arrington Remote Operations Center
BCL	Beam Combination Labratory
BSF	Beam Synthesis Facility
CCD	Charge Coupled Device
CHARA	Center for High Angular Resolution Astronomy
$F_{\rm BOL}$	Bolometric Flux
HST	Hubble Space Telescope
IDL	Interactive Data Language
IR	infrared
IRFM	Infrared Flux Method
km s^{-1}	kilometers per second
LBOI	Long Baseline Optical Interferometry
LO	Lunar Occultation
$L_{\odot}$	Solar Luminosity
mas	milli-arcseconds
$M_{\rm BOL}$	Bolometric Magnitude
MS	Main Sequence
$M_{\odot}$	Solar Mass
NASA	National Aeronautic and Space Administration
NIRO	Near Infrared Observer

OLBI	Optical Long Baseline Interferometry
OPLE	Optical Path Length Equalizer
pc	parsec
$R_{\odot}$	Solar Radius
SED	spectral energy distribution
SNR	Signal-to-noise ratio
T_{EFF}	Effective Temperature

– 1 –

Introduction

1.1 Motivation

1.1.1 Stellar Radii

The stellar radius is a fundamental physical characteristic of a star. Unfortunately, this property of a star is not well known due to the difficulty to measuring it directly. In eclipsing binary systems, the radii are measured by the combination of the binary's spectroscopic and photometric data, and absolute dimensions of their radii can be determined without the distance to the star being known. Although this is a straightforward approach to determining stellar radii, there are a limited amount of eclipsing binaries (52 individual components in the A, F, and G star range from the sample in Andersen 1991) to study in this manner.

Radii measurements of single stars are more challenging. They require special observing techniques to measure directly their small angular size, θ. The combination of θ with trigonometric parallax Π allows the linear radius to be determined. Thanks to the *HIPPARCOS* mission (ESA 1997; van Leeuwen 2007), we now know accurate parallaxes (out to a certain distance) to most of the bright stars in the sky. However, because stars are at such great distances from us, they are typically unresolved point sources of light, so their angular sizes can only be determined with clever techniques in astronomy such as using lunar or Jovian occultation (LO, JO) events, speckle interferometry, and long-baseline optical interferometry (LBOI).

The largest stars to be resolved in our sky are evolved stars (e.g. supergiants and giants), where although they reside at large distances from the Sun, their big intrinsic radii provide angular sizes that are large enough to be easily resolved by lunar occultation observations and by interferometers with modest baselines. Stars that have not evolved off the main sequence far outnumber the evolved stars is our sky, because $\approx 90\%$ of a star's life is spent on the main sequence. However, the radius of a main sequence star is typically one to three orders of magnitude (or $10 - 1000$) smaller than that of an evolved star, making it much smaller in angular size, despite its close vicinity to the Sun. These main sequence stars are also intrinsically several magnitudes dimmer than giants, due to their smaller radii.

The resolution limits to measuring the size of a single star using occultations (lunar or Jovian) or speckle interferometry depend on the size or diffraction limit of the telescope, and thus only the largest of stars may be observed with these techniques. Intensity interferometery can measure the size of a star to great accuracy (dependent on the baseline), but is limited to bright stars as in the case of the Narrabri Stellar Intensity Interferometer (Hanbury Brown et al. 1974), which only observed stars brighter than B=2.5 mag). The CHARA Array, an amplitude (Michelson-type) interferometer, has the highest resolution of any interferometer in the world due to its long baselines, and, although the telescopes are only 1-meter in diameter, the sensitivity of the CHARA Array depends on the beam combiner and wavelength used for observation.

1.1.2 Stellar Effective Temperatures

In addition to measuring the linear radius of a star, we may determine another fundamental property of a star, the effective temperature, $T_{\rm EFF}$. This property provides the link be-

tween the theory of stellar structure and evolution and model atmospheres. The effective temperature of a star is defined through the Stephan-Boltzmann law:

$$F = \sigma T_{\rm EFF}^4 \tag{1.1}$$

where F is the total emergent flux of the star and σ is the Stefan-Boltzmann constant. Transforming this equation to observables at Earth, we arrive at the expression:

$$F_{\rm BOL} = \frac{1}{4}\theta^2 \sigma T_{\rm EFF}^4 \tag{1.2}$$

where $F_{\rm BOL}$ is the bolometric flux received at Earth, and θ is the angular diameter of the star in radians. This is the only empirical method of determining a star's temperature, and it mostly depends on the tricky task of measuring the angular diameter of the star. Fortunately, the error in the effective temperature is relatively insensitive to errors in θ or $F_{\rm BOL}$. For instance, because $T_{\rm EFF} \propto \theta^{-2}$ then $\sigma(T_{\rm EFF}) \propto \frac{1}{2}\sigma(\theta)$, and because $T_{\rm EFF} \propto F_{\rm BOL}^4$ then $\sigma(T_{\rm EFF}) \propto \frac{1}{4}\sigma(F_{\rm BOL})$ (Booth 1997).

The renowned results from the survey of angular diameters of 32 stars conducted by the Narrabri Stellar Intensity Interferometer (Hanbury Brown et al. 1974; Code et al. 1976) extended from O to F type stars, eleven of which were on the main sequence. The average accuracy of these angular diameter determinations depended primarily on the brightness of the object, and was $\approx 6.5\%$ for the 32 stars measured. Distance errors at the time were not of high accuracy, and only eleven of the stars had less than a 20% error in parallax, limiting the results of the linear radius derived from the angular diameter measurement as well. This survey (conducted more than three decades ago), has been a key resource in calibrating several less direct relationships to stellar properties.

One such relation was first established by Barnes & Evans (1976), with the use of angular diameters of stars from lunar occultation (LO) measurements with other forms of direct measurements having been added to the calibration since this work was first published. It provides a relationship between the surface brightness of a star and its color index to the angular diameter of the star. Another technique, the Infrared Flux Method (IRFM), was first established by Blackwell & Shallis (1977). The IRFM embraces the idea that one can determine the angular diameter and temperature of a star simultaneously. A monochromatic version of the method was developed by Gray (1967), where the observed spectral energy distribution is compared to a model spectral energy distribution of a star, so that by conservation of energy:

$$4\pi R^2 F = 4\pi d^2 F_{\rm BOL} \tag{1.3}$$

where R is the radius of the star, F is the total flux emitted at the surface of the star, and d is the distance to Earth. Because $\theta = 2R/d$, then we have the relation:

$$\frac{F}{F_{\rm BOL}} = \theta^2/4. \tag{1.4}$$

The IRFM performs this same task, but assumes that the flux in the ratio of $F/F_{\rm BOL}$ holds for monochromatic wavelengths, in particular in the IR. In their work, Blackwell & Shallis (1977) justify this relation by arguing that there is a weak influence in the IR due to the temperature of the star versus the flux distribution (i.e., the monochromatic flux in the IR depends only on temperature to the first power, whereas the full integrated flux depends on the temperature to the fourth power). Smaller effects due to line-blanketing and opacity sources are more well known in this region as well. This method has developed sophistication

over the years to take these issues into account (see González Hernández & Bonifacio 2009, and references therein) and boasts a 1% accuracy on effective temperature determinations.

These relationships are extremely useful in extending our knowledge to a larger number of stars, at distances too far to resolve accurately their sizes. However, it has been noted over the years that in the absence of a more complete sample of stars, these relationships are only as good as the data upon which the calibrations were based (McAlister 1985).

1.1.3 Angular Diameters of Main Sequence Stars

As mentioned before, the Narrabri Stellar Intensity Interferometer (Hanbury Brown et al. 1974; Code et al. 1976) measured the angular diameters of eleven main sequence stars, providing the means to calibrate properties of stars on the hot, massive end of the main sequence. For several decades, luminosity class I, II, and III stars were observed with interferometry, but no main sequence star earlier than A7 was observed (Davis 1997). As an update, the CHARM2 Catalogue[1] (Richichi et al. 2005) is a compilation of stellar diameters by means of direct measurements by high angular resolution methods, as well as indirect estimates. The CHARM2 Catalogue includes all results as of July 2004, a total of 8231 entries, for 3238 unique sources. Of these 8231 entries, 905 are from direct measurements, and 458 of these are unique sources. Of the latter sample, 242 have errors in the angular diameter measurements of <5%, and only 24 of these reside on the main sequence (luminosity class V or IV). In a recent work by Holmberg et al. (2008), they remark that measurements of the angular diameters of main sequence F and G stars need to be better than 2%, yielding temperatures to 1%, in order for offsets in the color-temperature calibrations to be minimal.

[1] http://vizier.u-strasbg.fr/viz-bin/VizieR?-source=J/A+A/431/773

At that time, only nine stars met this criterion. This accuracy limit reiterates the target accuracy proposed by Blackwell et al. (1979) for the limits to the Infrared Flux Method, that a good $T_{\rm EFF}$ determination goal should be 1% to match the best atomic data available for abundance determinations and $\log g$ estimates (Davis 1985; Booth 1997).

The determination of accurate temperatures also becomes an important issue when determining stellar ages. Holmberg et al. (2007) give several good examples of how an offset in effective temperature will, in turn, offset the metallicity [Fe/H] measurements, and that these effects double up when determining the ages of the stars, thereby producing false age-metallicity relations. With 1% errors in the effective temperature scale, it is also possible to challenge stellar models to achieve greater accuracy than now attainable, by constraining mixing length theory and convective overshooting, to name a few issues at hand. The long baselines of the CHARA Array are uniquely suited for observing diameters of main-sequence stars to great accuracy.

1.2 Interferometry

We gain high spatial resolution in astronomical observations through the use of an interferometer. An interferometer is an array of telescopes that synthesizes the aperture of a giant telescope with the diameter equal to the separation of the arms of the interferometer. Mount Wilson Observatory is famous for interferometry historically and at the present day. It is the site where interferometry was first used to measure the diameters of stars when Michelson & Pease (1921) observed the diameter of the star α Orionis (Betelgeuse) with the 20-foot Michelson interferometer, which was mounted to the frame of the 100-inch Hooker telescope.

The first operational two-telescope optical interferometer was developed by A. Labeyrie (Labeyrie 1975) who detected interference fringes on α Lyra (Vega) in 1974. In the cartoon of such an interferometer (Figure 1.1), light is collected by two telescopes, Tel. #1 and Tel. #2, separated by baseline B. The light emitted by the star reaches each telescope at different times, where the extra light travel to Tel. #2 is called the "delay", and is quantified by the factor $B \sin\theta$. In order to detect interference fringes, this light delay to Tel. #2 must be compensated for, so the light collected from Tel. #1 must take a detour until the path lengths of light are equal. It is only then that interference fringes are formed when the beams are combined. The angular resolution of an interferometer is defined as $\lambda/2B$, where λ is the wavelength of observation. This is directly related to the condition of constructive interference in Young's double slit experiment (where the slits in this case are telescopes). This is slightly better than the angular resolution of a single telescope established by the Rayleigh Criterion that is defined as $1.22\lambda/D$, where D is the diameter of the telescope aperature.

1.3 The CHARA Array

1.3.1 Description of the Instrument

The CHARA Array is a six-telescope optical/infrared interferometric array located at Mount Wilson Observatory in the San Gabriel mountains of southern California (see Figure 1.2). The funding to build the CHARA Array came from Georgia State University, the National Science Foundation, the W. M. Keck Foundation, and the David and Lucile Packard Foundation. Continued operation of the Array after 'first fringes' (November 1999) is provided by

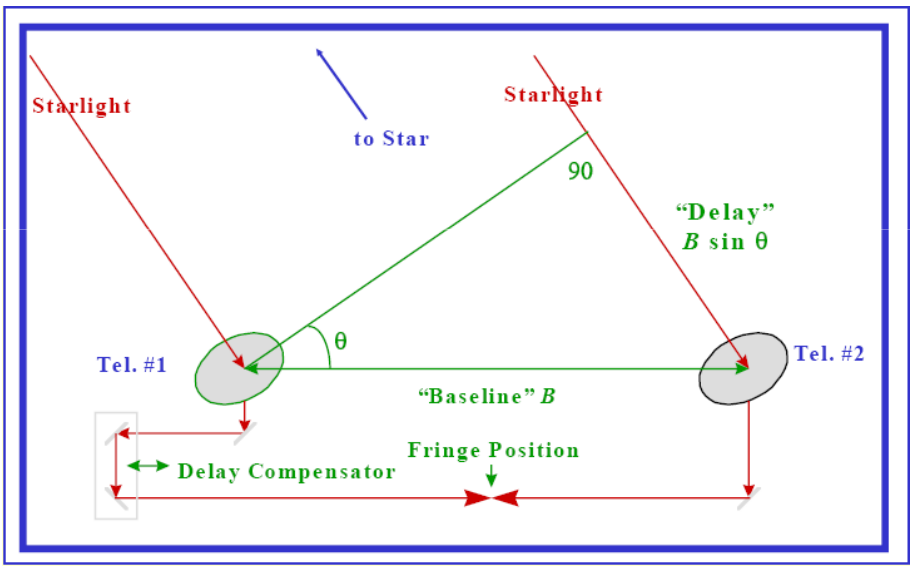

FIGURE 1.1: **The Two-Telescope Interferometer:** Cartoon of a two-telescope long baseline interferometer. Image courtesy of H. McAlister.

the College of Arts and Sciences of Georgia State University and the Division of Astronomical Sciences of the National Science Foundation. A detailed description of the instrument can be found in ten Brummelaar et al. (2005). The following text is a brief summary of the general elements and layout of the facility.

The CHARA Array consists of six, 1-meter aperture telescopes in a Y-shaped configuration spread across the mountaintop of the Observatory (Figure 1.3). With the six telescopes, there are fifteen available baseline combinations, ranging from 34 to 331 meters, at a variety of position angle orientations ψ (Table 1.1). There are two telescopes in each direction of South, East, and West, with the farthest telescope from the central OPLE building to which all light travels being named 1, the closer being named 2 (i.e. telescope S1 for the farthest southern telescope). The Array currently is the longest baseline optical/infrared interferometer in the world.

FIGURE 1.2: **Mount Wilson Observatory:** Pictorial overview of Mount Wilson Observatory. In the center of the image is the 100-inch Hooker telescope. CHARA telescopes are located at the right, bottom-left, and top-left of the image. (See also Figure 1.3.)

Each of the CHARA telescopes is connected to an evacuated light pipe (Figure 1.3), which channels the light collected at the telescope into the central "L"-shaped Beam Synthesis Facility (BSF). It is here in the Optical Path Length Equalizer (OPLE) building that the extra delay in the light arriving at each telescope is matched down to μm precision level using delay carts that move along rails in a lateral direction. This movement along the rails is fully automated and actively controlled in real-time to follow the stars' diurnal motion across the night sky.

Adjacent to the OPLE building in the BSF is the Beam Combination Laboratory (BCL), where the fringes are formed and detected. There are several beam combiners available for

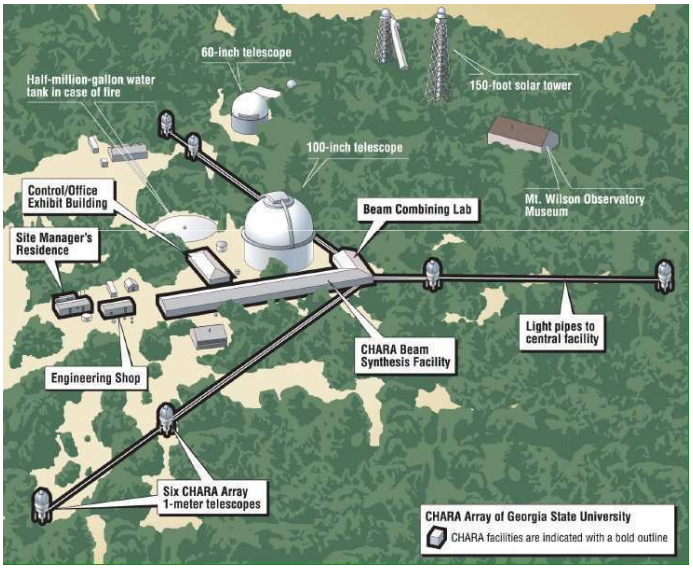

FIGURE 1.3: **Layout of the CHARA Array Facilities**

the CHARA Array, and for this project observations were made using the CHARA Classic beam combiner in two-telescope mode. CHARA Classic is a pupil-plane beam combiner, which is used primarily in K'-band (central wavelength of $\lambda_{K'} = 2.13 \pm 0.01 \mu$m). Fringes are detected and recorded on the Near Infrared Observer (NIRO) camera, which is based upon a HgCdTe PICNIC Array read out at high speed.

1.3.2 Observing and Data Reduction

Nearly all (98.5%) of the observing for this thesis was performed remotely from Georgia State University's Cleon Arrington Remote Operations Center (AROC) in Atlanta, GA. Here, almost everything needed to drive the CHARA Array can be done. We are able to

align the beams on the NIRO chip and on the sky, acquire targets, move the delay carts, scan for fringes, and record data. We are also able to monitor the weather and open and close the telescope optics and dome slits at any time during the evening. Night operators are on-site to alleviate any issues that may (and will) arise that require human interaction such as rebooting servers when they crash.

When observing, typically 200 scans are taken per data record, where the dither mirror scans the location of the last fringe offset[2]. An ideal night of observing will yield approximately 40 bracketed observations, but this is not typically the norm. Data recorded for each night of observing are stored on local machines at the Array.

The main data reduction package used to reduce CHARA Classic data for this project is VisUVCalc, written in MathCAD by H. A. McAlister and A. Jerkstrand. To process the data, the raw fringe signal is normalized and filtered using a low-pass filter to eliminate low frequency modulations in the fringe scan. A bandpass filter is then applied to the power spectrum of the fringe and inverted to smooth the data. The fringe visibility is then measured by fitting a model fringe to the data. The Signal-to-Noise (S/N) of the fringe data is also measured for each of the 200 scans. Zero weight is applied to scans with fringe visibility measurements with low S/N ratio, scans with unrealistically high visibility measurements (visibility greater than 0.75), and scans that detect fringes in a location far from the last fringe offset[3]. The total weight, mean and standard deviations of the individual visibilities are then calculated for the recorded data set. These outputs are stored in a text file to be calibrated (see Chapter 3 for details on calibrated observing methods and techniques).

[2]The fringe offset depends on the astrometric and baseline solutions for the star and baseline configuration used.

[3]The fringe servo keeps the fringe within the scan window while observing. In times of poor seeing, or other bad observing conditions, this tracking can be difficult, and scans can sometimes lose the fringe.

TABLE 1.1: CHARA Baseline Configurations

Telescope Pair	**B (m)**	ψ (°)
S1/S2	34.08	350.1
E1/E2	65.89	236.5
W1/W2	107.93	97.5
W2/E2	156.28	63.3
S2/W2	177.44	340.2
S1/W2	210.96	341.8
E1/W2	221.84	241.2
S2/E2	248.13	17.7
S2/W1	249.39	317.0
W1/E2	251.34	77.6
S1/W1	278.50	320.9
S1/E2	278.77	14.5
S2/E1	302.33	25.5
E1/W1	313.54	253.2
S1/E1	330.67	22.1

– 2 –

The Sample of A, F, and G Dwarfs

2.1 Selection Criteria

The motivation for this project extends from a long-standing need for accurate angular diameters for (roughly) main sequence stars. I selected the target list by aiming to meet several criteria, described below in detail. As discussed in the Introduction, several sources indicate that at least a 2% accuracy on the measured angular diameter is needed to refine the effective temperature scale to better than 1%, because $T_{\rm EFF} \propto \theta^{1/2}$. This limit will also allow us to calibrate color-temperature relations to a high degree of accuracy, and enable us to extend our knowledge to large populations of stars throughout the Galaxy. For this project, we aim to measure the angular diameter of a star to better than 4%, only to arrive at a sample that is large enough for an initial analysis; however, most of the stars observed will be sufficiently resolved down to the 2% level.

2.1.1 Resolution Limits

How accurately one can measure the angular diameter of a star depends on how far down the visibility curve you are able to sample. The visibility function of a single star is expressed as:

$$V = \frac{2J_1(\mathrm{x})}{\mathrm{x}}, \tag{2.1}$$

where

$$\mathrm{x} = \pi B \theta \lambda^{-1}, \tag{2.2}$$

where B is the projected baseline, θ is the angular diameter of the star, and λ is the wavelength of observation. By knowing the λ and B utilized in a given observation, we can estimate the optimum resolution range resulting from the accuracy with which we can measure the object visibility. For instance, assuming that we can readily measure the visibility of a star to 5% (McAlister, private communication), by evaluating Equation 2.1, we find that we must sample down to a visibility of V=0.55 to obtain better than 4% accuracy on the measured angular diameter of a star. To ensure that we will reach the resolution limit for our observations, we set the cutoff to obtain a visibility of 0.55 for CHARA's third longest baseline (S2/E1=302.2m). Thus, the limiting resolution that meets this criteria is $\theta = 0.65$ mas in K band and $\theta = 0.50$ mas in H band. By binning the spectral types and taking the nominal values for linear diameters for the stars from Cox (2000), the maximum distance for each spectral type bin is found (Figure 2.1).

I did not rely on assigned spectral types for stars because often it is difficult to find agreement from one catalogue to the next. Instead, in the *HIPPARCOS* Catalogue query, the ranges in spectral types were sampled by $(B - V)$ color indices, and luminosity classes were sampled by restricting the apparent V magnitudes of the stars to only admit roughly main sequence stars (Cox 2000). These sample criteria are listed in Table 2.1.

2.1.2 Instrumental Limits

In this project, the instrumental limits for observing are restricted only by the target declination, which must be greater than $-10°$. Stars approaching this declination suffer from baseline foreshortening. This is where the maximum projected baseline will never reach the full 330m on the longest S1/E1 baseline. Another factor in observing low-declination objects

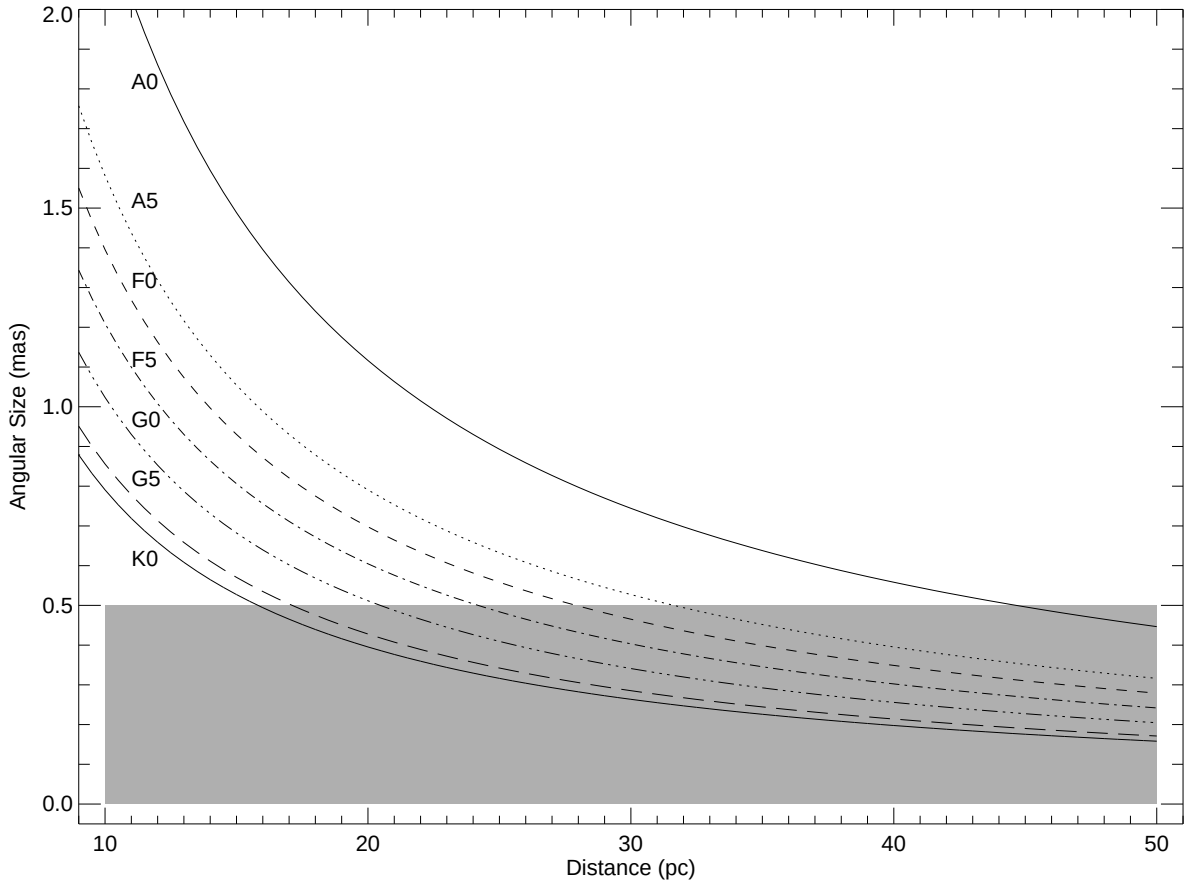

FIGURE 2.1: **Angular Size Versus Distance:** Plot of angular size of star by spectral type versus distance. The shaded region indicates distances where the star becomes too unresolved in H-band to achieve the goal of better than 4% accuracy on the angular diameter measurement. For example, we can observe a G0 dwarf to 20 pc using our adopted experimental setup.

is that they do not remain at their highest elevations for very long. Stars that are observed at lower than $\approx 30^\circ$ degrees elevation are thought to have calibration problems because one is observing through too much airmass, and seeing effects are more apparent at these low elevations. Additionally, the calibrator observed is likely to have a very different airmass, even if one is chosen to be very nearby, and these values change frequently when the objects are rising/setting. Last but not least, a very good reason not to observe a star too far south (and at low elevation) is that you are doomed to be glaring through the exhaust pipe of Los Angeles, which lies in the southern direction from Mount Wilson Observatory.

Magnitude limits are not a factor because of the resolution requirements set by the goals of the project ($\theta > 0.50$ mas for better than 4% accuracy in H-band). These are set by the distances of the target stars, and their predicted linear sizes. For instance, an A0 star has an absolute magnitude $M_V = 0.65$, so at the maximum distance of 33 pc it has an apparent magnitude of $m_V = 3.2$. For the late end of the sample, a K0 star has an absolute magnitude $M_V = 5.9$, so at the maximum distance of 16 pc this star has an apparent magnitude of $m_V = 6.9$. These translate into apparent K magnitudes of $m_K = 3.2$ and $m_K = 5.0$ for the A0 star and the K0 star, respectively (assuming $(V-K)_{\rm A0} = 0.0$ and $(V-K)_{\rm K0} = 1.96$; Cox 2000). Very conservative limits for observing with the CHARA Classic beam combiner require a K magnitude to be brighter than 7, much fainter than these values. This fact also gives some relief in finding suitable calibrators for the target stars, which are preferred to be of similar spectral type as the object, but must also be an unresolved source (i.e., farther and dimmer).

Figure 2.2 shows the relationship between a star's angular diameter as a function of effective temperature and observed K magnitude in a graphical representation. This uses the results from Code et al. (1976) where the angular diameters and effective temperatures are measured for eleven luminosity class V and IV stars[1]. For example, a $K = 5$ mag star with a temperature of ~ 4000 K will have an angular diameter of ~ 0.5 mas.

2.2 The *HIPPARCOS* Catalogue Query

A query of the *HIPPARCOS* Catalogue was preformed to compile a large list of objects to observe in this survey of (roughly) main sequence (MS) A, F, and G-type stars. The

[1]Computed K-magnitudes from line-blanketed model atmospheres developed by Robert Kurucz

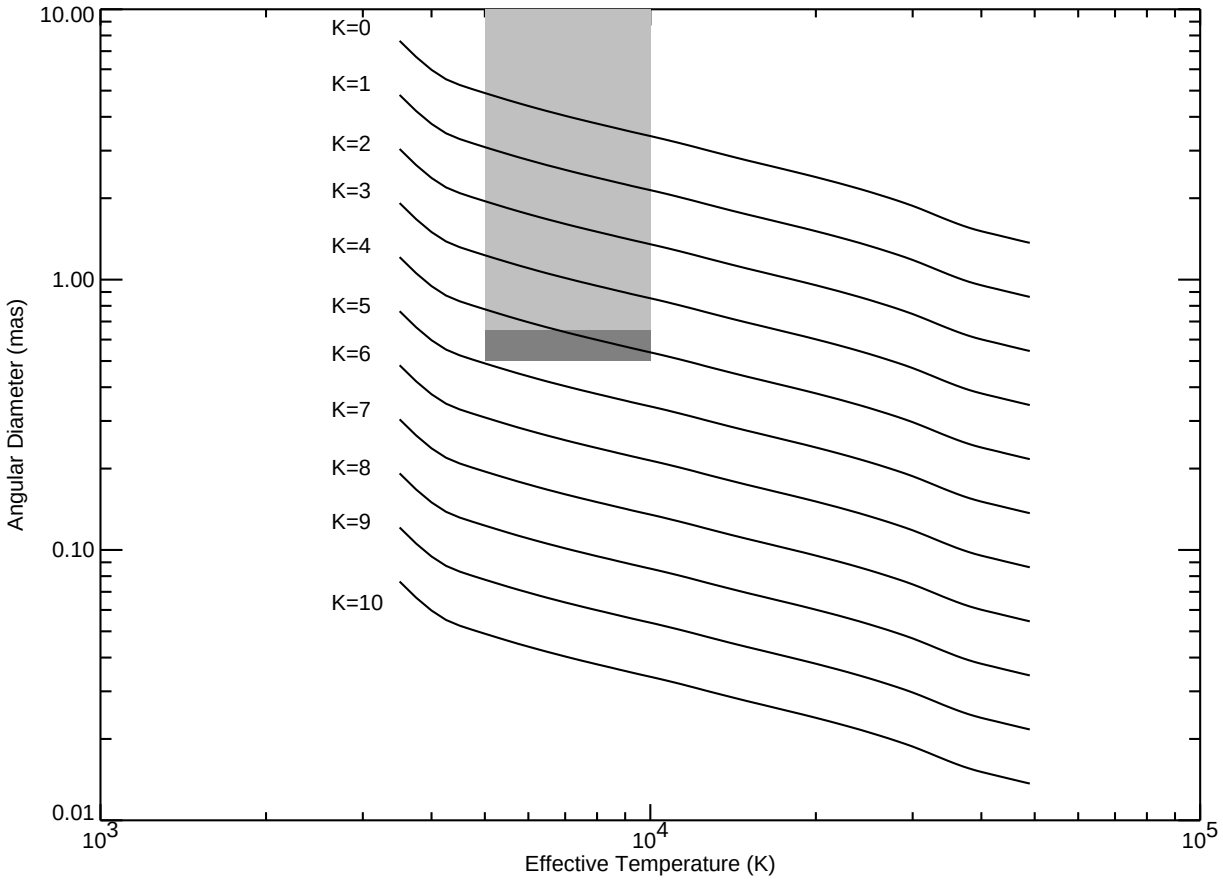

FIGURE 2.2: **Angular Diameter as a Function of Temperature and Magnitude:** The relationship between a star's angular diameter as a function of effective temperature and observed K magnitude. The shaded region indicates the observable region for an approximate temperature range of this survey (5−10 kK), with an angular diameter cutoff of 0.5 mas (H-band; dark gray) and 0.65 mas (K'-band; light gray).

HIPPARCOS Catalogue was queried through the online VizieR Service[2] with the constraints listed in Table 2.1. A total of 132 possible targets resulted in the initial query.

Next, each of these stars was individually scrutinized to find all relevant information that would prejudice good diameter measurements. For instance, each object was checked for entries in *The* 9^{th} *Catalogue of Spectroscopic Binary Orbits*[3] (SB9) and the *Washington Double Star Catalogue*[4] (WDS) to determine whether or not it was a known binary. The primary object was rejected if it harbored a companion with a separation ρ of less than 2

[2]http://vizier.u-strasbg.fr/viz-bin/VizieR
[3]http://sb9.astro.ulb.ac.be/
[4]http://ad.usno.navy.mil/wds/

arcsec (with the exception of μ Cas, $\rho = 1.3$ arcsec). The primary object was flagged if the companion was 2−5 arcsec away. In this range, light from the secondary may contaminate the visibility measurements of the primary star, and/or make it hard for the telescope's tip/tilt system to lock on the star. Detailed work was done in Boyajian et al. (2008) for the observations of μ Cas A to determine the contribution of light the secondary star contributes within our detector's field-of-view (See Appendix D). In summary, the amount of contributing light from the secondary has to do with the system separation, delta magnitude, and the seeing conditions at the time of observation.

A reference search for each target was also undertaken to determine if there were any extraordinary characteristics that could potentially hinder the accurate determination of the star's diameter measurement. These objects were also flagged. This includes stars with spots, pulsating stars, and rapid rotators. The status of the duplicity of each star was also checked for completeness and accuracy in the above mentioned catalogues in this reference search. This is mostly relevant in the SB9 Catalogue, whereas the WDS is updated daily.

Along with the reference search, stars with previously determined diameters via interferometry were removed from the sample that I will observe for this project[5]. Until very recently, main sequence stars in this range were unresolved, so very few fall into this category. However, the angular diameters of seven stars from Baines et al. (2008), who used the CHARA Array to measure the diameters of exoplanet host stars, fall within my sample criteria presented here and are eliminated from my sample in order not to be redundant.

[5]For results prior to 2004, these entries are found in the CHARM2 Catalogue: *An Updated Catalog of High Angular Resolution Measurements*[6] (Richichi et al. 2005).

These final candidates for the observing sample were sorted one last time. In order to estimate better angular sizes than ones merely defined by an estimated linear radius and distance to the star, I performed a fit of observed photometry to a model spectral energy distribution (SED). Information from this task also gives us a way to determine estimates of effective temperature, $T_{\rm EFF}$, and surface gravity, $\log g$, which are then used to determine the limb darkening coefficients μ_λ used in the final diameter fits to the data (Claret et al. 1995). When available, the magnitudes (Johnson UBV, Johnson et al. 1966; Strömgren $uvby$, Hauck & Mermilliod 1998; 2MASS JHK, Skrutskie et al. 2006) for each star were collected and then transformed into calibrated flux measurements using the methods described in Colina et al. (1996), Gray (1998), and Cohen et al. (2003). We then fitted a model SED[7] to the observed flux-calibrated photometry to determine the angular diameters $\theta_{\rm SED}$ for these stars. If the star has an observed infrared excess compared to the model, it was rejected because the presence of a companion is likely. A handful of stars also proved to be too small to be adequately resolved and were rejected as well. This unfortunate circumstance arose when we discovered that more often than not, the 2MASS JHK magnitudes had very large (>10%) errors due to saturation (usually occurring around $K = +4$ mag). In these cases, the fit was preformed with all data, and for any of the points with large errors that did not fit the SED for the star, the data in question were removed and the fit redone.

The resulting sample size for the survey came to 77 stars, 13 of them flagged for reasons stated in the above paragraphs. Table 2.2 shows a list of the full sample names, coordinates, and spectral types. Table 2.3 shows the list of the magnitudes and *HIPPARCOS* parallaxes in

[7]The model fluxes were interpolated from the grid of models from R. L. Kurucz available at http://kurucz.cfa.harvard.edu/

the final full sample, and Figure 2.3 plots these stars in a color-absolute magnitude diagram. The stars in Figure 2.3 range from spectral types A0V−K0V, and there is a nice intrinsic spread in the main sequence due to the evolutionary state of the stars within the band of the main sequence. The SED fit for each star can be found in Appendix A.

2.2.1 *RECONS* Stars

The *RECONS* project[8] is aimed at acquiring information about nearby stars, with particular emphasis on stars within 10 parsecs of the Sun. Given the selection criteria in this survey, all main sequence A, F, and G stars within 10 parsecs, and above -10° declination will now be observed with interferometry. Prior to this survey, Vega, Sirius, Altair, and Procyon were the only *RECONS* stars studied with interferometry (Aufdenberg et al. 2006; Kervella et al. 2003; Domiciano de Souza et al. 2005; Kervella et al. 2004b). In this survey, I will add an additional twelve stars, which will triple the number of *RECONS* stars with interferometric observations to date. All twelve stars have spectral types later than Procyon (F5IV-V, the latest spectral type of the above four mentioned), ranging from F6V−K0V. This leaves only four A, F and G *RECONS* stars (HD 98230, HD 98231, HD 161797, and HD 170153) in the northern hemisphere that will not be observed in this survey, due to their duplicity.

[8]http://www.recons.org

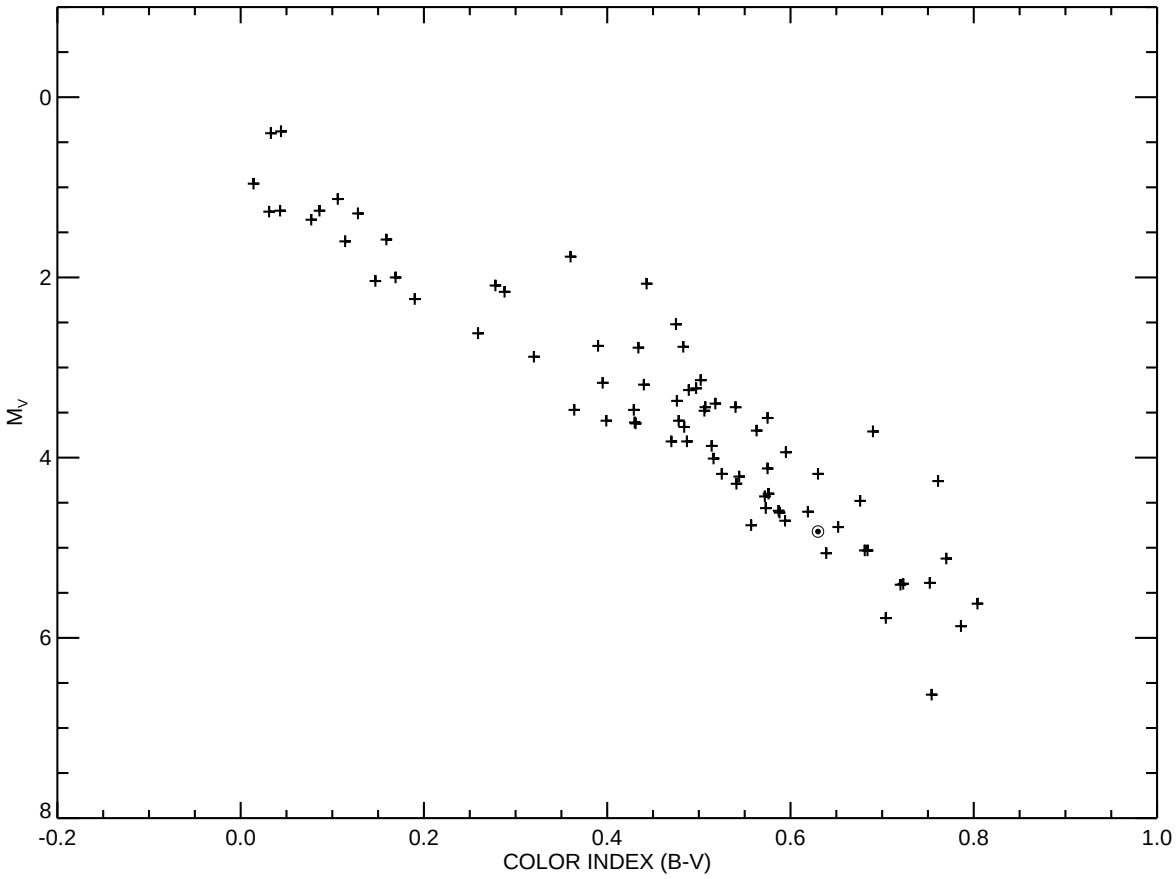

FIGURE 2.3: **Color Magnitude Diagram of Sample:** This is a Color-Magnitude plot of the data in Table 2.3, showing the full sample selected for the CHARA observational program to determine angular diameters.

TABLE 2.1: Sample Criteria for *HIPPARCOS* Catalogue Querry†

Spectral Type	V **(mag)**	$(B-V)$ **(mag)**	π **(mas)**	**Distance (pc)**	**# of stars**
A0V-A5V	<6.0	−0.02-0.15	>30	<33	11
A6V-F0V	<6.4	0.15-0.30	>34	<29	6
F1V-F5V	<6.7	0.30-0.44	>41	<25	11
F6V-G0V	<7.0	0.44-0.58	>47.6	<21	27
G1V-G5V	<7.3	0.58-0.68	>58.8	<17	9
G6V-K0V	<7.5	0.68-0.81	>62.5	<16	13

† Declination north of −10°.

TABLE 2.2: The Sample of A, F, and G Dwarfs

HD	**HR**	**HIP**	**Other Name**[a]	**RA (hh mm ss.xx)**	**DEC (dd mm ss)**	**Spectral Type**[b]	**Spectral Type**[c]
166	8	544	GJ 5	00 06 36.78	29 01 17.41	G8V	K0V
4614	219	3821	24 η Cas A	00 49 06.29	57 48 54.67	F9V	G0V
5015	244	4151	GJ 41	00 53 04.20	61 07 26.29	F8V	F8V
6582	321	5336	34 μ Cas A	01 08 16.39	54 55 13.22	G5Vb	G5Vp
10780	511	8362	GJ 75	01 47 44.84	63 51 09.00	G9V	K0V
16895	799	12777	13 θ Per A	02 44 11.99	49 13 42.41	F7V	F7V
19373	937	14632	ι Per	03 09 04.02	49 36 47.80	G0IV-V	G0V
20630	996	15457	κ Cet	03 19 21.70	03 22 12.71	G5V	G5Vvar
22484	1101	16852	10 Tau	03 36 52.38	00 24 05.98	F9IV-V	F9V
25457	1249	18859	GJ 159	04 02 36.75	−00 16 08.12	F7V	F5V
27045	1329	19990	50 ω Tau	04 17 15.66	20 34 42.93	···	A3m
30652	1543	22449	1 π^3 Ori	04 49 50.41	06 57 40.59	F6IV-V	F6V
34411	1729	24813	15 λ Aur	05 19 08.47	40 05 56.59	G1V	G0V
33564	1686	25110	GJ 196	05 22 33.53	79 13 52.14	F7V	F6V
35296	1780	25278	111 Tau	05 24 25.46	17 23 00.72	F8V	F8V
38858	2007	27435	GJ 1085	05 48 34.94	−04 05 40.73	G2V	G4V
39587	2047	27913	54 χ^1 Ori	05 54 22.98	20 16 34.23	G0IV-V	G0V
43042	2220	29650	71 Ori	06 14 50.88	19 09 23.21	F5.5IV-V	F6V
43386	2241	29800	74 k Ori	06 16 26.62	12 16 19.79	F5V	F5IV-V
48737	2484	32362	31 ξ Gem	06 45 17.37	12 53 44.13	F5IV-V	F5IV
46588	2401	32439	23 H Cam	06 46 14.15	79 33 53.32	F8V	F8V
48682	2483	32480	56 ψ^5 Aur	06 46 44.34	43 34 38.74	F9V	G0V
50692	2569	33277	37 Gem	06 55 18.67	25 22 32.51	G0V	G0V
55575	2721	35136	GJ 1095	07 15 50.14	47 14 23.87	F9V	G0V
56537	2763	35350	54 λ Gem	07 18 05.58	16 32 25.38	···	A3V
58946	2852	36366	62 ρ Gem	07 29 06.72	31 47 04.38	···	F6V
58855	2849	36439	22 Lyn	07 29 55.96	49 40 20.87	F6V	F6V
69897	3262	40843	18 χ Cnc	08 20 03.86	27 13 03.74	F6V	F6V
78209	3619	44901	15 f UMa	09 08 52.26	51 36 16.73	···	A1m
78154	3616	45038	13 σ^2 UMa	09 10 23.55	67 08 02.46	···	F7IV-V
81937	3757	46733	23 h UMa	09 31 31.71	63 03 42.70	···	F0IV
82328	3775	46853	25 θ UMa	09 32 51.43	51 40 38.28	F5.5IV-V	F6IV
82885	3815	47080	11 LMi	09 35 39.50	35 48 36.48	G8+V	G8IV-V
86728	3951	49081	20 LMi	10 01 00.66	31 55 25.22	G4V	G3V
87696	3974	49593	21 LMi	10 07 25.76	35 14 40.90	A7V(n)	A7V
90839	4112	51459	36 UMa	10 30 37.58	55 58 49.93	F8V	F8V
90089	4084	51502	GJ 9330	10 31 04.66	82 33 30.92	F4V	F2V
95418	4295	53910	48 β UMa	11 01 50.48	56 22 56.74	A1IV	A1V
97603	4357	54872	68 δ Leo	11 14 06.50	20 31 25.38	A5IV(n)	A4V

Continued on Next Page...

TABLE 2.2 – Continued

HD	HR	HIP	Other Name[a]	RA (hh mm ss.xx)	DEC (dd mm ss)	Spectral Type[b]	Spectral Type[c]
101501	4496	56997	61 UMa	11 41 03.02	34 12 05.89	G8V	G8V
102870	4540	57757	5 β Vir	11 50 41.72	01 45 52.98	F8.5IV-V	F8V
103095	4550	57939	CF UMa	11 52 58.77	37 43 07.24	K1V	G8Vp
103287	4554	58001	64 γ UMa	11 53 49.85	53 41 41.14	A1IV(n)	A0V
106591	4660	59774	69 δ UMa	12 15 25.56	57 01 57.42	A2Vn	A3V
109358	4785	61317	8 β CVn	12 33 44.55	41 21 26.93	G0V	G0V
110897	4845	62207	10 CVn	12 44 59.41	39 16 44.10	F9V	G0V
114710	4983	64394	43 β Com	13 11 52.39	27 52 41.46	G0V	G0V
116842	5062	65477	80 g UMa	13 25 13.54	54 59 16.65	A6Vnn	A5V
118098	5107	66249	79 ζ Vir	13 34 41.59	−00 35 44.95	A2Van	A3V
126660	5404	70497	23 θ Boo	14 25 11.80	51 51 02.68	F7V	F7V
126868	5409	70755	105 ϕ Vir	14 28 12.14	−02 13 40.65	G2IV	G2IV
128167	5447	71284	28 σ Boo	14 34 40.82	29 44 42.47	F4VkF2mF1	F3V
131156	5544	72659	37 ξ Boo	14 51 23.38	19 06 01.66	G7V	G8V
134083	5634	73996	45 c Boo	15 07 18.07	24 52 09.10	F5V	F5V
140538	5853	77052	23 ψ Ser	15 44 01.82	02 30 54.62	G5V	G5V
141795	5892	77622	37 ϵ Ser	15 50 48.97	04 28 39.83	kA2hA5mA7V	A2m
142860	5933	78072	41 γ Ser	15 56 27.18	15 39 41.82	F6V	F6V
146233	6060	79672	18 Sco	16 15 37.27	−08 22 09.99	G2V	G1V
157214	6458	84862	72 w Her	17 20 39.57	32 28 03.88	G0V	G0V
162003	6636	86614	31 ψ Dra	17 41 56.36	72 08 55.84	F5IV-V	F5IV-V
161868	6629	87108	62 γ Oph	17 47 53.56	02 42 26.19	A1VnkA0mA0	A0V
164259	6710	88175	57 ζ Ser	18 00 29.01	−03 41 24.97	F2V	F3V
165777	6771	88771	72 Oph	18 07 20.98	09 33 49.85	A5V	A4IVs
168151	6850	89348	36 Dra	18 13 53.83	64 23 50.23	···	F5V
173667	7061	92043	110 Her	18 45 39.73	20 32 46.71	F5.5IV-V	F6V
177724	7235	93747	17 ζ Aql	19 05 24.61	13 51 48.52	A0IV-Vnn	A0Vn
182572	7373	95447	31 b Aql	19 24 58.20	11 56 39.90	···	G8IV
185144	7462	96100	61 σ Dra	19 32 21.59	69 39 40.23	G9V	K0V
185395	7469	96441	13 θ Cyg	19 36 26.54	50 13 15.97	F3+V	F4V
187013	7534	97295	17 Cyg	19 46 25.60	33 43 39.35	F5.5IV-V	F7V
187691	7560	97675	54 Aql	19 51 01.64	10 24 56.62	F8V	F8V
195564	7845	101345	GJ 792.1 A	20 32 23.70	−09 51 12.20	G2V	G2.5IV
210418	8450	109427	26 θ Peg	22 10 11.99	06 11 52.31	···	A2V
211336	8494	109857	23 ϵ Cep	22 15 02.19	57 02 36.91	···	F0IV
213558	8585	111169	7 α Lac	22 31 17.50	50 16 56.97	···	A1V
215648	8665	112447	46 ξ Peg	22 46 41.58	12 10 22.40	F6V	F7V
222368	8969	116771	17 ι Psc	23 39 57.04	05 37 34.65	F7V	F7V

Notes: a) Bayer-Flamsteed or GJ (Kostjuk 2004), b) Gray et al. (2001, 2003), c) *SIMBAD* (Wenger et al. 2000).

TABLE 2.3: Magnitudes and Colors of the Sample

HD	V (mag)	K (mag)	$(B-V)$ (mag)	π (mas)	$\sigma(\pi)$ (mas)	M_V (mag)
166	6.07	4.31	0.752	73.16	0.56	5.39
4614	3.46	1.99	0.587	168.01	0.48	4.59
5015	4.80	3.64	0.540	53.35	0.33	3.44
6582	5.17	3.51	0.704	132.40	0.60	5.78
10780	5.63	4.01	0.804	99.34	0.53	5.62
16895	4.10	2.70	0.514	89.88	0.23	3.87
19373	4.05	2.72	0.595	94.87	0.23	3.94
20630	4.84	2.96	0.681	109.39	0.27	5.03
22484	4.29	2.84	0.575	71.60	0.54	3.56
25457	5.38	4.18	0.516	53.09	0.32	4.01

Continued on Next Page...

TABLE 2.3 – Continued

HD	V (mag)	K (mag)	$(B-V)$ (mag)	π (mas)	$\sigma(\pi)$ (mas)	M_V (mag)
27045	4.93	4.36	0.259	34.55	0.38	2.62
30652	3.19	1.60	0.484	123.94	0.17	3.66
33564	5.08	3.91	0.506	47.88	0.21	3.48
34411	4.69	3.04	0.630	79.18	0.28	4.18
35296	5.00	4.04	0.544	69.50	0.38	4.21
38858	5.97	4.41	0.639	65.90	0.41	5.06
39587	4.39	3.00	0.594	115.42	0.27	4.70
43042	5.20	4.13	0.430	48.06	0.34	3.61
43386	5.04	4.25	0.431	51.98	0.27	3.62
46588	5.44	4.14	0.525	55.95	0.27	4.18
48682	5.24	4.13	0.575	59.82	0.30	4.12
48737	3.35	1.69	0.443	55.55	0.19	2.07
50692	5.74	4.29	0.573	58.02	0.41	4.56
55575	5.54	4.12	0.576	59.21	0.33	4.40
56537	3.58	3.54	0.106	32.36	0.22	1.13
58855	5.35	4.18	0.470	49.41	0.36	3.82
58946	4.16	2.98	0.320	55.41	0.25	2.88
69897	5.13	3.87	0.487	54.73	0.32	3.82
78154	4.80	3.56	0.489	49.07	0.37	3.25
78209	4.46	4.04	0.288	34.70	0.25	2.16
81937	3.65	2.86	0.360	41.99	0.16	1.77
82328	3.17	1.97	0.475	74.18	0.13	2.52
82885	5.40	3.69	0.770	87.96	0.32	5.12
86728	5.37	3.82	0.676	66.47	0.32	4.48
87696	4.49	4.00	0.190	35.41	0.18	2.24
90089	5.25	4.27	0.399	46.51	1.40	3.59
90839	4.82	3.64	0.541	78.26	0.29	4.29
95418	2.34	2.29	0.033	40.89	0.16	0.40
97603	2.56	2.14	0.128	55.82	0.25	1.29
101501	5.31	3.59	0.723	104.03	0.26	5.40
102870	3.59	2.27	0.518	91.50	0.22	3.40
103095	6.42	4.37	0.754	109.98	0.41	6.63
103287	2.41	2.43	0.044	39.20	0.40	0.38
106591	3.32	3.10	0.077	40.50	0.14	1.36
109358	4.24	2.85	0.588	118.49	0.20	4.61
110897	5.95	4.47	0.557	57.55	0.32	4.75
114710	4.23	2.92	0.572	109.53	0.17	4.43
116842	3.99	3.15	0.169	39.91	0.14	2.00
118098	3.38	3.22	0.114	44.01	0.19	1.60
126660	4.04	2.74	0.497	68.83	0.14	3.23
126868	4.84	3.07	0.693	27.58	1.01	2.05
128167	4.47	3.34	0.364	63.16	0.26	3.47
131156	4.54	1.97	0.720	149.03	0.48	5.41
134083	4.93	3.86	0.429	51.14	0.31	3.47
140538	5.86	4.30	0.684	68.21	0.66	5.03
141795	3.71	3.43	0.147	46.28	0.19	2.04
142860	3.85	2.70	0.478	88.85	0.18	3.59
146233	5.49	4.19	0.652	71.93	0.37	4.77
157214	5.38	3.91	0.619	69.80	0.25	4.60

Continued on Next Page...

TABLE 2.3 – Continued

HD	V (mag)	K (mag)	$(B-V)$ (mag)	π (mas)	$\sigma(\pi)$ (mas)	M_V (mag)
161868	3.75	3.62	0.043	31.73	0.21	1.26
162003	4.57	3.50	0.434	43.79	0.45	2.78
164259	4.62	3.64	0.390	42.44	0.33	2.76
165777	3.71	3.41	0.159	37.56	0.22	1.58
168151	4.99	3.94	0.440	43.63	0.17	3.19
173667	4.19	3.19	0.483	52.06	0.24	2.77
177724	2.99	2.88	0.014	39.27	0.17	0.96
182572	5.17	3.04	0.761	65.89	0.26	4.26
185144	4.67	2.90	0.786	173.77	0.18	5.87
185395	4.49	3.54	0.395	54.55	0.15	3.17
187013	5.00	3.83	0.476	47.11	0.26	3.37
187691	5.12	3.90	0.563	52.11	0.29	3.70
195564	5.65	4.00	0.690	40.98	0.33	3.71
210418	3.52	3.38	0.086	35.34	0.85	1.26
211336	4.18	3.54	0.278	38.17	0.97	2.09
213558	3.76	3.85	0.031	31.80	0.12	1.27
215648	4.20	2.96	0.502	61.37	0.20	3.14
222368	4.13	2.95	0.507	72.91	0.15	3.44

– 3 –

Interferometric Calibrators

3.1 The Calibrator

3.1.1 Calibrator Selection

I used the web interface of getCal[1] for the preliminary calibrator search. This tool allows you to search for objects around your science star. It has many handy additional features such as limiting the luminosity classes or maximum angular diameters of the stars in the output.

Very basic selection guidelines to find near-perfect calibrators (as the perfect calibrator is impossible to find) are as follows: they must be close to your target, normal (single stars with very boring atmospheric properties), and close to unresolved in angular diameter. Because the goal of this project is to determine very accurate, indisputable angular diameters, I paid very close attention to calibrator selection and often observed an object with more than one calibrator to ensure that the results on the science star were calibrated correctly. Details of this can be found later in this chapter in the section on Observing Techniques.

Identifying calibrator stars that are close to your science target has many justifications. A good rule of thumb is to have the calibrator $< 10^{\circ}$ from the science target. This allows for quick transitions from calibrator to object and back to calibrator. Additionally, the effects from astronomical seeing change over time during the night, and could also vary greatly

[1] http://nexsciweb.ipac.caltech.edu/gcWeb/gcWeb.jsp

depending on what part of the sky you are observing your objects. A long lapse of time between observations of the calibrator and object may ruin the data calibration.

A second quality that we must have in the calibrator star is that it is normal, which is a very tough characteristic to find in stellar astronomy. Fortunately, much work has been done on the nearby bright stars (the ones we typically observe with LBOI), and the online catalogues are fairly up-to-date, so there are not many surprises from a star that appears to be normal but ends up not normal at all. I classify a normal star to be one that is not rotationally distorted, pulsating, or spotty. The normal calibrator star must also be single or have a companion with separation no less than 10 arcsec. This is to ensure that the companion does not contaminate the data collected, and that the measured visibilities will only be from the light of the primary star. Additionally, this separation limit will ensure us that the photometry collected for the SED fit to determine the calibrator's angular diameter is only detected from the primary star.

The final requirement in selecting a good calibrator is that it must be unresolved at the baselines that we are observing. The uncertainty in the calibrator star's angular diameter propagates through in the final data calibration. If the calibrator is very unresolved, there is much less influence of the error of the estimated angular diameter with the calibration of the data. This is discussed in more detail in the paragraphs to follow.

Typically, the output of getCal yields dozens of calibrators, depending on the selection criteria set by the user. Each star in the output must then be double checked for its goodness as a calibrator, taking into consideration the topics listed above. Table 3.1 lists the calibrators used in the thesis giving their right ascension RA, declination DEC, V and K magnitudes, and the relevant science object(s) it was observed with for this project. SED fits were

preformed on each of these calibrators to estimate their angular diameters in the same manner as the object SED fits (discussed in the previous chapter). Table 3.2 shows the calibrator HD number, effective temperature $T_{\rm EFF}$, gravity $\log g$, and SED diameters $\theta_{\rm SED}$ of the calibrator stars used in this work. The last column shows which targets were observed using each calibrator. Appendix B shows the plots of the SED fits for these calibrators.

3.2 Calibrating Interferometric Data

Observations made with the CHARA Array, like all other optical interferometers, need to be calibrated to convert the data we record (the instrumental Visibility, or (V_i)) into the true Visibility (V_t). The V_i is affected by several components of either the instrument and/or the observing conditions, which we assume to know very well, and we also assume to be somewhat stable and linear with time.

In order to calibrate the data we take on an object, we make observations in a sequence bracketed with observations of a calibrator star. For example, to record one bracket, the sequence Calibrator−Object− Calibrator is performed, where V_i is recorded for both the calibrator's observations ($V_{i,\rm C}$), and the object's ($V_{i,\rm O}$). Calibration of interferometric data then uses the relation to find the true Visibility of the object ($V_{t,\rm O}$):

$$V_{t,\rm O} = V_{t,\rm C} \times \frac{V_{i,\rm O}}{V_{i,\rm C}} \tag{3.1}$$

The angular diameter of the calibrator star is needed to calculate the true visibility of the calibrator $V_{t,\rm C}$. We derive the angular diameter of the calibrator star by fitting flux-calibrated broad-band photometric observations to a Kurucz model spectral energy distribution (SED)

(see Table 3.2 and Appendix B). This method is much more precise than the simple technique of estimating the linear diameter of a calibrator star based on its spectral type, and converting this linear diameter to an angular diameter by applying the tiny triangle formula ($\theta_{\mathrm{Sp.Ty.}}$ = diameter/distance).

Thus, once we have the estimated angular diameter of the calibrator star θ_{SED}, the true visibility of the calibrator star $V_{t,\mathrm{C}}$ at the time of observations is determined by evaluating the Bessel Function J_1 for the θ_{SED} of the calibrator star (evaluated at the central wavelength of $\lambda = 2.15$ μm and the baseline at the time the object observation was made B):

$$V = \frac{2J_1(\pi B\theta_{\mathrm{SED}}\lambda^{-1})}{\pi B\theta_{\mathrm{SED}}\lambda^{-1}} \tag{3.2}$$

Afterwards, we perform a linear interpolation of the calibrator's visibilities to the times of the object observations, and solve Equation 3.1 above to get $V_{t,\mathrm{O}}$.

The errors in the final true visibility of the object are then a combination of the instrumental errors in the object and calibrator visibilities, as well as the uncertainty in the calibrator's true visibility (arising from the error in the estimated θ_{SED} of the calibrator star). Adding each of these errors in quadrature, we use the formula (derived from Equation 3.1) to get the calibrated visibility errors for the object $\delta V_{t,\mathrm{O}}$:

$$\delta V_{t,\mathrm{O}} = \sqrt{\left(\frac{V_{i,\mathrm{O}}}{V_{i,\mathrm{C}}}\delta V_{t,\mathrm{C}}\right)^2 + \left(\frac{V_{t,\mathrm{O}}V_{i,\mathrm{O}}}{V_{i,\mathrm{C}}^2}\delta V_{i,\mathrm{C}}\right)^2 + \left(\frac{V_{t,\mathrm{C}}}{V_{i,\mathrm{C}}}\delta V_{i,\mathrm{O}}\right)^2} \tag{3.3}$$

From simple inspection of the equations above, we can see that the largest error is that propagated from the uncertainty of the calibrator's estimated diameter. The effect of the uncertainty of a calibrator's diameter increases the more resolved (closer to zero visibility)

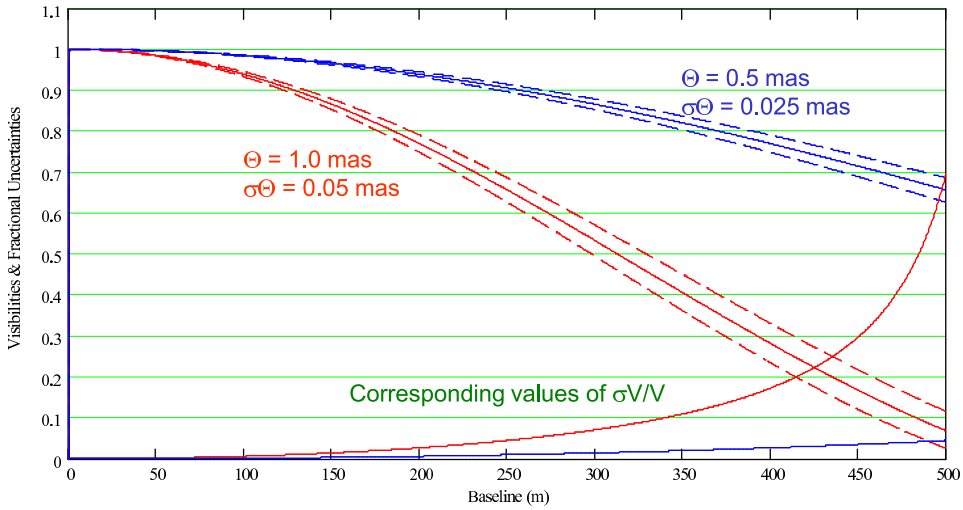

FIGURE 3.1: **The Calibrator's Diameter:** The effect on the errors of a calibrator's estimated diameter depend on its angular size. Seen here are visibility curves of two stars, one with a diameter of $\theta = 1.0$ mas and the other with $\theta = 0.5$ mas. With the same percentage uncertainty in the estimated diameter (5%), the error propagated (σ V/V) for the star of the smaller diameter is much smaller. Plot courtesy of H. A. McAlister.

it is during observations. Figure 3.1 shows a graphical representation of this effect for two hypothetical stars of different sizes. At long baselines, where the $\theta = 1.0$ mas star starts to become resolved, the corresponding values of σV/V start to rise much quicker than that for the smaller star which is still moderately unresolved at these baselines. If the calibrator is small enough, even a 100% error on the diameter does not yield noticeable effects at CHARA's baselines.

3.3 Observing Techniques

Many of the following sections describing observing techniques are typically topics for which the observer has a pre-chosen preference. However, each of these points has never been formally tested at the CHARA Array. Here, I show limits of several observing techniques and, in turn, how successful the data calibration process is with each method. This results in what should be referred to as "Tabby's *bona fide* observing techniques ".

3.3.1 When Is a Good Time to Align NIRO?

The NIRO (**N**ear **I**nfra**R**ed **O**bserver) camera alignment is very important when it comes to calibrating interferometric visibilities. The input optics into the NIRO camera must allow for the light to fall on the center of the chip for data to be collected (in either 1×1 or 2×2 pixel arrays). Slight changes over time as an object moves across the sky during a short amount of time can offset the alignment of the system. For example, Figure 3.2 and Figure 3.3 show a sequence of bracketed observations for HD 215648 and a calibrator, HD 214923 (2007-07-21), taken over the course of approximately 2.5 hours. In Figure 3.2, one can see that just before 1.5 hours have passed, the system alignment starts to degrade, although the object and calibrator visibilities are still tracking one another. This sudden drop in the measured instrumental visibility for each is significant enough to show two effects in the object's calibrated visibilities: (1) the visibility errors become increasingly larger, and (2) the calibrated visibility measurements fit to a single star visibility function show larger residuals (demonstrated in Figure 3.3, at baselines < 300 meters).

NIRO alignment should not be done in the middle of a bracket, for the simple reason that it is an adjustment to the system, and calibration can be offset. The observer should complete the bracket, perform the alignment, then start a new bracket after the alignment is complete.

3.3.2 Classic Observing: 1×1 Versus 2×2 Pixels

The light collecting area on the NIRO camera chip can be set to 1×1 or 2×2 pixels. During the start of my observing days with CHARA Classic, it was taught to be a good rule of thumb to observe with 2×2 pixels. In preparation for H-band observations (which need to

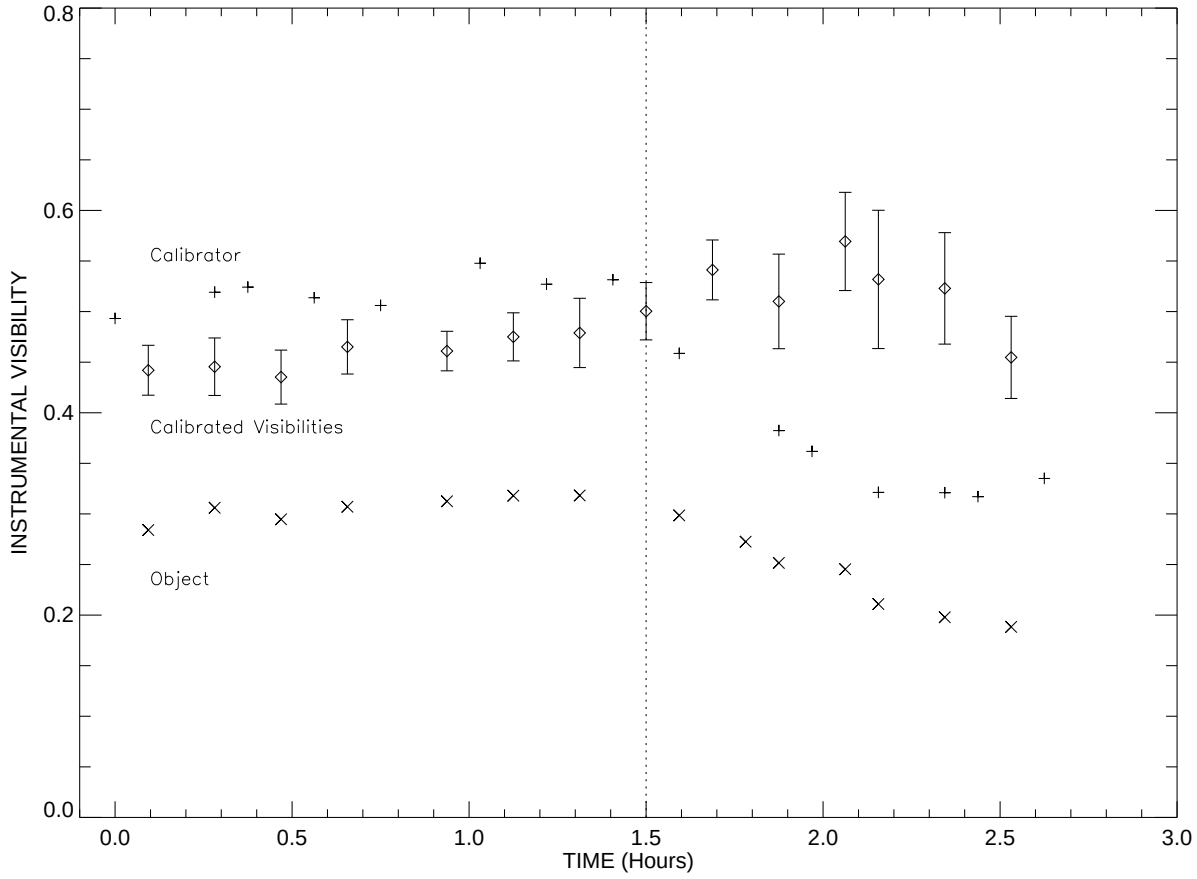

FIGURE 3.2: **Bad NIRO Alignment Effects:** Data for HD 215648 and its calibrator taken on 2007-07-21. Instrumental visibilities for the calibrator (*plusses*), object (*crosses*), and the object's calibrated visibilities (*diamonds*) and 1-σ errors are shown with respect to time. The *dotted* line marks a time where NIRO should have been realigned.

be done in 1×1)[2], I decided to perform a test of the calibration of the data made with the different pixel array sizes, mainly to see how poor seeing will affect the data quality on 2×2 pixel observing.

On 2007-11-16, I observed 5 brackets of HD 90839 (with the calibrator HD 89389) in both 2×2 and 1×1 pixel arrays. Figure 3.4 shows the results of the test with data calibration, and Figure 3.5 shows the resulting diameter fit with data taken in each observing mode. Two things are learned from this test. The first is that the errors are smaller by a modest amount

[2]The readout mode for H band is different than in K band, and saturation is an issue. If the camera is set to read out in 2×2 pixel arrays, saturation can occur on one pixel at a time during the scan, making data reduction hopeless.

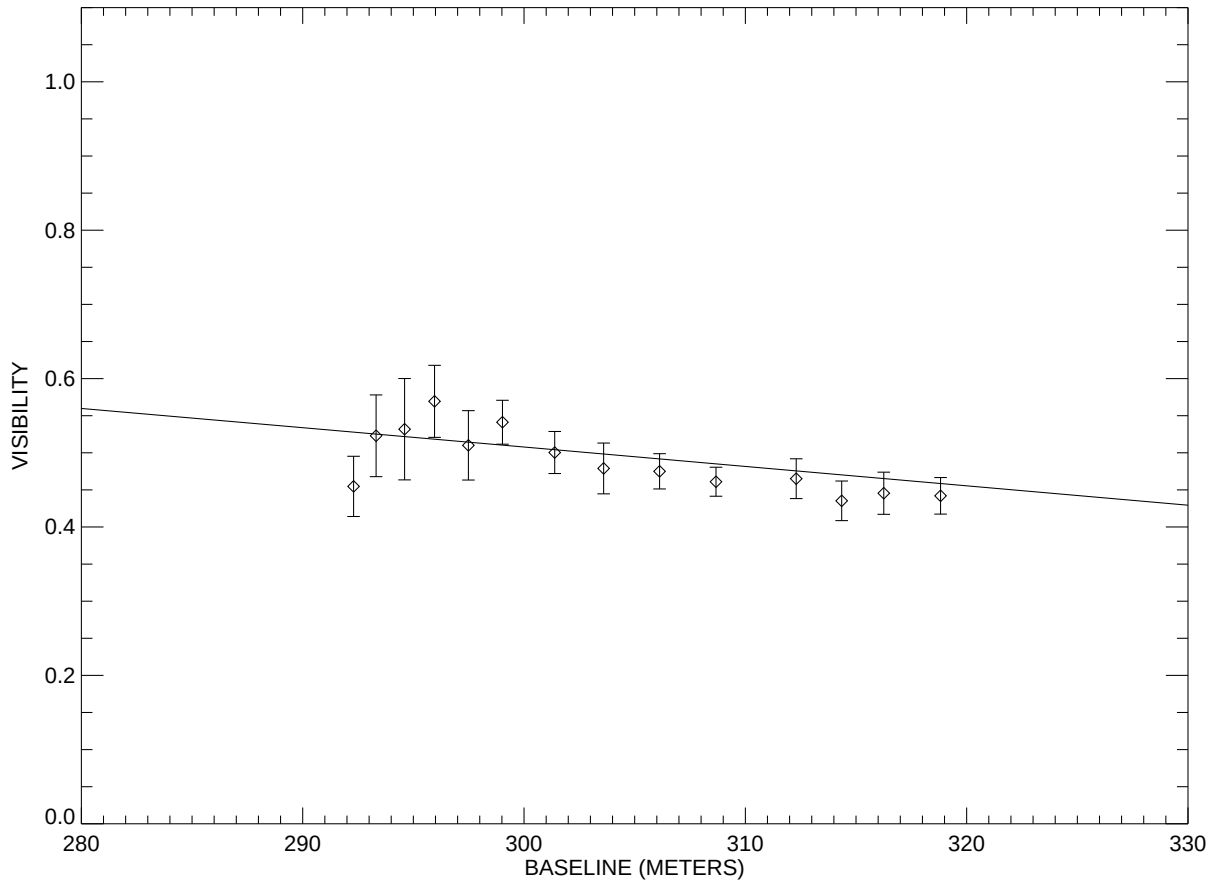

FIGURE 3.3: **Bad NIRO Alignment Effects:** Limb darkened diameter fit to the calibrated visibilities of HD 215648 taken on 2007-07-21. In this case, Time= 0 in Figure 3.2 represents the points at the longest projected baseline shown here. Data obtained with baselines shorter than 300 meters are those where NIRO re-alignment should have been done (after 1.5 hours of observing, Figure 3.2).

when observing with a 1×1 pixel array. The second is that the measured visibilities, and therefore the calibrated visibilities, are much more stable and have much less scatter in the diameter fit while observing with a 1×1 pixel array. Because of these results, it is thought that when the chip is set to read out in a 1×1 pixel array, it acts like a spatial filter.

3.3.3 Night-to-Night Repeatability

The previous section shows the greatly improved stability in the measured visibilities for HD 90839 when observing with 1×1 pixels. An additional test was performed to investigate the night-to-night repeatability of the calibrated visibilities in 1×1 observing mode. Fig-

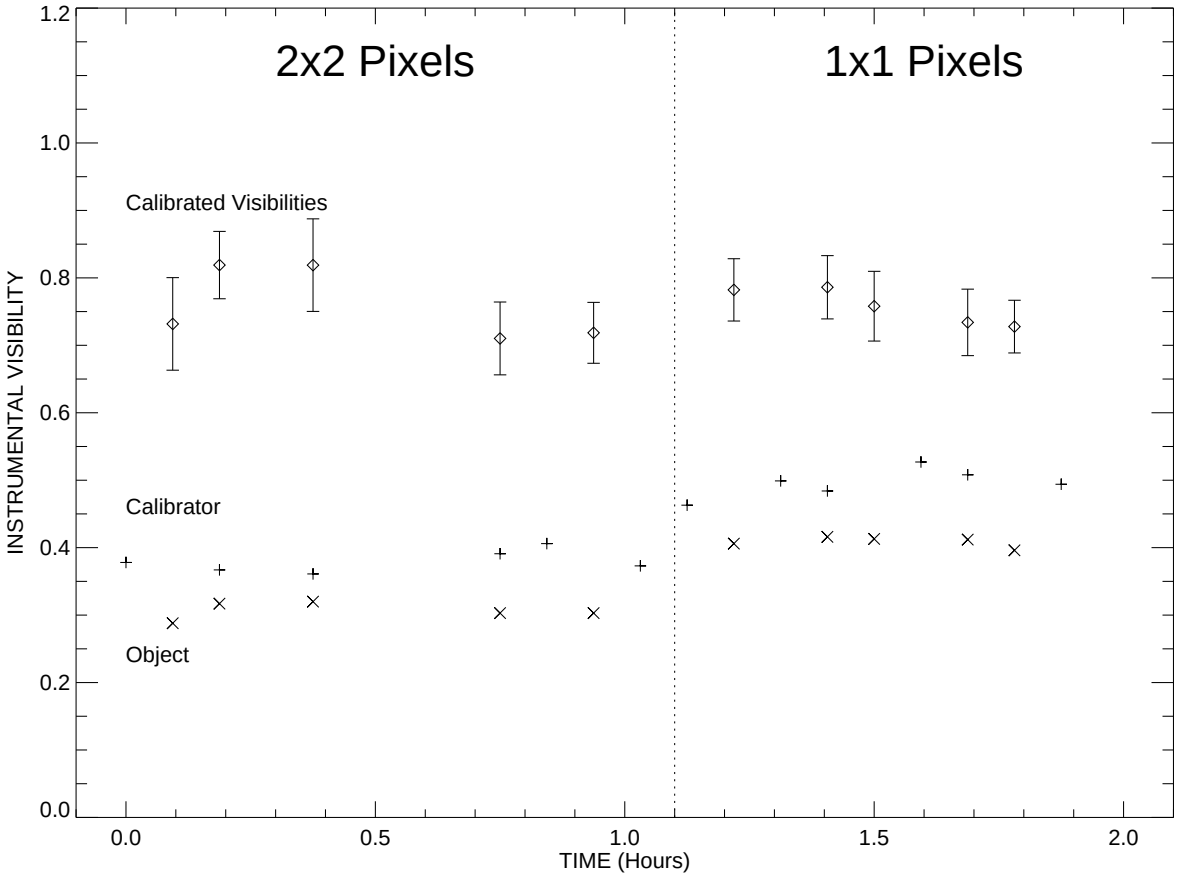

FIGURE 3.4: **NIRO 1×1 Versus 2×2 Pixels:** Data for HD 90839 and its calibrator taken on 2007-11-16. Instrumental visibilities for the calibrator (*plusses*), object (*crosses*), and the objects calibrated visibilities (*diamonds*) are shown with respect to time. The *dotted* line marks the time when NIRO was changed to collect data in 1×1 mode.

ure 3.6 and Figure 3.7 show calibrated visibilities and the resulting diameter fit for HD 103095 taken on 2007-11-16 and 2007-12-24. In comparing the raw, instrumental visibilities of the calibrator and the object in Figure 3.6, we can see that they are offset by about 0.1 in the raw insturmental visibility from the November to the December observations. This offset in the raw visibilities is not a concern (rather expected), and is only an effect of the observing conditions. The results in the night-to-night repeatability are actually seen in Figure 3.7. Here, the values of the object's calibrated visibilities for each night agree exceptionally well

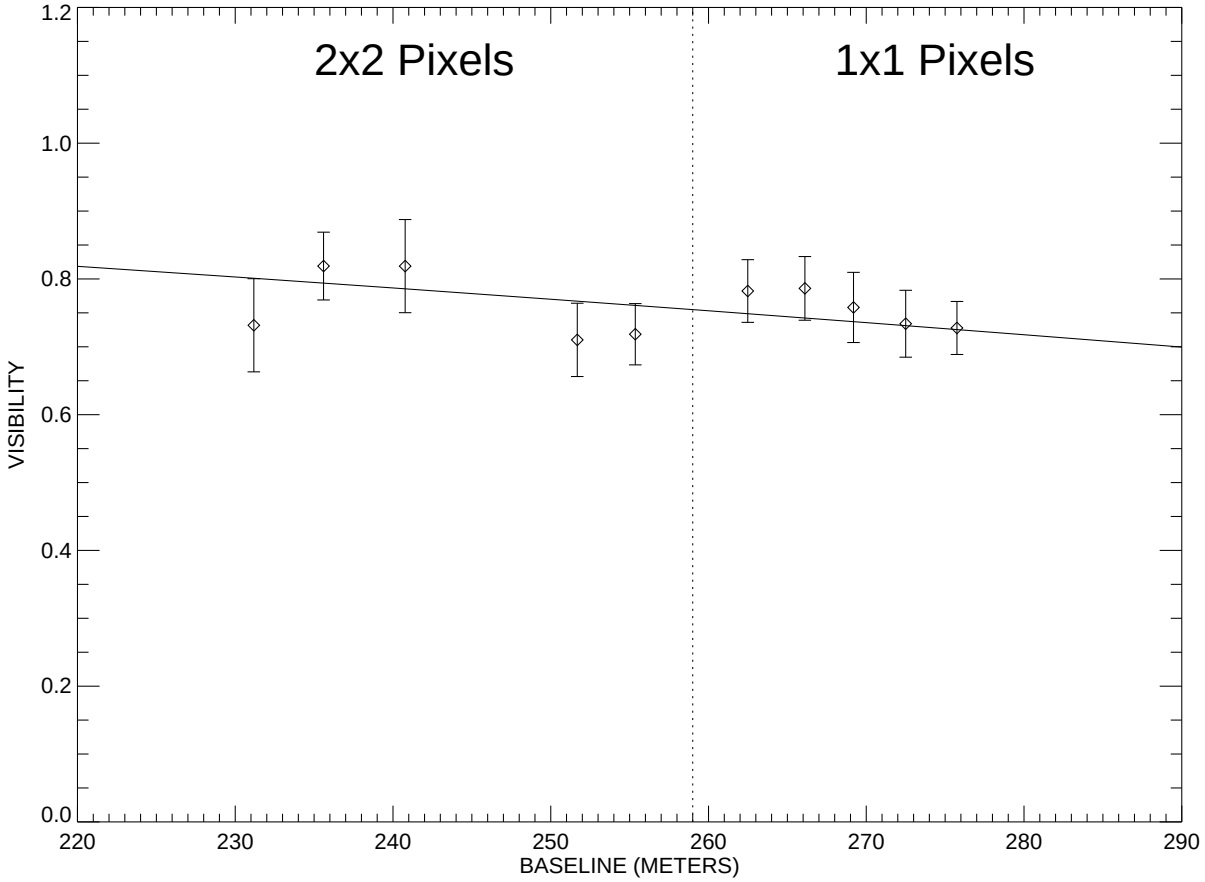

FIGURE 3.5: **NIRO 1×1 Versus 2×2 Pixels:** Limb darkened diameter fit to the calibrated visibilities of HD 90839 taken on 2007-11-16. The scatter in the calibrated visibilities when observing with 2×2 pixels is apparent here.

in the resulting diameter fit, proving that both the choice of calibrator was good and that the data calibration in this observing mode was successful.

3.3.4 Object/Calibrator Brightness Offsets and Calibration

A good calibrator is unresolved at long baselines and thus is almost always intrinsically fainter than your science star (unless you use a very early-type calibrator). There exist four sampling rates to choose from when observing with CHARA Classic, namely 1000, 750, 500, and 250 Hz. The default is set to observe at 750 Hz, but for stars fainter than $K \sim 5$ mag, a slower frequency (e.g. 500 Hz) may be desired, depending on the signal to noise of the data.

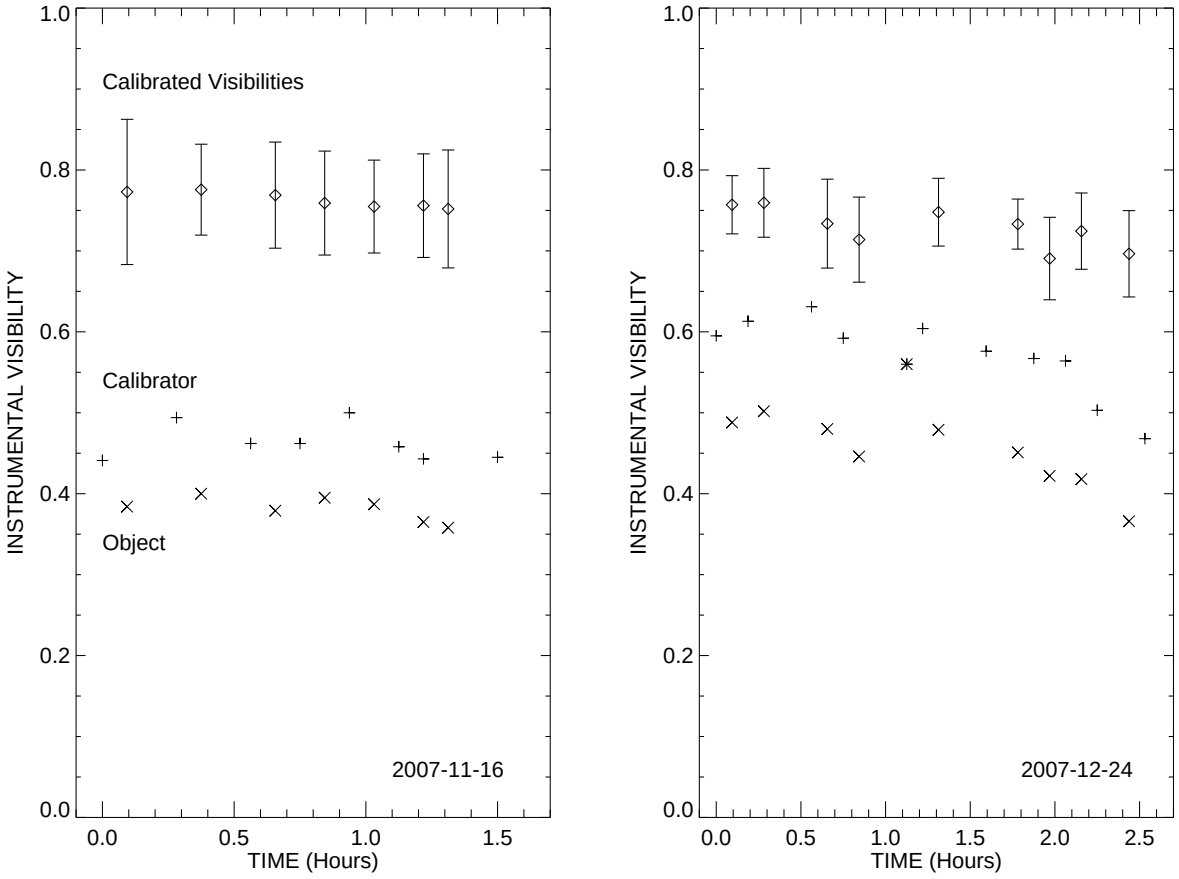

FIGURE 3.6: **Night-to-Night Repeatability:** Data for HD 103095 and its calibrator taken on 2007-11-16 and 2007-12-24. Instrumental visibilities for the calibrator (*plusses*), object (*crosses*), and the object's calibrated visibilities (*diamonds*) are shown with respect to time. In the right panel, the asterisk symbol is a placeholder to indicate when NIRO was aligned.

Almost all calibrators in this thesis are fainter than this limit, but 500 Hz was only used when seeing conditions were very poor. I performed a calibration check to ensure that although the counts appear low on the NIRO SUM window (on the NIRO server), the reduced data still calibrate well.

The test bracket went as follows:

- Calibrator at 500 Hz
- Calibrator at 750 Hz
- Object at 500 Hz

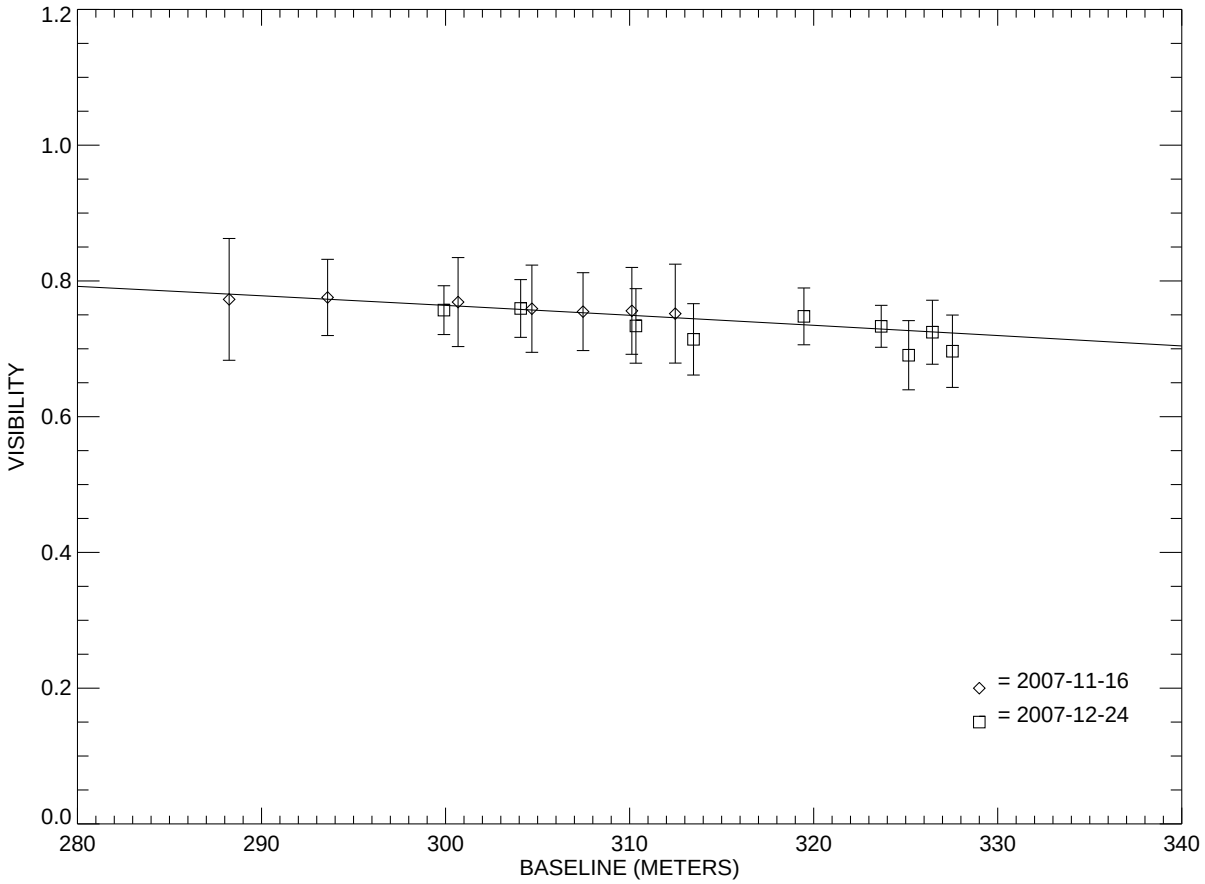

FIGURE 3.7: **Night-to-Night Repeatability:** Limb darkened diameter fit to the calibrated visibilities of HD 103095 taken on 2007-11-16 (*diamonds*) and 2007-12-24 (*squares*). Excellent agreement is seen in the resulting diameter fit for observations taken over a month apart.

- Object at 750 Hz
- Calibrator at 500 Hz
- Calibrator at 750 Hz

Calibrating the records of different frequencies independently (the error in the calibrated visibility is $\sim 10\%$), the calibrated visibilities when reduced with MathCAD are: $V_{500\ \mathrm{Hz}} = 0.82$, and $V_{750\ \mathrm{Hz}} = 0.83$ and the resulting calibrated visibilities when reduced in reduceir are: $V_{500\ \mathrm{Hz}} = 0.86$, and $V_{750\ \mathrm{Hz}} = 0.85$. This test shows that the calculated error of the visibilities

of $\sim 10\%$ is much greater than the deviation in the two program's calibrated visibilities ($\sim$ 2%), as well as the difference produced by the two recording frequencies ($\sim 1\%$).

3.3.5 Observing with Two Calibrators

There exist several reasons to observe with more than one calibrator, as discussed in the beginning of this chapter. The typical observing cadence of observing with one calibrator is C-O-C-O-C-O-C-O-C..., where 'C' denotes a calibrator observation, and 'O' denotes an object observation.

If you have chosen a good pair of calibrators, the object's calibrated visibilities should agree with each other perfectly. The observer may choose to observe with one calibrator on one night, and another calibrator on the next, and rotate back to test if the calibrated data agree with one another.

An alternative way to take brackets with two calibrators follows the sequence:

C1-C2-O-C2-C1-O-C1-C2-O-C2-C1-O-C1-C2...

Here, the object is always closely bracketed between either the first calibrator 'C1' or the second calibrator 'C2'. This way of observing also allows you to track the calibrator's visibilities against one another. The data can also be calibrated with both calibrators, giving higher weight to the calibrator data observed closer in time to the object. The downside of observing in this sequence is that a *NIRO* alignment is usually needed by the time the second or third bracket is completed.

In Figure 3.8, I have illustrated the agreement of calibrated observations for HD 30652, taken on 2008-10-01. On this night, the object was observed with two calibrators, rotating 3 brackets with each one, taken in the order:

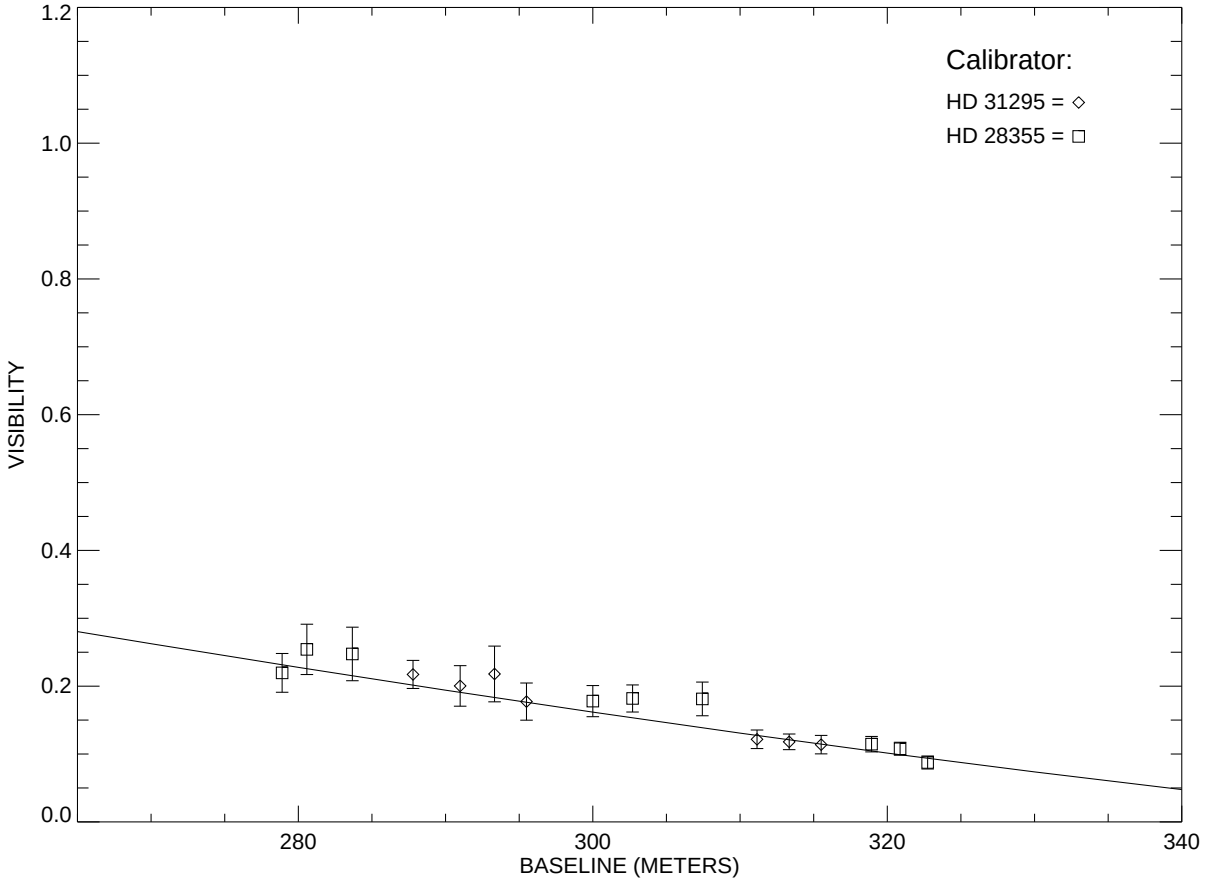

FIGURE 3.8: **Two Calibrator Diameter Fit:** Limb darkened diameter fit to the calibrated visibilities of HD 30652 taken on 2008-10-01. The *diamonds* represent data calibrated with the star HD 31295, and the *squares* represent the data calibrated with the star HD 28355. Excellent agreement is seen in the resulting diameter fit for observations calibrated with both calibrators.

C1-O-C1-O-C1-O-C1 – C2-O-C2-O-C2-O-C2 – C1-O-...

(aligning NIRO or moving carts where a '–'is indicated). Observing in this fashion has proven to be the most efficient and beneficial way to observe with two calibrators. In Figure 3.8, the calibrated visibilities for HD 30652 are shown in a single diameter fit. The agreement from one calibrator to the next (in an alternating observing pattern), is excellent, over a range of projected baselines.

3.3.6 Signs of a Bad Calibrator

Estimates of the instrumental visibility V_i are recorded during observing by the Grand Wazoo for each data record. These numbers can help identify the use of a bad calibrator. This is especially the case if the calibrator you are observing has visibilities smaller than those of the object, and the estimated size of the calibrator is thought to be smaller (i.e., unresolved). It is then the likely case that your calibrator is a previously undetected binary, or the observer did a poor job checking the calibrator's '*goodness* '.

Another hint that the calibrator is bad (a binary) is that the calibrator visibility estimates change drastically over the few hours you are taking brackets, while the object visibility estimates stay constant. Although detecting this pattern can also mean that the object could also be a previously undetected binary, or the instrumental system and/or seeing is unstable, one can deduce the real source of the variability by looking at the entire night's data set. Figure 3.9 shows the unmistakable signature of a bad calibrator (HD 41074), taken with the target star HD 48682 on 2007-12-24. In this data set, Figure 3.9 shows that the calibrated visibilities reach values >1, purely indicative of a calibrator star that is a binary, and the calibrated visibility observations for this star need to be thrown away.

Bad calibrators may appear less conspicuous when observing over the course of a few hours if there is not much change in position angle of the baseline projected on the sky during the time when the object is observed. More subtle effects may also arise if the chosen calibrator is single, but not round (i.e., rapidly rotating or has a disk). The four stars in Table 3.3 were observed and have been identified as bad calibrators, or in other words, newly discovered binaries.

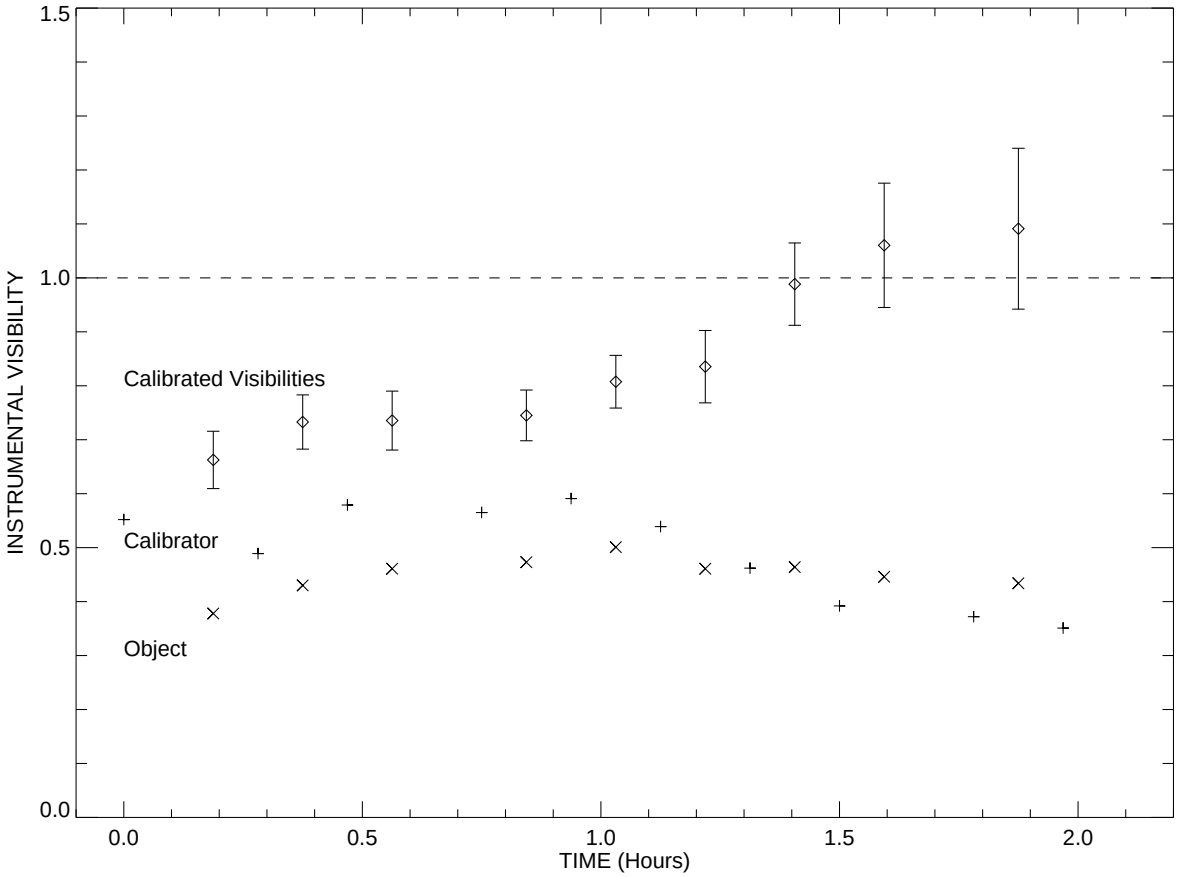

FIGURE 3.9: **Binary Calibrator Brackets:** Brackets of HD 48682 and its calibrator taken on 2007-12-24. Instrumental visibilities for the calibrator (*plusses*), object (*crosses*), and the object's calibrated visibilities (*diamonds*) are shown with respect to time. The change in the calibrator visibilities with respect to time are a good indicator that this calibrator (HD 41074) is a binary. Also note that the calibrated visibilities reach values greater than 1.0, a tell-tale sign that the calibrator used is a binary.

3.4 Miscellaneous

3.4.1 The Baseline Test

Due to the fact that the star is moving across the sky when observing, the moving delay cart must compensate for this motion to obtain interference fringes. Each data record takes ≈200 scans, with shutter sequences in the beginning and end of the record to enable us to remove background and noise from the data. The time it takes to take one data record depends on scan length (short, medium, or long), and the sampling rate (250, 500, 750, or 1000 Hz), all

of which are chosen by the observer[3]. The amount of change in projected baseline depends on where the object is in the sky and which baseline is being used. The combination of these conditions can change the projected baseline calculated from the beginning of the record to the end of the record by an amount on the order of meters. In our diameter fits for stars in this thesis, the projected baseline at the time of mid-observation is used.

We tested this effect on the diameter fit for the calibrated visibilities when we used the projected baseline at the start of the record versus the projected baseline at the end of the record for observations of HD 6582 taken on 2007-7-17. These data were taken at 500 Hz (slower than the normal 750 Hz sampling rate) using a long scan (which also contributes to a longer observation record), where each data record is ≈ 7.1 minutes in duration. There is an average difference of three meters of projected baseline between the beginning to the end of each observation[4]. Performing diameter fits to each set of calibrated points (one using B from the beginning of the observations and one using B from the end of the observation), we find that the baseline motion during observing is an insignificant contribution (about 0.2% out of 1.5%) to the overall uncertainty in diameter.

3.4.2 Lab Vibrations

Vibrations in the lab may cause spurious visibility measurements and lead to calibration errors. They are likely to manifest while observing due to cooling fans in electrical devices or due to mechanical devices in the lab being moved in some manner. Things that have caused issues in the past are: the PICO #3 micrometer driven control box, the HVAC

[3]Time for one observation takes place over $\approx 3-8$ minutes

[4]The change in baseline also depends on where the object is in the sky and the bsaeline used for observation.

(which sits on a bed of springs to alleviate most of the effects), and the vacuum pumps for the vacuum light tubes. Figure 3.10 and Figure 3.11 show data taken on lab fringes that T. ten Brummelaar obtained and analyzed on 2007-01-27. Here, we can clearly see that in Figure 3.11, where the HVAC unit is turned on, the power spectrum is much lumpier and wider than the power spectrum of the data when it is turned off in Figure 3.10. Relocation of the offending components and the adoption of appropriate observing practices can nearly completely eliminate these problems.

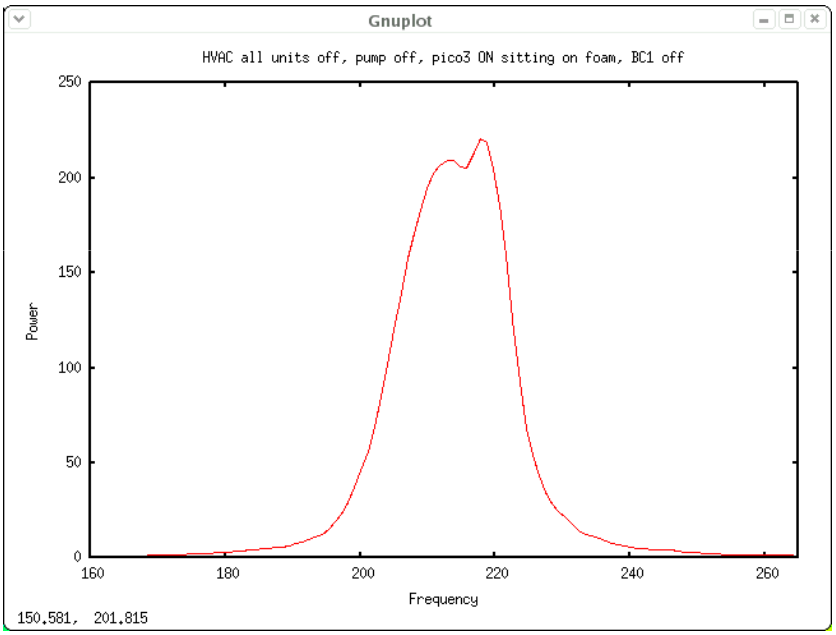

FIGURE 3.10: **Lab Vibrations:** Plot of data reduced from lab fringes with the HVAC units turned off.

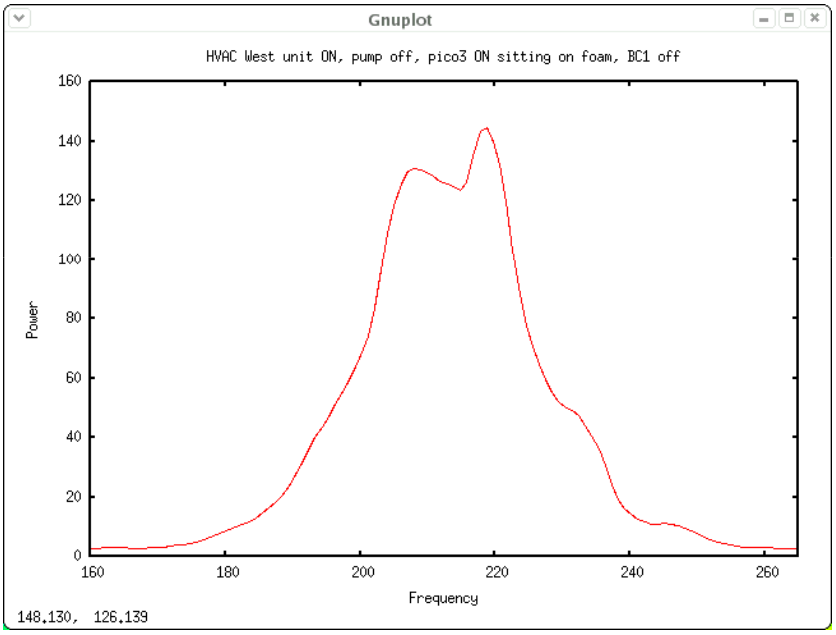

FIGURE 3.11: **Lab Vibrations:** Plot of data reduced from lab fringes with the HVAC unit turned on.

TABLE 3.1: Calibrators Observed

Calibrator HD	**RA (hh mm ss.xx)**	**DEC (dd mm ss)**	V **(mag)**	K **(mag)**	**Target (s) HD**
71	00 05 39.73	55 42 36	7.0	4.2	4614
6210	01 04 19.45	61 34 49	5.8	4.4	4614, 5015, 6582, 10780
9407	01 34 33.26	68 56 53	6.5	4.9	4614
20675	03 21 52.53	49 04 15	5.9	4.9	16895, 19373
21790	03 30 37.06	−05 04 31	4.7	4.9	20630, 22484, 25457
22879	03 40 22.06	−03 13 01	6.7	5.2	20630, 22484, 25457
28355	04 28 50.16	13 02 51	5.0	4.5	30652
30739	04 50 36.72	08 54 00	4.3	4.2	30652
31295	04 54 53.73	10 09 03	4.6	4.6	30652
34904	05 22 50.31	41 01 45	5.5	5.1	34411
38558	05 47 26.20	17 43 45	5.5	4.5	39587
42807	06 13 12.50	10 37 38	6.4	4.6	48737
43042	06 14 50.88	19 09 23	5.2	4.1	39587
43795	06 20 16.04	42 47 60	7.7	5.4	48682
50277	06 52 49.47	08 22 49	5.8	5.1	48737
58551	07 26 50.25	21 32 08	6.5	5.2	56537
59037	07 29 20.44	28 07 06	5.1	4.7	58946
65583	08 00 32.13	29 12 44	6.9	5.1	58946
83951	09 42 42.70	35 05 36	6.1	5.2	82885, 86728
87141	10 04 36.32	53 53 30	5.7	4.5	82328
88986	10 16 28.08	28 40 57	6.5	4.9	86728
89389	10 20 14.79	53 46 46	6.5	5.0	90839, 95418
91480	10 35 09.69	57 04 57	5.2	4.3	81937, 90839, 95418
99285	11 25 36.37	16 27 24	5.6	4.6	97603
99984	11 41 34.26	31 44 45	5.7	4.5	103095
102124	11 45 17.04	08 15 29	4.8	4.4	102870
102634	11 49 01.28	00 19 07	6.2	4.9	102870
103799	11 57 14.58	40 20 37	6.6	5.3	101501, 103095, 109358
110897	12 44 59.41	39 16 44	6.0	4.5	109358
114093	13 08 02.41	24 49 52	6.8	4.6	114710
120066	13 46 57.12	06 21 01	6.3	4.9	118098
128093	14 34 11.71	32 32 04	6.3	5.2	128167
129153	14 40 42.39	13 32 04	5.9	5.4	131156
132254	14 56 23.04	49 37 42	5.6	4.4	126660
135101	15 12 43.48	19 17 10	6.7	5.0	131156
139225	15 36 29.23	16 07 09	5.9	5.0	142860
140775	15 45 23.48	05 26 50	5.6	5.4	141795
145607	16 12 07.32	−08 32 51	5.4	5.1	146233
150177	16 39 39.13	−09 33 17	6.3	5.0	146233
154099	16 56 16.74	73 07 40	6.3	5.6	162003
158352	17 28 49.70	00 19 49	5.4	4.8	164259
158633	17 25 00.10	67 18 24	6.4	4.5	168151
162004	17 41 58.11	72 09 25	5.8	4.5	162003
167564	18 15 59.93	−03 37 05	6.3	5.8	165259
174897	18 52 18.64	14 32 08	6.5	4.1	182572
176303	18 59 05.74	13 37 20	5.3	3.9	173667, 177724, 182572, 187691
180317	19 15 17.36	21 13 56	5.7	5.3	173667, 177724

Continued on Next Page...

TABLE 3.1 – Continued

Calibrator HD	**RA (hh mm ss.xx)**	**DEC (° ′ ″)**	V **(mag)**	K **(mag)**	**Target (s) HD**
183534	19 27 25.96	52 19 13	5.7	5.7	185395
184499	19 33 27.08	33 12 07	6.6	5.1	187013
189395	19 58 37.98	30 59 01	5.5	5.6	187013
191195	20 06 13.85	53 09 56	5.9	4.8	185395
193555	20 20 15.38	15 32 34	6.8	5.5	187691
193664	20 17 31.33	66 51 13	5.9	4.5	185144
195838	20 34 11.70	−13 43 16	6.1	4.8	195564
204485	21 28 08.25	32 13 31	5.8	5.0	201091, 201092
210715	22 11 09.89	50 49 24	5.4	5.0	213558
211976	22 20 55.80	08 11 12	6.2	5.0	210418, 215648
214923	22 41 27.72	10 49 53	3.4	3.6	215648
216735	22 55 13.67	08 48 58	4.9	4.8	215648, 222368
218470	23 07 45.38	49 17 45	5.7	4.6	213558
222603	23 42 02.80	01 46 48	4.5	4.1	222368
225003	00 02 29.70	08 29 08	5.7	4.9	222368

TABLE 3.2: Calibrator SED Diameters

Calibrator HD	$T_{\rm EFF}$ **(K)**	$\log g$ **(cgs)**	$\theta_{\rm SED}$ **(mas)**	**Target (s) HD**
71	4500	4.50	0.682 ± 0.024	4614
6210	6100	3.80	0.519 ± 0.012	4614, 5015, 6582, 10780
9407	5800	4.50	0.430 ± 0.017	4614
20675	6600	4.20	0.415 ± 0.012	16895, 19373
21790	11500	3.70	0.308 ± 0.009	20630, 22484, 25457
22879	6250	4.25	0.342 ± 0.021	20630, 22484, 25457
28355	8000	4.00	0.425 ± 0.030	30652
30739	9450	3.90	0.461 ± 0.018	30652
31295	8800	4.10	0.439 ± 0.043	30652
34904	7900	4.00	0.345 ± 0.013	34411
38558	7100	3.50	0.422 ± 0.008	39587
42807	5850	4.45	0.429 ± 0.016	48737
43042	6650	4.25	0.591 ± 0.030	39587
43795	5000	2.50	0.376 ± 0.008	48682
50277	7400	4.00	0.346 ± 0.011	48737
58551	6200	4.00	0.357 ± 0.009	56537
59037	8450	4.20	0.389 ± 0.018	58946
65583	5550	4.50	0.406 ± 0.033	58946

Continued on Next Page...

TABLE 3.2 – Continued

Calibrator HD	$T_{\rm EFF}$ **(K)**	$\log g$ **(cgs)**	$\theta_{\rm SED}$ **(mas)**	**Target (s) HD**
83951	6750	4.00	0.360 ± 0.006	82885, 86728
87141	6400	4.00	0.476 ± 0.022	82328
88986	5850	4.00	0.432 ± 0.013	86728
89389	6100	4.20	0.398 ± 0.013	90839, 95418
91480	7050	4.25	0.518 ± 0.014	81937, 90839, 95418
99285	6800	3.90	0.456 ± 0.017	97603
99984	6200	3.80	0.483 ± 0.020	103095
102124	7950	4.20	0.466 ± 0.022	102870
102634	6350	4.25	0.404 ± 0.010	102870
103799	6300	4.50	0.343 ± 0.013	101501, 103095, 109358
110897	6150	4.25	0.492 ± 0.022	109358
114093	4900	4.40	0.572 ± 0.014	114710
120066	6000	4.50	0.428 ± 0.013	118098
128093	6600	4.10	0.351 ± 0.011	128167
129153	7650	4.25	0.309 ± 0.010	131156
132254	6350	4.00	0.520 ± 0.015	126660
135101	5750	4.40	0.409 ± 0.014	131156
139225	6900	4.00	0.380 ± 0.122	142860
140775	9000	4.00	0.275 ± 0.013	141795
145607	8400	4.00	0.325 ± 0.020	146233
150177	6250	4.00	0.391 ± 0.019	146233
154099	7300	4.00	0.283 ± 0.005	162003
158352	7450	3.90	0.407 ± 0.013	164259
158633	5400	4.50	0.542 ± 0.043	168151
162004	6250	4.20	0.498 ± 0.015	162003
167564	7500	4.00	0.259 ± 0.004	165259
174897	4950	3.50	0.652 ± 0.038	182572
176303	6200	4.25	0.659 ± 0.016	173667, 177724, 182572, 187691
180317	8050	4.00	0.309 ± 0.007	173667, 177724
183534	9500	4.00	0.241 ± 0.012	185395
184499	6050	4.50	0.383 ± 0.019	187013
189395	10650	3.50	0.235 ± 0.006	187013
191195	6650	4.25	0.432 ± 0.014	185395
193555	6150	4.00	0.328 ± 0.006	187691
193664	6100	4.50	0.494 ± 0.019	185144
195838	6300	4.25	0.421 ± 0.017	195564
204485	7100	4.25	0.381 ± 0.011	201091, 201092
210715	7950	4.20	0.366 ± 0.015	213558
211976	6600	4.00	0.373 ± 0.013	210418, 215648
214923	10100	3.75	0.611 ± 0.029	215648

Continued on Next Page...

TABLE 3.2 – Continued

Calibrator HD	$T_{\rm EFF}$ **(K)**	$\log g$ **(cgs)**	$\theta_{\rm SED}$ **(mas)**	**Target (s) HD**
216735	10150	3.50	0.321 ± 0.022	215648, 222368
218470	6650	4.00	0.462 ± 0.014	213558
222603	7750	4.00	0.577 ± 0.032	222368
225003	7200	4.00	0.386 ± 0.017	222368

TABLE 3.3: Bad Calibrators

HD	**RA (hh mm ss.xx)**	**DEC (dd mm ss)**	**Reason**
41074	06 05 03.38	42 58 54	visibility modulation
43153	06 15 25.13	16 08 35	separated fringe packet binary
101606	11 41 34.26	31 44 46	separated fringe packet binary
181655	19 19 39.00	37 19 50	separated fringe packet binary

– 4 –

Observations

Observations were taken using the CHARA Array, located on Mount Wilson, CA, and remotely operated from the Georgia State University AROC[1] facility in Atlanta, GA. Observing proposals for the full-year durations of 2007 and 2008 were submitted, and sufficient time was assigned to the project to collect data on forty-four stars to determine their angular diameters. This observed sample includes 7 A-type stars, 19 F-type stars and 18 G-type stars (also includes spectral type K0). Observations were made using the CHARA Classic beam combiner in the K'-band ($\lambda = 2.15 \pm 0.01$ μm).

The target sample was selected on the assumption that we could also observe many of these stars in H-band, which provides higher resolution than observing in K-band because of the shorter wavelength. H-band observations were desired for approximately half of the sample, allowing us to extend farther down the visibility curve to measure their diameter with better than 4% accuracy. A combination of H- and K-band observations were to be made for $\sim$10 of the objects, useful for comparison of data from different filters. The remaining objects are sufficiently resolved in the K-band only. H-band observations were attempted on several occasions; however, the brightness of the targets restricted us from taking any useful data[2].

Ideally, observations of the stars use a combination of the longest baselines for diameter determinations. In particular, the use of CHARA's longest baseline, S1/E1, is crucial to

[1]Arrington Remote Operations Center

[2]The faintest of the stars in the sample were observed in the fastest readout mode (1000 Hz) and the chip was still saturating three quarters of the way through the scan.

this work due to the small angular sizes of the targets. The length of the projected baseline changes naturally throughout the night due to the diurnal rotation of the Earth, so a large range in projected baselines (and thus visibility curve coverage) are obtainable with one pair of telescopes. In order to take advantage of an available orthogonal baseline configuration for better UV plane coverage for the observations, we found that either S1/W1 or E1/W1 provides a suitable complement to S1/E1. The UV plane can also be represented by the position angle of the baseline with respect to the object in the sky and it also changes throughout the night similar to the projected baseline length. Table 1.1 shows the current baseline configurations (2007) for the CHARA Array for each telescope pair's maximum projected baseline B and position angle ψ of the baseline on the sky.

Remote observing at AROC allows for easy data acquisition without travel to Mount Wilson, CA. Although a telescope operator must still be present on the mountain to do necessary lab alignment and other such things, nearly all the tasks to be done during the night can be done independently from AROC. This facility also allows for parallel observing of two independent programs using separate beam combiners and baselines. The data collected on my targets were promptly reduced and calibrated within a few days of the observations being made.

Table 4.1 lists the identifications of all (52) stars made for this work (column 1), UT date (column 2), the baseline used (column 3), the number of bracketed observations (column 4), and the calibrator(s) used on that date (column 5). The abbreviation (H) denotes H-band observations, which proved to be impossible to reduce and use for this work. Observations made with a bad calibrator are denoted with a †. Stars that are incomplete in their analysis to this date are labeled with a †† in Table 4.1. Table 4.2 lists these eight stars and gives a

reason why those analyses are incomplete. 'Binary (or Disk)' indicates that the star shows dramatic changes in visibility, either during single night of observations, or over a period of time. Stars that 'Need more data' are not sufficiently resolved to meet the goals of this project. Omission of these eight stars leaves 44 stars with sufficient observations for the final analysis.

Tables of the resulting calibrated visibilities for each star can be found in Appendix C, along with a plot of the final diameter fits.

TABLE 4.1: Observations of A, F, and G Dwarfs

Object HD	UT Date	Baseline	Number of Brackets	Calibrator HD
4614	2007/06/29	W1/E1	2	6210
	2007/06/30	W1/E1	5	6210
	2007/07/01	W1/E1	3	6210
	2007/07/18	S1/E1	3	6210
	2007/07/19	S1/E1	3	6210
	2007/11/16	S1/E1	4	6210
	2008/10/02	W1/E1	4	6210, 9407
5015	2007/10/10	W1/E1	10	6210
	2007/11/03	W1/E1	7	6210
	2007/11/17	S1/E1	8	6210
6582	2007/07/01	W1/E1	3	6210
	2007/07/17	S1/E1	6	6210
	2007/07/18	S1/E1	8	6210
	2007/09/08	S1/E1	10	6210
10780	2007/06/29	W1/E1	2	6210
	2007/07/19	S1/E1	10	6210
	2007/10/10	W1/E1	10	6210
16895	2007/09/08	S1/E1	7	20675
	2007/11/03	W1/E1	8	20675
	2007/12/24	S1/E1	6	20675
19373	2007/01/25	S1/E1	8	20675
	2007/08/28	W1/S1	2	20675
	2007/09/08	S1/E1	10	20675
	2007/11/04	W1/E1	6	20675
20630	2007/09/09	S1/E1	9	21790
	2007/09/10	S1/E1	6 (H)	21790
	2008/10/01	S1/E1	4	22879
	2008/11/17	S1/E1	5	22879
	2008/11/18	S1/E1	5	21790, 22879
22484	2006/12/05	S1/E1	1	21790
	2006/12/07	S1/E1	3	21790

Continued on Next Page...

TABLE 4.1 – Continued

Object HD	UT Date	Baseline	Number of Brackets	Calibrator HD
	2007/09/09	S1/E1	8	21790
	2008/10/01	S1/E1	6	22879
	2008/10/02	W1/E1	4	22879
25457††	2008/11/17	S1/E1	6	22879
	2008/11/18	S1/E1	3	21790, 22879
30652	2007/11/05	S1/E1	16	30739
	2008/10/01	S1/E1	10	28355, 31295
	2008/10/02	W1/E1	3	31295
34411	2007/01/26	S1/E1	5	34904
	2007/11/03	W1/E1	8	34904
	2007/11/15	S1/E1	4	34904
	2007/11/17	S1/E1	7	34904
39587	2006/12/07	S1/E1	3	38558
	2007/03/06	S1/E1	8	38558
	2008/11/18	S1/E1	11	38558, 43042
48682	2007/12/24	S1/E1	6	41074†
	2008/09/17	S1/E1	6	43795
	2008/10/02	W1/E1	3	43795
	2008/11/16	S1/E1	6	43795
48737	2006/12/07	S1/E1	4	50277
	2008/11/17	S1/E1	12	42807, 50277
	2008/11/18	S1/E1	11	42807, 50277
55575††	2007/11/03	W1/E1	5	56221
	2007/11/07	S1/E1	5	56221
	2007/11/17	S1/E1	1 + 1 (H)	56221
56537	2007/02/21	S1/E1	1	58551
	2007/02/25	S1/E1	7	58551
	2007/03/11	S1/E1	6	58551
	2007/11/04	S1/E1	5	58551
	2007/12/23	S1/E1	5	58551
58946	2007/01/25	S1/E1	6	65583

Continued on Next Page...

TABLE 4.1 – Continued

Object HD	UT Date	Baseline	Number of Brackets	Calibrator HD
	2007/11/16	S1/E1	7	59037
	2007/11/17	S1/E1	7	59037
81937	2007/11/29	S2/E2	9	91480
82328	2007/11/02	W2/E2	9	87141
82885	2007/02/03	S1/E1	2	83951
	2007/11/03	W1/E1	7	83951
	2007/11/07	S1/E1	9	83951
	2007/12/24	S1/E1	5	83951
86728	2007/11/15	S1/E1	10	83951
	2007/11/16	S1/E1	2	83951
	2007/12/24	S1/E1	6	83951
	2008/11/16	S1/E1	10	83951, 88986
90839	2007/11/16	S1/E1	10	89389
	2008/04/17	W1/S1	5	89389, 91480
95418††	2007/04/04	S1/E1	7	91480
	2007/11/07	S1/E1	6	91480
	2008/04/17	W1/S1	5	89389, 91480
97603	2007/02/21	S1/E1	10	99285
	2007/03/10	S1/E1	1	99285
	2007/03/11	S1/E1	5	99285
101501	2007/11/15	S1/E1	7	103799
	2007/12/24	S1/E1	3	103799
102870	2007/03/09	S1/E1	6	102124
	2007/12/23	S1/E1	4	102124
	2008/04/19	W1/S1	8	102124
	2008/04/22	S1/E1	9	102124
	2008/04/23	S1/E1	7	102634
103095	2007/11/16	S1/E1	7	103799
	2007/12/24	S1/E1	10	103799

Continued on Next Page...

TABLE 4.1 – Continued

Object HD	UT Date	Baseline	Number of Brackets	Calibrator HD
109358	2007/05/26	S1/E2	3	110897
	2008/04/18	W1/S1	5	103799, 110897
114710	2008/04/21	W1/S1	10	114093
	2008/06/27	S1/E1	6	114093
118098	2007/03/10	S1/E1	6	120066
	2007/03/30	S1/E1	5	120066
	2007/12/23	S1/E1	2	120066
126660	2007/05/24	W1/S1	5	132254
	2007/07/16	S1/E1	6	132254
	2008/07/25	S1/E1	4	132254
128167	2008/06/28	S1/E1	5	128093
	2008/07/06	S1/E1	12	128093
	2008/07/24	S1/E2	10	128093
131156	2007/03/12	S1/E1	5	135101
	2008/04/18	W1/S1	5	135101, 129153
	2008/04/19	W1/S1	6	135101
	2008/06/27	S1/E1	9	135101, 129153
141795	2008/07/22	S1/E1	8	140775
142860	2007/07/20	S1/E1	3	139225
	2007/07/21	S1/E1	6	139225
	2008/04/21	W1/S1	10	139225
146233	2008/04/19	W1/S1	11	145607, 150177
	2008/04/21	W1/S1	6	145607, 150177
	2008/04/22	S1/E1	9	145607, 150177
	2008/04/23	S1/E1	6	145607, 150177
	2008/05/16	W1/E2	4	150177
162003	2007/07/17	S1/E1	8	154099
	2007/07/18	S1/E1	2	162004
	2007/10/10	W1/E1	6	162004
	2007/11/17	S1/E1	4	162004
	2008/06/26	S1/E1	5	162004

Continued on Next Page...

TABLE 4.1 – Continued

Object HD	UT Date	Baseline	Number of Brackets	Calibrator HD
164259	2008/04/22	S1/E1	6	167564, 158352
	2008/04/23	S1/E1	3	158352
	2008/06/20	W1/S1	3	158352
	2008/06/28	S1/E1	5	158352
	2008/07/27	W1/S1	6	158352
168151††	2008/07/21	S1/E1	4	158633
173667	2007/07/20	S1/E1	3	180317
	2007/07/21	S1/E1	9	176303
	2007/09/10	S1/E1	12 (H)	176303
	2008/04/21	W1/S1	3	176303
	2008/06/28	S1/E1	8	176303
	2008/07/07	W1/S1	1	176303
	2008/07/21	W1/S1	1	176303
	2008/07/22	S1/E1	6	176303
	2008/07/23	W1/E1	6	176303
177724	2008/06/28	S1/E1	10	176303
	2008/07/07	W1/S1	5	176303
	2008/07/21	W1/S1	4	176303
	2008/07/22	S1/E1	6	176303
	2008/07/23	W1/E1	6	176303
	2008/10/01	S1/E1	4	176303
182572	2007/07/21	S1/E1	6	174897
	2007/09/09	S1/E1	10	174897
	2008/07/22	S1/E1	5	174897
	2008/07/24	S1/E2	5	174897
	2008/09/30	S1/E1	7	176303
185144	2007/05/24	W1/S1	3	193664
	2007/05/25	W1/S1	4	193664
	2007/06/28	W1/E1	1	193664
	2007/06/29	W1/E1	4	193664
	2007/06/30	W1/E1	1	193664
	2007/07/01	W1/E1	2	193664
185395	2007/05/26	S1/E2	3	183534

Continued on Next Page...

TABLE 4.1 – Continued

Object HD	UT Date	Baseline	Number of Brackets	Calibrator HD
	2007/07/19	S1/E1	11	191195
	2007/11/02	W1/E2	5	191195
	2008/07/25	S1/E1	8	191195
187013††	2008/04/17	W1/S1	2	181655†
	2008/07/23	S1/E1	10	184499, 189395
	2008/07/24	S1/E2	5	184499
187691††	2007/09/09	S1/E1	8	193555
	2008/06/27	S1/E1	7	193555
	2008/09/30	S1/E1	3	176303
195564††	2008/06/20	W1/S1	3	196838
	2008/06/27	S1/E1	11	196838
210418	2008/06/28	S1/E1	6	211976
	2008/07/22	S1/E1	9	211976
	2008/07/24	S1/E2	4	211976
	2008/10/01	S1/E1	3	211976
211336††	2008/10/02	W1/E1	4	204965
213558	2007/09/08	S1/E1	7	218470
	2007/10/10	W1/E1	10	210715
	2007/12/24	S1/E1	6	218470
	2008/07/21	S1/E1	5	218470
215648	2007/07/16	S1/E1	4	211976
	2007/07/21	S1/E1	14	214923
	2008/07/24	S1/E2	5	214923
	2008/09/30	S1/E1	4	211976
	2008/10/01	S1/E1	8	211976, 216735
222368	2006/12/07	S1/E1	4	222603
	2007/07/20	S1/E1	11	222603
	2007/09/09	S1/E1	5	222603
	2007/09/10	S1/E1	5 (H)	222603
	2008/09/30	S1/E1	10	222603, 225003
	2008/10/01	S1/E1	8	216735

†Bad calibrator used. ††Incomplete.

TABLE 4.2: Problem Stars

Star	**Reason**
25457	Need more data
55575	Binary?
95418	Binary and/or Disk?
168151	Need more data
187013	Need more data
187691	Binary?
195564	Need more data
211336	Need more data

– 5 –

Stellar Diameters

5.1 Diameter Fit to a Single Star

Angular diameters for each star were determined by fitting the calibrated visibilities to the visibility curve for a single star's uniform-disk and limb-darkened angular diameters. We calculate the uniform-disk $\theta_{\rm UD}$ (Equation 5.1) and limb-darkened $\theta_{\rm LD}$ (Equation 5.2) angular diameters from the calibrated visibilities by χ^2 minimization of the following relations from Brown et al. (1974):

$$V = \frac{2J_1(\mathrm{x})}{\mathrm{x}}, \tag{5.1}$$

$$V = \left(\frac{1-\mu_\lambda}{2} + \frac{\mu_\lambda}{3}\right)^{-1} \times \left[(1-\mu_\lambda)\frac{J_1(\mathrm{x})}{\mathrm{x}} + \mu_\lambda\left(\frac{\pi}{2}\right)^{1/2}\frac{J_{3/2}(\mathrm{x})}{\mathrm{x}^{3/2}}\right], \tag{5.2}$$

and

$$\mathrm{x} = \pi B\theta\lambda^{-1}, \tag{5.3}$$

where J_n is the n^{th}-order Bessel function and μ_λ is the linear limb darkening coefficient at the wavelength of observation. In Equation 5.3, B is the projected baseline in the sky, θ is the UD angular diameter of the star when applied to Equation 5.1 and the LD angular diameter when used in Equation 5.2, and λ is the central wavelength of the observational bandpass ($\lambda = 2.15$ μm).

The error of the diameter fit is based upon the values on either side of the minimum for which $\chi^2 = \chi^2_{\rm min} + 1$ (Press et al. 1992; Wall & Jenkins 2003). We find in most cases that

the value of the reduced χ^2 is less than 1.0, meaning that we have overestimated the errors on the calibrated visibilities for the star. In the results presented here, we adjusted those error estimates to force the reduced χ^2 to unity to compensate for the uncertainty in the visibility error estimates.

These measured angular diameters are converted to limb darkened angular diameters $\theta_{\rm LD}$ using the limb darkening coefficients in K-band μ_K found in Claret et al. (1995). Although observations with CHARA Classic are in the K'-band, to find the limb darkening coefficients here we assume that $K \approx K'$, since there is a negligible difference in limb darkening corrections in this wavelength region. Overall, for stars of these spectral types, the correction from $\theta_{\rm UD}$ to $\theta_{\rm LD}$ is $\approx 2\%$, and therefore we expect little offset due to the dependence of stellar models in determining the limb darkening coefficients used.

Table 5.1 shows the input $T_{\rm EFF}$ and $\log g$ used for generating the model SED fit for each program star. The Claret et al. (1995) limb darkening coefficients (μ_K) are then found through a bilinear interpolation of these $T_{\rm EFF}$ and $\log g$ estimates. Table 5.1 also shows the $\theta_{\rm SED}$, $\theta_{\rm UD}$, and $\theta_{\rm LD}$ for the stars observed in this project. Finally, we are able to determine the linear radii R of each of the stars observed by simply combining the measured parallax from van Leeuwen (2007) and the measured limb darkened angular diameter $\theta_{\rm LD}$ (column 9). Note that this table includes only the 44 stars that meet the criteria of better than 4% accuracy on the measured angular diameter (i.e., excludes problem stars). The mean percentage error of the measured limb darkened angular diameter is 1.5%, with 0.2% as the best and 3.5% the worst. A short summary of the results for each star can be found in Appendix C, which includes tables of the calibrated visibilities for each star and plots of their diameter fits.

In Figure 5.1, the $\theta_{\rm SED}$ values are plotted against the $\theta_{\rm LD}$ angular diameters, with the color corresponding to the $(B-V)$ color index of the star. Here we see that most stars lie above the 1:1 ratio line, meaning that the $\theta_{\rm SED}$ is typically underestimated for the sample, especially for stars under ≈ 0.9 mas, and for the bluer stars in the sample. Figure 5.2 shows the percent difference in the measured $\theta_{\rm LD}$ and the $\theta_{\rm SED}$ versus the $(B-V)$ color index. The average offset is $\sim 10\%$ for all 44 stars, while diameters of stars bluer than $(B-V)$=0.2 are all overestimated.

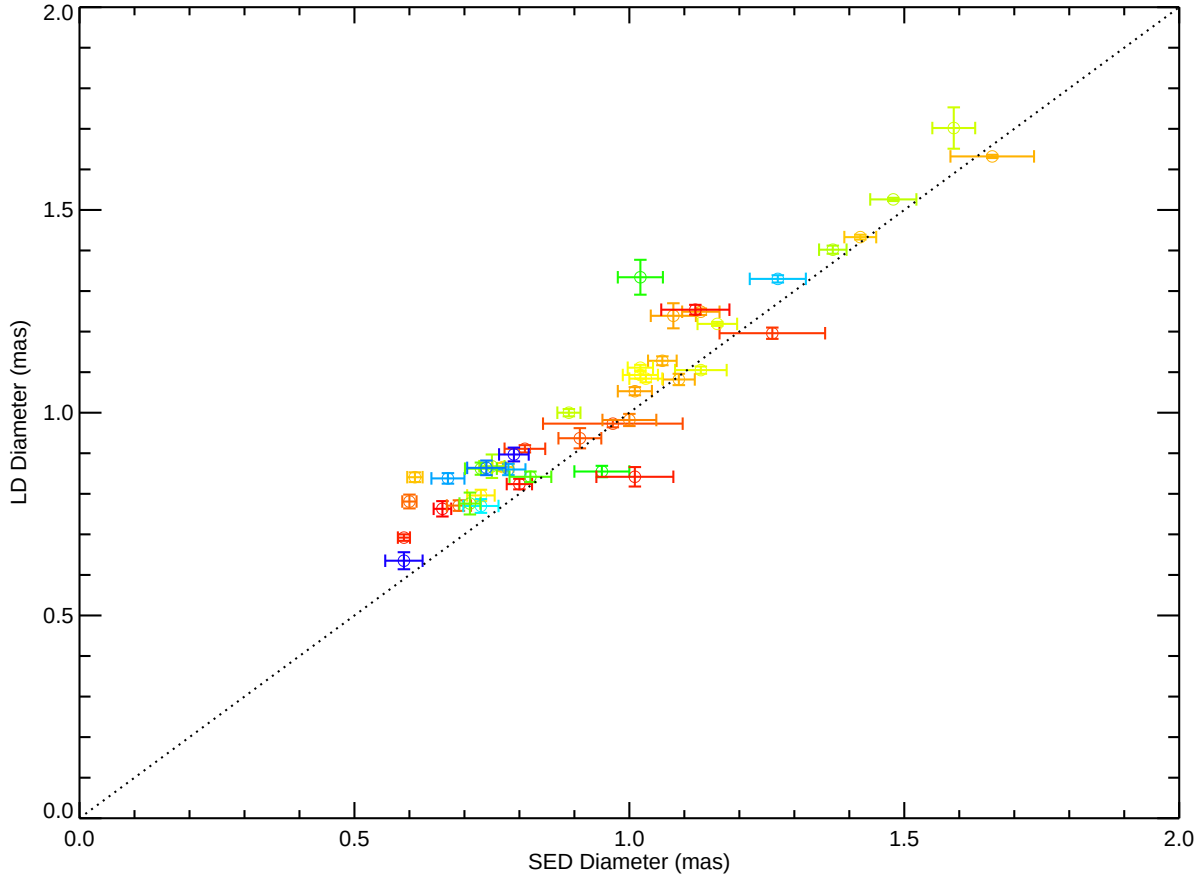

FIGURE 5.1: **SED Versus LD Diameters with Respect to $(B-V)$ Color:** Plot of SED versus LD angular diameters and the dependence on color index $(B-V)$. The color of the data point corresponds to the $(B-V)$ color index of the star, where blue indicates the bluest star in the sample $(B-V) = 0.013$), and red indicates the reddest star in the sample $(B-V) = 0.804$). The dotted line shows a 1:1 ratio.

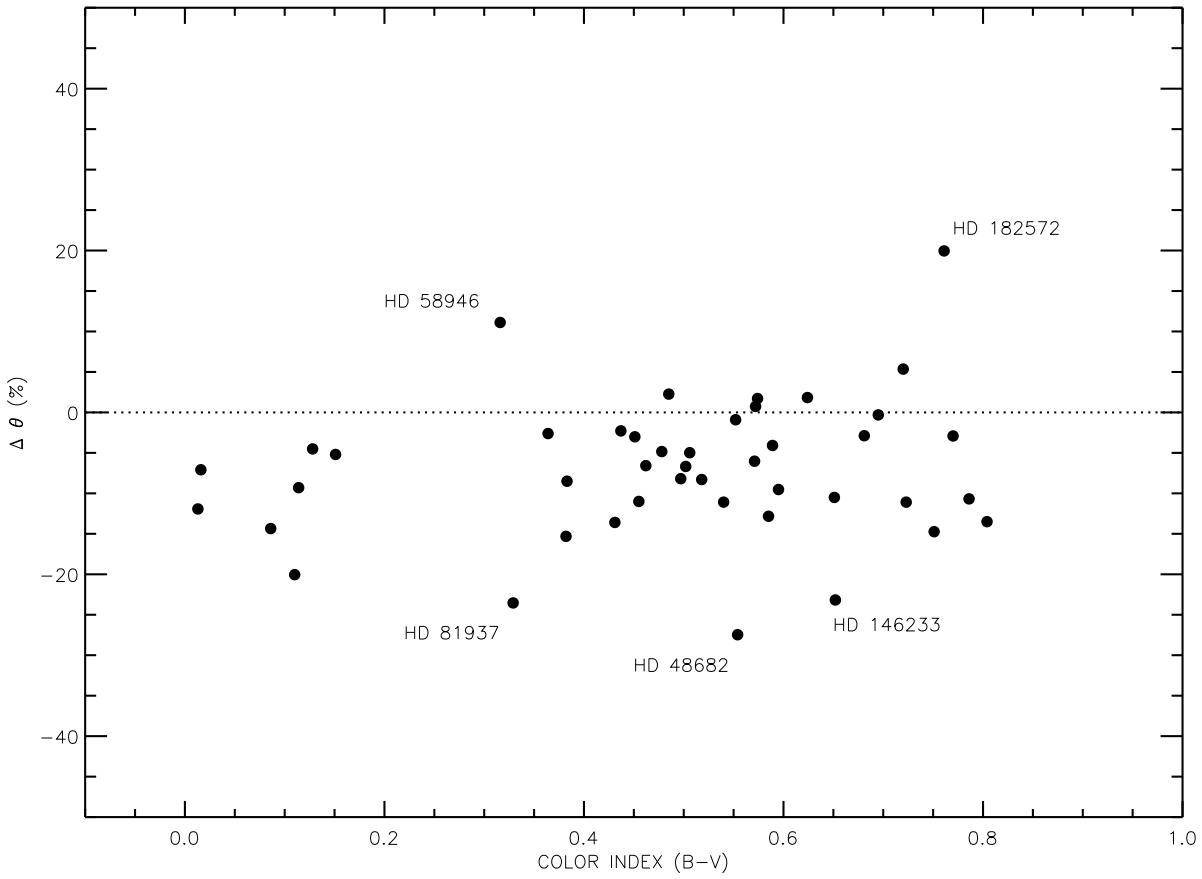

FIGURE 5.2: **Comparison of SED to LD Diameters with Respect to $(B-V)$ Color:** Plot of the percentage difference between the angular diameters found by SED fits and observational data ($\Delta\theta$), and the dependence on color index $(B-V)$.

5.2 CHARA Versus Palomar Testbed Interferometer Diameters

The sample of stars for this project was selected in terms of how resolved they would be with the longest baselines of the CHARA Array. Recently, angular diameters of a few dozen main sequence stars measured with the Palomar Testbed Interferometer (PTI) were released in van Belle & von Braun (2009). This work provides measurements of 14 stars in common with the CHARA stars measured in this work and is the only alternate source of angular diameter measurements of these stars. The longest baseline obtainable with PTI is 110 m, a factor of three shorter than those of the CHARA Array, and accurate measurements are quite difficult with this instrument due to the small angular sizes of these stars.

Table 5.2 lists the 14 stars in common with the van Belle & von Braun (2009) work, the limb darkened angular diameters and errors, and how many σ the two values differ from each other. For these stars, the errors on the PTI angular diameters are anywhere from 2−12 times (with an average of 6.5 times) the errors on the CHARA angular diameters presented here. However, this comparison can still point to any systematic offsets in the results from each instrument. Comparing the angular diameters from this work and van Belle & von Braun (2009), I find that the weighted mean ratio of CHARA to PTI diameters is $\overline{\theta_{\rm CHARA}/\theta_{\rm PTI}} = 1.052 \pm 0.062$. van Belle & von Braun (2009) make this same comparison of their diameters compared to diameters from Baines et al. (2008), who used the CHARA Array to measure the diameters of exoplanet host stars, and find that the ratio of the four stars they have in common is $\overline{\theta_{\rm CHARA}/\theta_{\rm PTI}} = 1.06 \pm 0.06$, very similar to the results found here, indicating again that there is a slight preference for smaller PTI diameters, and larger

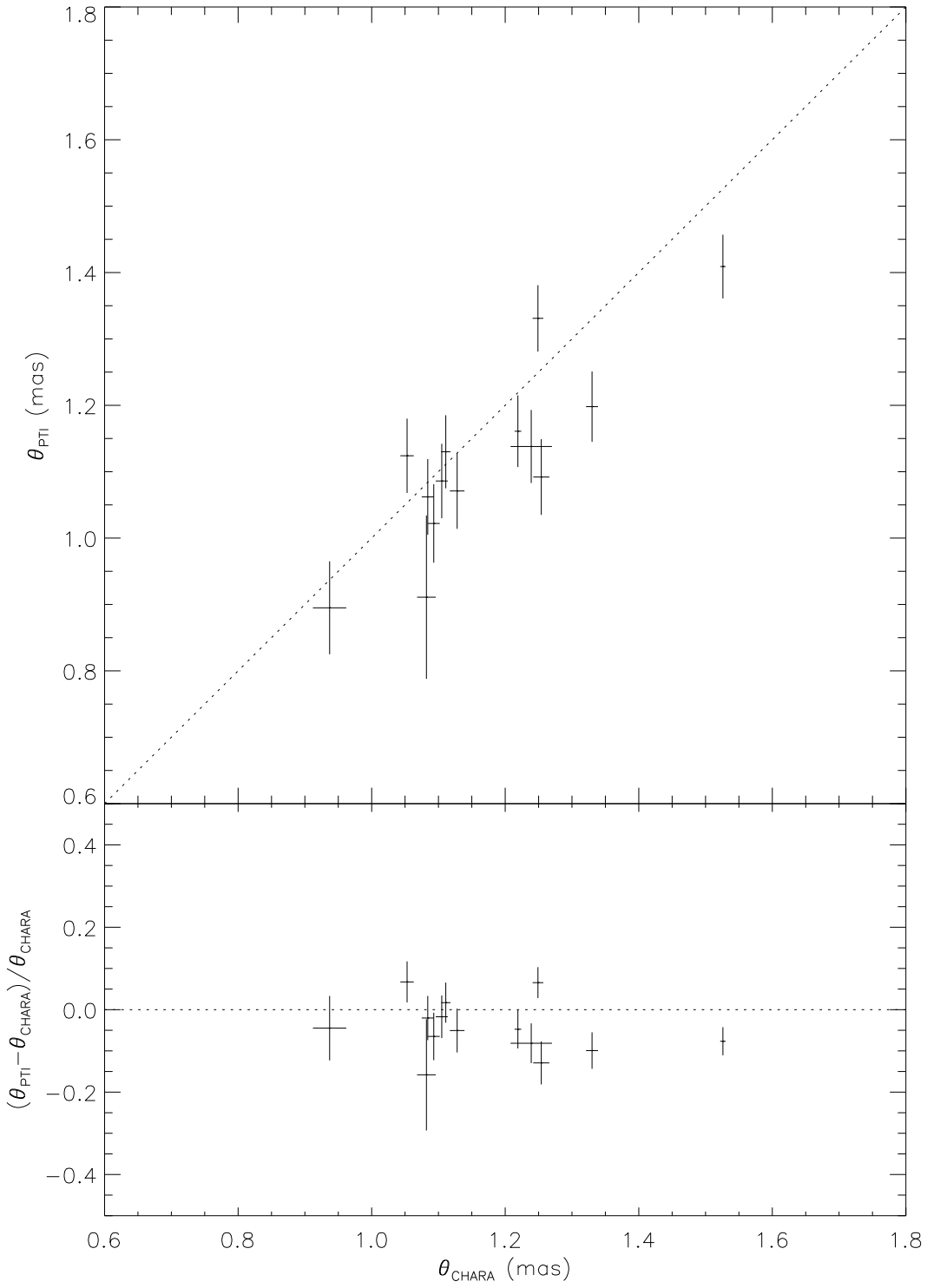

FIGURE 5.3: **CHARA Versus PTI Diameters:** TOP: Plot of CHARA versus PTI limb-darkened angular diameters for the stars in common from this work (CHARA) and van Belle & von Braun (2009) (PTI). The dotted line shows a 1:1 ratio. BOTTOM: Plot showing the fractional difference between the CHARA and PTI limb-darkened angular diameters. The dotted line shows an equal agreement of both measurements.

CHARA diameters. Figure 5.3 shows this comparison in a graphical representation for the stars in common in each work, where most of the stars fall below the 1:1 line, but typically agree within 1-σ of each other.

This is also seen in Boyajian et al. (2009), where I measure the diameters of the four Hyades giants with the CHARA Array. In that work, two of the stars, ϵ Tau and δ^1 Tau, were measured previously with other interferometers (Mark III, NPOI, and PTI), all which lead to smaller diameters than those measured with CHARA. However, we find that models for the Hyades age and metallicity match flawlessly with the CHARA observations, and the smaller angular diameters from other works in turn lead to temperatures that are much too hot for these stars.

A main distinction that could lead to offsets in measured diameters are the estimated sizes of the calibrator stars. van Belle & von Braun (2009) also discuss their calibrator selection in their work compared to Baines et al. (2008). van Belle & von Braun (2009) set a limit to a sufficiently unresolved calibrator at CHARA to be < 0.5 mas in diameter, a criterion which all but a few calibrators in this work meet. The stars that were observed with calibrators > 0.5 mas were also observed with calibrators < 0.5 mas in order to catch any inconsistencies in the calibration process. The reality of this $<$ 1-σ systematic displacement is questionable.

To investigate the possibility that the estimated size of the calibrators in this work are offset to the calibrators used in van Belle & von Braun (2009), I compare the estimated sizes of the calibrators in the *Palomar Testbed Interferometer Calibrator Catalog* (PTICC, van Belle et al. 2008) to the ones derived here. Twenty-nine of the 63 calibrators used in

this work are included in the PTICC. Overall, the ratio of the estimated diameter of the calibrator in this work to the PTICC is 0.97 ± 0.06, a less than 1-σ difference.

Twelve of the 14 stars in common with both works were observed with calibrators whose diameters are also included in the PTICC. For each of these 12 calibrators, the estimated angular diameter $\theta_{\rm SED}$ is presented in Table 5.3, along with the ratio of the CHARA to PTI SED diameters. The object that the calibrator was observed with is also listed in Table 5.3 along with the ratio of the CHARA to PTI measured limb darkened diameters. Here, there is no pattern in the calibrator SED diameter ratio and the object diameter ratio. In fact, the effects of a slight offset in the calibrator's estimated diameter listed above (ratio $\theta_{\rm CHARA}/\theta_{\rm PTI} = 0.97 \pm 0.06$) would actually contribute counterproductively to the slight offset in the diameter measurements (ratio $\theta_{\rm CHARA}/\theta_{\rm PTI} = 1.05 \pm 0.06$). For instance, for the case of my data, the size of the calibrator $\theta_{\rm SED}$ is typically smaller, thus the true visibility of the calibrator would be bigger (i.e., it would be more unresolved). If the true visibility of the calibrator is bigger, it would in turn make the true visibility of the object bigger in the calibration process (see Equation 3.1). Thus, the object would appear more unresolved (having larger calibrated visibilities) if I were using a SED diameter of the same calibrator but with a larger value. Because we do not see the case of smaller CHARA diameters, then this indicates that the calibrators are not the cause of any offset, if present, in each data set.

5.3 Systematics of CHARA Versus Other OLBI Diameters

The diameters measured in this project are $\sim 5\%$ larger than what is expected from SED fits, as well as compared to the measurements of some of the same stars in van Belle & von

Braun (2009). Here, we utilize a version of the surface brightness relation (for example, see Kervella et al. 2004a) to compare the diameters measured with CHARA Classic to diameters measured with other Optical Long Baseline Interferometry (OLBI) to determine whether there are systematic differences in our measurements. On this relation:

$$5 \log \theta_{\rm LD} = -(K_{\rm Obs} - \Delta K_{T_{\rm EFF}}) + C \tag{5.4}$$

the $\theta_{\rm LD}$ is the limb-darkened angular diameter, $K_{\rm Obs}$ is the observed K magnitude, and C is the constant relating your measured K magnitude to the angular diameter. The term $\Delta K_{T_{\rm EFF}} = K_{T_{\rm EFF}} - K_{\rm 10kK}$ are the Kurucz model K magnitudes including a temperature correction term relative to a 10 kK, $\log g = 4.5$ star.

The big problem is getting good K mags for bright stars, since the $2MASS$ mags are saturated and unreliable. However, there is an old Two-Micron Sky Survey[1] that is good for northern targets to $K < 3$ mags (Neugebauer & Leighton 1969). Thus, the collection of interferometric diameters used for this fit includes only BAFGK dwarfs with $T_{\rm EFF} > 5000$ (so that the Kurucz relation is valid) and with $K < 3$ mags (so they are listed in Neugebauer & Leighton 1969). There are 55 stars that meet this criteria, and Figure 5.4 shows the plot ($K - \Delta K_{T_{\rm EFF}}$, $5 \log \theta_{\rm LD}$). The solution for the fit of Equation 5.4 finds a mean trend for a constant $C = 2.49626$. We can see that CHARA Classic (the set of stars in this work) is a little high, but falls well within 1 σ of the constant. The PTI values are on the low side, but also within 1 σ of the constant. Note that the single SUSI point for β Vir is probably

[1]made at Mount Wilson; http://vizier.cfa.harvard.edu/viz-bin/VizieR?-source=II/2B

not meaningful since the errors here are dominated by its K mag (± 0.06 mag), so it is likely within errors of the main trend.

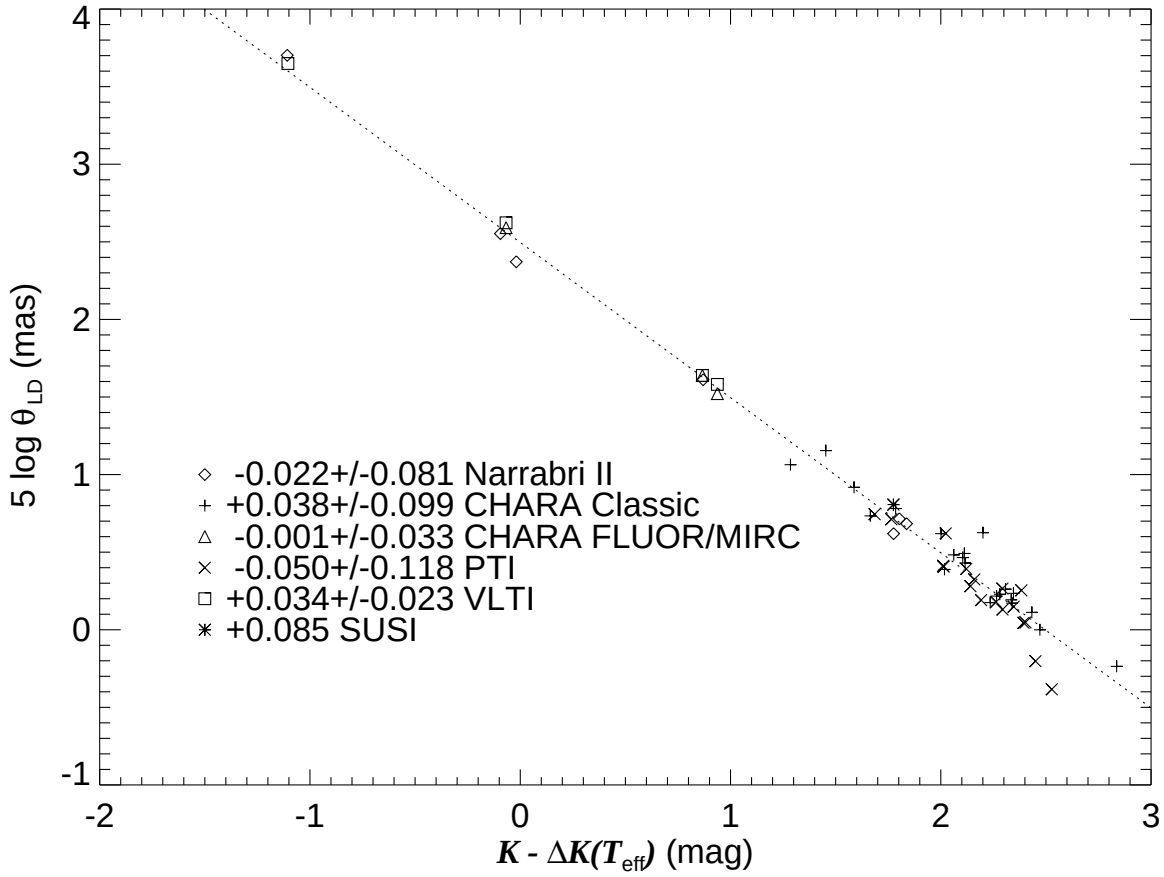

FIGURE 5.4: **Offsets in Various OLBI Data Sets:** Plot showing the solution to the relation in Equation 5.4 for a constant $C = 2.49626$ (dotted line). The legend presents the symbols indicating data sets from each OLBI, and the relative offset and standard deviation to this constant for each data set.

TABLE 5.1: Angular Diameters

Star HD	$T_{\rm EFF}$ † **(K)**	$\log g$ † **(cgs)**	μ_λ	$\theta_{\rm SED}$ **(mas)**	$\theta_{\rm UD}$ **(mas)**	$\theta_{\rm LD}$ **(mas)**	$\theta_{\rm LD}$ **% error**	**Radius** ($R_\odot$)
4614	6000	4.4	0.255	1.656 ± 0.076	1.592 ± 0.004	1.632 ± 0.004	0.2	1.044 ± 0.004
5015	6250	4.0	0.239	0.771 ± 0.019	0.850 ± 0.010	0.866 ± 0.010	1.2	1.746 ± 0.023
6582	5450	4.5	0.287	0.973 ± 0.127	0.951 ± 0.009	0.973 ± 0.009	0.9	0.791 ± 0.008
10780	5650	4.5	0.276	0.659 ± 0.016	0.747 ± 0.018	0.763 ± 0.019	2.5	0.819 ± 0.024
16895	6200	4.5	0.246	1.127 ± 0.047	1.082 ± 0.009	1.105 ± 0.009	0.8	1.322 ± 0.011
19373	6150	4.3	0.246	1.130 ± 0.034	1.222 ± 0.007	1.249 ± 0.008	0.6	1.415 ± 0.009
20630	5850	4.5	0.265	0.914 ± 0.039	0.918 ± 0.024	0.937 ± 0.025	2.7	0.922 ± 0.025
22484	6050	4.0	0.249	1.092 ± 0.029	1.060 ± 0.014	1.082 ± 0.014	1.3	1.625 ± 0.024
30652	6600	4.5	0.227	1.477 ± 0.042	1.494 ± 0.004	1.526 ± 0.004	0.3	1.325 ± 0.004
34411	5850	4.5	0.265	1.000 ± 0.049	0.961 ± 0.015	0.982 ± 0.015	1.5	1.334 ± 0.020
39587	6100	4.5	0.251	1.013 ± 0.031	1.031 ± 0.009	1.053 ± 0.010	0.9	0.981 ± 0.009
48682	6350	4.3	0.236	0.606 ± 0.014	0.825 ± 0.012	0.841 ± 0.012	1.4	1.511 ± 0.023

Continued on Next Page...

TABLE 5.1 – Continued

Star HD	$T_{\rm EFF}$ † **(K)**	$\log g$ † **(cgs)**	μ_λ	$\theta_{\rm SED}$ **(mas)**	$\theta_{\rm UD}$ **(mas)**	$\theta_{\rm LD}$ **(mas)**	$\theta_{\rm LD}$ **% error**	**Radius** $(R_\odot)$
48737	6550	3.8	0.222	1.366 ± 0.025	1.375 ± 0.009	1.402 ± 0.010	0.7	2.715 ± 0.021
56537	9000	4.0	0.166	0.673 ± 0.030	0.827 ± 0.013	0.838 ± 0.013	1.6	2.784 ± 0.048
58946	6600	4.3	0.225	0.952 ± 0.050	0.840 ± 0.013	0.855 ± 0.014	1.6	1.659 ± 0.038
81937	7000	4.0	0.209	1.016 ± 0.041	1.312 ± 0.042	1.334 ± 0.043	3.2	3.496 ± 0.078
82328	6400	4.0	0.231	1.586 ± 0.039	1.671 ± 0.050	1.702 ± 0.051	3.0	2.467 ± 0.074
82885	5550	4.5	0.281	0.797 ± 0.023	0.806 ± 0.013	0.824 ± 0.013	1.6	1.008 ± 0.016
86728	5850	4.3	0.263	0.694 ± 0.022	0.755 ± 0.012	0.771 ± 0.013	1.7	1.247 ± 0.021
90839	6400	4.3	0.234	0.731 ± 0.025	0.782 ± 0.014	0.796 ± 0.014	1.8	1.093 ± 0.020
97603	8150	4.0	0.190	1.267 ± 0.051	1.309 ± 0.009	1.330 ± 0.009	0.7	2.563 ± 0.020
101501	5650	4.6	0.277	0.805 ± 0.037	0.890 ± 0.009	0.911 ± 0.009	1.0	0.941 ± 0.010
102870	6150	4.2	0.245	1.419 ± 0.029	1.401 ± 0.006	1.433 ± 0.006	0.4	1.684 ± 0.008
103095	5500	4.5	0.284	0.594 ± 0.011	0.677 ± 0.008	0.692 ± 0.008	1.2	0.677 ± 0.008
109358	6100	4.5	0.251	1.077 ± 0.041	1.214 ± 0.030	1.239 ± 0.031	2.5	1.125 ± 0.028
114710	6150	4.5	0.248	1.057 ± 0.026	1.105 ± 0.011	1.128 ± 0.011	1.0	1.107 ± 0.011
118098	8800	4.0	0.170	0.777 ± 0.031	0.849 ± 0.014	0.860 ± 0.014	1.6	2.102 ± 0.036
126660	6450	4.0	0.229	1.020 ± 0.023	1.090 ± 0.007	1.111 ± 0.007	0.6	1.735 ± 0.011
128167	6650	4.4	0.224	0.818 ± 0.038	0.827 ± 0.013	0.842 ± 0.013	1.5	1.434 ± 0.023
131156	5500	4.5	0.284	1.256 ± 0.096	1.168 ± 0.014	1.196 ± 0.014	1.2	0.863 ± 0.011
141795	8250	4.2	0.188	0.728 ± 0.032	0.759 ± 0.017	0.770 ± 0.017	2.2	1.789 ± 0.040
142860	6450	4.3	0.231	1.159 ± 0.036	1.195 ± 0.005	1.219 ± 0.005	0.4	1.475 ± 0.007
146233	6050	4.5	0.253	0.601 ± 0.013	0.766 ± 0.017	0.781 ± 0.017	2.2	1.167 ± 0.026
162003	6650	4.0	0.221	0.753 ± 0.023	0.853 ± 0.028	0.868 ± 0.029	3.3	2.131 ± 0.074
164259	6800	4.0	0.215	0.710 ± 0.019	0.764 ± 0.027	0.776 ± 0.027	3.5	1.967 ± 0.071
173667	6650	4.0	0.221	0.892 ± 0.021	0.983 ± 0.009	1.000 ± 0.009	0.9	2.066 ± 0.021
177724	9950	4.0	0.154	0.790 ± 0.027	0.887 ± 0.016	0.897 ± 0.017	1.9	2.457 ± 0.047
182572	5400	4.5	0.290	1.009 ± 0.070	0.823 ± 0.024	0.842 ± 0.024	2.9	1.374 ± 0.040
185144	5550	4.5	0.281	1.118 ± 0.062	1.224 ± 0.012	1.254 ± 0.012	1.0	0.776 ± 0.007
185395	6900	4.0	0.212	0.732 ± 0.029	0.848 ± 0.015	0.862 ± 0.015	1.7	1.699 ± 0.030
210418	8550	4.0	0.177	0.740 ± 0.035	0.852 ± 0.017	0.864 ± 0.018	2.1	2.629 ± 0.083
213558	9350	4.2	0.160	0.594 ± 0.034	0.628 ± 0.021	0.635 ± 0.021	3.3	2.197 ± 0.076
215648	6350	4.1	0.235	1.015 ± 0.032	1.072 ± 0.008	1.093 ± 0.009	0.8	1.915 ± 0.016
222368	6350	4.0	0.234	1.032 ± 0.030	1.063 ± 0.009	1.084 ± 0.009	0.8	1.598 ± 0.014

†Kurucz model estimates for SED fit.

TABLE 5.2: CHARA Versus PTI Angular Diameters

HD	**CHARA** $\theta_{\rm LD} \pm \sigma$	**error** (%)	**PTI** $\theta_{\rm LD} \pm \sigma$	**error** (%)	$\Delta\theta_{\rm LD}/\sigma_{\rm C}$ †
16895	1.105 ± 0.009	0.8	1.086 ± 0.056	5.2	0.3
19373	1.249 ± 0.008	0.6	1.331 ± 0.050	3.8	−1.6
20630	0.937 ± 0.025	2.7	0.895 ± 0.070	7.8	0.6
22484	1.082 ± 0.014	1.3	0.911 ± 0.123	13.5	1.4
30652	1.526 ± 0.004	0.3	1.409 ± 0.048	3.4	2.4
39587	1.053 ± 0.010	0.9	1.124 ± 0.056	5.0	−1.2
97603	1.330 ± 0.009	0.7	1.198 ± 0.053	4.4	2.5
109358	1.239 ± 0.031	2.5	1.138 ± 0.055	4.8	1.6
114710	1.128 ± 0.011	1.0	1.071 ± 0.057	5.3	1.0
126660	1.111 ± 0.007	0.6	1.130 ± 0.055	4.9	−0.3

Continued on Next Page...

TABLE 5.2 – Continued

HD	CHARA $\theta_{LD} \pm \sigma$	error (%)	PTI $\theta_{LD} \pm \sigma$	error (%)	$\Delta\theta_{LD}/\sigma_C$ †
142860	1.219 ± 0.005	0.4	1.161 ± 0.054	4.7	1.1
185144	1.254 ± 0.012	1.0	1.092 ± 0.057	5.2	2.8
215648	1.093 ± 0.009	0.8	1.022 ± 0.059	5.8	1.2
222368	1.084 ± 0.009	0.8	1.062 ± 0.057	5.4	0.4

†Here, $\Delta\theta_{LD}$ is the difference between PTI and CHARA limb darkened angular diameters, and σ_C is the combined error, $\sigma_C = (\sigma^2_{CHARA} + \sigma^2_{PTI})^{0.5}$.

TABLE 5.3: CHARA Versus PTI Calibrators

Calibrator HD	CHARA θ_{SED} (mas)	PTI θ_{SED} (mas)	Calibrator SED $\theta_{CHARA}/\theta_{PTI}$	Object HD	Object Measured $\theta_{CHARA}/\theta_{PTI}$
20675	0.415±0.012	0.424±0.020	0.98±0.05	16895	1.02±0.05
20675	0.415±0.012	0.424±0.020	0.98±0.05	19373	0.94±0.04
22879	0.342±0.021	0.369±0.009	0.93±0.06	20630	1.05±0.09
22879	0.342±0.021	0.369±0.009	0.93±0.06	22484	1.19±0.16
28355	0.425±0.030	0.401±0.012	1.06±0.08	30652	1.08±0.04
30739	0.461±0.018	0.544±0.025	0.85±0.05	30652	1.08±0.04
31295	0.439±0.043	0.470±0.022	0.93±0.10	30652	1.08±0.04
38558	0.422±0.008	0.442±0.033	0.95±0.07	39587	0.94±0.05
43042	0.591±0.030	0.655±0.017	0.90±0.05	39587	0.94±0.05
99285	0.456±0.017	0.454±0.026	1.00±0.07	97603	1.11±0.05
110897	0.492±0.022	0.504±0.009	0.98±0.05	109358	1.09±0.06
132254	0.520±0.015	0.542±0.013	0.96±0.04	126660	0.98±0.05
193664	0.494±0.019	0.552±0.011	0.89±0.04	185144	1.15±0.06
211976	0.373±0.013	0.377±0.009	0.99±0.04	215648	1.07±0.06
214923	0.611±0.029	0.552±0.094	1.11±0.20	215648	1.07±0.06
216735	0.321±0.022	0.330±0.020	0.97±0.09	215648	1.07±0.06
216735	0.321±0.022	0.330±0.020	0.97±0.09	222368	1.02±0.06
222603	0.577±0.032	0.533±0.014	1.08±0.07	222368	1.02±0.06

– 6 –

Luminosities and Temperatures

6.1 Luminosities and Temperatures

The absolute luminosity of a star may be determined by several methods. The simplest, and albeit the most model dependent, is the use of bolometric corrections (BCs). For instance, the absolute magnitude of a star at a particular photometric band M_λ is determined by knowing the parallax of the star Π and the apparent magnitude m_λ (what we observe from Earth). The BC is a scalar number that converts this M_λ to compensate for all light not accounted for in the spectrum of that waveband into the bolometric magnitude $M_{\rm BOL}$. The luminosity in solar units (assuming $M_{\rm BOL,\odot} = 4.74$) is then found using the equation:

$$L = 10^{(M_{\rm BOL} - 4.74)/-2.5}. \tag{6.1}$$

However, BCs depend on several stellar parameters not easily determined (such as metallicity and $\log g$) and there exist offsets from one source to the next (see discussion in Torres et al. 1997).

A more thorough method to determine the absolute luminosity of a star is by collecting flux calibrated photometry (or spectrophotometry) covering the entire stellar spectrum. However, this approach is also impractical because it is impossible to measure the flux of a star at all wavelengths of the electromagnetic spectrum. Therefore, models are typically fit

to the available data, and by integrating the flux over the spectrum, the bolometric flux $F_{\rm BOL}$ is determined. Incorporating the distance to the star d, the luminosity is found through:

$$L = F_{\rm BOL} 4\pi d^2. \tag{6.2}$$

For this work, published values of BC and/or $F_{\rm BOL}$ are averaged and used to determine the absolute luminosity of the star. Table 6.1 shows the values for the resulting bolometric flux with each reference and the standard deviation of the values for each star. Interstellar extinction is negligible for all of the stars in the sample due to their close proximity to the Earth. Table 6.2 lists the absolute luminosity L of each of the stars. Errors are added in quadrature, where the standard deviation of the $F_{\rm BOL}$ for each star is applied as well as the *HIPPARCOS* parallax error. For stars with only one measurement of $F_{\rm BOL}$, we apply a 3% error to the flux measurement, which corresponds to the average percentage standard deviation of the other stars with more than one value for $F_{\rm BOL}$.

By measuring the angular diameter of a star, we can calculate the effective temperature in a purely empirical manner. Beginning with the expression of luminosity:

$$L = 4\pi r^2 \sigma T_{\rm EFF}^4 \tag{6.3}$$

we divide both sides of the equation by the square of the distance, which then produces the relation:

$$F_{\rm BOL} = \frac{1}{4}\theta_{\rm LD}^2 \sigma T_{\rm EFF}^4 \tag{6.4}$$

where θ is the angular diameter of the star and σ is the Stefan-Boltzmann constant. Solving for temperature we arrive at the expression:

$$T_{\rm EFF} = 2341(F_{\rm BOL}/\theta^2_{\rm LD})^{\frac{1}{4}} \tag{6.5}$$

where θ is in units of milliarcsec, and $F_{\rm BOL}$ in 10^{-8} erg cm^{-2} s^{-1}. Effective temperatures are found for all stars using Equation 6.5 and are presented in Table 6.2. For the whole sample, I have reached an average error on the effective temperature of 1.2%, where 20 of the stars observed have temperature errors of <1%. My goal to measure temperatures to better than 2% was achieved for all but 2 of the 44 stars (which have errors of 2.1%).

6.2 Discussion of the CHARA Determined Fundamental Parameters

Figure 6.1 through Figure 6.10 show the relationships between all the fundamental quantities measured for the stars in this survey. The information is displayed for parameter pairs with two methods. The first shows the errors of the measurements (for example, see Figure 6.1). The second shows no errors, but has the additional information of either the stellar size or metallicity which is represented as the size or color (respectively) of the data point (for example, see Figure 6.2 or Figure 6.3).

In Figure 6.1 and Figure 6.4, the two most metal poor stars (μ Cas A = HD 6582 and Gmb 1830 = HD 103095), are labeled. In Figure 6.1, where temperature is the x-axis, the two points are not offset from the ZAMS line of the rest of the sample. However, in Figure 6.4, we plot luminosity against the color index ($B-V$), which is much bluer for these

stars because of their low metal abundances. As a result of this, they lie below the ZAMS for the rest of the sample, appearing under-luminous for their apparent $(B-V)$ color index. It is thus safe to say that the use of the color index $(B-V)$ by itself is not a good indicator of a star's effective temperature. Also shown in Figure 6.1 are lines of constant radius from the relation:

$$L = 4\pi r^2 \sigma T_{\rm EFF}^4 \tag{6.6}$$

where stars of the same radius fall on this line on the logarithmic luminosity-temperature plane:

$$\log \frac{L}{L_\odot} = 4 \log \frac{T_{\rm EFF}}{T_{\rm EFF,\odot}} + 2 \log \frac{R}{R_\odot}. \tag{6.7}$$

Evolution within the main sequence band is clearly apparent from these figures. For instance, in Figure 6.2 and Figure 6.5, we can see that in both the $(B-V)$ and temperature dependent plots, there is a significant amount of evolution where the stars evolve to larger radii in the direction of up and to the right on these plots. Figure 6.3 and Figure 6.6 show that the nearby main sequence stars observed in this survey span a range of metallicities at all stages of evolution within the main sequence band. Figure 6.7 demonstrates evolution from the main sequence in a different manner, showing that even the star with the largest radius is not the hottest star in the sample. The spread in these plots due to evolution is remarkable. For instance, in Figure 6.7 and Figure 6.8, at any given point on the x-axis ($T_{\rm EFF}$ or color index), several different values of radius appear, with the error bars close to overlapping (very pronounced at $\log T_{\rm EFF} \approx 3.78$, where there are stars of both 1 $R_\odot$ and

3.5 $R_{\odot}$). Figure 6.9 beautifully shows the thickening of the main sequence with increasing mass (up and right) and consequently accelerated evolution.

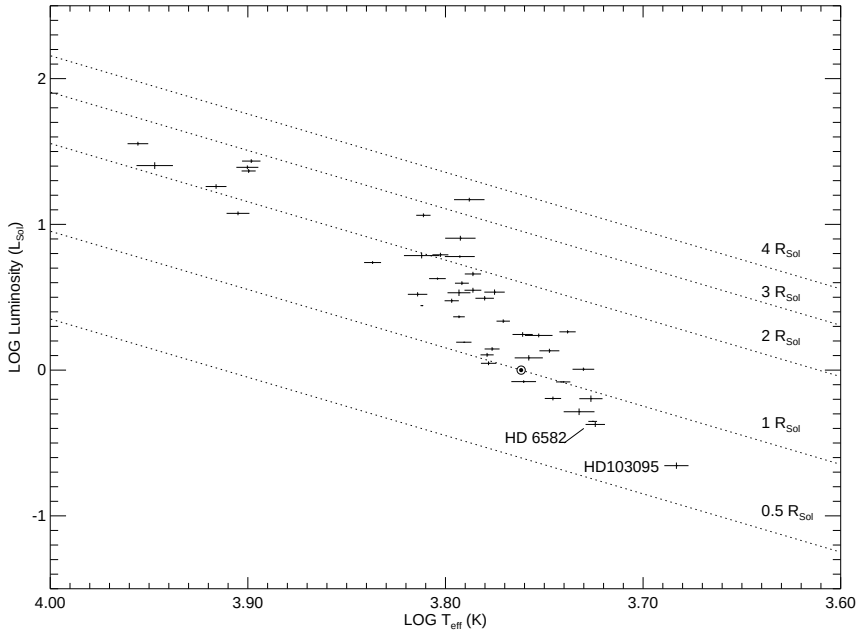

FIGURE 6.1: **CHARA Luminosity Versus Temperature:** The luminosities and temperatures of the stars in the survey are plotted with their 1-σ errors. Lines of constant radii are plotted as dotted lines.

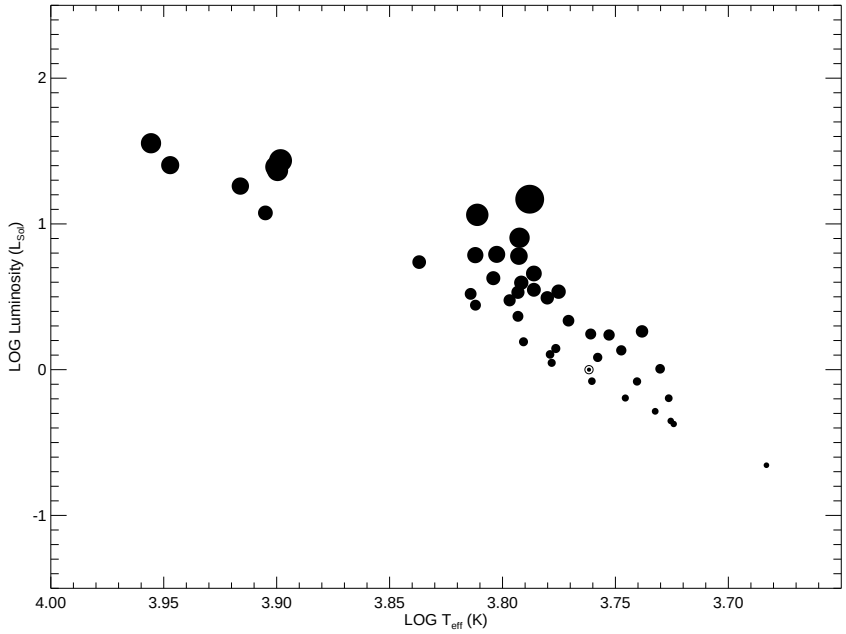

FIGURE 6.2: **CHARA Luminosity Versus Temperature and Radius:** The luminosities and temperatures of the stars in the survey are plotted. The size of the symbol represents the linear radius of the star.

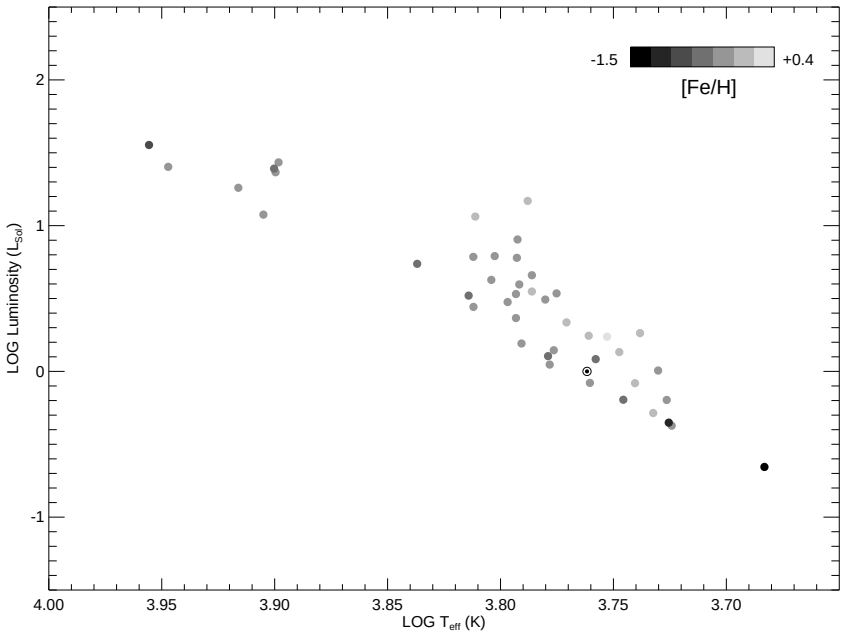

FIGURE 6.3: **CHARA Luminosity Versus Temperature and Metallicity:** The luminosities and temperatures of the stars in the survey are plotted. The shading of the symbols represents the metallicity of the star [Fe/H] from Holmberg et al. (2007). For stars without metallicity estimates from Holmberg et al. (2007), the [M/H] values from Gray et al. (2003, 2006) (HD 82885, HD 97603, HD 118098, HD 131156, HD 177724, HD 210418), and Takeda et al. (2005) (HD 182572) are used. Stars without metallicity measurements have [Fe/H]=0 (HD 56537, HD 141795, HD 213558).

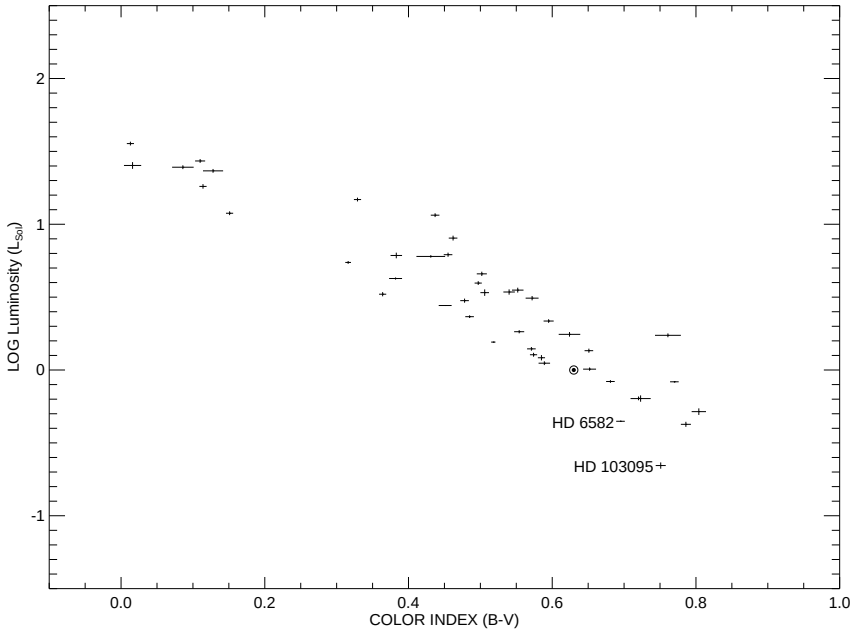

FIGURE 6.4: **CHARA Luminosity Versus $(B-V)$:** The luminosity and color index $(B-V)$ of the stars in the survey are plotted with their 1-σ errors.

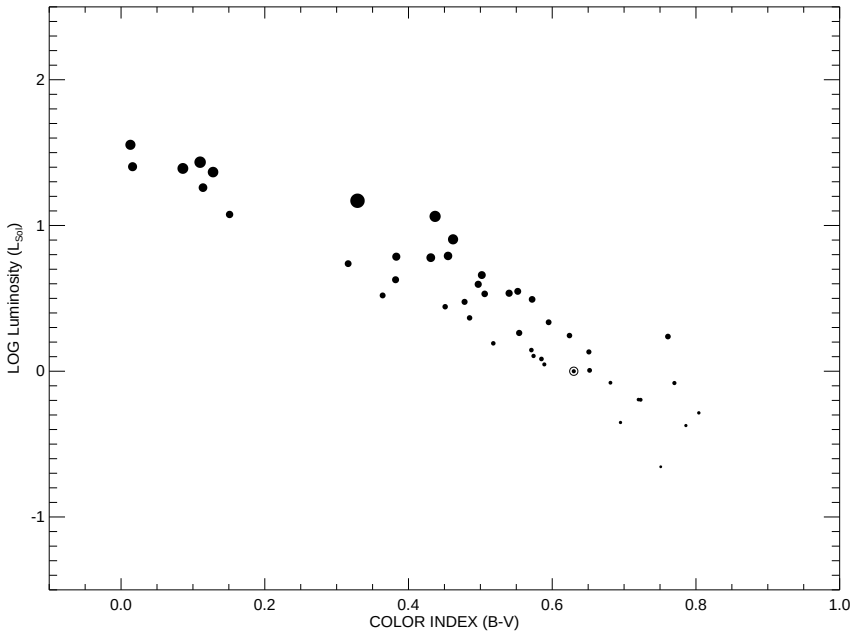

FIGURE 6.5: **CHARA Luminosity Versus $(B-V)$ and Radius:** The luminosity and color index $(B-V)$ of the stars in the survey are plotted. The size of the symbol represents the linear radius of the star.

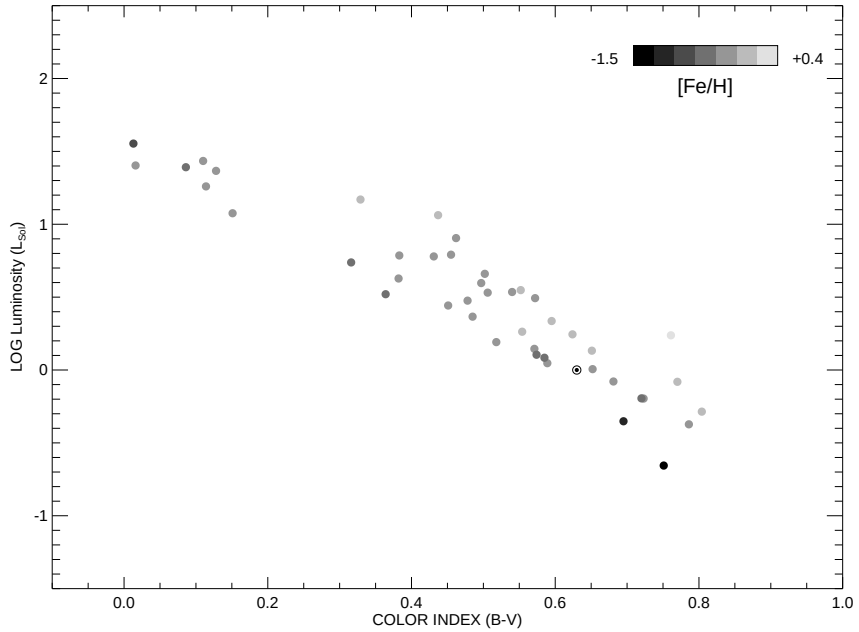

FIGURE 6.6: **CHARA Luminosity Versus $(B-V)$ and Metallicity:** The luminosity and color index $(B-V)$ of the stars in the survey are plotted. The shading of the symbol represents the metallicity of the star [Fe/H] (with the same references as in Figure 6.3).

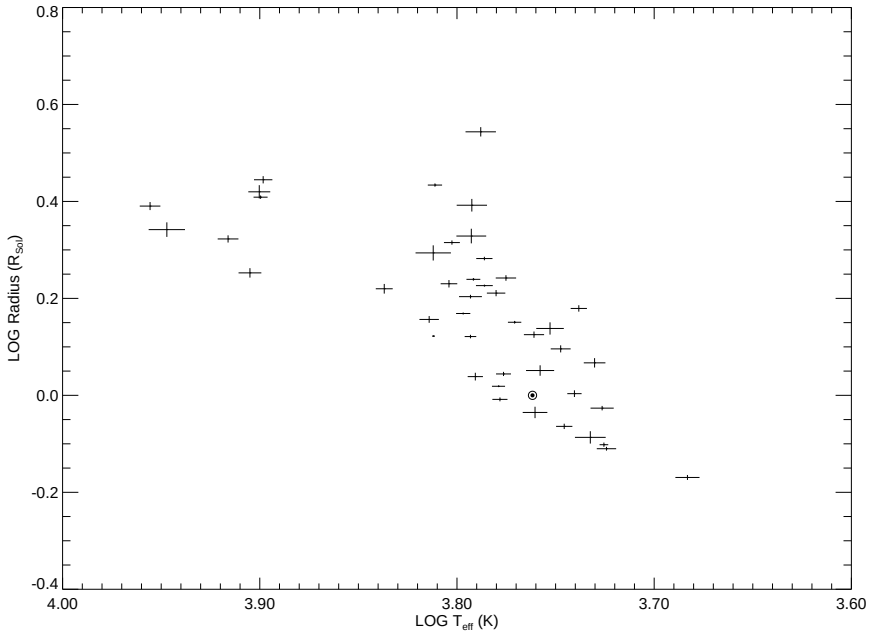

FIGURE 6.7: **CHARA Temperature Versus Radius:** The effective temperatures and radii of the stars in the survey are plotted with their 1-σ errors.

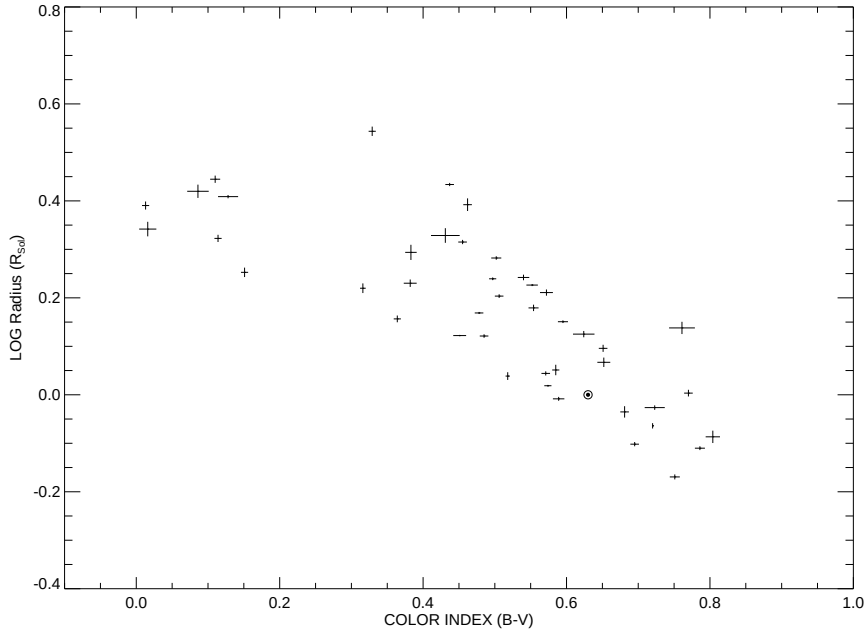

FIGURE 6.8: **CHARA Radius Versus $(B-V)$:** The color index $(B-V)$ and radii of the stars in the survey are plotted with their 1-σ errors.

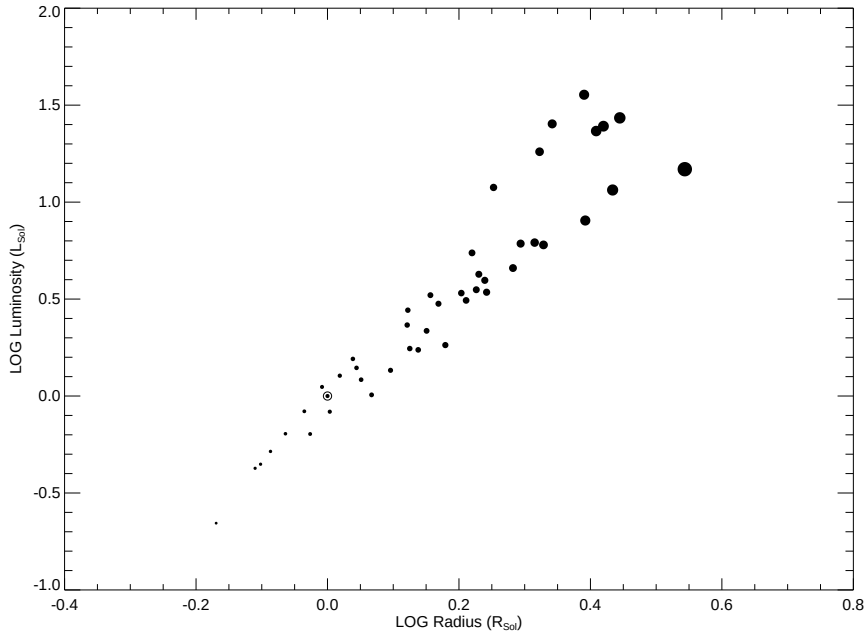

FIGURE 6.9: **CHARA Luminosity Versus Radius:** The absolute luminosities and radii of the stars in the survey are plotted. The symbol size is proportional to the linear radius of the star.

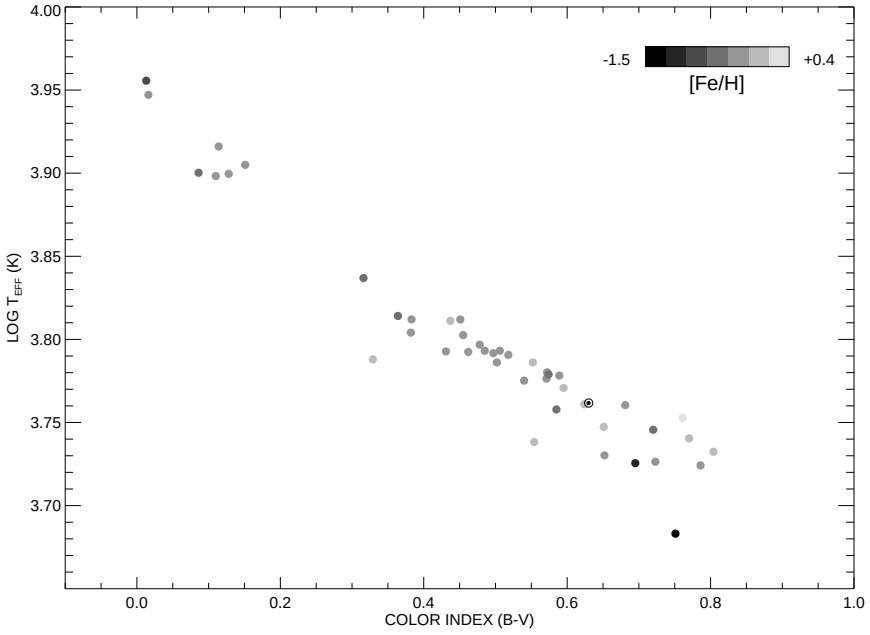

FIGURE 6.10: **CHARA Temperature Versus $(B-V)$ and Metallicity:** The temperature and color index $(B-V)$ of the stars in the survey are plotted. The shading of the symbol represents the metallicity of the star [Fe/H] (with the same references as in Figure 6.3).

TABLE 6.1: Bolometric Fluxes†

Star HD	BLG98††	BG89††	AAMR95, AAMR96††	APL99††	TOSKS05††	Average Flux	Std. Dev. Flux
4614	···	119.3	114.0	111.8	118.2	115.8	3.51
5015	···	···	31.4	30.2	32.8	31.5	1.31
6582	25.0	···	25.3	···	···	25.2	0.21
10780	···	···	15.9	···	17.1	16.5	0.85
16895	···	···	59.7	59.8	62.0	60.5	1.30
19373	64.1	···	63.7	60.9	···	62.9	1.77
20630	32.2	···	31.8	31.7	33.1	32.2	0.68
22484	51.3	···	51.9	49.3	53.5	51.5	1.76
30652	137.8	···	137.0	136.9	···	137.2	0.49
34411	35.2	···	35.1	34.4	37.4	35.5	1.28
39587	···	···	46.4	47.9	49.3	47.9	1.42
48682	···	···	20.8	21.5	···	21.1	0.53
48737	···	···	···	114.9	···	114.9	···
56537	···	···	···	91.6	···	91.6	···
58946	52.8	···	55.2	54.5	···	54.2	1.22
81937	···	···	···	84.0	···	84.0	···
82328	···	···	141.0	138.2	148.8	142.6	5.47
82885	···	···	20.9	···	20.5	20.7	0.24
86728	···	···	19.3	18.7	20.0	19.3	0.63
90839	···	···	30.6	30.8	···	30.7	0.15
97603	···	···	···	233.6	···	233.6	···
101501	···	23.2	21.0	···	22.5	22.2	1.12
102870	95.9	···	94.2	91.3	100.1	95.4	3.68
103095	8.3	···	8.4	···	9.1	8.6	0.44
109358	···	54.1	53.2	···	57.6	55.0	2.33
114710	52.6	55.1	52.4	54.0	56.0	54.0	1.56
118098	116.6	···	···	110.8	···	113.7	4.12
126660	···	···	···	60.3	···	60.3	···
128167	40.9	···	43.3	42.1	44.1	42.6	1.41
131156	···	···	···	···	45.8	45.8	···
141795	···	···	···	82.3	···	82.3	···
142860	···	···	75.9	73.9	78.8	76.2	2.47
146233	···	···	16.6	17.2	···	16.9	0.44
162003	···	···	37.7	36.7	···	37.2	0.73
164259	···	···	36.6	34.4	···	35.5	1.59
173667	53.2	···	53.8	52.5	56.6	54.0	1.76
177724	···	···	···	178.0	···	178.0	···
182572	24.5	···	23.7	23.6	25.1	24.2	0.73
185144	···	42.5	40.1	···	···	41.3	1.69
185395	40.1	···	41.5	40.6	···	40.7	0.70
210418	···	···	···	99.2	···	99.2	···
213558	···	···	79.4	85.6	···	82.5	4.38
215648	55.7	···	55.6	53.0	57.6	55.5	1.88
222368	···	···	58.7	55.0	60.9	58.2	2.97

†units in 10^{-8} erg cm^{-2} s^{-1}. ††Blackwell & Lynas-Gray (1998) (BLG98), Bell & Gustafsson (1989) (BG89), Alonso et al. (1995, 1996) (AAMR95,AAMR96), Allende Prieto & Lambert (1999) (APL99), Takeda et al. (2005) (TOSKS05).

TABLE 6.2: Luminosities and Temperatures

Star HD	L ($L_\odot$)	$T_{\rm EFF}$ **(K)**	**% error** $T_{\rm EFF}$
4614	1.27 ± 0.04	6011 ± 46	0.8
5015	3.43 ± 0.14	5959 ± 71	1.2
6582	0.445 ± 0.004	5315 ± 27	0.5
10780	0.52 ± 0.03	5400 ± 97	1.8
16895	2.32 ± 0.05	6211 ± 42	0.7
19373	2.17 ± 0.06	5899 ± 46	0.8
20630	0.834 ± 0.018	5760 ± 83	1.4
22484	3.11 ± 0.10	6028 ± 65	1.1
30652	2.7707 ± 0.0098	6486 ± 10	0.2
34411	1.76 ± 0.06	5767 ± 68	1.2
39587	1.11 ± 0.03	6001 ± 53	0.9
48682	1.83 ± 0.05	5473 ± 52	1.0
48737	11.5 ± 0.3	6474 ± 54	0.8
56537	27.2 ± 0.8	7912 ± 85	1.1
58946	5.47 ± 0.12	6869 ± 68	1.0
81937	14.8 ± 0.4	6137 ± 109	1.8
82328	8.0 ± 0.3	6201 ± 110	1.8
82885	0.8300 ± 0.0098	5501 ± 46	0.8
86728	1.36 ± 0.04	5590 ± 65	1.2
90839	1.554 ± 0.008	6176 ± 55	0.9
97603	23.3 ± 0.7	7936 ± 65	0.8
101501	0.64 ± 0.03	5326 ± 72	1.4
102870	3.53 ± 0.13	6111 ± 60	1.0
103095	0.221 ± 0.011	4821 ± 68	1.4
109358	1.21 ± 0.05	5726 ± 94	1.6
114710	1.40 ± 0.04	5976 ± 52	0.9
118098	18.2 ± 0.7	8243 ± 100	1.2
126660	3.95 ± 0.11	6190 ± 50	0.8
128167	3.31 ± 0.11	6518 ± 74	1.1
131156	0.639 ± 0.019	5567 ± 53	1.0
141795	11.9 ± 0.4	8035 ± 107	1.3
142860	2.99 ± 0.09	6264 ± 52	0.8
146233	1.01 ± 0.02	5373 ± 68	1.3
162003	6.02 ± 0.11	6205 ± 108	1.7
164259	6.1 ± 0.3	6487 ± 134	2.1
173667	6.2 ± 0.2	6347 ± 59	0.9
177724	35.8 ± 1.1	9029 ± 109	1.2
182572	1.73 ± 0.05	5660 ± 91	1.6

Continued on Next Page...

TABLE 6.2 – Continued

Star HD	L ($L_\odot$)	$T_{\rm EFF}$ **(K)**	**% error** $T_{\rm EFF}$
185144	0.424 ± 0.017	5299 ± 60	1.1
185395	4.24 ± 0.07	6369 ± 62	1.0
210418	24.6 ± 0.7	7948 ± 102	1.3
213558	25.3 ± 1.3	8854 ± 188	2.1
215648	4.57 ± 0.15	6111 ± 58	0.9
222368	3.39 ± 0.17	6211 ± 83	1.3

– 7 –

Analysis

7.1 Comparative Analysis of Linear Radii

Thirty-seven out of the 44 stars that I observed were also included in the work from Allende Prieto & Lambert (1999). Allende Prieto & Lambert (1999) identified several fundamental parameters by fitting model evolutionary tracks from Bertelli et al. (1994) to observed photometry. The directly determined linear radii found for our stars are compared with the results Allende Prieto & Lambert (1999) in Figure 7.1, where the dotted line indicates the 1:1 ratio of radii (top panel) or 0% difference of radii (bottom panel). We can see that for stars larger than $\approx 1R_{\odot}$, the model radii are under-predicted by an average of $\approx 12\%$ (and up to 28%) of the radius.

Figure 7.2 shows the percent difference in the Allende Prieto & Lambert (1999) radii versus the CHARA radii plotted against metallicity values [Fe/H] from Holmberg et al. (2007). For stars without [Fe/H] measurements from Holmberg et al. (2007), [M/H] abundances are used from Gray et al. (2003, 2006) (HD 97603, HD 118098, HD 177724, HD 210418) and Takeda et al. (2005) (HD 182572). The stars HD 56537, HD 141795, and HD 213558 have no published values of metallicity, and their values are set to zero for this plot. Figure 7.2 shows that only one star above solar metallicity ([Fe/H]=0.0) has an accurately predicted radius from the models used in Allende Prieto & Lambert (1999). The most populated region in this plot ranging from solar metallicity down to [Fe/H]≈ -0.3 has a few stars which do have accurately predicted radii, but most points fall well above the line even in this region.

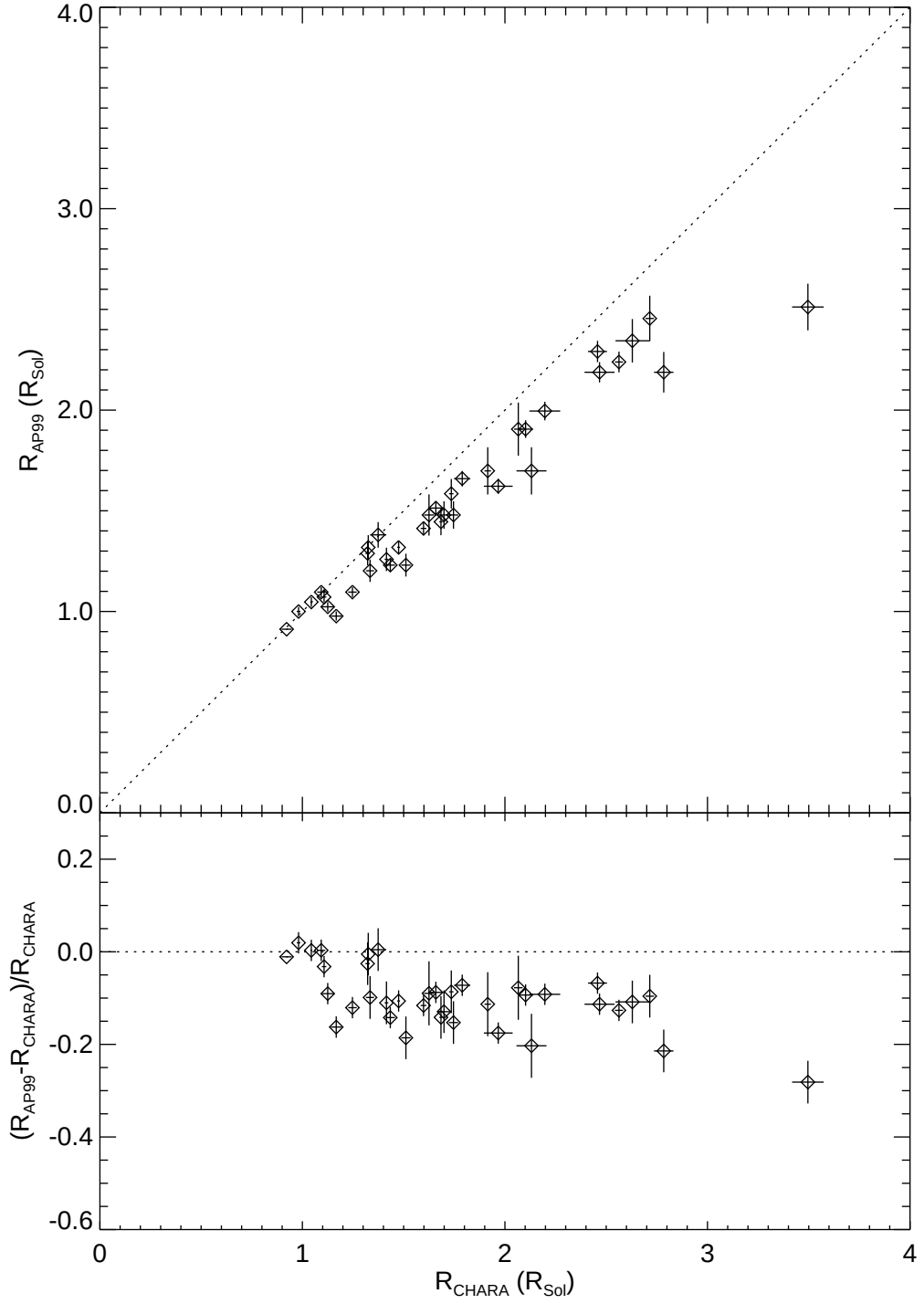

FIGURE 7.1: **Measured Versus Model Radii:** TOP: The data plotted show the difference between model radii determined by Allende Prieto & Lambert (1999) (AP99) and radii measured for this project, along with 1-σ errors for each. The dotted line marks a 1:1 relation between the two values. BOTTOM: The percent difference between model radii determined by Allende Prieto & Lambert (1999) (AP99) and radii measured for this project.

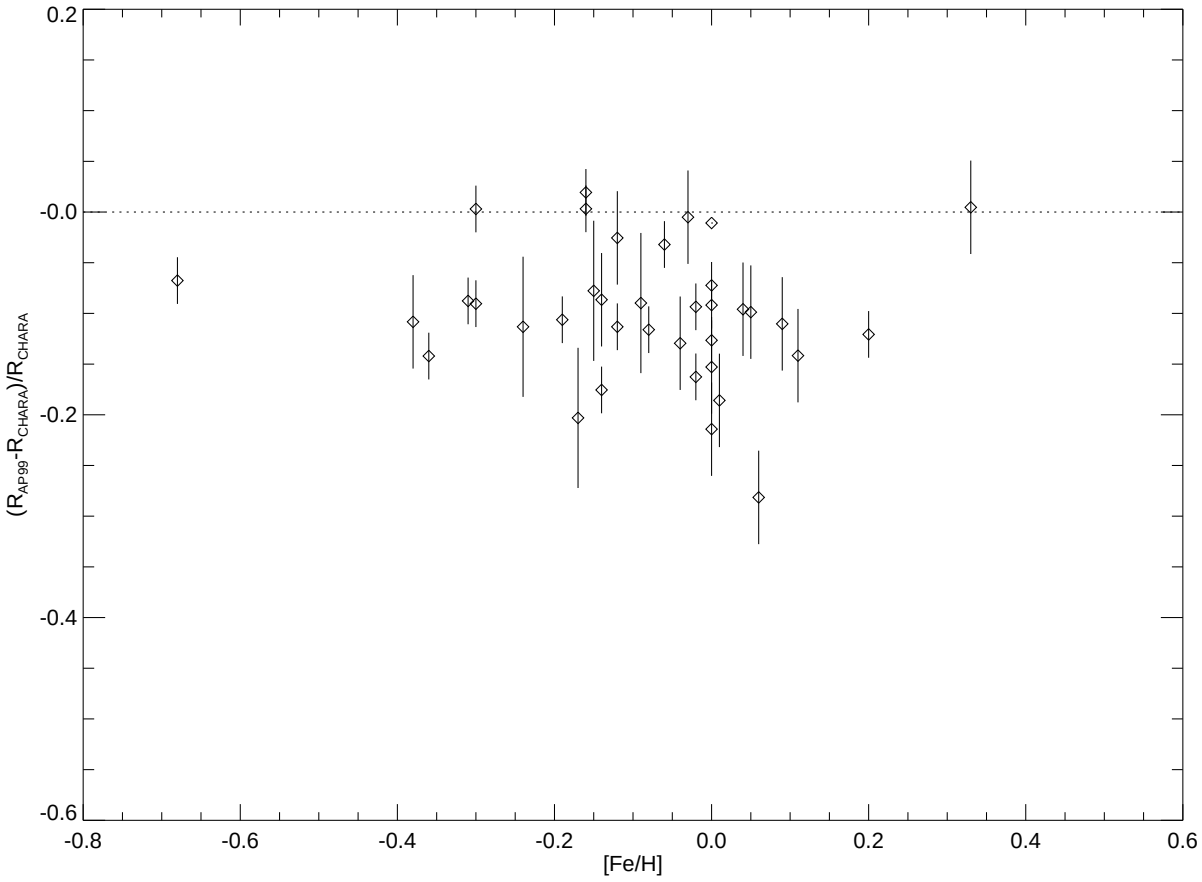

FIGURE 7.2: **Effects of Metallicity on Radii Offsets:** The data plotted show the differences between model radii determined by Allende Prieto & Lambert (1999) (AP99) and radii measured for this project, and the metallicities of the stars. The dotted line marks a 0% difference between the measured and model radii values.

7.2 Comparative Analysis of Effective Temperatures

There are three surveys of nearby stars that I will compare my results to in this analysis: Allende Prieto & Lambert (1999); Holmberg et al. (2007); Takeda (2007). While each of these covers a large number of stars, none encompasses all the stars I have observed with the CHARA Array for this work. The number of stars in common with each survey are 37, 34, and 25 for Allende Prieto & Lambert (1999); Holmberg et al. (2007); Takeda (2007), respectively. Effective temperatures for stars from each of these surveys are compared to my direct measurements and are discussed in the sections to follow.

7.2.1 CHARA Versus Allende Prieto & Lambert (1999)

The new empirical effective temperatures are compared here to those determined by models in Allende Prieto & Lambert (1999), where available. Figure 7.3 shows the relationship between the two temperature determinations, where the dotted line indicates the 1:1 ratio. For most cases seen here, Allende Prieto & Lambert (1999) overestimates the effective temperature of the star through the entire range of effective temperatures by about 5%, up to 15% (Figure 7.4). Figure 7.5 and Figure 7.6 show the dependence on metallicity and $(b-y)$ color index (respectively) of the star versus the fractional offset from each method. It is apparent that neither the metallicity nor the color index influences the offset in temperature.

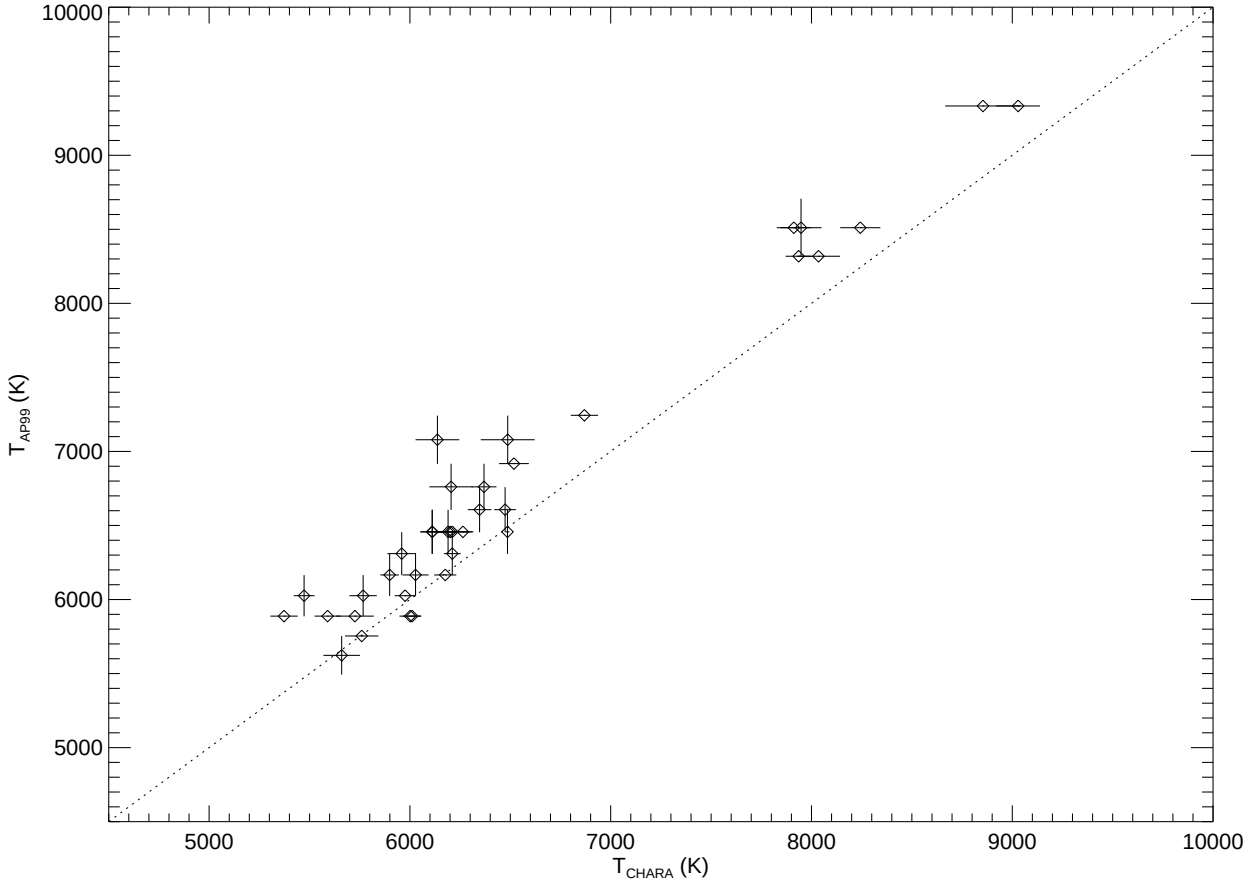

FIGURE 7.3: **Empirical Versus Model Effective Temperatures:** The data plotted show the differences between model temperatures determined by Allende Prieto & Lambert (1999) (AP99) and the empirical values determined in this project. The dotted line marks equal temperatures from each source.

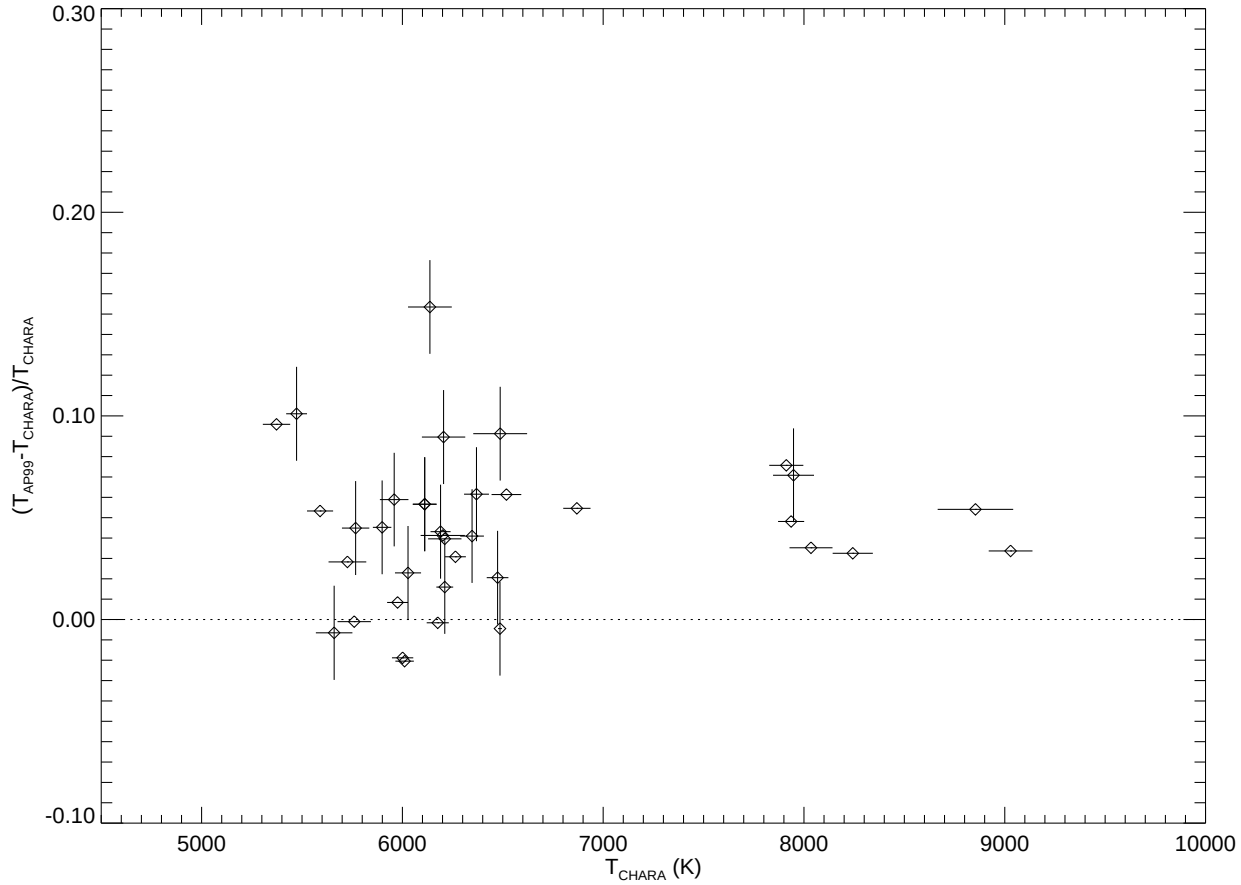

FIGURE 7.4: **Empirical Versus Model Effective Temperatures:** The data plotted show the fractional difference between model temperatures determined by Allende Prieto & Lambert (1999) (AP99) and the empirical values determined in this project.

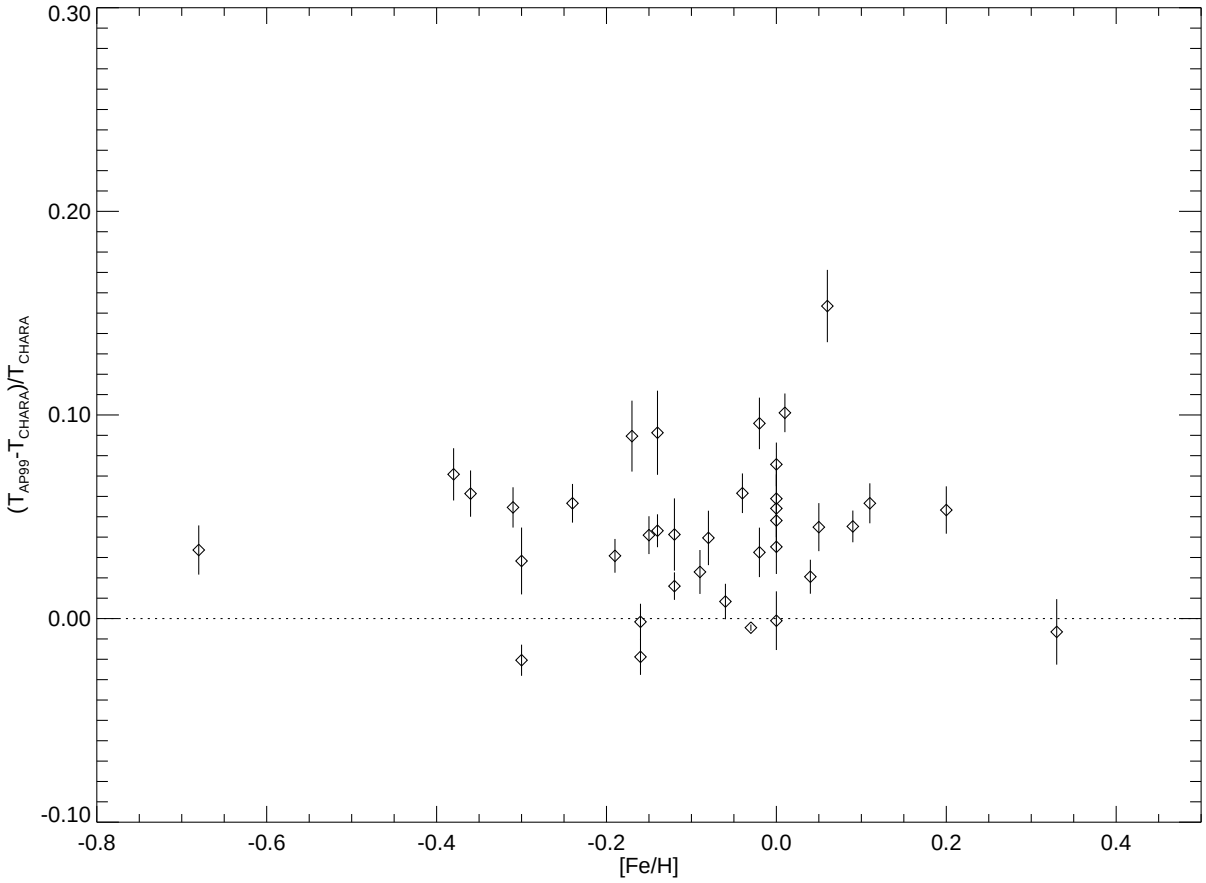

FIGURE 7.5: **Effects of Metallicity on Temperature Offsets:** The data plotted show the differences between model temperatures determined by Allende Prieto & Lambert (1999) (AP99) and the empirical values determined in this project versus metallicity. The dotted line marks a 0% difference between the temperature values from each source.

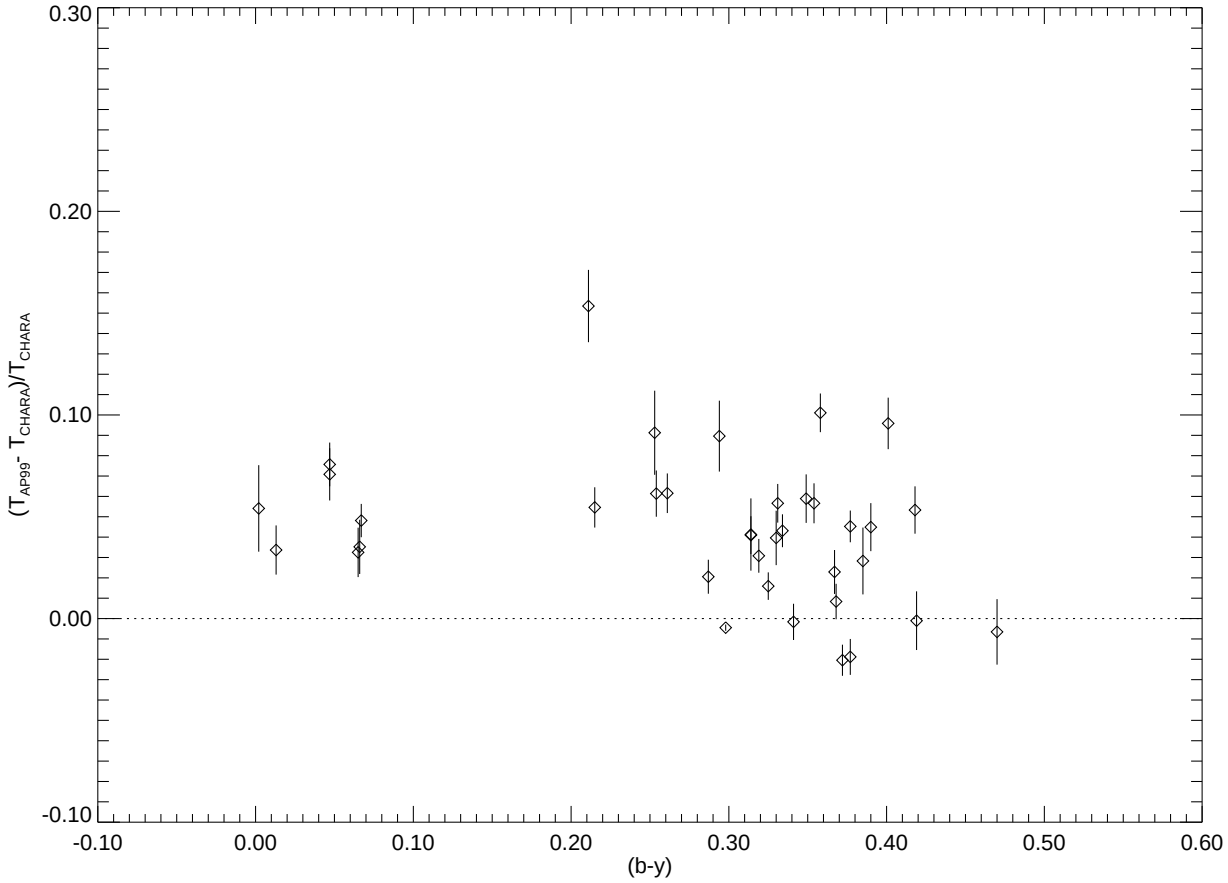

FIGURE 7.6: **Effects of $(b-y)$ on Temperature Offsets:** The data plotted show the differences between model temperatures determined by Allende Prieto & Lambert (1999) (AP99) and the empirical values determined in this project versus $(b-y)$ color index. The dotted line marks a 0% difference between the temperature values from each source.

7.2.2 CHARA Versus Holmberg et al. (2007)

We now compare the temperatures from the Geneva-Copenhagen survey (GC07; Holmberg et al. 2007) to the empirically determined temperatures found here. The stars that are not included in the Holmberg et al. (2007) sample that were observed with CHARA are the A stars HD 56537, HD 97603, HD 118098, HD 141795, HD 177724, HD 210418, and HD 213558, and three G8 stars HD 82885, HD 131156, and HD 182572. Figure 7.7 shows the differences in the effective temperatures of the two data sets (there are no errors given for the GC07 temperatures). The agreement between the two is much better than that with Allende Prieto & Lambert (1999), but there is still a slight trend seen in the temperature offsets of the models to prefer higher temperatures than what we measure with CHARA, with the largest deviation in temperature value of 13% (Figure 7.8). Figure 7.9 shows the fractional deviation between the two values and the dependence on metallicity measured for each source in Holmberg et al. (2007), where again, there is no trend seen in the offset in temperatures of each source due to the metallicity of the star. Figure 7.10 displays the relationship between the $(b-y)$ color index and the fractional temperature offsets, showing again that the color index of the star has no relation to the offset in temperature from models to observations.

The stars with the largest offsets in the effective temperatures are HD 81937 (13%), HD 48682 (10%) and HD 146233 (7%). Interestingly enough, these stars also have high deviations in the SED diameter versus the limb darkened diameter measured with CHARA (See Figure 5.2). However, stars such as HD 10780 and HD 109358 also have high deviation in the SED diameter versus the limb darkened diameter measured with CHARA, but their

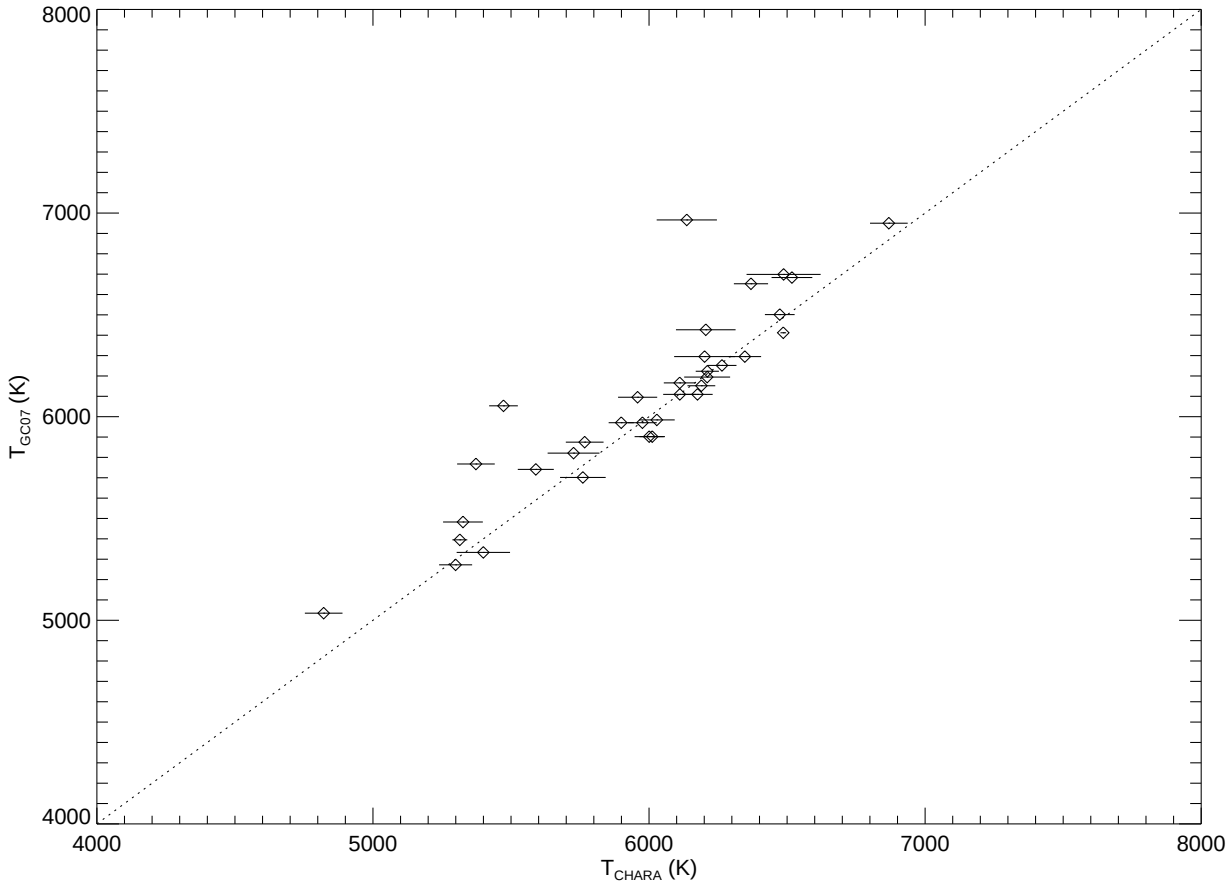

FIGURE 7.7: **Empirical Versus Model Effective Temperatures:** The data plotted show the differences between model temperatures determined by Holmberg et al. (2007) (GC07) and the empirical values determined in this project. The dotted line marks a 1:1 ratio between the temperature values from each source.

agreement with the temperature from Holmberg et al. (2007) is at the ≈1% level. It is interesting to note that the star HD 146233 (18 Sco), that was first identified by Porto de Mello & da Silva (1997) to be a solar twin, is one of these stars with a large offset in effective temperature.

7.2.3 CHARA Versus Takeda (2007)

CHARA stars that do not overlap with the study by Takeda (2007) are HD 19373, HD 48682, HD 48737, HD 56537, HD 58946, HD 81937, HD 90839, HD 97603, HD 118098, HD 126660, HD 146233, HD 162003, HD 164259, HD 177724, HD 210418 and HD 213558. Figure 7.11

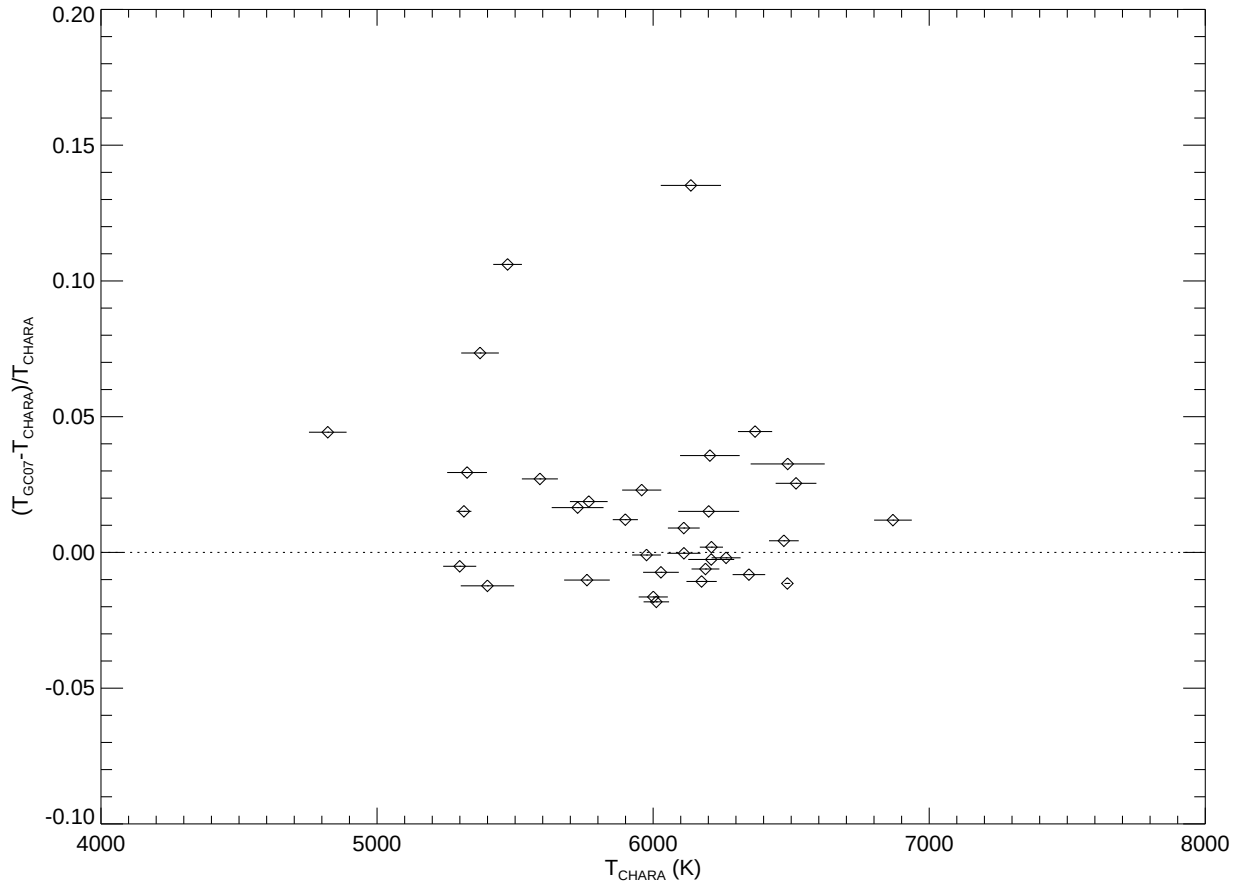

FIGURE 7.8: **Empirical Versus Model Effective Temperatures:** The data plotted show the fractional differences between model temperatures determined by Holmberg et al. (2007) (GC07) and the empirical values determined in this project.

shows the differences in the effective temperatures of the two data sets (there are no errors given for the Takeda 2007 temperatures). The agreement between the two is under the 6% level, much better than that of Allende Prieto & Lambert (1999) and Holmberg et al. (2007), but again temperature estimates from Takeda (2007) are higher than the value we measure with the CHARA Array. The largest outliers in temperature offsets are HD 128167 (6.5%), HD 103095 (5.4%), and HD 86728 (4.3%) (Figure 7.12). Comparing these outliers to the Holmberg et al. (2007) outliers, there are no two stars in each that show large deviations from the model versus CHARA temperature, with the exception of the very metal poor star HD 103095. The metallicities measured in Takeda (2007) are compared to the fractional

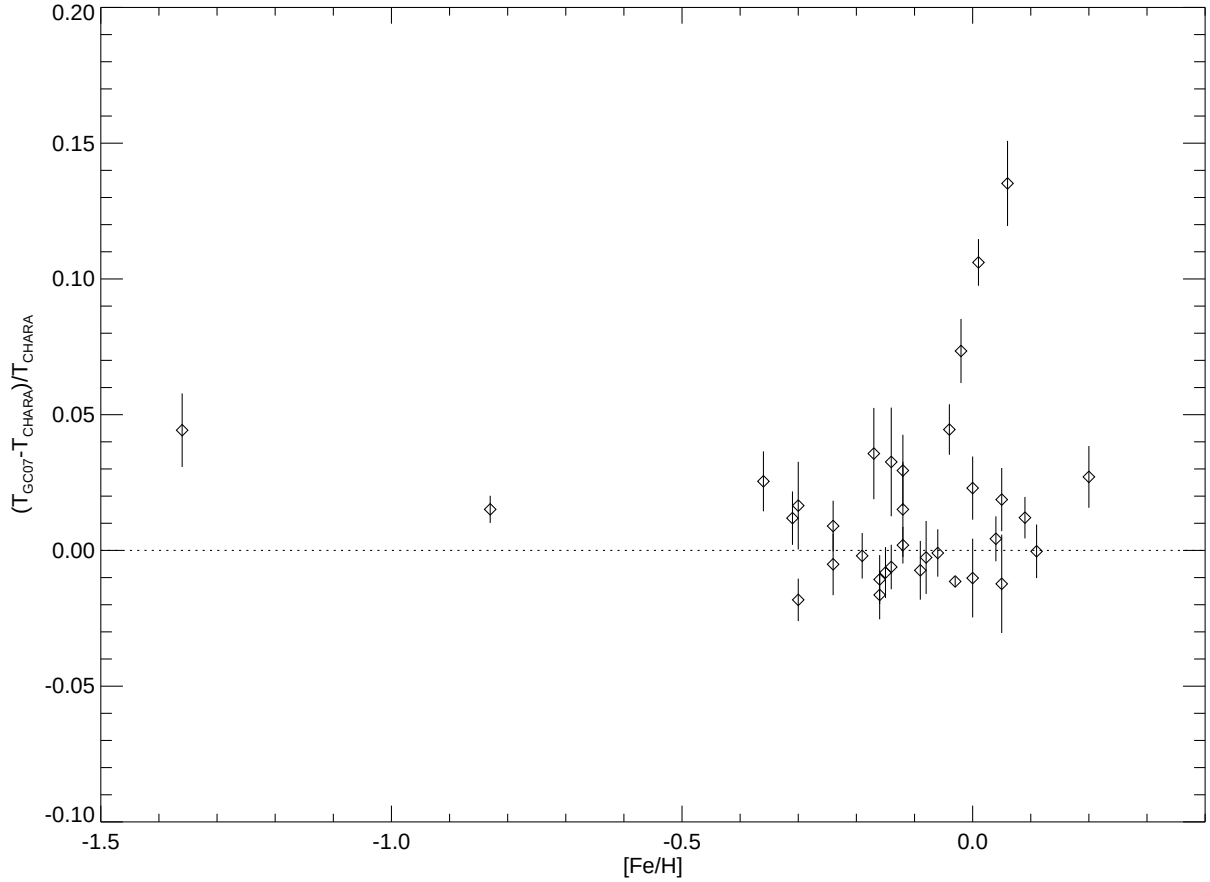

FIGURE 7.9: **Effects of Metallicity on Temperature Offsets:** The data plotted show the differences between model temperatures determined by Holmberg et al. (2007) (GC07) and the empirical values determined in this project versus metallicity. The dotted line marks a 0% difference between the temperature values from each source.

deviation in the temperature values for Takeda (2007) and CHARA in Figure 7.13, and the $(b-y)$ color index is compared to the fractional deviation in the temperature values for Takeda (2007) and CHARA in Figure 7.14. Again, it does not appear that a star's metallicity or color index is related to the deviation in temperatures of each source.

7.3 Model Mass and Age Relations to Measured CHARA Data

The work done by Allende Prieto & Lambert (1999), Holmberg et al. (2007) and Takeda (2007) all use model isochrones to determine the masses and ages of each star. Here, I show

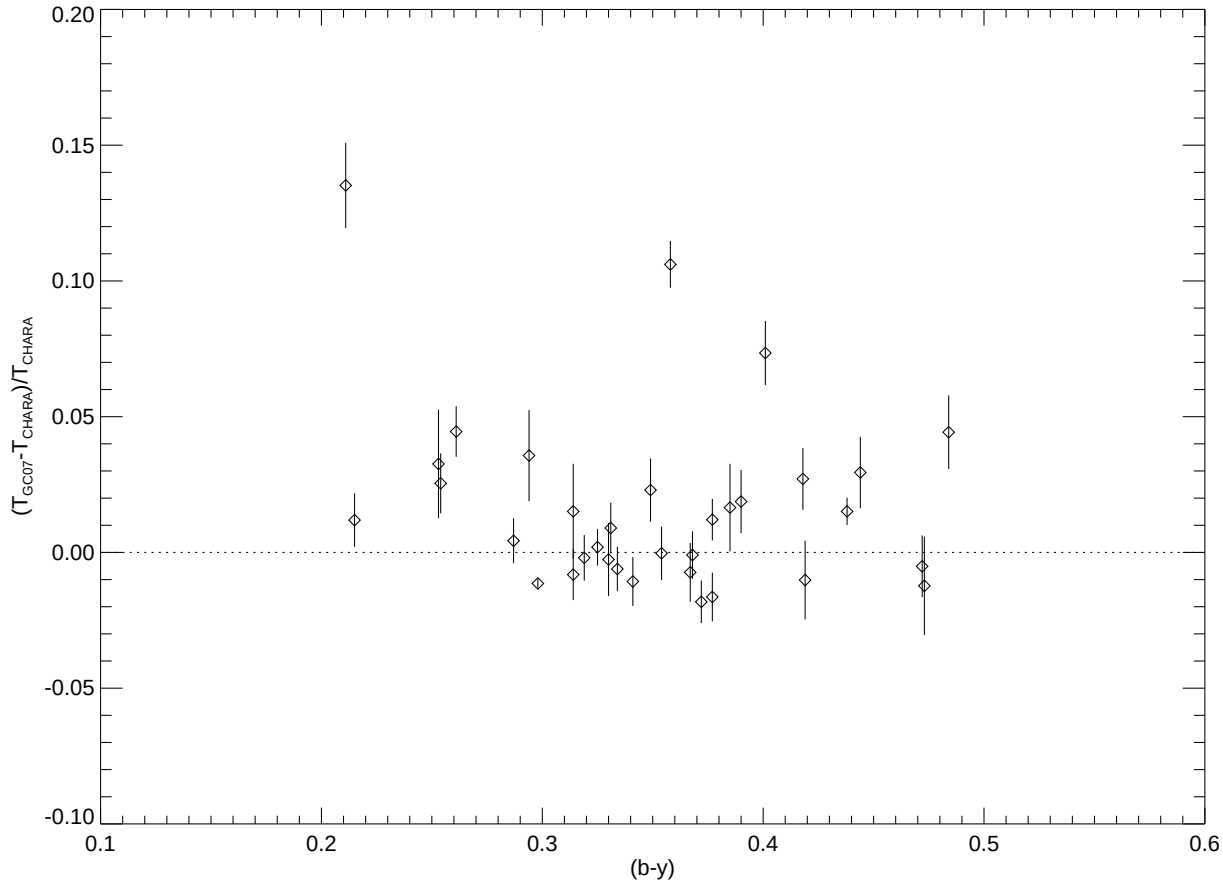

FIGURE 7.10: **Effects of $(b-y)$ on Temperature Offsets:** The data plotted show the differences between model temperatures determined by Holmberg et al. (2007) (GC07) and the empirical values determined in this project versus $(b-y)$ color index. The dotted line marks a 0% difference between the temperature values from each source.

relationships using these quantities for the stars observed in each survey that overlap with the CHARA stars. In Figure 7.15, Figure 7.16, and Figure 7.17, the CHARA determined temperatures and linear radii are plotted with the symbol size proportional to the model mass of the star. The most massive of the stars observed are also the biggest in linear size. The sample in Figure 7.15 includes the largest dispersion in mass, temperature and radius. It is most apparent here that a star with a linear radius of $R = 2R_{\odot}$ has quite a large range in mass, as well as a potential 3000° K range in temperature. On the other hand, a star with $T_{\rm EFF} = 6200$ K ranges from $1 - 3.5R_{\odot}$ at a range in masses as well. This is an important

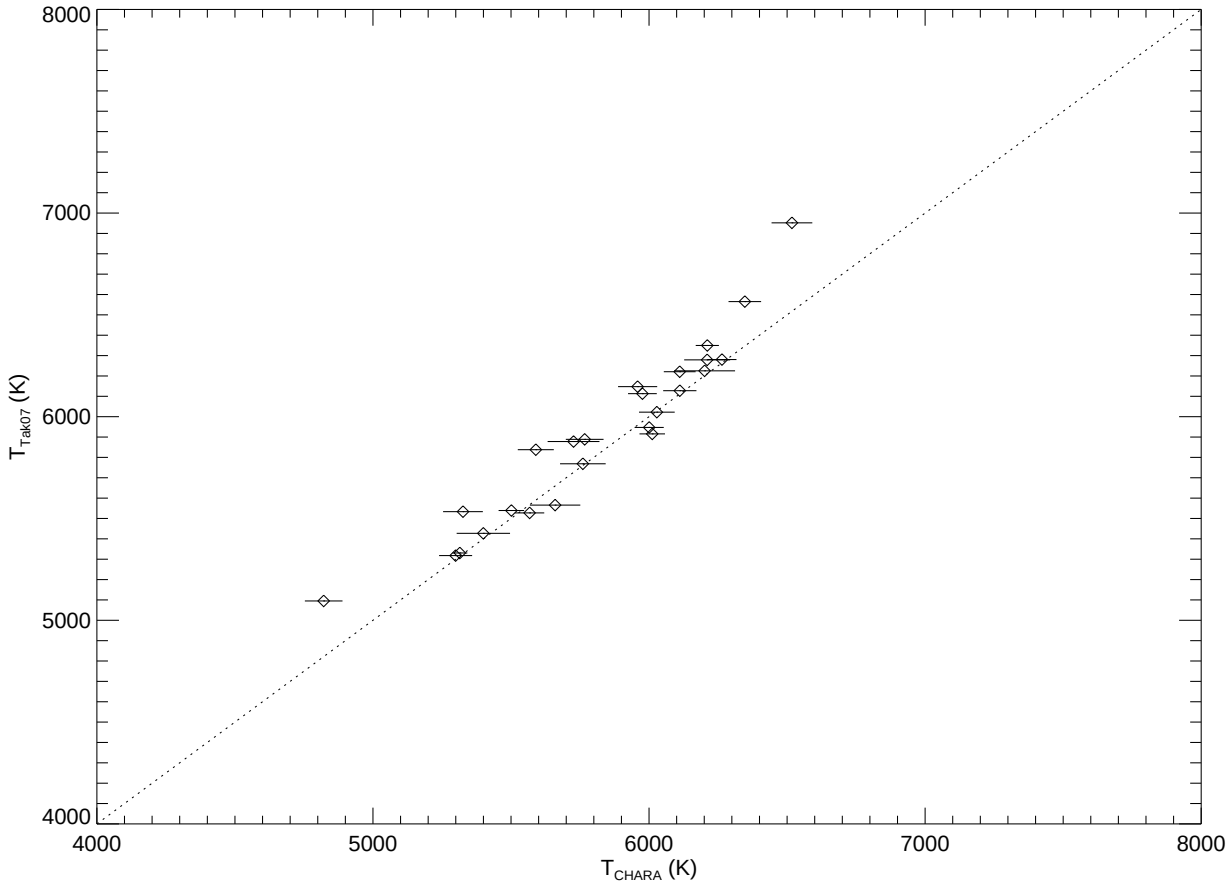

FIGURE 7.11: **Empirical Versus Model Effective Temperatures:** The data plotted show the differences between model temperatures determined by Takeda (2007) (Tak07) and the empirical values determined in this project. The dotted line marks a 1:1 ratio between the temperature values from each source.

effect resulting from stellar evolution on the main sequence where the more massive stars evolve to be cooler and have larger radii.

The temperatures and radii of the stars are compared with the model-determined ages in Figure 7.18 and Figure 7.19 (Allende Prieto & Lambert 1999 do not determine ages in their work). In Figure 7.18 we can see that for stars hotter than $\approx$ 6300 K, only younger stars were observed, but interestingly enough, they exhibit a range in stellar radii. For the later type stars with an effective temperature of less than $\approx$ 6300 K, the stars observed cover a full range of ages and show a moderate spread in radii. In Figure 7.18, only the oldest stars

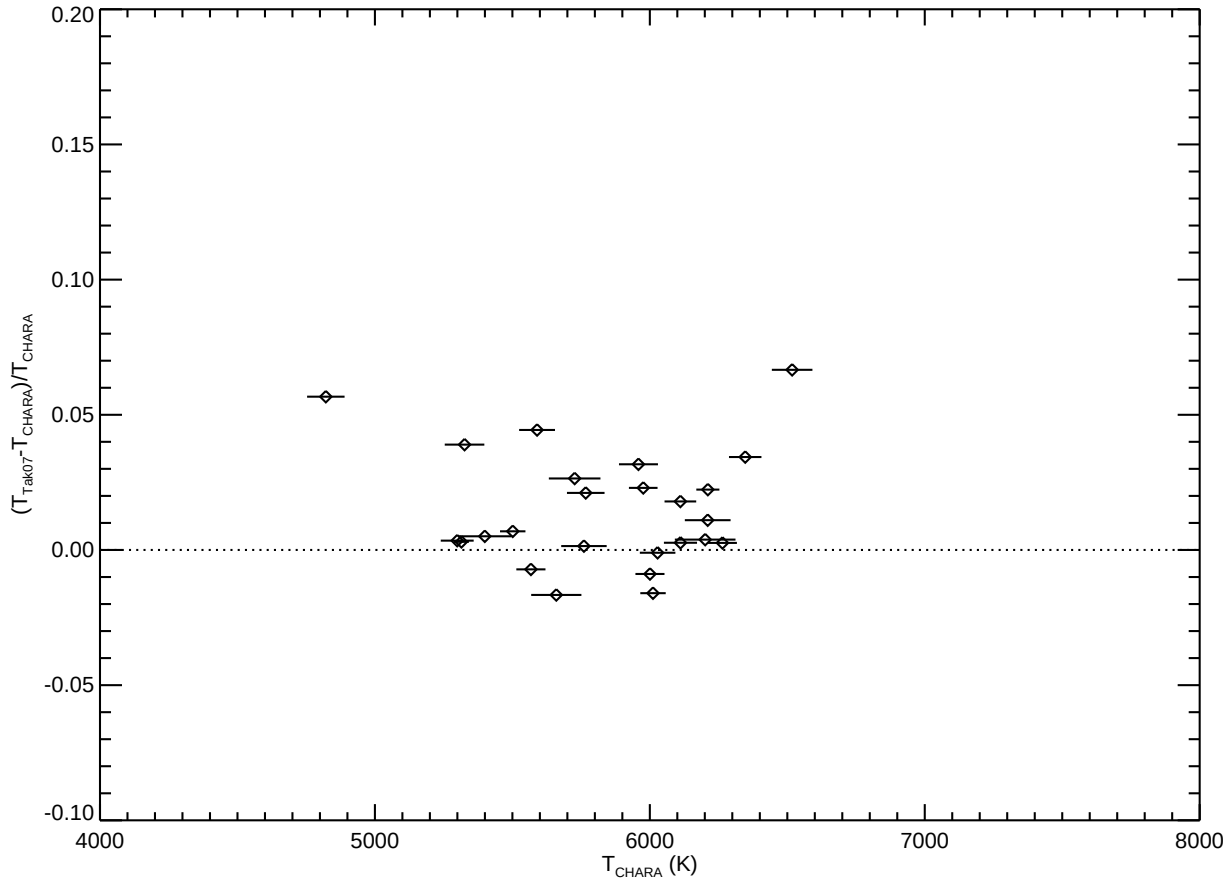

FIGURE 7.12: **Empirical Versus Model Effective Temperatures:** The data plotted show the fractional differences between model temperatures determined by Takeda (2007) (Tak07) and the empirical values determined in this project.

are observed at temperatures cooler than ≈ 5500 K, whereas a mixture of observations are made for the remainder of the sample.

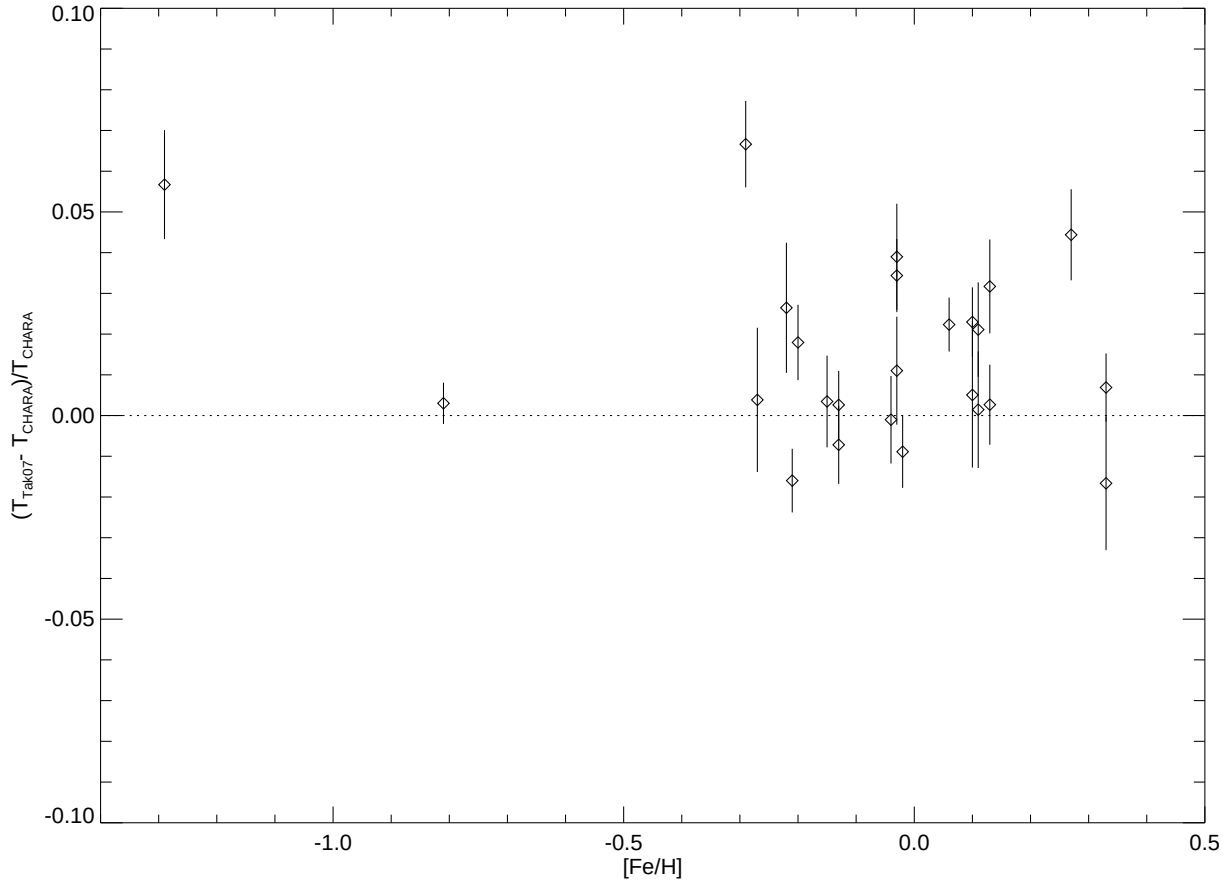

FIGURE 7.13: **Effects of Metallicity on Temperature Offsets:** The data plotted show the differences between model temperatures determined by Takeda (2007) (Tak07) and the empirical values determined in this project versus metallicity. The dotted line marks a 0% difference between the temperature values from each source.

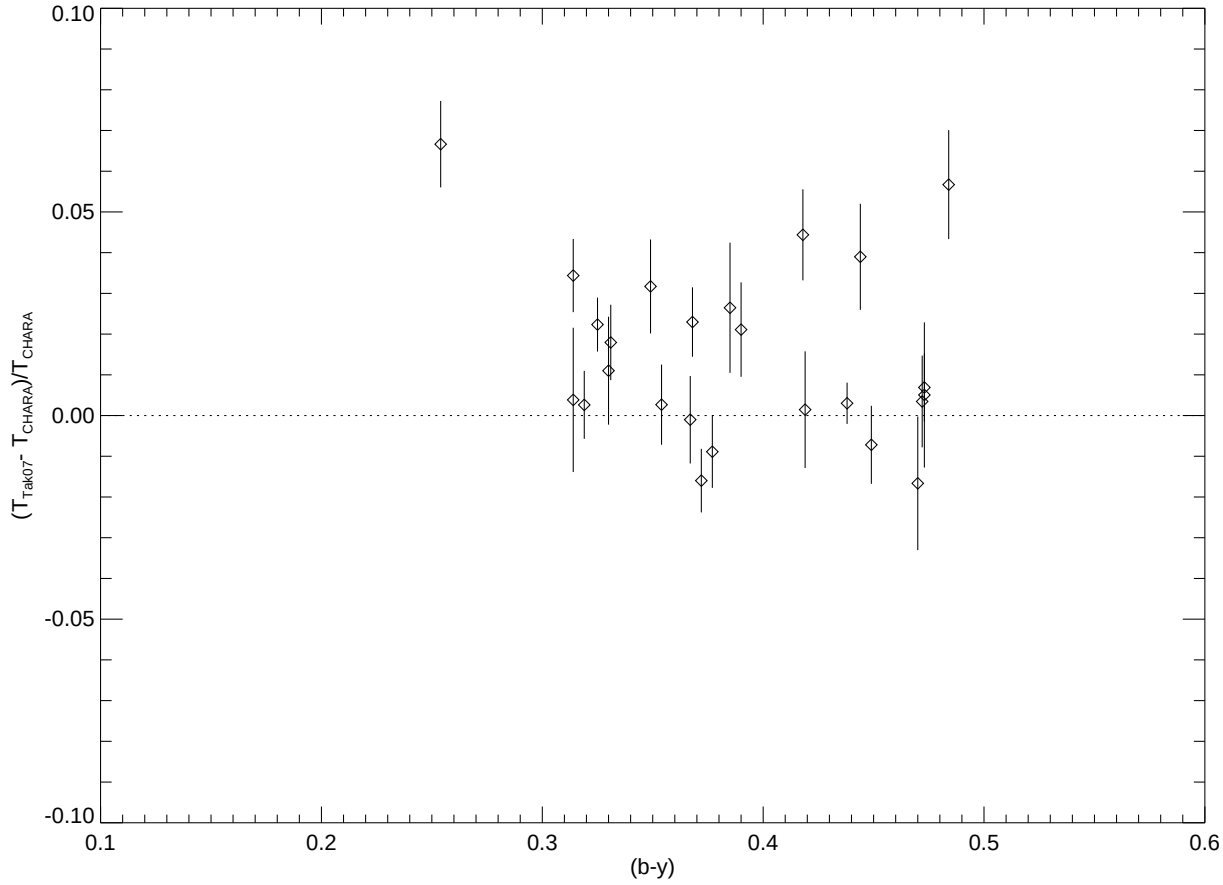

FIGURE 7.14: **Effects of $(b-y)$ on Temperature Offsets:** The data plotted show the differences between model temperatures determined by Takeda (2007) (Tak07) and the empirical values determined in this project versus $(b-y)$ color index. The dotted line marks a 0% difference between the temperature values from each source.

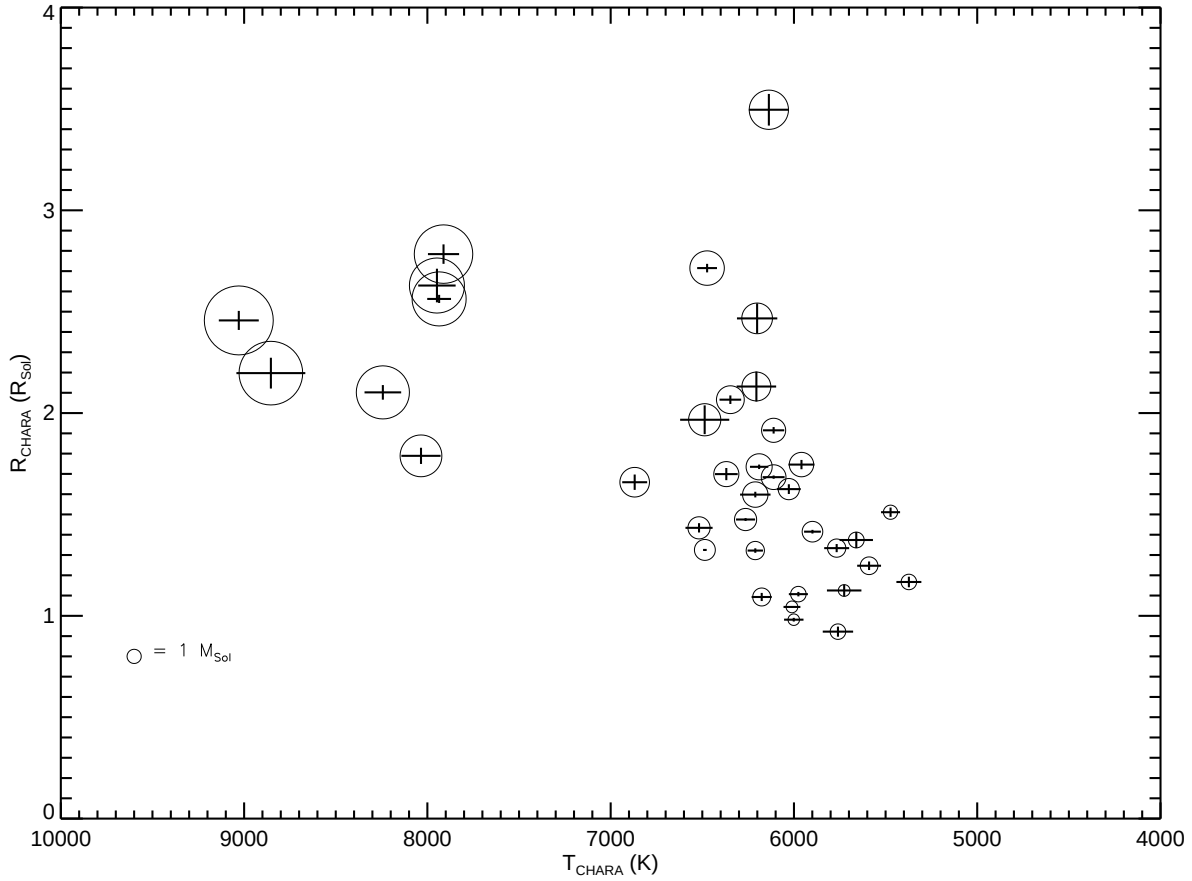

FIGURE 7.15: **Radius-Temperature-Mass:** The CHARA radii and temperatures (and the 1-σ errors) are plotted for stars in common with the Allende Prieto & Lambert (1999) (AP99) survey. The size of the circle is proportional to the mass of the star determined from models in Allende Prieto & Lambert (1999). To show the scale of the plot, a star of 1 $M_{\rm Sol}$ is plotted on the lower left.

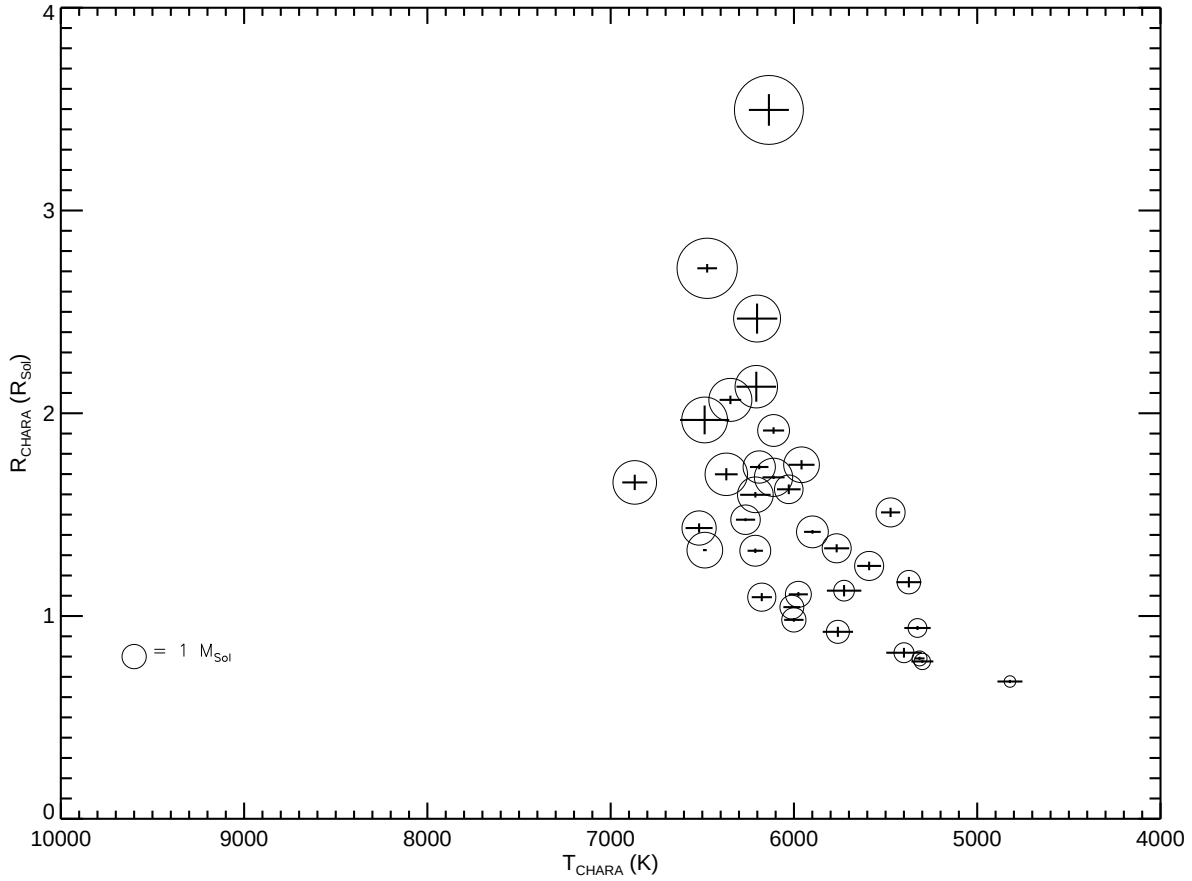

FIGURE 7.16: **Radius-Temperature-Mass:** The CHARA radii and temperatures (and the 1-σ errors) are plotted for stars in common with the Holmberg et al. (2007) (GC07) survey. The size of the circle is proportional to the mass of the star determined from models in Holmberg et al. (2007).

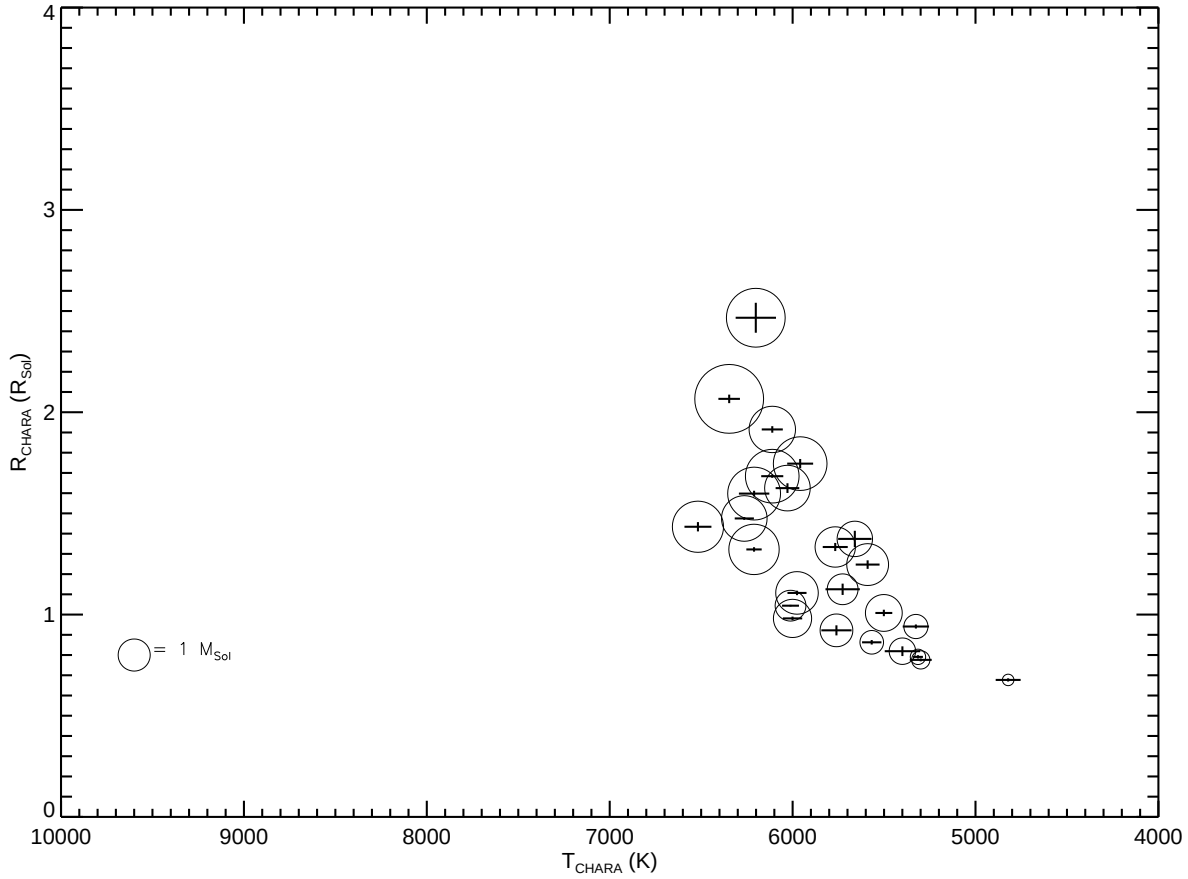

FIGURE 7.17: **Radius-Temperature-Mass:** The CHARA radii and temperatures (and the 1-σ errors) are plotted for stars in common with the Takeda (2007) (Tak07) survey. The size of the circle is proportional to the mass of the star determined from models in Takeda (2007).

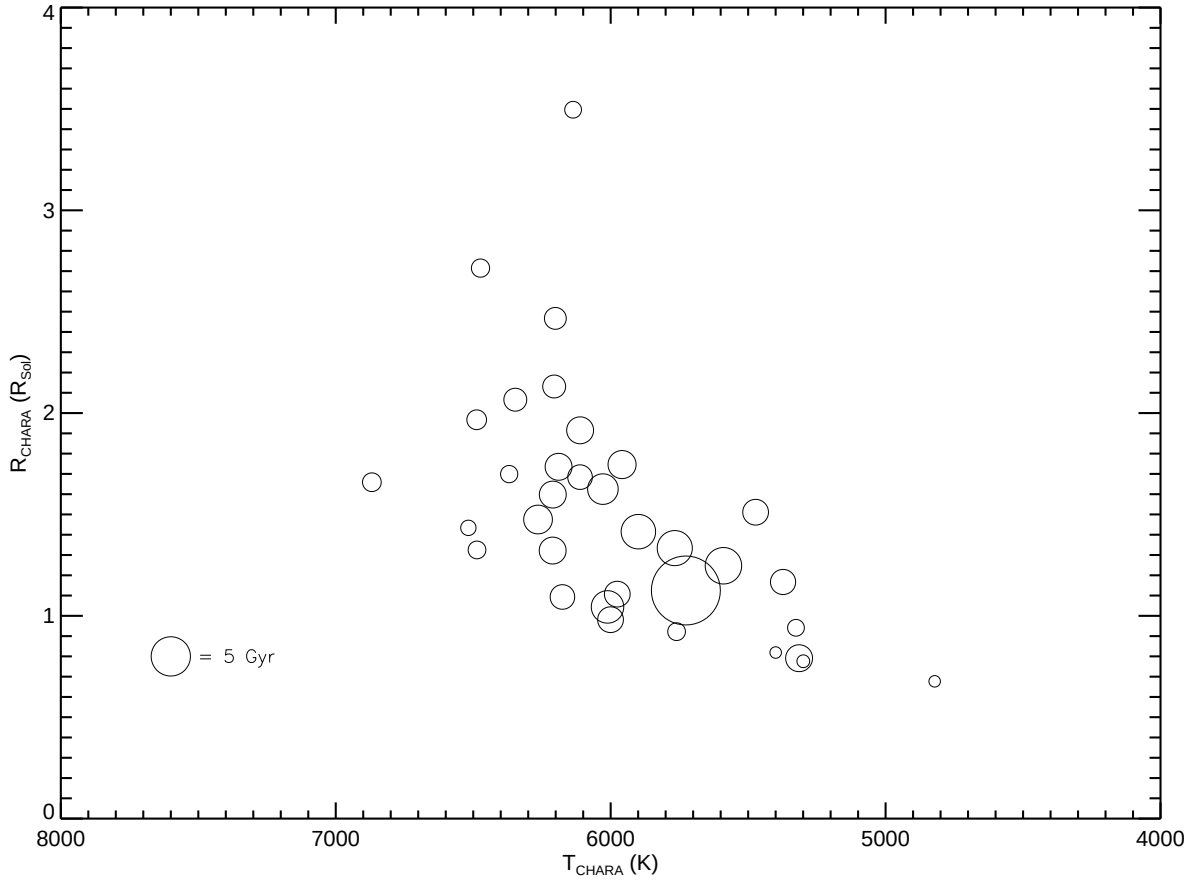

FIGURE 7.18: **Radius-Temperature-Age:** The CHARA radii and temperatures are plotted for stars in common with the Holmberg et al. (2007) survey. The size of the circle is proportional to the age of the star in Gyr determined from models in Holmberg et al. (2007). Errors in our measurements are not shown here for clarity.

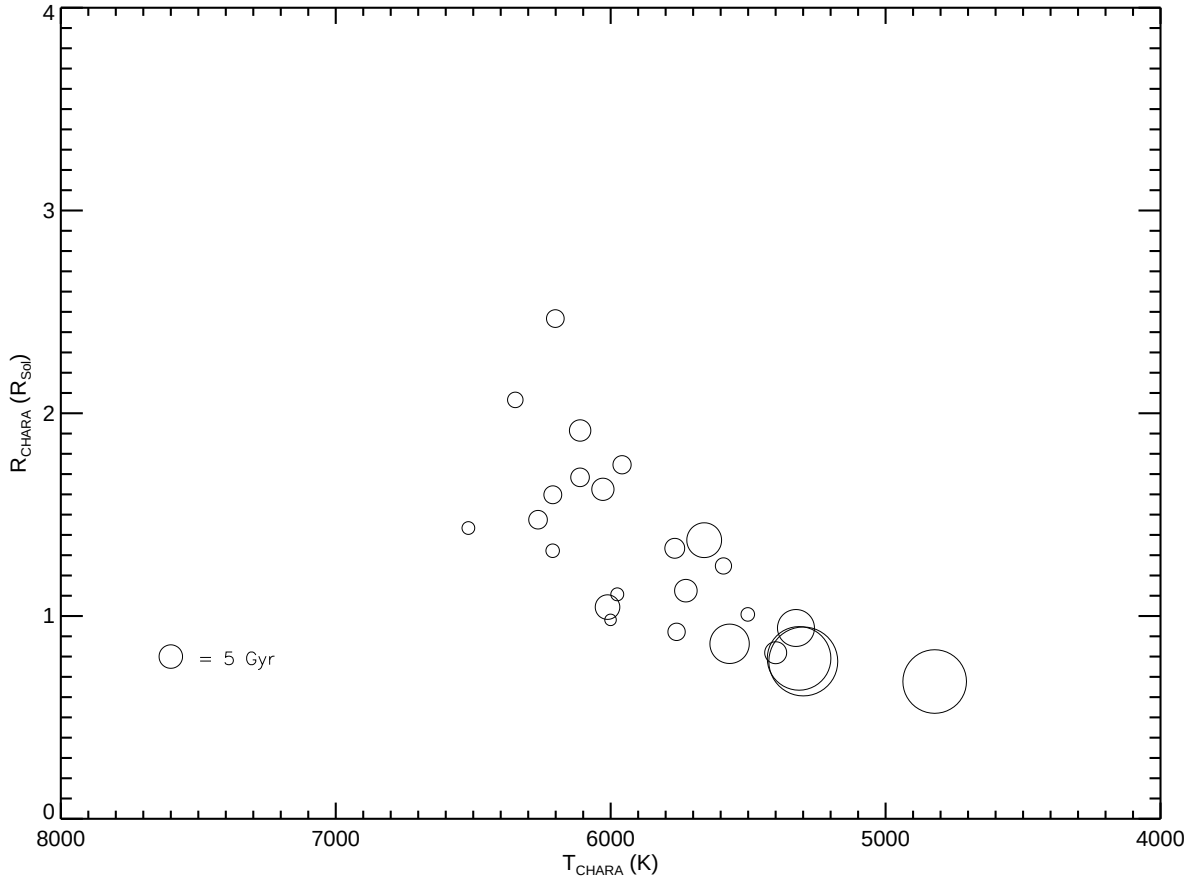

FIGURE 7.19: **Radius-Temperature-Age:** The CHARA radii and temperatures are plotted for stars in common with the Takeda (2007) survey. The size of the circle is proportional to the age of the star in Gyr determined from models in Takeda (2007). Errors in our measurements are not shown here for clarity.

Figure 7.20 and Figure 7.21 show the radius-age relation for stars in common in the Holmberg et al. (2007) and Takeda (2007) surveys and this one. Figure 7.20 shows that the smaller the star is, the larger the error on the model age. It also shows that stars above $\approx 2R_{\odot}$, are all under ≈ 2.5 Gyrs old. Age errors are not listed for Takeda (2007), but we can see that the large spread in age for the smaller stars is similar to the spread in Holmberg et al. (2007) for stars of these types. This can be attributed to the lifetime of a star on the main sequence and slower evolution of the less massive stars. Thus, there are more stages of evolution on the main sequence seen in these types of stars. The more massive stars that evolve quicker have shorter main sequence lifetimes, and thus there are few seen at very different ages in this range (before they become giants).

The relationship between stellar radius and mass is explored in Figure 7.22, Figure 7.24, and Figure 7.26 with stars in common in the Allende Prieto & Lambert (1999), Holmberg et al. (2007) and Takeda (2007) surveys, respectively. Again, Takeda (2007) does not present errors on mass, so they are not included in the plot. All of these figures show fairly tight correlations between observed radii and model masses from each reference. In Figure 7.22 (CHARA versus Allende Prieto & Lambert 1999), the spread in masses for stars larger than $2R_{\odot}$ becomes two times greater than that for stars of smaller radii. The upwards trend is consistent in each figure, but it is unclear whether or not the curve levels out at around $2R_{\odot}$ (Figure 7.26) or continues to rise (Figure 7.24) due to lack of data in this range of higher mass stars. Figure 7.23, Figure 7.25, and Figure 7.27 show the same relation of the CHARA measured stellar radius versus mass for the stars in common in the Allende Prieto & Lambert (1999), Holmberg et al. (2007), and Takeda (2007) surveys. Here, the metallicity of each

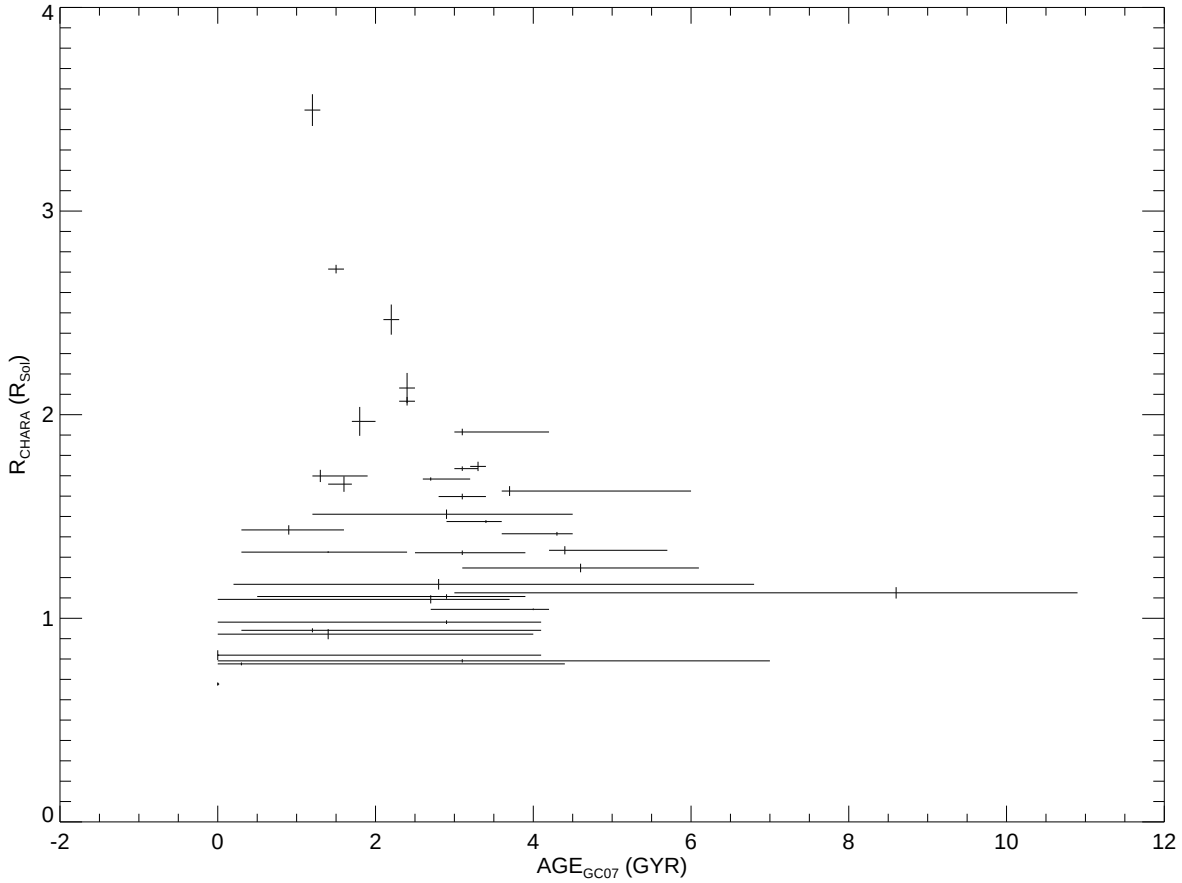

FIGURE 7.20: **Radius-Age:** The CHARA radii are plotted for stars in common with the Holmberg et al. (2007) survey. The 1-σ errors on radius and age (asymmetric in most cases) are plotted.

point is shaded to a grayscale value corresponding to the metallicity estimate determined from each reference.

Temperature and mass relations of the three surveys versus the new CHARA results are presented in Figure 7.28, Figure 7.29, and Figure 7.30. Each of these figures shows that, in general, there is a range of $\approx 0.3 M_{\odot}$ for a given temperature. They also show that for main sequence stars of these types, the relation between temperature and mass is somewhat linear.

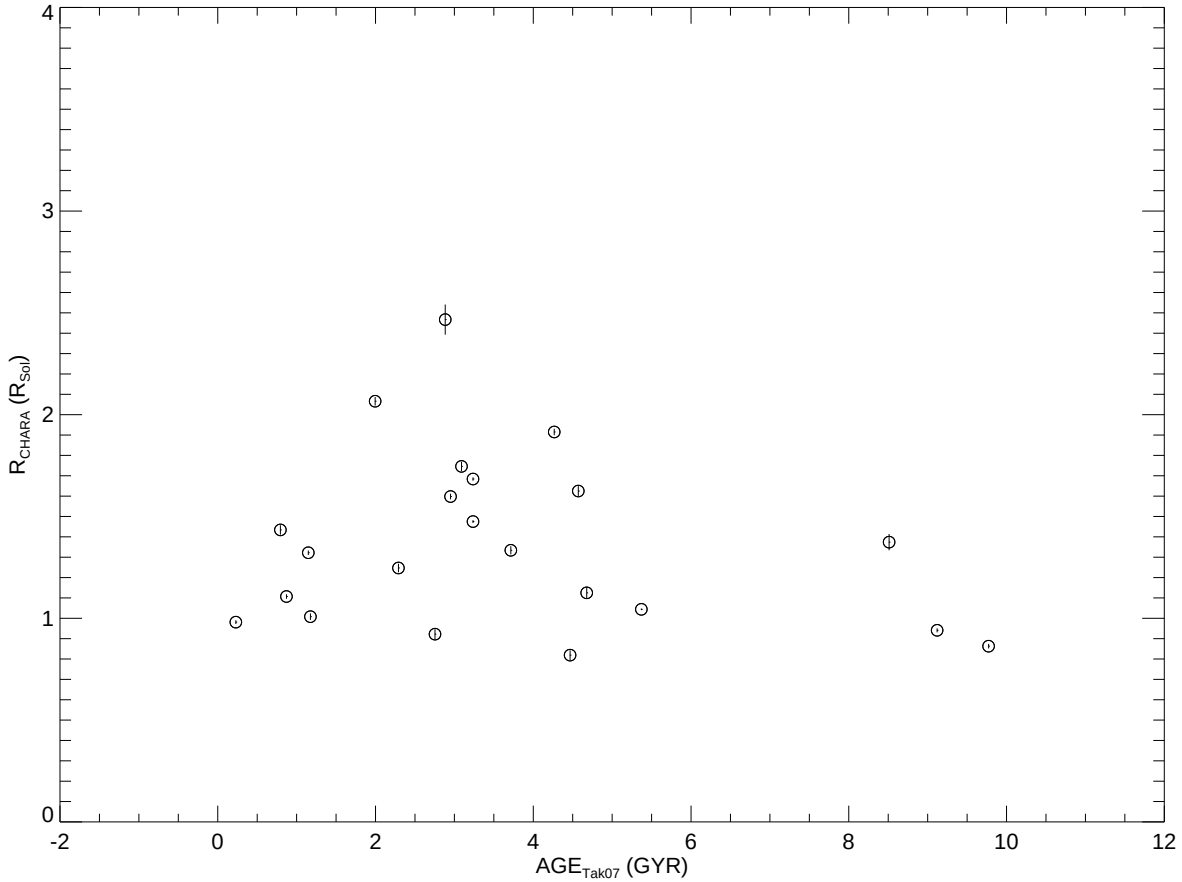

FIGURE 7.21: **Radius-Age:** The CHARA radii are plotted for stars in common with the Takeda (2007) survey. Each point is represented by a circle, and the 1-σ errors in radius are shown (Takeda 2007 does not provide age errors).

7.4 CHARA Masses

With the linear radii known for all stars in the CHARA sample, I am able to determine the mass of a star using $\log g$ estimates found in Allende Prieto & Lambert (1999) and Takeda (2007) using the relation:

$$g_\star = \frac{GM_\star}{R_\star^2} \tag{7.1}$$

where G is the gravitational constant, $M_\star$ is the mass of the star, $R_\star$ is the radius of the star, and $g_\star$ is the surface gravity of the star. Figure 7.31 and Figure 7.32 show the results of this

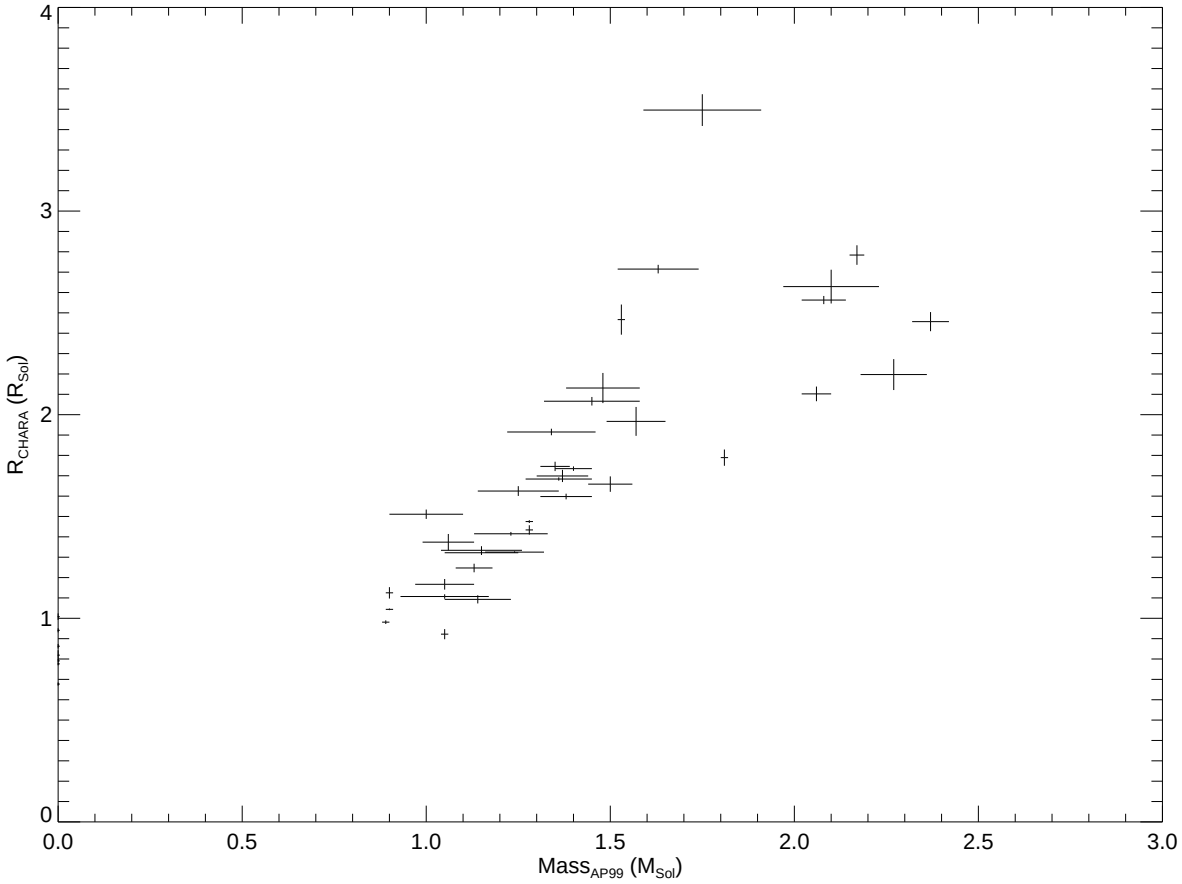

FIGURE 7.22: **Radius-Mass:** The CHARA radii and model masses are plotted for stars in common with the Allende Prieto & Lambert (1999) survey (AP99). The 1-σ errors on radius and mass are also shown.

approach, and compares these derived masses to the masses derived by Allende Prieto & Lambert (1999) and Takeda (2007). The errors on the CHARA derived masses are hard to determine, but are suspected to be quite high due to the uncertainty in $\log g$ estimates used in the determination of the masses. It is interesting to note that in Figure 7.31, the CHARA masses are larger than AP99 for stars more massive than $\approx 1.3 M_{\odot}$, and the more massive the star, the more deviation there is from the 1:1 ratio line. The reason for this discrepancy is likely to be because the Allende Prieto & Lambert (1999) stars are also underestimated in radius (Figure 7.1), which in turn, leads models to predict a smaller mass. It could also be caused by an offset in the $\log g$ estimates for these more massive stars by some unknown

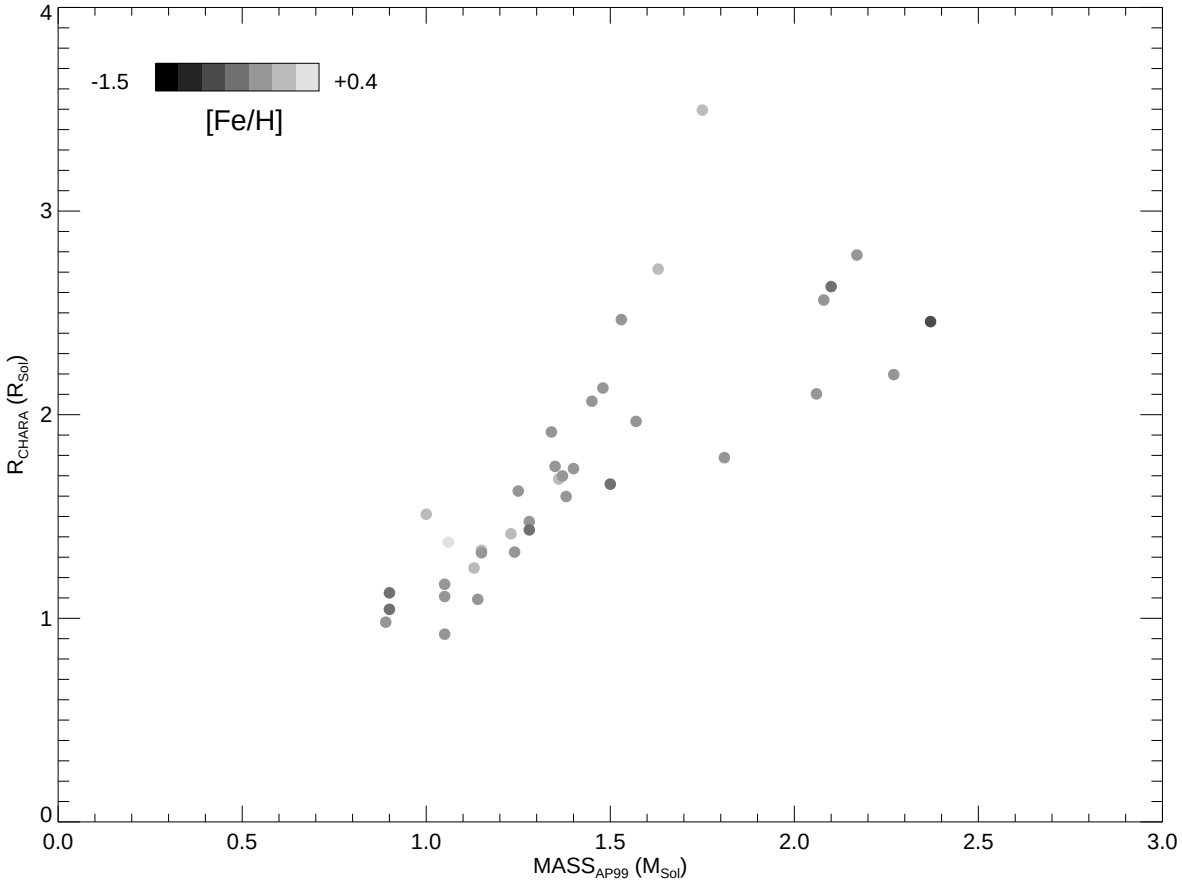

FIGURE 7.23: **Radius-Mass-Metallicity:** The CHARA radii and model masses are plotted for stars in common with the Allende Prieto & Lambert (1999) survey (AP99). The grayscale color corresponds to the metallicity [Fe/H] of the star.

property in the stellar atmosphere. This could tie into the model temperatures used to fit the star's gravity (that is overestimated in most cases). The relation in Figure 7.32 shows much more scatter, but points seem to follow the 1:1 trendline. The two outliers (different from the ones in Figure 7.31), are the hottest stars in the Tak07 survey that overlap with the CHARA stars.

7.5 Comparative Analysis to Eclipsing Binaries

Andersen (1991) provides a compilation of data on all eclipsing binaries (EB) known at the time - a total of 90 stars, most of which are on the main sequence. Section 4 in Andersen

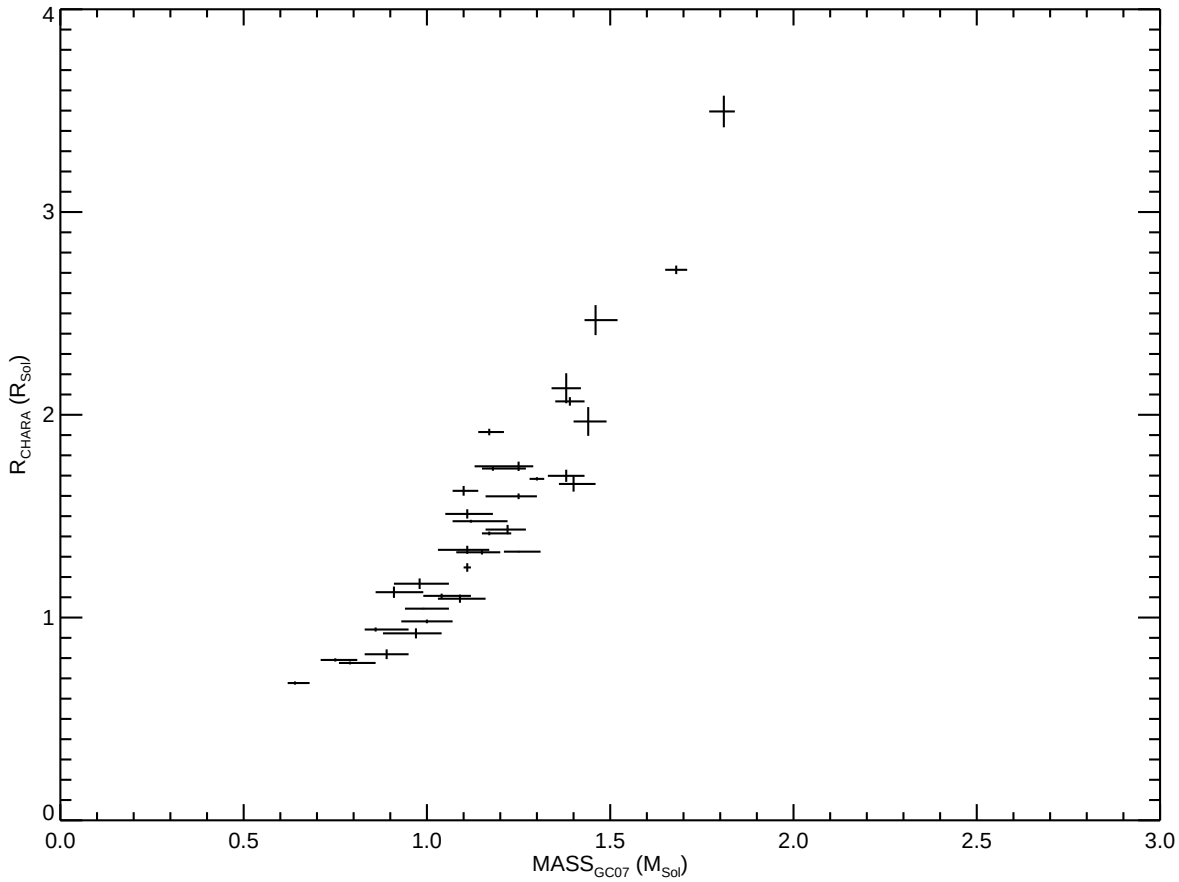

FIGURE 7.24: **Radius-Mass:** The CHARA radii and model masses are plotted for stars in common with the Holmberg et al. (2007) survey (GC07). The 1-σ errors on radius and mass are also shown.

(1991) argues that the motivation for compiling the EB data is to aid in the prediction of single star properties where masses and radii are unobtainable by direct measurements for a large number of stars. We use these data on eclipsing binaries to compare with our results for single stars in this section.

Effective temperatures of EB stars are not able to be determined directly because the distances to the systems are not known to great accuracy. Due to the fact that the stars are in binaries, their parallaxes could be difficult to determine because the orbital motion of the binary in the sky around the center of mass of the system is particularly difficult to deconvolve from the parallactic displacement. In addition, interstellar reddening is also a

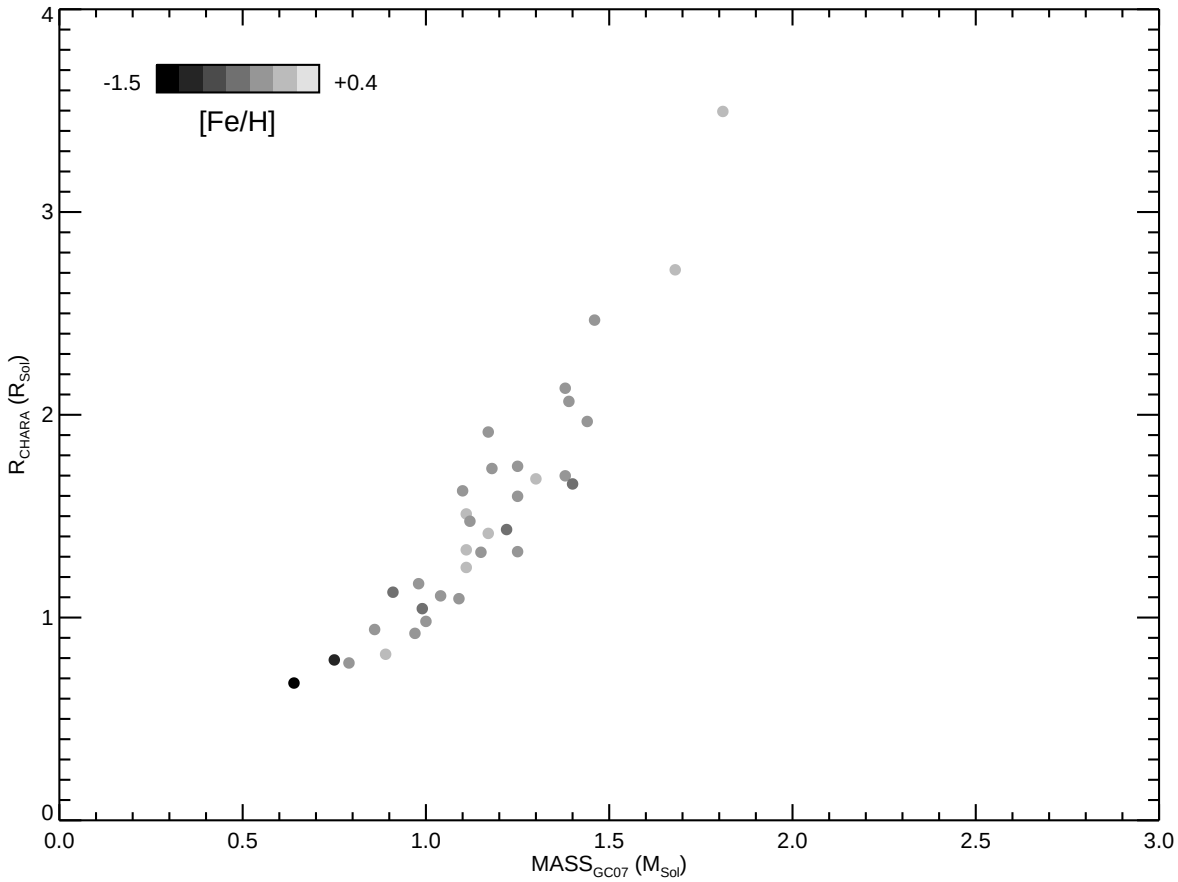

FIGURE 7.25: **Radius-Mass-Metallicity:** The CHARA radii and model masses are plotted for stars in common with the Holmberg et al. (2007) survey (GC07). The grayscale color corresponds to the metallicity [Fe/H] of the star.

factor in the distant systems when converting observed photometry to absolute magnitudes. Thus, a primary advantage of measuring the angular diameters of single stars for which we know the distances with great accuracy is that reddening can be ignored. Nearby stars will provide the means to calibrate the temperature relations for EB's and can also be applied to a large number of stars. Also, in Andersen (1991) the luminosities are derived via the Stefan-Boltzmann equation, using the measured EB radii and model derived $T_{\rm EFF}$. In the discussions to follow, keep in mind that these EB luminosities and temperatures might have systematic offsets due to the indirect determination of these quantities.

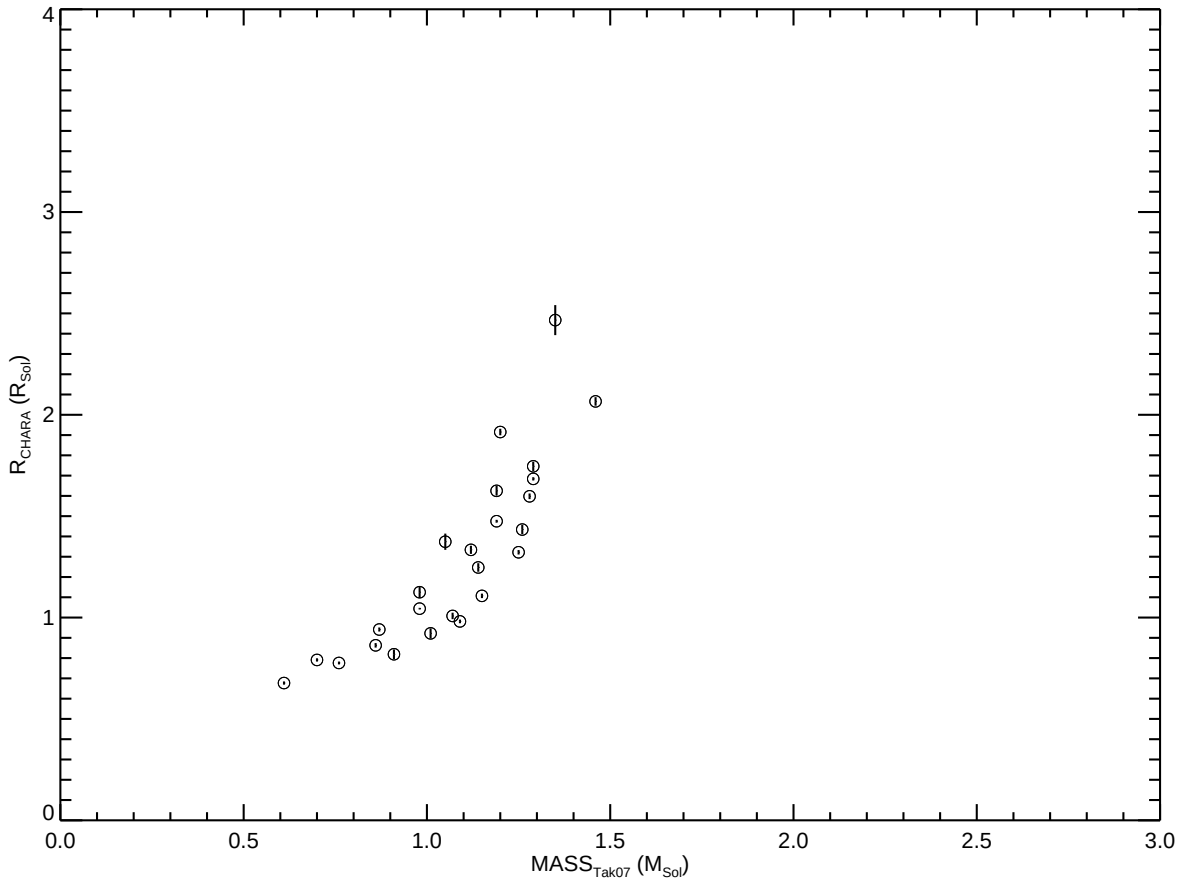

FIGURE 7.26: **Radius-Mass:** The CHARA radii and model masses are plotted for stars in common with the Takeda (2007) survey (Tak07). Each point is represented by a circle, and the 1-σ errors in radius are shown (Takeda 2007 does not provide mass errors).

Eclipsing binary star and single star radii versus $(B-V)$ color index are compared in Figure 7.33. The general direction of evolution off the main sequence is marked in the top right of the plot. One can see that for stars even on the main sequence there is quite a spread in radius for a given $(B-V)$. It is interesting to note that for stars redder than $B-V \approx 0.5$, EB stars are more evolved than CHARA stars (although the data are sparse in this region for EBs). For stars bluer than $B-V \approx 0.5$, the CHARA stars are more evolved than the EB stars. This might be from a selection effect that all nearby stars observed with CHARA are field stars, and hence older than EBs found in dense young clusters. The important conclusion here is that there is no systematic offset seen when comparing the radii from

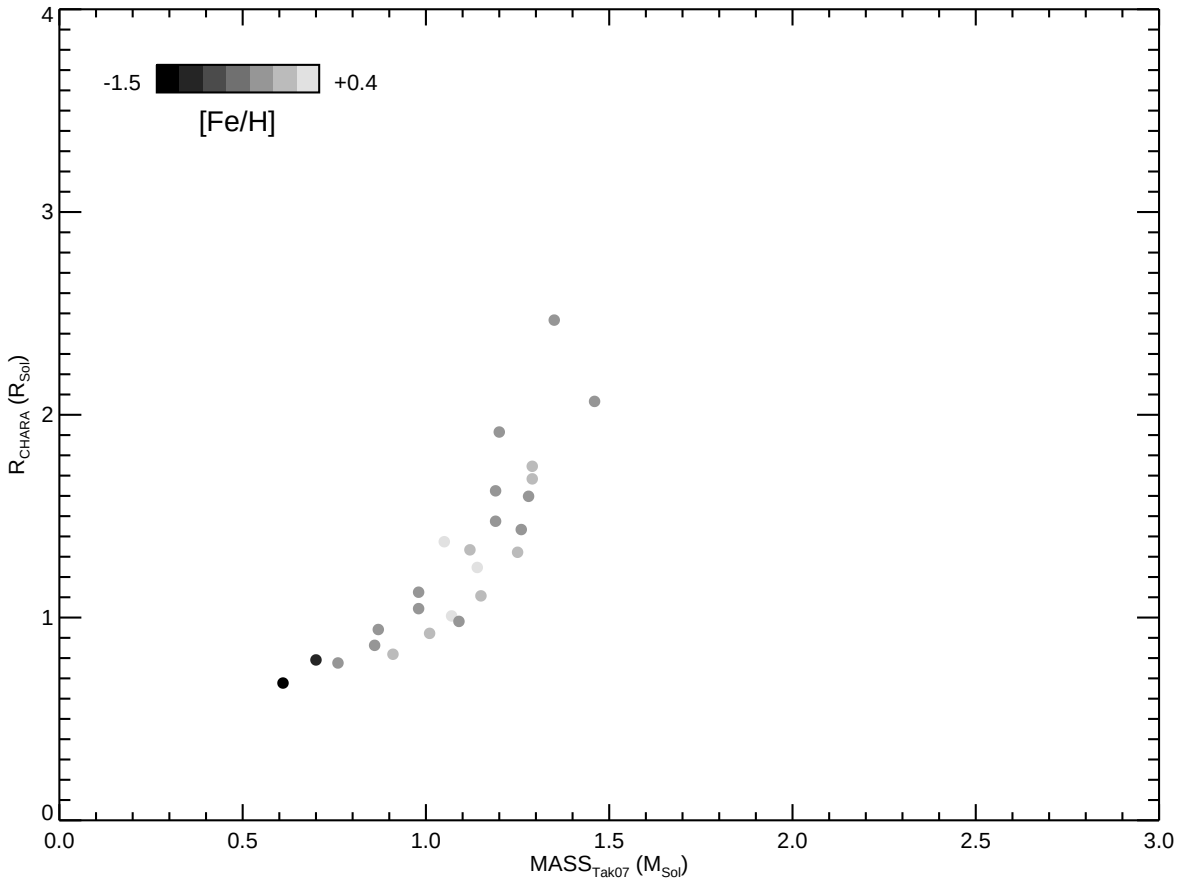

FIGURE 7.27: **Radius-Mass-Metallicity:** The CHARA radii and model masses are plotted for stars in common with the Takeda (2007) survey (Tak07). The grayscale color corresponds to the metallicity [Fe/H] of the star.

eclipsing binary and single stars. This supports the conclusion that models are doing a poor job of predicted radii for single stars (§7.1).

Exploring the mass-radius relations in single versus binary stars, we find a similar relationship. Figure 7.34 shows that there is still much scatter in the mass-radius relation for main sequence stars and that there is no systematic offset when comparing values from binary to single stars. The masses used here are the masses derived from our measured CHARA radii and $\log g$ estimates. In the previous section, Figure 7.31 and Figure 7.32 showed that for stars of larger masses, there were increasingly larger differences between the model masses from the references, and our derived CHARA masses. In the region of higher

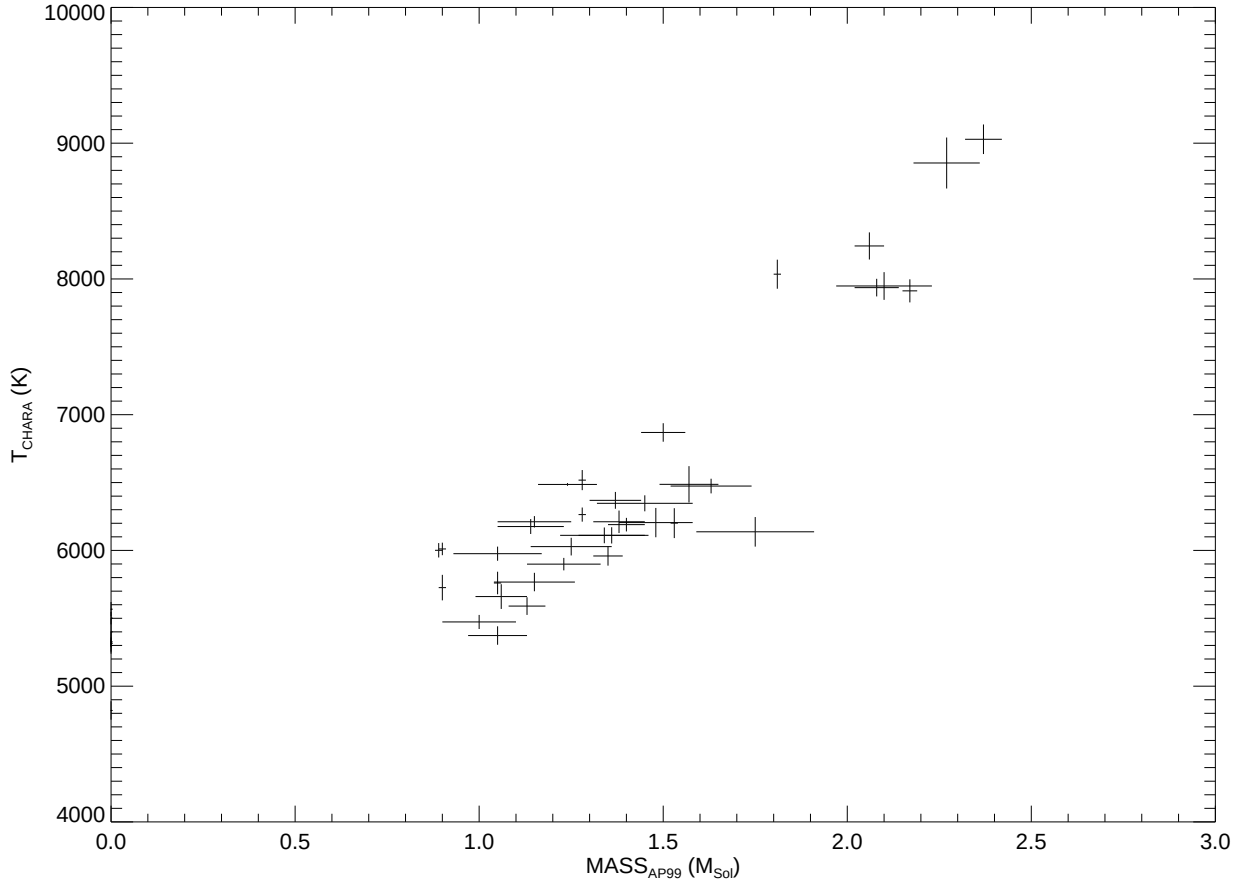

FIGURE 7.28: **Temperature-Mass:** The CHARA temperatures and model masses are plotted for stars in common with the Allende Prieto & Lambert (1999) survey (AP99). The 1-σ errors on temperature and mass are also shown.

masses in Figure 7.34, the derived CHARA masses are very consistent with the EB values, so perhaps the errors in gravity are not as large as previously thought, and the techniques for determining masses from the models need to be tweaked. The mass-radius relation of $R \propto M^{0.8}$ is shown as the dotted line, which holds for both binary and single main sequence stars of less than $\approx 3.5 M_{\odot}$.

Figure 7.35 is the radius-luminosity relation for both the EB stars and the single CHARA stars. The larger the radii, the more spread in luminosity is found in these stars. For the main sequence stars observed with CHARA this spread is minimal. For the eclipsing binary stars, whose spectral types range from O8−M1, the spread on the luminosity-radius plane

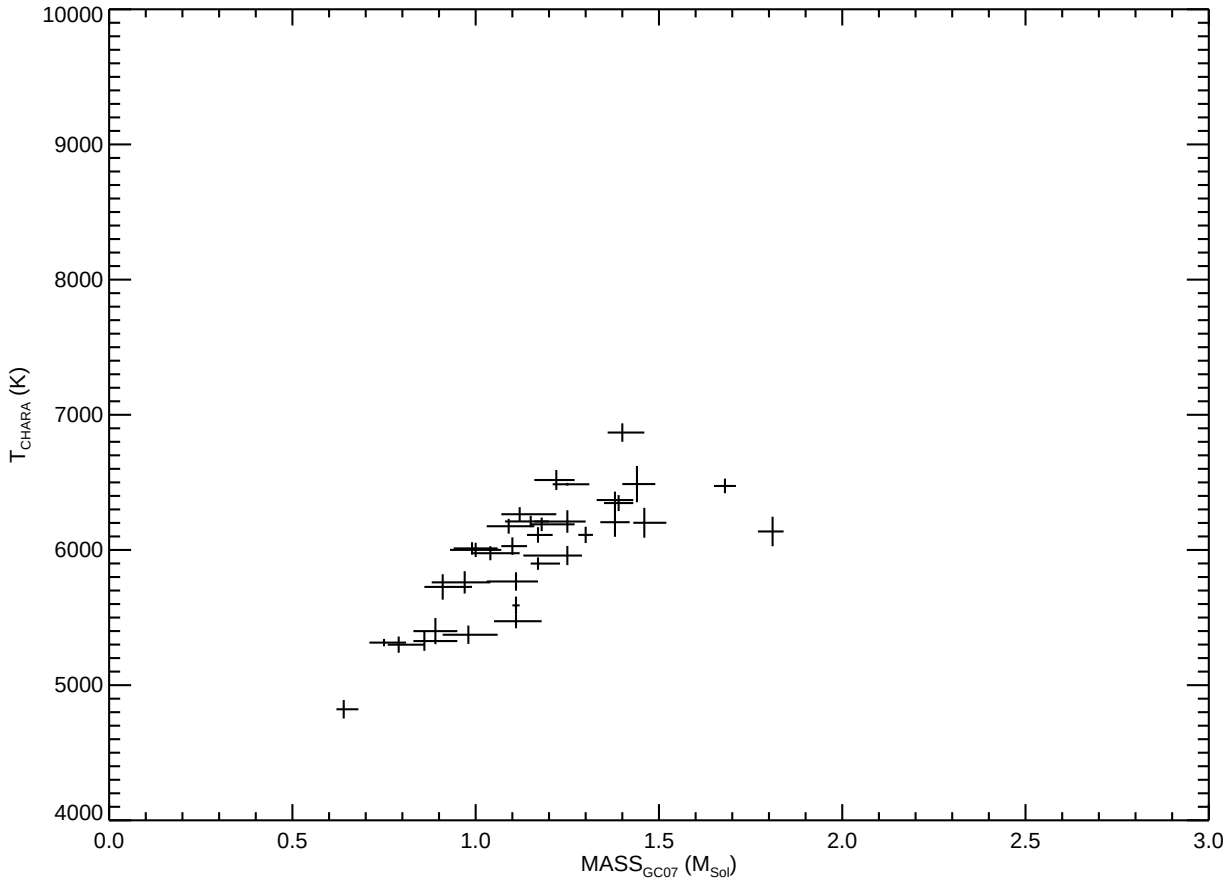

FIGURE 7.29: **Temperature-Mass:** The CHARA temperatures and model masses are plotted for stars in common with the Holmberg et al. (2007) survey (GC07). The 1-σ errors on temperature and mass are shown.

is significant. Within the range of radii measured with CHARA ($\log R/R_\odot \approx -0.2$ to 0.6), there is a tight relation of binary stars to single stars up to $\log R/R_\odot \approx 0.15$. For stars larger than this radius, there is a minimum luminosity for a given radius consistent within each data set, but the spread to higher luminosities of the EB sample increases significantly more than the single stars.

Figure 7.36 shows the mass to color index ($B - V$) relation for EB and CHARA stars with masses derived from $\log g$ estimates. For the sample of EBs, Andersen (1991) points out that stellar evolution on the main sequence can be seen by the fact that for a certain color index, there is a range of masses (EB mass error is typically $\approx 1.4\%$). This effect is

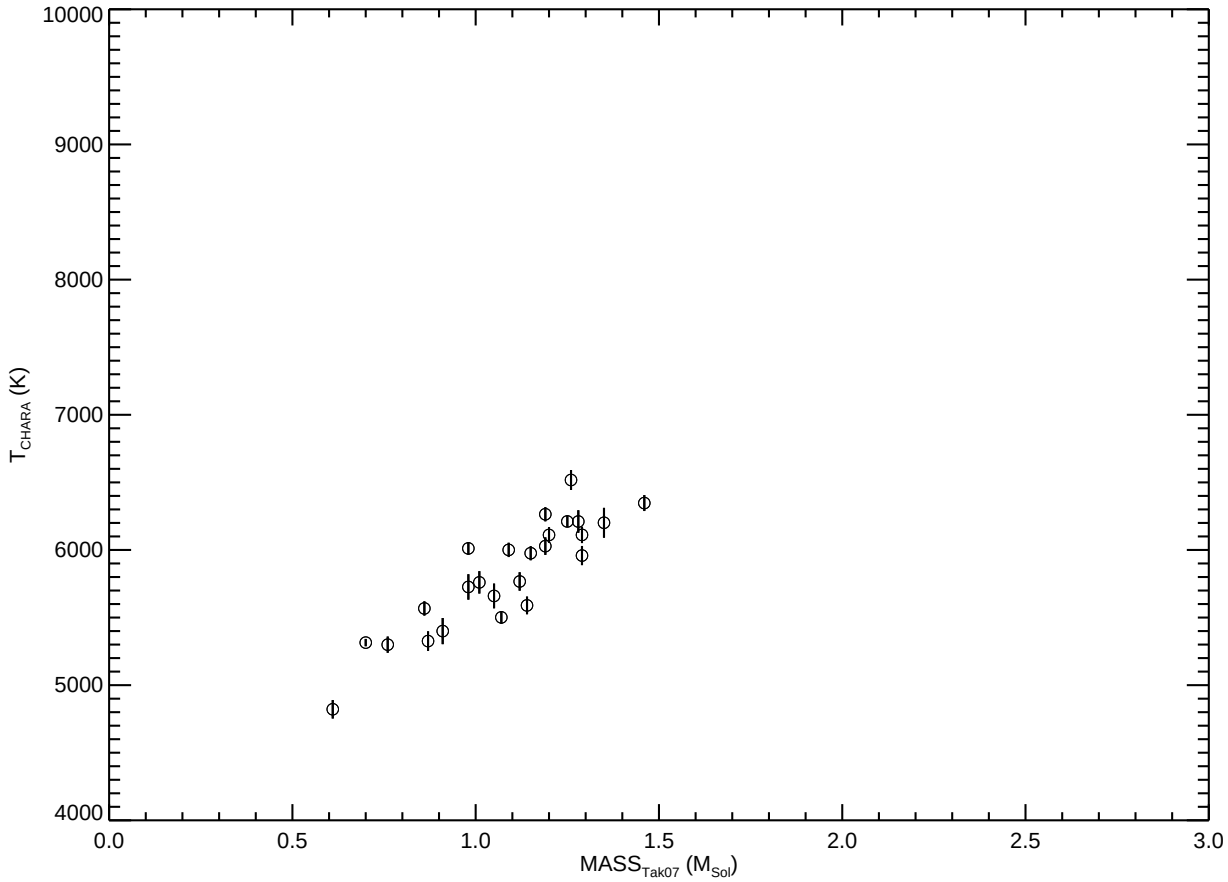

FIGURE 7.30: **Temperature-Mass:** The CHARA temperatures and model masses are plotted for stars in common with the Takeda (2007) survey (Tak07). Each point is represented by a circle, and the 1-σ errors in temperatures are shown (Takeda 2007 does not provide mass errors).

most apparent in spectral types A-F ($0.0 \lesssim B-V \lesssim 0.5$), where for the EB data points, there is a spread in the right direction of the plot (the direction of stellar evolution). For the CHARA stars, the error in mass is much larger. However, the same trend seen in Figure 7.33 (radius versus color index) is seen with respect to stellar mass versus color index, where the stars bluer than $B-V \lesssim 0.45$ are more evolved than the stars in the EB sample.

There does seem to be a systematic offset between EB masses and CHARA masses derived from gravity when plotted against luminosity, as seen in Figure 7.37. Although the scatter is large, the systematics appear for stars with $M \geq 1.5 M_{\odot}$, the same position as in Figure 7.31, where the CHARA masses are larger than they should be if $\log g$ estimates are

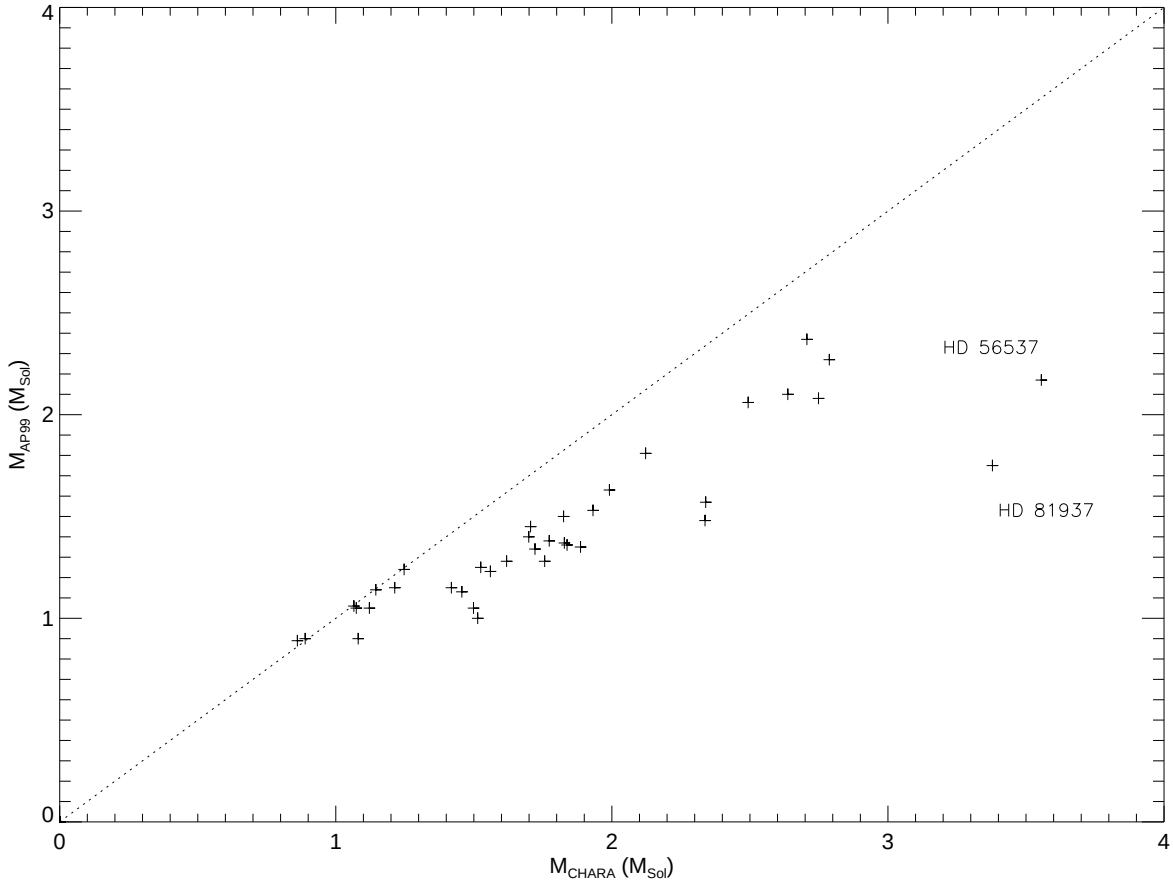

FIGURE 7.31: **CHARA Masses Versus Model Masses:** The CHARA masses derived from measured radii and $\log g$ estimates from Allende Prieto & Lambert (1999) (AP99) compared to model masses of the same stars included in Allende Prieto & Lambert (1999). The dotted line shows the 1:1 relation. Errors are not shown, however the errors for the CHARA derived masses are $\approx 20\%$ due to uncertainty in gravity estimates.

overestimated. However, the errors in CHARA derived masses may diminish the significance of this effect. An equally likely contributor to this effect is that this could be a problem with the derived EB luminosities.

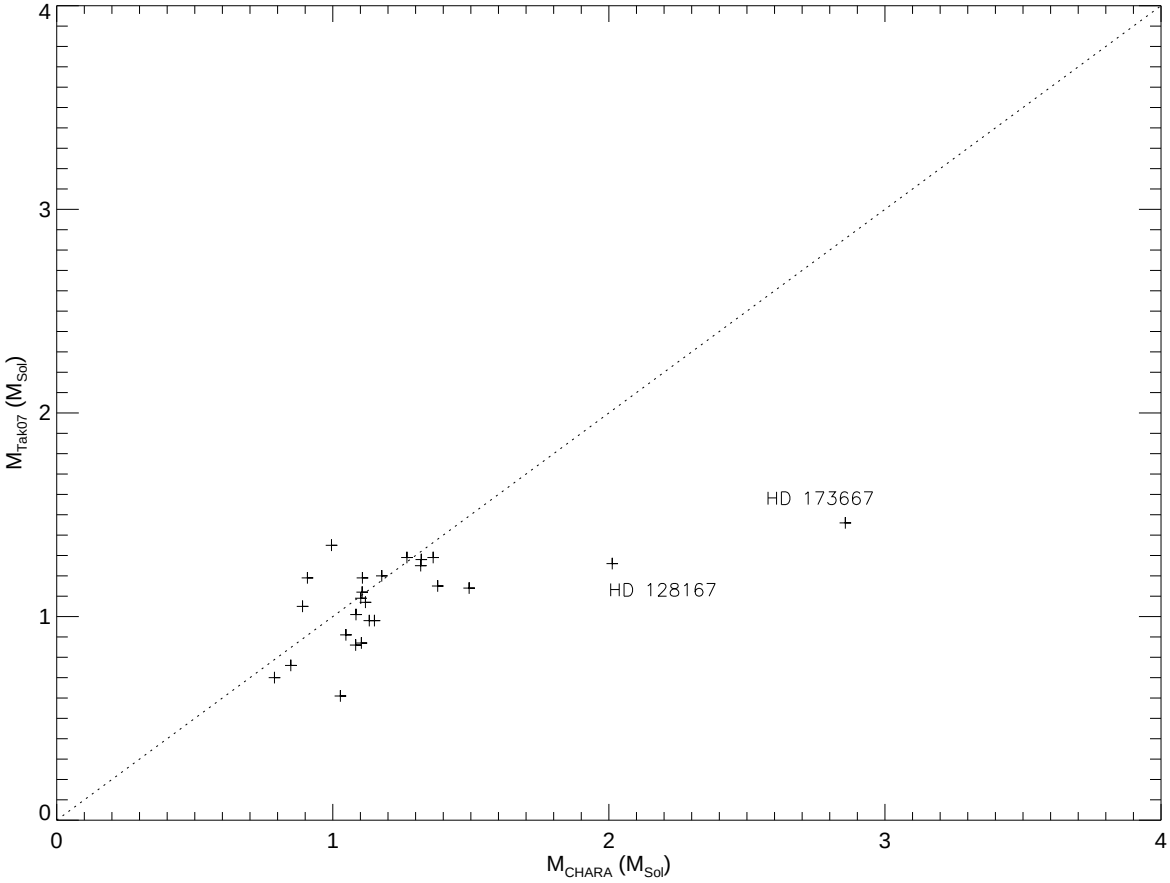

FIGURE 7.32: **CHARA Masses Versus Model Masses:** The CHARA masses derived from measured radii and $\log g$ estimates from Takeda (2007) (Tak07) compared to model masses of the same stars included in Allende Prieto & Lambert (1999). The dotted line shows the 1:1 relation. Errors are not shown, however the errors for the CHARA derived masses are $\approx 20\%$ due to uncertainty in gravity estimates.

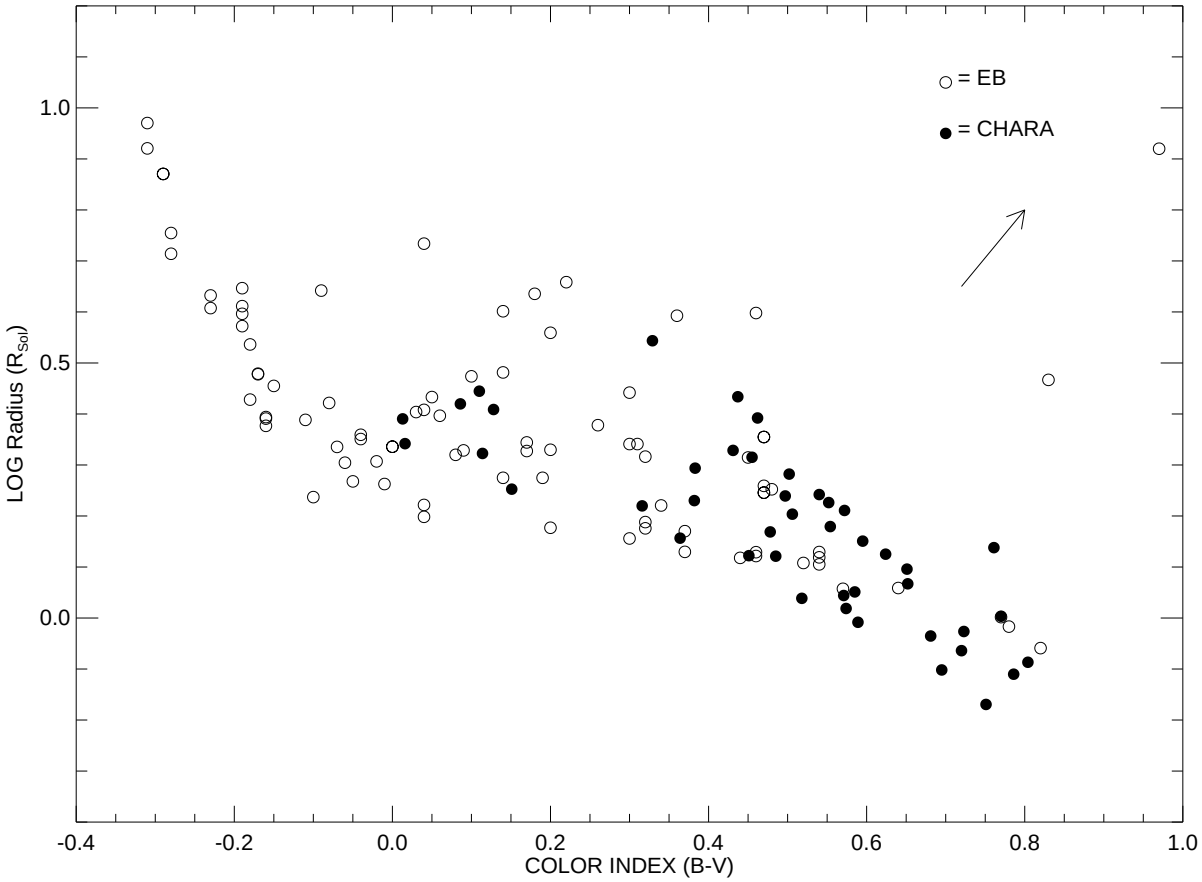

FIGURE 7.33: **Eclipsing Binary and CHARA Radii Versus (B-V):** The CHARA radii (filled circles) and eclipsing binary radii (open circles) are plotted against color index ($B - V$). In most cases, the errors in radii are smaller than the data points. The arrow in the top right side of the plot indicates the direction of evolution off the main sequence.

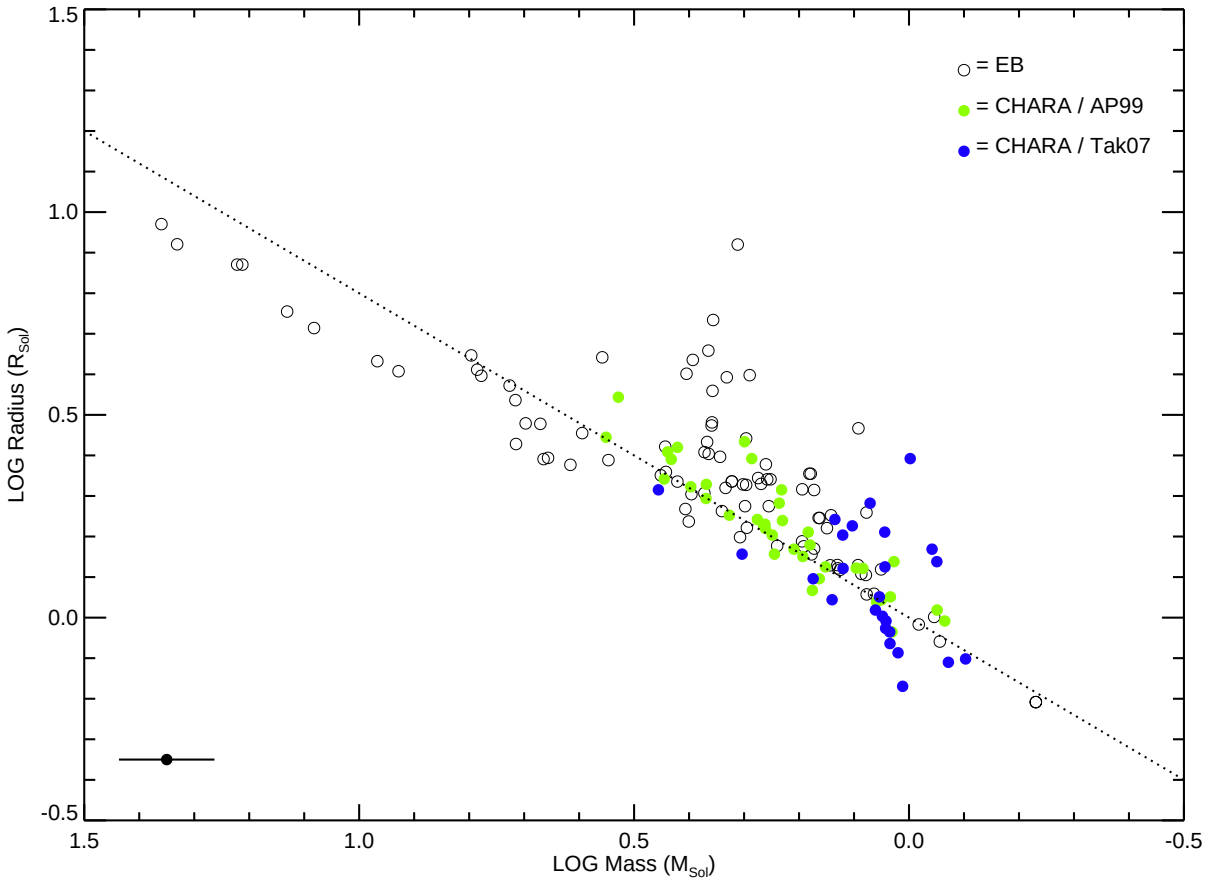

FIGURE 7.34: **Eclipsing Binary and CHARA Masses Versus Radius:** The EB radii and masses (open circles) are from Andersen (1991). CHARA data from this work are plotted, where the mass is derived from the $\log g$ estimates combined with CHARA radii for stars in Allende Prieto & Lambert (1999) (AP99) and Takeda (2007) (Tak07). In most cases, the errors in radii are smaller than the data points. Mass errors for EB's are typically smaller than the data point. A representative error in CHARA mass is plotted on the bottom left of the plot window. The dotted line is the mass-radius relation for main sequence stars $R \propto M^{0.8}$.

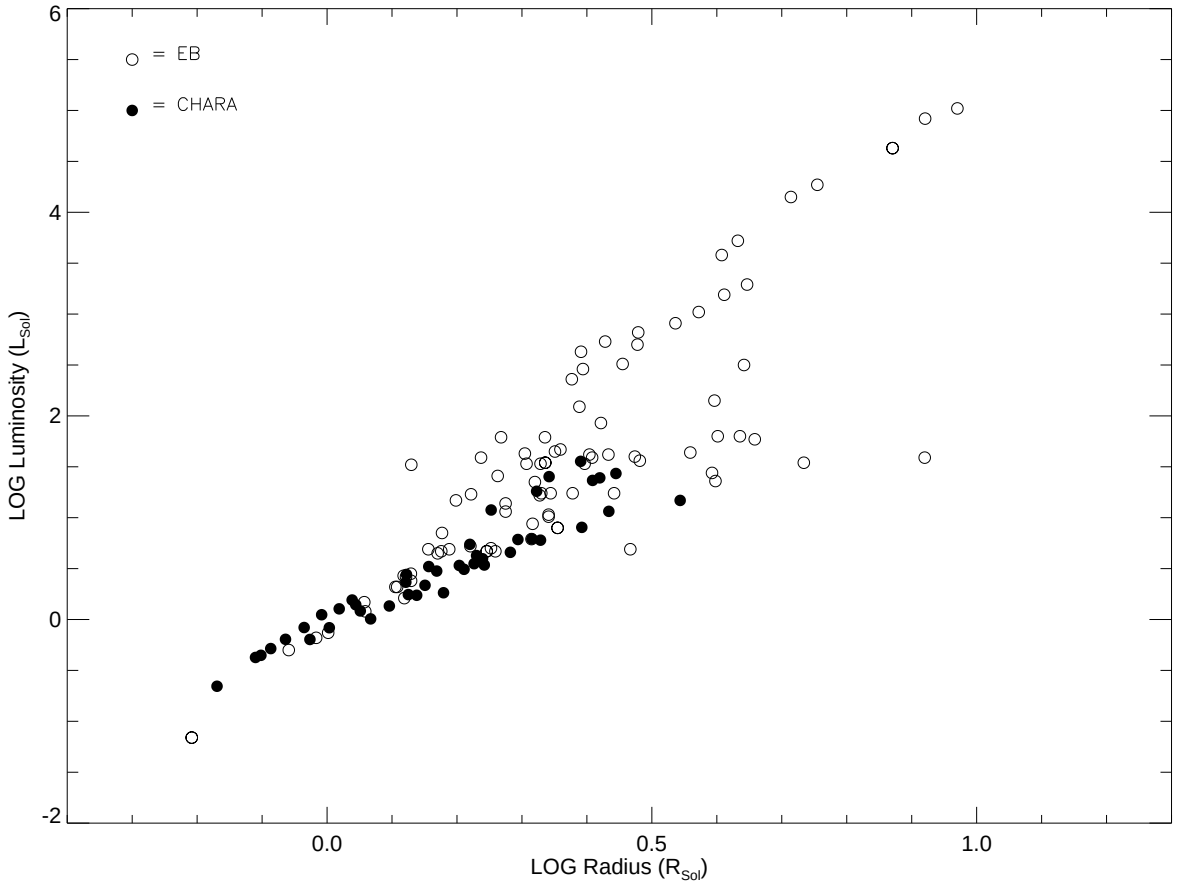

FIGURE 7.35: **Eclipsing Binary and CHARA Luminosities Versus Radii:** The EB data are from Andersen (1991) and are plotted as open circles. CHARA data from this work are plotted as closed circles. In most cases, the errors in radii and luminosities are smaller than the data points.

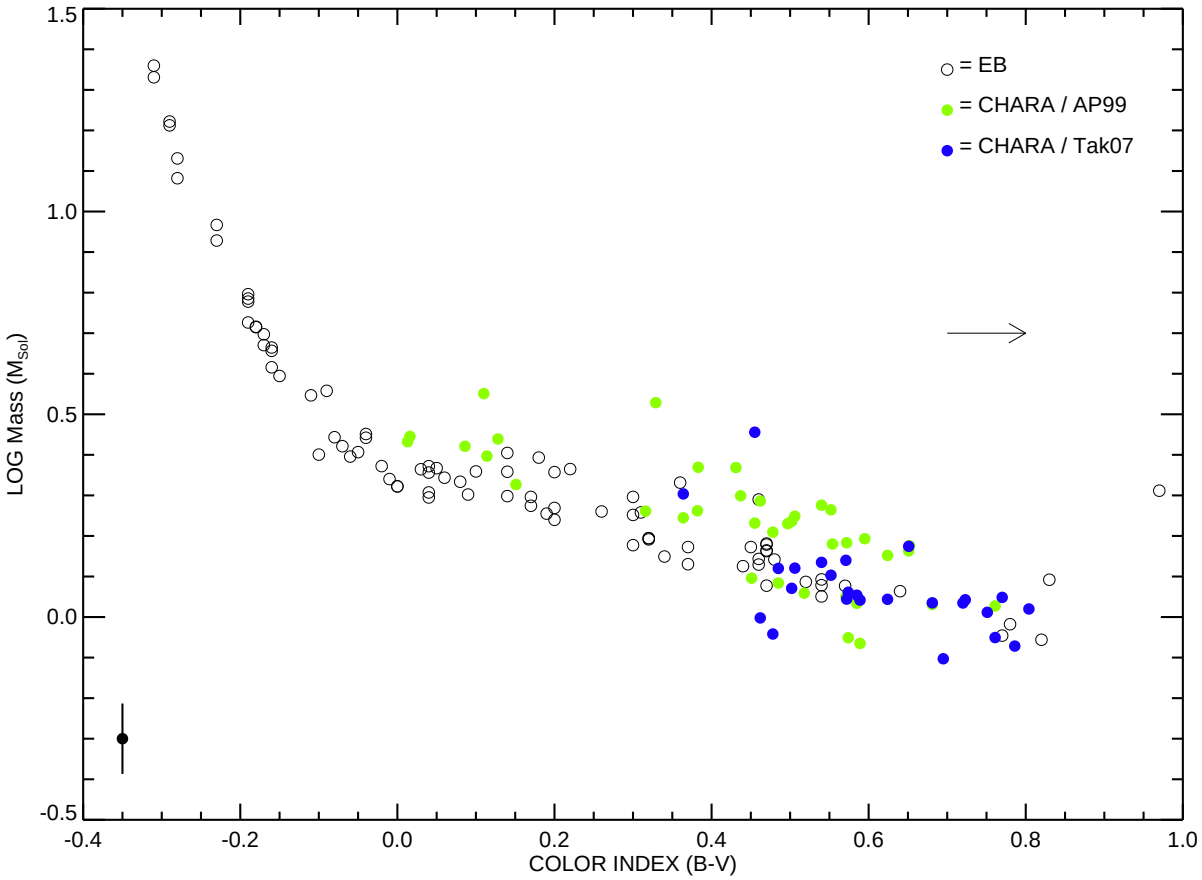

FIGURE 7.36: **Eclipsing Binary and CHARA Mass Versus ($B-V$):** The EB data are from Andersen (1991) and are plotted as open circles. The mass is derived from the $\log g$ estimates combined with CHARA radii for stars in Allende Prieto & Lambert (1999) (AP99) and Takeda (2007) (Tak07) are plotted as green and blue filled circles, respectively. In most cases, the errors in color index ($B-V$) are smaller than the data point. Mass errors for EB's are typically smaller than the data point. A representative error in CHARA mass is plotted on the bottom left of the plot window. The arrow in the upper right position of the plot points in the direction of stellar evolution.

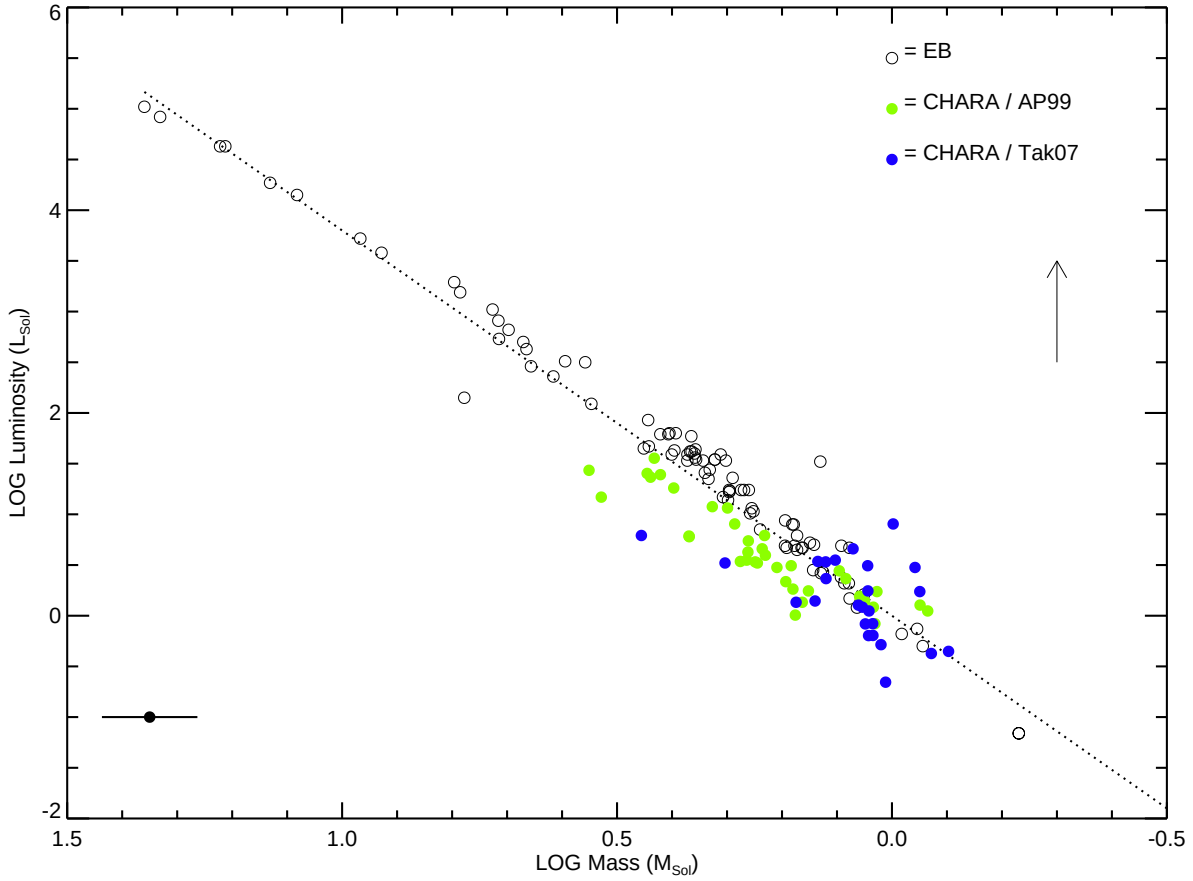

FIGURE 7.37: **Eclipsing Binary and CHARA Mass Versus Luminosity:** The EB data are from Andersen (1991) and are plotted as open circles. The mass is derived from the $\log g$ estimates combined with CHARA radii for stars in Allende Prieto & Lambert (1999) (AP99) and Takeda (2007) (Tak07) are plotted as filled green and blue circles, respectively. In most cases, the error in luminosity is smaller than the data point. Mass errors for EB's are typically smaller than the data point, whereas the error in CHARA masses are much larger (representative CHARA mass error shown in the bottom left position of the plot window). The dotted line is the relation: $M \propto L^{3.8}$. The arrow in the upper right position of the plot points in the direction of stellar evolution.

– 8 –

Yonsei-Yale Models

8.1 Introduction

The previous chapter compares ages of our stars in common with the stars in the survey work from Holmberg et al. (2007) and Takeda (2007). In those works, Holmberg et al. (2007) use the Padova models (Girardi et al. 2000; Salasnich et al. 2000), and Takeda (2007) uses the Yonsei-Yale (Y^2) stellar isochrones (Yi et al. 2001; Kim et al. 2002; Yi et al. 2003; Demarque et al. 2004). Holmberg et al. (2007) demonstrate that these model isochrones (among others) show minimal differences when compared to each other (also seen in Boyajian et al. 2008).

In order to determine ages of all the CHARA stars observed in this work, the Yonsei-Yale (Y^2) stellar isochrones, which apply the color table from Lejeune et al. (1998), are fit to the temperatures and luminosities determined here. To run the model isochrones, input estimates are required for the abundance of iron [Fe/H] and α-elements [α/Fe], both of which contribute to the overall heavy-metal mass fraction Z. Table 8.1 shows the model input values used in generating its isochrones for each of the 44 stars. For each star, model isochrones are generated for every 0.1 Gyr, in the range of 0.1−15 Gyr, and Table 8.1 has the resulting best fit age isochrone (in the temperature-luminosity plane), along with the associated mass for this best fit isochrone.

Appendix C shows the results for the Y^2 model isochrones for each star. There are four plots generated, all with 0.1, 1, 5, and 10 Gyr isochrones lines[1] along with the best fit

[1]Isochrone lines for 15 Gyr are also plotted for the stars HD 6582, HD48682, HD 101501, HD 103095, HD 109358, and HD 146233

isochrone line for the star's measured temperature and luminosity (also plotted with the 1-σ errors). The results for each star are also presented in Table 8.1, which includes the star name, best fit model isochrone age in Gyr, and the mass that corresponds to the position of the star on the fitted isochrone. The stars HD 6582 and HD 103095 are the only two stars which require non-zero [α/Fe] estimates as inputs to the model. Still, however, the solution for the best fit isochrone age is unphysical (>15 Gyr) showing that the models need further adjustment to match observations (see the discussion in Boyajian et al. 2008 for details on HD 6582). The star HD 146233 also shows a solution for an age >15 Gyr, unexplainable with the data at hand here.

8.2 Discussion

We fit the model isochrones in the theoretical temperature-luminosity (T-L) plane, where the solutions from the model are purely from the theory of stellar structure. In Appendix C, we also show the these results from the model isochrones and observations with respect to the observational color index ($B-V$)-luminosity (($B-V$)-L) plane. For almost all of the stars, the solutions are offset, and different ages can be inferred by matching the isochrone to the data in the observational plane of the color index ($B-V$). For instance, the age of HD 4614 in the T-L plane is 5.7 Gyr, however in the ($B-V$)-L plane, the age would be closer to $\sim$10 Gyr. The opposite is true for HD 86728, where the age in the T-L plane is 9.2 Gyr, and the ($B-V$)-L plane the age is closer to $\sim$5 Gyr. Very rarely do the two ages agree with one another. I suspect that this is due to an offset in the color table used in transforming the model isochrone temperatures to ($B-V$) colors (Lejeune et al. 1998). In

the next chapter, I will determine a color-temperature relation for the stars observed here with CHARA.

It is worth noting that the metallicity input for the model isochrones has an impact on the derived age (and in turn also on the derived mass). Lower metallicity isochrones shift down and to the left on these diagrams, so for a star with a true metallicity less than the input value, a higher isochrone age would be found. The opposite is true for stars with higher values of metallicity, where a younger age would result. For stars on the cool end of the main sequence, the isochrone lines are not very sensitive to age. For example, see HD 185144, a K0V, which has an age of 7.6 Gyr. Here, the errors in the temperature and luminosity alone (which are at the 1% level) result in acceptable values for its age from $\sim 1 - 10$ Gyr. An uncertainty in its metallicity value makes this acceptable range in age even wider. Because of this, no age errors are computed for these stars, and only fixed values of metallicity measured from a uniform source are used in the model input for computations. Thus relative ages may be correct while absolute ages are highly uncertain.

There are a few additional items to mention with respect to fitting these model isochrones to our measurements. The most metal poor stars observed, HD 6582 and HD 103095, have large deviations of the model compared to the observations, where the model overestimates the temperatures and underestimates the radii for each star and even 15 Gyr isochrones do not fit the data (see Boyajian et al. 2008 for details on HD 6582).

The star HD 146233 (18 Sco) also has this issue, and the isochrone age found for this star is >15 Gyr. I find this result very puzzling and interesting because HD 146233 is identified as a solar twin (Porto de Mello & da Silva 1997). Solar twins as defined in Cayrel de Strobel (1996) are stars that 1) have a temperature within $\sim 10^{\circ}$ K, of the Sun, 2) have a metallicity

within ~ 0.05 dex of the Sun, 3) have an age within ~ 1 Gyr of the Sun, and 4) have no known stellar companion. We measure an angular diameter of this star as $\theta_{\rm LD} = 0.781 \pm 0.017$ mas, much larger than the expected SED diameter of $\theta_{\rm SED} = 0.601 \pm 0.013$ mas. It was extensively observed over five nights, with three different baselines and using two calibrators, for a total of 25 data points used in the final diameter fit. The observed angular diameter forces this star to have a temperature much less than that of the Sun, $T_{\rm EFF} = 5373 \pm 68$ K ($T_{\rm EFF,\odot} = 5777$ K). While the luminosity of HD 146233 is very similar to the Solar value, $L = 1.01 \pm 0.03 L_{\odot}$, the radius is measured to be $\approx 17\%$ larger, indicating that it is much more evolved. Meléndez & Ramírez (2007) recently determined that indeed HD 146233 is more luminous than the Sun ($L = 1.06 \pm 0.09 L_{\odot}$), and while still finding the temperature close to solar, the radius is then predicted to be larger than solar by $0.03 R_{\odot}$, still showing a large discrepancy to our measurements. The best explanation of this offset may be from an undetected stellar companion, making the star appear more resolved by interferometry. Although long-term, high-resolution spectroscopic surveys have been conducted on HD 146233 to determine its abundances as well as radial velocity searches for exo-planets, a low-mass star could be undetected if it is far enough separated from the primary, producing no radial velocity changes over time. A hidden companion (nearly identical to the primary) would also mask the true abundance of the star, raising the continuum and making the absorption lines of the primary star appear weaker than they truly are. Further work should be done on HD 146233 to uncover the real reason for this discrepancy and possibly rule out its status of being a solar twin.

8.3 Comparative Analysis to Results from Other Works

For the stars in common in Holmberg et al. (2007) and Takeda (2007), I compare in Figure 8.1 the model ages I find with the Y^2 isochrones fits to my observations, to the ages they derive. The ages found for each reference compared to mine are significantly different, with the most pronounced differences in the ages from Holmberg et al. (2007), where their ages are typically lower than the my values. Because we are using the metallicity values from Holmberg et al. (2007) in computing the model isochrones in this work, we can assume that the difference is from one of two things. First, if the temperatures they are fitting to the models are higher (as seen in the last chapter when comparing the our temperatures to theirs), then a younger age will be found. Secondly, the models used are different in each work, but this effect should not contribute to such a high difference in the ages derived. We associate the effect seen to be a consequence of overestimating the temperature for the stars in Holmberg et al. (2007). The youngest ages we find for the stars in the sample do not agree with the Holmberg et al. (2007) or Takeda (2007) ages, where we find ages of 0.2 Gyr, while their ages are significantly higher, at 1.5 to 6.5 Gyr. These outliers are on the cool end of the sample (HD 10780; K0V and HD 20630; G5V), where the best isochrones are extremely sensitive to the data.

To investigate the possibility of an age-metallicity relation I plot the Y^2 isochrone age versus metallicity in Figure 8.2. The overall scatter in the diagram shows that for the nearby stars observed, there is no correlation between age and metallicity. Also shown in this figure is the color index for each star, coded to indicate its $(B-V)$ color, ranging from HD 177724 (bluest; $(B-V) = 0.013$; A0Vn) to HD 10780 (reddest; $(B-V) = 0.804$; K0V), where the

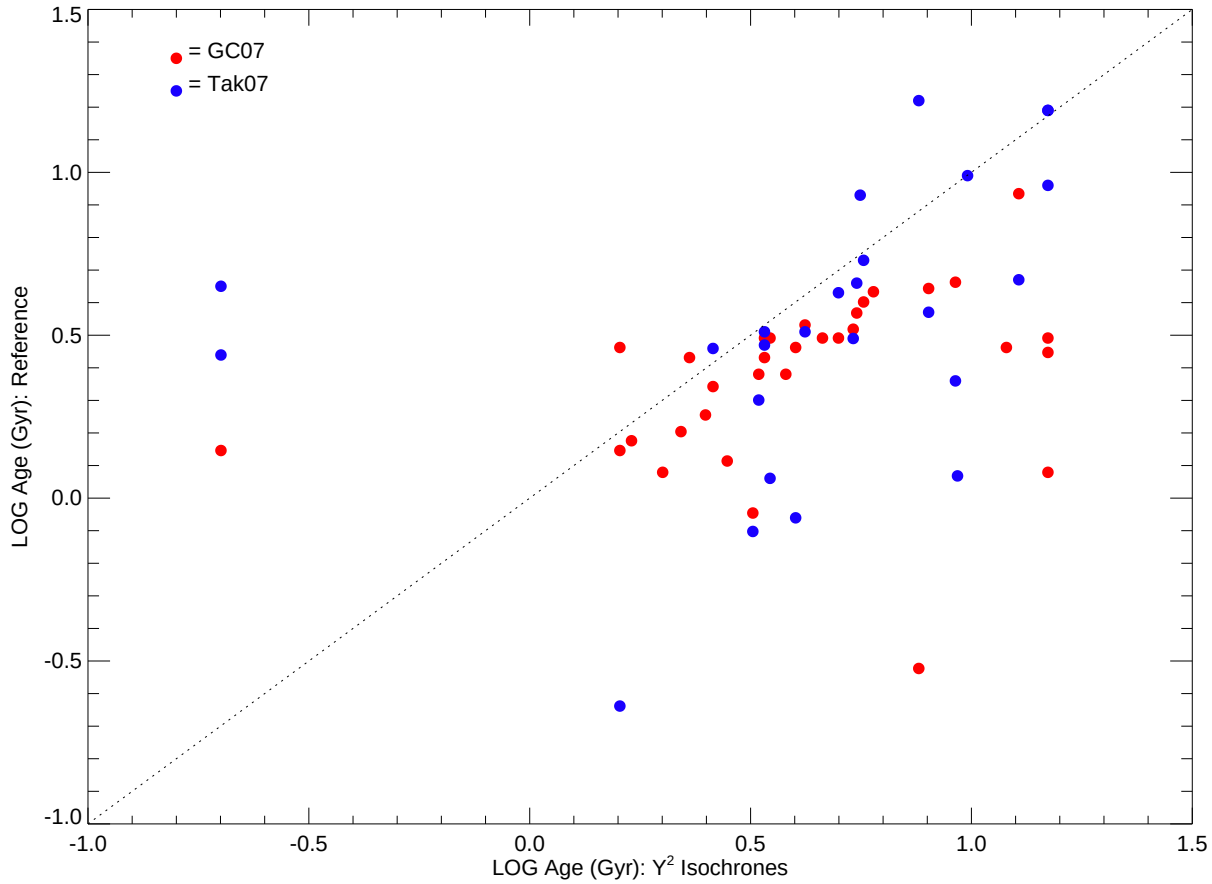

FIGURE 8.1: **Y^2 Model Ages Versus Ages from Holmberg et al. (2007) and Takeda (2007):** Ages derived from the Y^2 isochrones compared to ages of stars in common with Holmberg et al. (2007) and Takeda (2007). The dotted line shows a 1:1 relation.

color of the Sun ($(B-V) = 0.64$; G2V; shown as black in the figure) is yellow. For the reddest stars in the sample, we find stars ranging from the extreme of ages and metallicities. The bluest stars in the sample plotted do seem to show a slight downwards trend towards younger ages at higher metallicities. However, these bluest stars are also rapid rotators, which may make determining the [Fe/H] values difficult due to the rotational broadening of their spectral lines.

The masses I found from the best fit Y^2 isochrones compared to the masses derived for the stars in common in Allende Prieto & Lambert (1999), Holmberg et al. (2007), and Takeda (2007) are compared to each other in Figure 8.3. There is excellent agreement here for each

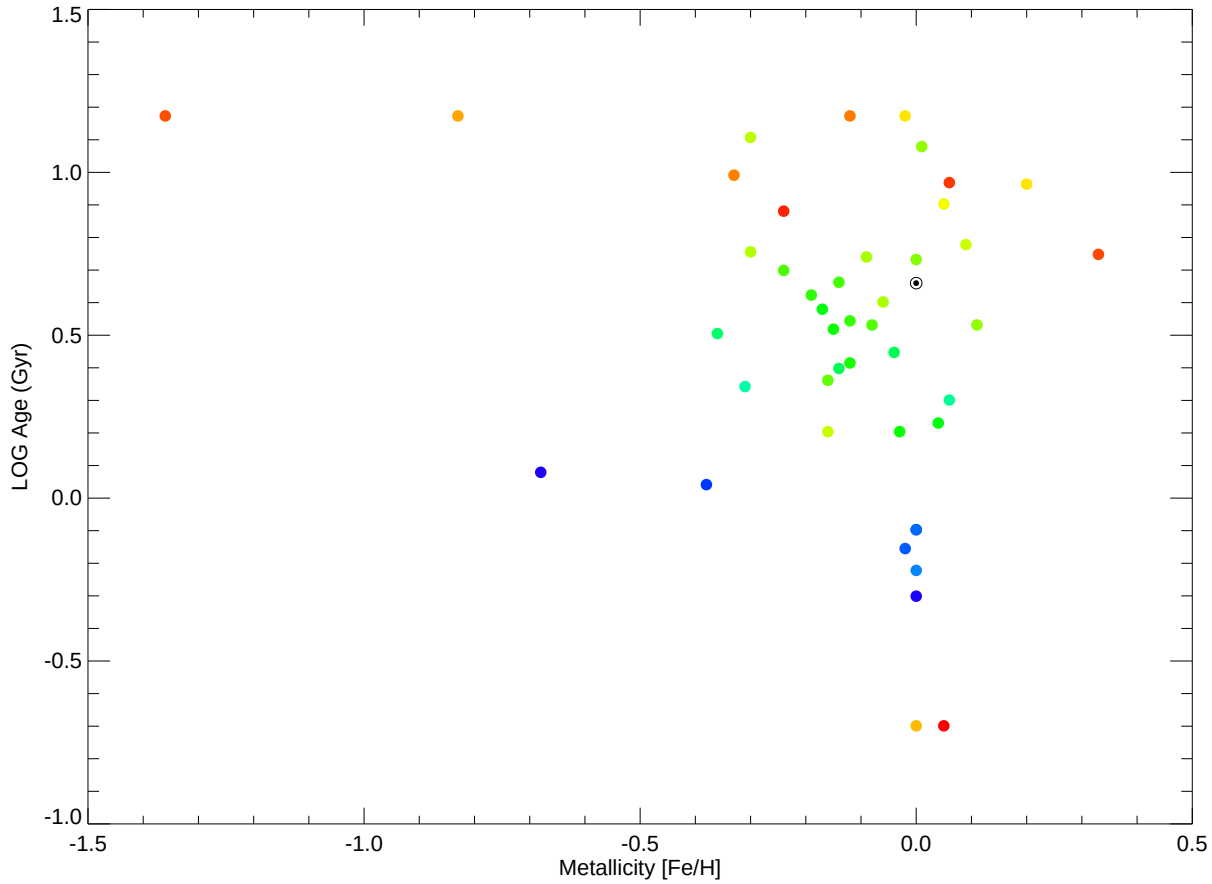

FIGURE 8.2: **Y^2 Model Ages Versus Metallicity:** Ages derived from the Y^2 isochrones as a function of metallicity for each star observed. The Sun is shown as $\odot$. The color-scale represents the $(B-V)$ color index of each star, where the $(B-V)_{\rm min} = 0.013$ is the bluest shade, $(B-V)_{\rm max} = 0.804$ is the reddest shade, and $(B-V)_{\odot}$ is yellow for an age of 4.57 Gyr (Bonanno et al. 2002).

reference, with a slight tendency for the mass in each reference to be higher than my derived mass. This is likely because the ages derived for the stars are mostly overestimated in each reference compared to these new results, a cause which links back to the temperature offsets. An overestimated temperature will lead to a slightly more massive star, because hotter stars on the main sequence are more massive than their cooler counterparts, as well as a younger age.

In the previous chapter, I derived masses using the CHARA measured radius of a star in combination with $\log g$ estimates for stars in common with Takeda (2007) and Allende Prieto

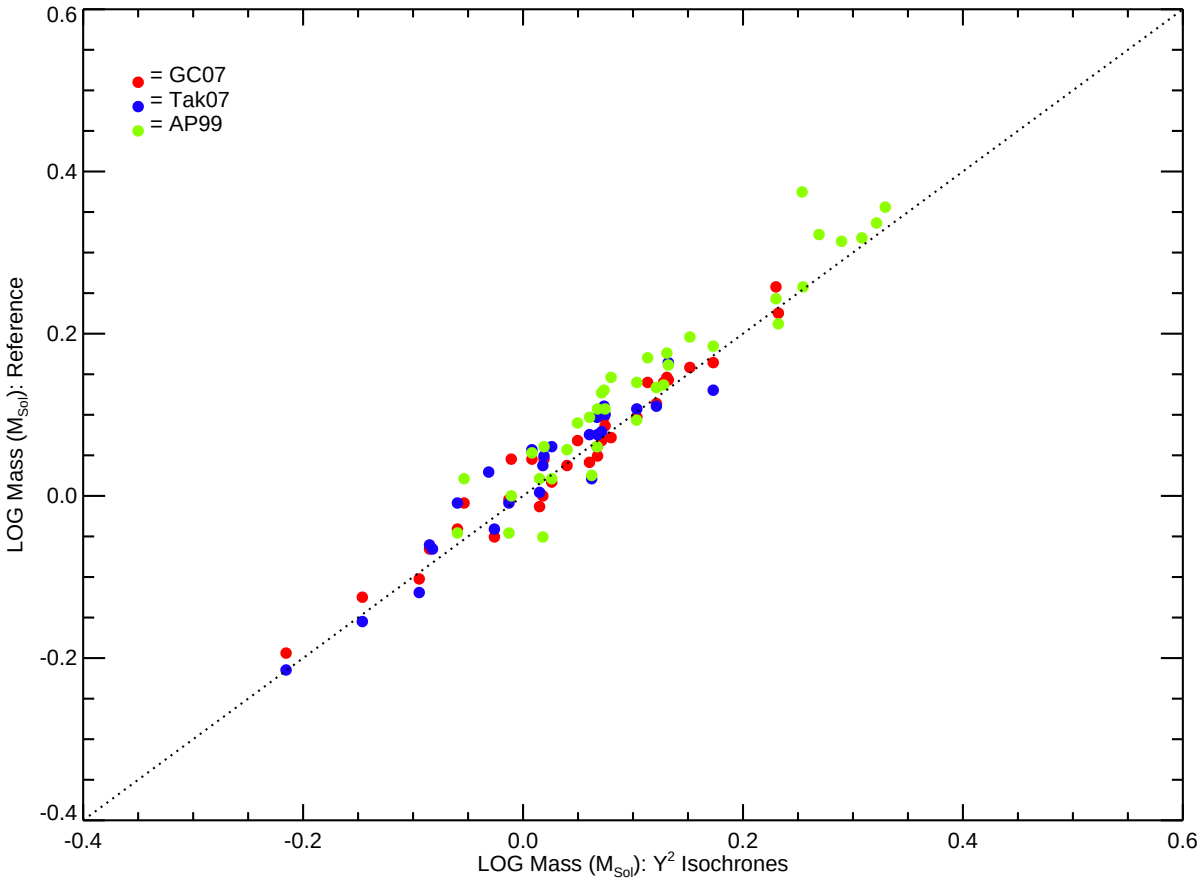

FIGURE 8.3: **Y^2 Model Masses Versus Masses from Allende Prieto & Lambert (1999), Holmberg et al. (2007), and Takeda (2007):** Masses derived from the Y^2 isochrones compared to masses of stars in common with Allende Prieto & Lambert (1999), Holmberg et al. (2007), and Takeda (2007). The dotted line shows a 1:1 relation.

& Lambert (1999). Figure 8.4 shows the relation between the masses derived from the Y^2 isochrones, compared to the masses found from the combination of $\log g$ and CHARA radii. There is significant scatter in the plot, especially for the stars in common with the Takeda (2007) survey. The stars in the Allende Prieto & Lambert (1999) work show an interesting trend for masses bigger than $\sim 1 M_{\odot}$, where the derived mass from $\log g$ and radii are larger than the model mass solutions from the Y^2 isochrones. This can be attributed to the $\log g$ values being overestimated, producing in turn higher masses than expected. It is possible that the reason why the $\log g$ values are being overestimated is a consequence of stars'

overestimated temperatures. If the model temperature that is used to fit the spectral lines to determine $\log g$ values for the stars is offset, it will in turn lead to spurious values of $\log g$ for the stars. This idea is enforced in the previous chapter that showed that the temperatures in Allende Prieto & Lambert (1999) are much more offset to higher temperatures than the temperatures for stars in Takeda (2007), especially for the hotter (more massive) stars.

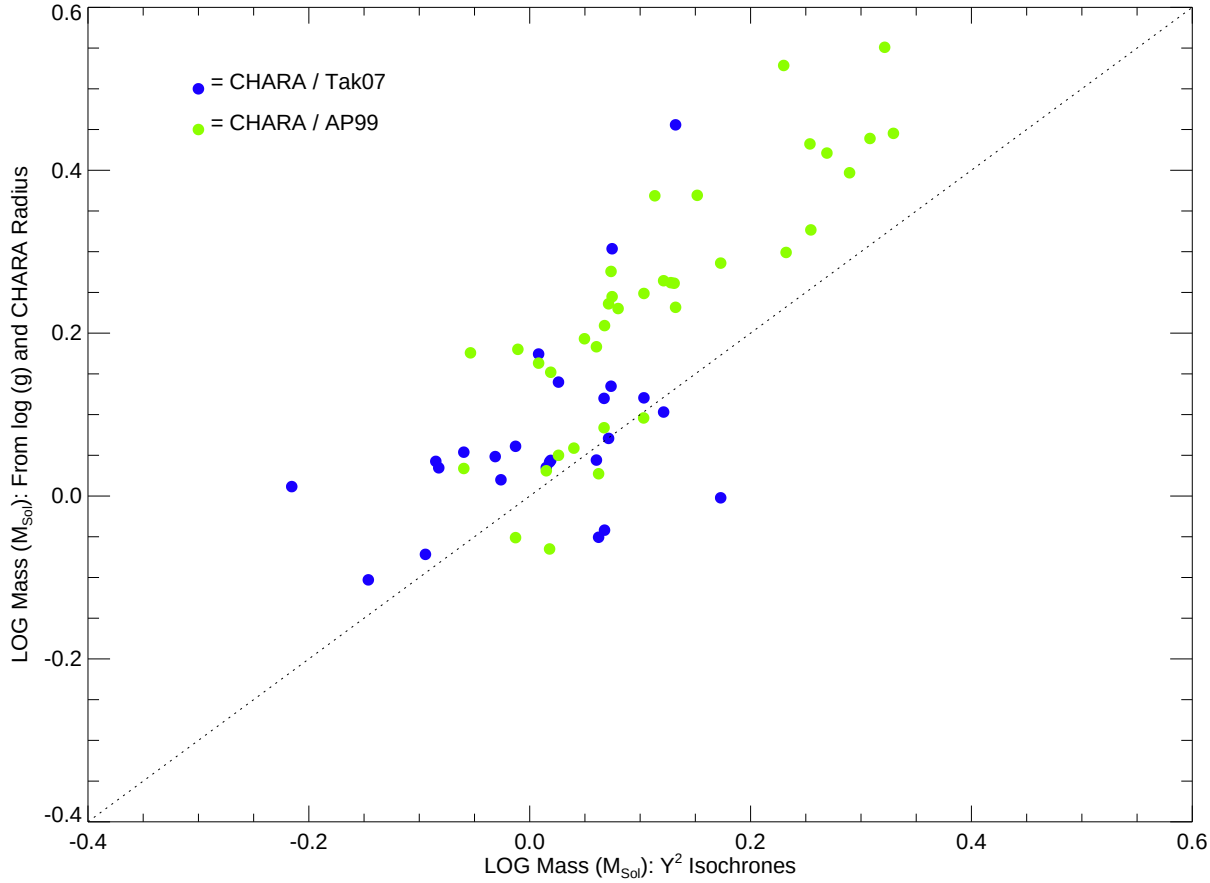

FIGURE 8.4: **Y^2 Model Masses Versus Masses Derived from $\log g$:** Masses derived from the Y^2 isochrones compared to masses of stars calculated from the combination of $\log g$ estimates and our CHARA Radii. Reference for $\log g$ estimates are for stars in common with the Allende Prieto & Lambert (1999), and Takeda (2007) surveys. The dotted line shows a 1:1 relation.

In Figure 8.5, I show the relation between $(B-V)$ color index and stellar mass. Eclipsing binary data from Andersen (1991) are plotted, as well as the masses for stars in this project derived from the Y^2 isochrones, and masses derived from the combination of the CHARA

radii and $\log g$ estimates from each source (AP99 or Tak07). In the previous chapter, inspection of this plot revealed that the stars observed in this survey were slightly evolved compared to eclipsing binary systems. Introducing the Y^2 masses in this figure, I find that that result is likely misinterpreted. The Y^2 masses I found are in excellent agreement with the unevolved sample of eclipsing binaries from Andersen (1991). The higher masses found from the $\log g$/radii method made the stars appear to be more evolved than they really are. This offset of higher $\log g$ estimates (forcing higher derived masses) also ties into the reference's results for slightly higher model masses (Figure 8.3), leading to younger ages (Figure 8.1), all factors that are results of overestimated temperatures.

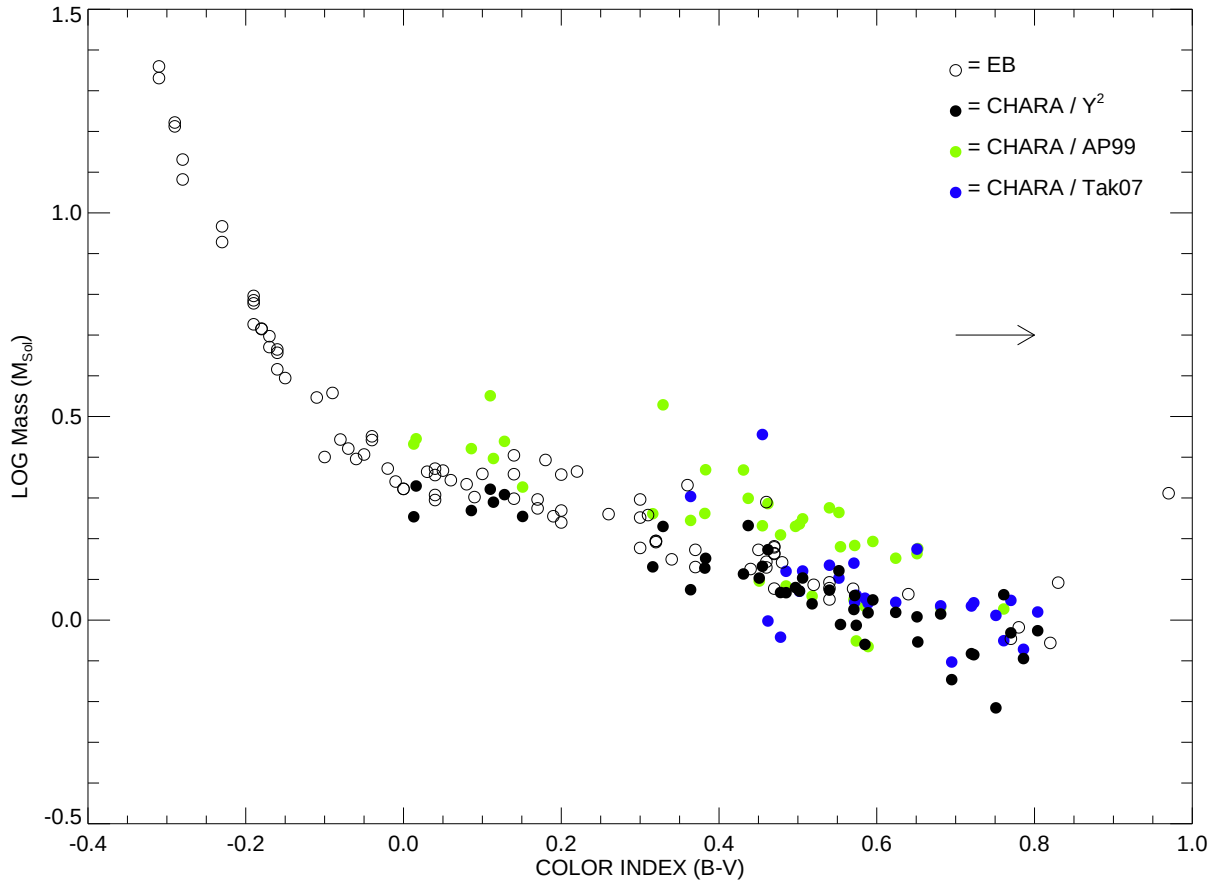

FIGURE 8.5: **Mass Versus Color Index:** Mass versus color index for eclipsing binaries plotted with masses derived from the Y^2 isochrones, and masses of stars calculated from the combination of $\log g$ estimates and our CHARA radii. Reference for $\log g$ estimates are for stars in common with the Allende Prieto & Lambert (1999), and Takeda (2007) surveys. The arrow points in the direction of evolution.

The mass-luminosity relation for the stars in this project are plotted against the sample of eclipsing binaries in Andersen (1991) in Figure 8.6. Masses found from the Y^2 isochrones are again in excellent agreement with the eclipsing binaries. The masses derived from the CHARA radii/$\log g$ method again show an offset to prefer higher masses, forcing them to appear under-luminous compared to the EB sample. This effect leads to a false sense of younger ages, along with the higher $\log g$'s and under-predicted radius values from Allende Prieto & Lambert (1999).

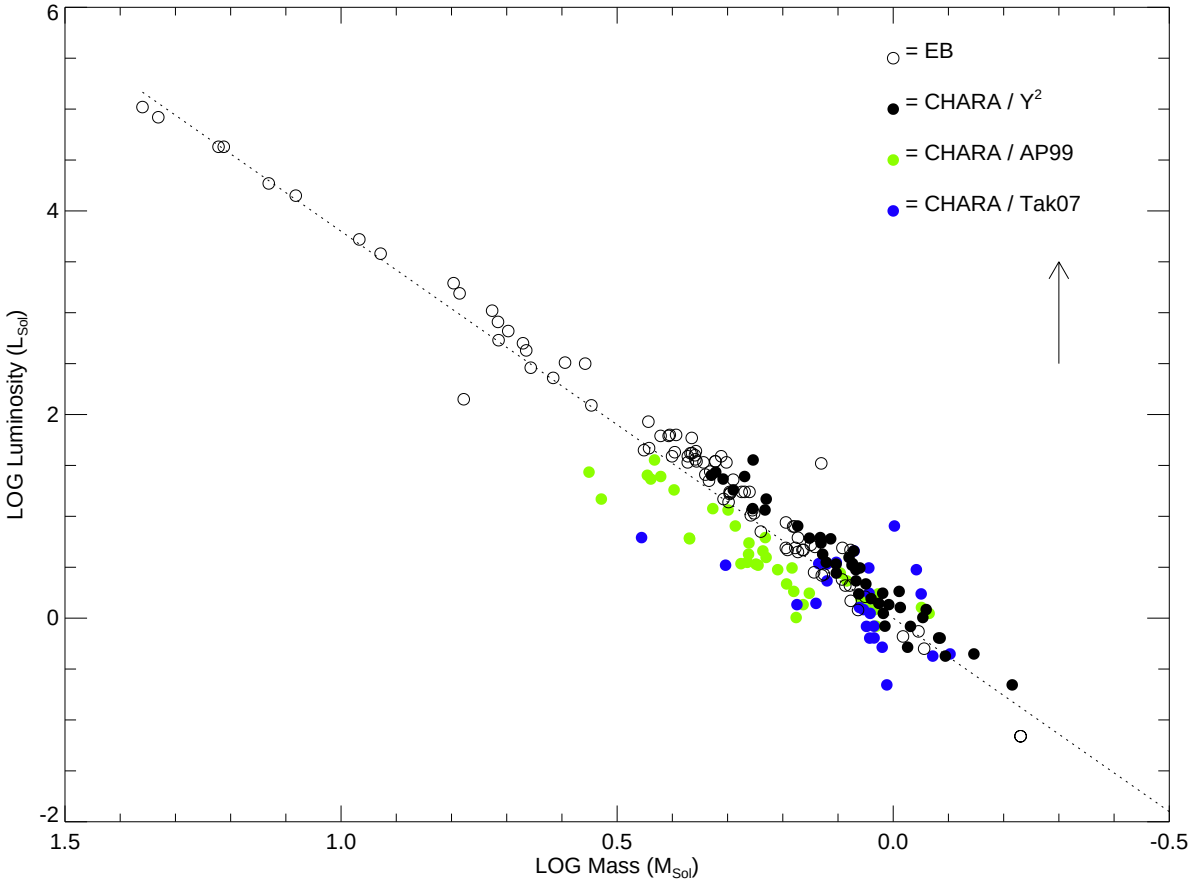

FIGURE 8.6: **Mass Versus Luminosity:** Mass versus luminosity for eclipsing binaries and CHARA masses derived from the Y^2 isochrones, as well as masses of stars calculated from the combination of $\log g$ estimates and our CHARA radii. Reference for $\log g$ estimates are for stars in common with the Allende Prieto & Lambert (1999), and Takeda (2007) surveys. The arrow points in the direction of evolution. The dotted line is the relation $M \propto L^{3.8}$.

TABLE 8.1: Y^2 Model Isochrone Results

Star HD	**[Fe/H]** †	**[α/Fe]** † †	**Age (Gyr)**	**Mass ($M_\odot$)**
4614	−0.30	0.0	5.7	0.97
5015	0.00	0.0	5.4	1.18
6582	−0.83	0.3	>15.0	0.71
10780	0.05	0.0	0.2	0.94
16895	−0.12	0.0	3.5	1.17
19373	0.09	0.0	6.0	1.12
20630	0.00	0.0	0.2	1.04
22484	−0.09	0.0	5.5	1.15
30652	−0.03	0.0	1.6	1.27
34411	0.05	0.0	8.0	1.04
39587	−0.16	0.0	1.6	1.04
48682	0.01	0.0	12.0	0.98
48737	0.04	0.0	1.7	1.71
56537	0.00	0.0	0.8	2.10
58946	−0.31	0.0	2.2	1.35
81937	0.06	0.0	2.0	1.70
82328	−0.12	0.0	2.6	1.49
82885	0.06	0.0	9.3	0.93
86728	0.20	0.0	9.2	1.02
90839	−0.16	0.0	2.3	1.10
97603	0.00	0.0	0.8	2.03
101501	−0.12	0.0	14.9	0.82
102870	0.11	0.0	3.4	1.32
103095	−1.36	0.3	>15.0	0.61
109358	−0.30	0.0	12.8	0.87
114710	−0.06	0.0	4.0	1.06
118098	−0.02	0.0	0.7	1.95
126660	−0.14	0.0	4.6	1.20
128167	−0.36	0.0	3.2	1.19
131156	−0.33	0.0	9.8	0.83
141795	0.00	0.0	0.6	1.80
142860	−0.19	0.0	4.2	1.17
146233	−0.02	0.0	>15.0	0.88
162003	−0.17	0.0	3.8	1.30
164259	−0.14	0.0	2.5	1.42
173667	−0.15	0.0	3.3	1.36
177724	−0.68	0.0	1.2	1.79
182572	0.33	0.0	5.6	1.15

Continued on Next Page...

TABLE 8.1 – Continued

Star HD	**[Fe/H]** †	**[α/Fe]** † †	**Age (Gyr)**	**Mass ($M_\odot$)**
185144	−0.24	0.0	7.6	0.80
185395	−0.04	0.0	2.8	1.34
210418	−0.38	0.0	1.1	1.86
213558	0.00	0.0	0.5	2.13
215648	−0.24	0.0	5.0	1.18
222368	−0.08	0.0	3.4	1.27

†[Fe/H] values from Holmberg et al. (2007), when available. For stars without metallicity estimates from Holmberg et al. (2007), the [M/H] values from Gray et al. (2003, 2006) (HD 82885, HD 97603, HD 118098, HD 131156, HD 177724, HD 210418), and Takeda et al. (2005) (HD 182572) are used. Stars without metallicity measurements have [Fe/H]=0.0 (HD 56537, HD 141795, HD 213558).

† † The [α/Fe] for all stars are zero, except for HD 6582 and HD 103095 where we set [α/Fe] = 0.3 (the average value for stars with [Fe/H]< -0.6 (Carney 1996)).

– 9 –

Effective Temperature Calibrations

Obtaining an empirical effective temperature scale provides the means to estimating the temperatures of a large number of stars at great distances where they are too unresolved to measure their temperature directly with interferometry. This is particularly important when studying clusters of stars, allowing the transformation of their observed properties on a color-color diagram to the theoretical version of a temperature-luminosity diagram.

There exist theoretical color-temperature relations as well as empirical color-temperature relations (and some semi-empirical). The most robust methods implement the metallicity of the star into the relation as well, for this is a contributing factor to the observed color index of a star along with the effective temperature.

The typical expression used to fit the temperature, color, and metallicity is expressed in Equation 1 of Alonso et al. (1996):

$$\theta_{\rm EFF} = a_0 + a_1 X + a_2 X^2 + a_3 X[{\rm Fe/H}] + a_4[{\rm Fe/H}] + a_5[{\rm Fe/H}]^2 \tag{9.1}$$

where $\theta_{\rm EFF} = 5040/T_{\rm EFF}$, X is the color index $(B-V)$, [Fe/H] is the metallicity, and a_i $(i = 0 \ldots 5)$ are the coefficients of the fit. This formula has been used in temperature calibrations derived from the Infrared Flux Method (IRFM, Blackwell & Shallis 1977) in more recent works including Ramírez & Meléndez (2005); Casagrande et al. (2006); González Hernández & Bonifacio (2009).

In this work, the solution of coefficients a_i is found using a nonlinear, least-squares fit implementing the Levenberg-Marquardt algorithm in *Mathematica*. The stars in this sample are bright, and $2MASS\ K$ magnitudes are typically saturated and have a photometric quality flag grade of C, or worse. For this reason, I derive a calibration using the well-determined $(B-V)$ colors. The data were fit in the full range of color index ($0.013 \leq (B-V) \leq 0.804$) and full range in metallicity ($-1.36 \leq$ [Fe/H] ≤ 0.33) to arrive at the solution:

$$\begin{aligned}\theta_{\rm EFF} = 0.563 + 0.629(B-V) - 0.209(B-V)^2 - 0.100(B-V)[{\rm Fe/H}] \\ +0.050[{\rm Fe/H}] + 0.049[{\rm Fe/H}]^2\end{aligned} \tag{9.2}$$

where the standard deviation of the fit is $\sigma(\theta_{\rm EFF}) = 0.025$. Ordinarily, there are several iterations performed of the fit, with outliers greater than 2.5σ clipped out of the following fit (see González Hernández & Bonifacio 2009, and references therein). This solution includes all data points (one iteration for the fit), and there are two outliers: HD 48682 (368°K) and HD 81937 (363°K). Following the accepted policy of clipping data with fit residuals $> 2.5\sigma$, a second iteration is performed with a resulting $\sigma(\theta_{\rm EFF}) = 0.018$ and, according to policy, only one outlier must be removed HD 146233 (282°K) for the next (and final) iteration. In the final iteration, all the data have fit residuals within 2.5σ, with a standard deviation of the fit of $\sigma(\theta_{\rm EFF}) = 0.0156$. This is the final form of the solution:

$$\begin{aligned}\theta_{\rm EFF} = 0.561 + 0.585(B-V) - 0.152(B-V)^2 - 0.094(B-V)[{\rm Fe/H}] \\ +0.022[{\rm Fe/H}] + 0.032[{\rm Fe/H}]^2.\end{aligned} \tag{9.3}$$

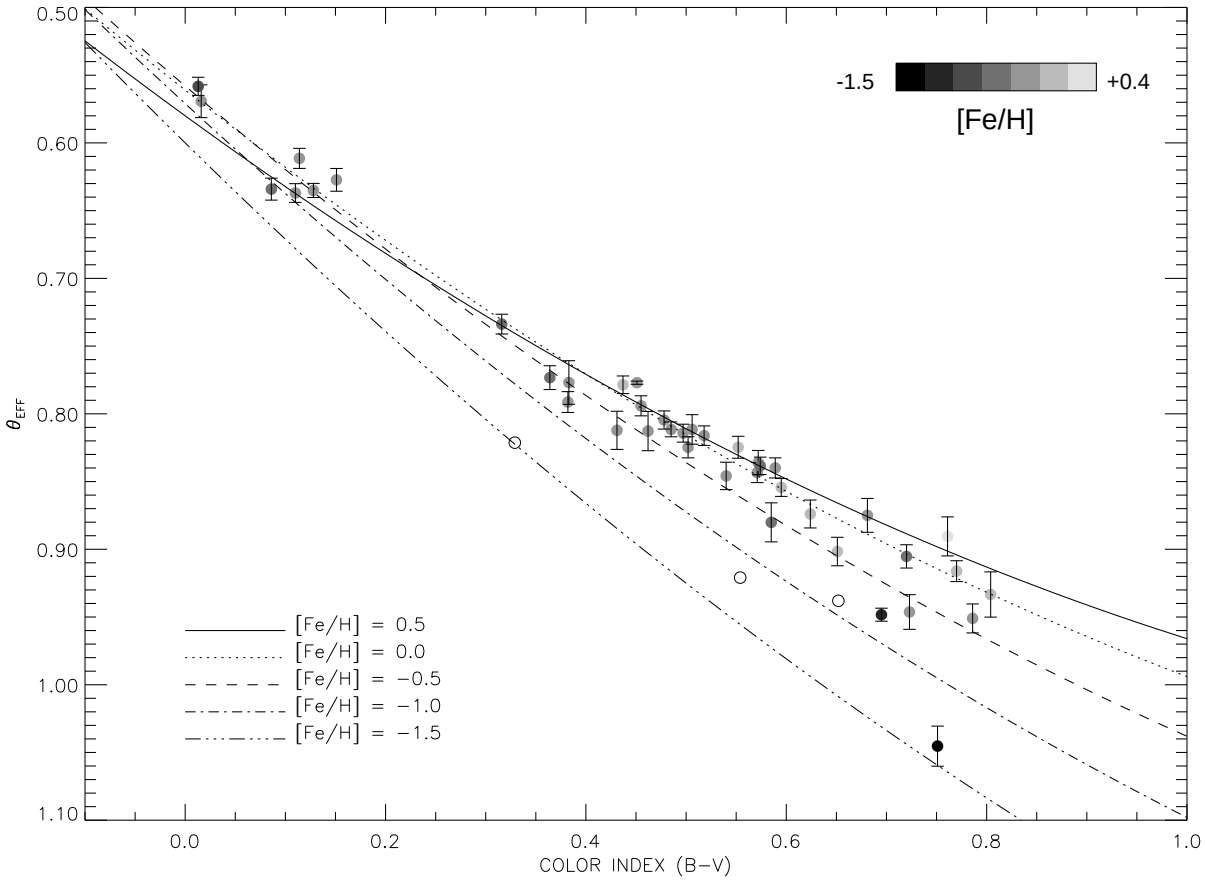

FIGURE 9.1: **Color-Temperature-Metallicity:** The star temperature $\theta_{\rm EFF} = 5040/T_{\rm EFF}$ versus $(B-V)$ color index, with grayscale levels indicating the metallicity [Fe/H]. The three stars clipped in the final solution are plotted as open circles. The final solution is plotted for lines of constant metallicity values (see legend).

Figure 9.1 shows the new results and the relation I derived for lines of constant metallicity.

There are three stars in the sample with very low metallicity, HD 6582, HD 103095, and HD 177724 (($\theta_{\rm EFF}$, $(B-V)$,[Fe/H]) = (0.948, 0.695, −0.83), (1.045, 0.751, −1.36), (0.558, 0.013, −0.68), respectively). The metallicity dependence for metal-poor, late-type stars is mostly defined by HD 6582 and HD 103095, and there are several dozen other stars used in the fit for this region to define the characteristics for stars of various higher metallicities.

There is a paucity of data in the hotter region of this sample that includes only the 7 A-type stars observed with CHARA. One star in particular, HD 177724, is one of the most rapidly rotating A-stars known, with a projected rotational velocity v $\sin i$ = 317 km s^{-1}

(Royer et al. 2006). For this work, I give the average diameter of all measurements, which agrees exceptionally well with the predicted mean angular diameter of the star from Absil et al. (2008)[1]. However, although we measure a mean angular diameter of the star, there are several issues that manifest due to its rapid rotation. The star will have apparent gravity darkening (in addition to limb darkening), which results in hotter temperatures at its pole than at its equator. Due to this temperature gradient (which is likely to be on the order of a few hundred degrees Kelvin), its spectra will contain the absorption lines of elements with different ionization states corresponding to both the hotter and cooler regions of the star. The spectral lines are also very rotationally broadened, making abundances measured from equivalent widths difficult. I suspect that the low metallicity of HD 177724 ([Fe/H]=−0.68; Gray et al. 2003) is a product of these circumstances. It is more probable that HD 177724 has a metallicity nearer to solar, because it has such a young age ($\mathrm{Age_{ISO}} = 1.2$ Gyr). With this in mind, the solution derived above is likely close to the truth for low-metallicity hot stars, because metal lines become weak at hotter temperatures, and so there would be less dependence of a stars metallicity on both the $(B - V)$ color and bolometric flux (the basis for temperature).

Figure 9.2 shows a visual representation of the fit compared to the solutions from other publications. Code et al. (1976) derived a relation of temperature versus color for the main sequence stars they observed (assuming solar metallicity) for the bluer end of the range. However, most works following this do not apply their calibration for stars bluer than $(B - V) \sim 0.3$. The relation from Lejeune et al. (1998) (red dashed line) is based upon synthetic

[1]Further work on this star is warranted, and is discussed in the chapter on Conclusions and Future Work.

colors and model atmospheres, and extends through the whole range of temperature and colors.

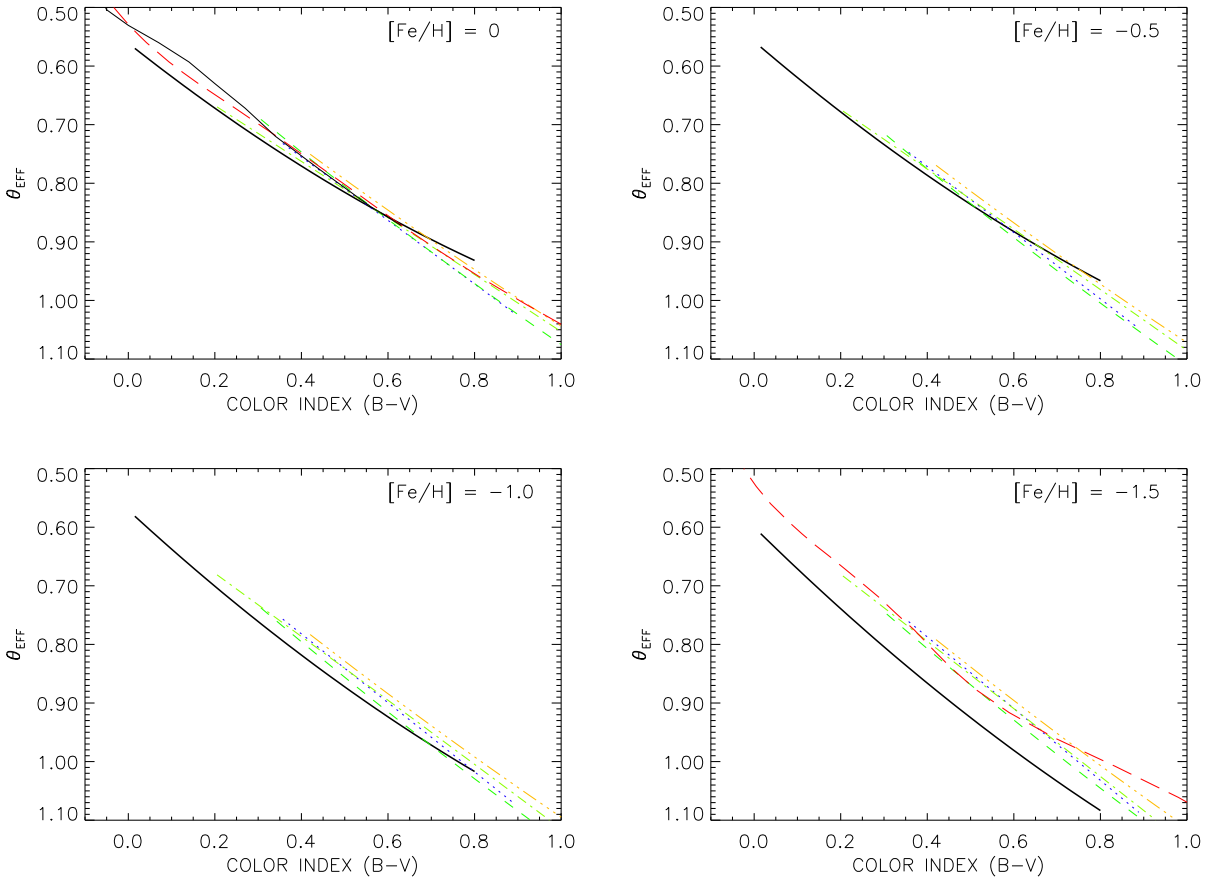

FIGURE 9.2: **Comparing Color-Temperature-Metallicity Relations:** The solutions for color temperature calibrations for 4 different metallicities. The lines correspond to the following: this work (thick-solid), Code et al. (1976) (solid), Alonso et al. (1996) (blue dotted), Ramírez & Meléndez (2005) (green dashed), González Hernández & Bonifacio (2009) (lime dotted-dashed), Casagrande et al. (2006) (orange triple-dotted-dashed), and Lejeune et al. (1998) (red long-dashed).

For a solar metallicity relation, my solution predicts cooler temperatures compared to Code et al. (1976) and Lejeune et al. (1998) by $\sim 200°$ K on the bluest end of the sequence, converging to a difference of only around $\sim 100°$ K at $(B-V) \sim 0.3$. The overall spread in temperature for all other relations on the red end of the sequence is $\sim 100°$ K, where my temperatures are typically cooler for stars bluer than the Sun and hotter for stars redder than the Sun (where $\theta_{\mathrm{EFF},\odot} = 0.872$). The same applies for a metallicity [Fe/H]$= -0.5$,

although the spread in temperatures here approaches $\sim 300^{\circ}$ K for the stars of $(B-V) \sim 0.8$. At a metallicity of [Fe/H] $= -1$, the solution from this work predicts temperatures cooler than most of the other references compared here for the whole range of colors. The solution for the lowest metallicity of [Fe/H] $= -1.5$ is quite interesting. My temperatures are $\sim 200^{\circ}$ K lower than any of the other temperature scales it is compared to here.

To compare my results to solutions in previous works, I use the color-temperature-metallicity scales presented in Alonso et al. (1996), Ramírez & Meléndez (2005), and González Hernández & Bonifacio (2009) to determine the residuals when my data are applied to their solution (only valid for stars in the ranges of $(B-V) \gtrsim 0.3$). Figure 9.3 shows the residual in the predicted temperature of the polynomial solution for each star's color and metallicity versus the CHARA temperature found from interferometry (δT). The results for this work are also shown (top panel), and the standard deviation of the residuals is also displayed in the lower left hand corner of each panel. Each solution reproduces the CHARA temperatures with a mean error of $< 100^{\circ}$K, however, slight systematic residuals are seen for stars bluer than $(B-V) \sim 0.5$, where the predictions in the published references lead to hotter temperatures. Cooler temperatures are predicted (with a significant amount of scatter) for the redder stars in this region, most pronounced in the Alonso et al. (1996) and Ramírez & Meléndez (2005) temperature scales.

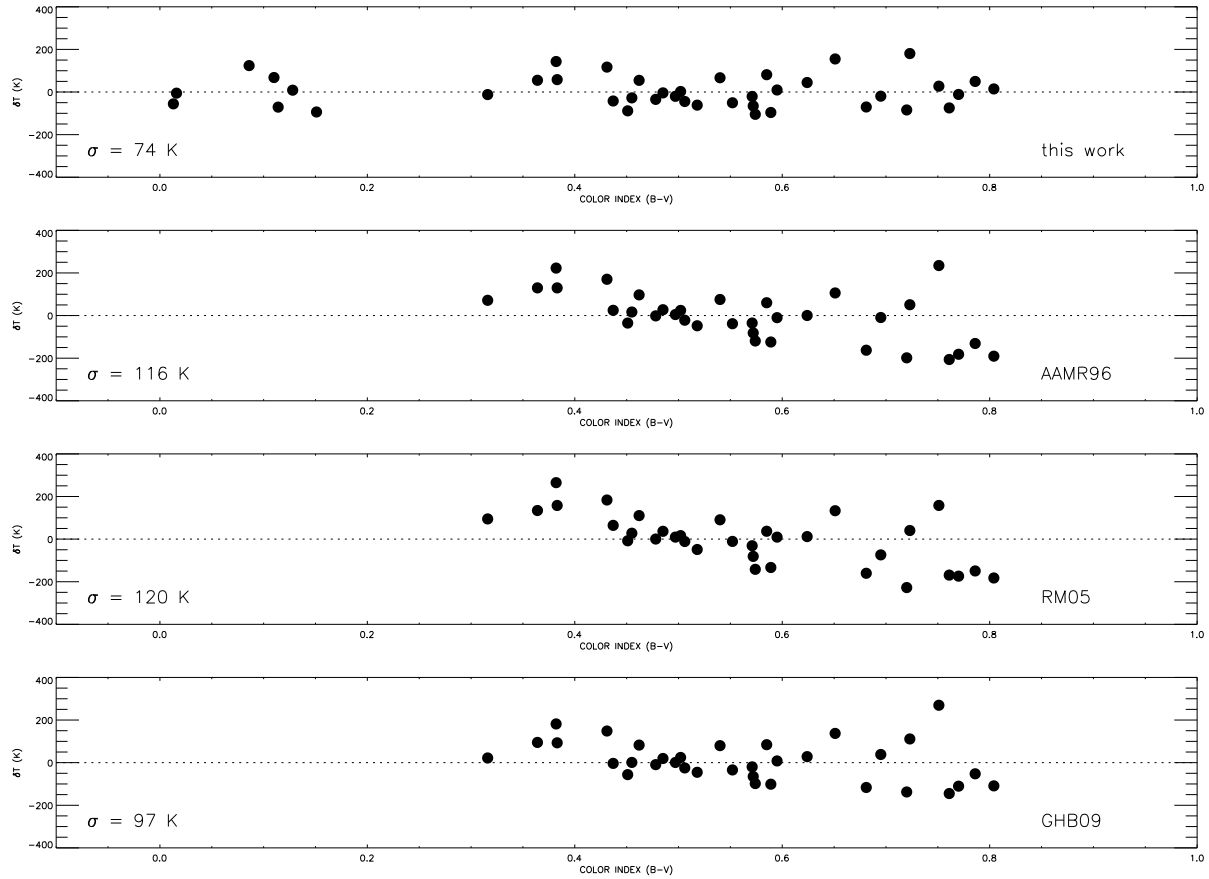

FIGURE 9.3: **Residuals of Color-Temperature-Metallicity Relations:** The color-temperature-metallicity relations in Alonso et al. (1996) (AAMR96), Ramírez & Meléndez (2005) (RM05), and González Hernández & Bonifacio (2009) (GHB09) are used to predict the temperature of each star and are compared with the measured CHARA temperature (δT). The standard deviation in the predicted versus measured temperature residuals is shown in the lower left region of each plot.

– 10 –

Summary and Future Work

During the 2007-2008 observing seasons, I observed a total of 69 nights with the CHARA Array. A total of 943 bracketed observations were collected for 44 of the 77 stars chosen for this survey; this includes 7 A-stars, 19 F-stars, and 18 G-stars. The measurements of these 44 stars meet the main goal of the project, to determine their angular diameters to better then 4% accuracy. These results also yield linear radii of the 44 stars to better than 4% accuracy. Twenty of these stars have effective temperatures measured to <1% accuracy, all of which are measured to better than 2.1%. Contact has been established with several different groups who are interested in using these results to refine the effective temperature scale of main sequence stars of these types to better improve models and color-temperature transformations.

The temperatures and luminosities presented here were used in conjunction with Yonsei-Yale model isochrones to derive ages and masses for these 44 stars, and excellent agreement is seen with the results from a large sample of eclipsing binary stars. On the other hand, indirect determination of stellar parameters (exclusively using photometric observations) show a discrepancy compared to my results. For most cases, the indirectly determined properties lead the models to underestimate the radius of the star by $\sim 12\%$, while in turn they overestimate the effective temperature by $\sim 1.5 - 4\%$, with no apparent correlation to the star's metallicity or color index. The overestimated temperatures and underestimated radii in these works appear to cause an additional offset in the star's surface gravity measure-

ments, which consequently yields higher masses and younger ages, in particular for stars with masses greater than $\sim 1.3\ M_{\odot}$.

To fully take advantage of the excellent accuracy available on measuring the angular diameters with the CHARA Array, a few things need to be studied further. The first is the effective wavelength of the CHARA Classic filter. Modeling of the transmission of the filter, mirror reflection properties and incorporating the flux distribution of the star in the K' waveband, McAlister et al. (2005) concluded that we know the effective wavelength as $\lambda = 2.15 \pm 0.01\ \mu$m. A project is underway by Ms Emily Bowsher to characterize the properties of the filter. Her investigation will cover a range in spectral types from O to M, at different luminosity classes, and is anticipated to be completed by Spring 2010.

Next, a more robust method for determining the bolometric flux for each star is needed. Lacking this improvement, we will ultimately make the errors on the $T_{\rm EFF}$ determination through the angular diameter of the star be limited by the $F_{\rm BOL}$ error, which for these stars is currently at the 3% level, on average.

A collaboration with Dr Gerard van Belle (ESO) has been established to determine the bolometric flux's for these stars in the same way as described in van Belle et al. (2008). Briefly put, this implies fitting a template SED from Pickles (1998) to observed photometry, in addition to accounting for additional wavelength dependent reddening factors (assumed to be zero in this work). Due to time constraints, we performed only a test run to estimate $F_{\rm BOL}$ for these stars using van Belle's routine. For this test run, the SED template from Pickles (1998) was fixed to the spectral type given in Table 2.2 (majority of spectral types from Gray et al. 2001, 2003). However, a main drawback from this approach is that incorrect spectral typing is possible, and if the star is off by a subclass (or two) in spectral type, this

can lead to spurious results. Likewise, there is a nasty degeneracy between incorrect spectral typing and apparent reddening, which can also lead to inaccurate results. When the time comes for the final analysis, we plan to search through a larger grid of suitable spectral type templates to find the best fit solution of $F_{\rm BOL}$ estimates for each star.

The $F_{\rm BOL}$ estimated from a test run of van Belle's routine compared with the literature values in I used for this work (summarized in Table 6.1) have an average absolute difference of 5.1%[1]. Although these new values need to be scrubbed, it is quite decent to say that the errors estimated for the $F_{\rm BOL}$ in Chapter 6 are likely to be underestimated. This is in part because the rms value of multiple measurements was taken as the error, and the values without multiple measurements were assigned the mean percentage error (3%) for the stars with more than one $F_{\rm BOL}$ estimate. To view the consequences of this mishap, we impose a conservative 4.5% error on the average literature values for $F_{\rm BOL}$ in Table 6.1 (where 4.5% is the median absolute difference between the various values found in Table 6.1). Overall, this is an increased error of $F_{\rm BOL}$ for almost all of the stars (which is directly proportional to the error on the absolute luminosity, quoted here in Table 6.2). This increase in $F_{\rm BOL}$ error, also changes the errors in temperature because the error of $F_{\rm BOL}$ is propagated through to the final error in temperature (along with the error of the angular diameter). The effective temperature errors for the 44 stars now range from 1.1−2.1% (compared to 0.2−2.1% with the old method), with an average error of 1.4% (compared to 1.2% with the old method). This simple exercise provides us with solid proof that picking $F_{\rm BOL}$ values from the literature

[1]However, taking into account the issues described in the previous paragraph, we suspect that in the end the agreement will not fall below $\sim 3\%$

to determine the stellar temperature is the weakest point in our method, and attention to revising this matter is currently underway.

Also, special attention of the following stars is required:

- Rapid rotators

  A-type stars are approaching the range at which stars begin to be seen with the highest rotational velocities (B-type stars). HD 177724 was observed for this project and its average diameter is given. However, it is among one of the fastest rotating A-stars, with a rotational velocity of $v\sin i = 317$ km s^{-1} (Royer et al. 2006), which leads to a predicted apparent oblateness of 1.307 (Absil et al. 2008). This oblateness factor depends on the limb-darkened angular diameter, $v\sin i$ and mass of the star (see Equation 5 in (Absil et al. 2008)). Our mean angular diameter of HD 177724 of $\theta = 0.897 \pm 0.017$ mas is in excellent agreement with their predicted mean angular diameter of $\theta = 0.880 \pm 0.018$ mas.

  In fact, the rotational velocities for all of the A-type stars in this project (except for HD 141795) are fairly high (HD 56537 = 154 km s^{-1}, HD 97603 = 180 km s^{-1}, HD 118098 = 222 km s^{-1}, HD 210418 = 144 km s^{-1}, and HD 213558 = 128 km s^{-1}, Royer et al. 2006). Although their predicted oblateness is likely to be undetectable with the precision of our measurements we should consider the angular diameter measured for these stars as the mean angular diameter.

- Visual and/or spectroscopic binaries

  The diameters of the primary stars in several binary systems were measured in this survey. The work for the population II binary HD 6582 has been published already by

Boyajian et al. (2008). The other systems observed are widely separated (ρ >10 arcsec), and have fainter late K to M dwarf companions (HD 4614, HD 16895, HD 39587, HD 131156, and HD 162003). These orbits have not been updated in several decades, despite data continually being collected on the systems. An effort needs to be made to update the orbital parameters for these stars to obtain dynamical masses. In combination with the results from these interferometric observations of their angular diameters, we will be able to determine all of the fundamental properties of these stars, the masses, luminosities, temperatures and radii, providing a more powerful probe into models of stellar theory, star formation, and evolution.

- Visibility Binaries

  There are several stars that I observed for this work having visibility measurements that do not lead to an angular diameter for a single star, namely, HD 55575, HD 95418, and HD 187691. These stars are likely previously undetected binaries, and more observations may confirm their multiplicity status, as well as enable us to define their orbital motions.

- Incomplete diameter determination

  The stars HD 25457, HD 168151, HD 187013, HD 195564, and HD 211336 presently have an insufficient amount of data to reliably determine their angular diameters to the accuracy goals of this project. New improvements to the CHARA Array will allow for H-band observations of brighter targets that were previously saturating. Observations at a shorter wavelength will adequately resolve these targets to meet the goal of better than 4% accuracy.

I would also like to build a database (similar to the CHARM2 Catalogue) of stars with diameter measurements. Georgia State University could be known as "Diameter Central " because the CHARA Array has enabled us to advance the field of fundamental stellar properties.

I have received a Hubble Fellowship to further pursue the determination of fundamental properties of main sequence stars with the CHARA Array. In the fellowship proposal, I aimed to carry out a program encompassing several astrophysically interesting stars to determine their diameters to great accuracy. I have selected stars with special astrophysical significance in three primary areas: exoplanet host stars, low-mass, main-sequence K and M stars, and metal-poor stars.

By successfully measuring the angular diameters for all objects described in this project, the fundamental properties of effective temperature, stellar radius, and absolute luminosity will be determined. Stellar ages will then be able to be determined by fitting the data to model evolutionary isochrones as well as activity isochrones. With these quantities in hand, I will explore the connection between activity rates and the deviation between model predictions about radius and temperature. The ranges of ages and metallicities of these nearby stars will in turn help reveal details about the star formation history of the local region of the Galactic disk. These relevant issues are fundamentally connected to the NASA Cosmic Origins themes. I will accomplish a foundation for establishing an empirical temperature scale for late-type, main sequence stars, enabling the means for calibrating less direct relationships to extend our knowledge to a larger number of stars. This includes the practical application of plotting positions of stars in the temperature-luminosity version of the H-R diagram through newly established color-temperature-metallicity transformations. By accomplishing

a survey of the very oldest metal-poor stars, to the typical local population of nearby stars, and to those stars that have known exoplanets, we will better understand the processes of star formation, chemical enrichment, planetary formation, and Galactic evolution to the present day, all important themes for the NASA Cosmic Origins Missions.

References

Absil, O. et al. 2008, A&A, 487, 1041

Allende Prieto, C., & Lambert, D. L. 1999, A&A, 352, 555

Alonso, A., Arribas, S., & Martinez-Roger, C. 1995, A&A, 297, 197

——. 1996, A&AS, 117, 227

Andersen, J. 1991, A&A Rev., 3, 91

Aufdenberg, J. P. et al. 2006, ApJ, 645, 664

Baines, E. K., McAlister, H. A., ten Brummelaar, T. A., Turner, N. H., Sturmann, J., Sturmann, L., Goldfinger, P. J., & Ridgway, S. T. 2008, ArXiv e-prints, 803

Barnes, T. G., & Evans, D. S. 1976, MNRAS, 174, 489

Bell, R. A., & Gustafsson, B. 1989, MNRAS, 236, 653

Bertelli, G., Bressan, A., Chiosi, C., Fagotto, F., & Nasi, E. 1994, A&AS, 106, 275

Blackwell, D. E., & Lynas-Gray, A. E. 1998, A&AS, 129, 505

Blackwell, D. E., & Shallis, M. J. 1977, MNRAS, 180, 177

Blackwell, D. E., Shallis, M. J., & Selby, M. J. 1979, MNRAS, 188, 847

Bonanno, A., Schlattl, H., & Paternò, L. 2002, A&A, 390, 1115

Booth, A. J. 1997, in IAU Symposium, Vol. 189, IAU Symposium, ed. T. R. Bedding, A. J. Booth, & J. Davis, 147–152

Boyajian, T. S. et al. 2008, ArXiv e-prints, 804

——. 2009, ApJ, 691, 1243

Brown, R. H., Davis, J., Lake, R. J. W., & Thompson, R. J. 1974, MNRAS, 167, 475

Carney, B. W. 1996, PASP, 108, 900

Casagrande, L., Portinari, L., & Flynn, C. 2006, MNRAS, 373, 13

Cayrel de Strobel, G. 1996, A&A Rev., 7, 243

Claret, A., Diaz-Cordoves, J., & Gimenez, A. 1995, A&AS, 114, 247

Code, A. D., Bless, R. C., Davis, J., & Brown, R. H. 1976, ApJ, 203, 417

Cohen, M., Wheaton, W. A., & Megeath, S. T. 2003, AJ, 126, 1090

Colina, L., Bohlin, R., & Castelli, F. 1996, HST Instrument Science Report, CAL/SCS-008 (Baltimore: STScI)

Cox, A. N. 2000, Allen's astrophysical quantities (Allen's astrophysical quantities, 4th ed. Publisher: New York: AIP Press; Springer, 2000. ed. Arthur N. Cox. ISBN: 0387987460)

Davis, J. 1985, in IAU Symposium, Vol. 111, Calibration of Fundamental Stellar Quantities, ed. D. S. Hayes, L. E. Pasinetti, & A. G. D. Philip, 193–208

Davis, J. 1997, in IAU Symposium, Vol. 189, IAU Symposium, ed. T. R. Bedding, A. J. Booth, & J. Davis, 31–38

Demarque, P., Woo, J.-H., Kim, Y.-C., & Yi, S. K. 2004, ApJS, 155, 667

Domiciano de Souza, A., Kervella, P., Jankov, S., Vakili, F., Ohishi, N., Nordgren, T. E., & Abe, L. 2005, A&A, 442, 567

ESA. 1997, The Hipparcos and Tycho Catalogues ESA SP - 1200 (Noordwijk, Netherlands: ESA/ESTEC)

Girardi, L., Bressan, A., Bertelli, G., & Chiosi, C. 2000, A&AS, 141, 371

González Hernández, J. I., & Bonifacio, P. 2009, A&A, 497, 497

Gray, D. F. 1967, ApJ, 149, 317

Gray, R. O. 1998, AJ, 116, 482

Gray, R. O., Corbally, C. J., Garrison, R. F., McFadden, M. T., Bubar, E. J., McGahee, C. E., O'Donoghue, A. A., & Knox, E. R. 2006, AJ, 132, 161

Gray, R. O., Corbally, C. J., Garrison, R. F., McFadden, M. T., & Robinson, P. E. 2003, AJ, 126, 2048

Gray, R. O., Napier, M. G., & Winkler, L. I. 2001, AJ, 121, 2148

Hanbury Brown, R., Davis, J., & Allen, L. R. 1974, MNRAS, 167, 121

Hauck, B., & Mermilliod, M. 1998, A&AS, 129, 431

Holmberg, J., Nordström, B., & Andersen, J. 2007, A&A, 475, 519

——. 2008, ArXiv e-prints

Johnson, H. L., Iriarte, B., Mitchell, R. I., & Wisniewskj, W. Z. 1966, Communications of the Lunar and Planetary Laboratory, 4, 99

Kervella, P., Thévenin, F., Di Folco, E., & Ségransan, D. 2004a, A&A, 426, 297

Kervella, P., Thévenin, F., Morel, P., Berthomieu, G., Bordé, P., & Provost, J. 2004b, A&A, 413, 251

Kervella, P., Thévenin, F., Morel, P., Bordé, P., & Di Folco, E. 2003, A&A, 408, 681

Kim, Y.-C., Demarque, P., Yi, S. K., & Alexander, D. R. 2002, ApJS, 143, 499

Kostjuk, N. D. 2004, VizieR Online Data Catalog, 4027, 0

Labeyrie, A. 1975, ApJ, 196, L71

Lejeune, T., Cuisinier, F., & Buser, R. 1998, A&AS, 130, 65

McAlister, H. A. 1985, ARA&A, 23, 59

McAlister, H. A. et al. 2005, ApJ, 628, 439

Meléndez, J., & Ramírez, I. 2007, ApJ, 669, L89

Michelson, A. A., & Pease, F. G. 1921, ApJ, 53, 249

Neugebauer, G., & Leighton, R. B. 1969, Two-micron sky survey. A preliminary catalogue (NASA SP, Washington: NASA, 1969)

Pickles, A. J. 1998, PASP, 110, 863

Porto de Mello, G. F., & da Silva, L. 1997, ApJ, 482, L89+

Press, W. H., Teukolsky, S. A., Vetterling, W. T., & Flannery, B. P. 1992, Numerical recipes in C. The art of scientific computing (Cambridge: University Press, —c1992, 2nd ed.)

Ramírez, I., & Meléndez, J. 2005, ApJ, 626, 465

Richichi, A., Percheron, I., & Khristoforova, M. 2005, A&A, 431, 773

Royer, F., Zorec, J., & Gomez, A. E. 2006, VizieR Online Data Catalog, 346, 30671

Salasnich, B., Girardi, L., Weiss, A., & Chiosi, C. 2000, A&A, 361, 1023

Skrutskie, M. F. et al. 2006, AJ, 131, 1163

Takeda, Y. 2007, PASJ, 59, 335

Takeda, Y., Ohkubo, M., Sato, B., Kambe, E., & Sadakane, K. 2005, PASJ, 57, 27

ten Brummelaar, T. A. et al. 2005, ApJ, 628, 453

Torres, G., Stefanik, R. P., & Latham, D. W. 1997, ApJ, 485, 167

van Belle, G. T. et al. 2008, ApJS, 176, 276

van Belle, G. T., & von Braun, K. 2009, ApJ, 694, 1085

van Leeuwen, F. 2007, Hipparcos, the New Reduction of the Raw Data (Hipparcos, the New Reduction of the Raw Data. By Floor van Leeuwen, Institute of Astronomy, Cambridge University, Cambridge, UK Series: Astrophysics and Space Science Library, Vol. 350 20 Springer Dordrecht)

Wall, J. V., & Jenkins, C. R. 2003, Practical Statistics for Astronomers (Princeton Series in Astrophysics)

Wenger, M. et al. 2000, A&AS, 143, 9

Yi, S., Demarque, P., Kim, Y.-C., Lee, Y.-W., Ree, C. H., Lejeune, T., & Barnes, S. 2001, ApJS, 136, 417

Yi, S. K., Kim, Y.-C., & Demarque, P. 2003, ApJS, 144, 259

Appendices

– A –

Appendix A

SED plots for the all objects in the sample. The *solid* line is the Kurucz model atmosphere for the star's effective temperature and gravity and the *diamonds* are flux calibrated photometry.

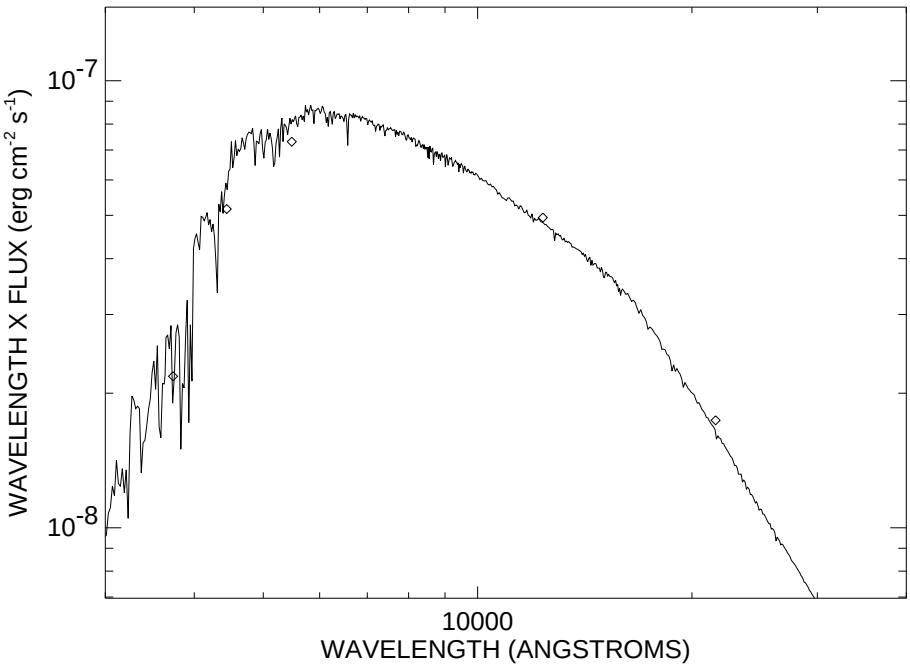

FIGURE A.1: SED plot for HD 166.

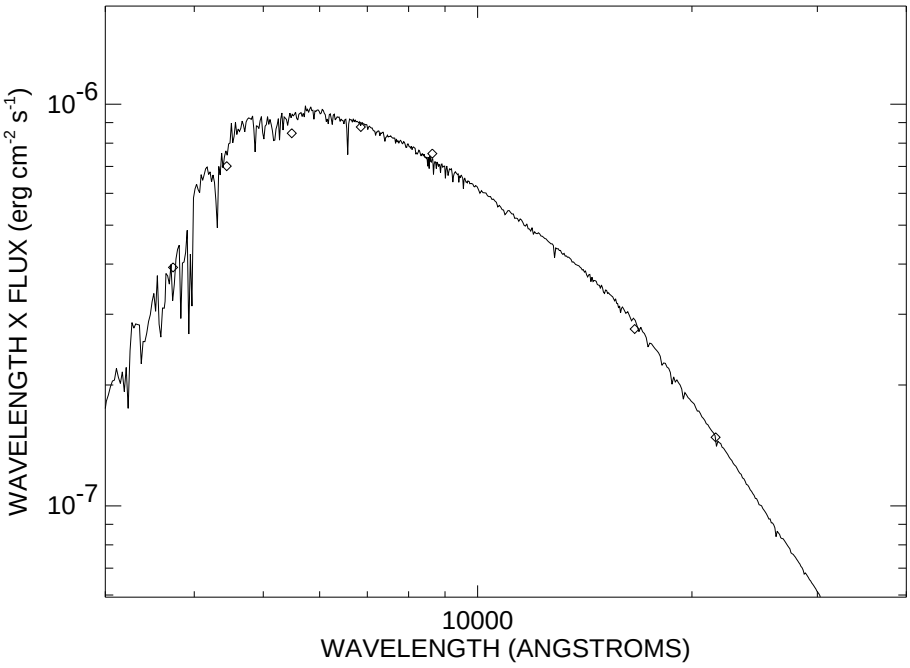

FIGURE A.2: SED plot for HD 4614.

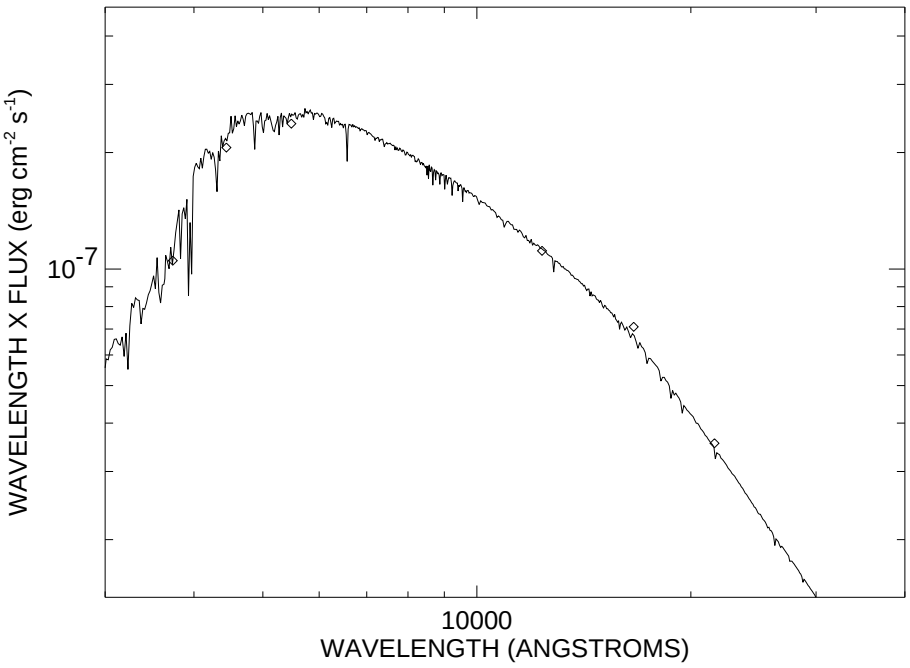

FIGURE A.3: SED plot for HD 5015.

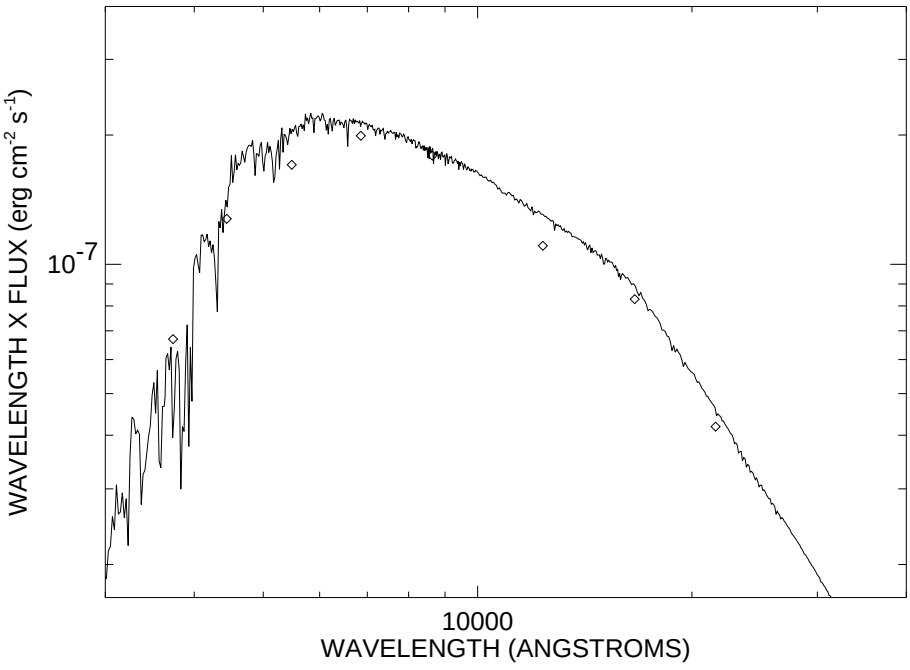

FIGURE A.4: SED plot for HD 6582.

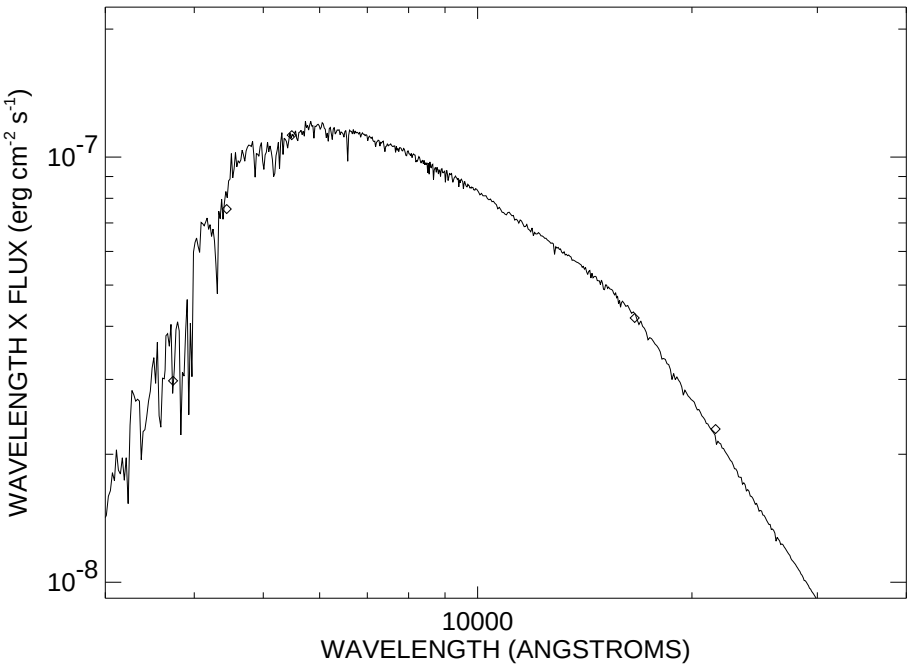

FIGURE A.5: SED plot for HD 10780.

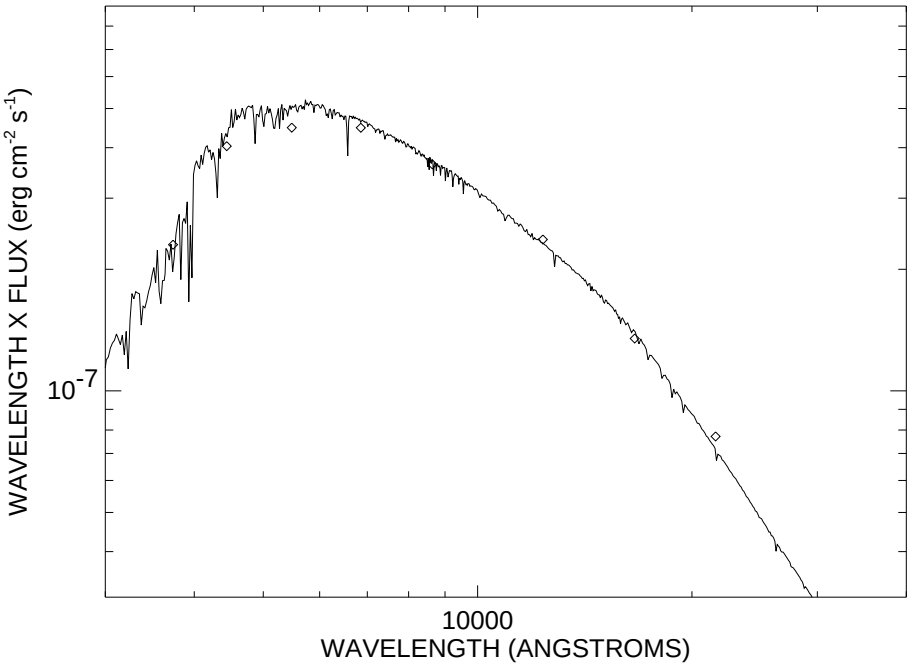

FIGURE A.6: SED plot for HD 16895.

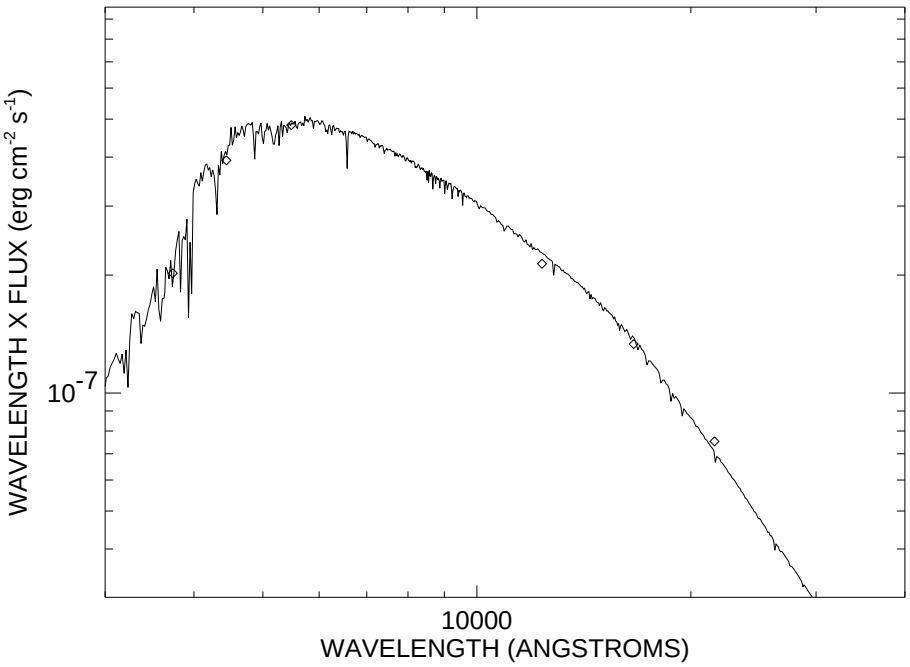

FIGURE A.7: SED plot for HD 19373.

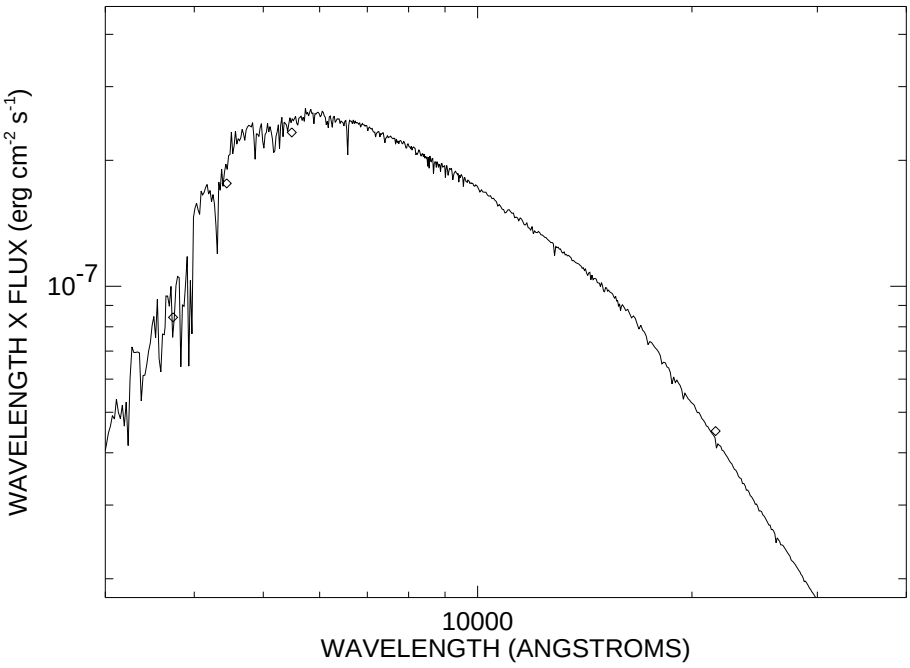

FIGURE A.8: SED plot for HD 20630.

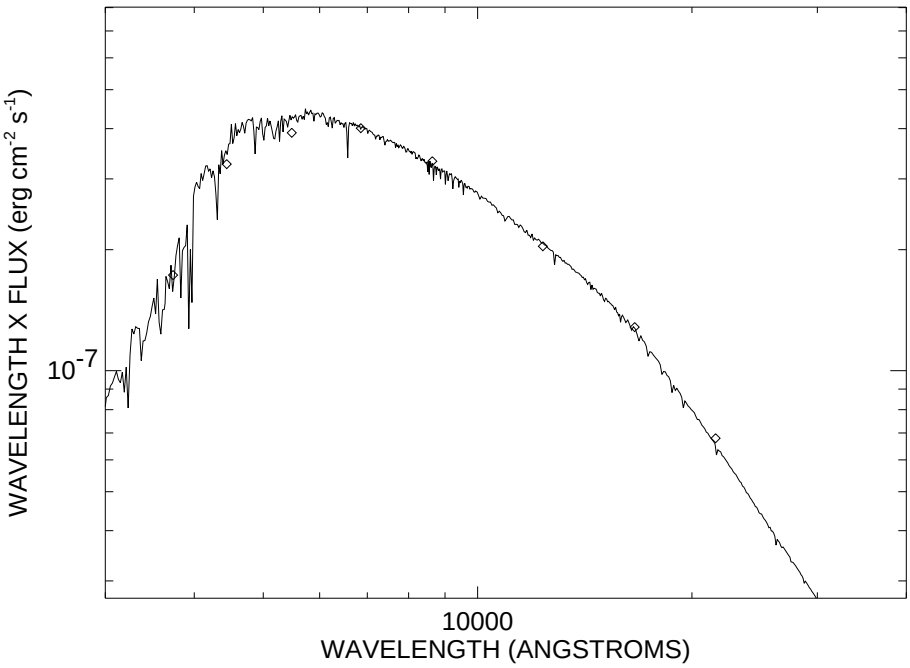

FIGURE A.9: SED plot for HD 22484.

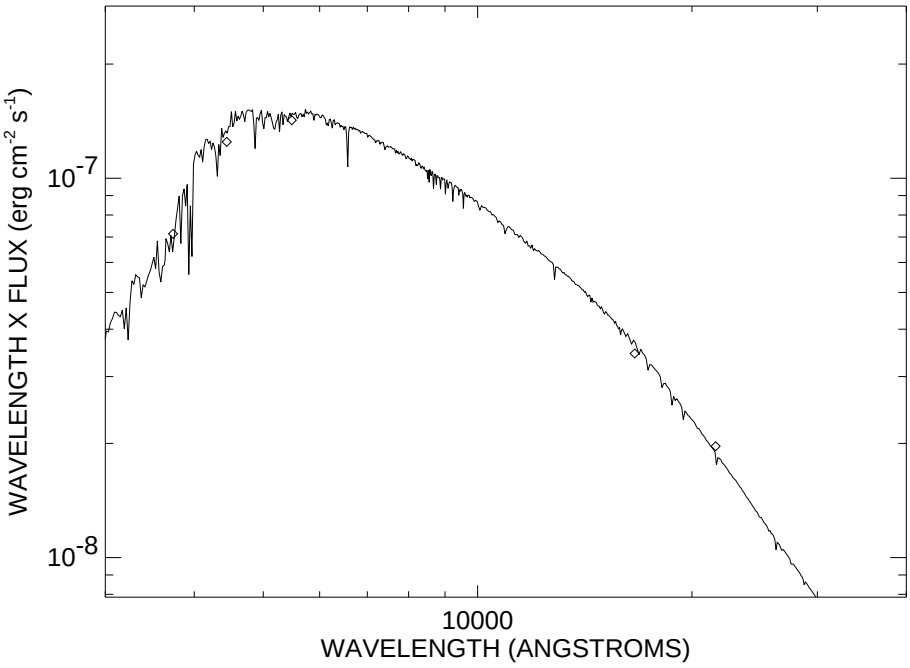

FIGURE A.10: SED plot for HD 25457.

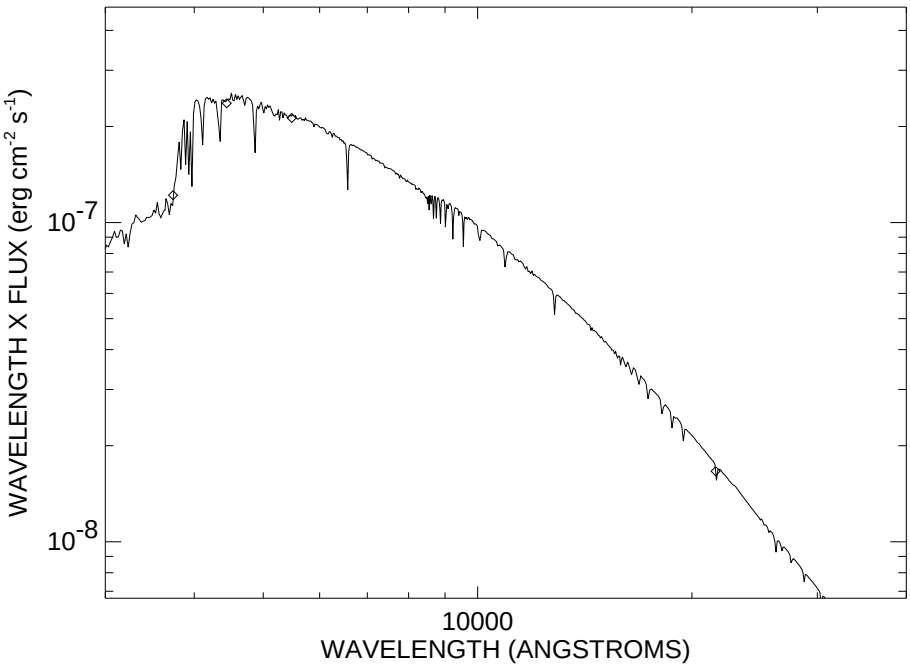

FIGURE A.11: SED plot for HD 27045.

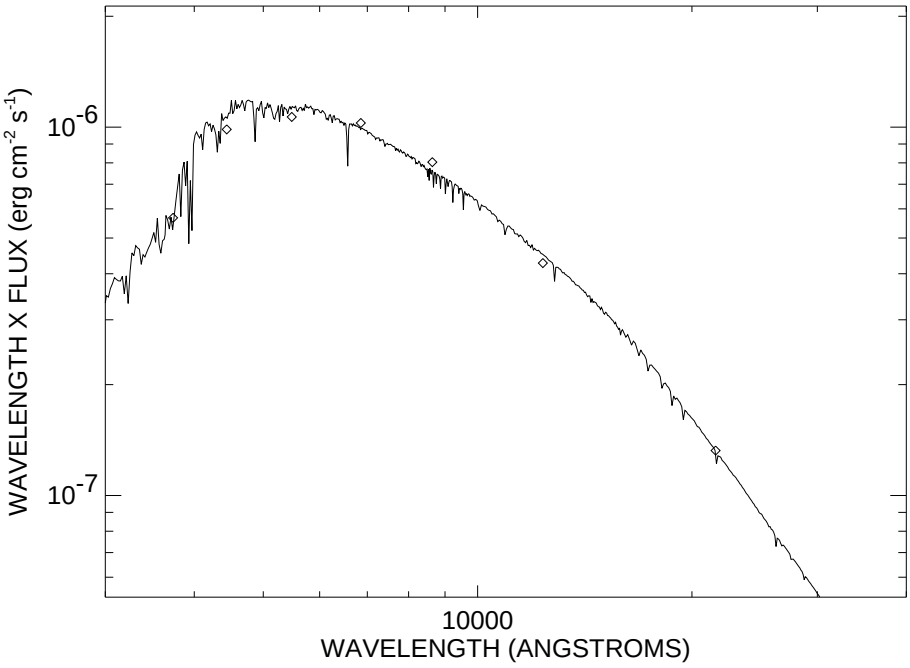

FIGURE A.12: SED plot for HD 30652.

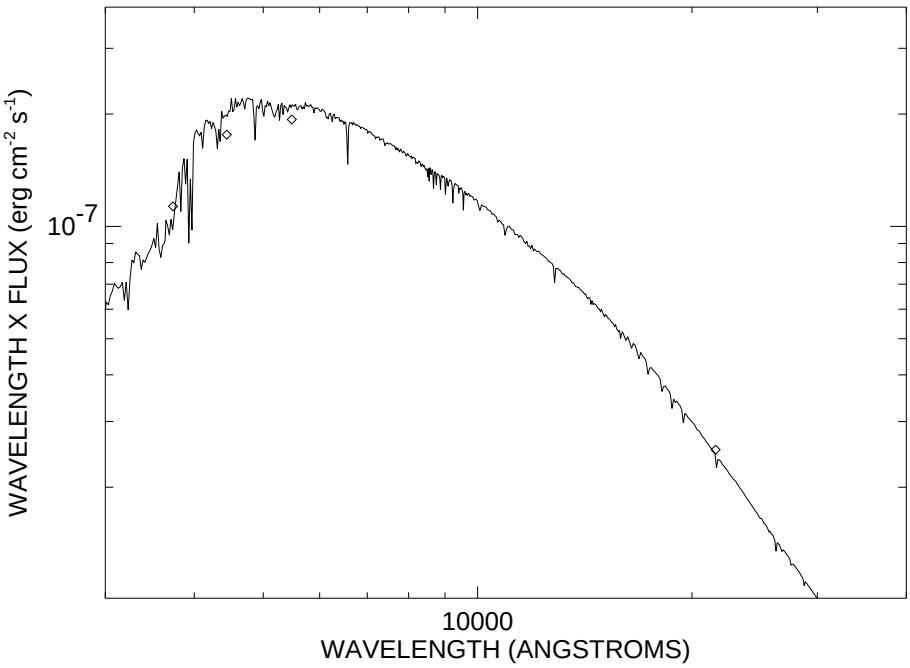

FIGURE A.13: SED plot for HD 33564.

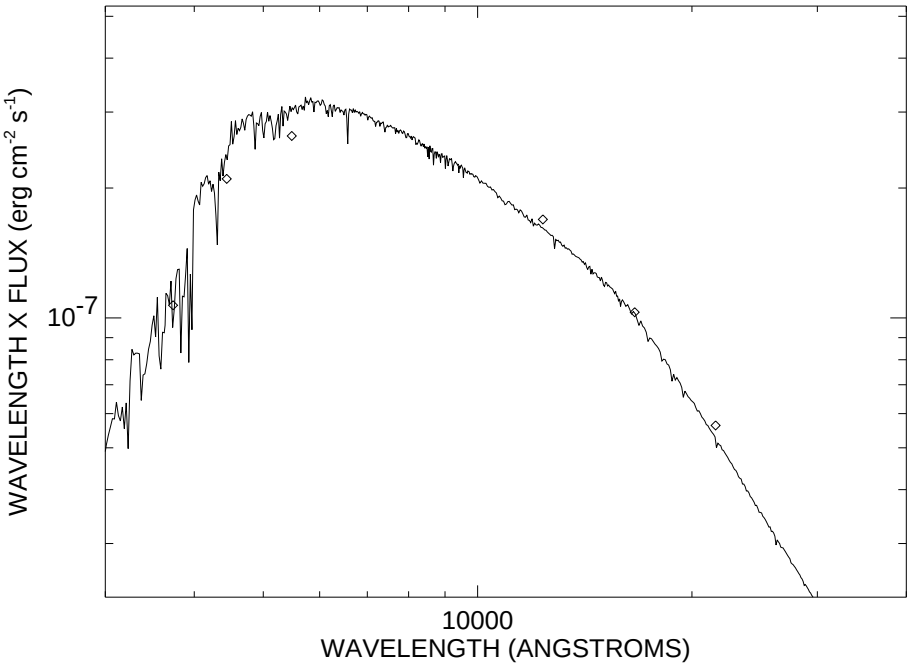

FIGURE A.14: SED plot for HD 34411.

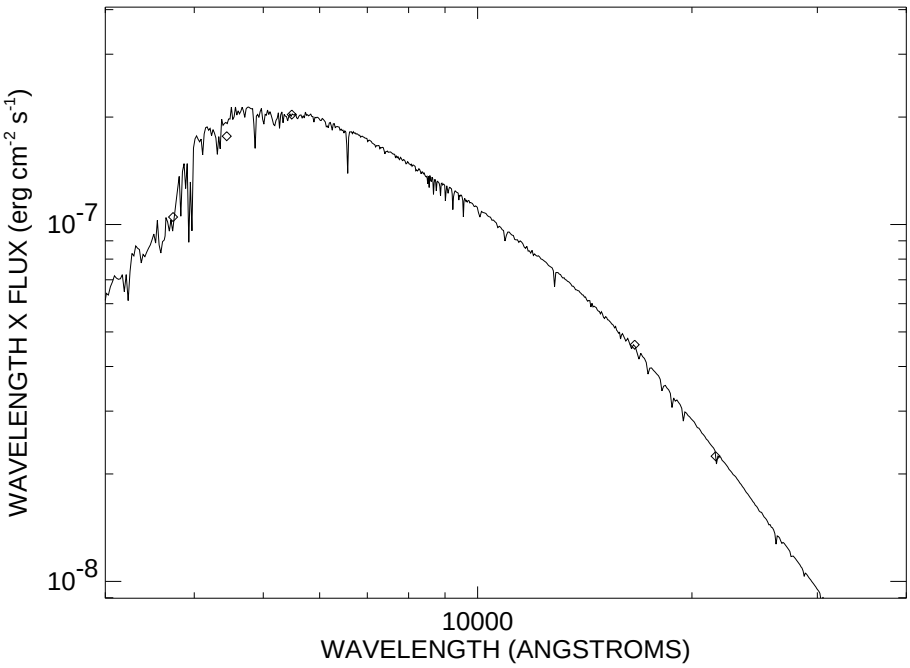

FIGURE A.15: SED plot for HD 35296.

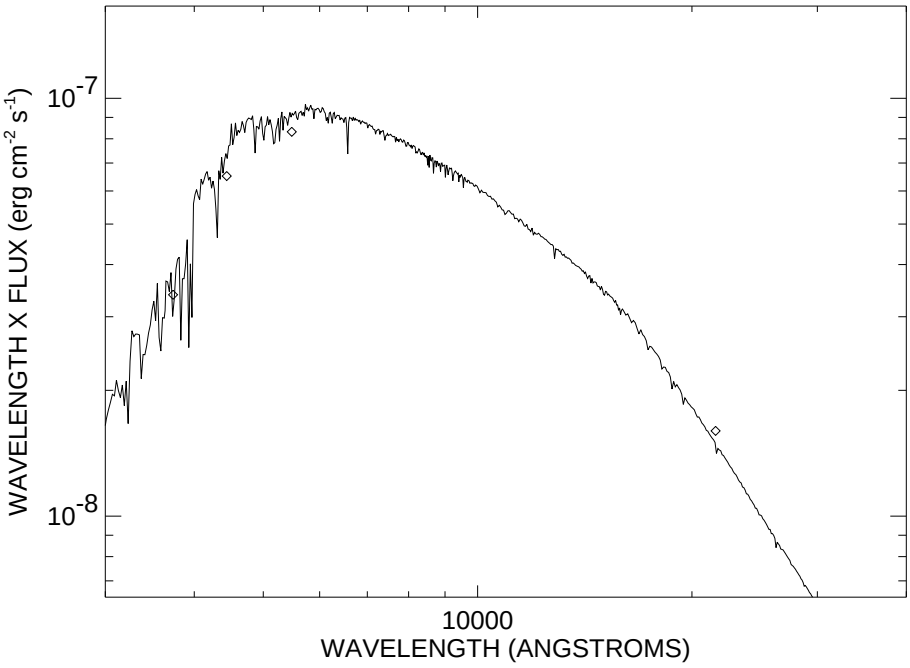

FIGURE A.16: SED plot for HD 38858.

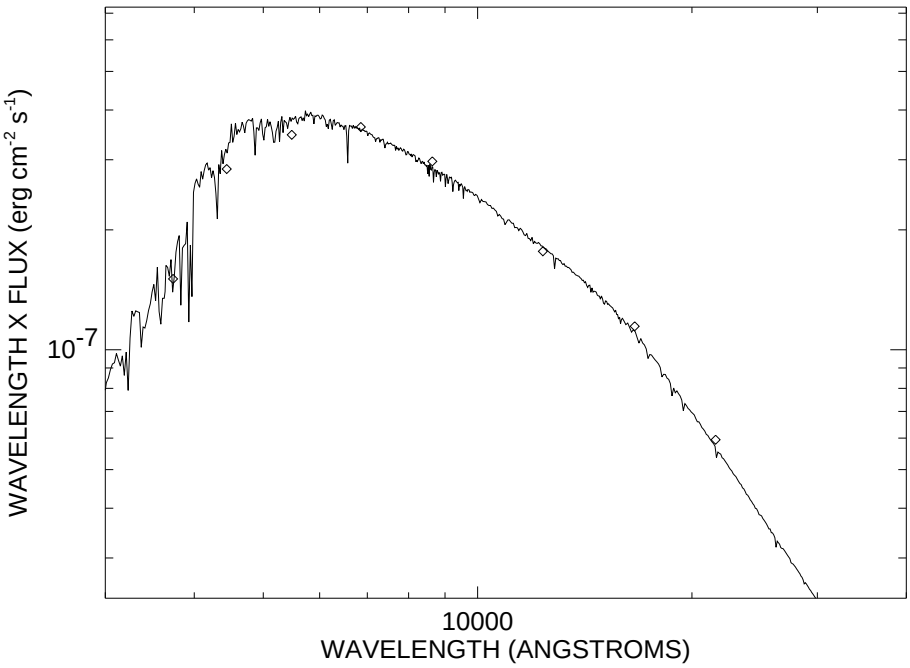

FIGURE A.17: SED plot for HD 39587.

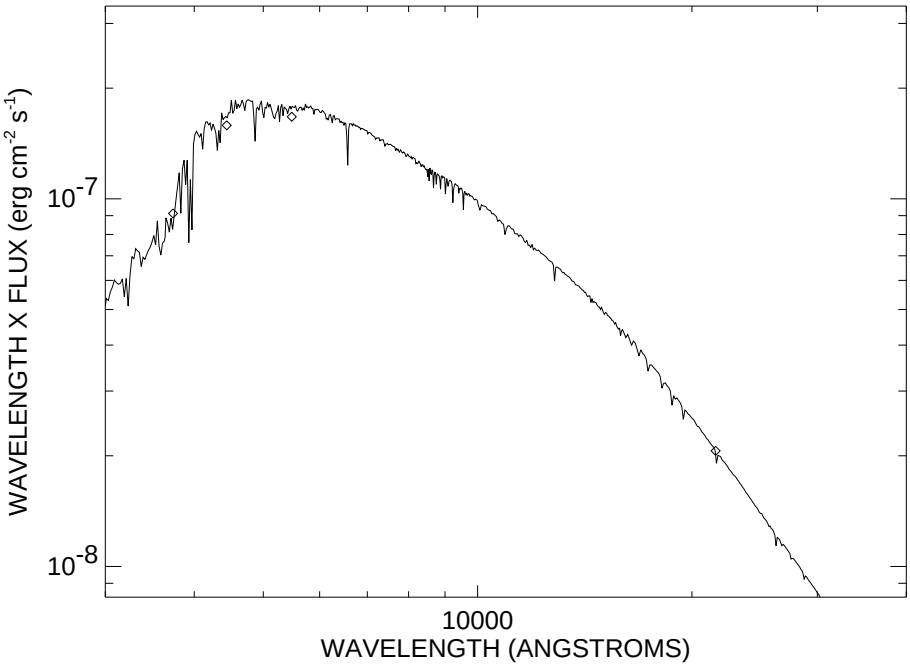

FIGURE A.18: SED plot for HD 43042.

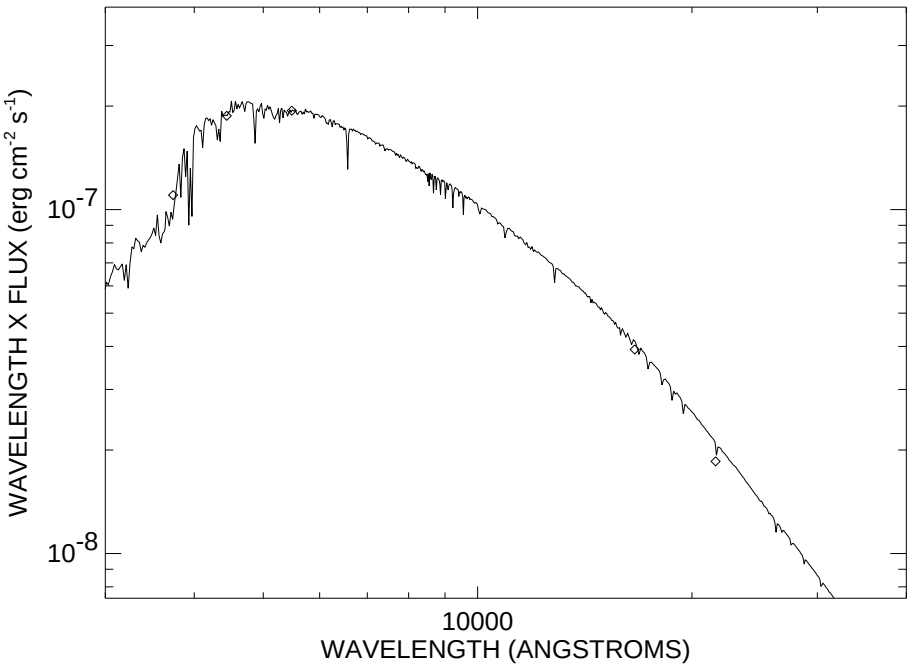

FIGURE A.19: SED plot for HD 43386.

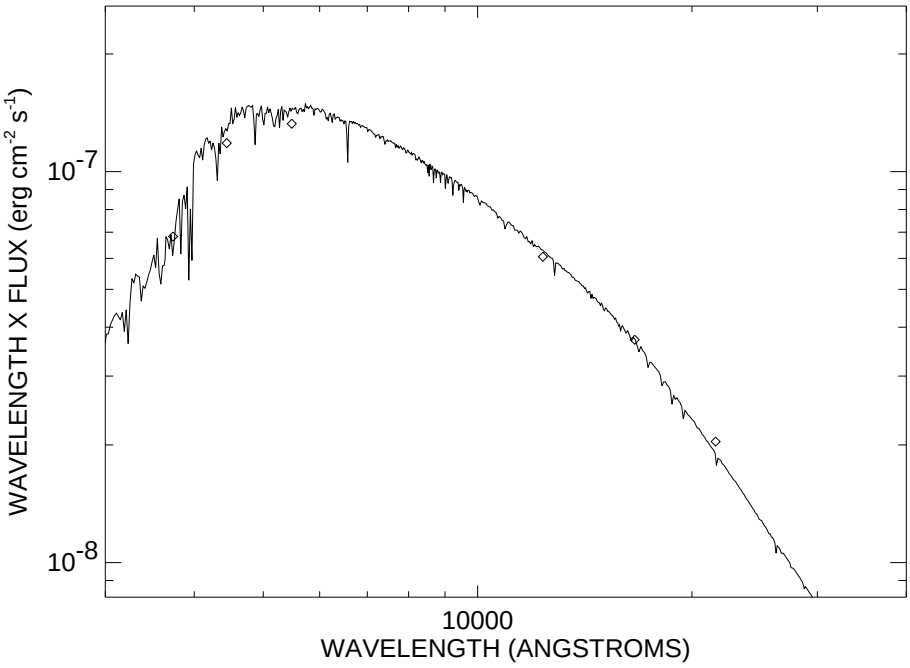

FIGURE A.20: SED plot for HD 46588.

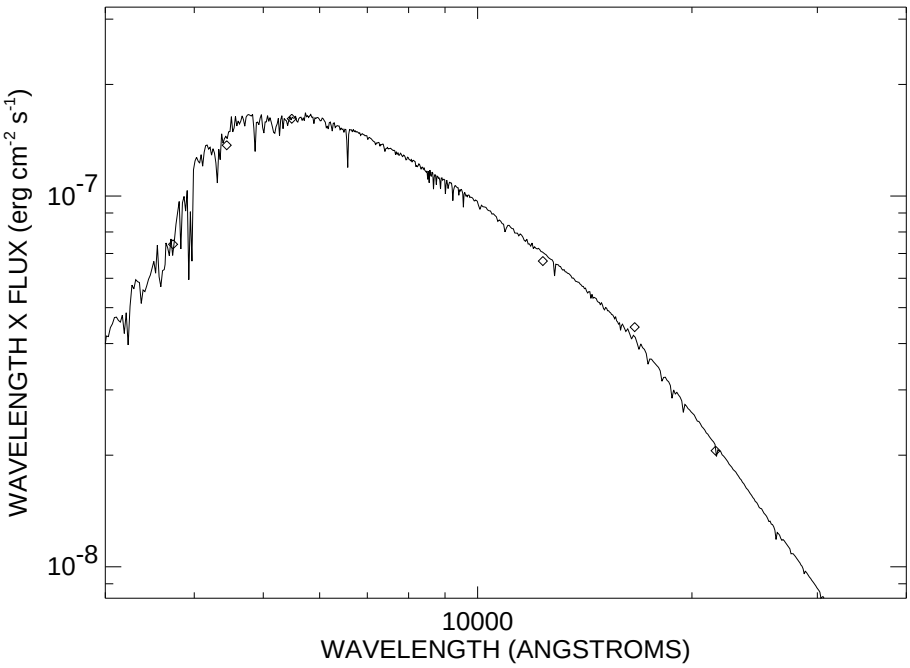

FIGURE A.21: SED plot for HD 48682.

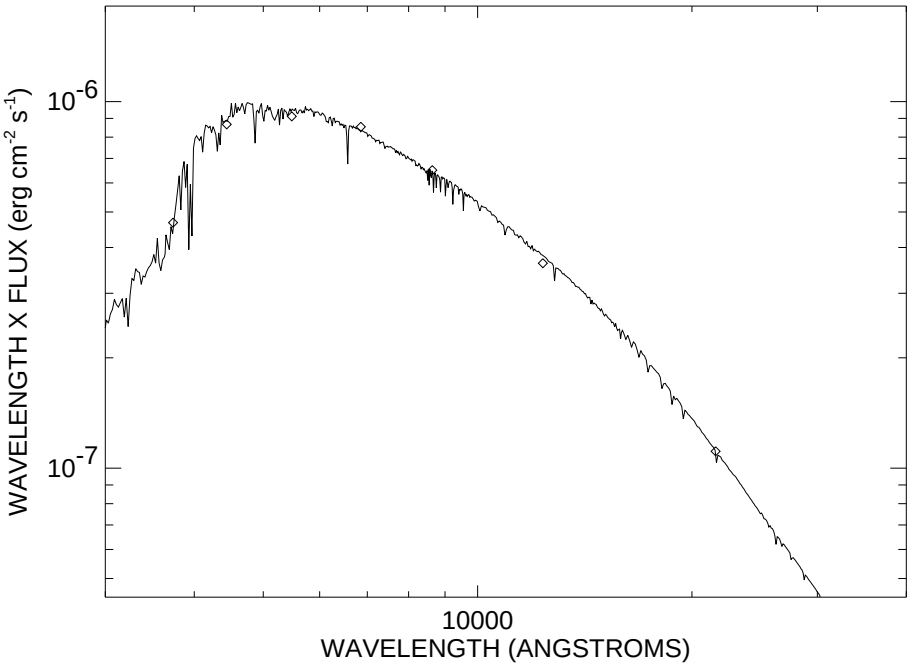

FIGURE A.22: SED plot for HD 48737.

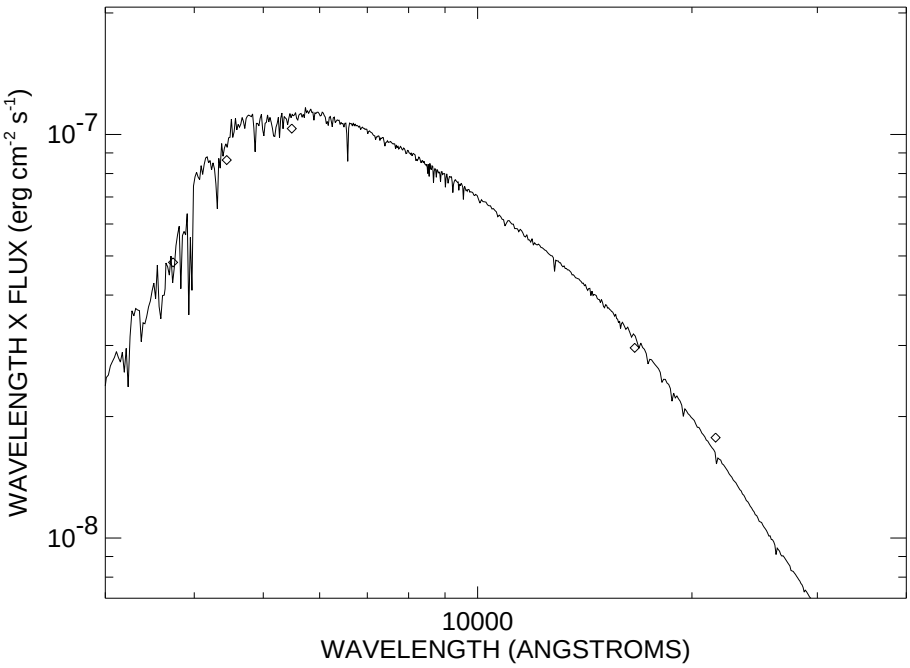

FIGURE A.23: SED plot for HD 50692.

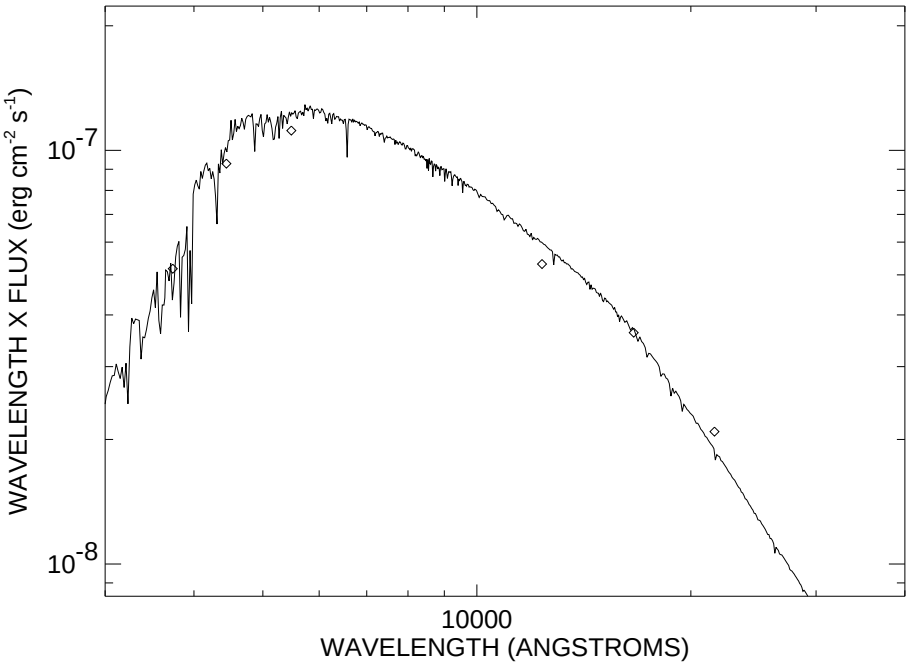

FIGURE A.24: SED plot for HD 55575.

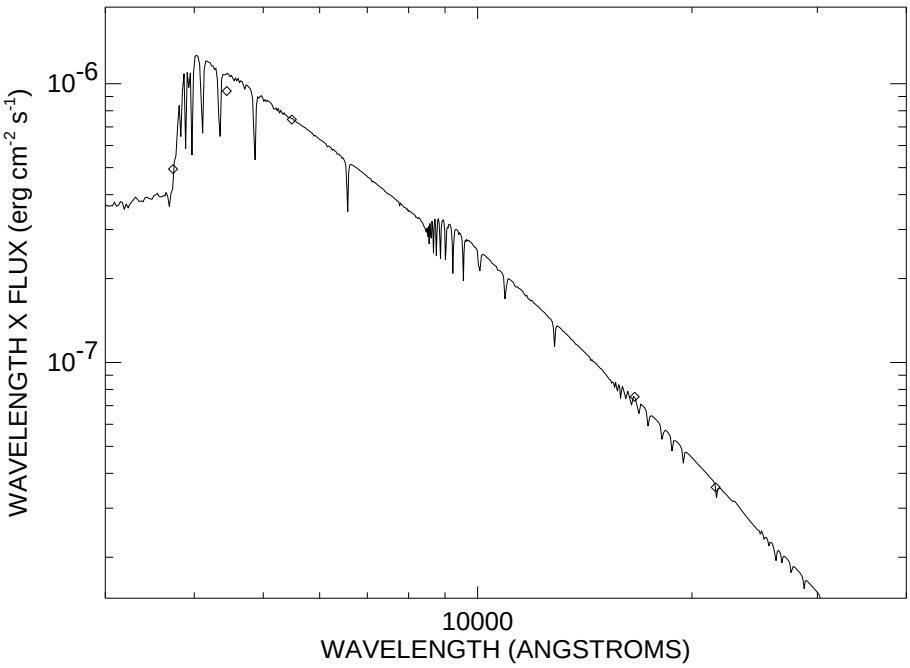

FIGURE A.25: SED plot for HD 56537.

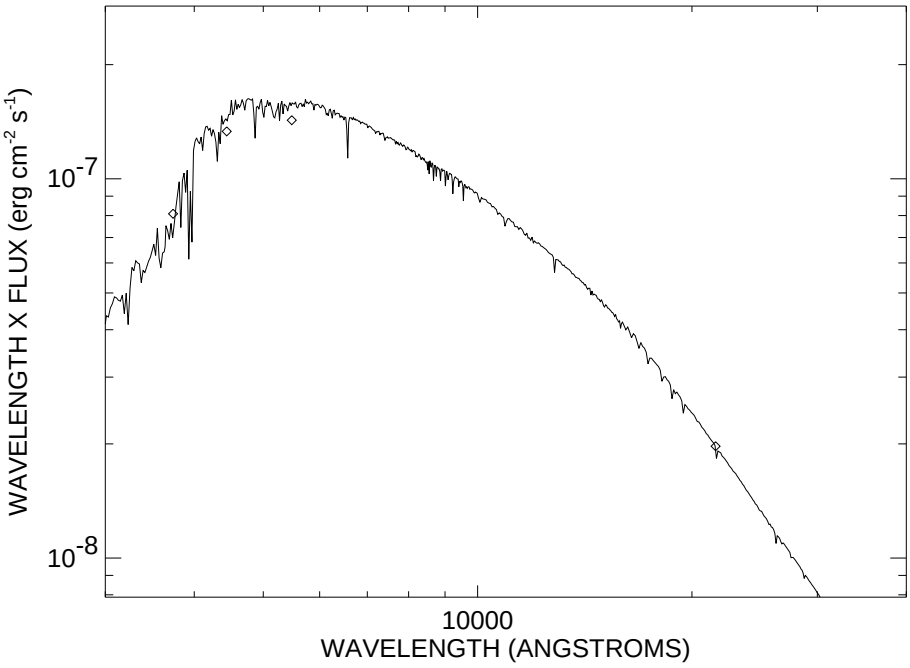

FIGURE A.26: SED plot for HD 58855.

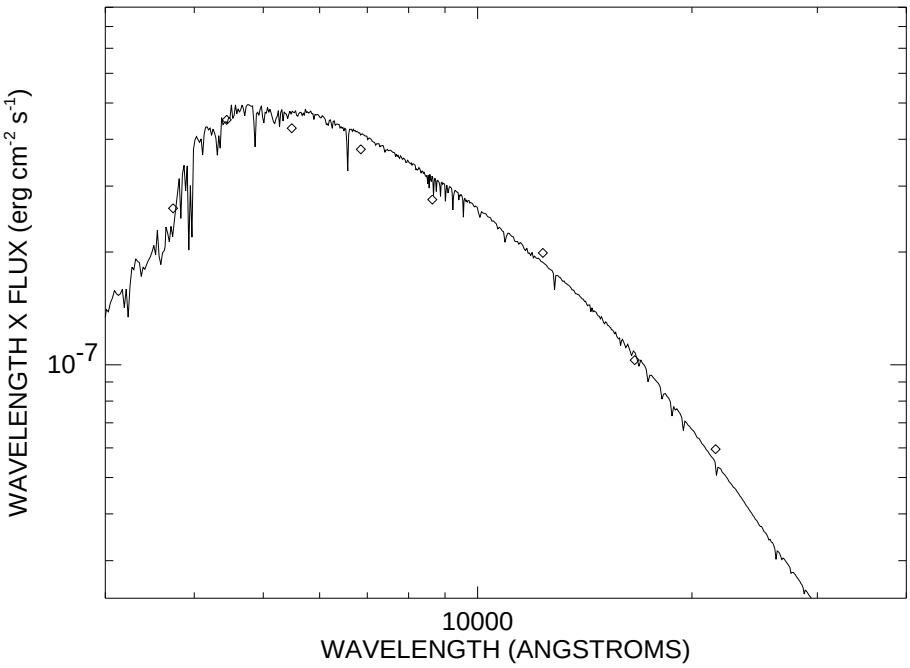

FIGURE A.27: SED plot for HD 58946.

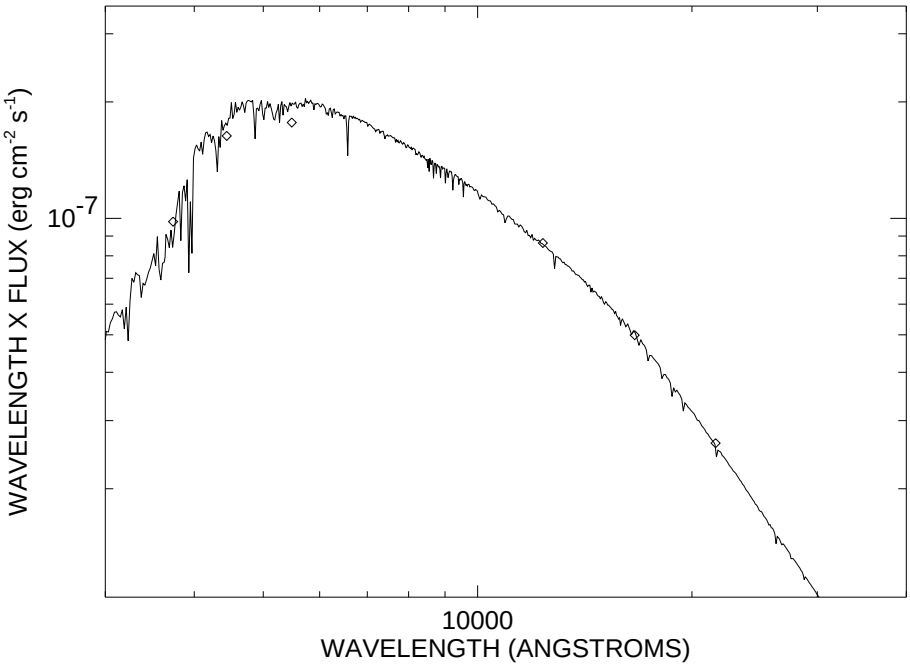

FIGURE A.28: SED plot for HD 69897.

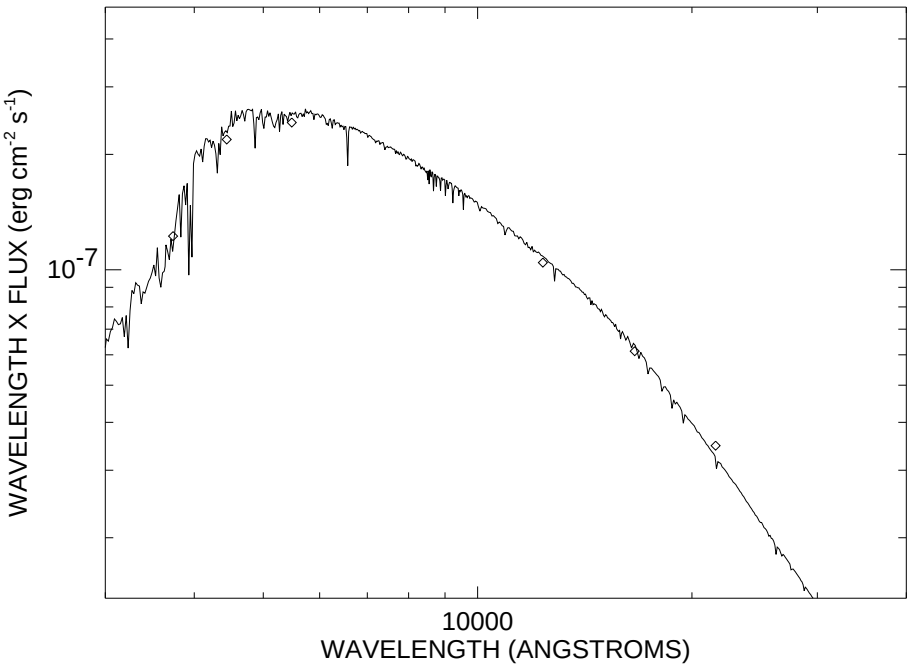

FIGURE A.29: SED plot for HD 78154.

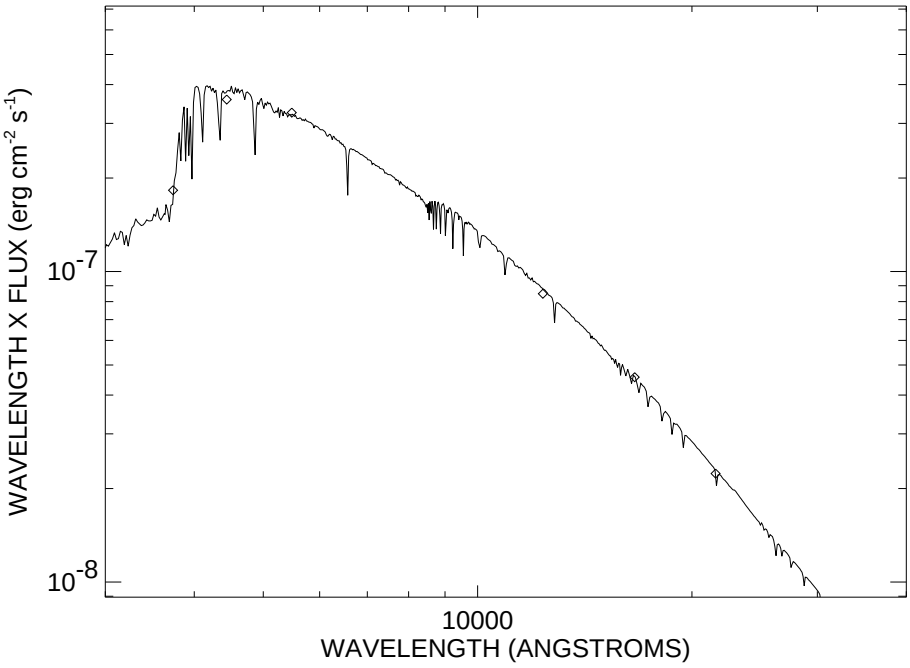

FIGURE A.30: SED plot for HD 78209.

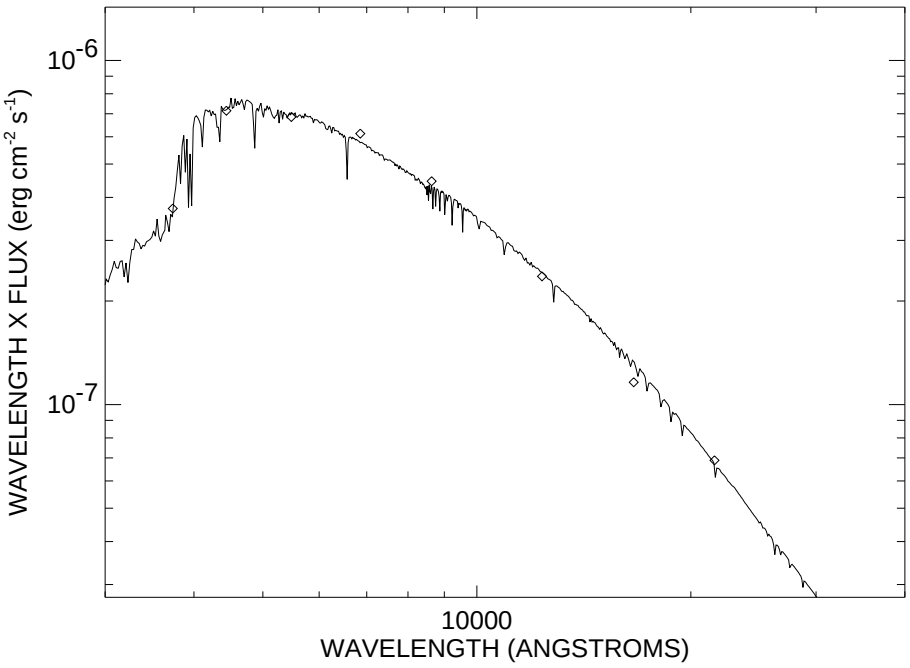

FIGURE A.31: SED plot for HD 81937.

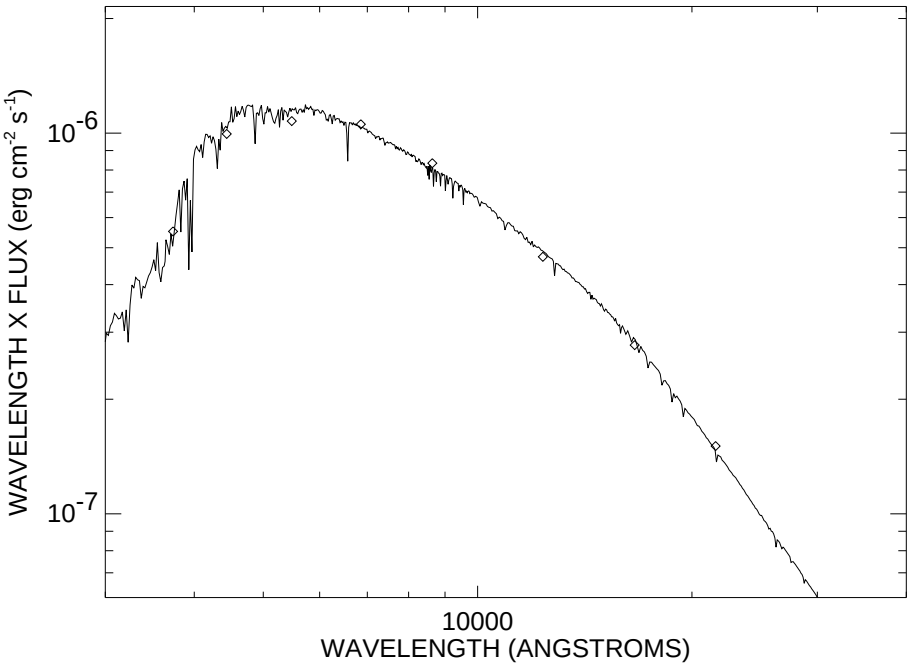

FIGURE A.32: SED plot for HD 82328.

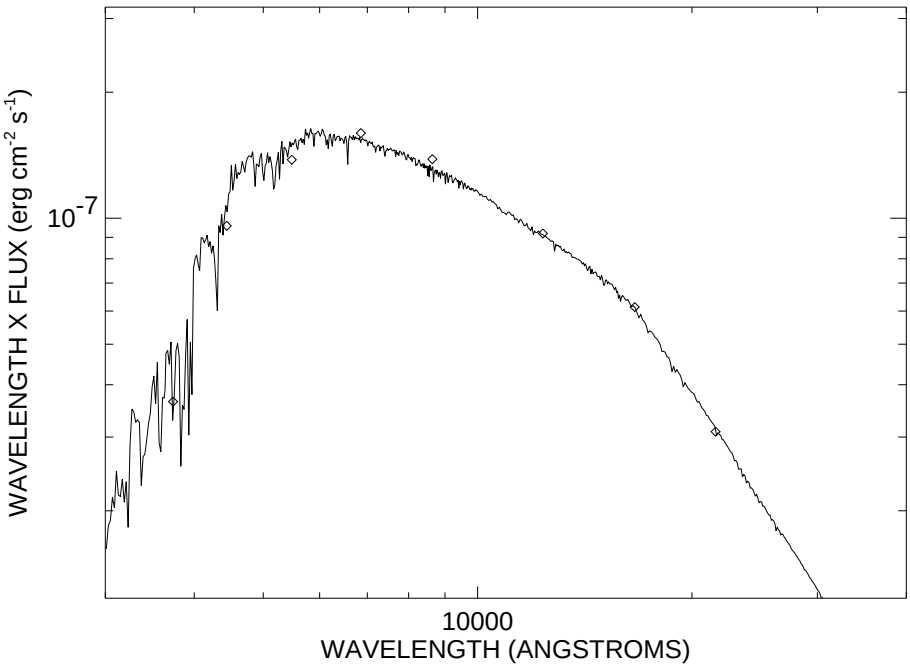

FIGURE A.33: SED plot for HD 82885.

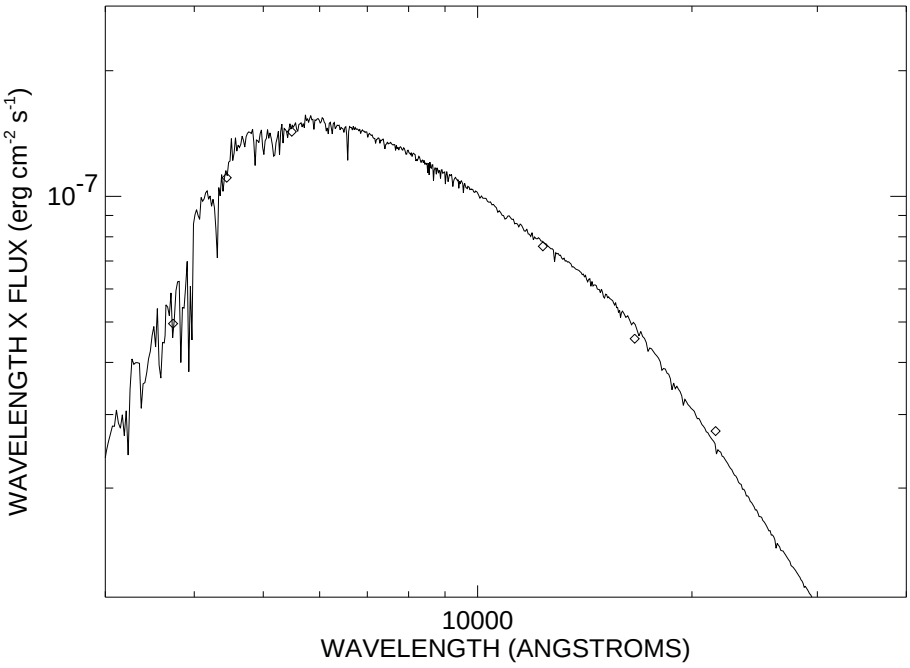

FIGURE A.34: SED plot for HD 86728.

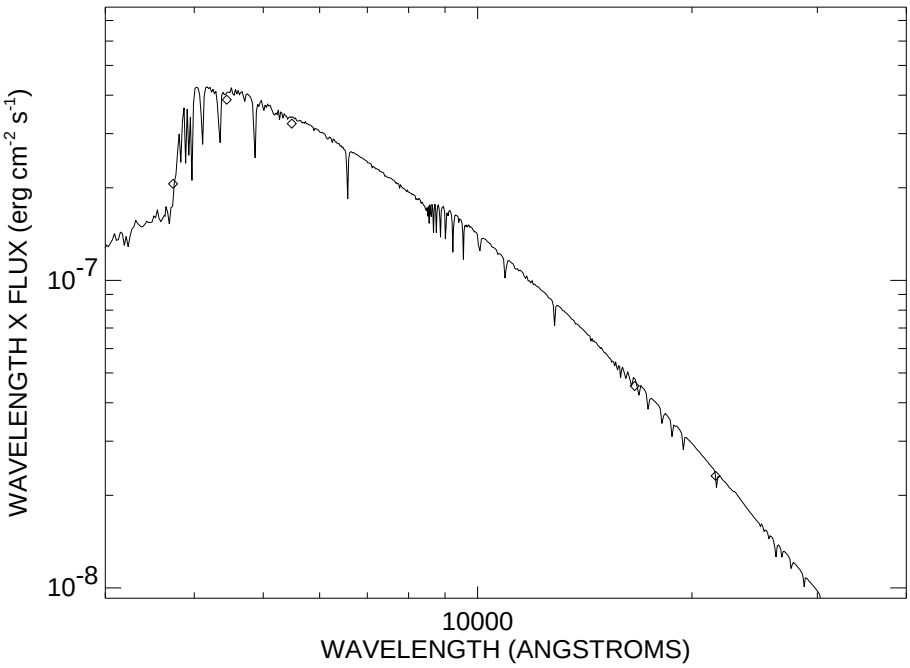

FIGURE A.35: SED plot for HD 87696.

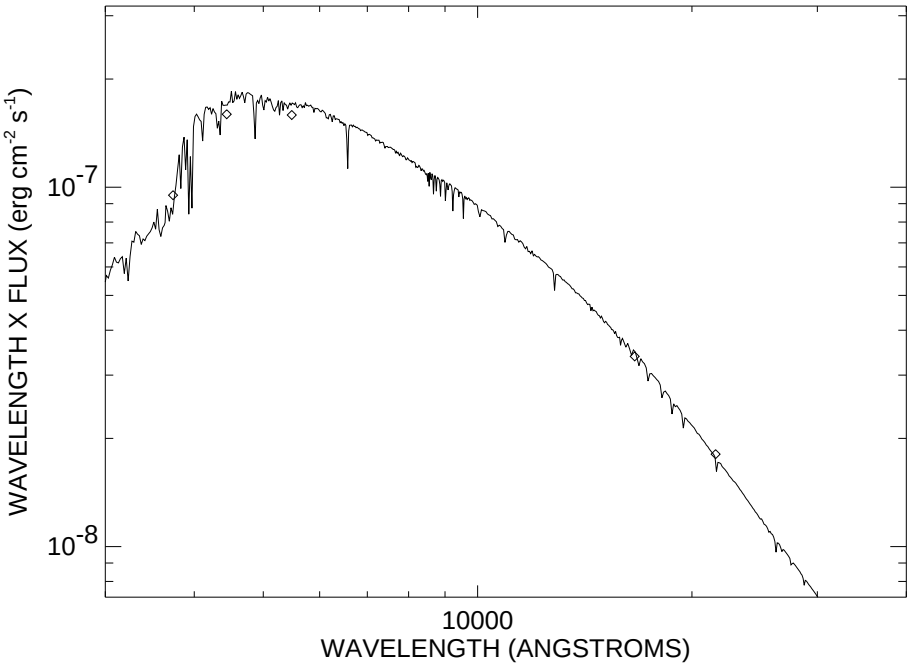

FIGURE A.36: SED plot for HD 90089.

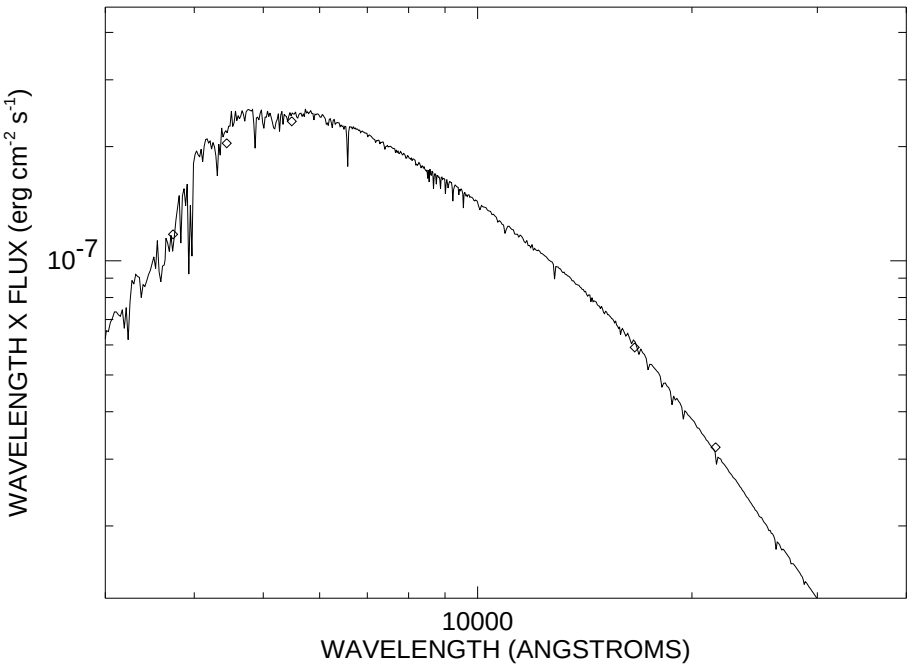

FIGURE A.37: SED plot for HD 90839.

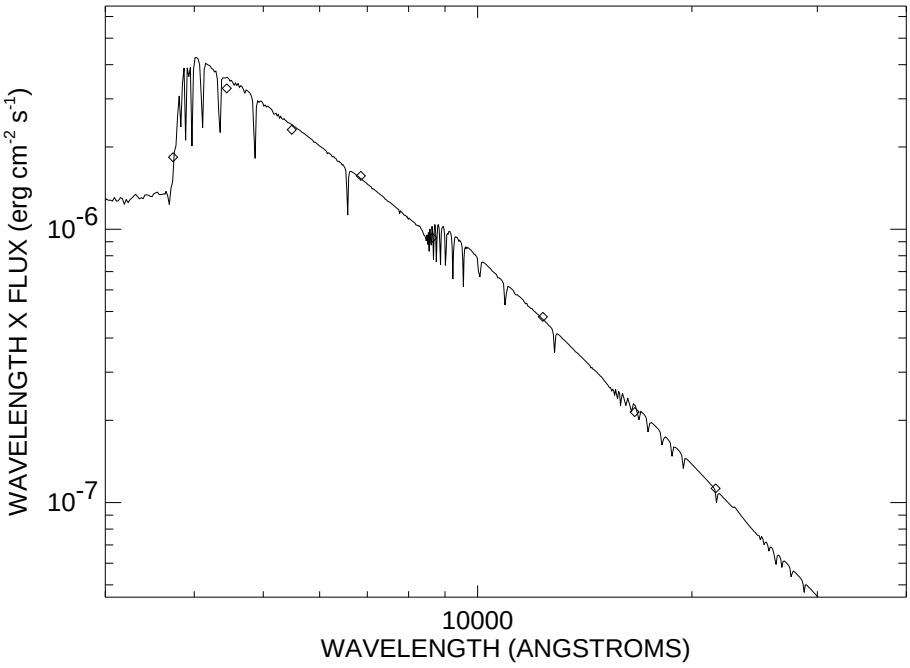

FIGURE A.38: SED plot for HD 95418.

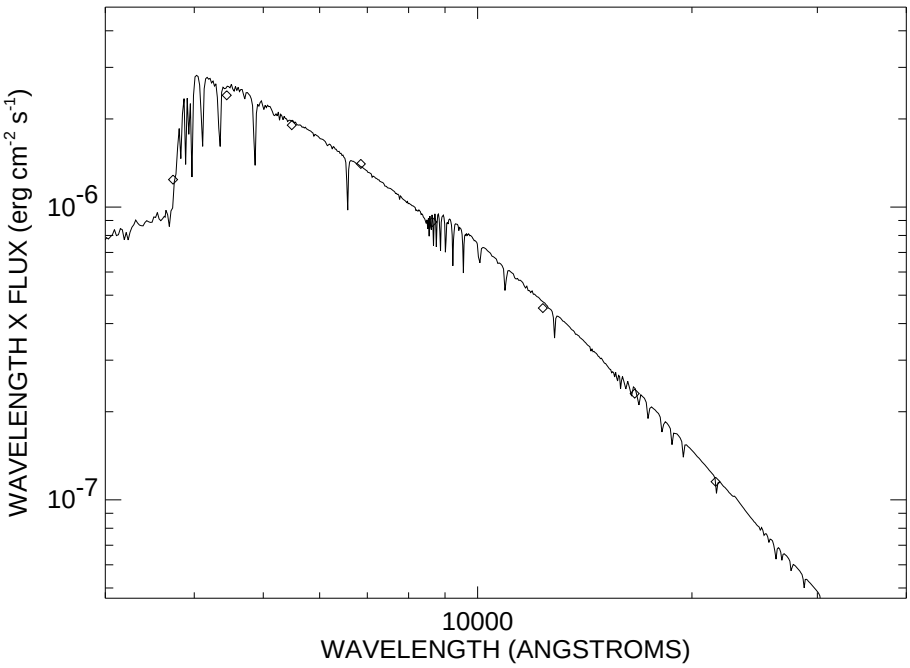

FIGURE A.39: SED plot for HD 97603.

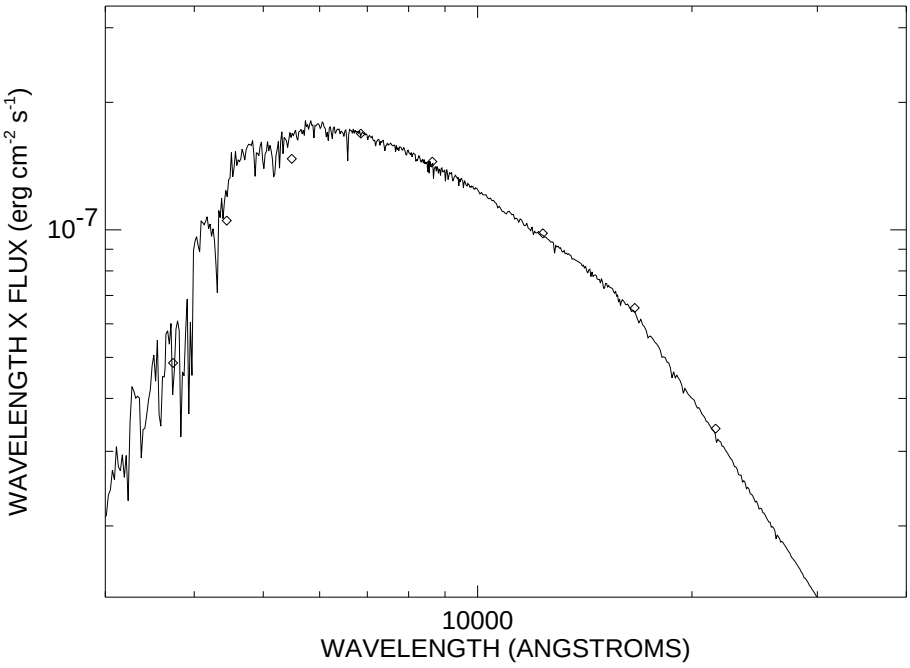

FIGURE A.40: SED plot for HD 101501.

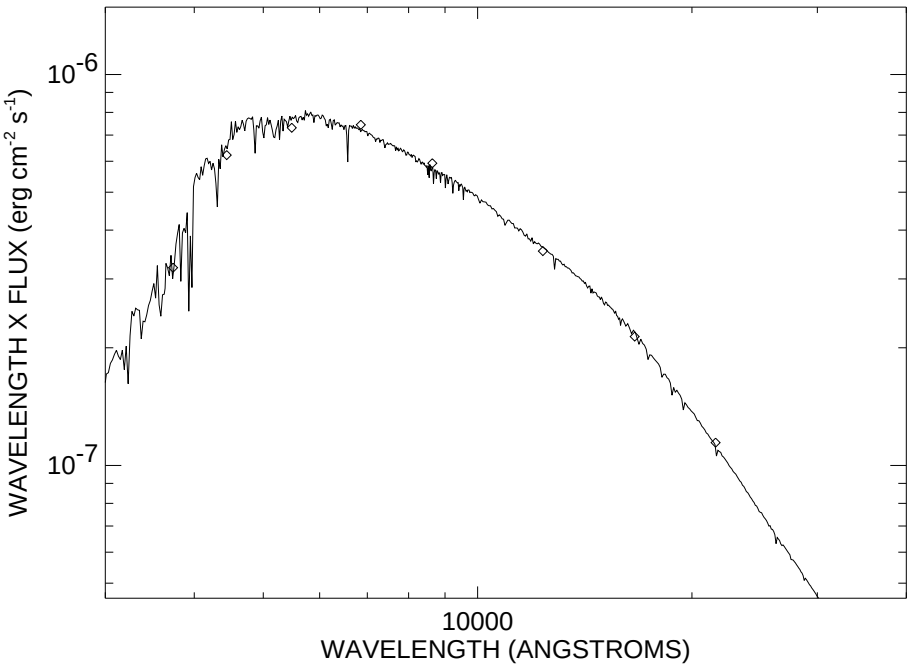

FIGURE A.41: SED plot for HD 102870.

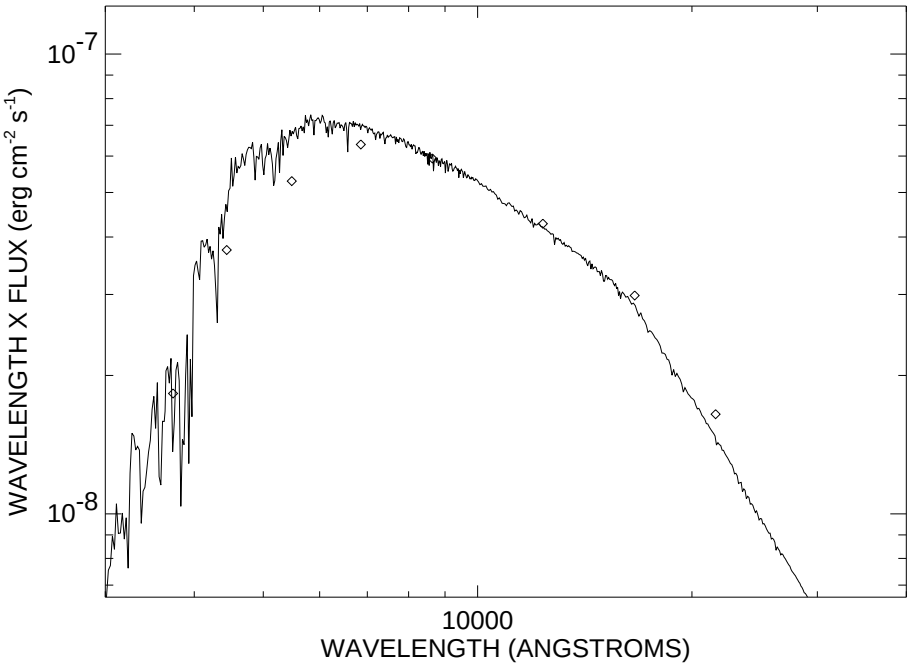

FIGURE A.42: SED plot for HD 103095.

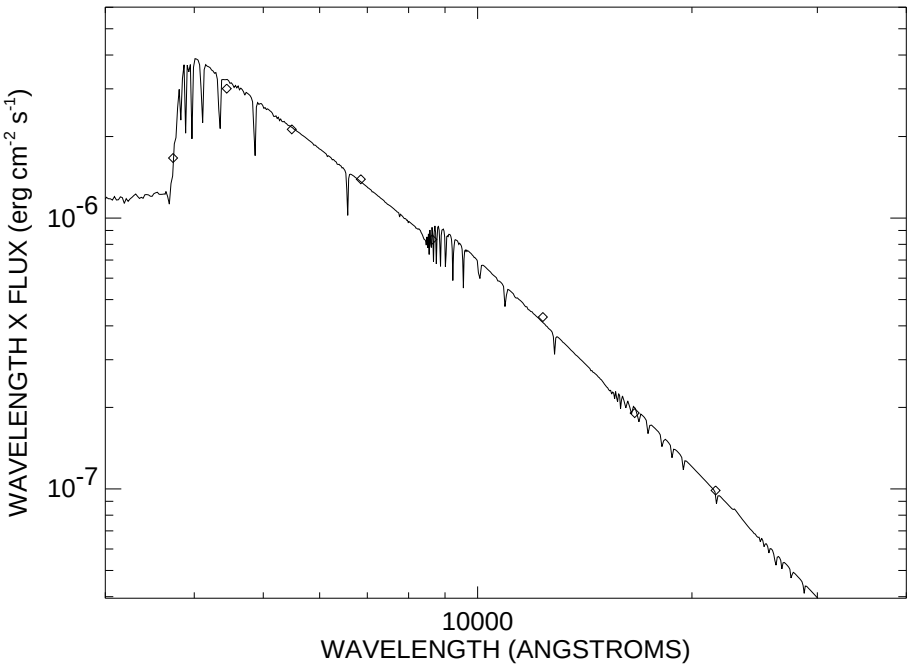

FIGURE A.43: SED plot for HD 103287.

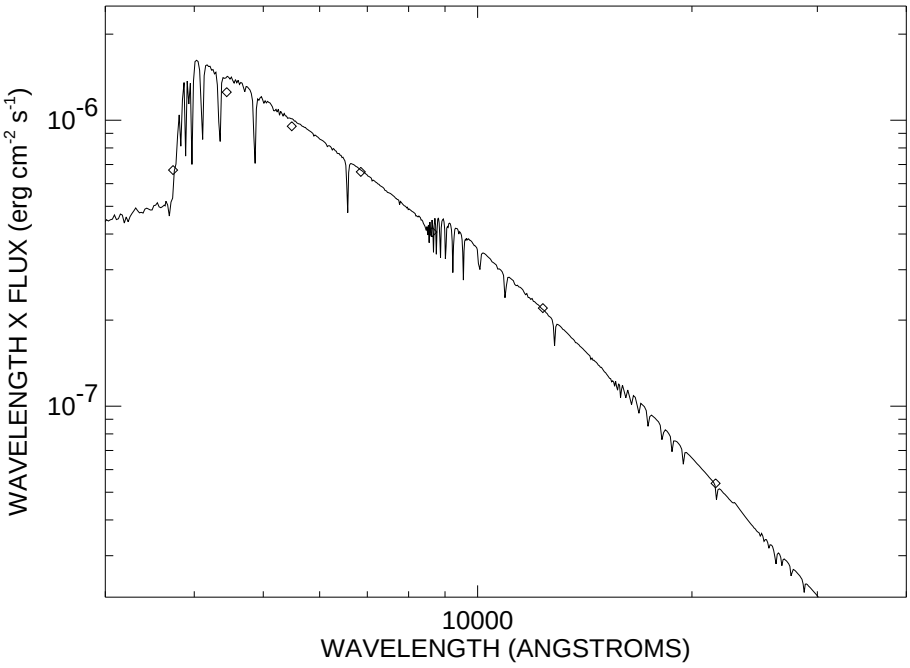

FIGURE A.44: SED plot for HD 106591.

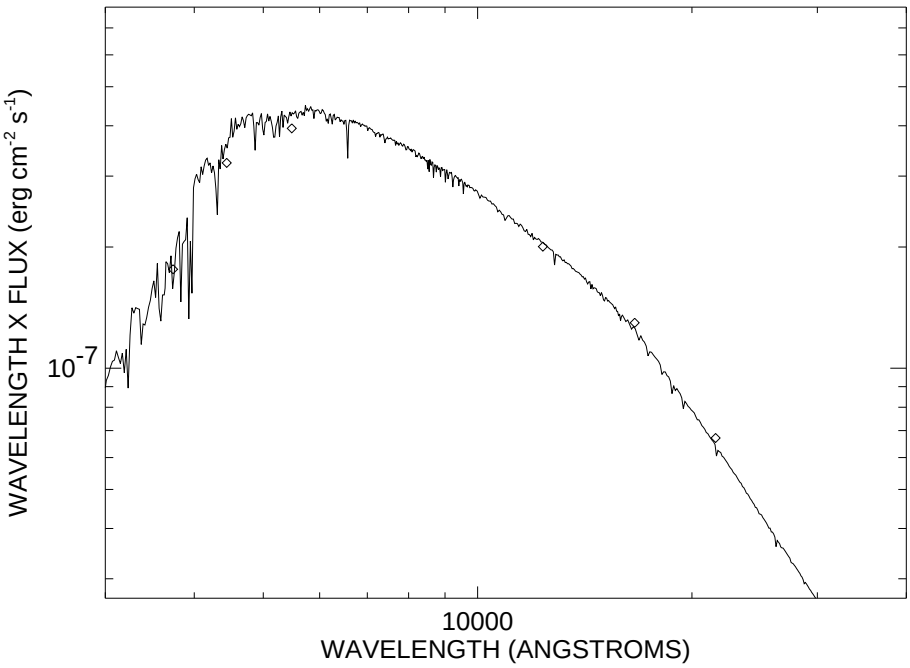

FIGURE A.45: SED plot for HD 109358.

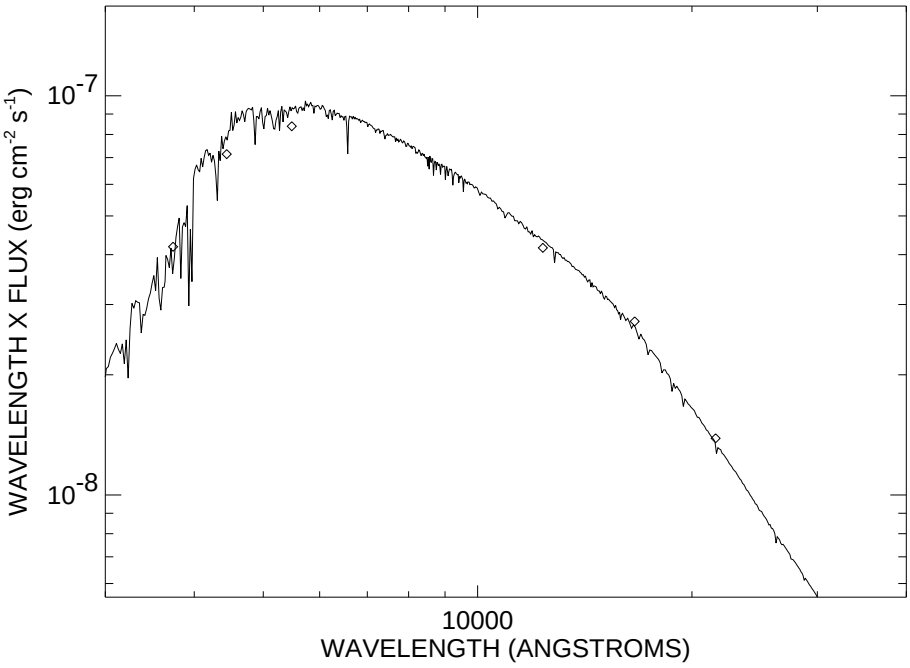

FIGURE A.46: SED plot for HD 110897.

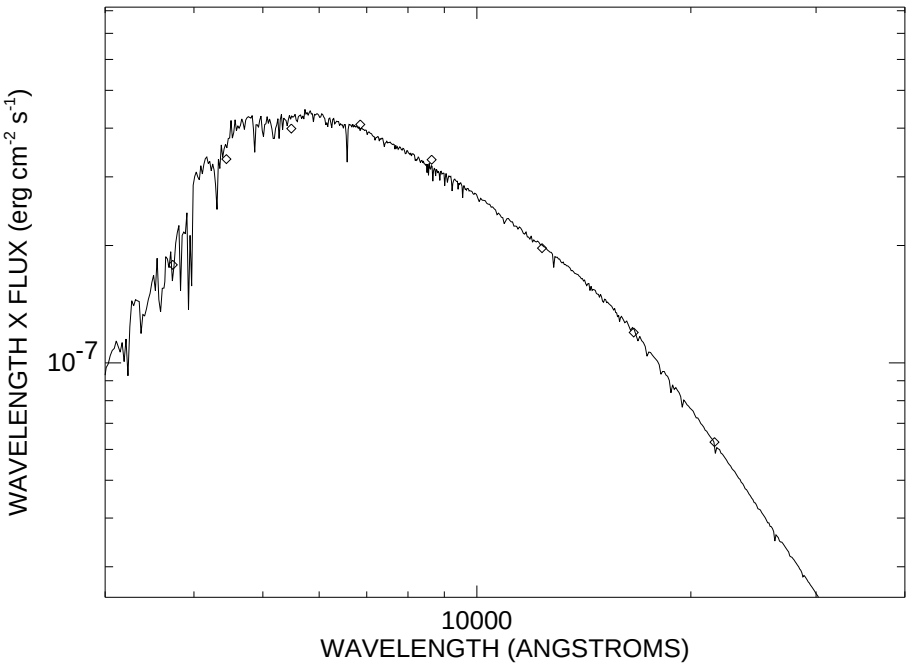

FIGURE A.47: SED plot for HD 114710.

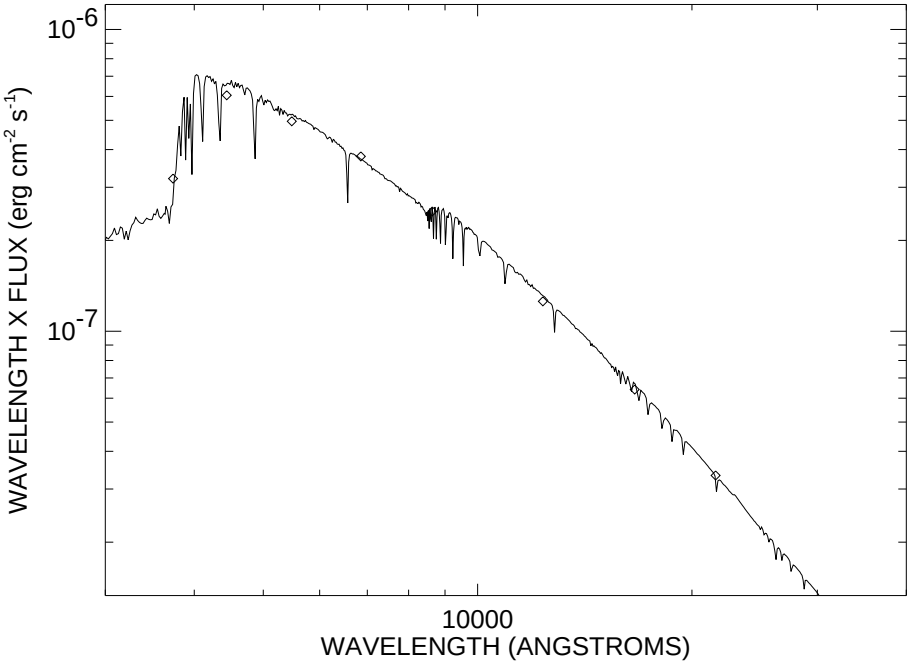

FIGURE A.48: SED plot for HD 116842.

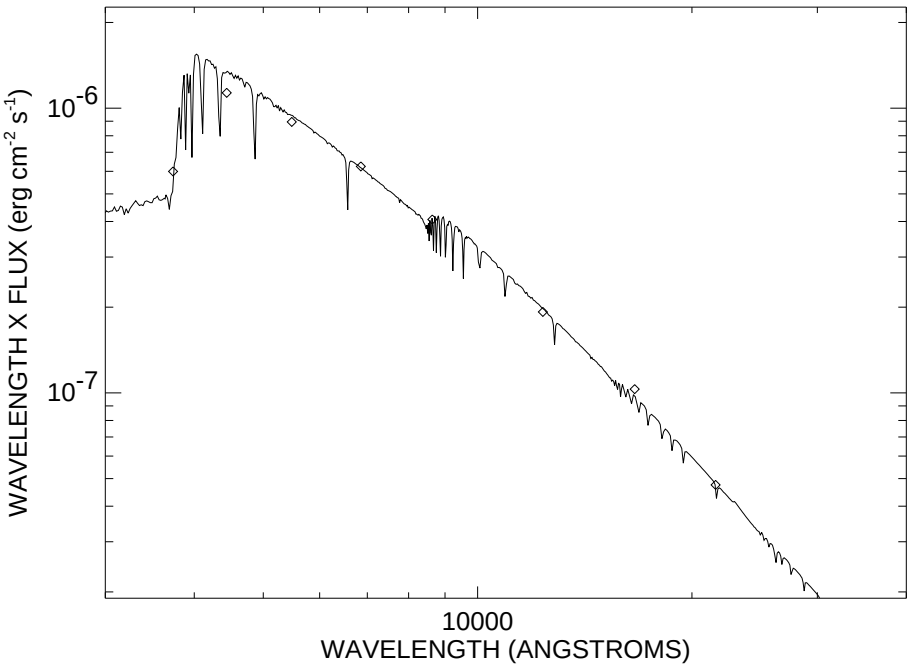

FIGURE A.49: SED plot for HD 118098.

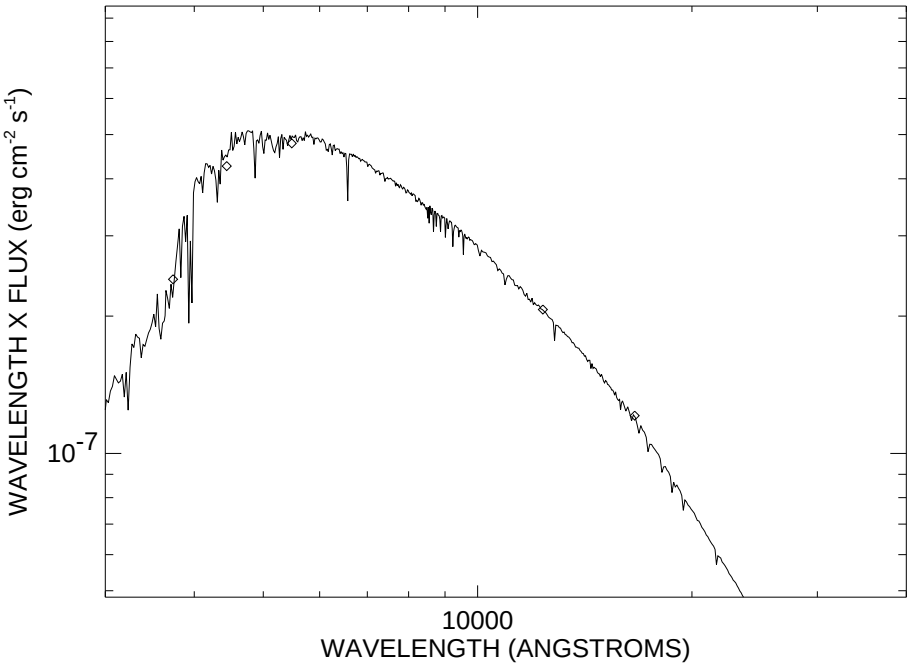

FIGURE A.50: SED plot for HD 126660.

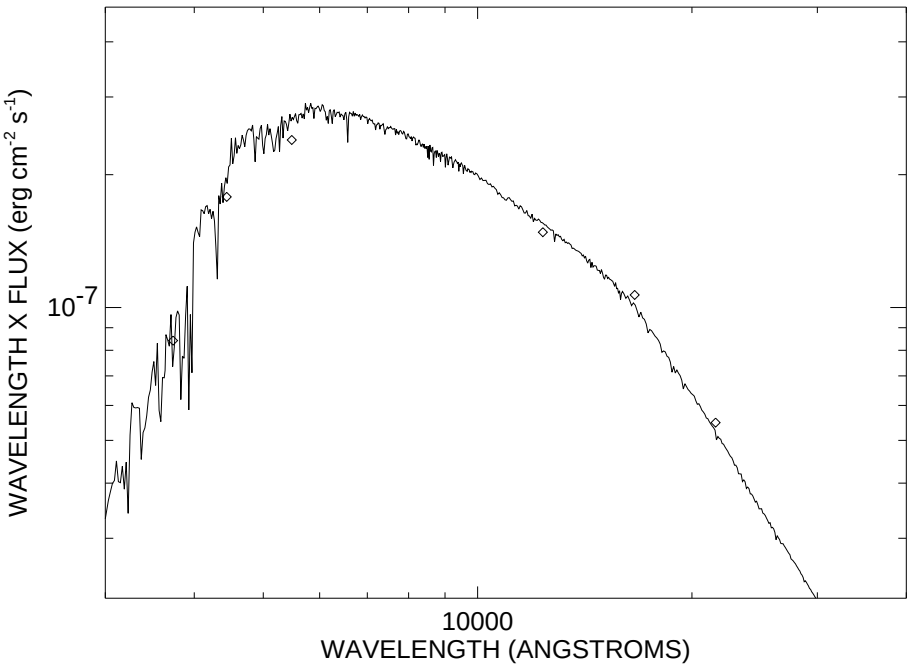

FIGURE A.51: SED plot for HD 126868.

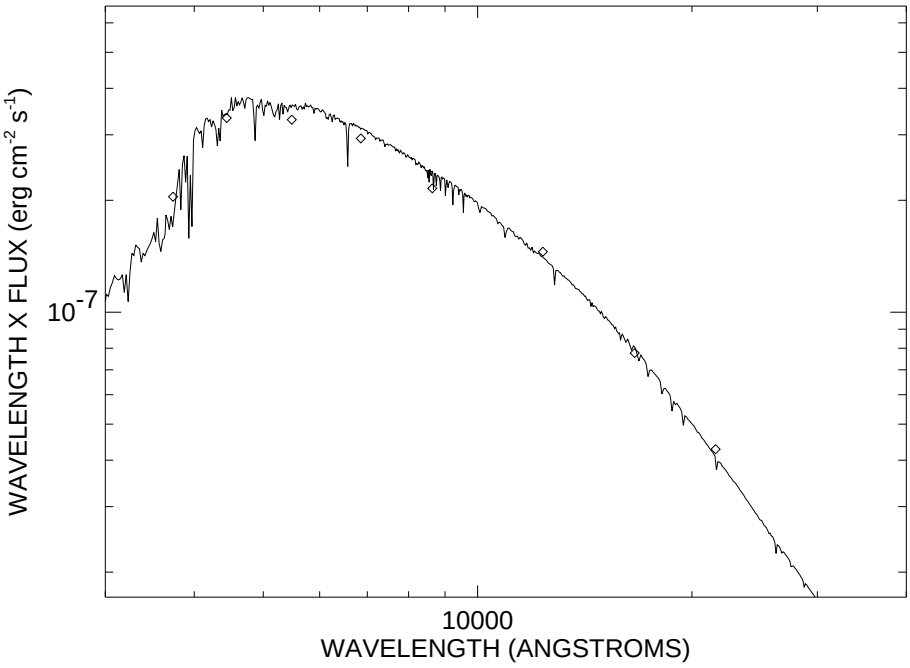

FIGURE A.52: SED plot for HD 128167.

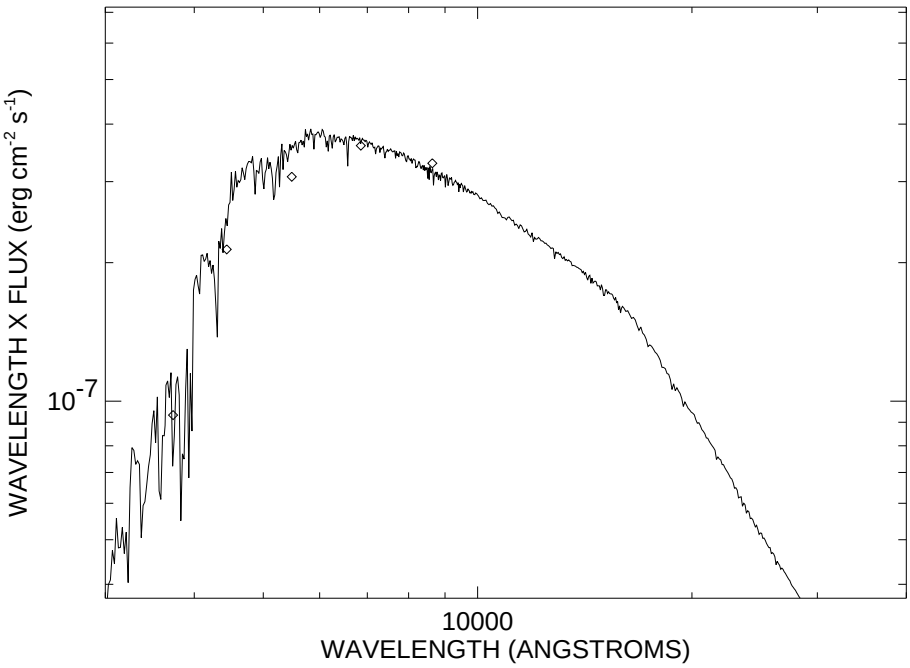

FIGURE A.53: SED plot for HD 131156.

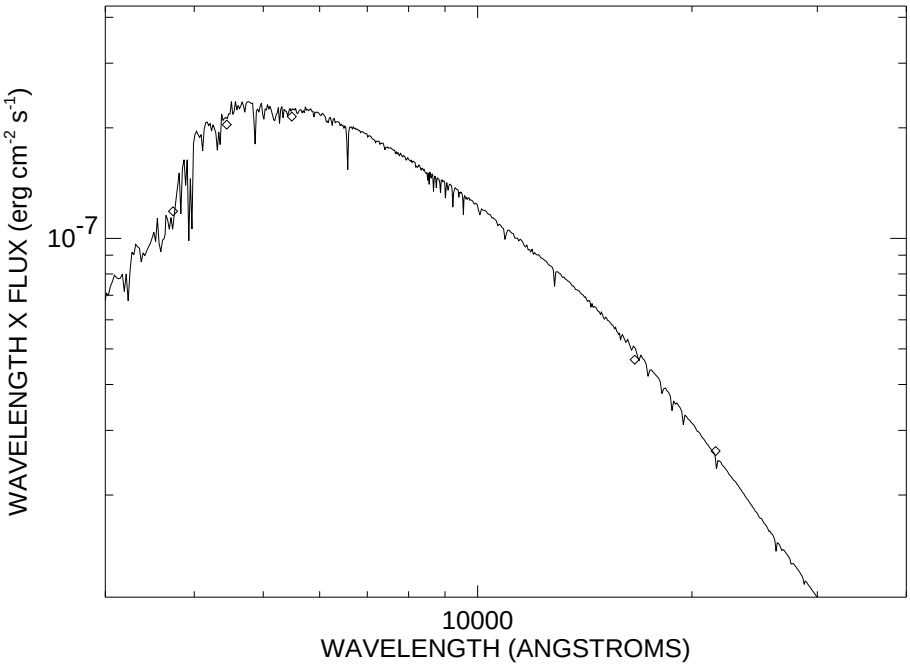

FIGURE A.54: SED plot for HD 134083.

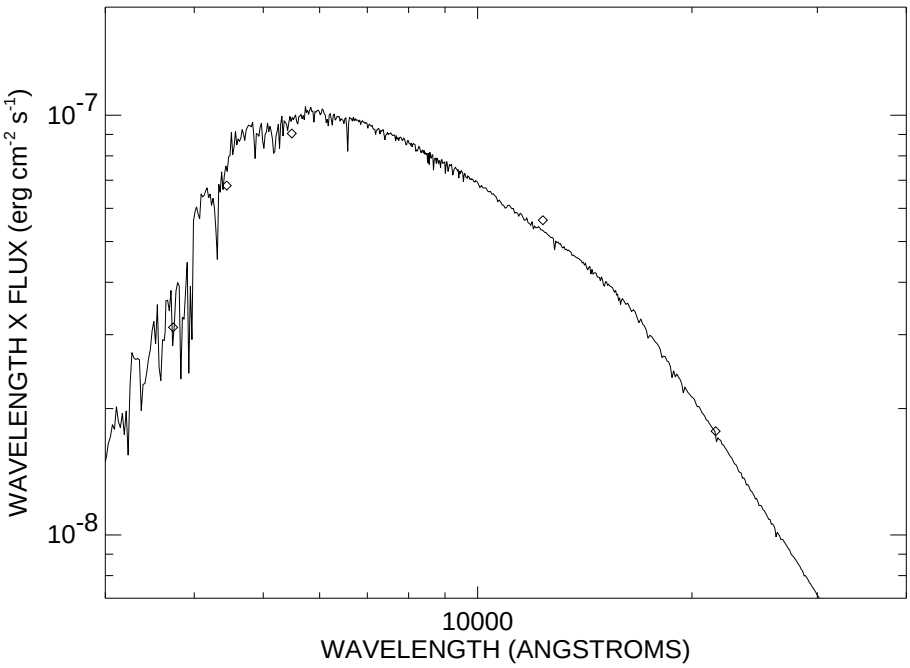

FIGURE A.55: SED plot for HD 140538.

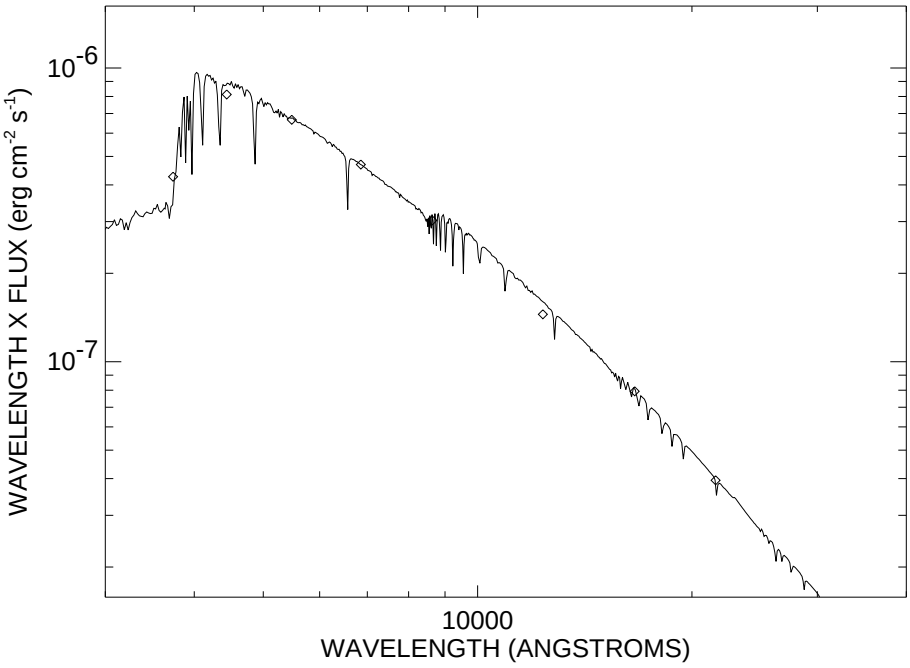

FIGURE A.56: SED plot for HD 141795.

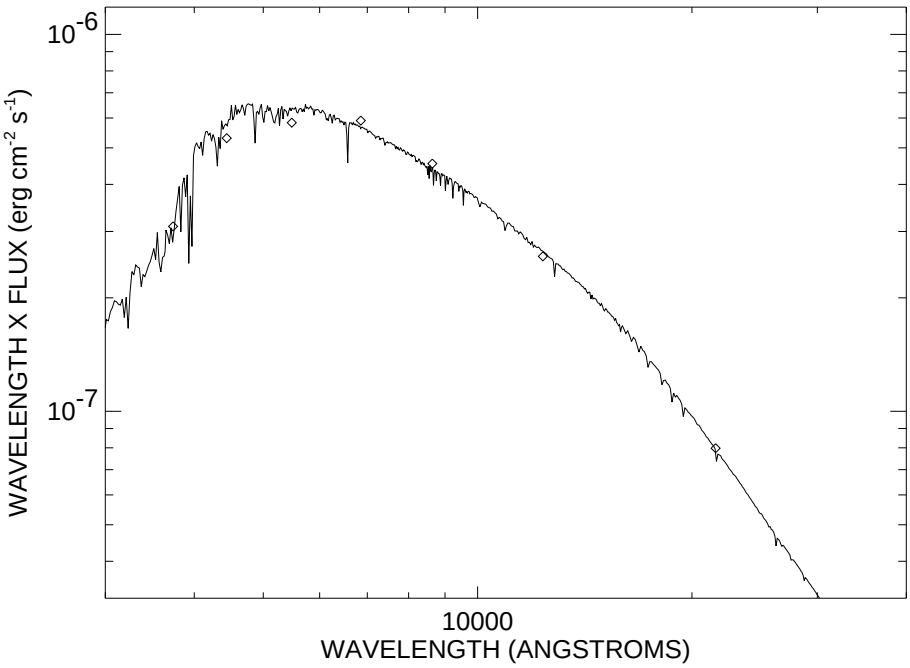

FIGURE A.57: SED plot for HD 142860.

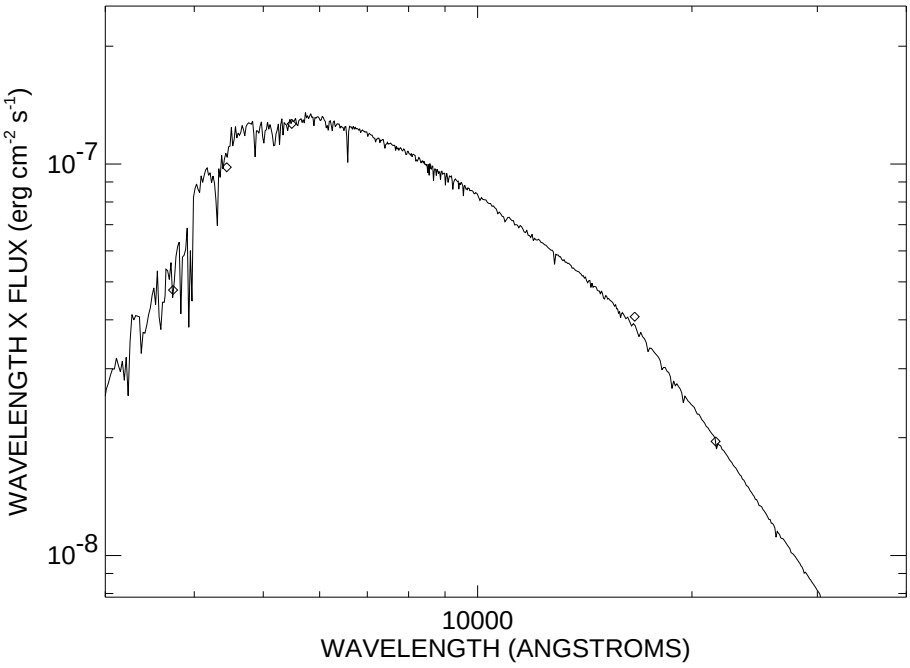

FIGURE A.58: SED plot for HD 146233.

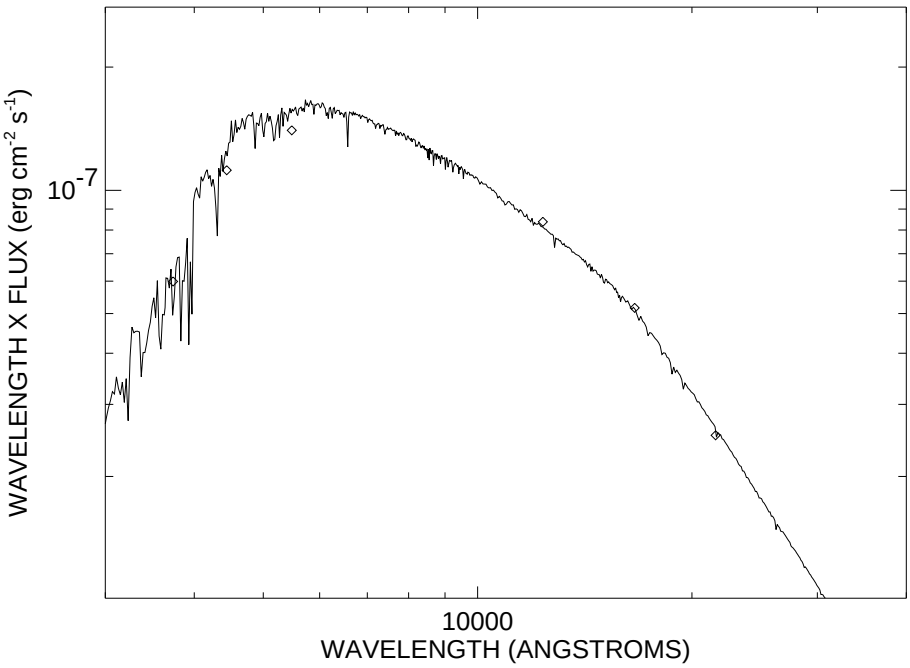

FIGURE A.59: SED plot for HD 157214.

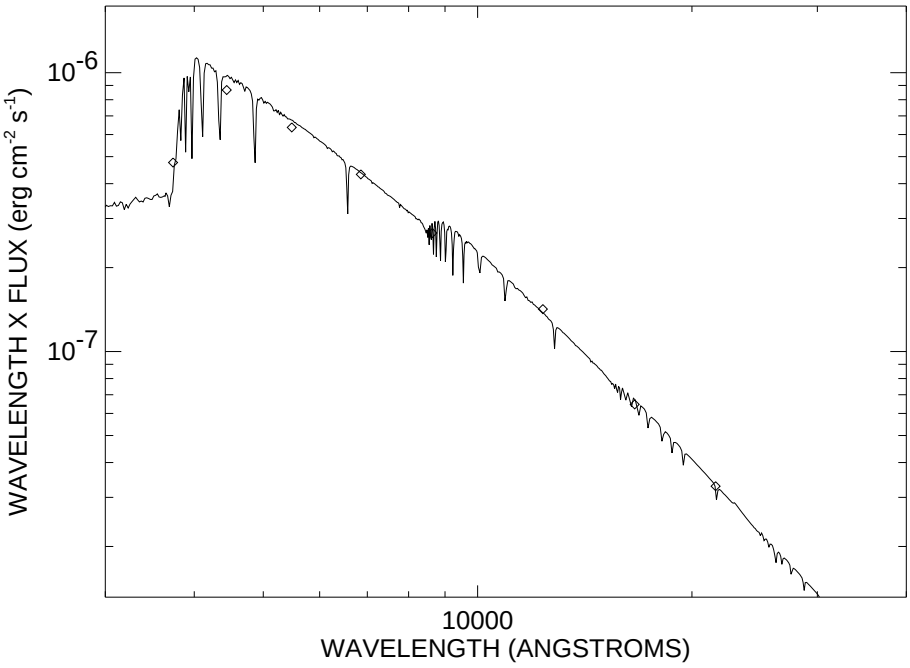

FIGURE A.60: SED plot for HD 161868.

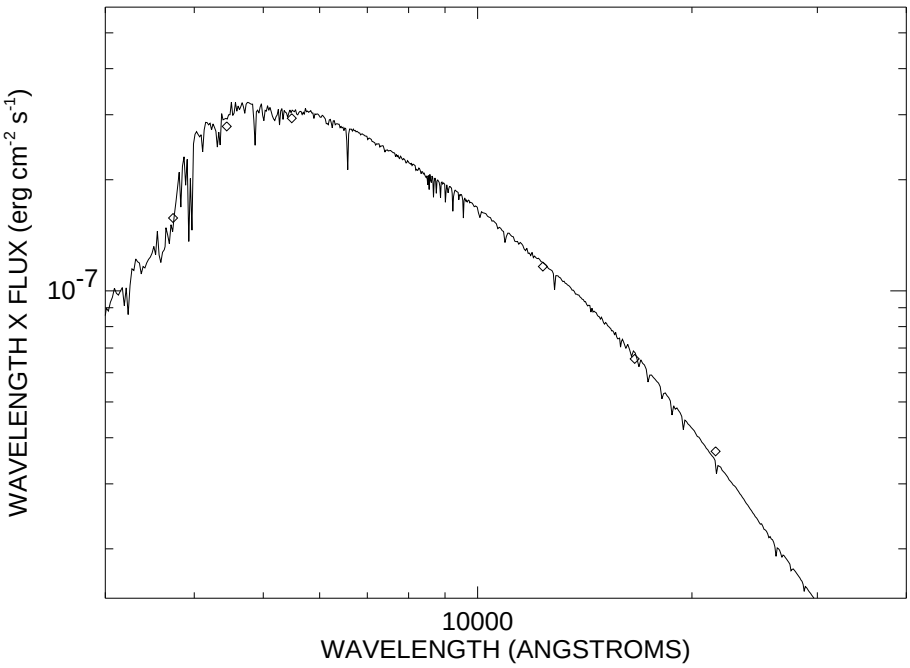

FIGURE A.61: SED plot for HD 162003.

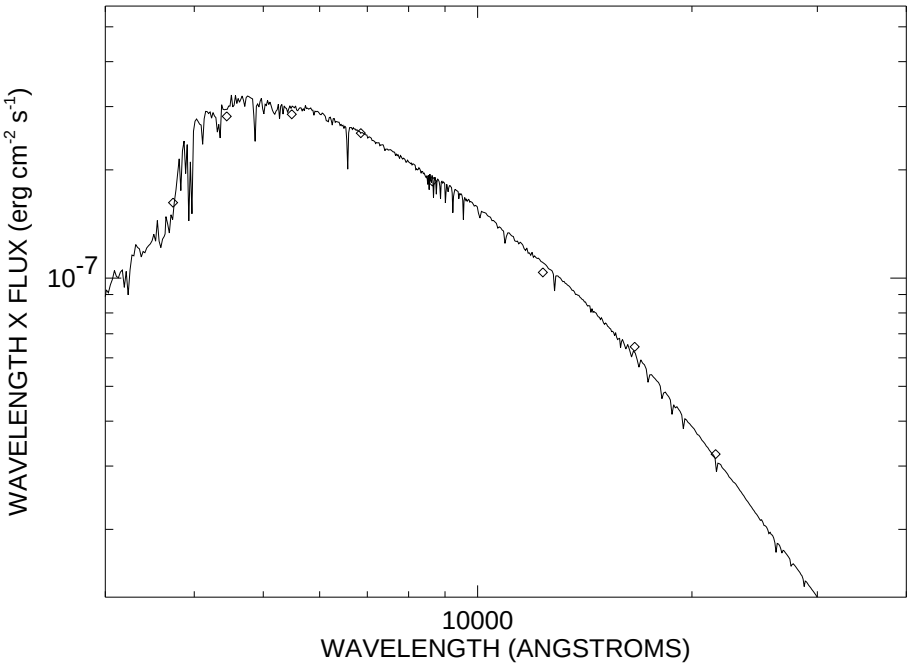

FIGURE A.62: SED plot for HD 164259.

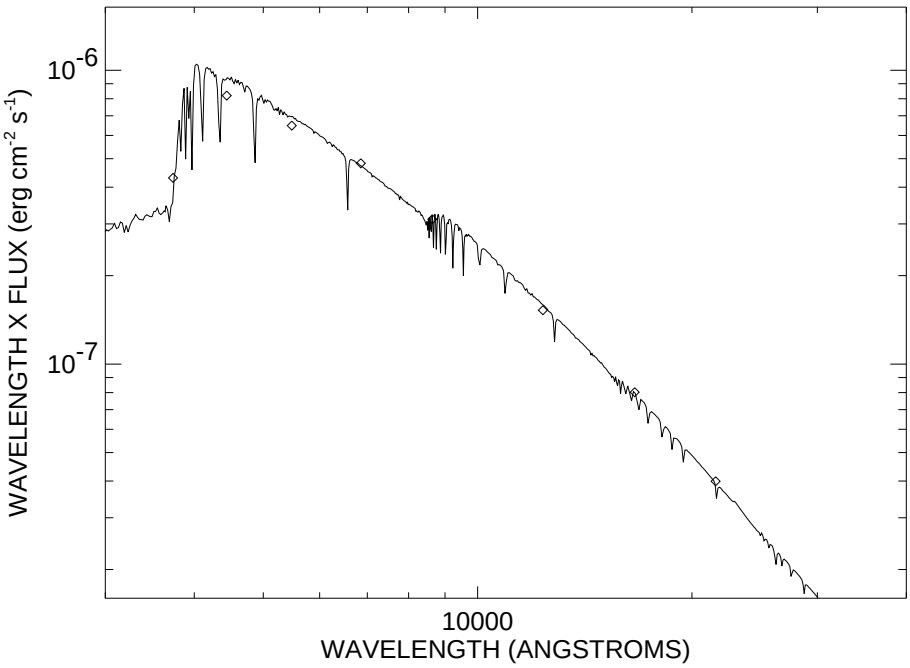

FIGURE A.63: SED plot for HD 165777.

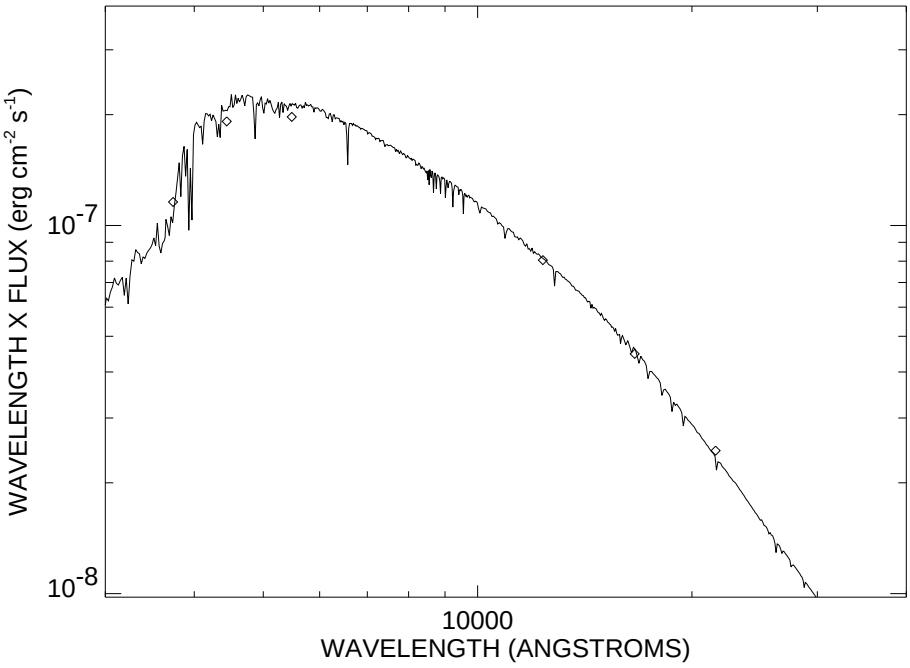

FIGURE A.64: SED plot for HD 168151.

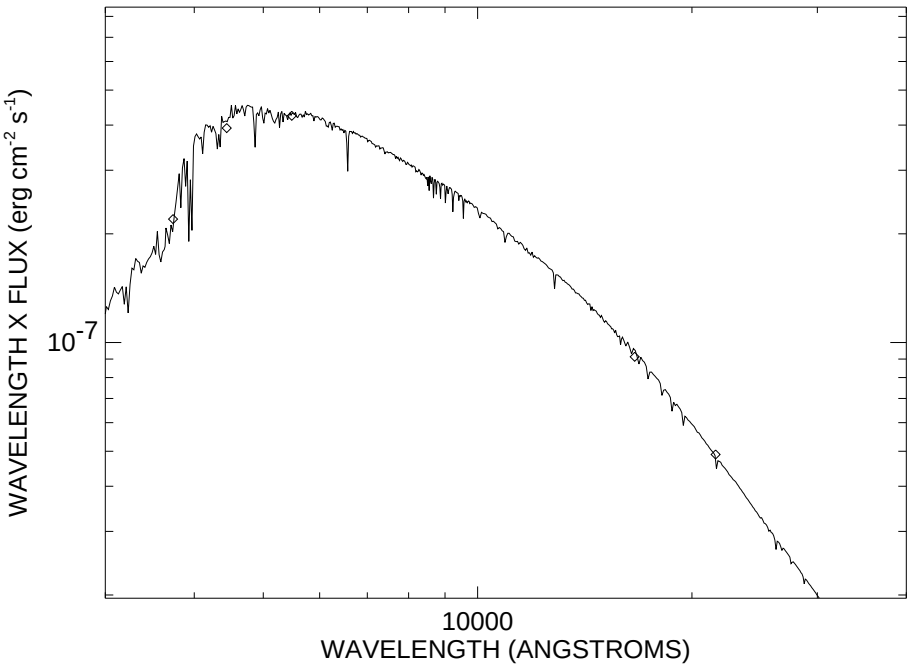

FIGURE A.65: SED plot for HD 173667.

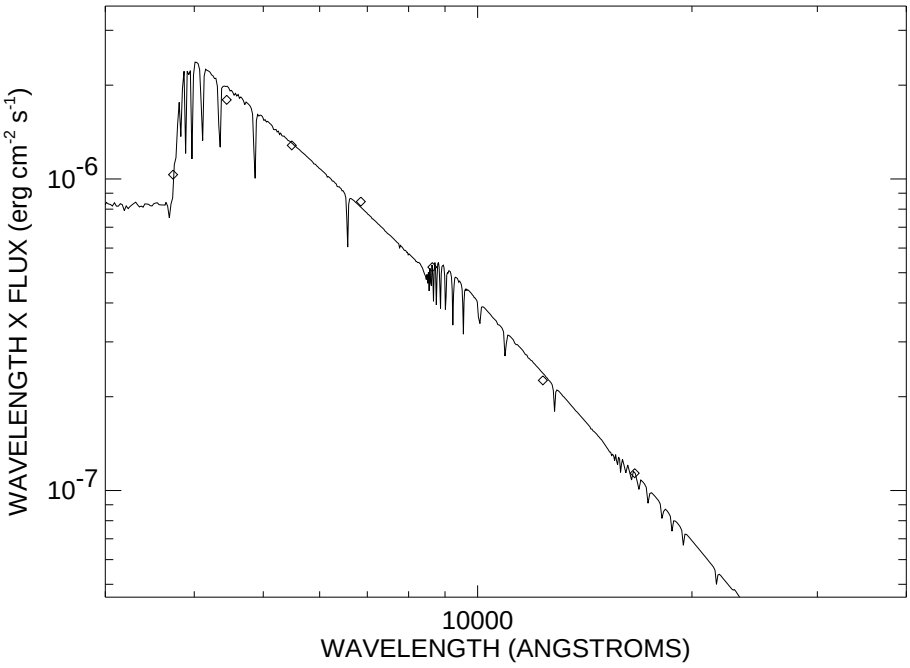

FIGURE A.66: SED plot for HD 177724.

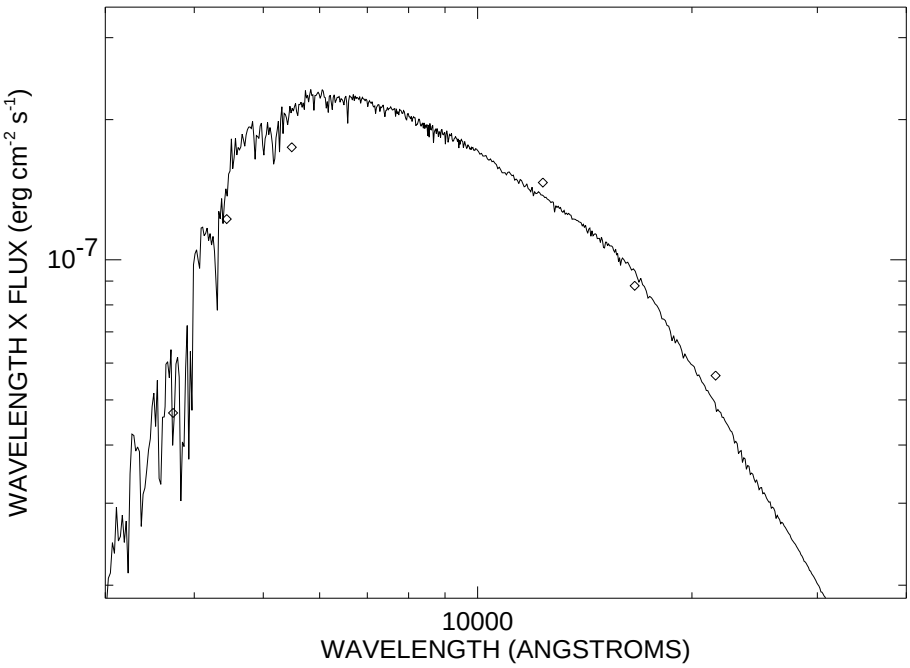

FIGURE A.67: SED plot for HD 182572.

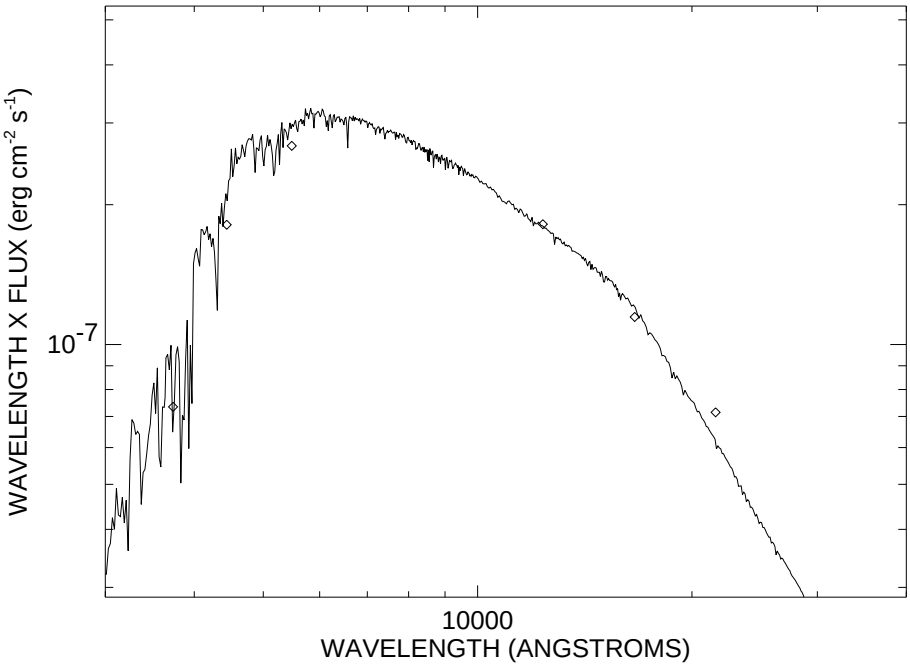

FIGURE A.68: SED plot for HD 185144.

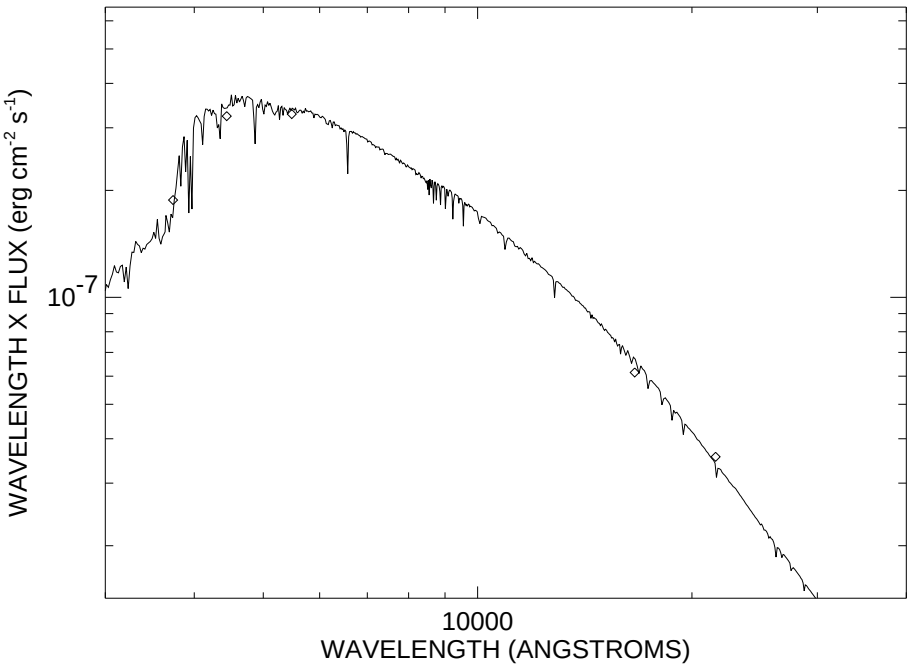

FIGURE A.69: SED plot for HD 185395.

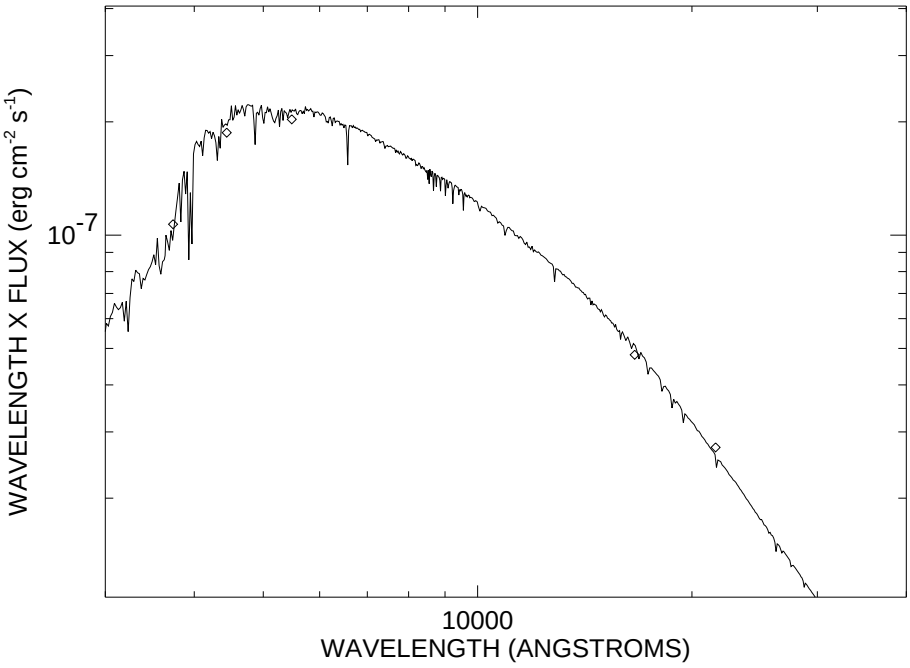

FIGURE A.70: SED plot for HD 187013.

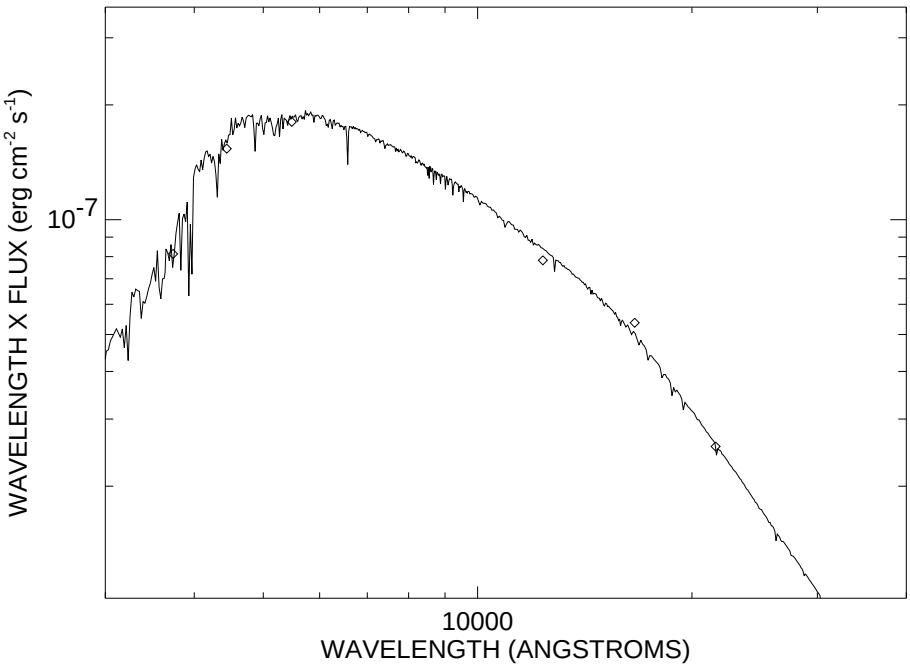

FIGURE A.71: SED plot for HD 187691.

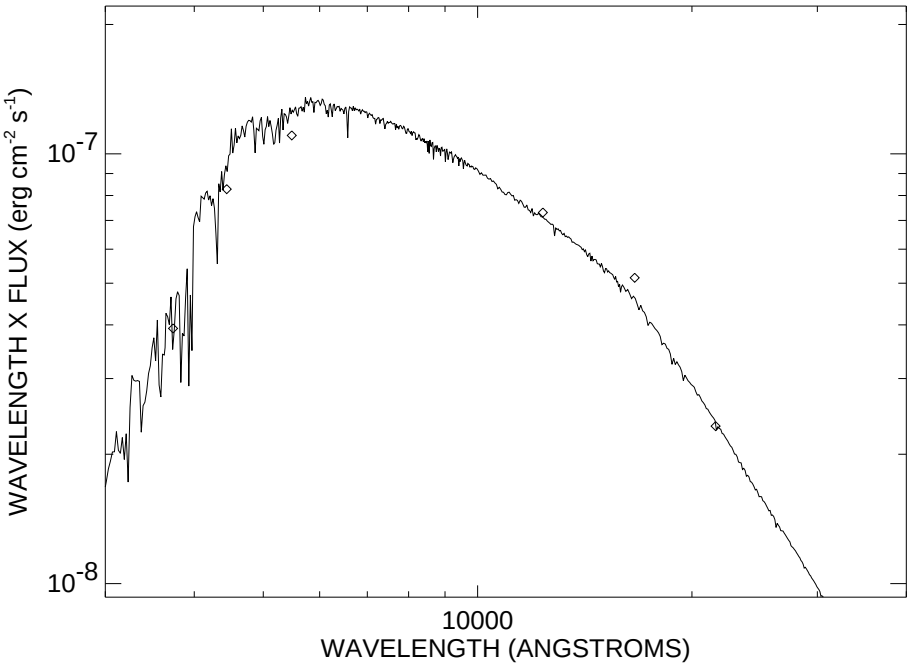

FIGURE A.72: SED plot for HD 195564.

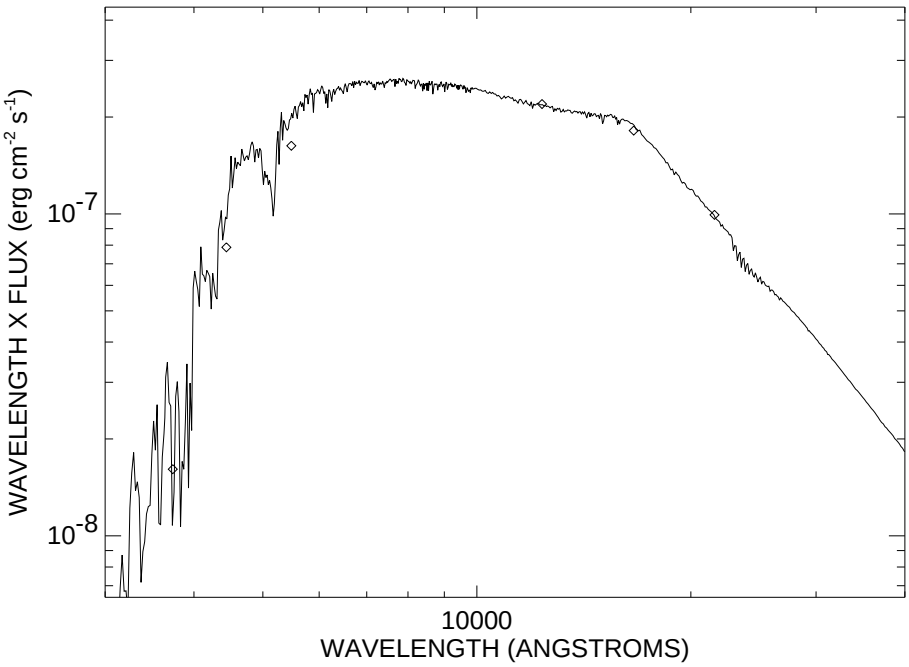

FIGURE A.73: SED plot for HD 201091.

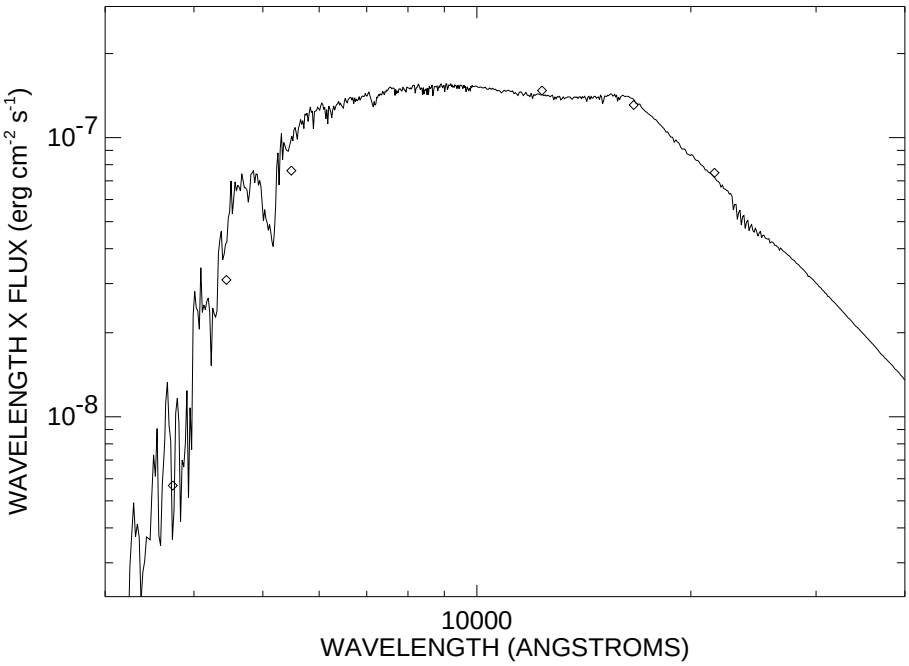

FIGURE A.74: SED plot for HD 201092.

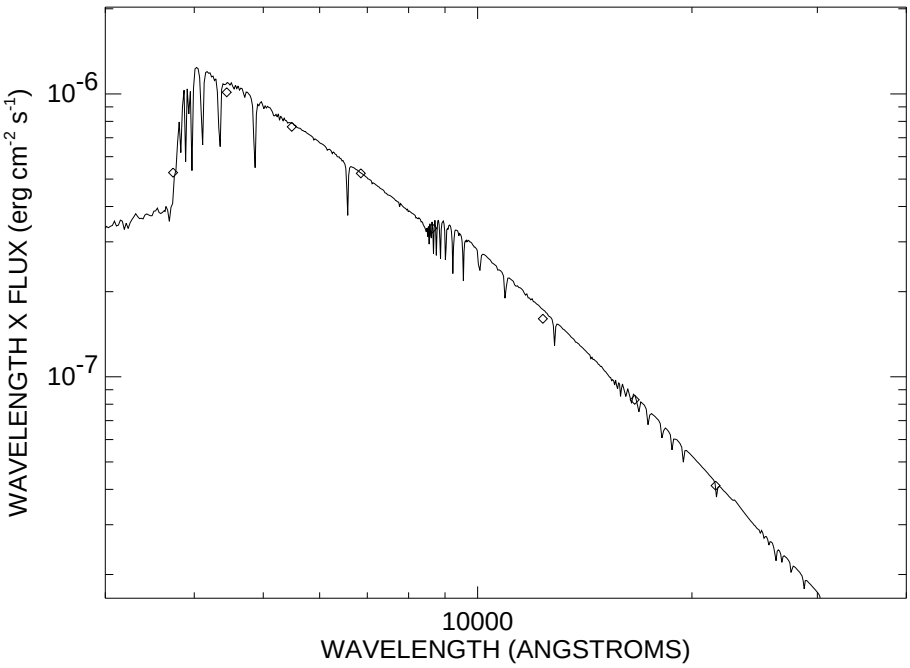

FIGURE A.75: SED plot for HD 210418.

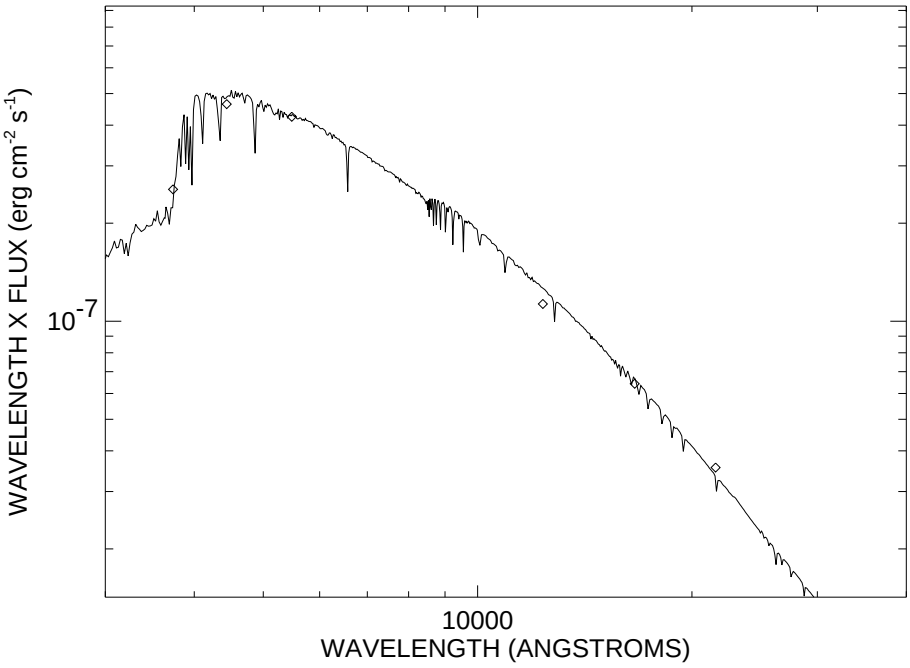

FIGURE A.76: SED plot for HD 211336.

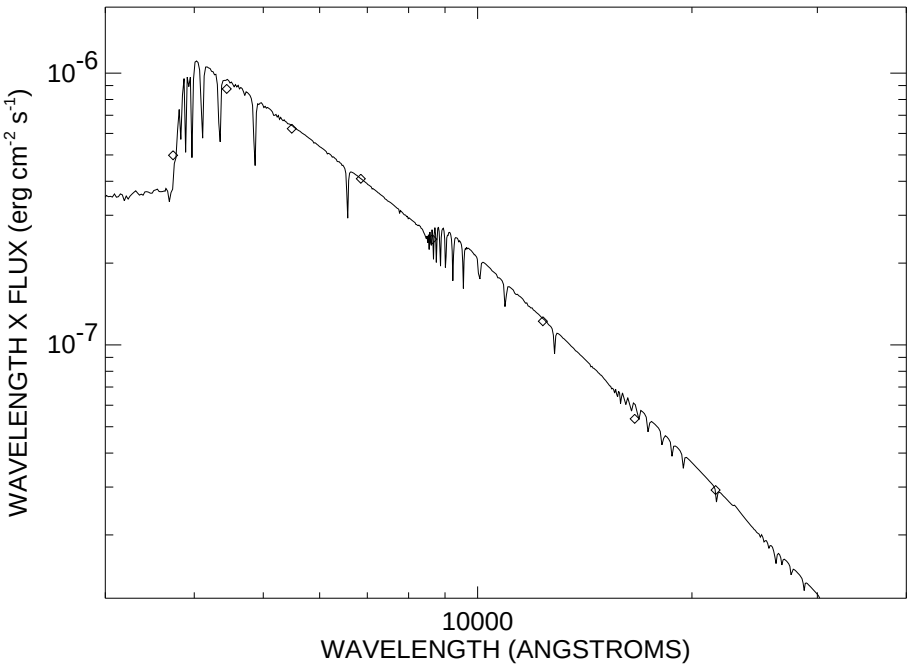

FIGURE A.77: SED plot for HD 213558.

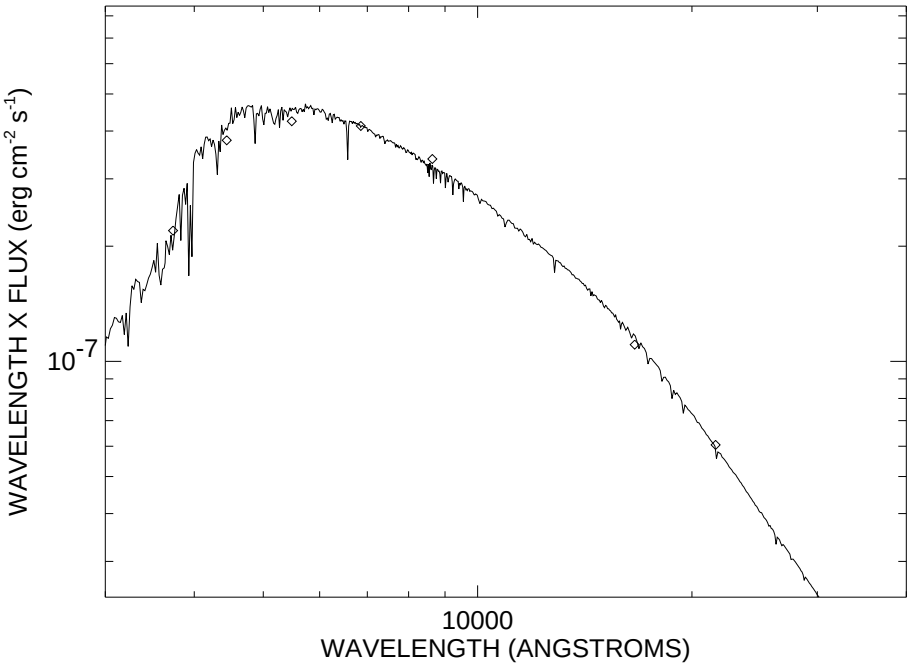

FIGURE A.78: SED plot for HD 215648.

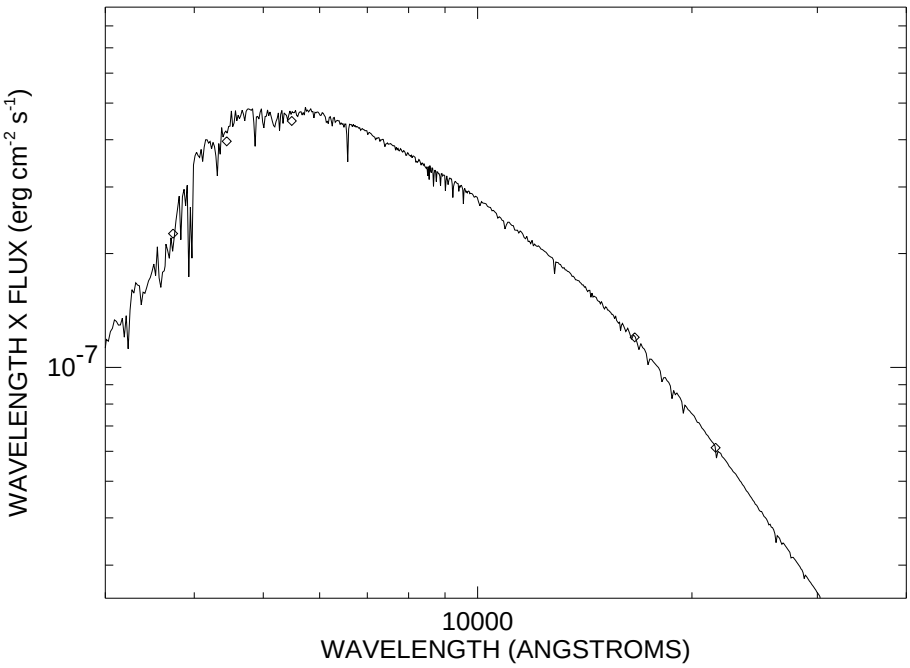

FIGURE A.79: SED plot for HD 222368.

– B –

Appendix B

SED plots for the calibrators used in the thesis. The *solid* line is the Kurucz model atmosphere for the star's effective temperature and gravity and the *diamonds* are flux calibrated photometry.

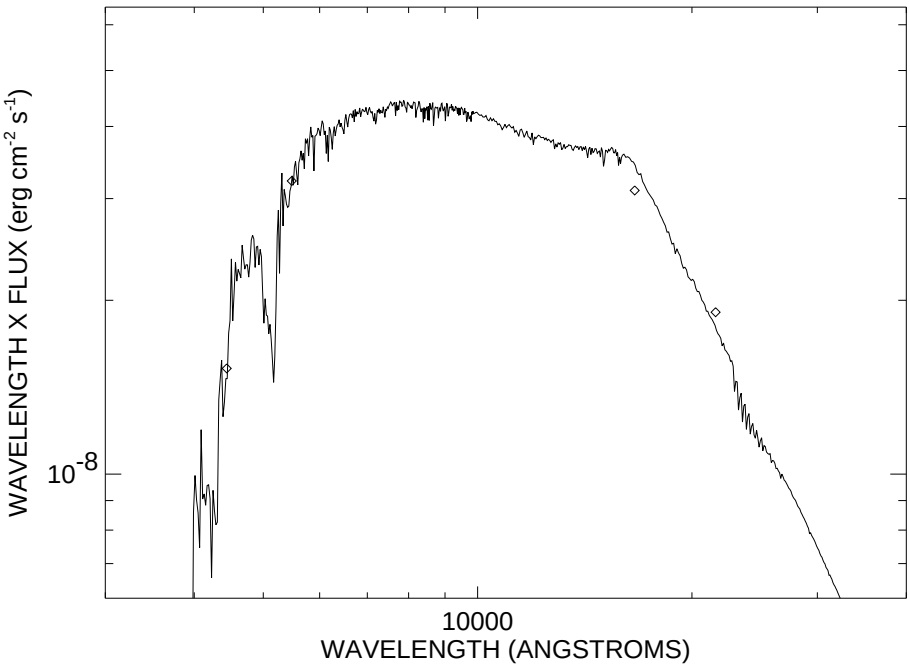

FIGURE B.1: SED plot for HD 71.

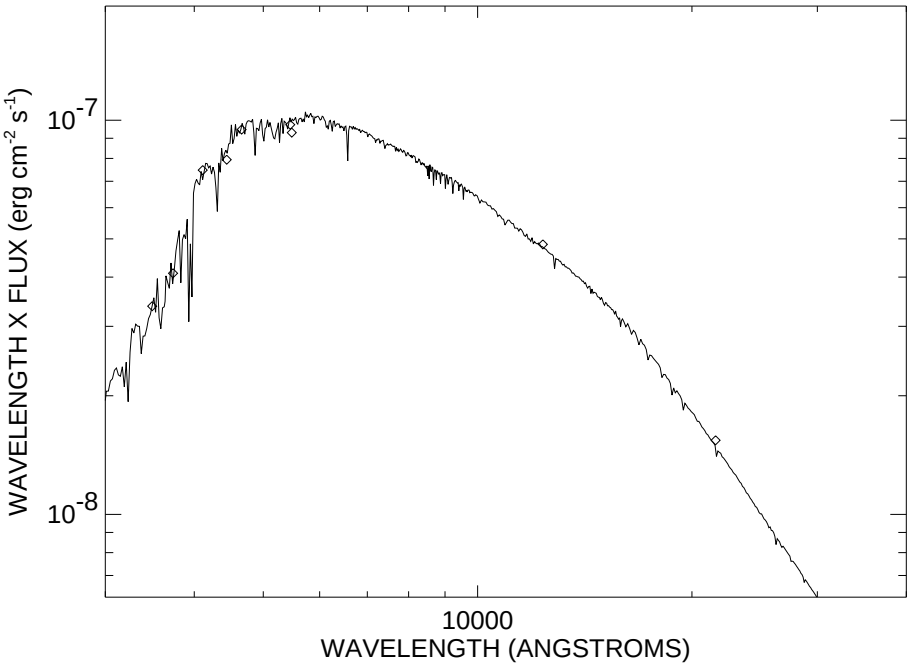

FIGURE B.2: SED plot for HD 6210.

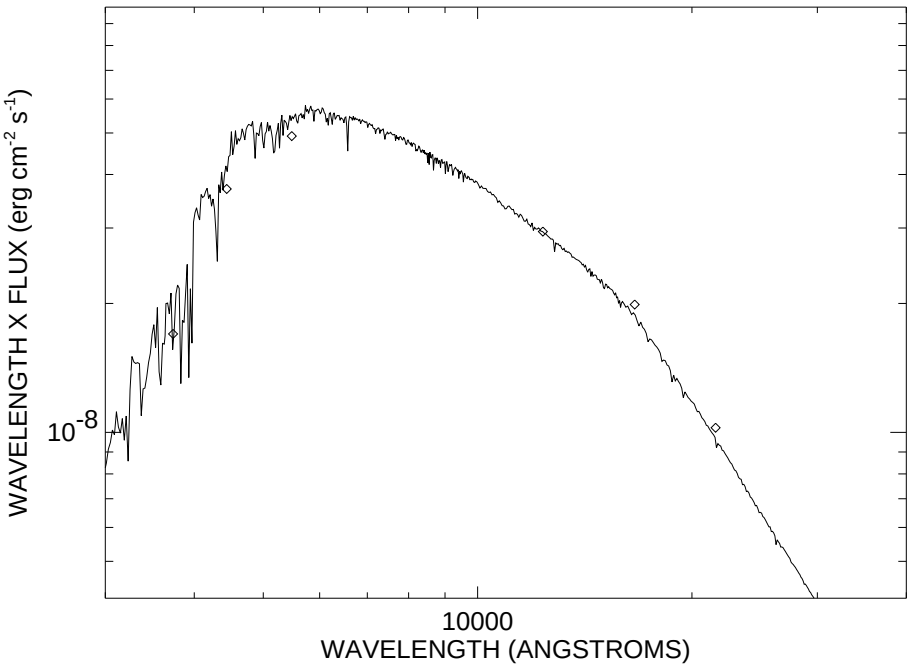

FIGURE B.3: SED plot for HD 9407.

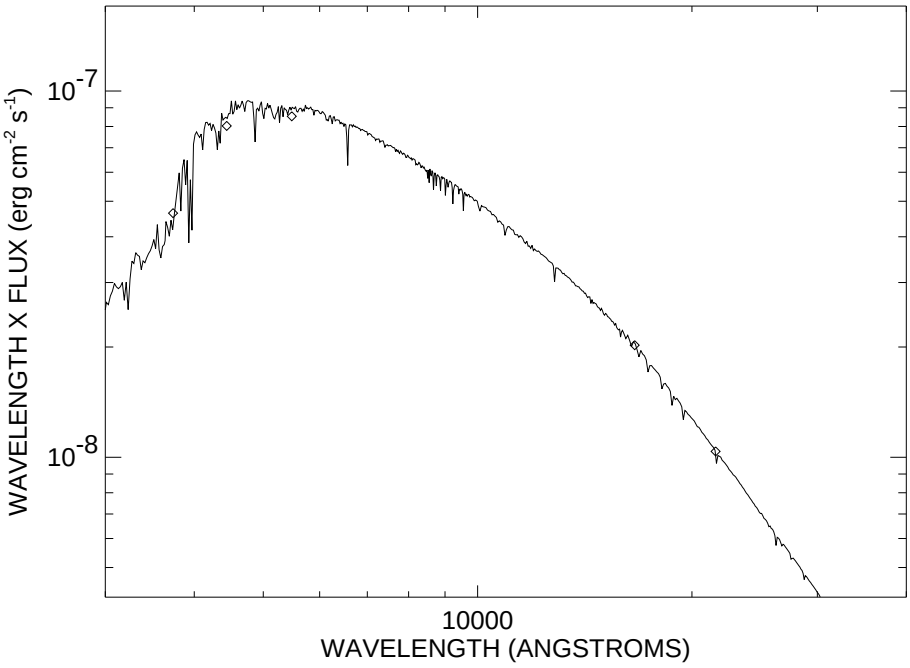

FIGURE B.4: SED plot for HD 20675.

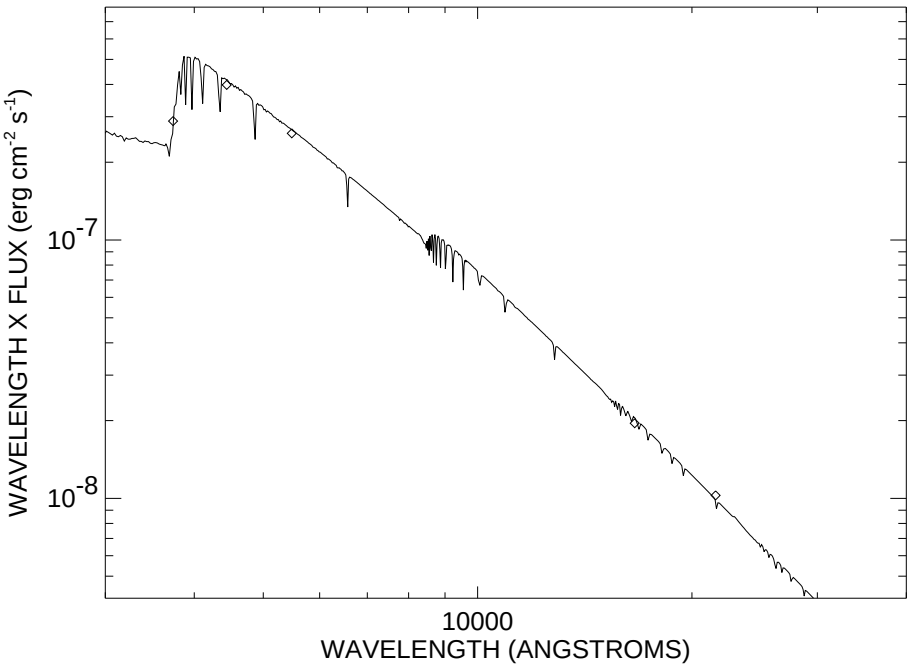

FIGURE B.5: SED plot for HD 21790.

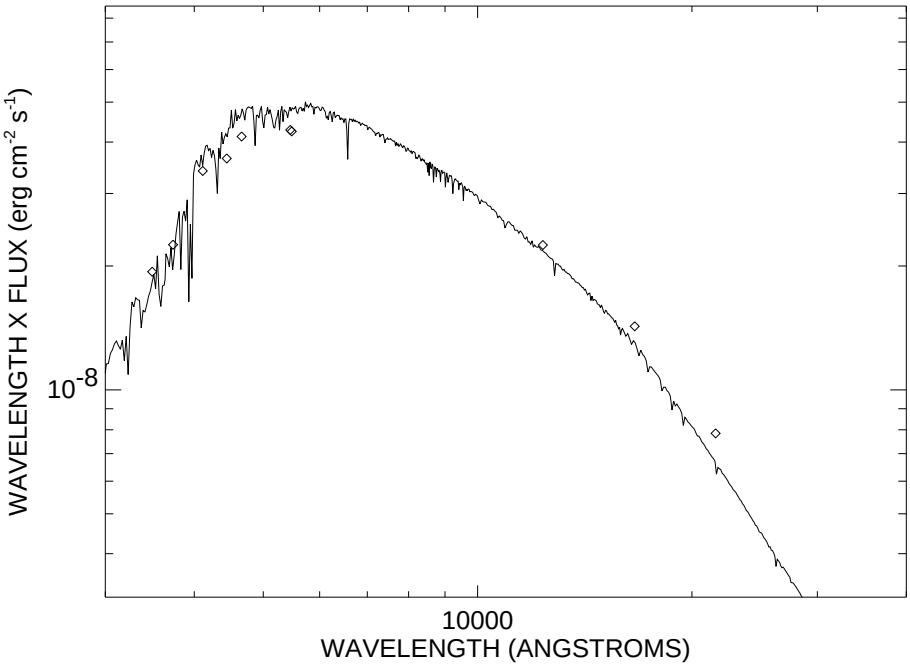

FIGURE B.6: SED plot for HD 22879.

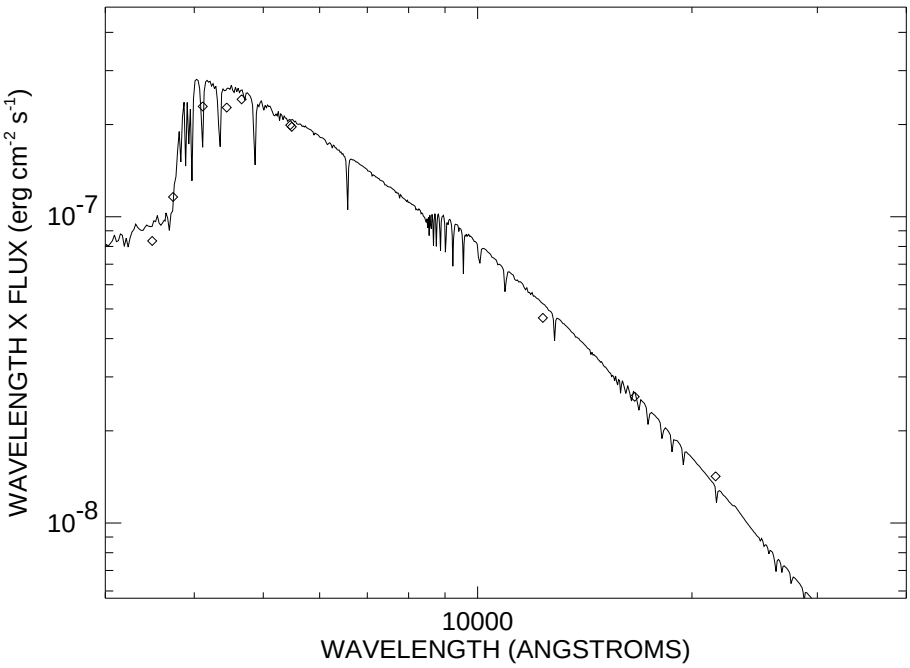

FIGURE B.7: SED plot for HD 28355.

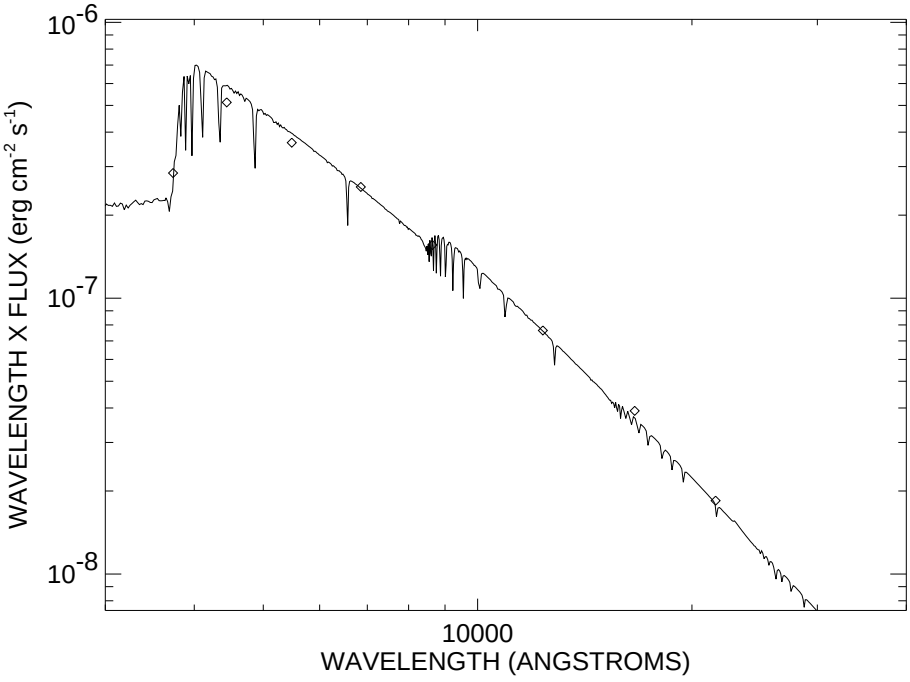

FIGURE B.8: SED plot for HD 30739.

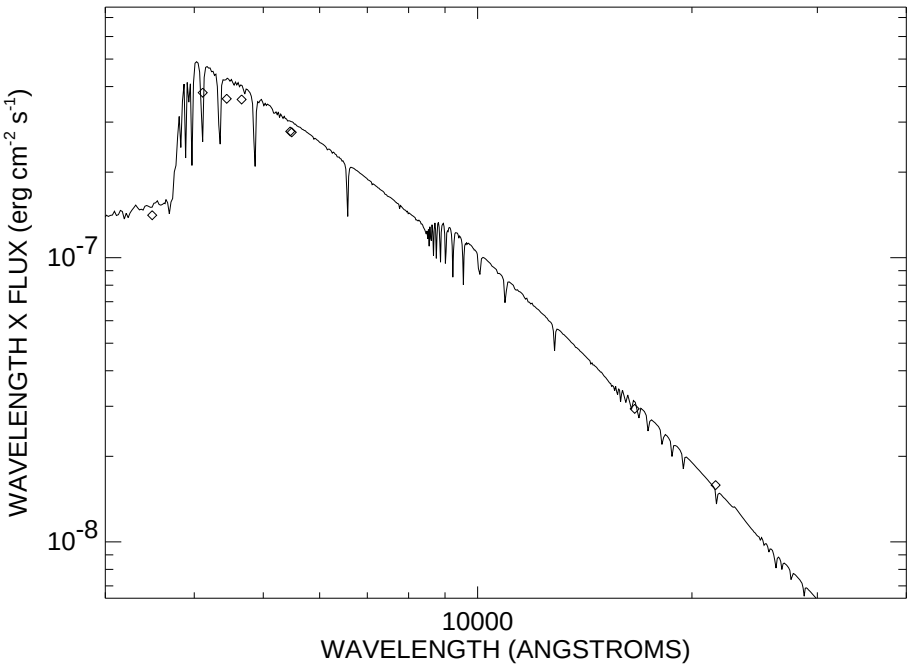

FIGURE B.9: SED plot for HD 31295.

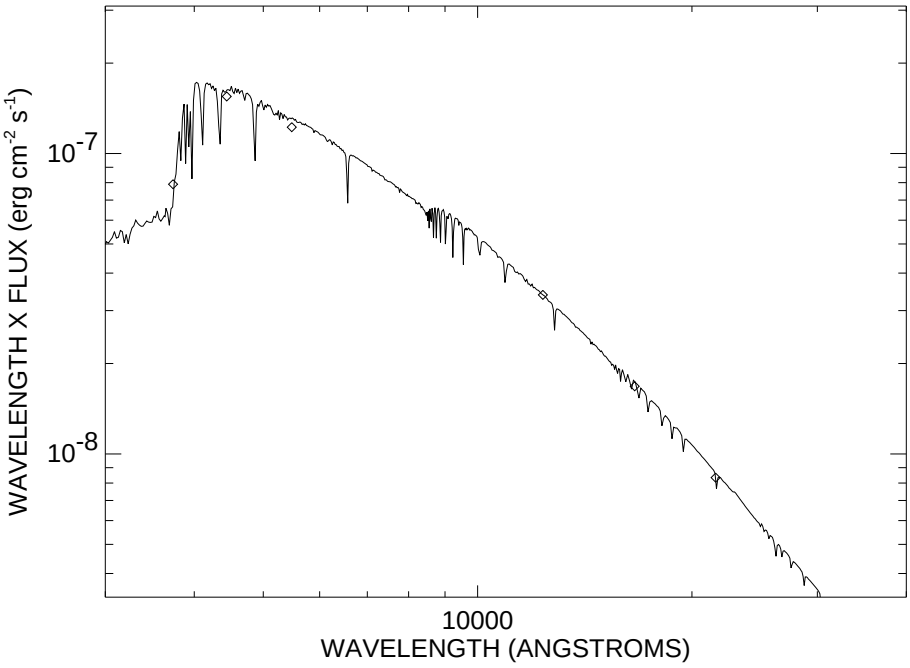

FIGURE B.10: SED plot for HD 34904.

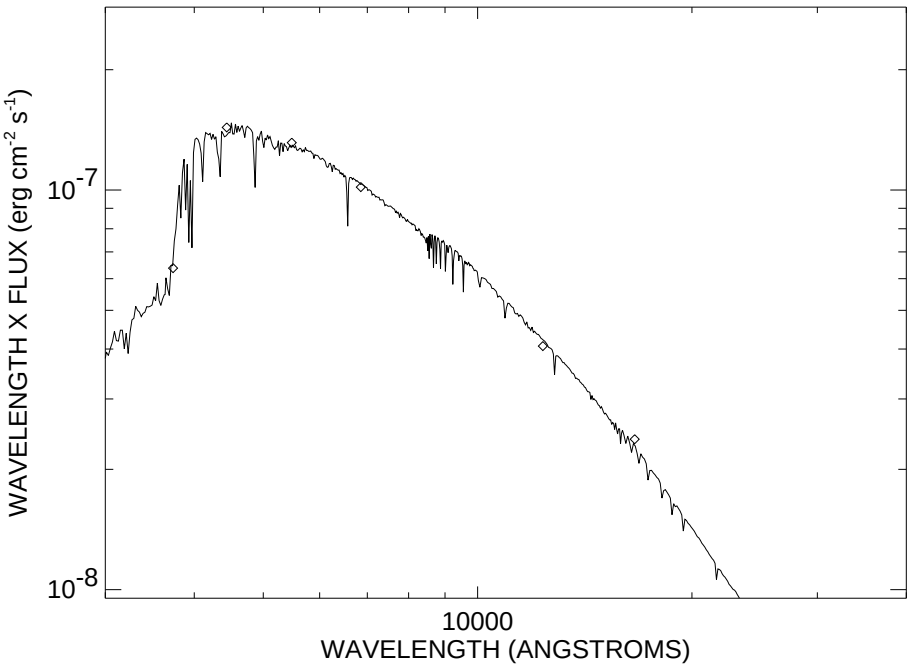

FIGURE B.11: SED plot for HD 38558.

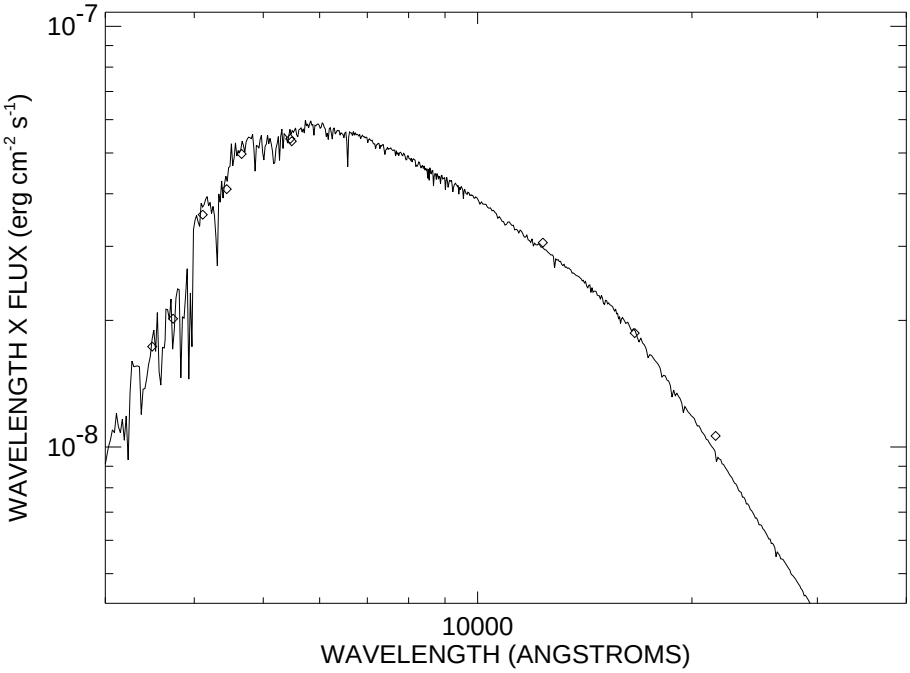

FIGURE B.12: SED plot for HD 42807.

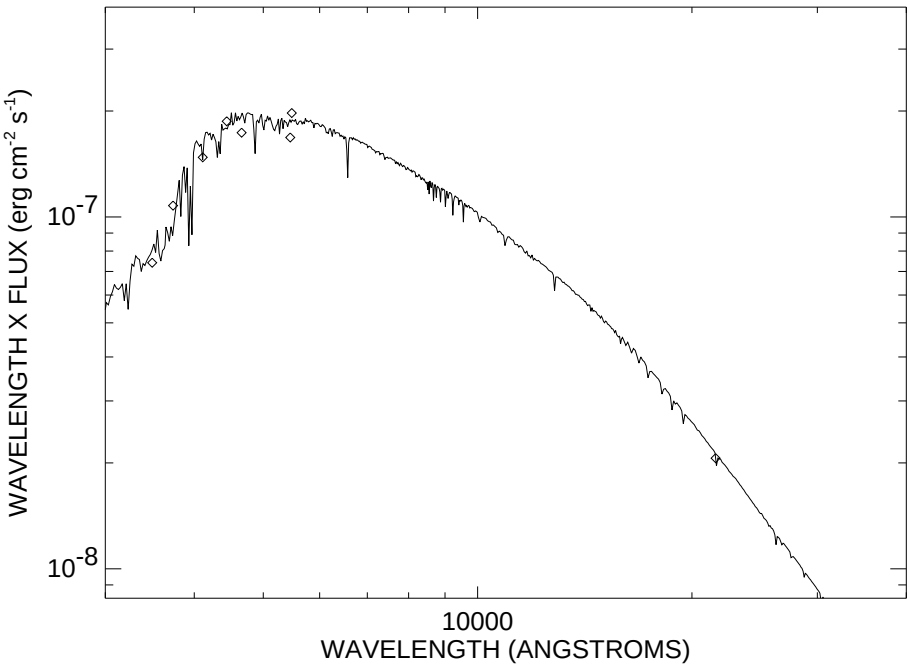

FIGURE B.13: SED plot for HD 43042.

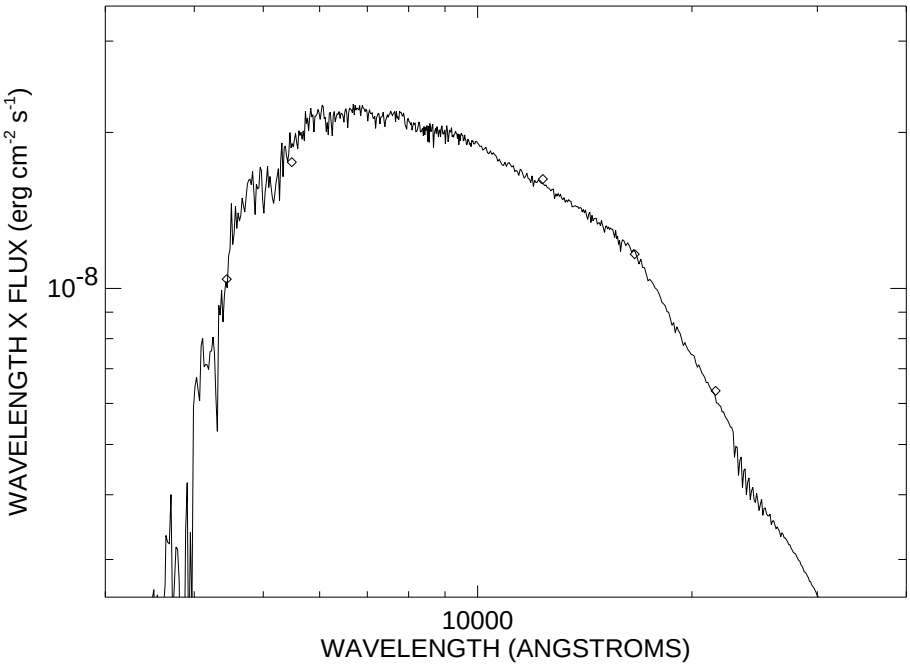

FIGURE B.14: SED plot for HD 43795.

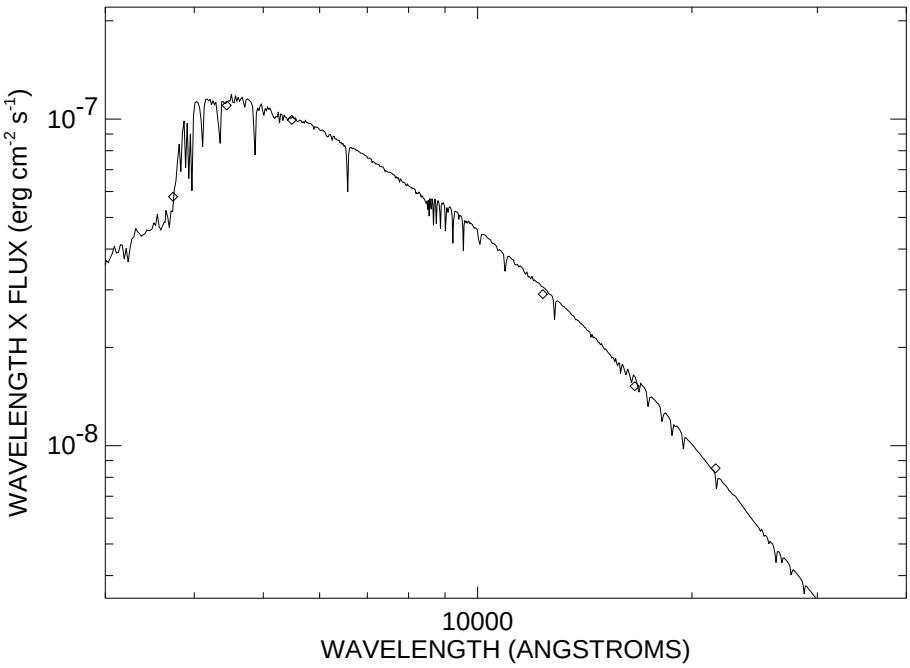

FIGURE B.15: SED plot for HD 50277.

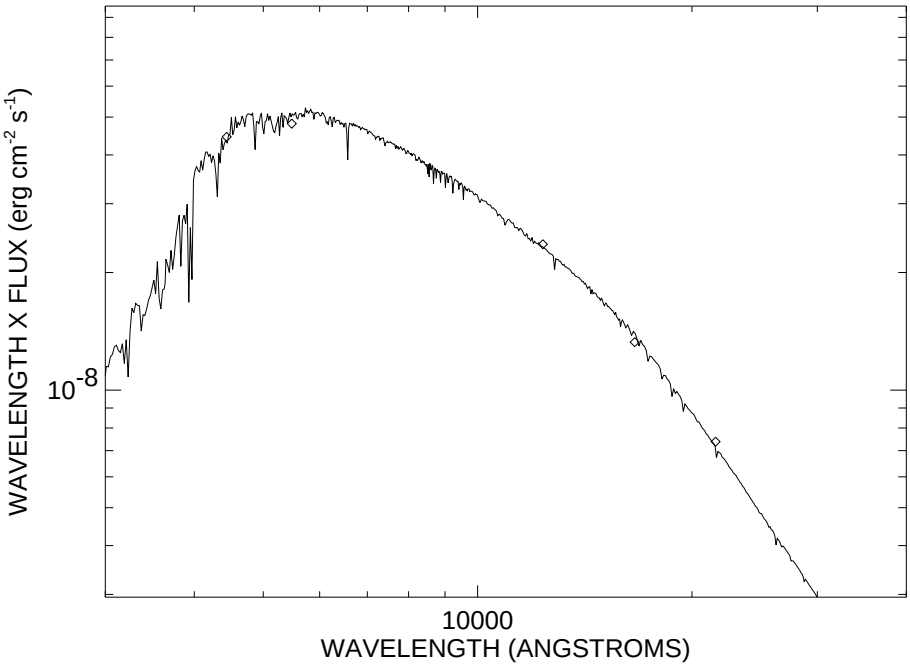

FIGURE B.16: SED plot for HD 58551.

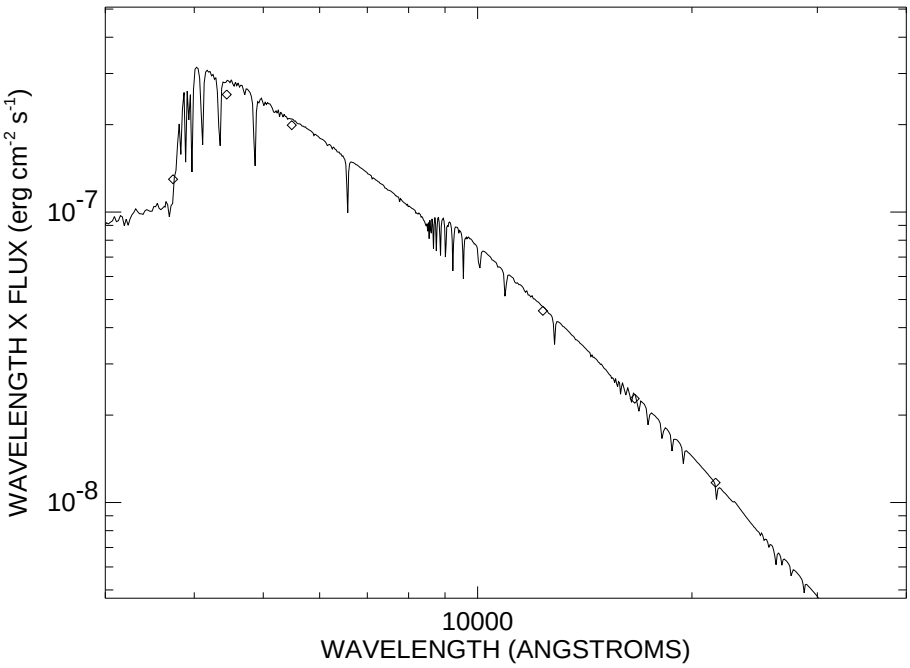

FIGURE B.17: SED plot for HD 59037.

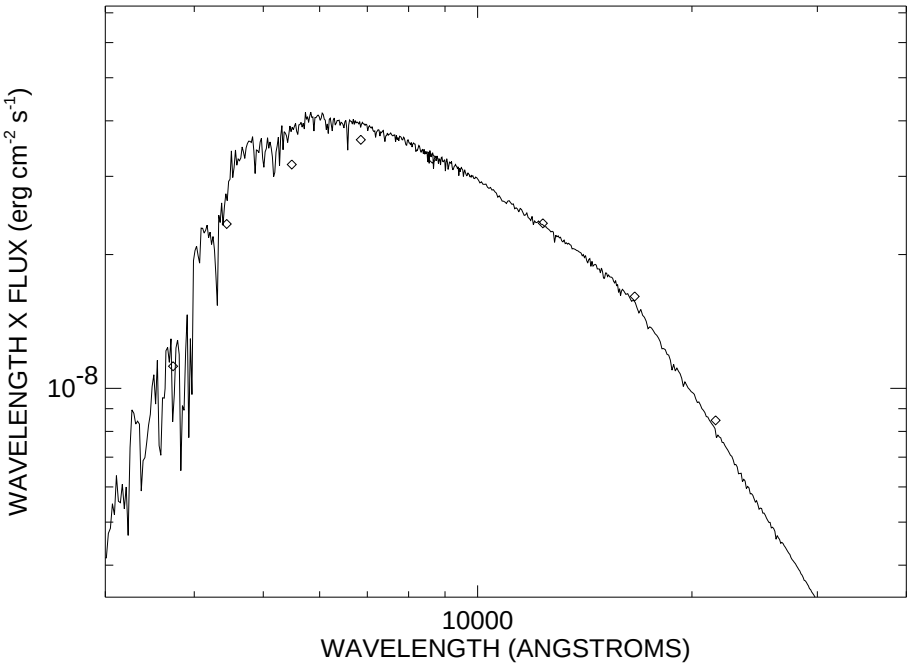

FIGURE B.18: SED plot for HD 65583.

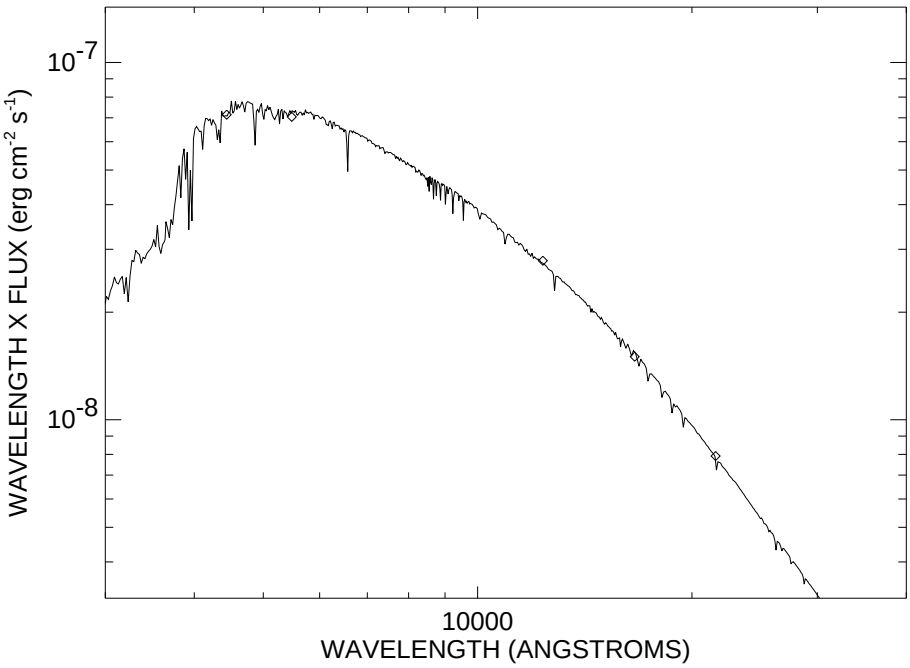

FIGURE B.19: SED plot for HD 83951.

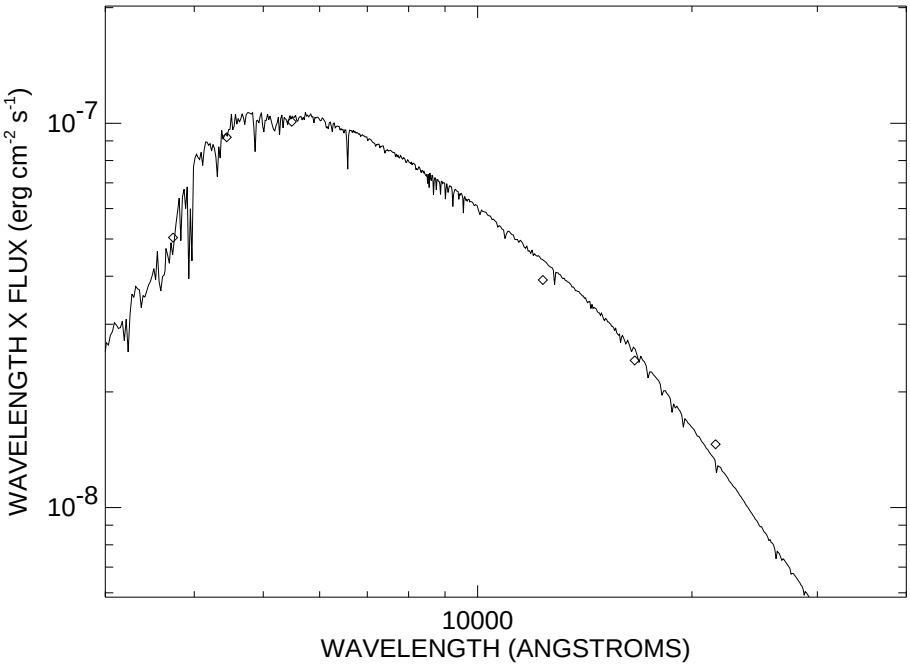

FIGURE B.20: SED plot for HD 87141.

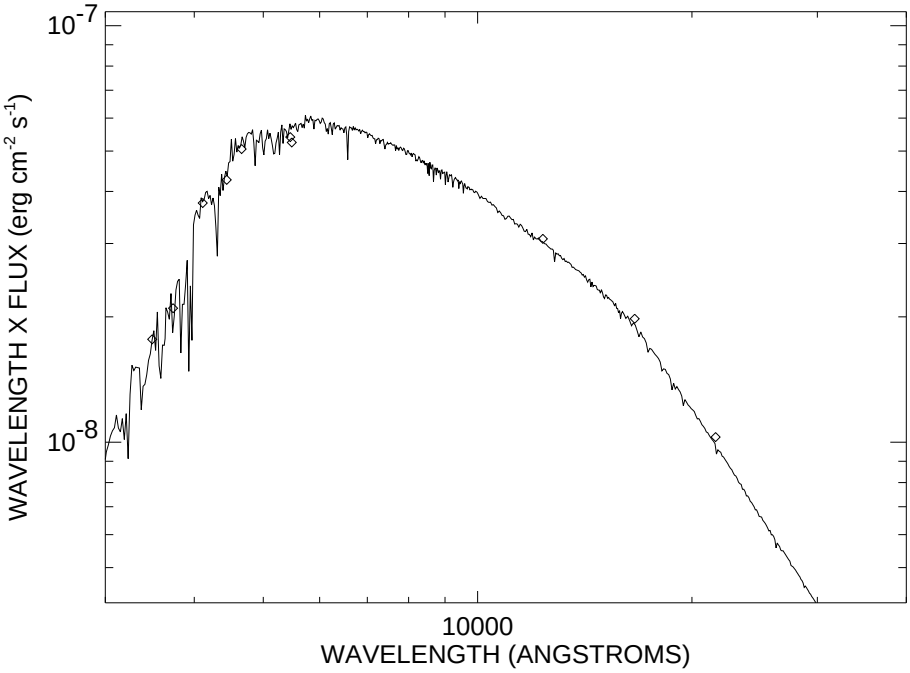

FIGURE B.21: SED plot for HD 88986.

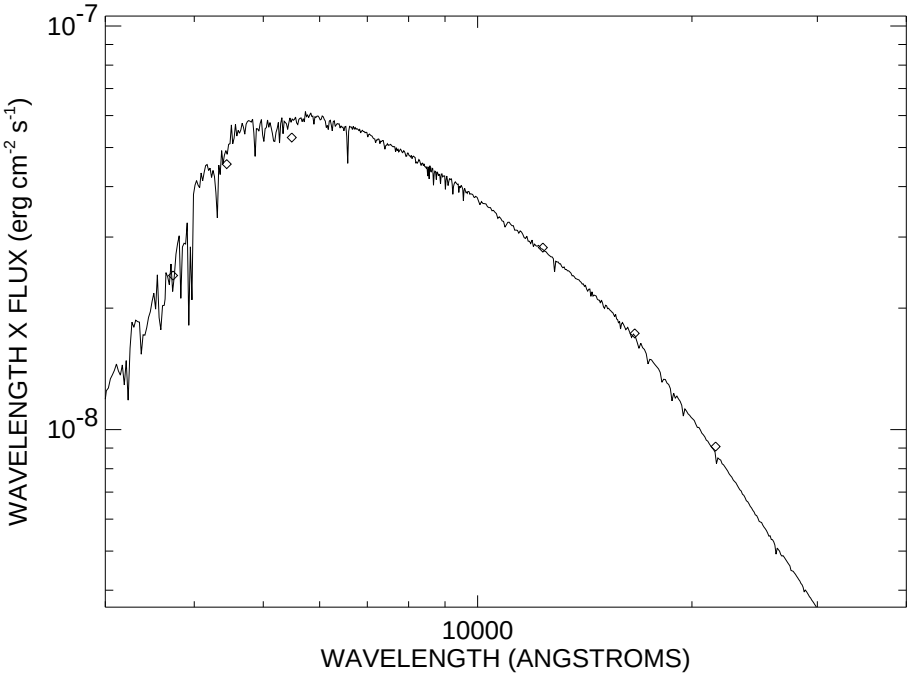

FIGURE B.22: SED plot for HD 89389.

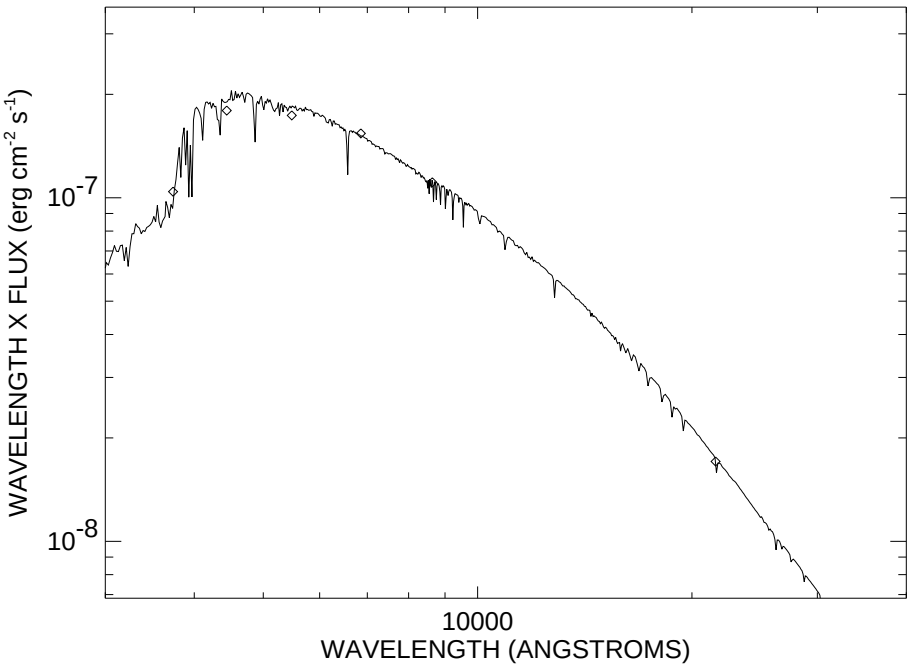

FIGURE B.23: SED plot for HD 91480.

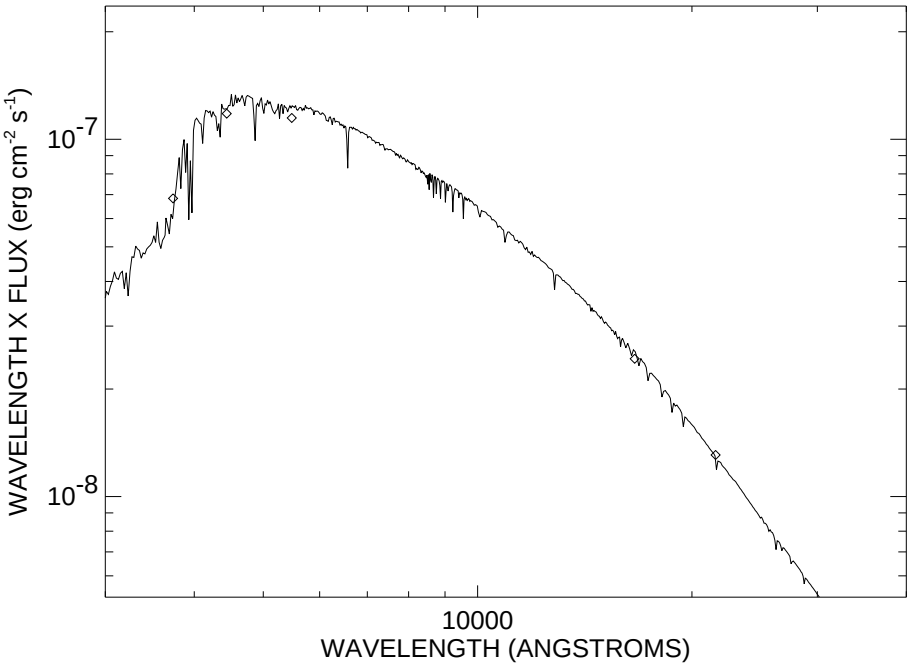

FIGURE B.24: SED plot for HD 99285.

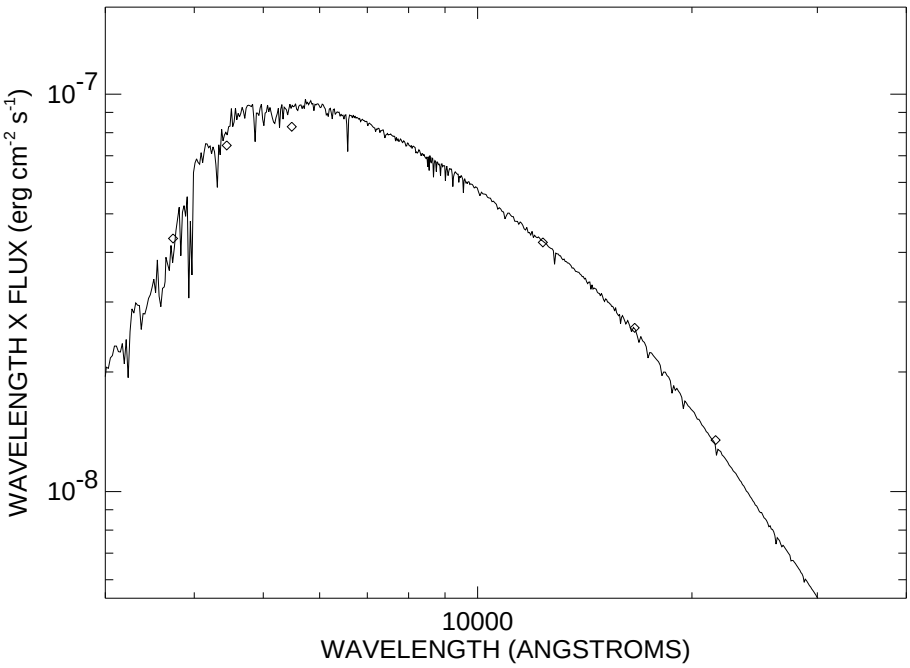

FIGURE B.25: SED plot for HD 99984.

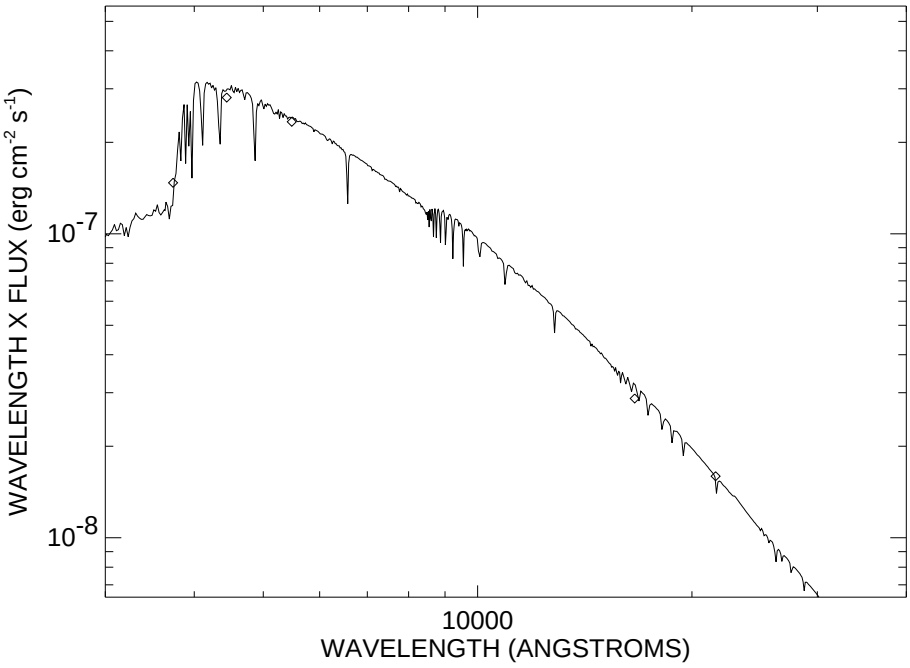

FIGURE B.26: SED plot for HD 102124.

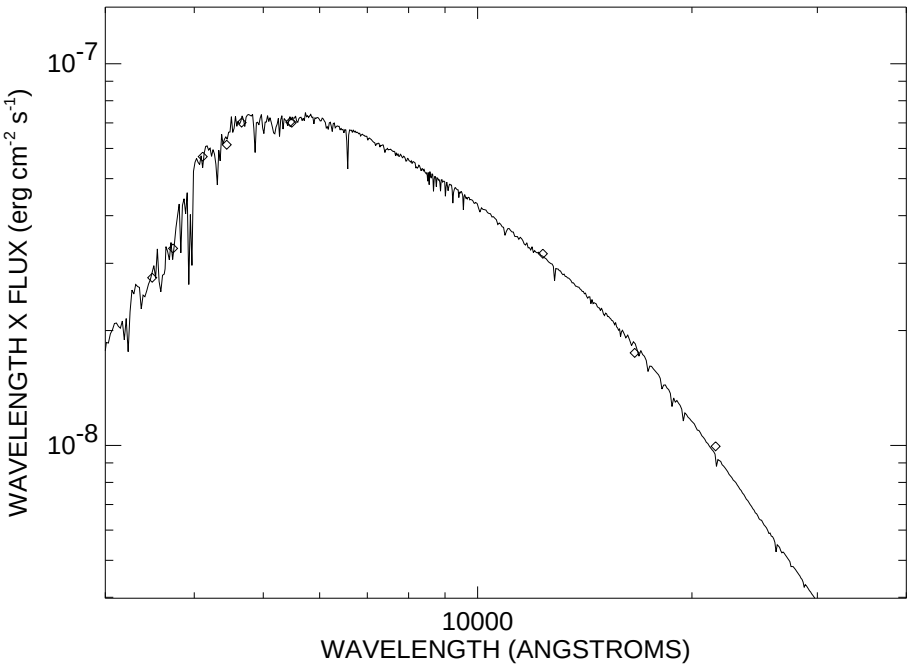

FIGURE B.27: SED plot for HD 102634.

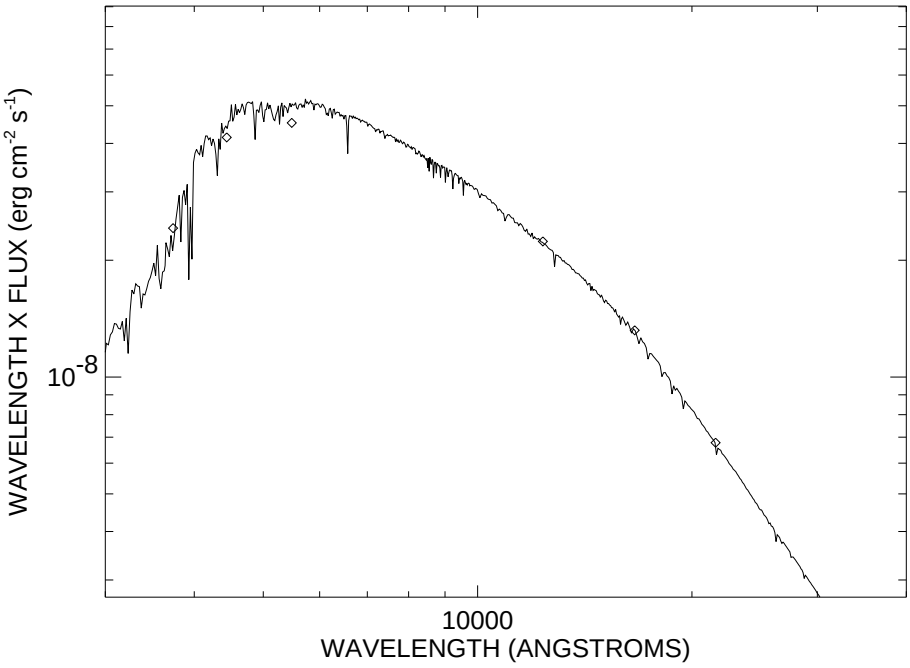

FIGURE B.28: SED plot for HD 103799.

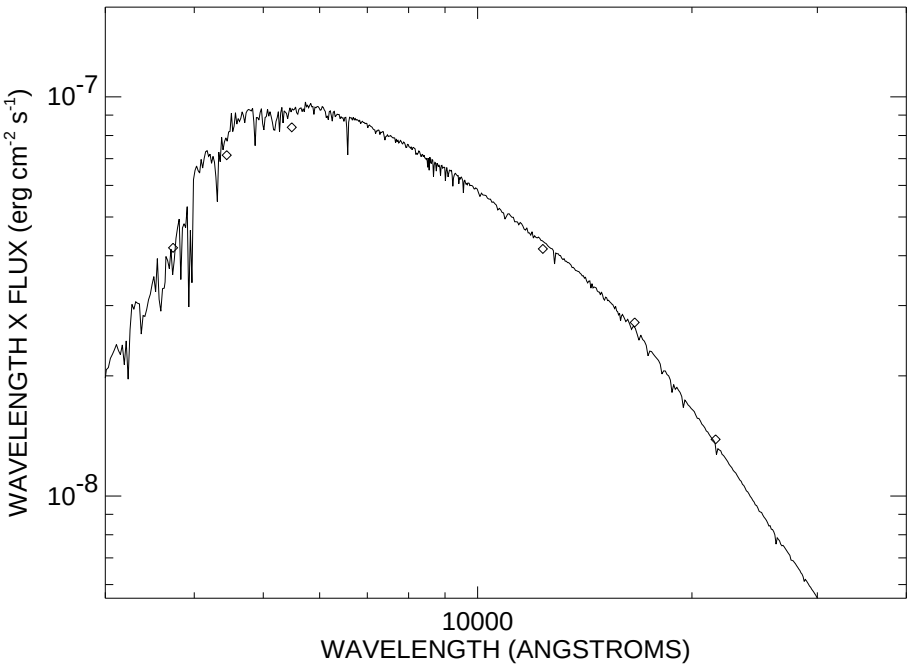

FIGURE B.29: SED plot for HD 110897.

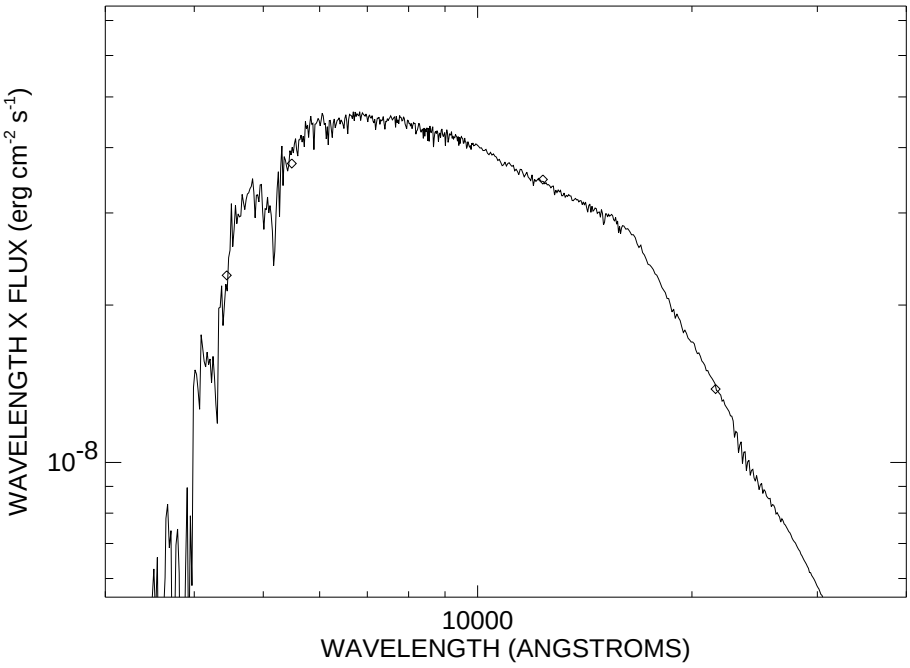

FIGURE B.30: SED plot for HD 114093.

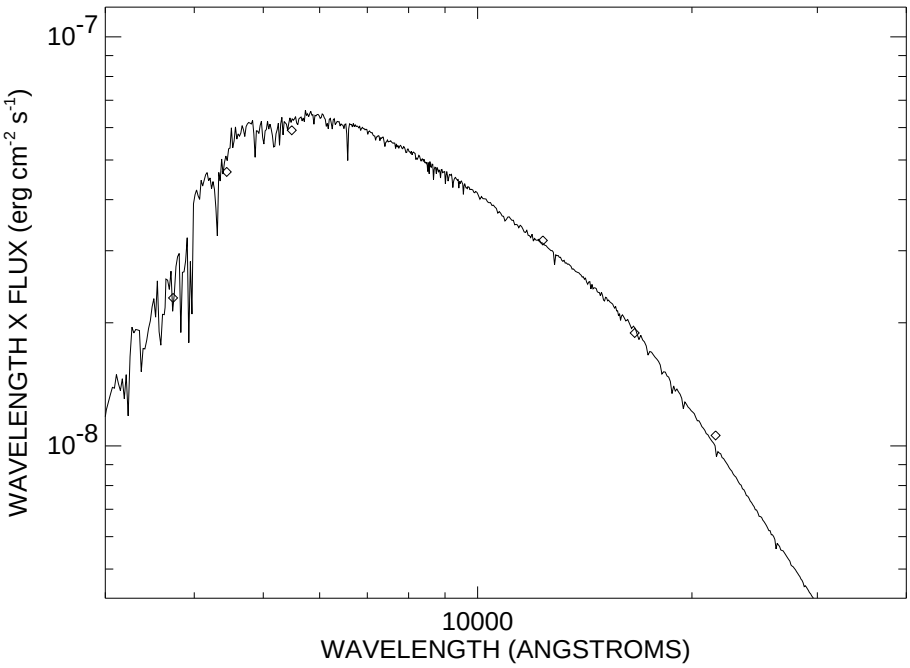

FIGURE B.31: SED plot for HD 120066.

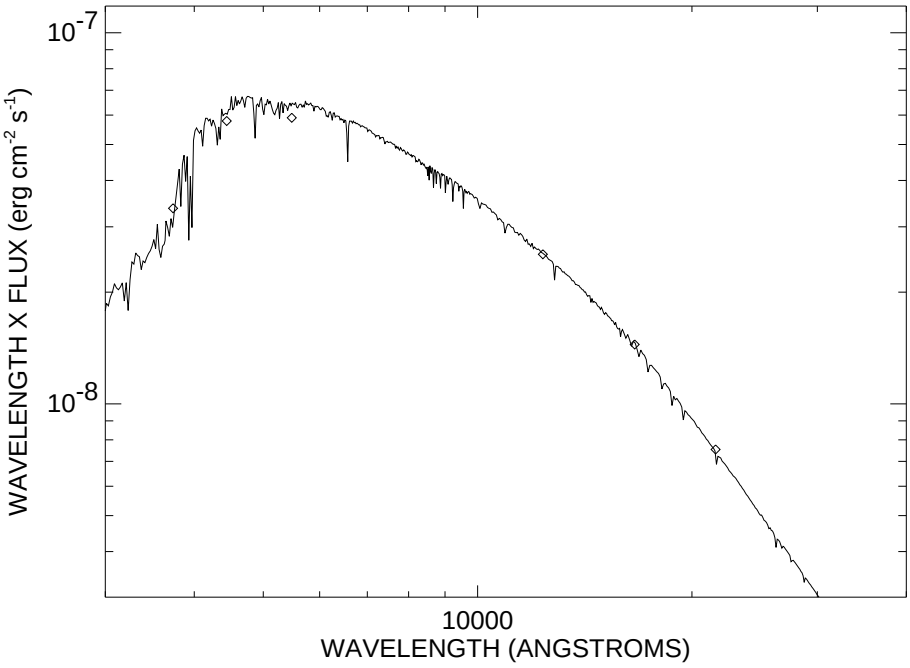

FIGURE B.32: SED plot for HD 128093.

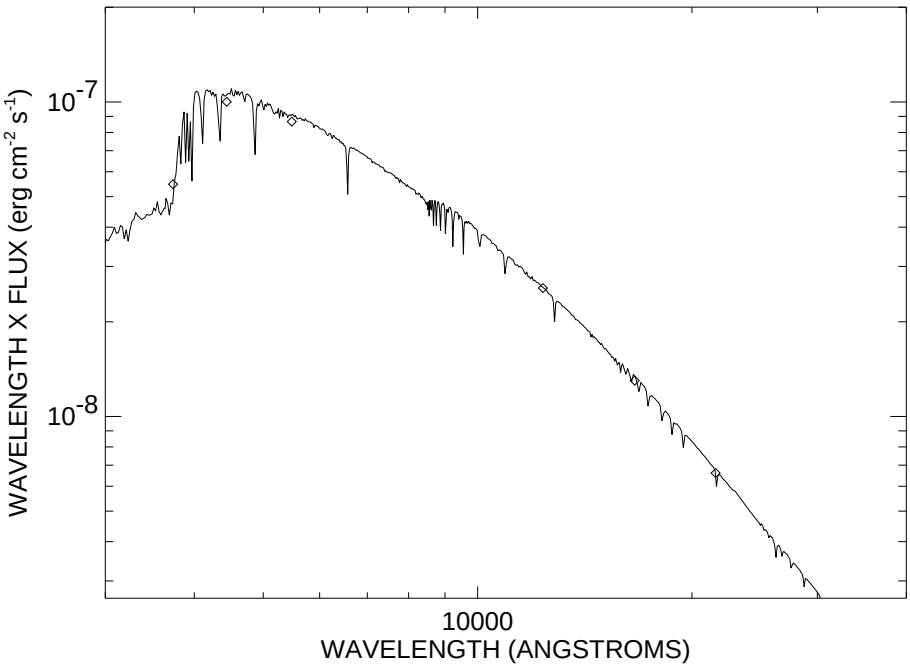

FIGURE B.33: SED plot for HD 129153.

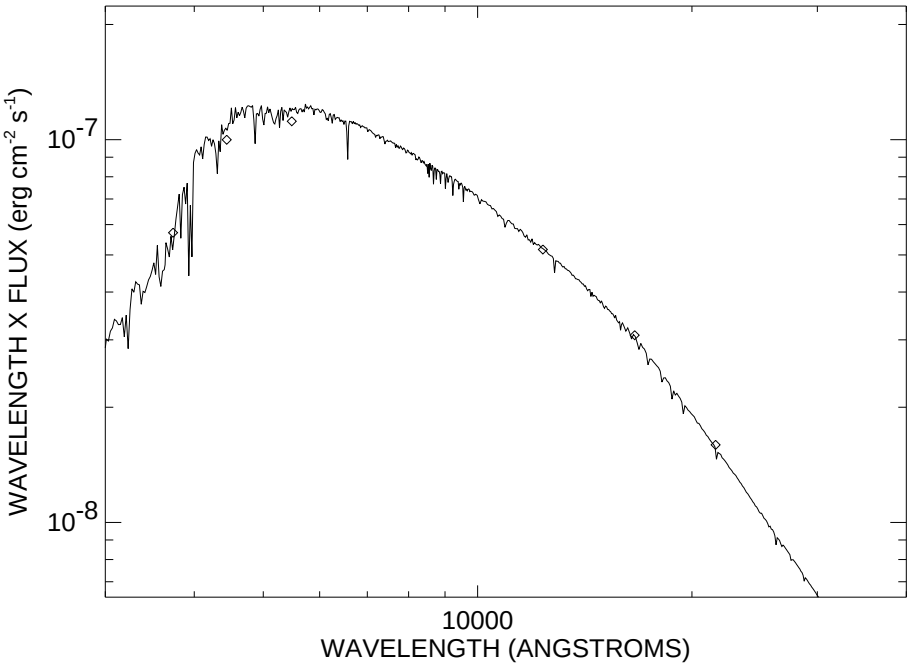

FIGURE B.34: SED plot for HD 132254.

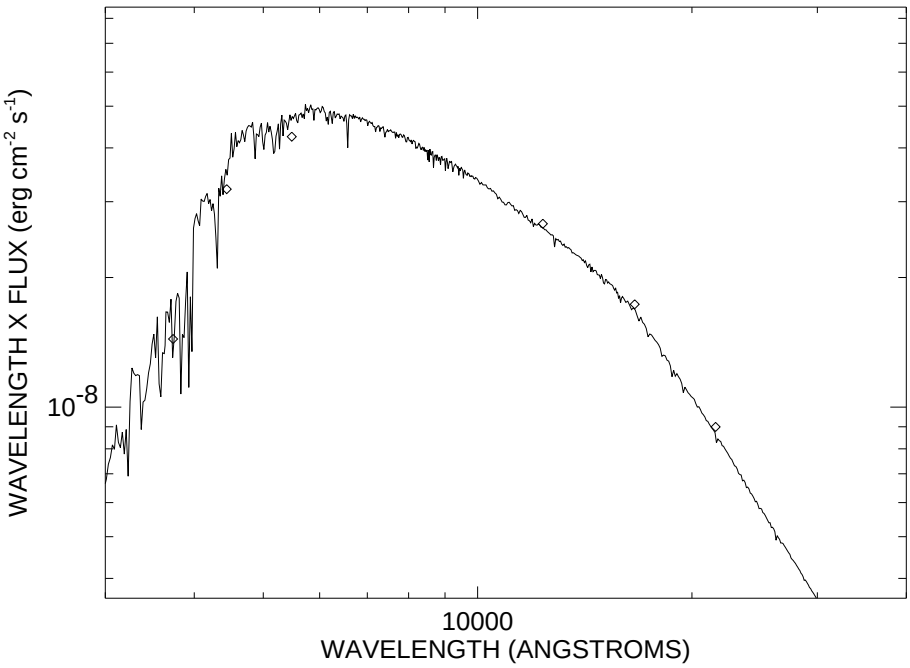

FIGURE B.35: SED plot for HD 135101.

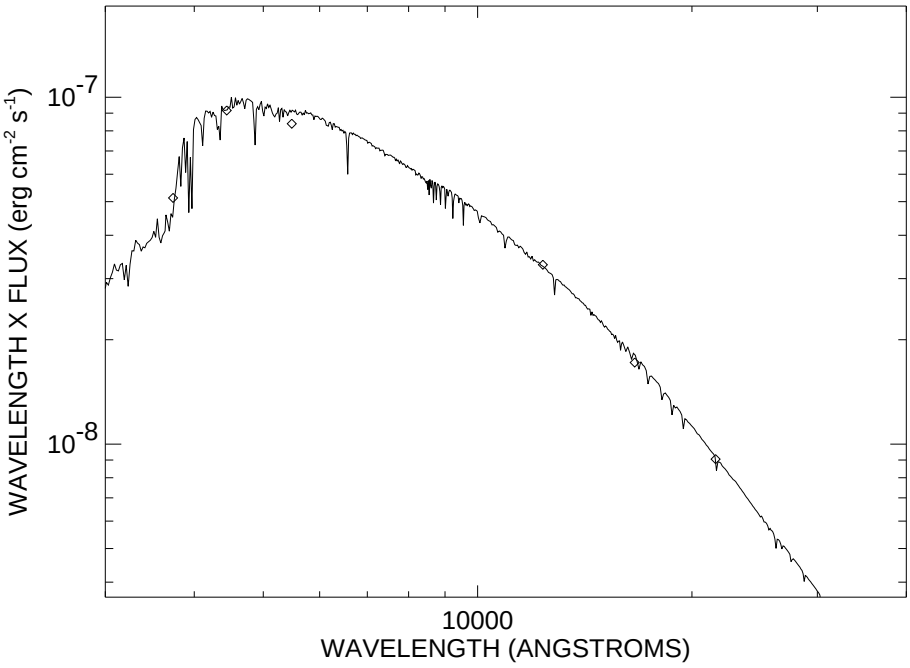

FIGURE B.36: SED plot for HD 139225.

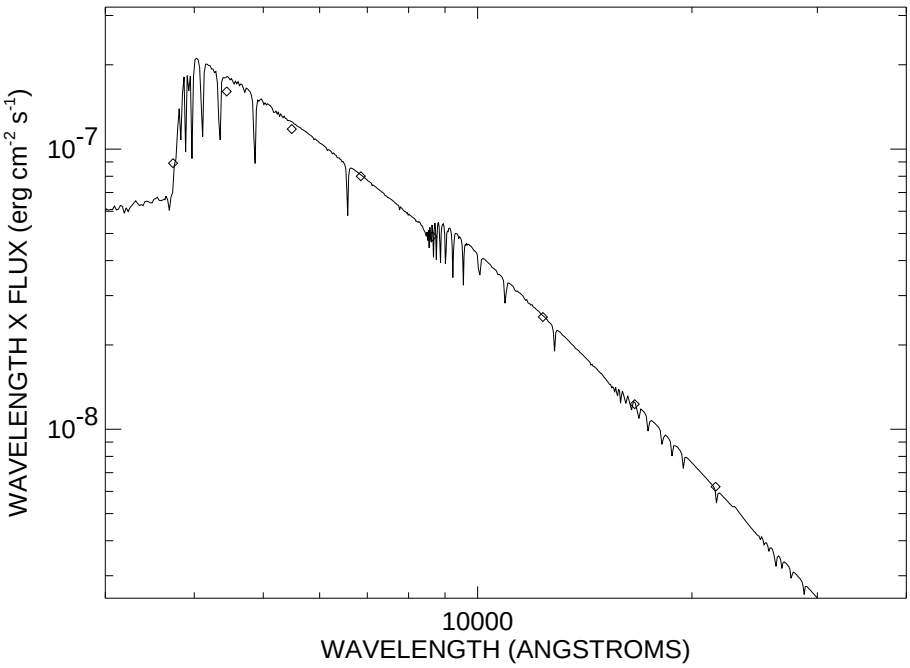

FIGURE B.37: SED plot for HD 140775.

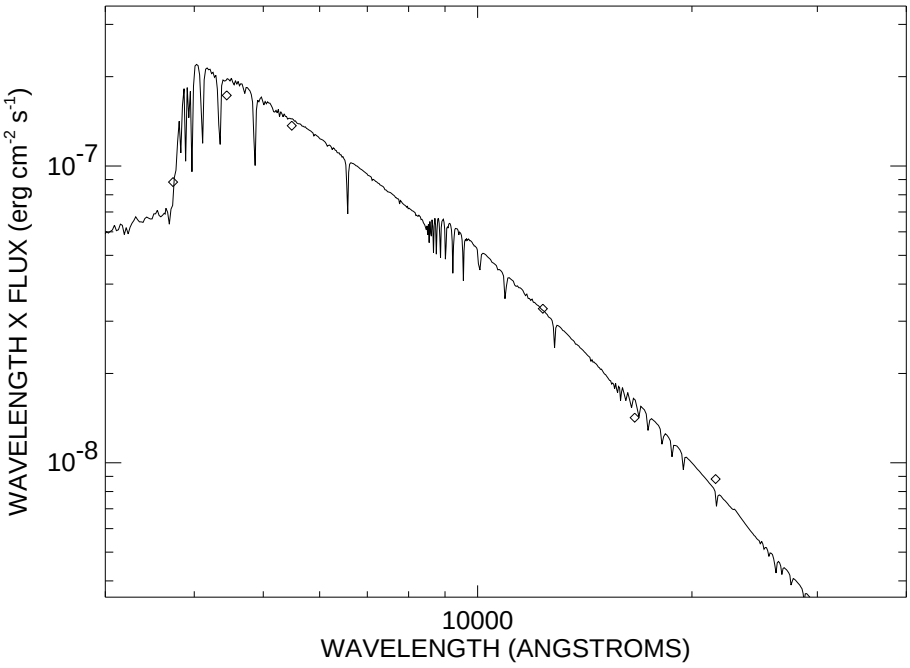

FIGURE B.38: SED plot for HD 145607.

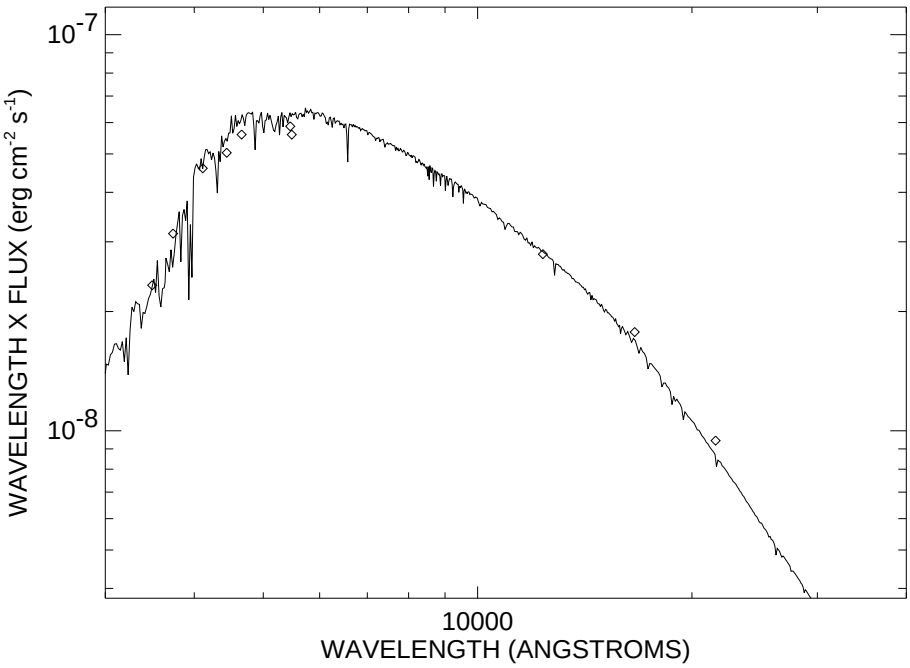

FIGURE B.39: SED plot for HD 150177.

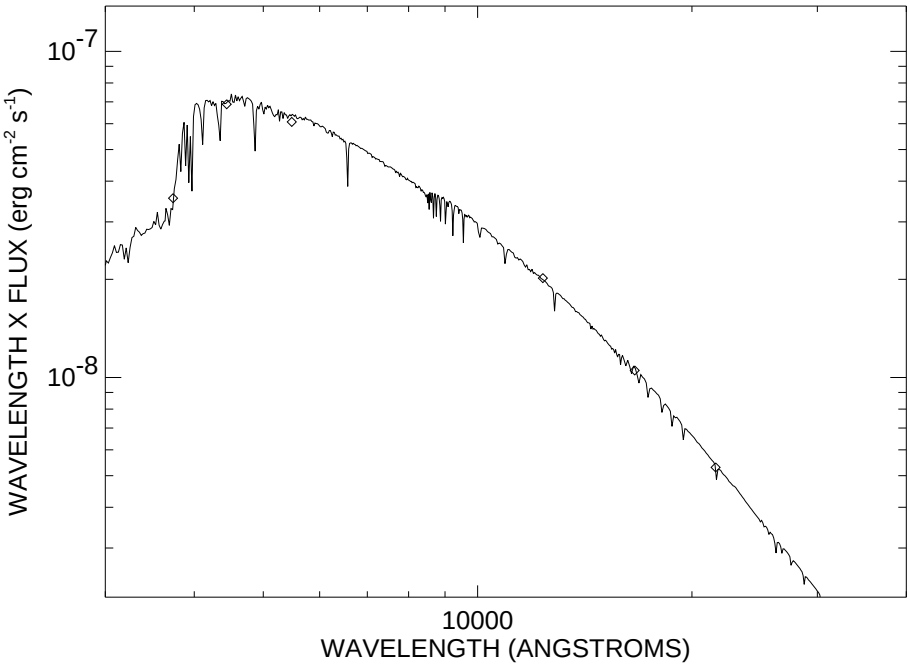

FIGURE B.40: SED plot for HD 154099.

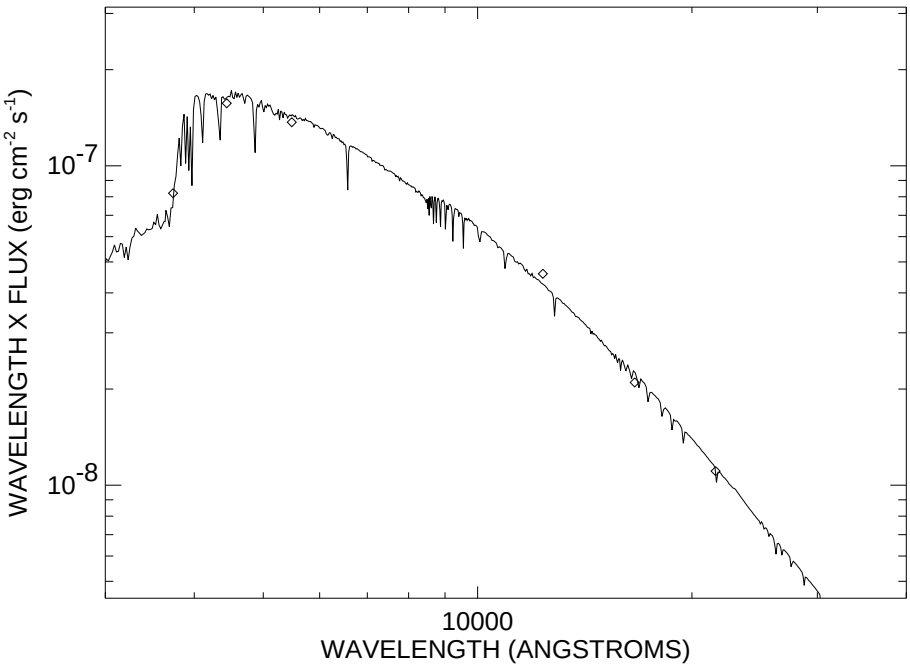

FIGURE B.41: SED plot for HD 158352.

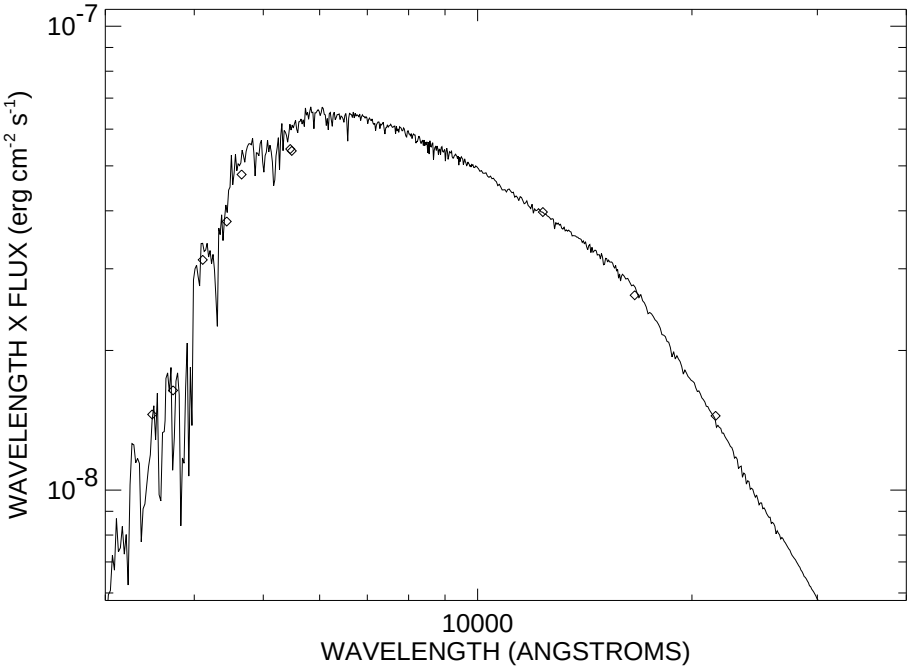

FIGURE B.42: SED plot for HD 158633.

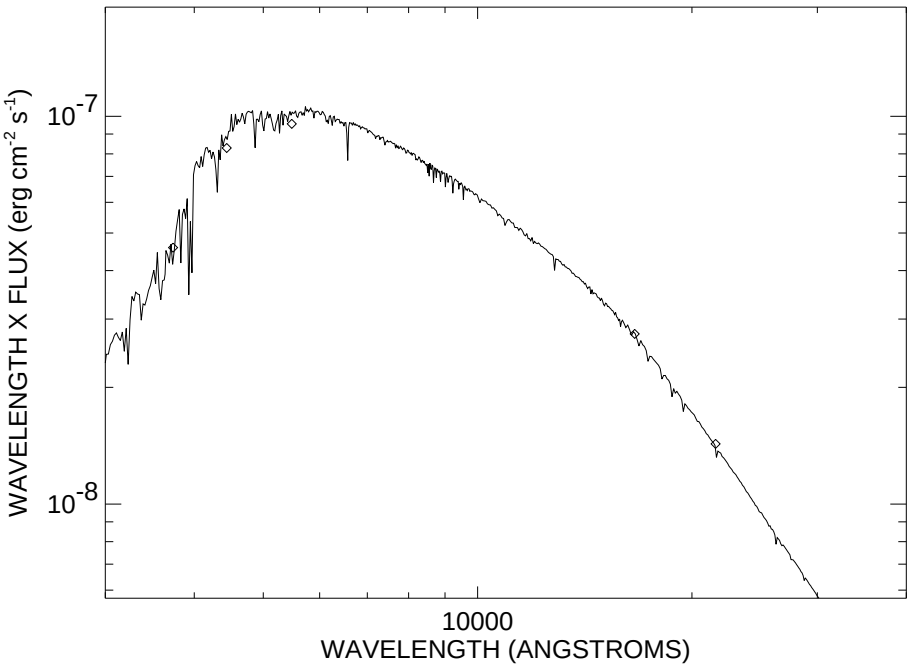

FIGURE B.43: SED plot for HD 162004.

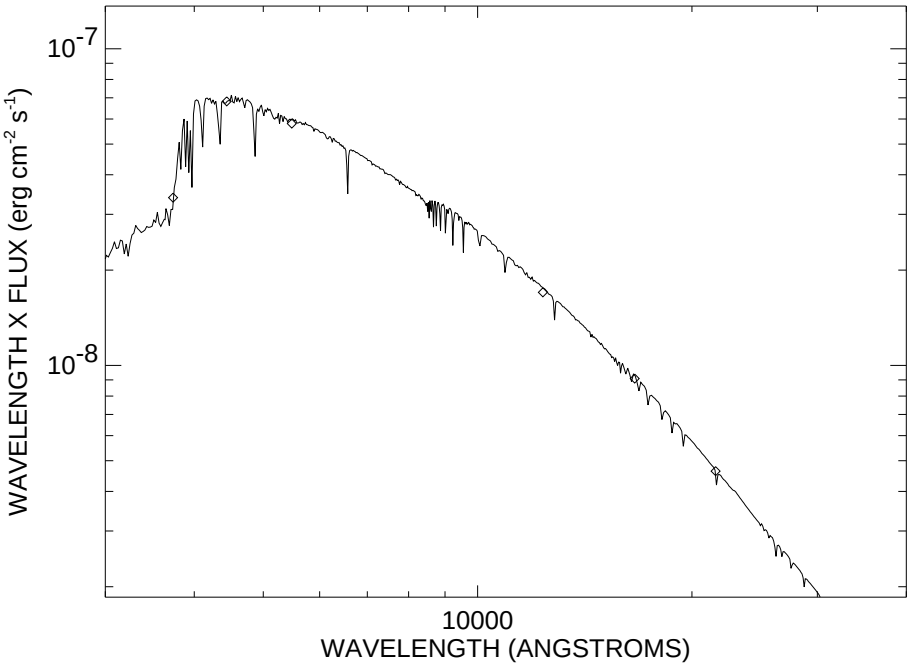

FIGURE B.44: SED plot for HD 167564.

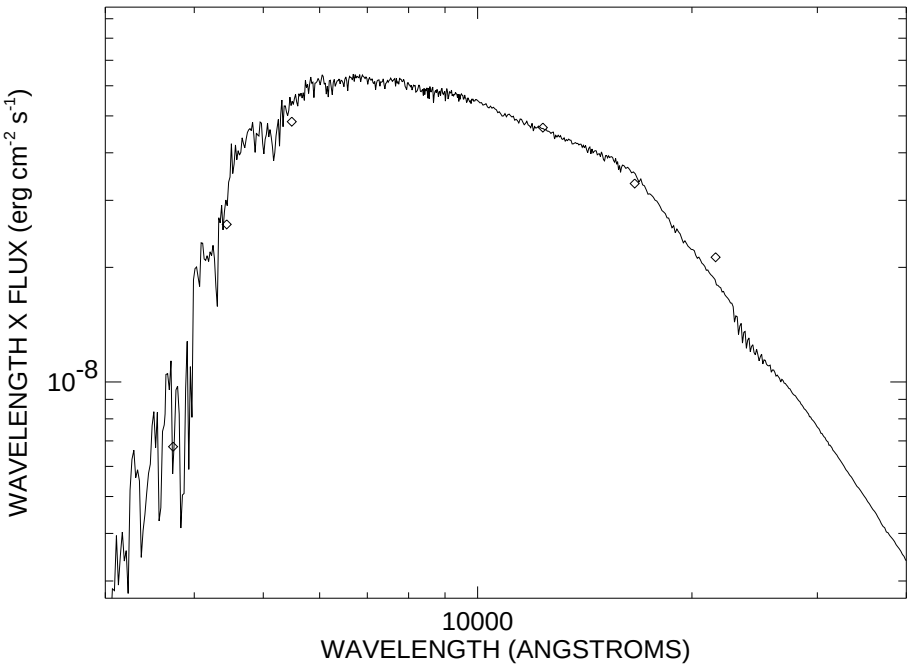

FIGURE B.45: SED plot for HD 174897.

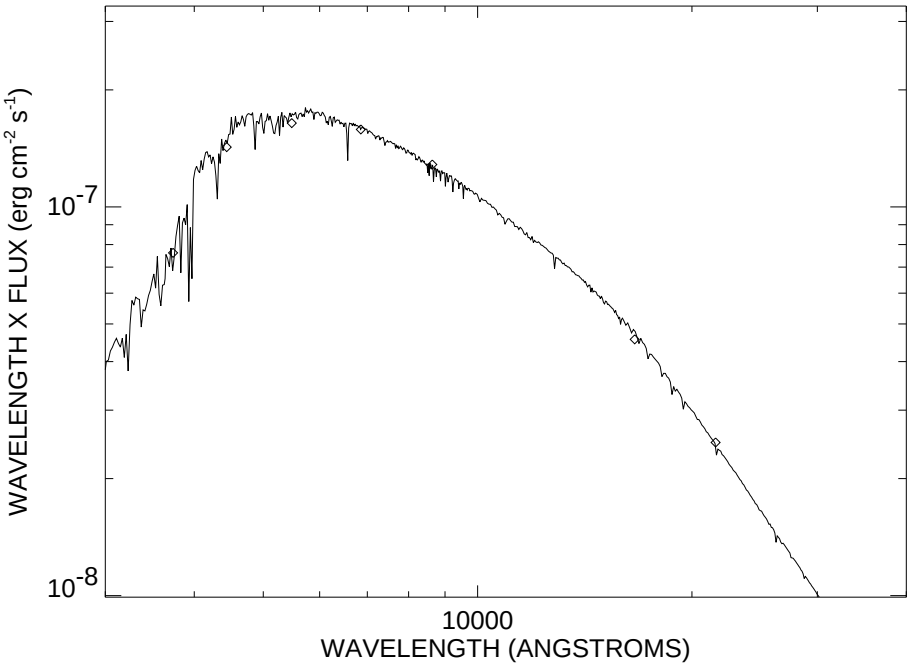

FIGURE B.46: SED plot for HD 176303.

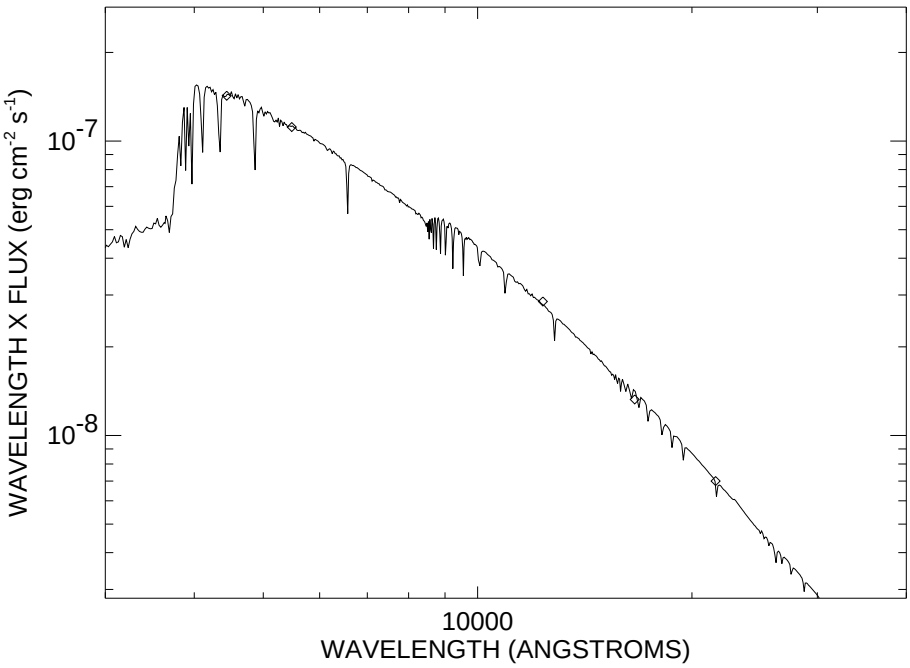

FIGURE B.47: SED plot for HD 180317.

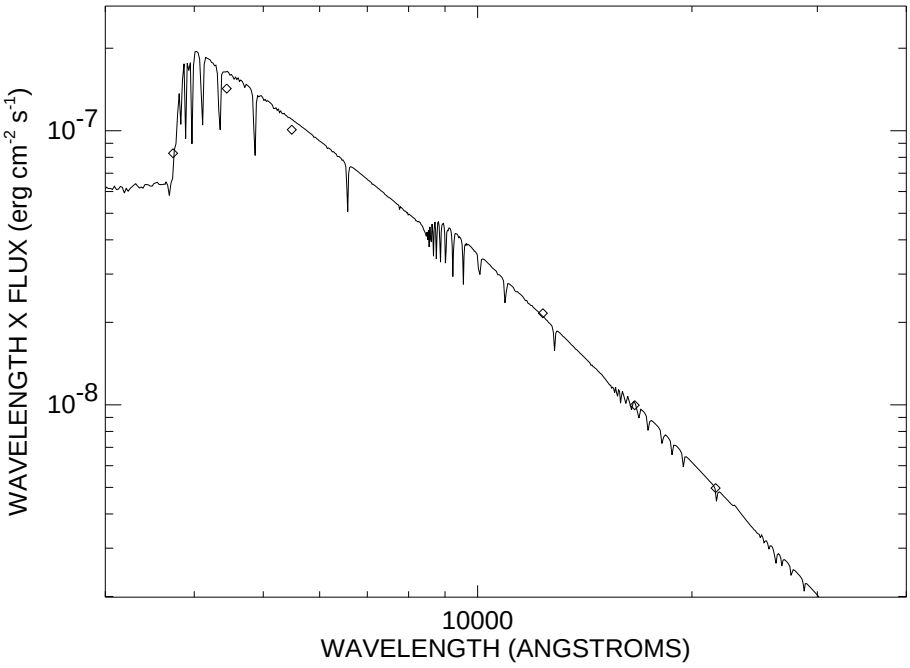

FIGURE B.48: SED plot for HD 183534.

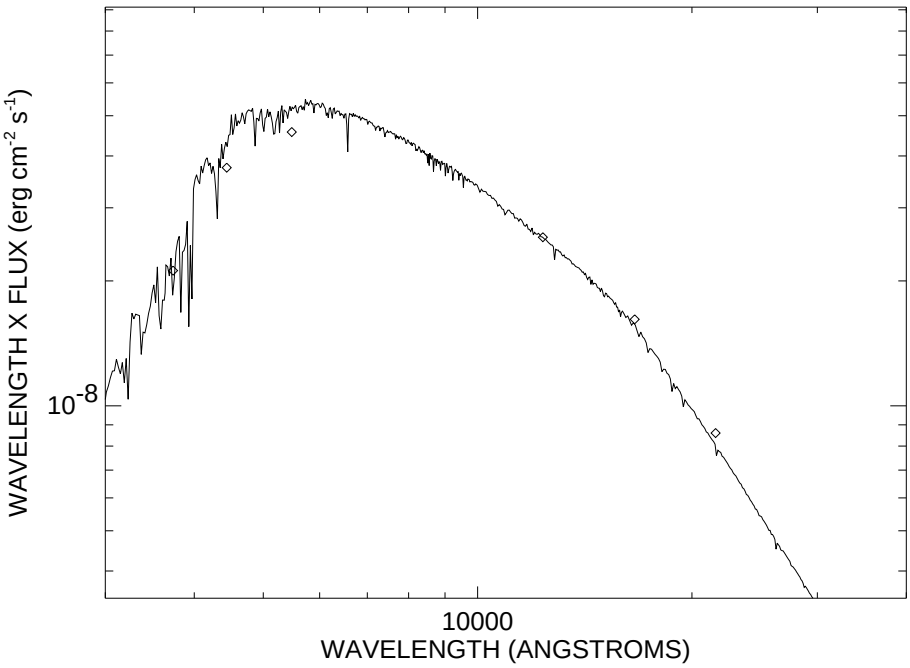

FIGURE B.49: SED plot for HD 184499.

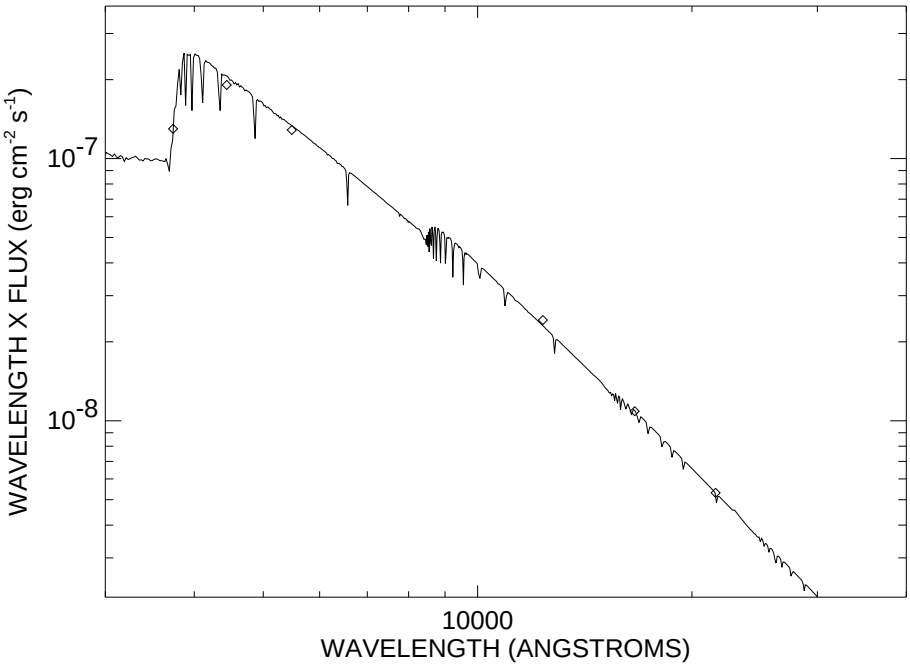

FIGURE B.50: SED plot for HD 189395.

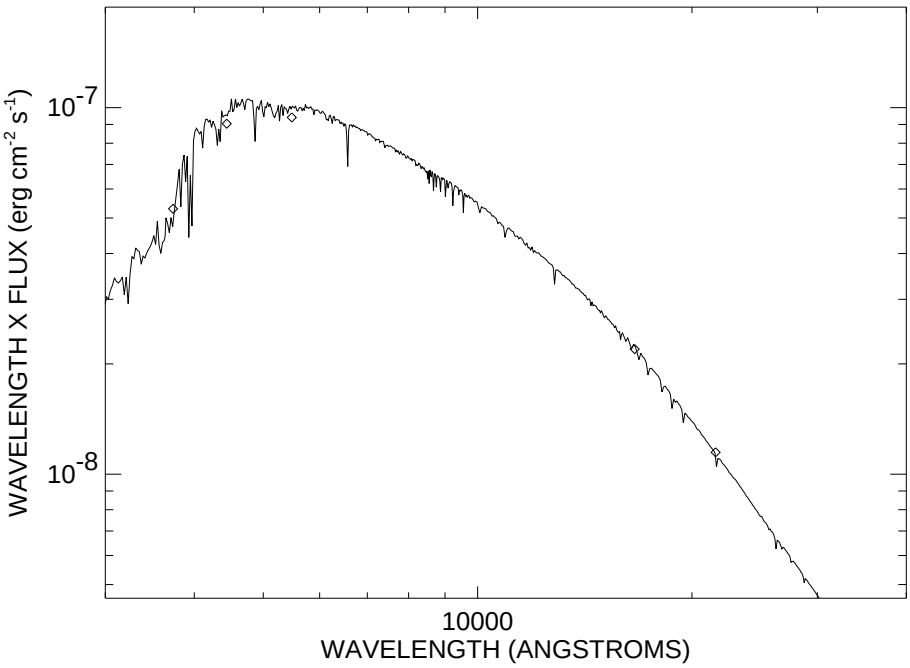

FIGURE B.51: SED plot for HD 191195.

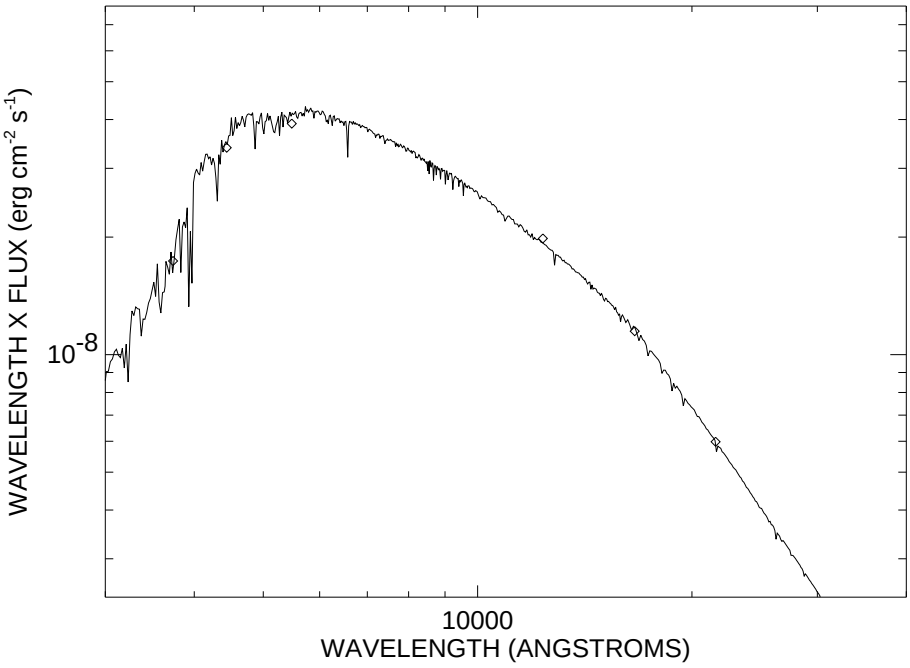

FIGURE B.52: SED plot for HD 193555.

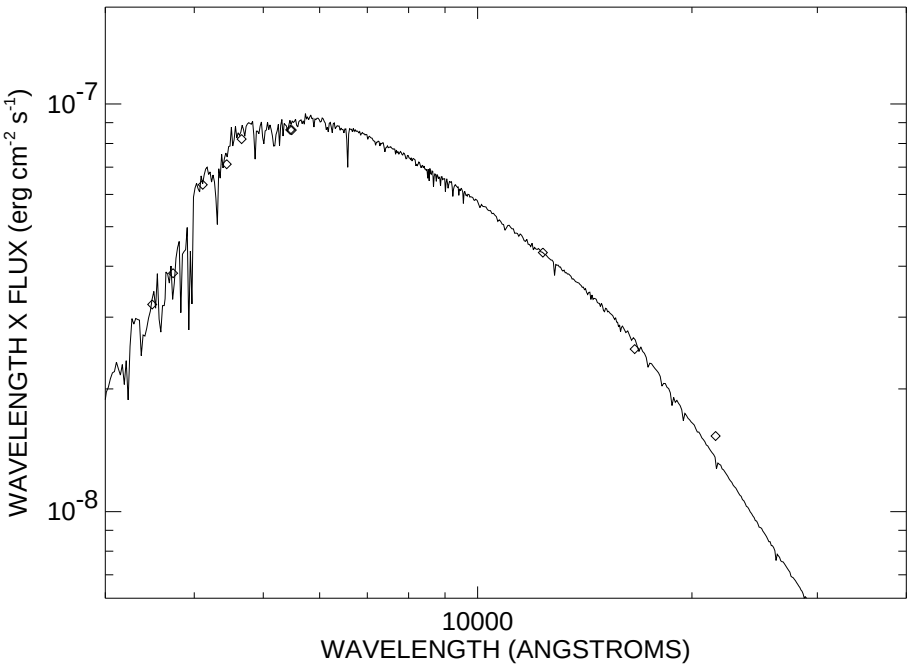

FIGURE B.53: SED plot for HD 193664.

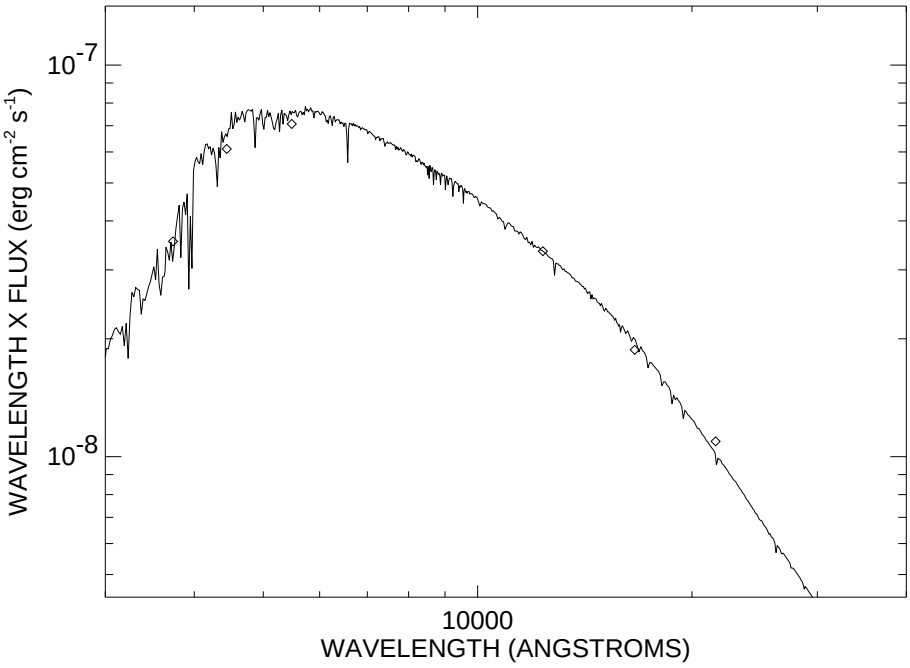

FIGURE B.54: SED plot for HD 195838.

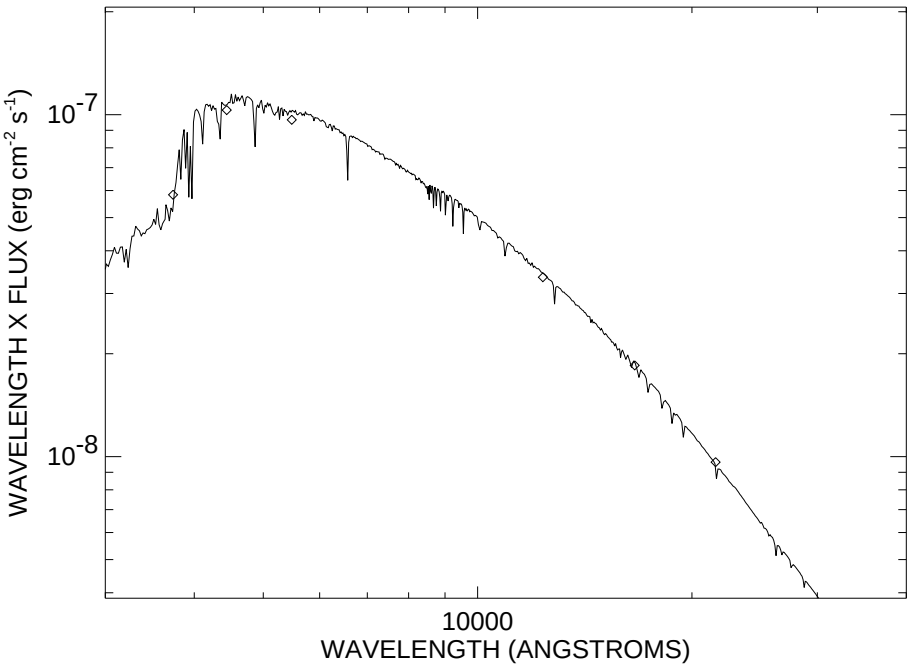

FIGURE B.55: SED plot for HD 204485.

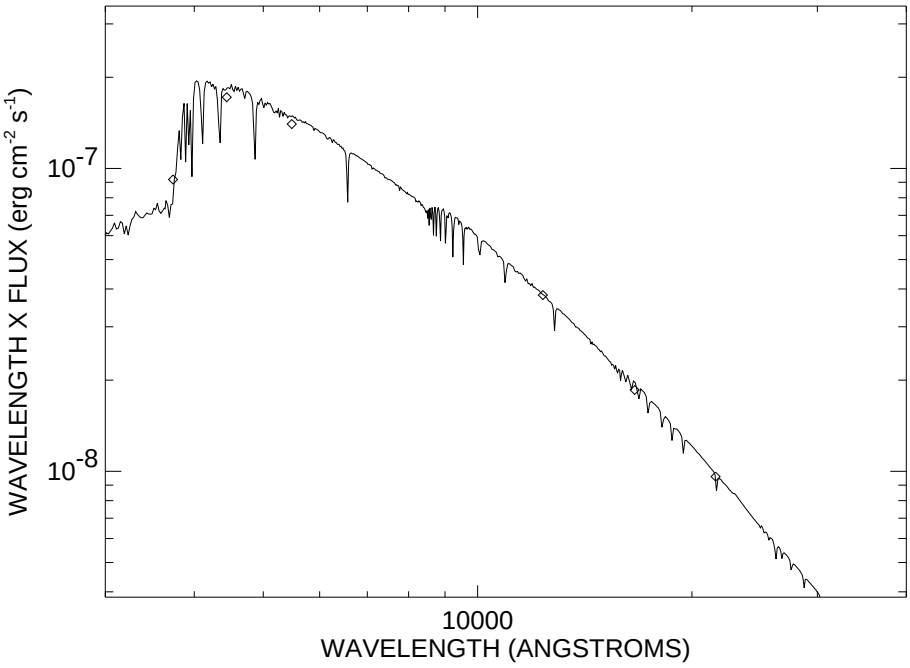

FIGURE B.56: SED plot for HD 210715.

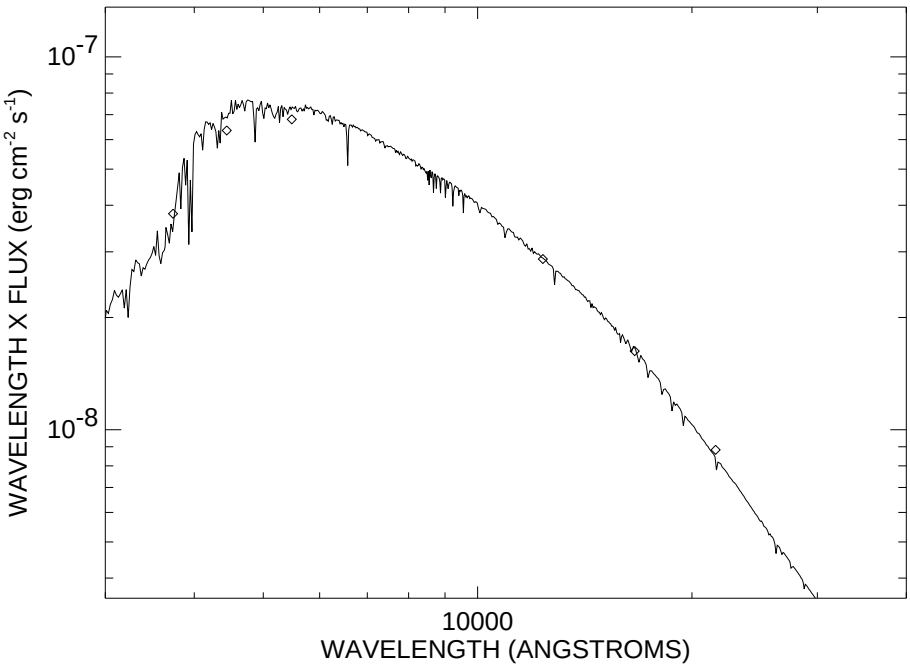

FIGURE B.57: SED plot for HD 211976.

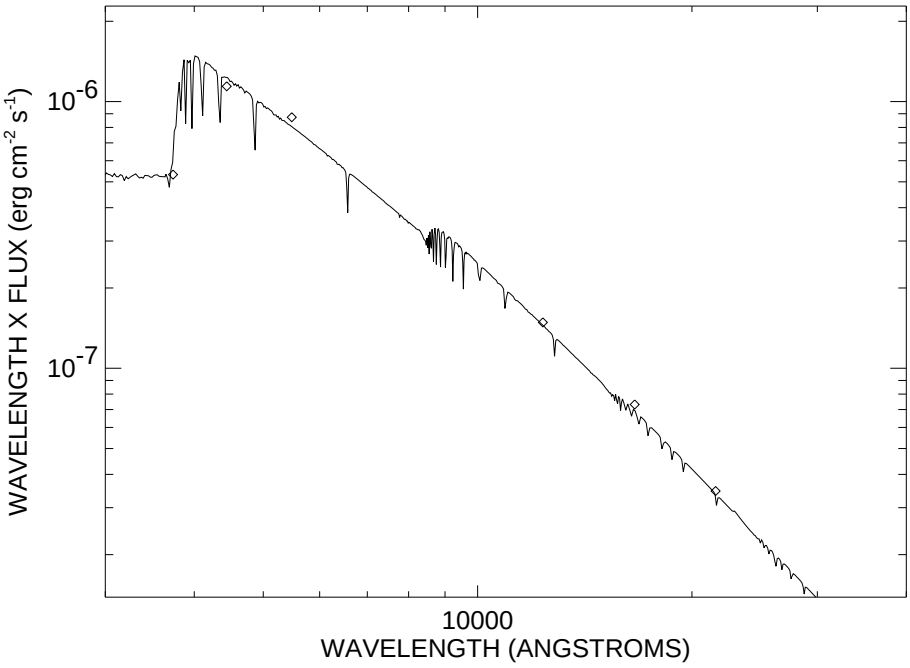

FIGURE B.58: SED plot for HD 214923.

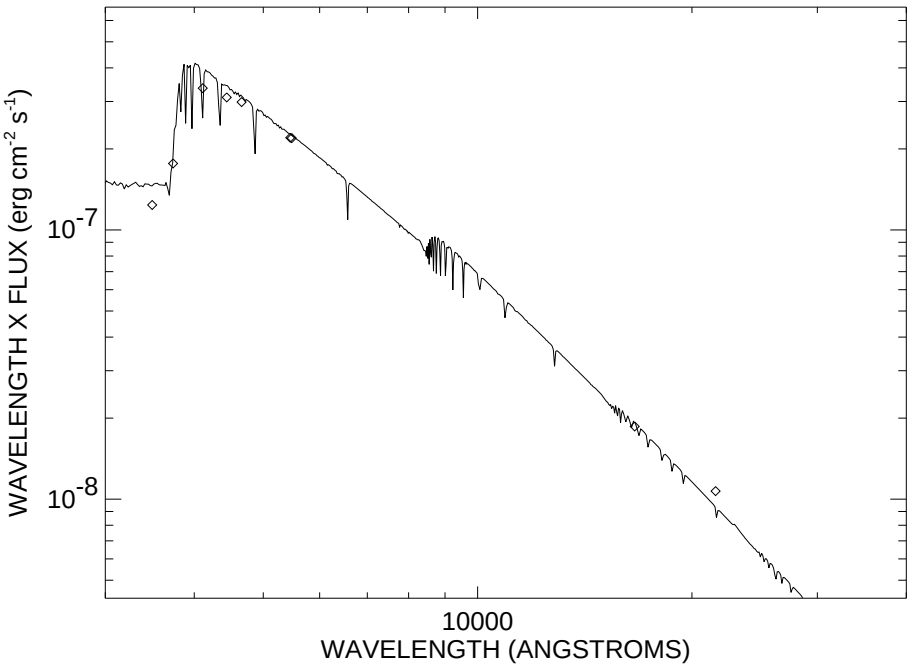

FIGURE B.59: SED plot for HD 216735.

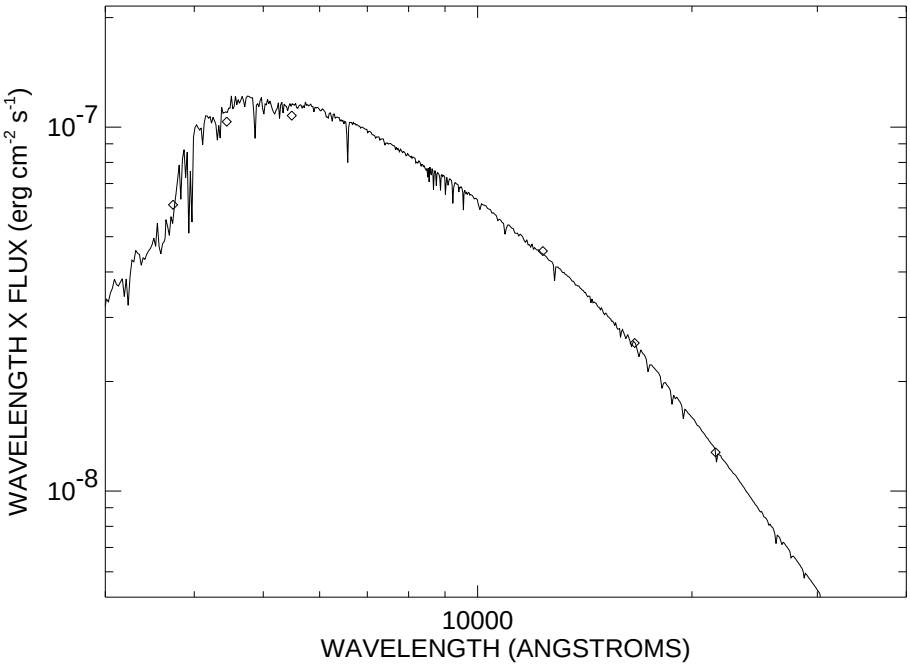

FIGURE B.60: SED plot for HD 218470.

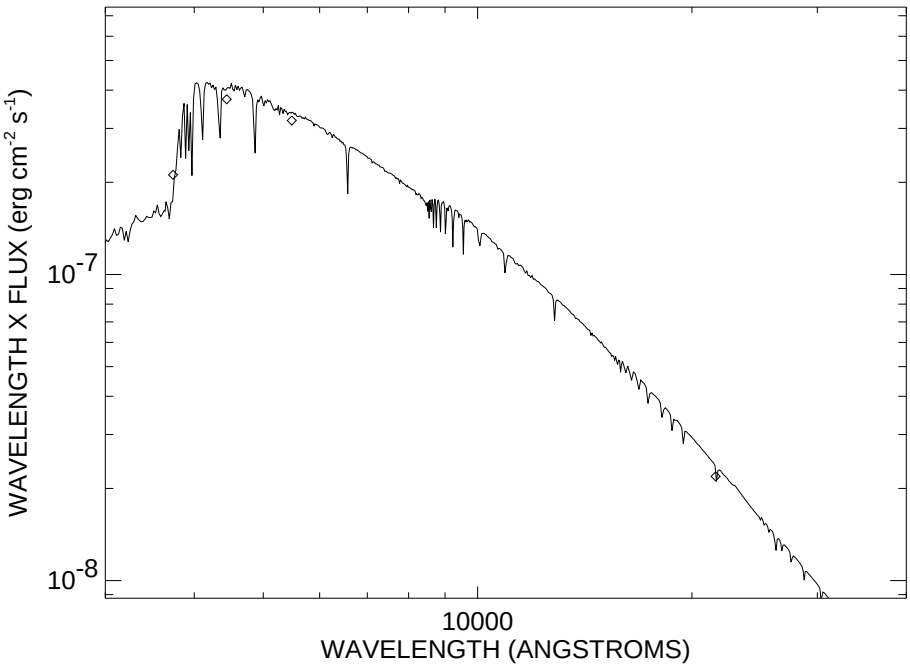

FIGURE B.61: SED plot for HD 222603.

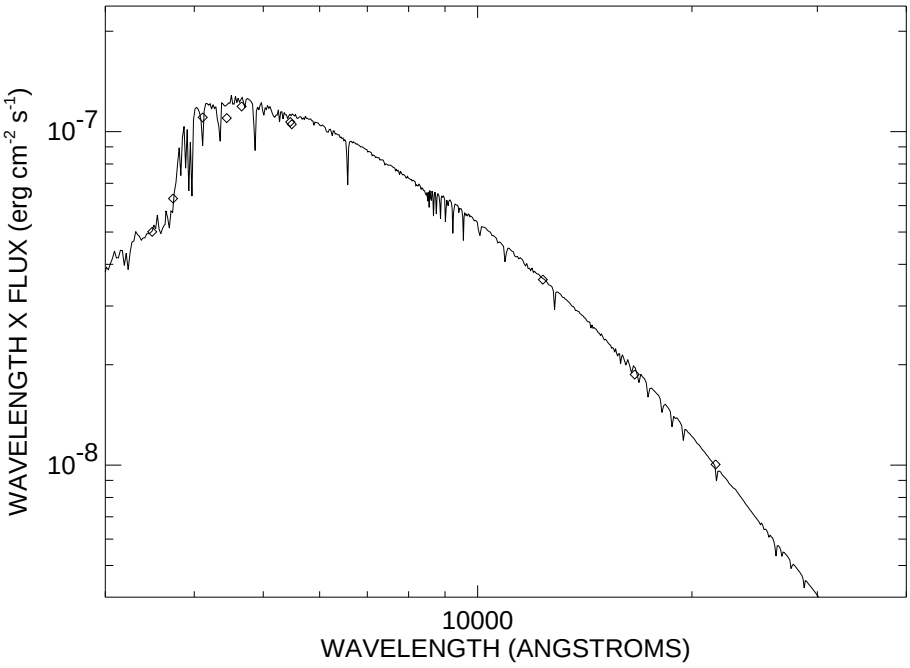

FIGURE B.62: SED plot for HD 225003.

– C –

Appendix C

C.1 HD 4614

TABLE C.1: HD 4614 Visibilities

MJD	B (m)	ψ (°)	V	σV
54280.969	270.8	−23.2	0.212	0.016
54280.990	280.7	−16.0	0.162	0.009
54281.943	259.3	−31.6	0.239	0.014
54281.954	264.5	−27.7	0.229	0.023
54281.964	269.5	−24.1	0.186	0.019
54281.974	274.7	−20.4	0.168	0.014
54281.988	281.1	−15.8	0.147	0.012
54282.889	234.7	−52.4	0.337	0.038
54282.903	240.9	−46.4	0.288	0.033
54282.938	258.1	−32.5	0.253	0.017
54300.928	275.7	40.4	0.200	0.009
54300.940	280.7	42.9	0.176	0.010
54300.950	285.0	45.2	0.163	0.007
54301.869	244.8	28.1	0.309	0.014
54301.879	251.3	30.4	0.282	0.015
54301.891	258.3	33.0	0.264	0.015
54420.695	306.7	27.4	0.092	0.009
54420.714	309.9	22.9	0.100	0.009
54420.720	310.9	21.3	0.084	0.006
54420.732	312.3	18.6	0.078	0.008
54741.743	286.3	101.9	0.145	0.018
54741.759	292.6	96.8	0.124	0.013
54741.775	298.1	92.0	0.097	0.013
54741.826	310.3	76.5	0.087	0.014

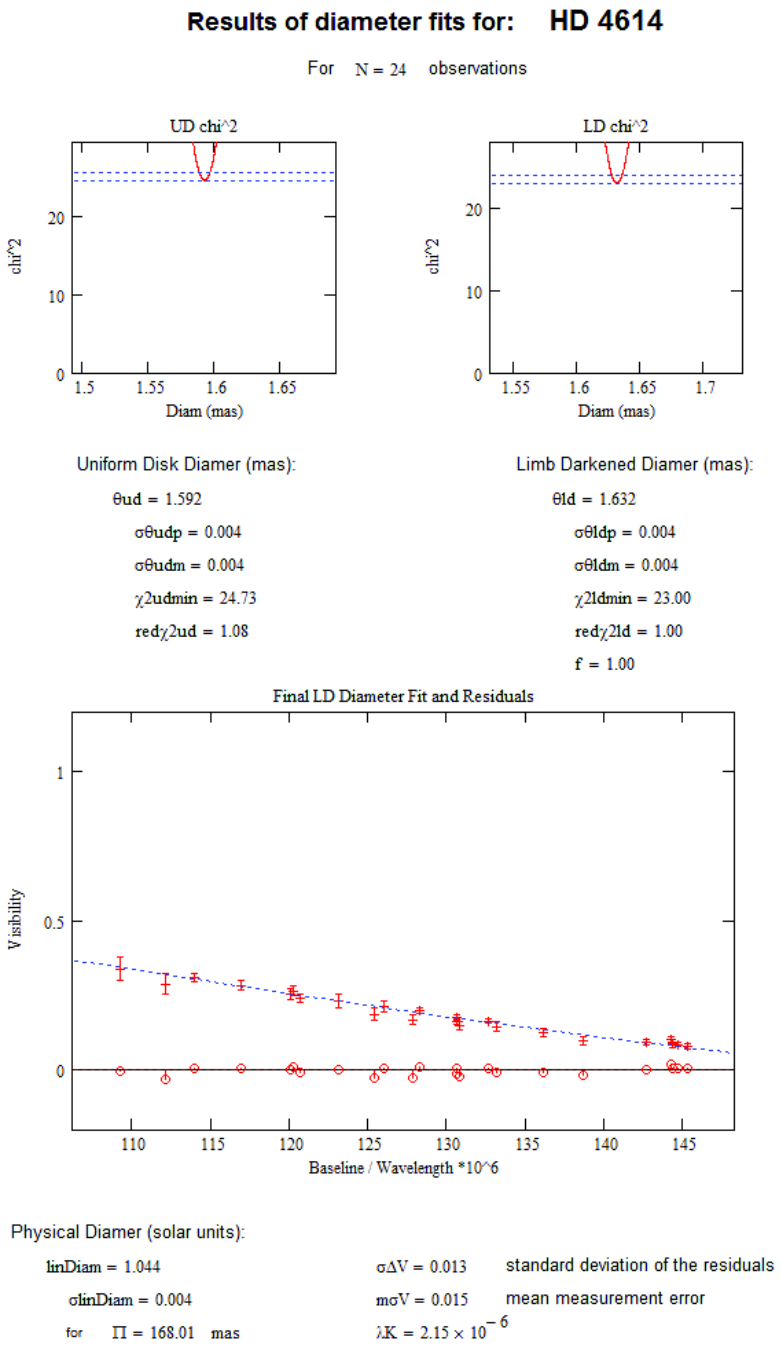

FIGURE C.1: **Diameter fit for HD 4614**

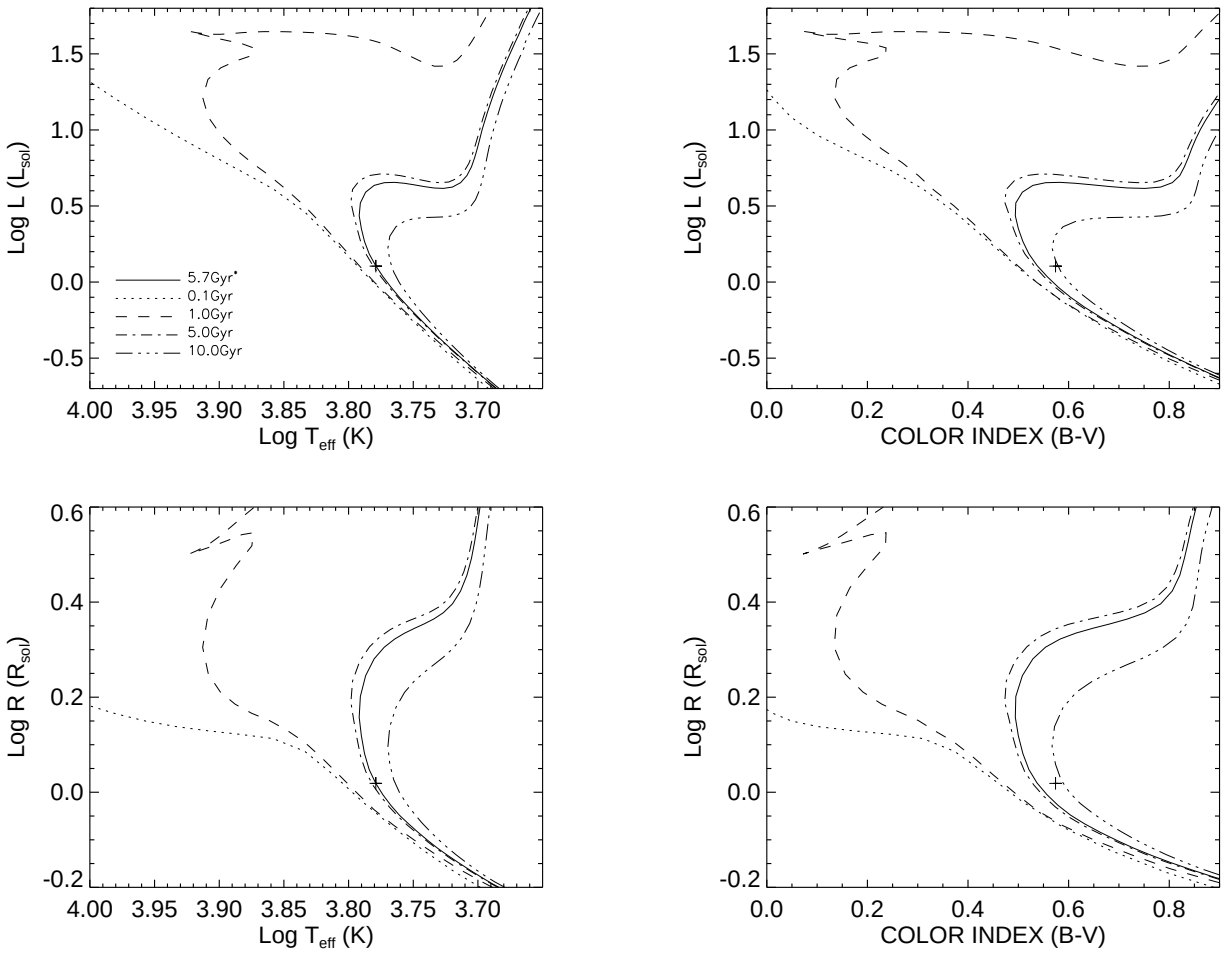

FIGURE C.2: **Y^2 Model Isochrones for HD 4614:** HD 4614 data (and 1-σ errors) plotted against Y^2 models isochrones ([α/Fe]=0.0, [Fe/H]=$-$0.3.)

C.2 HD 5015

TABLE C.2: HD 5015 Visibilities

MJD	B (m)	ψ (°)	V	σV
54383.903	312.2	47.3	0.629	0.048
54383.908	311.8	45.4	0.618	0.040
54383.915	311.3	43.3	0.594	0.108
54383.921	310.8	41.2	0.660	0.047
54383.927	310.3	39.1	0.688	0.053
54383.978	305.8	21.7	0.603	0.057
54383.984	305.4	19.5	0.662	0.039
54383.990	304.9	17.3	0.619	0.059
54383.996	304.6	15.2	0.638	0.064
54384.009	303.9	10.5	0.697	0.061
54407.614	269.1	119.5	0.585	0.121
54407.620	272.0	117.1	0.692	0.151
54407.627	274.6	114.8	0.708	0.124
54407.634	277.5	112.3	0.726	0.097
54407.668	290.5	100.9	0.587	0.080
54407.674	292.7	98.8	0.590	0.078
54407.681	295.2	96.3	0.697	0.093
54421.671	294.5	34.0	0.605	0.057
54421.676	295.9	32.6	0.665	0.040
54421.682	297.3	31.2	0.599	0.038
54421.688	298.6	29.7	0.654	0.044
54421.694	299.8	28.2	0.624	0.039
54421.700	301.0	26.8	0.565	0.053
54421.706	302.0	25.4	0.640	0.040
54421.711	303.0	24.1	0.650	0.048

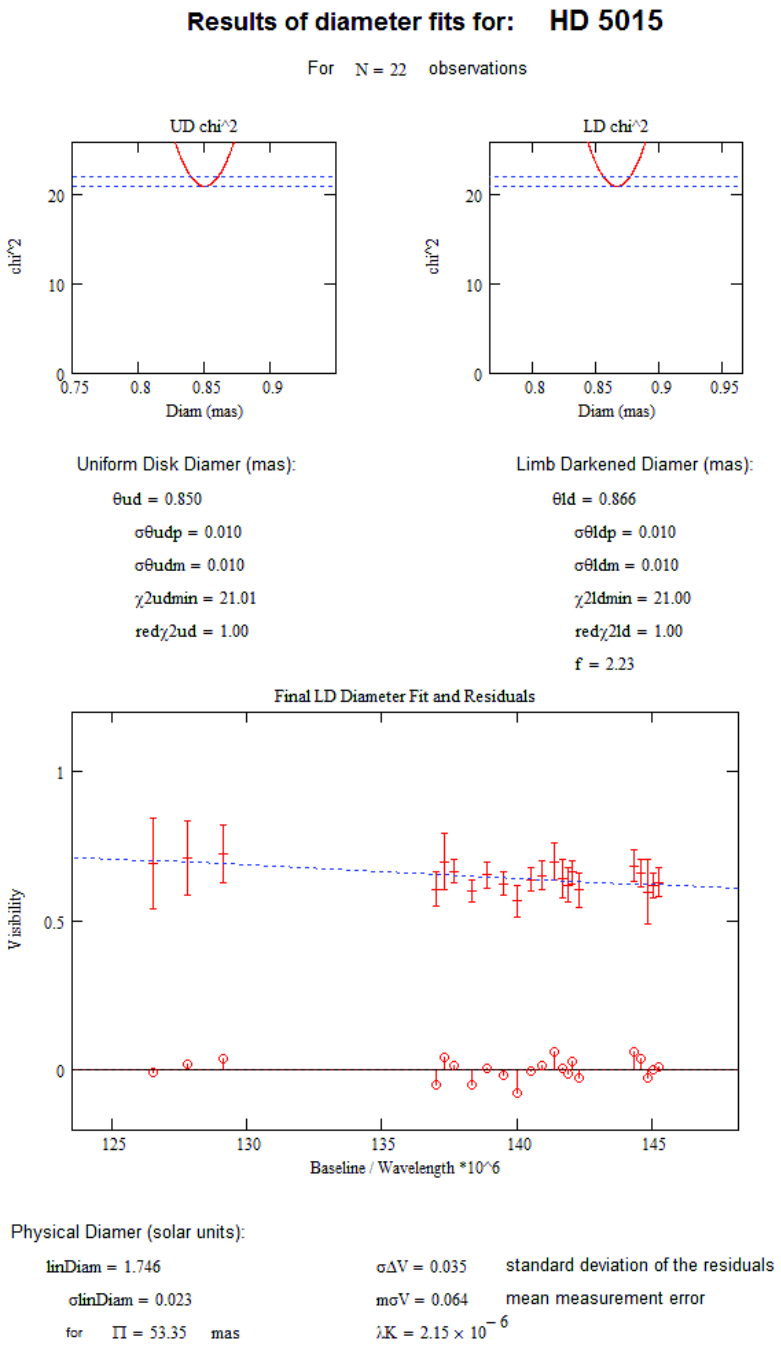

FIGURE C.3: **Diameter fit for HD 5015**

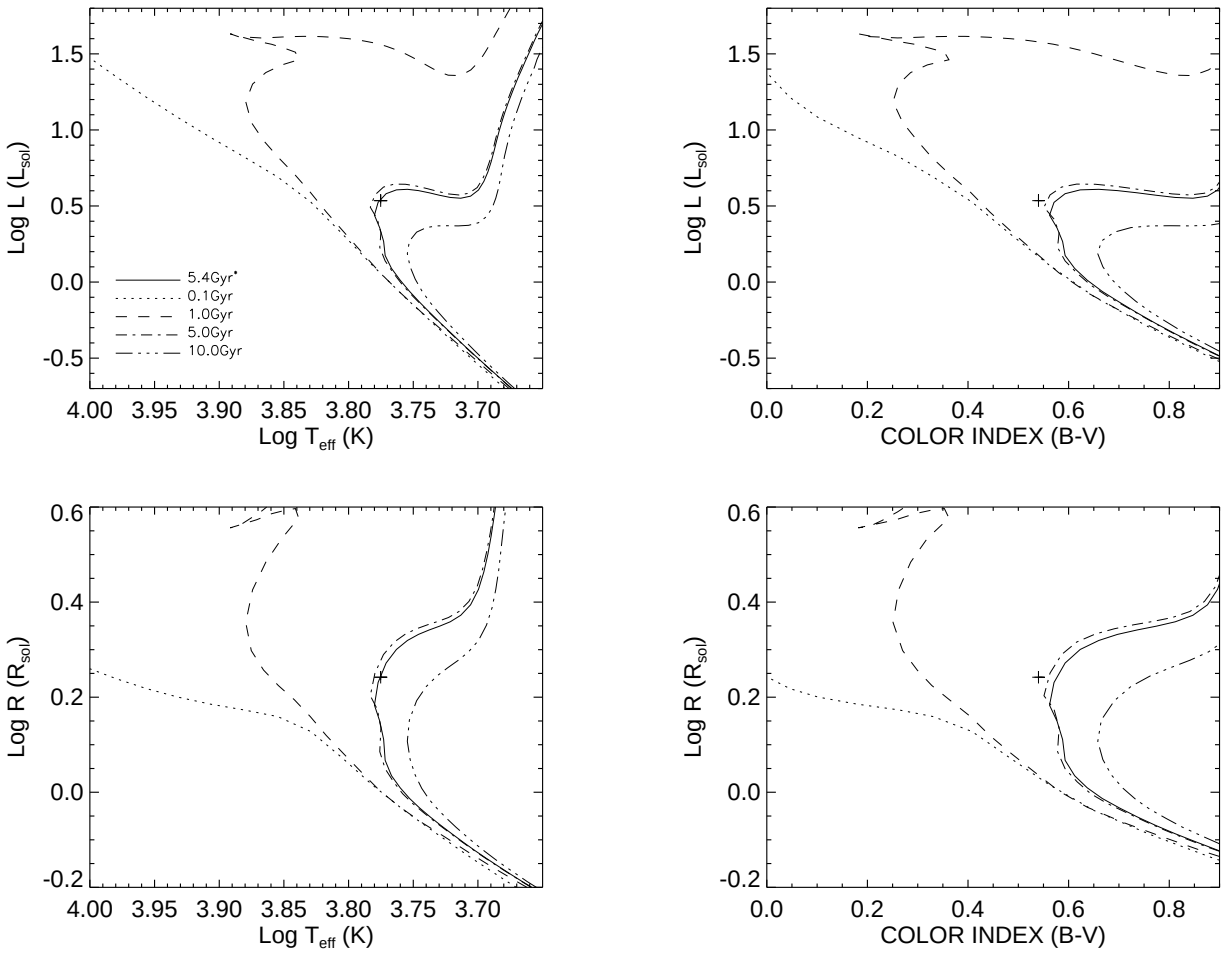

FIGURE C.4: **Y^2 Model Isochrones for HD 5015:** HD 5015 data (and 1-σ errors) plotted against Y^2 models isochrones ([α/Fe]=0.0, [Fe/H]=0.0).

C.3 HD 6582

Results on this star have been published in Boyajian et al. (2008). To re-iterate the important information, we give the calibrated visibilities and Diameter fit below.

TABLE C.3: HD 6582 Visibilities

MJD	B (m)	ψ (°)	V	σV
54282.917	233.2	135.0	0.739	0.093
54282.929	239.8	130.0	0.692	0.071
54282.954	253.8	120.4	0.652	0.065
54298.915	266.4	234.3	0.682	0.038
54298.929	274.0	231.4	0.672	0.023
54298.942	280.7	228.6	0.638	0.024
54298.957	287.1	225.6	0.625	0.020
54298.971	292.7	222.7	0.580	0.024
54298.986	298.0	219.4	0.550	0.026
54299.885	249.2	239.9	0.636	0.027
54299.896	256.2	237.8	0.629	0.023
54299.905	262.2	235.8	0.694	0.030
54299.917	268.9	233.4	0.639	0.028
54299.961	290.0	224.1	0.583	0.035
54299.973	294.6	221.5	0.568	0.038
54299.984	298.2	219.2	0.549	0.026
54299.996	301.9	216.6	0.547	0.035
54351.787	275.7	219.2	0.566	0.037
54351.795	279.4	220.8	0.612	0.030
54351.802	282.8	222.3	0.605	0.026
54351.809	285.9	223.8	0.618	0.040
54351.816	288.9	225.3	0.660	0.045
54351.831	294.5	228.4	0.569	0.034
54351.839	297.3	230.2	0.604	0.047
54351.851	301.3	232.9	0.576	0.036
54351.875	307.6	238.3	0.601	0.055

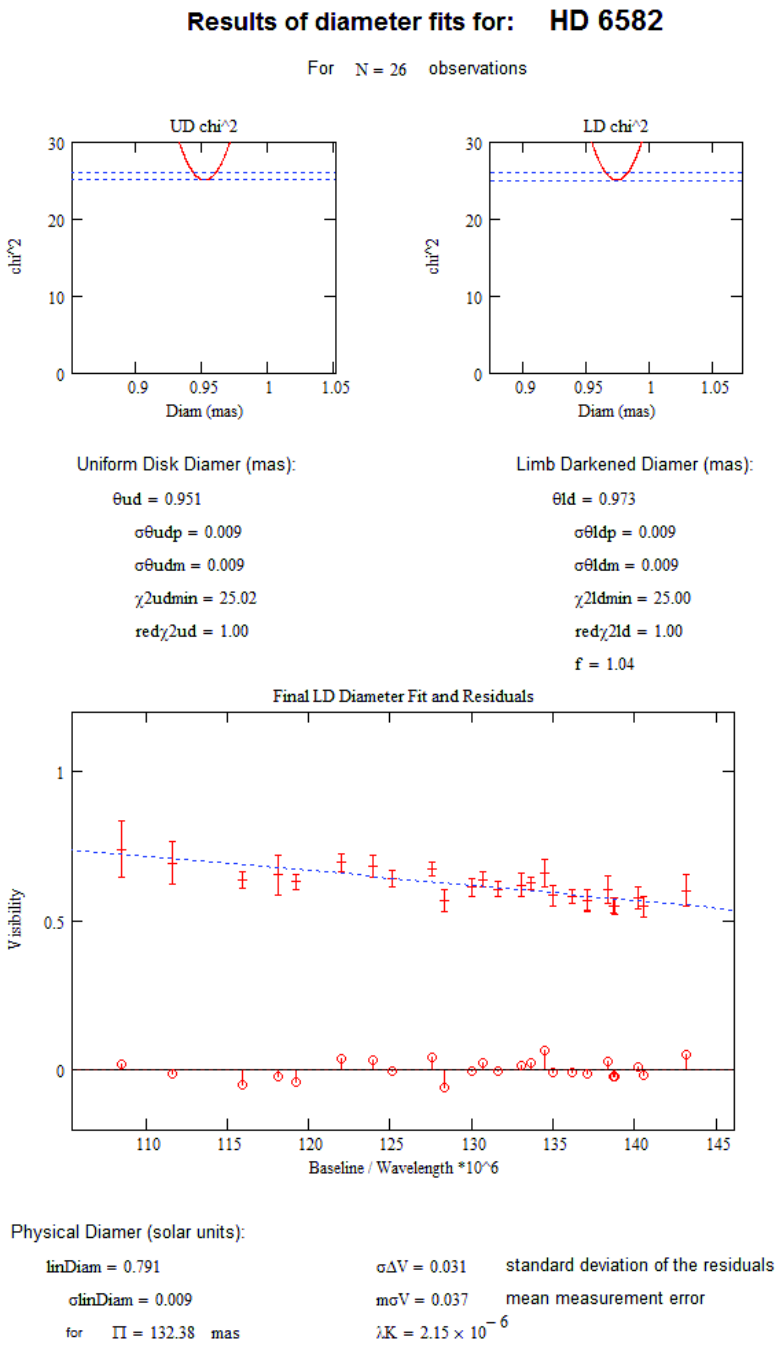

FIGURE C.5: **Diameter fit for HD 6582**

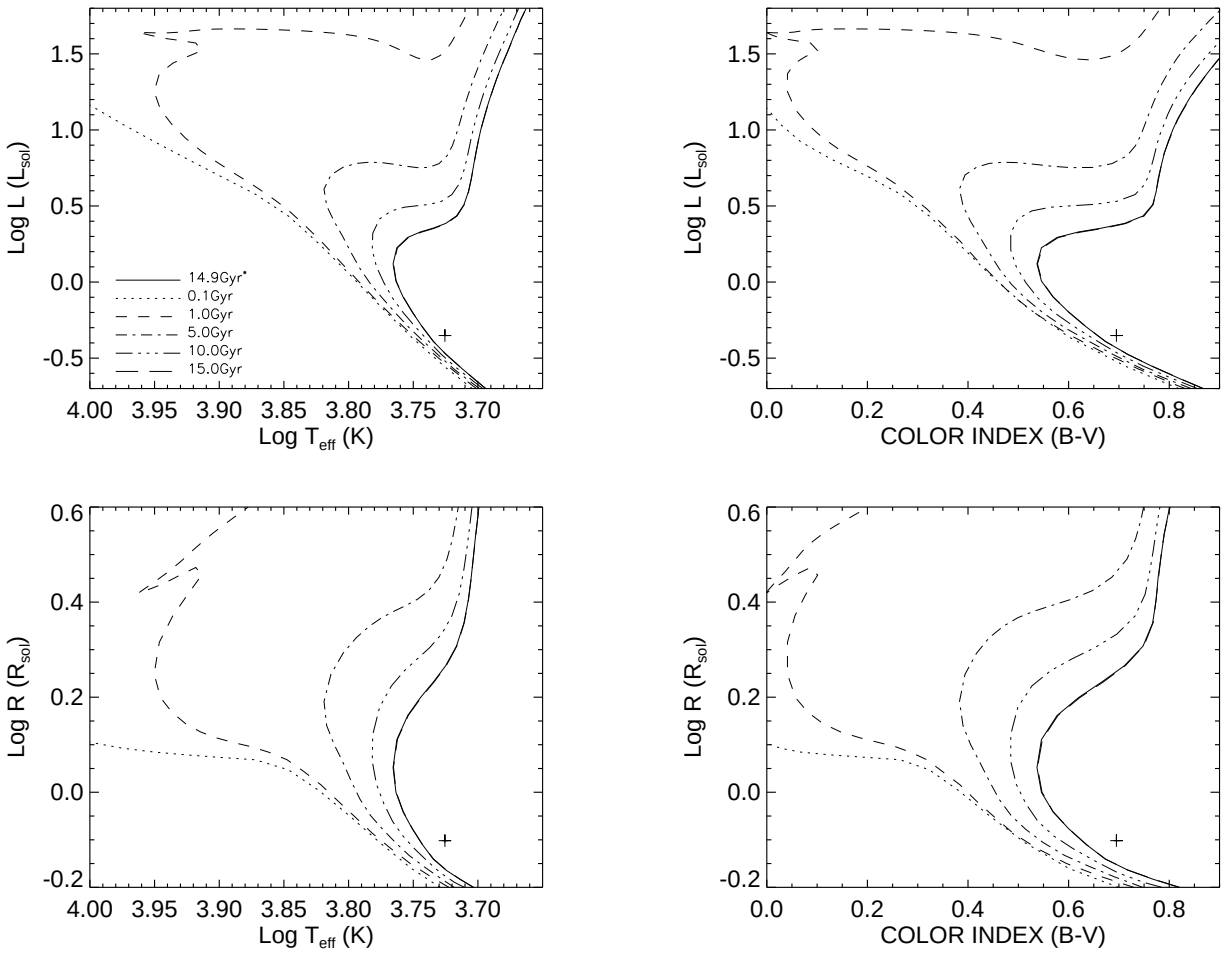

FIGURE C.6: **Y^2 Model Isochrones for HD 6582:** HD 6582 data (and 1-σ errors) plotted against Y^2 models isochrones ([α/Fe]=0.3, [Fe/H]=$-$0.83).

C.4 HD 10780

Results on this star have been published in Boyajian et al. (2008). To re-iterate the important information, we give the calibrated visibilities and Diameter fit below.

TABLE C.4: HD 10780 Visibilities

MJD	B (m)	ψ (°)	V	σV
52922.857	235.2	137.4	0.890	0.092
52922.867	233.3	140.4	0.947	0.076
54280.952	256.8	138.4	0.730	0.063
54280.979	266.4	127.5	0.738	0.043
54301.903	230.1	248.9	0.834	0.037
54301.913	236.4	246.2	0.879	0.053
54301.924	242.5	243.4	0.819	0.054
54301.935	248.7	240.5	0.802	0.062
54301.946	254.3	237.7	0.758	0.056
54301.957	259.4	235.0	0.780	0.035
54301.968	264.5	232.2	0.787	0.062
54301.979	269.0	229.5	0.783	0.072
54301.989	273.2	226.8	0.856	0.058
54302.000	276.9	224.2	0.824	0.059
54383.935	313.2	220.9	0.742	0.059
54383.943	312.8	223.7	0.694	0.069
54383.950	312.5	226.2	0.614	0.059
54383.958	312.1	228.7	0.688	0.071
54383.971	311.3	233.2	0.627	0.045
54384.017	308.5	249.0	0.692	0.078
54384.025	308.1	251.6	0.582	0.145
54384.031	307.8	253.9	0.708	0.077

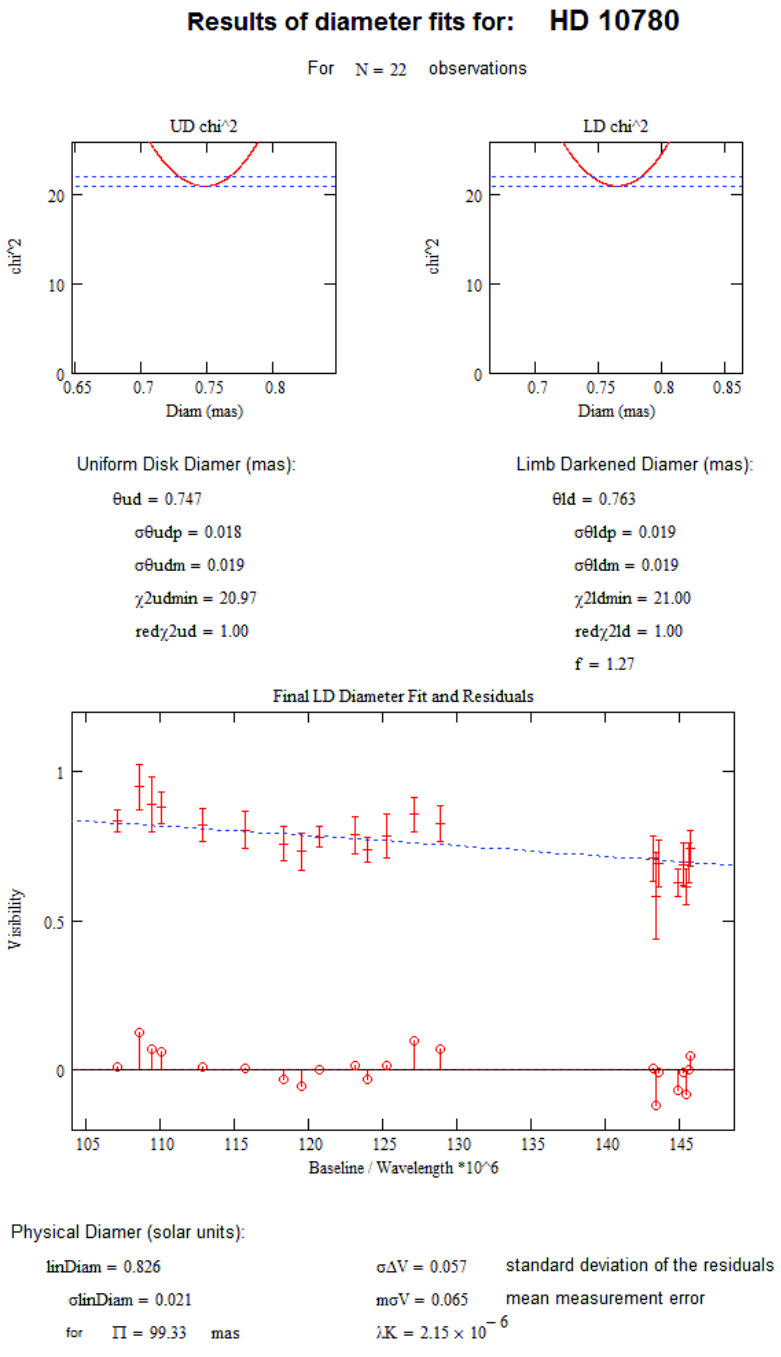

FIGURE C.7: **Diameter fit for HD 10780**

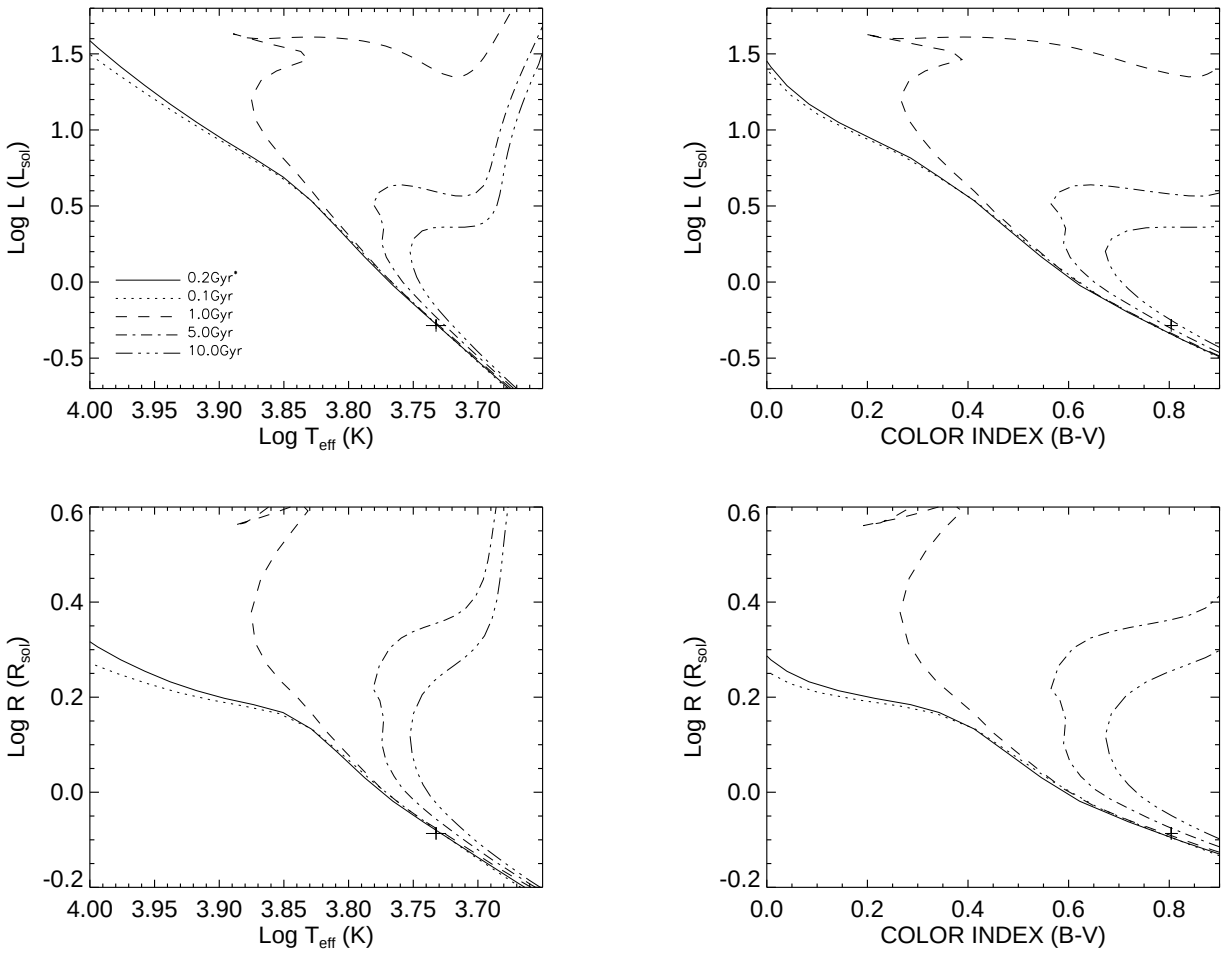

FIGURE C.8: **Y^2 Model Isochrones for HD 10780:** HD 10780 data (and 1-σ errors) plotted against Y^2 models isochrones ([α/Fe]=0.0, [Fe/H]=0.05).

C.5 HD 16895

TABLE C.5: HD 16895 Visibilities

MJD	B (m)	ψ (°)	V	σV
54351.917	310.9	36.0	0.518	0.050
54351.936	315.5	32.0	0.461	0.019
54351.946	317.5	29.9	0.408	0.026
54351.956	319.3	27.7	0.413	0.026
54351.966	320.9	25.5	0.403	0.028
54351.973	321.8	24.0	0.365	0.027
54351.983	323.0	21.6	0.471	0.031
54407.710	266.5	106.1	0.544	0.074
54407.718	271.3	103.8	0.470	0.073
54407.725	276.0	101.4	0.517	0.052
54407.733	280.3	99.3	0.551	0.049
54407.741	284.7	97.0	0.455	0.060
54407.765	296.4	90.2	0.396	0.049
54407.775	300.3	87.5	0.489	0.080
54407.783	303.0	85.4	0.465	0.061
54458.694	323.3	21.1	0.383	0.025
54458.702	324.1	19.1	0.415	0.023
54458.711	324.8	17.1	0.406	0.019
54458.719	325.4	15.2	0.379	0.033
54458.728	325.9	13.2	0.381	0.027
54458.737	326.3	11.0	0.396	0.029

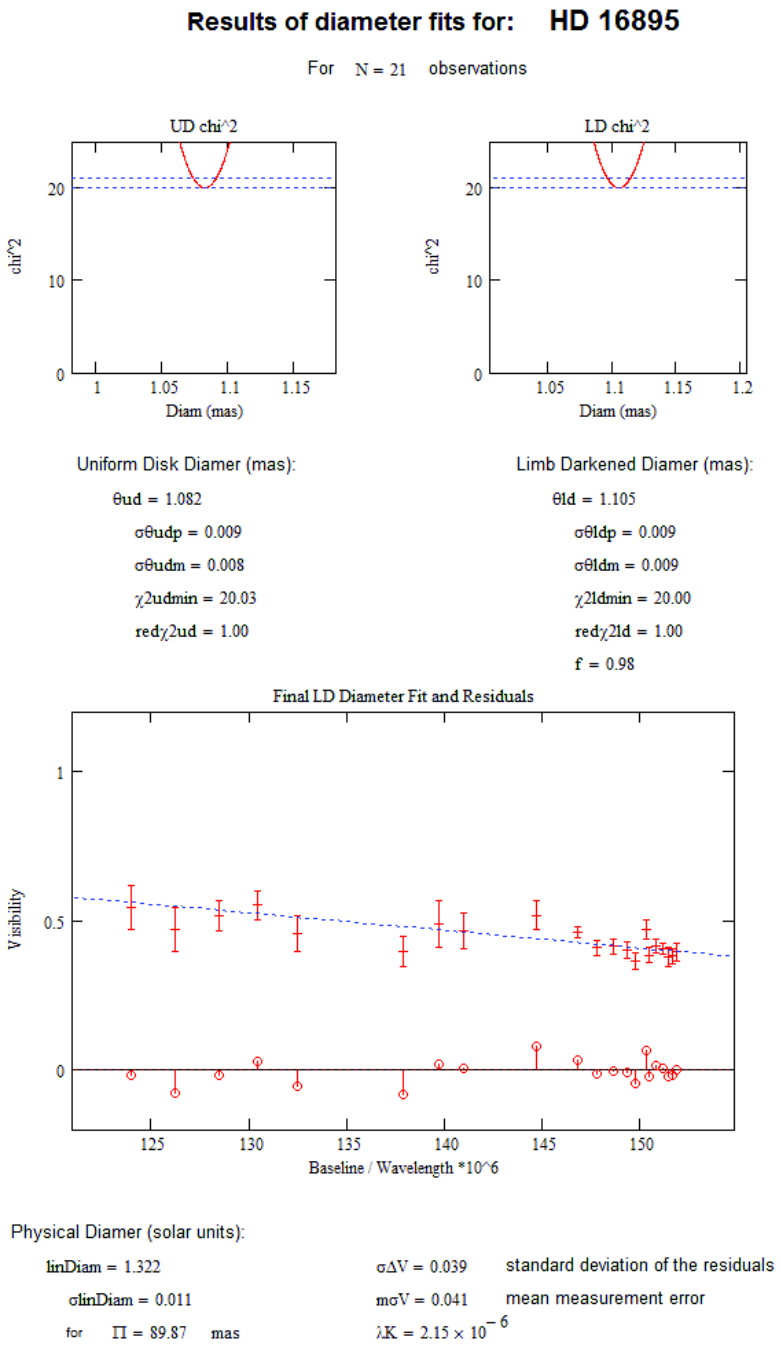

FIGURE C.9: **Diameter fit for HD 16895**

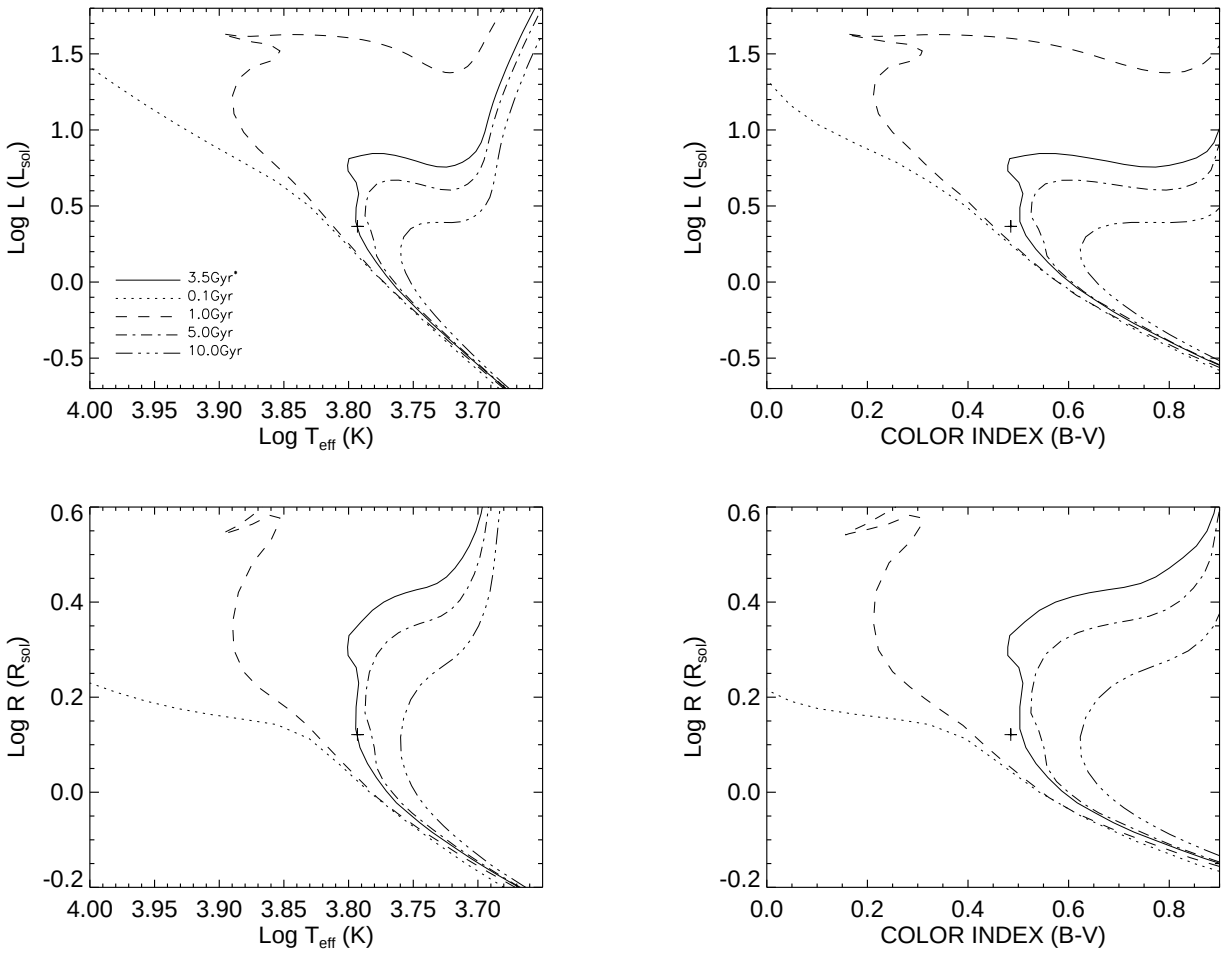

FIGURE C.10: **Y^2 Model Isochrones for HD 16895:** HD 16895 data (and 1-σ errors) plotted against Y^2 models isochrones ([α/Fe]=0.0, [Fe/H]=$-$0.12).

C.6 HD 19373

TABLE C.6: HD 19373 Visibilities

MJD	B (m)	ψ (°)	V	σV
54125.655	325.5	76.7	0.290	0.037
54125.666	326.0	79.3	0.282	0.028
54125.676	326.4	81.6	0.288	0.029
54125.686	326.6	83.9	0.292	0.029
54125.709	326.9	89.4	0.260	0.024
54125.718	326.9	−88.2	0.261	0.034
54125.728	326.8	−85.9	0.268	0.035
54340.996	277.1	147.6	0.399	0.023
54341.007	276.3	144.8	0.366	0.027
54351.902	299.9	42.4	0.416	0.034
54351.909	302.3	41.1	0.378	0.034
54351.923	307.0	38.3	0.334	0.033
54351.939	311.7	35.0	0.326	0.022
54351.949	314.1	32.9	0.347	0.018
54351.959	316.3	30.8	0.314	0.026
54351.976	319.4	27.0	0.310	0.024
54351.987	320.9	24.7	0.294	0.026
54351.993	321.7	23.3	0.293	0.025
54351.999	322.5	21.9	0.308	0.019
54408.699	249.2	114.9	0.621	0.170
54408.715	260.6	109.4	0.619	0.172
54408.728	269.2	105.1	0.542	0.059
54408.735	273.1	103.2	0.457	0.047
54408.741	277.0	101.3	0.473	0.048
54408.751	282.6	98.4	0.441	0.083

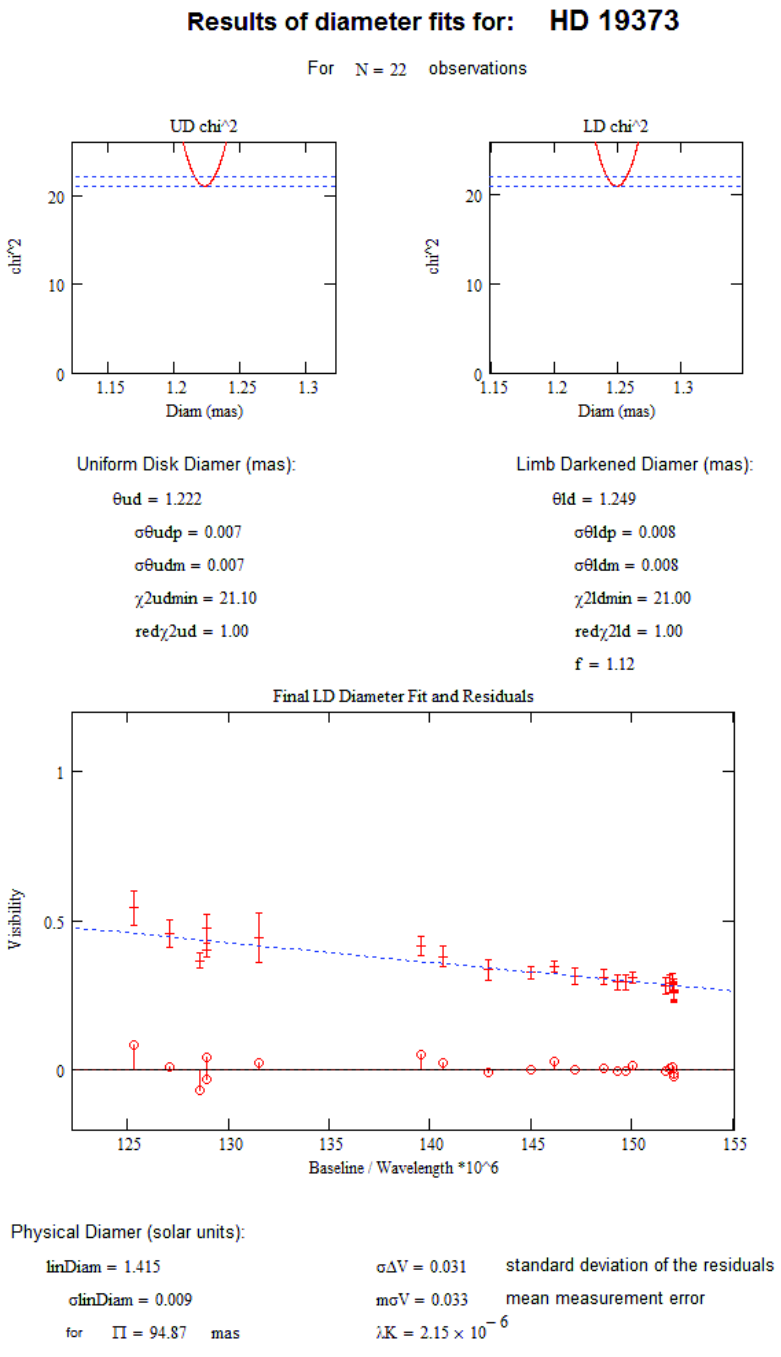

FIGURE C.11: **Diameter fit for HD 19373**

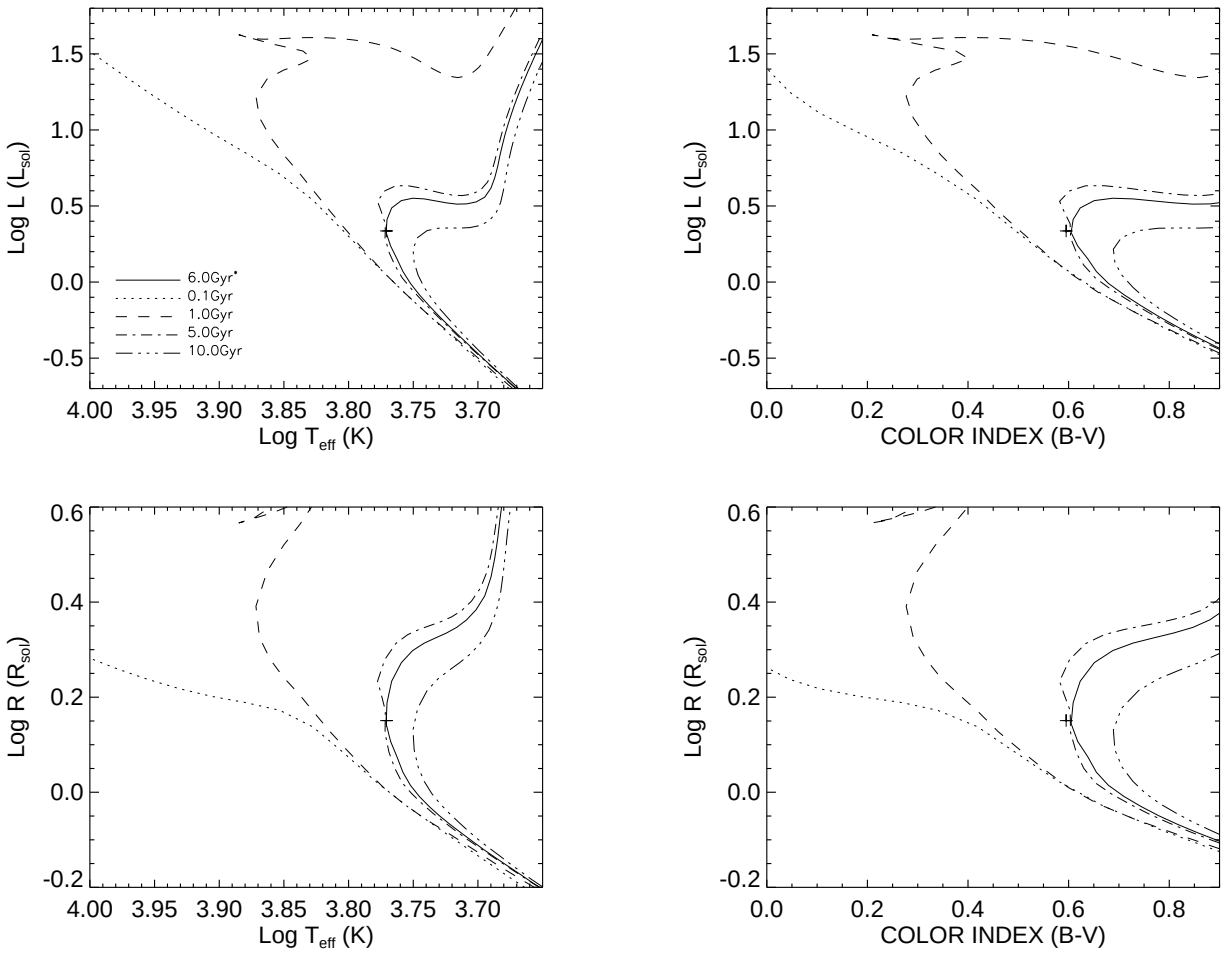

FIGURE C.12: **Y^2 Model Isochrones for HD 19373:** HD 19373 data (and 1-σ errors) plotted against Y^2 models isochrones ([α/Fe]=0.0, [Fe/H]=0.9).

C.7 HD 20630

TABLE C.7: HD 20630 Visibilities

MJD	B (m)	ψ (°)	V	σV
54352.907	324.4	38.5	0.560	0.080
54352.938	314.6	35.5	0.604	0.106
54352.953	308.6	33.6	0.682	0.106
54352.964	303.9	32.0	0.660	0.079
54352.978	297.7	29.7	0.786	0.115
54352.989	292.7	27.7	0.804	0.121
54353.003	286.6	25.0	0.750	0.101
54353.013	282.3	22.9	0.697	0.083
54353.020	279.4	21.2	0.570	0.072
54740.872	316.2	36.0	0.614	0.060
54740.883	312.0	34.7	0.621	0.079
54740.902	304.2	32.1	0.577	0.057
54740.912	299.8	30.5	0.560	0.087
54787.776	303.3	31.8	0.548	0.081
54787.794	295.3	28.8	0.613	0.075
54787.823	282.5	22.9	0.557	0.067
54787.836	277.3	19.9	0.638	0.067
54788.780	300.0	30.6	0.446	0.064
54788.792	294.6	28.5	0.586	0.101
54788.811	286.5	25.0	0.619	0.068
54788.827	279.5	21.3	0.536	0.049
54788.849	271.5	15.8	0.762	0.138

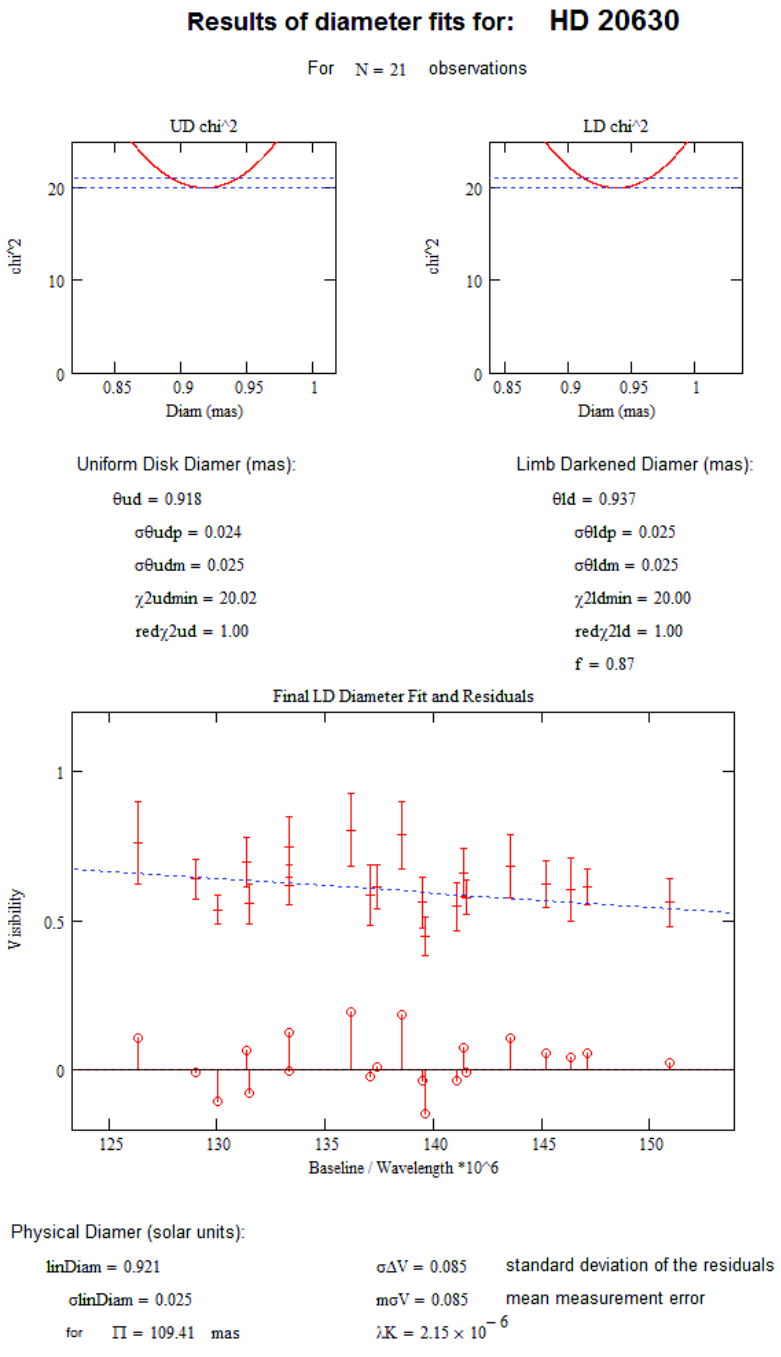

FIGURE C.13: **Diameter fit for HD 20630**

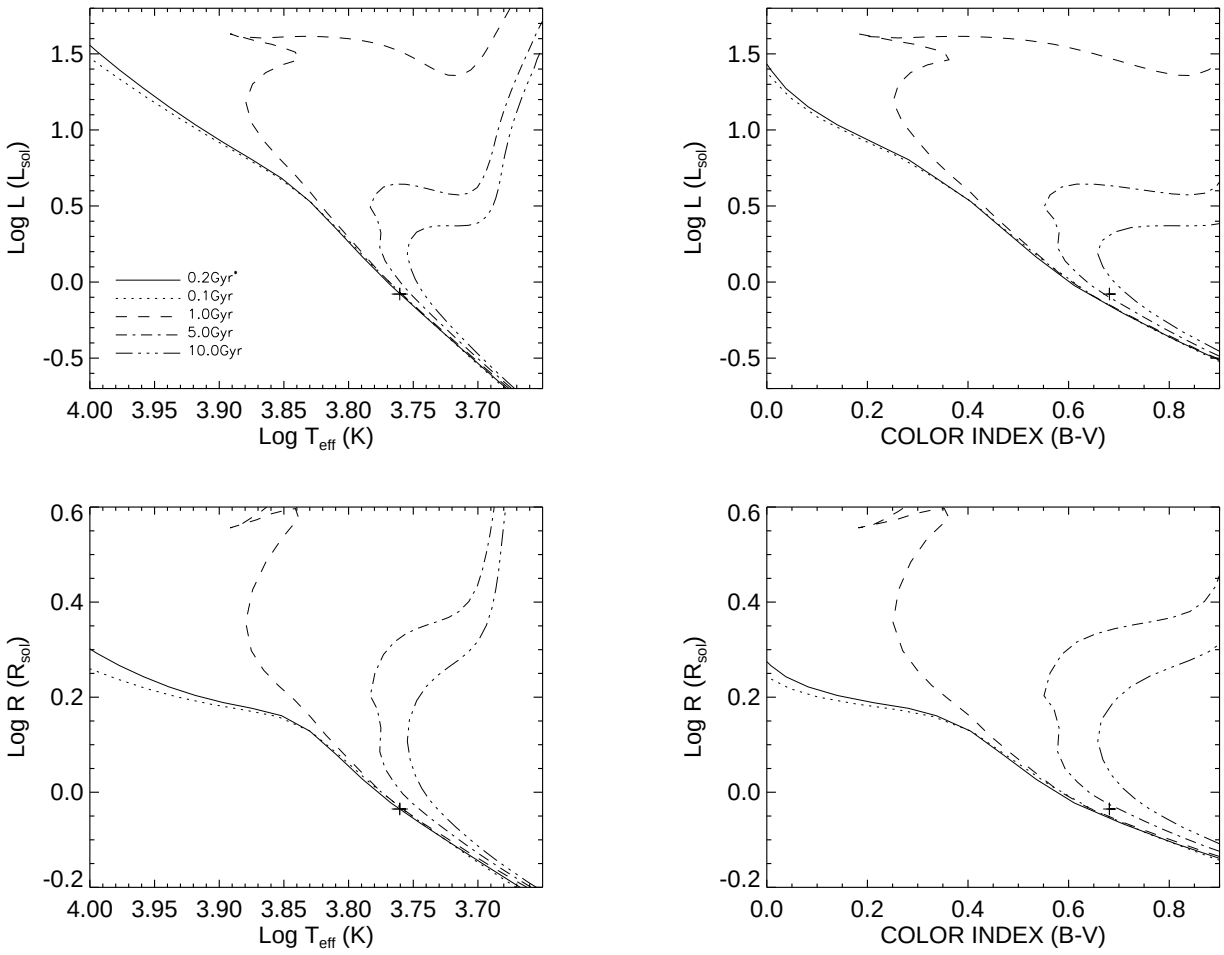

FIGURE C.14: **Y^2 Model Isochrones for HD 20630:** HD 20630 data (and 1-σ errors) plotted against Y^2 models isochrones ([α/Fe]=0.0, [Fe/H]=0.0).

C.8 HD 22484

TABLE C.8: HD 22484 Visibilities

MJD	B (m)	ψ (°)	V	σV
54074.707	310.8	36.8	0.505	0.074
54076.692	314.7	37.7	0.361	0.038
54076.705	309.3	36.4	0.413	0.051
54076.717	303.7	35.0	0.413	0.062
54076.729	297.9	33.4	0.431	0.041
54352.911	323.1	39.5	0.479	0.050
54352.919	320.7	39.1	0.481	0.043
54352.950	308.9	36.3	0.513	0.078
54352.961	303.7	35.0	0.510	0.055
54352.975	296.8	33.1	0.603	0.073
54352.986	291.2	31.4	0.655	0.131
54353.000	284.1	29.0	0.611	0.090
54353.010	278.9	27.1	0.594	0.063
54740.842	324.9	39.9	0.382	0.038
54740.858	320.4	39.0	0.472	0.055
54740.863	318.5	38.6	0.447	0.050
54740.879	312.7	37.3	0.400	0.054
54740.898	304.1	35.1	0.506	0.052
54740.909	299.1	33.8	0.490	0.066
54741.854	286.8	74.3	0.514	0.031
54741.865	294.4	74.7	0.501	0.032
54741.874	300.1	75.0	0.483	0.051
54741.886	305.8	75.4	0.543	0.048

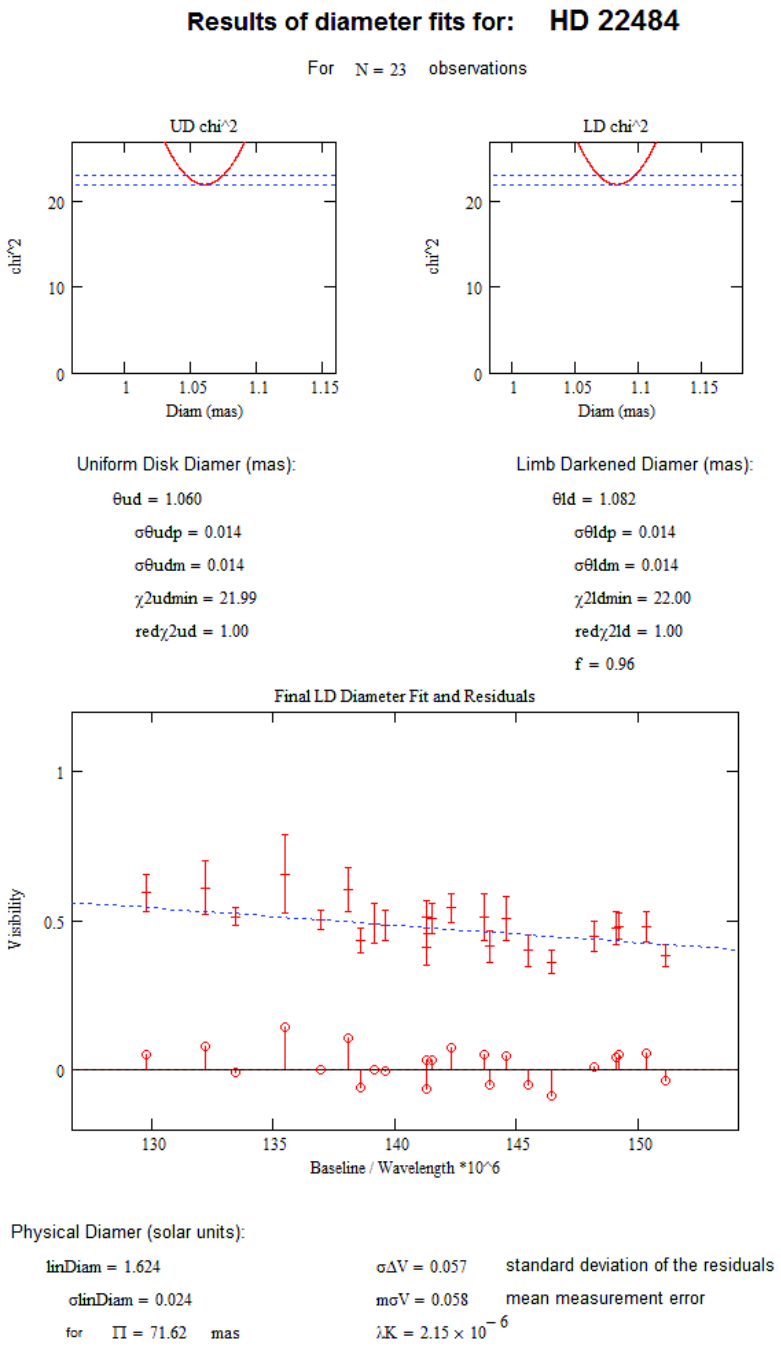

FIGURE C.15: **Diameter fit for HD 22484**

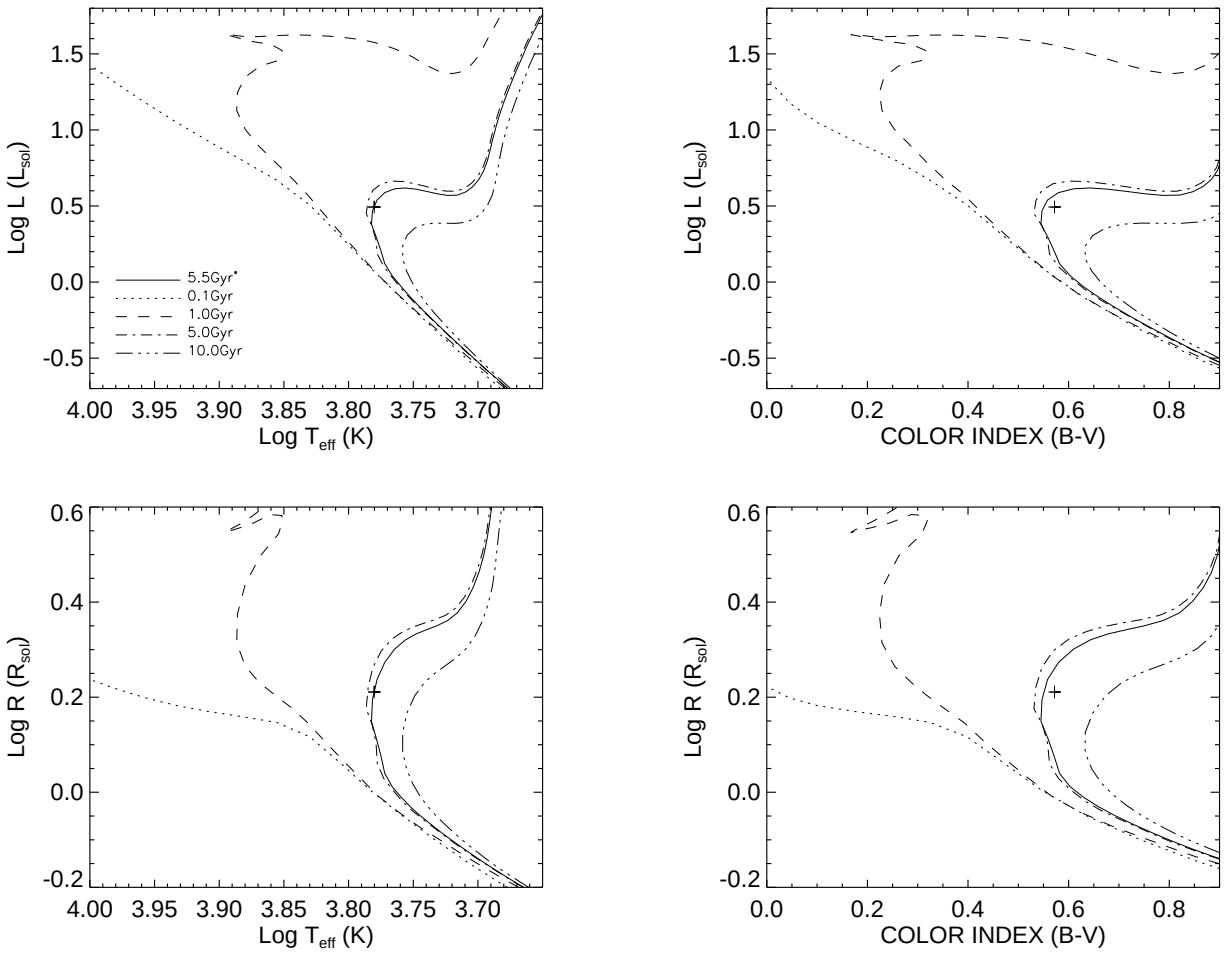

FIGURE C.16: **Y^2 Model Isochrones for HD 22484:** HD 22484 data (and 1-σ errors) plotted against Y^2 models isochrones ([α/Fe]=0.0, [Fe/H]=$-$0.09).

C.9 HD 30652

TABLE C.9: HD 30652 Visibilities

MJD	B (m)	ψ (°)	V	σV
54409.942	284.5	17.0	0.259	0.047
54409.948	282.7	15.5	0.264	0.035
54409.953	281.1	14.0	0.282	0.036
54409.959	279.6	12.4	0.296	0.048
54409.966	278.2	10.8	0.285	0.044
54409.976	276.3	7.9	0.269	0.027
54409.982	275.4	6.2	0.263	0.029
54409.990	274.6	4.0	0.260	0.035
54409.996	274.3	2.4	0.246	0.041
54410.001	274.1	0.9	0.211	0.033
54410.032	276.3	172.1	0.237	0.040
54410.038	277.3	170.5	0.244	0.040
54410.045	278.6	168.7	0.221	0.033
54410.051	280.0	167.1	0.249	0.033
54410.056	281.6	165.6	0.204	0.045
54410.023	275.1	174.7	0.262	0.036
54740.927	322.7	36.3	0.088	0.010
54740.934	320.9	35.5	0.108	0.010
54740.940	318.9	34.7	0.115	0.011
54740.973	307.4	30.0	0.181	0.025
54740.985	302.7	27.8	0.182	0.020
54740.992	300.0	26.5	0.178	0.023
54741.038	283.7	16.3	0.247	0.039
54741.049	280.6	13.5	0.254	0.037
54741.056	278.9	11.7	0.220	0.029
54740.951	315.5	33.3	0.114	0.014
54740.957	313.3	32.5	0.118	0.012
54740.963	311.2	31.6	0.122	0.014
54741.004	295.5	24.2	0.177	0.027
54741.010	293.3	22.9	0.218	0.041
54741.016	291.0	21.6	0.200	0.030
54741.025	287.8	19.5	0.217	0.021
54741.946	307.4	76.9	0.151	0.011
54741.955	310.4	76.6	0.152	0.014

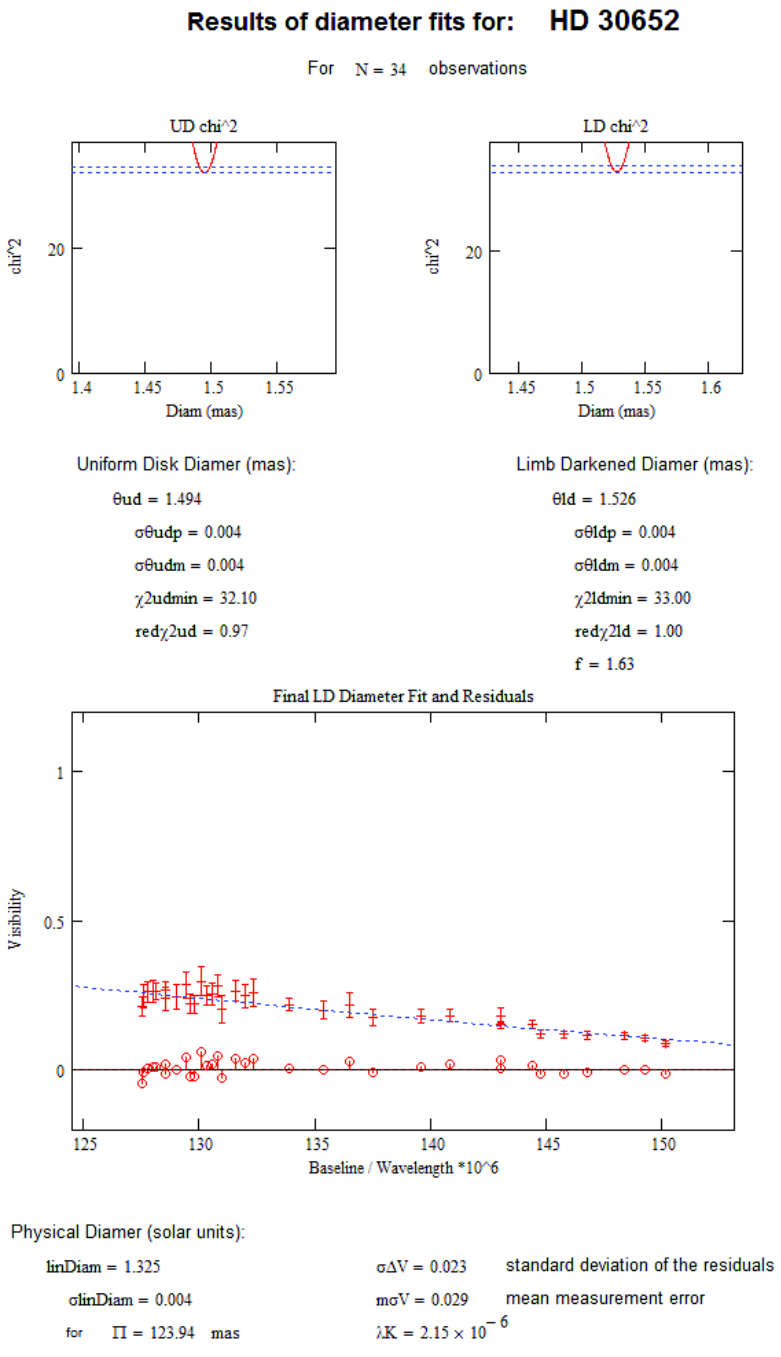

FIGURE C.17: **Diameter fit for HD 30652**

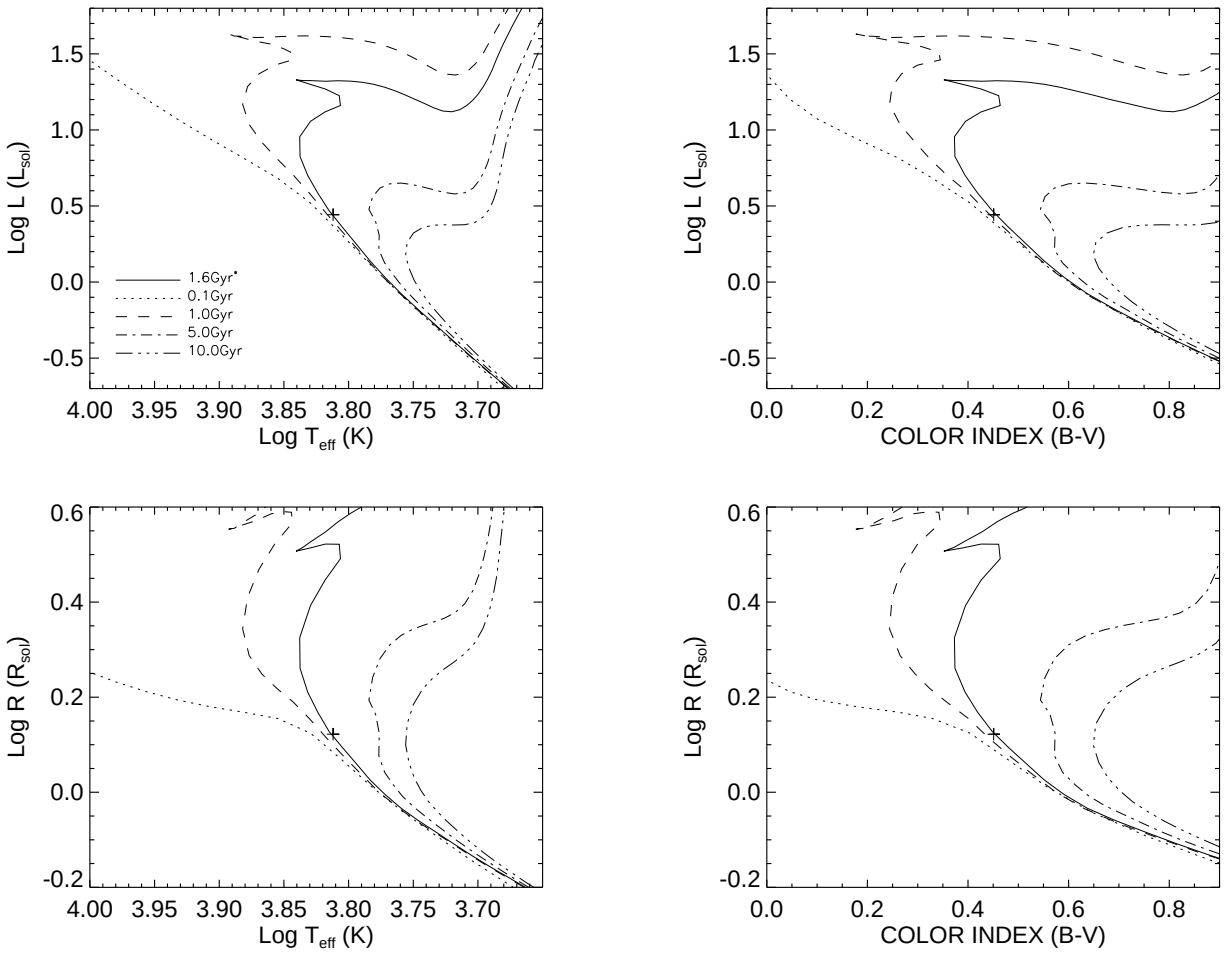

FIGURE C.18: **Y^2 Model Isochrones for HD 30652:** HD 30652 data (and 1-σ errors) plotted against Y^2 models isochrones ([α/Fe]=0.0, [Fe/H]=$-$0.03).

C.10 HD 34411

Table C.10: HD 34411 Visibilities

MJD	B (m)	ψ (°)	V	σV
54126.812	330.6	−86.8	0.566	0.105
54126.823	330.7	−84.3	0.470	0.046
54126.833	330.7	−81.9	0.428	0.063
54126.846	330.7	−78.8	0.463	0.051
54126.862	330.6	−75.2	0.391	0.059
54407.809	253.5	102.5	0.619	0.053
54407.819	261.2	100.1	0.595	0.048
54407.833	272.6	96.3	0.595	0.078
54407.840	277.3	94.7	0.698	0.163
54407.853	286.4	91.4	0.673	0.224
54407.865	293.0	88.7	0.686	0.191
54407.873	297.2	86.9	0.616	0.138
54419.718	269.2	52.3	0.563	0.104
54419.753	292.0	47.9	0.489	0.062
54419.778	304.4	44.4	0.507	0.060
54419.793	310.3	42.1	0.574	0.060
54421.730	281.6	50.2	0.661	0.031
54421.738	286.6	49.1	0.631	0.031
54421.747	291.7	48.0	0.535	0.043
54421.755	295.9	46.9	0.599	0.027
54421.763	299.8	45.8	0.569	0.041
54421.771	303.5	44.7	0.560	0.046
54421.778	306.7	43.6	0.587	0.042

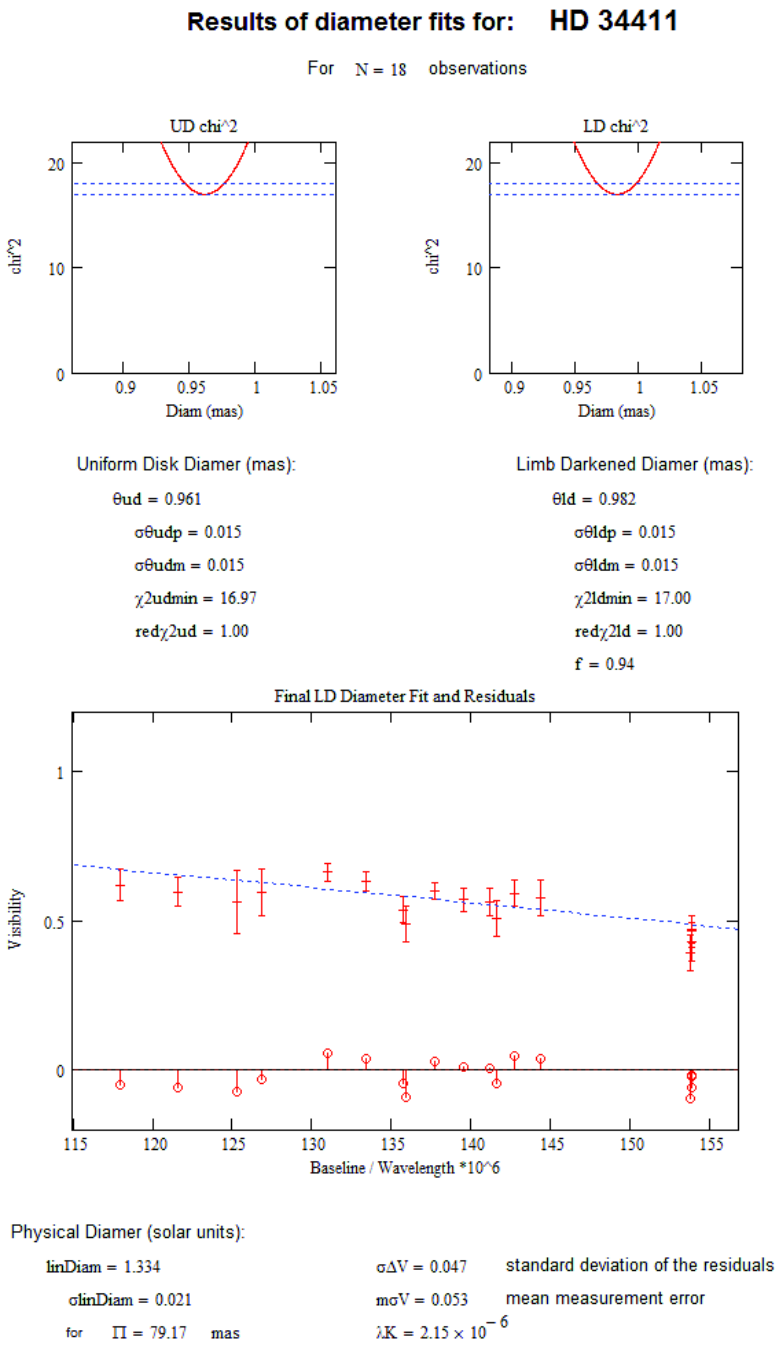

FIGURE C.19: **Diameter fit for HD 34411**

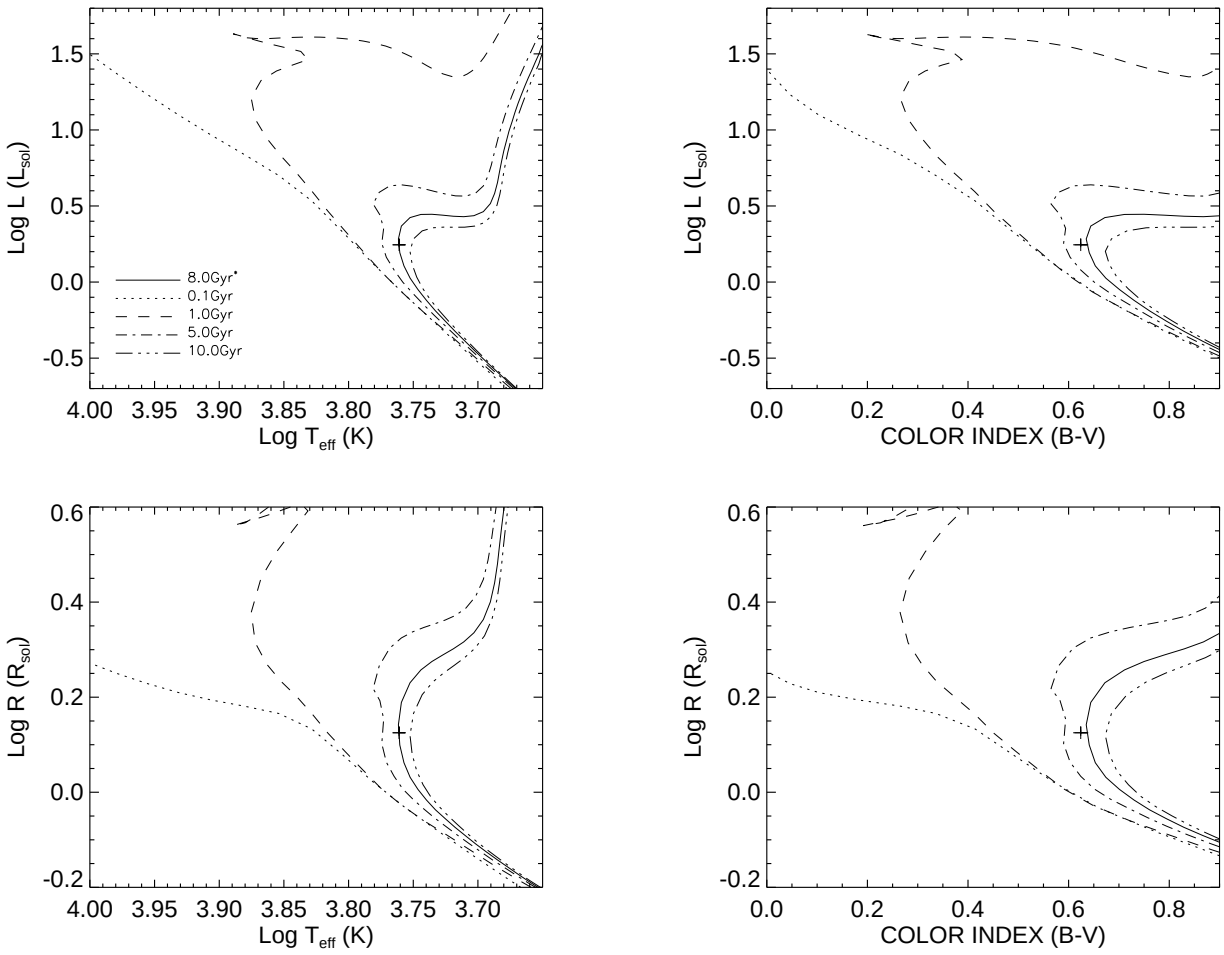

FIGURE C.20: **Y^2 Model Isochrones for HD 34411:** HD 34411 data (and 1-σ errors) plotted against Y^2 models isochrones ([α/Fe]=0.0, [Fe/H]=$-$0.05).

C.11 HD 39587

Table C.11: HD 39587 Visibilities

MJD	B (m)	ψ (°)	V	σV
54076.960	309.3	0.1	0.498	0.045
54076.970	309.5	−87.2	0.503	0.033
54076.981	310.0	−84.7	0.483	0.043
54165.694	310.1	84.3	0.533	0.051
54165.709	309.4	88.2	0.462	0.052
54165.725	309.4	−87.9	0.493	0.053
54165.734	309.8	−85.5	0.493	0.045
54165.744	310.5	−83.1	0.467	0.034
54165.753	311.4	−80.7	0.417	0.037
54165.763	312.5	−78.4	0.400	0.047
54165.775	314.2	−75.5	0.390	0.035
54788.874	327.6	30.3	0.398	0.058
54788.881	326.5	29.1	0.413	0.060
54788.891	324.9	27.3	0.440	0.111
54788.899	323.7	25.9	0.476	0.111
54788.906	322.3	24.5	0.372	0.066
54788.914	320.9	22.9	0.483	0.072
54788.927	318.6	20.3	0.438	0.051
54788.934	317.2	18.7	0.416	0.058
54788.941	316.1	17.2	0.502	0.061
54788.948	315.0	15.6	0.461	0.061
54788.954	314.0	14.2	0.344	0.044

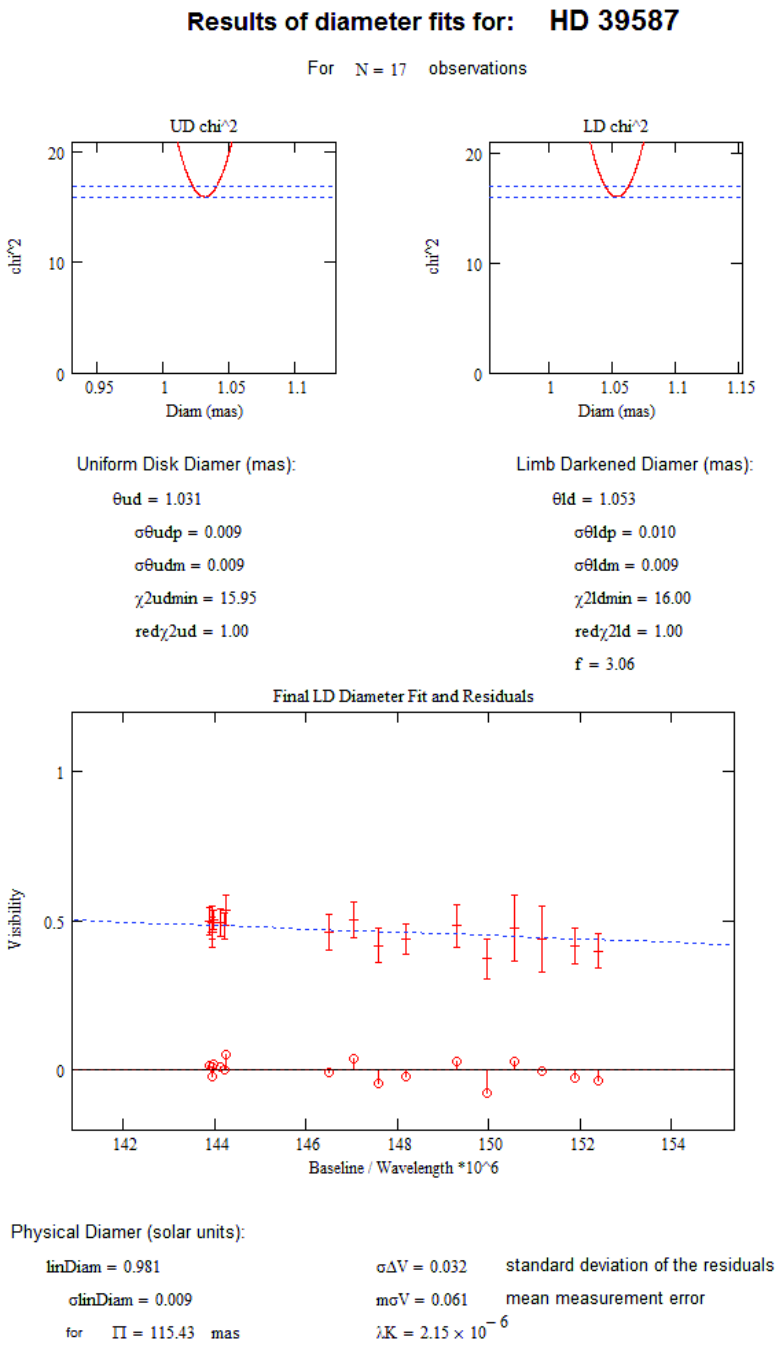

FIGURE C.21: **Diameter fit for HD 39587**

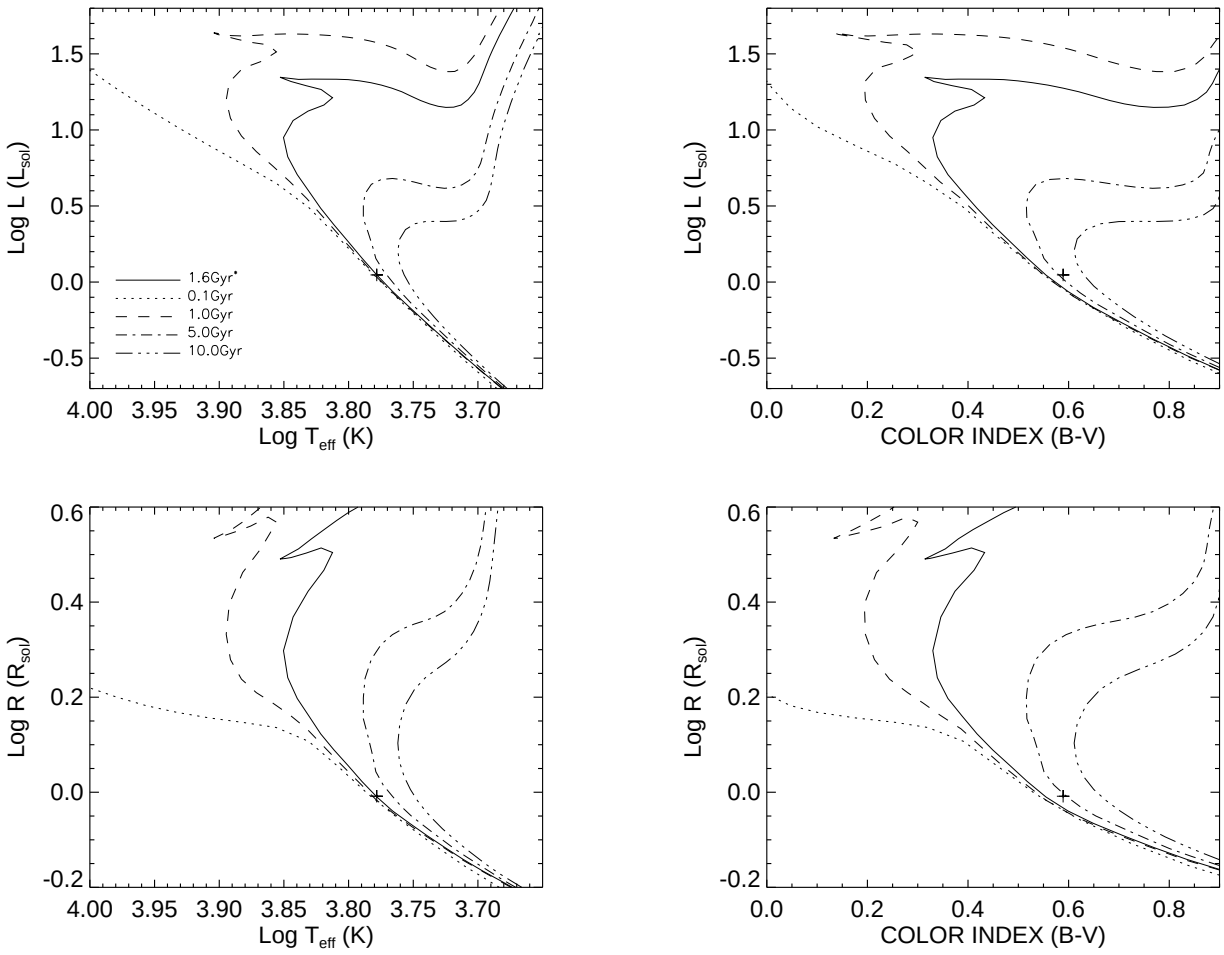

FIGURE C.22: **Y^2 Model Isochrones for HD 39587:** HD 39587 data (and 1-σ errors) plotted against Y^2 models isochrones ([α/Fe]=0.0, [Fe/H]=−0.16).

C.12 HD 48682

TABLE C.12: HD 48682 Visibilities

MJD	B (m)	ψ (°)	V	σV
54458.756†	308.2	41.6	0.663	0.053
54458.766†	311.5	39.9	0.736	0.050
54458.775†	314.5	38.1	0.735	0.055
54458.785†	317.1	36.4	0.745	0.047
54458.793†	319.1	34.8	0.807	0.049
54458.802†	320.9	33.1	0.836	0.067
54458.810†	322.5	31.5	0.989	0.076
54458.818†	323.8	29.9	1.060	0.115
54458.827†	325.0	28.1	1.091	0.149
54726.971	284.1	49.7	0.682	0.073
54726.979	288.6	48.6	0.734	0.105
54726.987	292.9	47.3	0.697	0.065
54726.995	297.0	46.0	0.615	0.053
54727.004	301.3	44.5	0.666	0.044
54727.036	313.1	39.0	0.690	0.048
54741.978	272.5	98.8	0.740	0.110
54741.989	280.0	95.8	0.654	0.093
54742.001	287.3	92.7	0.683	0.088
54786.827	294.7	46.8	0.679	0.056
54786.838	299.9	45.0	0.669	0.031
54786.846	303.7	43.6	0.648	0.042
54786.855	307.0	42.1	0.610	0.044
54786.922	324.0	29.6	0.848	0.089

† represents data calibrated with a bad calibrator.

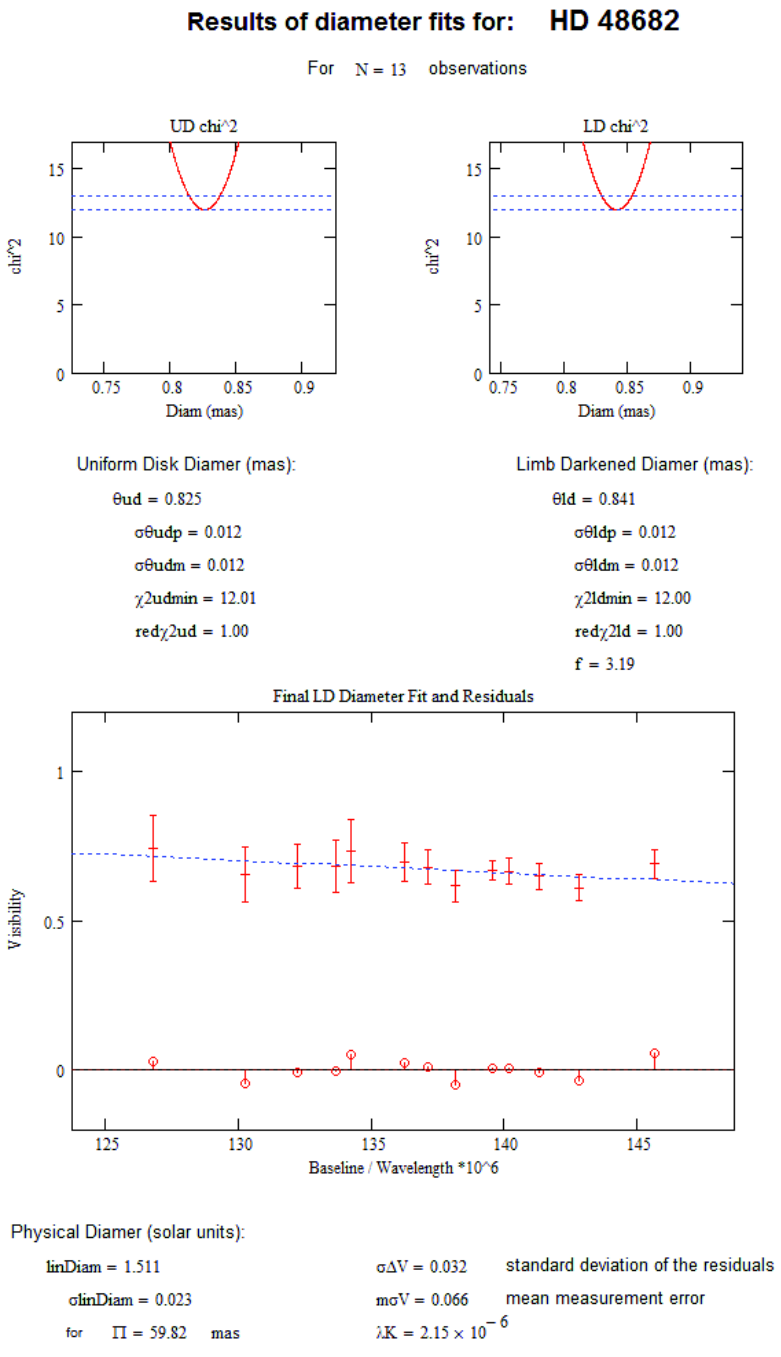

FIGURE C.23: **Diameter fit for HD 48682**

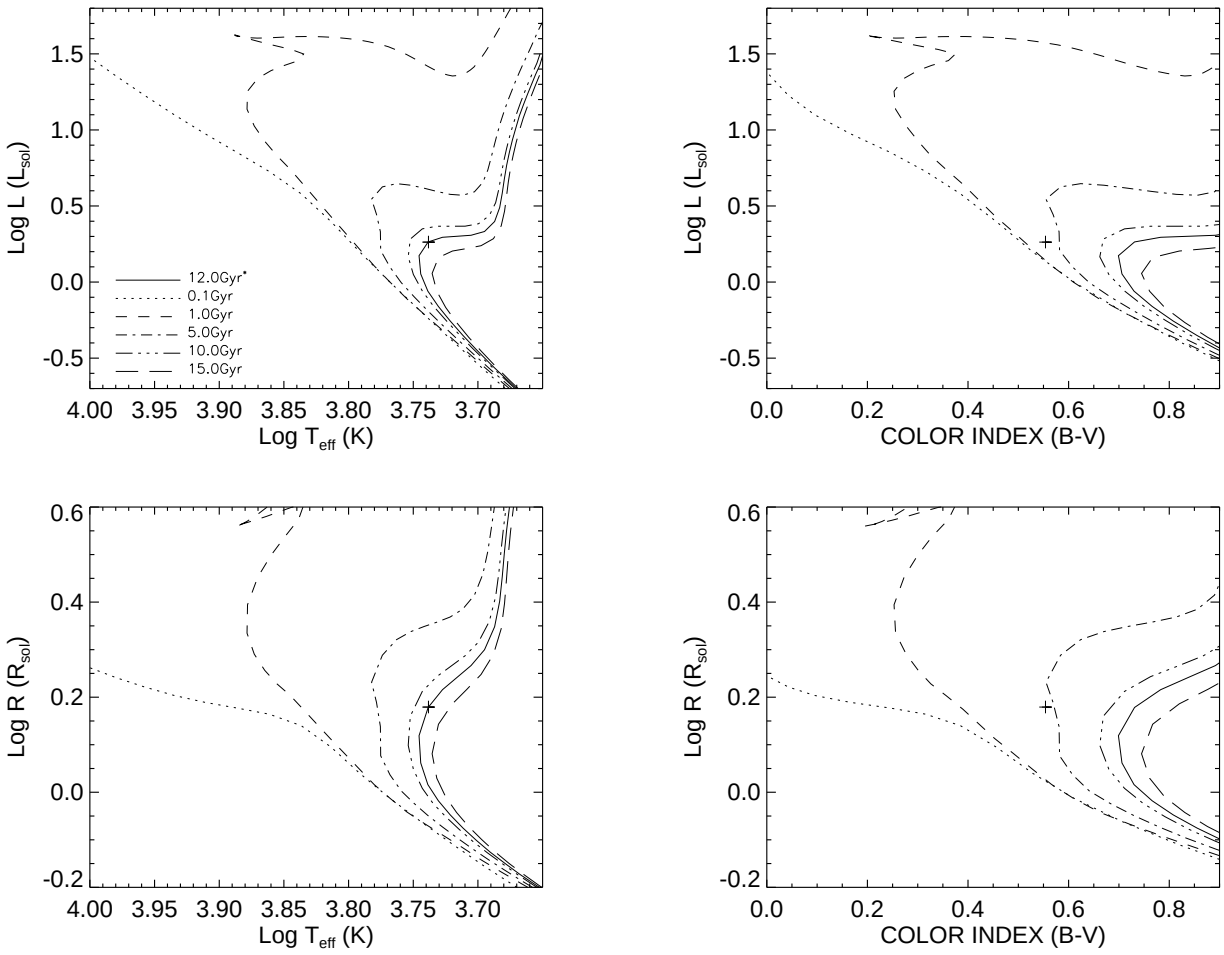

FIGURE C.24: **Y^2 Model Isochrones for HD 48682:** HD 48682 data (and 1-σ errors) plotted against Y^2 models isochrones ([α/Fe]=0.0, [Fe/H]=0.01).

C.13 HD 48737

TABLE C.13: HD 48737 Visibilities

MJD	B (m)	ψ (°)	V	σV
54076.900	308.4	66.8	0.192	0.027
54076.911	305.2	69.1	0.248	0.015
54076.923	302.1	71.7	0.253	0.016
54076.933	299.5	74.2	0.256	0.021
54787.943	312.1	25.8	0.280	0.036
54787.951	309.8	24.2	0.221	0.022
54788.026	293.0	6.3	0.262	0.039
54788.034	292.3	4.2	0.298	0.029
54788.050	291.7	90.0	0.263	0.029
54787.966	305.4	21.0	0.226	0.027
54787.974	303.2	19.2	0.193	0.020
54787.982	301.1	17.3	0.273	0.035
54787.996	297.8	14.0	0.222	0.024
54788.013	294.6	9.7	0.242	0.030
54788.970	303.5	19.5	0.233	0.031
54788.976	301.9	18.1	0.348	0.039
54788.985	299.6	15.9	0.287	0.028
54788.991	298.2	14.4	0.289	0.027
54789.003	295.8	11.4	0.280	0.031
54789.010	294.7	9.8	0.308	0.048
54789.016	293.8	8.2	0.294	0.040
54789.022	293.1	6.6	0.299	0.033
54789.029	292.4	4.8	0.263	0.034
54789.035	292.0	3.0	0.221	0.024
54789.041	291.8	1.4	0.212	0.025

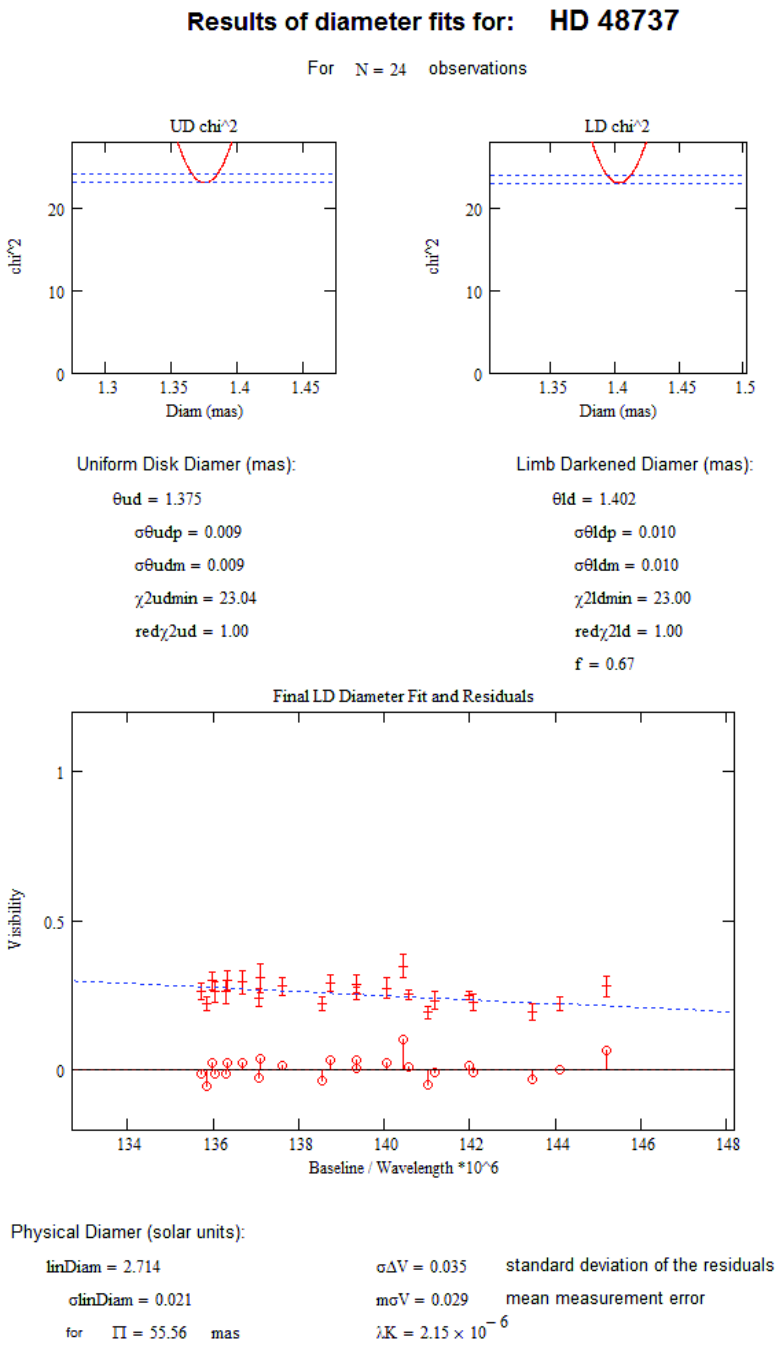

FIGURE C.25: **Diameter fit for HD 48737**

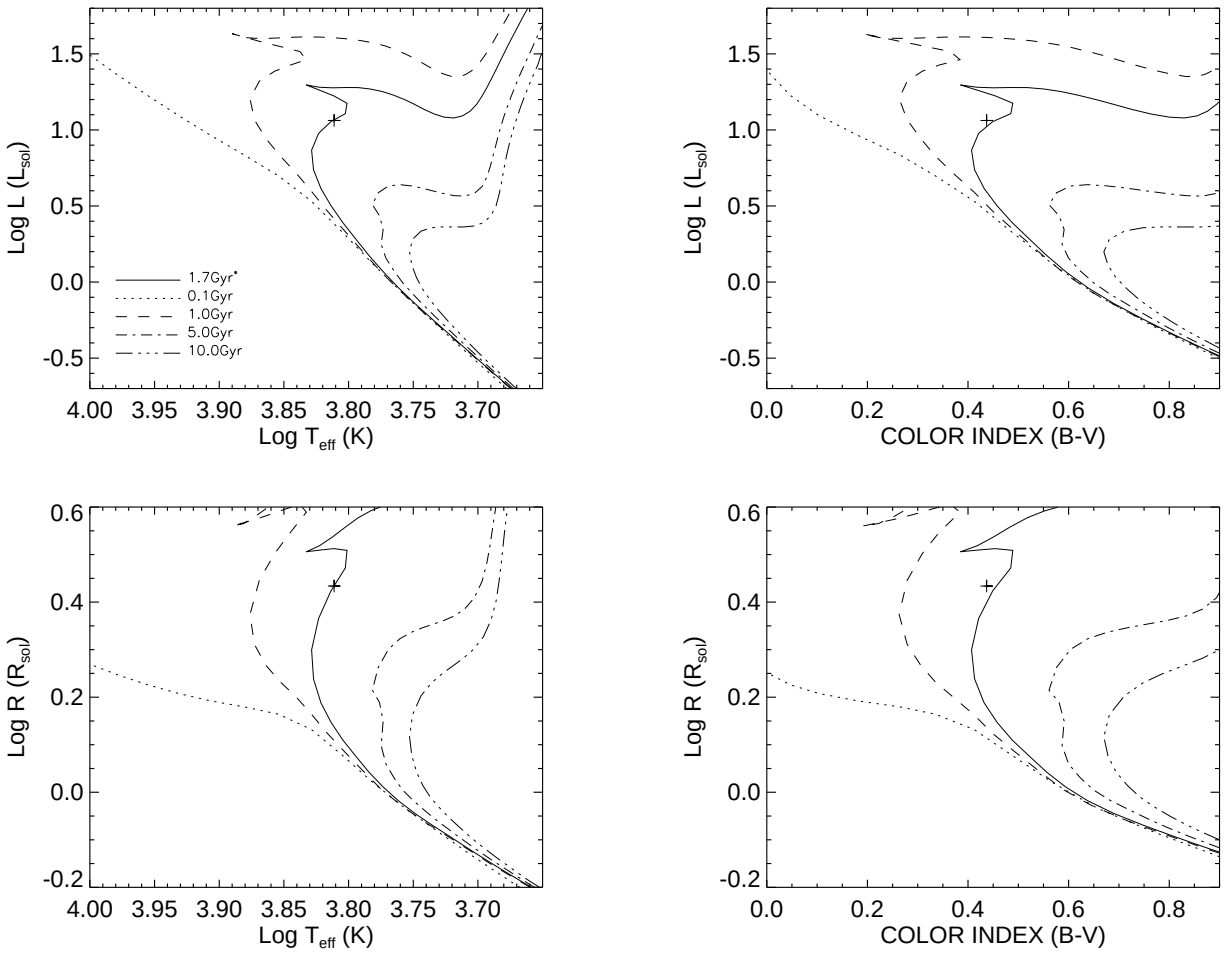

FIGURE C.26: **Y^2 Model Isochrones for HD 48737:** HD 48737 data (and 1-σ errors) plotted against Y^2 models isochrones ([α/Fe]=0.0, [Fe/H]=0.04).

C.14 HD 56537

TABLE C.14: HD 56537 Visibilities

MJD	B (m)	ψ (°)	V	σV
54156.743	306.6	75.8	0.581	0.066
54156.754	304.7	78.5	0.613	0.051
54156.765	303.1	81.3	0.663	0.076
54156.777	302.0	84.3	0.690	0.081
54156.789	301.2	87.5	0.676	0.080
54156.801	301.1	−89.5	0.665	0.085
54156.812	301.4	−86.7	0.677	0.053
54170.746	301.5	4.3	0.644	0.083
54170.760	301.1	0.7	0.661	0.056
54170.772	301.2	177.5	0.648	0.052
54170.784	301.9	174.4	0.648	0.063
54170.797	303.3	171.0	0.557	0.066
54409.003	317.6	25.1	0.720	0.066
54409.013	315.3	23.1	0.702	0.049
54409.018	322.4	22.8	0.919	0.066
54409.038	309.5	17.7	0.642	0.074
54409.048	307.6	15.5	0.584	0.058
54457.879	315.4	23.2	0.604	0.056
54457.889	313.1	21.2	0.561	0.041
54457.914	307.6	15.5	0.658	0.045
54457.923	306.0	13.4	0.672	0.049
54457.933	304.4	11.0	0.601	0.042
54457.947	302.5	7.4	0.699	0.096

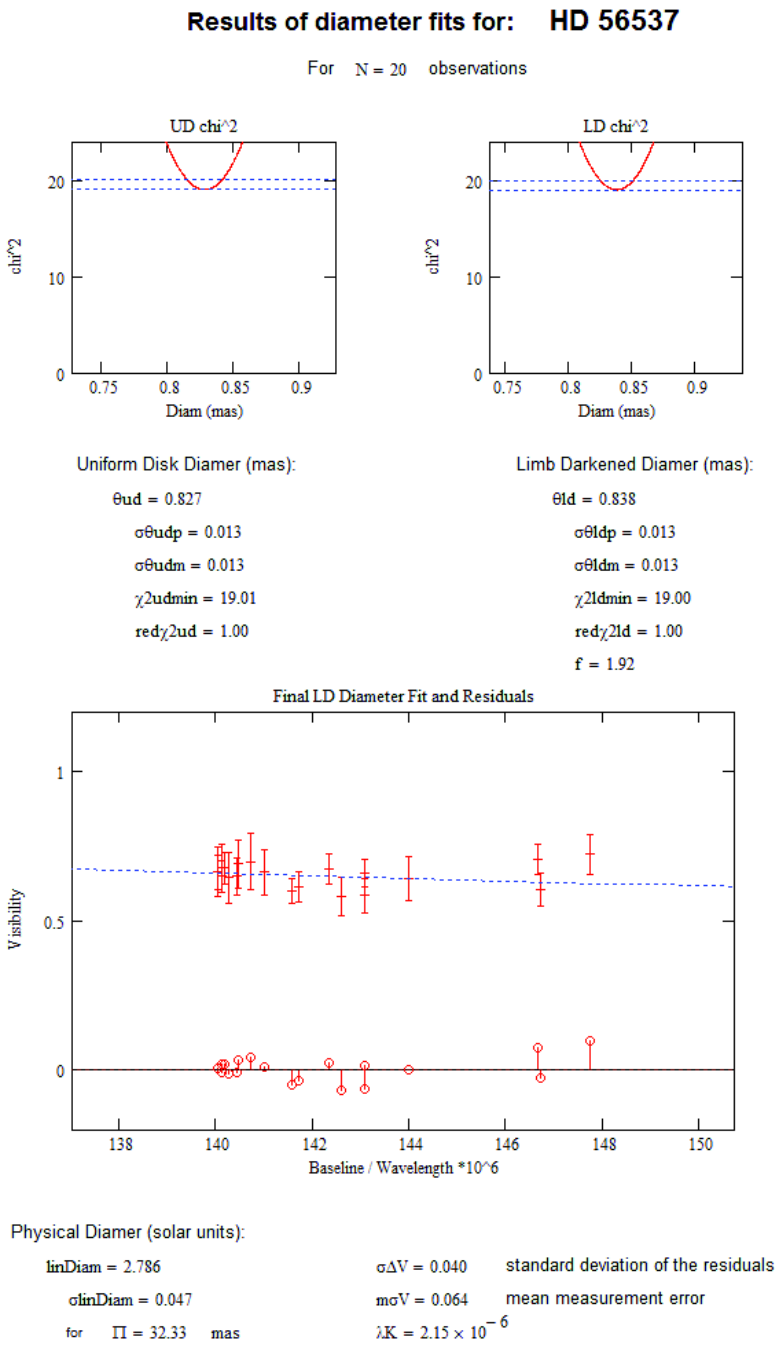

FIGURE C.27: **Diameter fit for HD 56537**

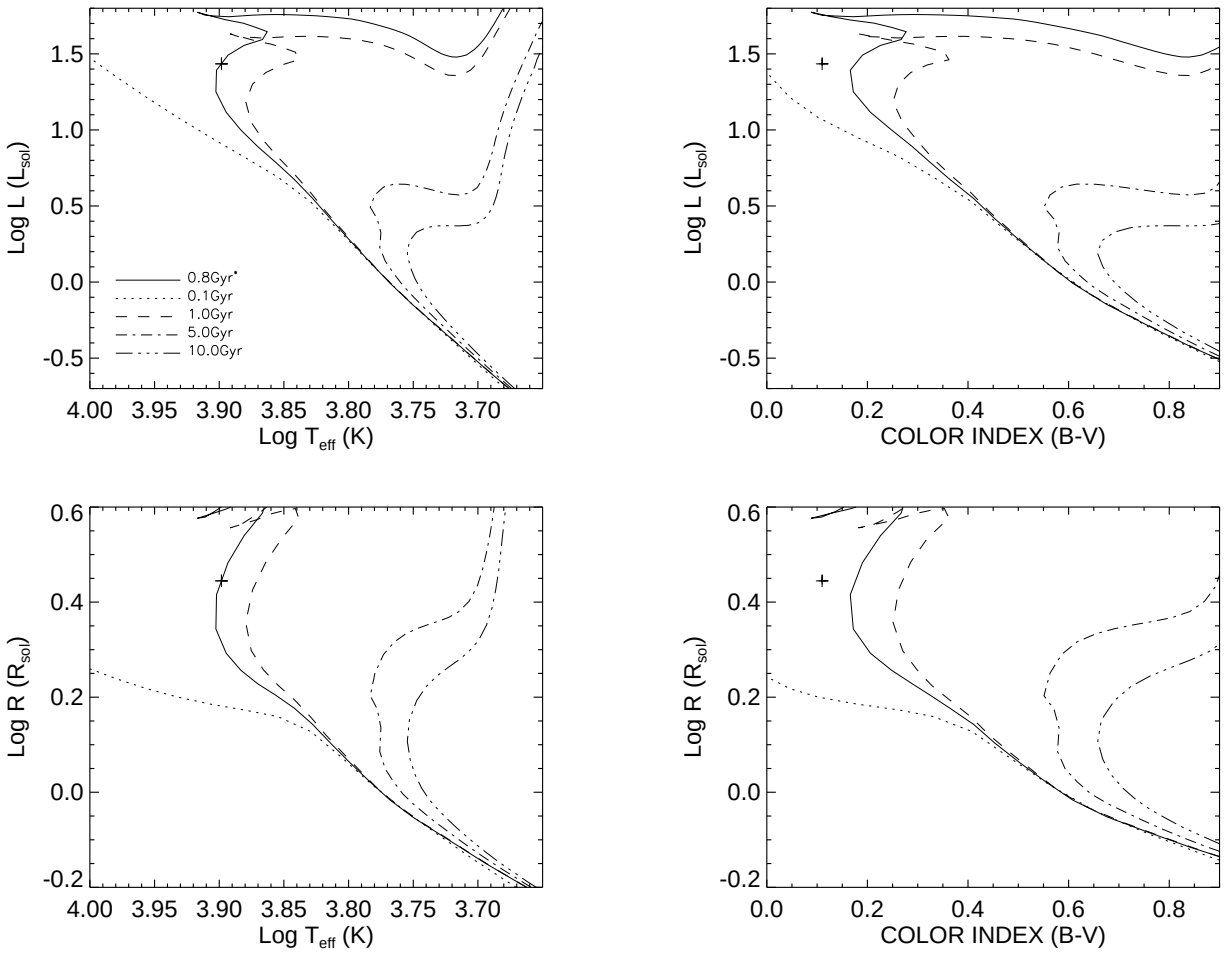

FIGURE C.28: **Y^2 Model Isochrones for HD 56537:** HD 56537 data (and 1-σ errors) plotted against Y^2 models isochrones ([α/Fe]=0.0, [Fe/H]=0.0).

C.15 HD 58946

Table C.15: HD 58946 Visibilities

MJD	B (m)	ψ (°)	V	σV
54125.881	326.5	87.6	0.609	0.046
54125.896	326.4	−88.9	0.461	0.070
54125.907	326.6	−86.2	0.507	0.094
54125.925	327.1	−82.0	0.689	0.061
54125.936	327.5	−79.5	0.564	0.054
54125.953	328.4	−75.5	0.542	0.040
54420.805	286.1	48.1	0.746	0.100
54420.815	291.9	47.4	0.694	0.072
54420.821	295.7	46.9	0.534	0.074
54420.842	306.7	44.9	0.666	0.077
54420.848	309.7	44.3	0.586	0.072
54420.854	312.2	43.6	0.585	0.045
54420.861	314.5	42.9	0.665	0.048
54421.800	284.2	48.3	0.761	0.059
54421.807	289.0	47.8	0.711	0.052
54421.815	293.9	47.2	0.656	0.064
54421.828	301.4	46.0	0.664	0.065
54421.836	305.3	45.3	0.654	0.063
54421.844	309.0	44.4	0.608	0.052
54421.852	312.5	43.5	0.622	0.054

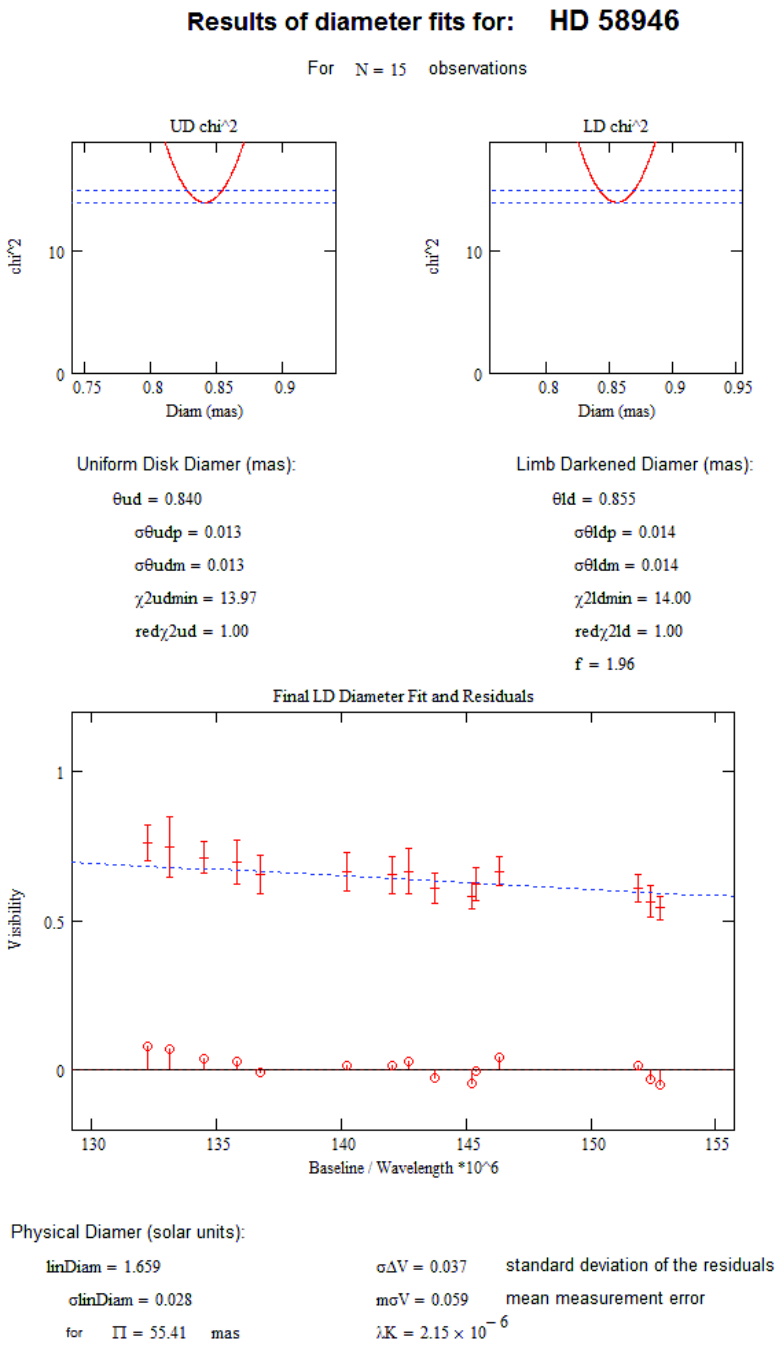

FIGURE C.29: **Diameter fit for HD 58946**

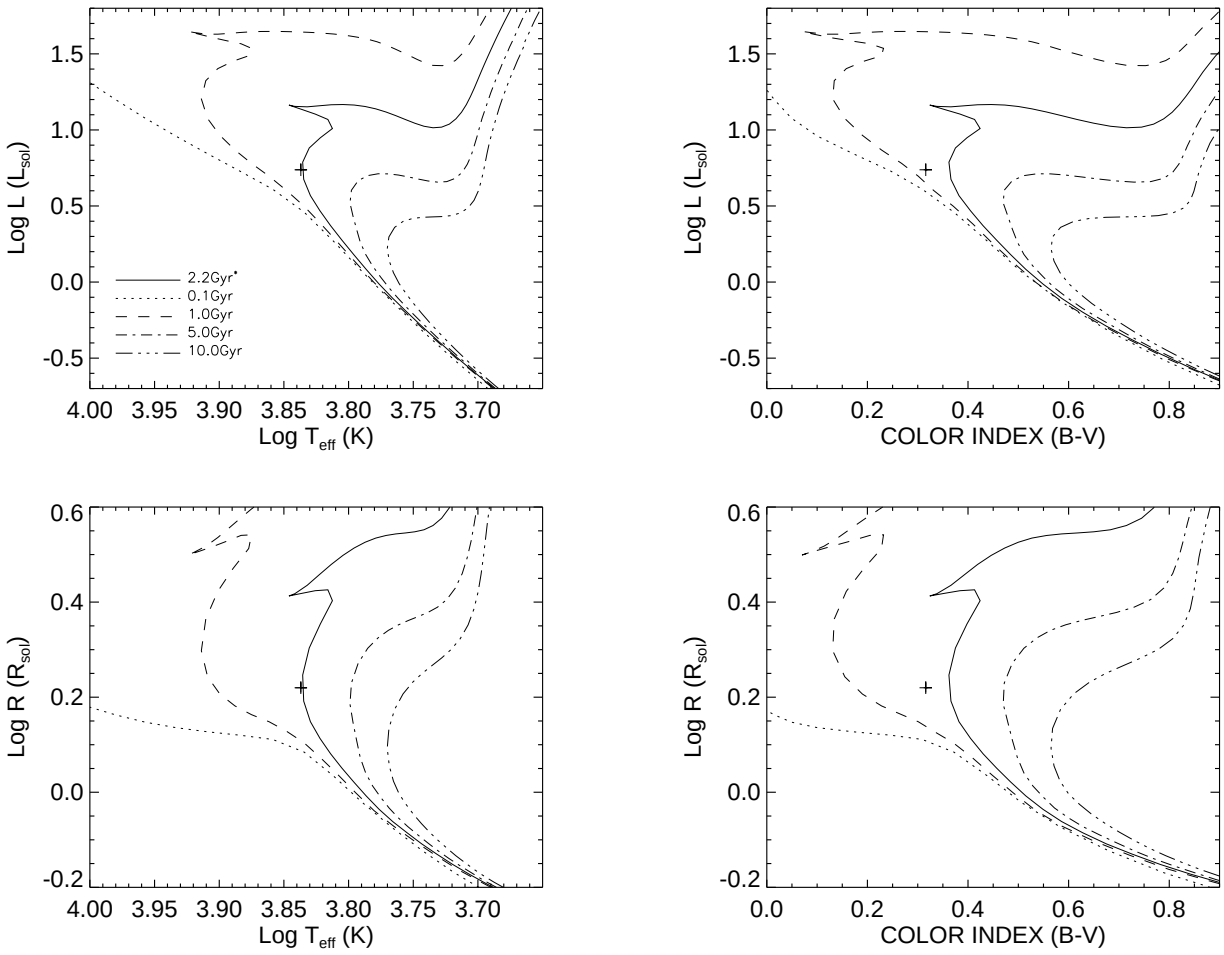

FIGURE C.30: **Y^2 Model Isochrones for HD 58946:** HD 58946 data (and 1-σ errors) plotted against Y^2 models isochrones ([α/Fe]=0.0, [Fe/H]=−0.31).

C.16 HD 81937

TABLE C.16: HD 81937 Visibilities

MJD	B (m)	ψ (°)	V	σV
54433.982	213.9	33.1	0.575	0.048
54433.991	215.5	31.0	0.629	0.050
54433.999	216.9	29.1	0.487	0.043
54434.010	218.7	26.4	0.543	0.050
54434.020	220.0	24.0	0.490	0.037
54434.033	221.7	20.7	0.599	0.052
54434.041	222.6	18.7	0.552	0.046
54434.052	223.6	16.0	0.565	0.047
54434.061	224.3	13.9	0.690	0.048

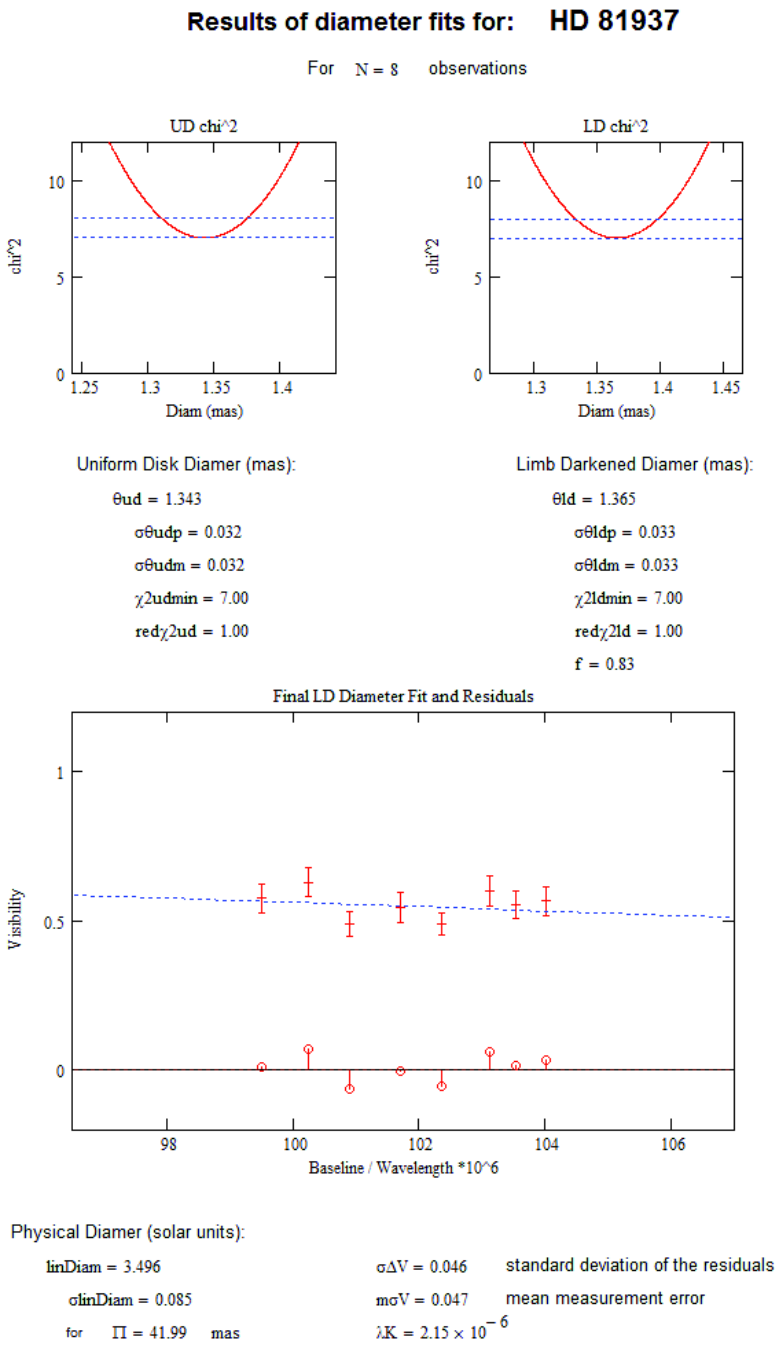

FIGURE C.31: **Diameter fit for HD 81937**

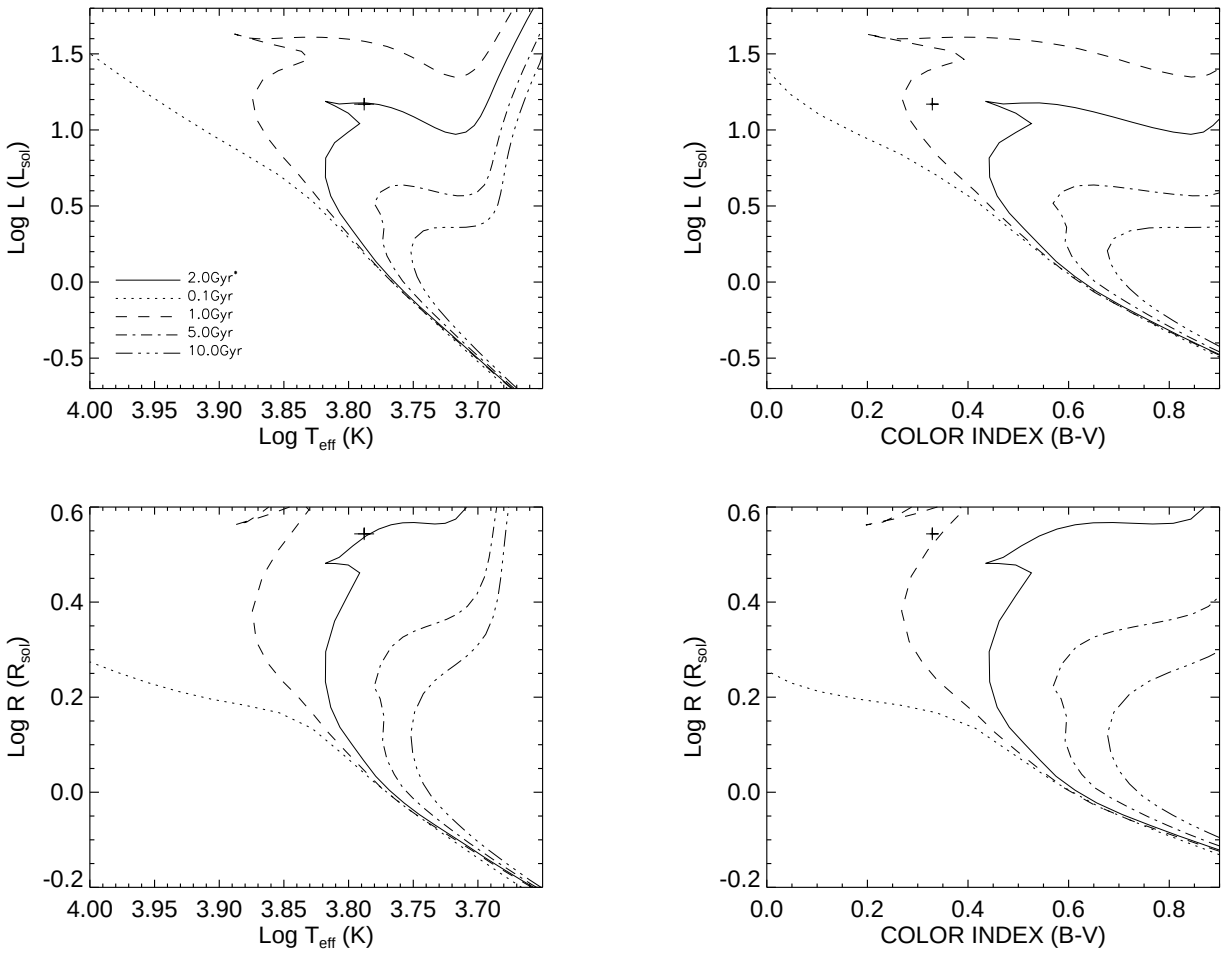

FIGURE C.32: **Y^2 Model Isochrones for HD 81937:** HD 81937 data (and 1-σ errors) plotted against Y^2 models isochrones ([α/Fe]=0.0, [Fe/H]=0.06).

C.17 HD 82328

Table C.17: HD 82328 Visibilities

MJD	B (m)	ψ (°)	V	σV
54406.988	130.600	97.8	0.705	0.1
54406.994	132.670	95.9	0.675	0.1
54407.001	134.650	94.0	0.687	0.1
54407.007	136.490	92.3	0.674	0.1
54407.013	138.260	90.5	0.658	0.1
54407.019	140.110	88.6	0.671	0.1
54407.027	142.220	86.4	0.717	0.1
54407.034	143.800	84.6	0.739	0.1
54407.041	145.340	82.8	0.750	0.1

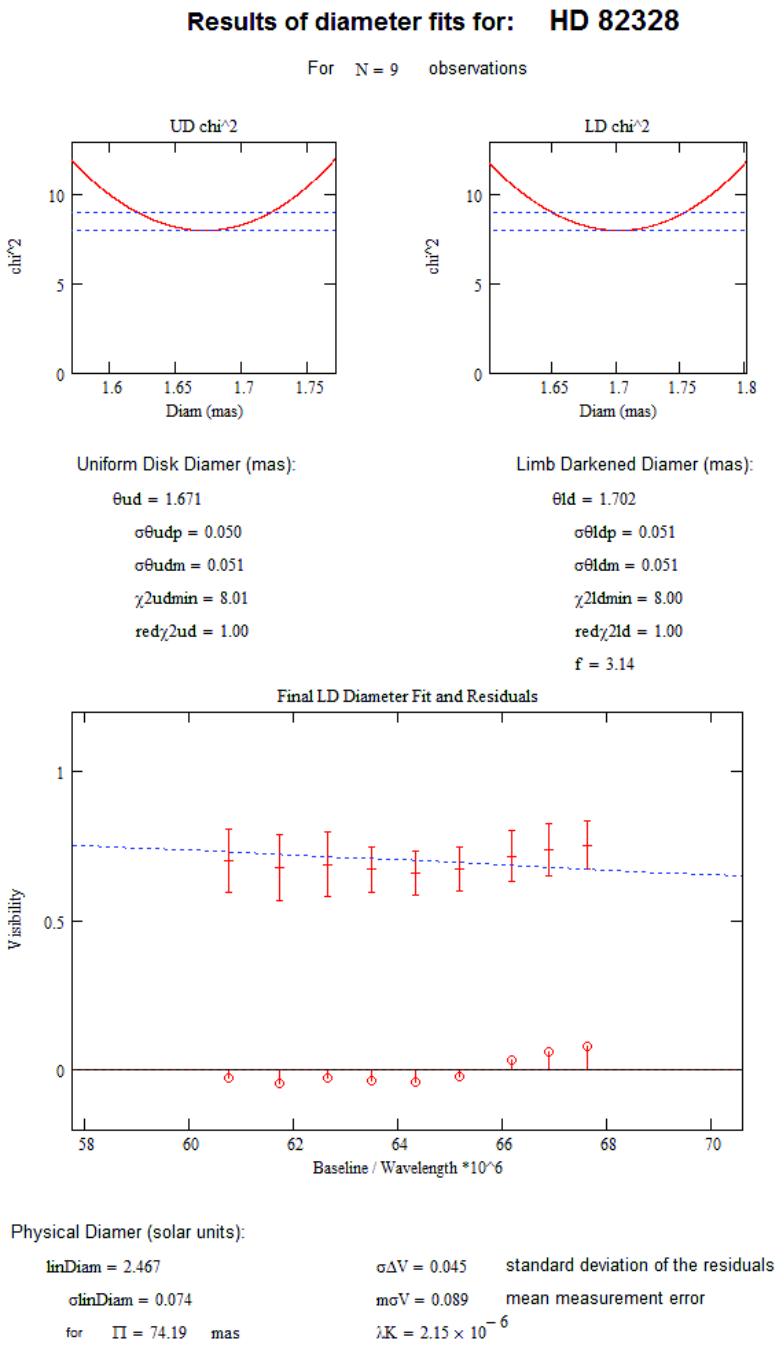

FIGURE C.33: **Diameter fit for HD 82328**

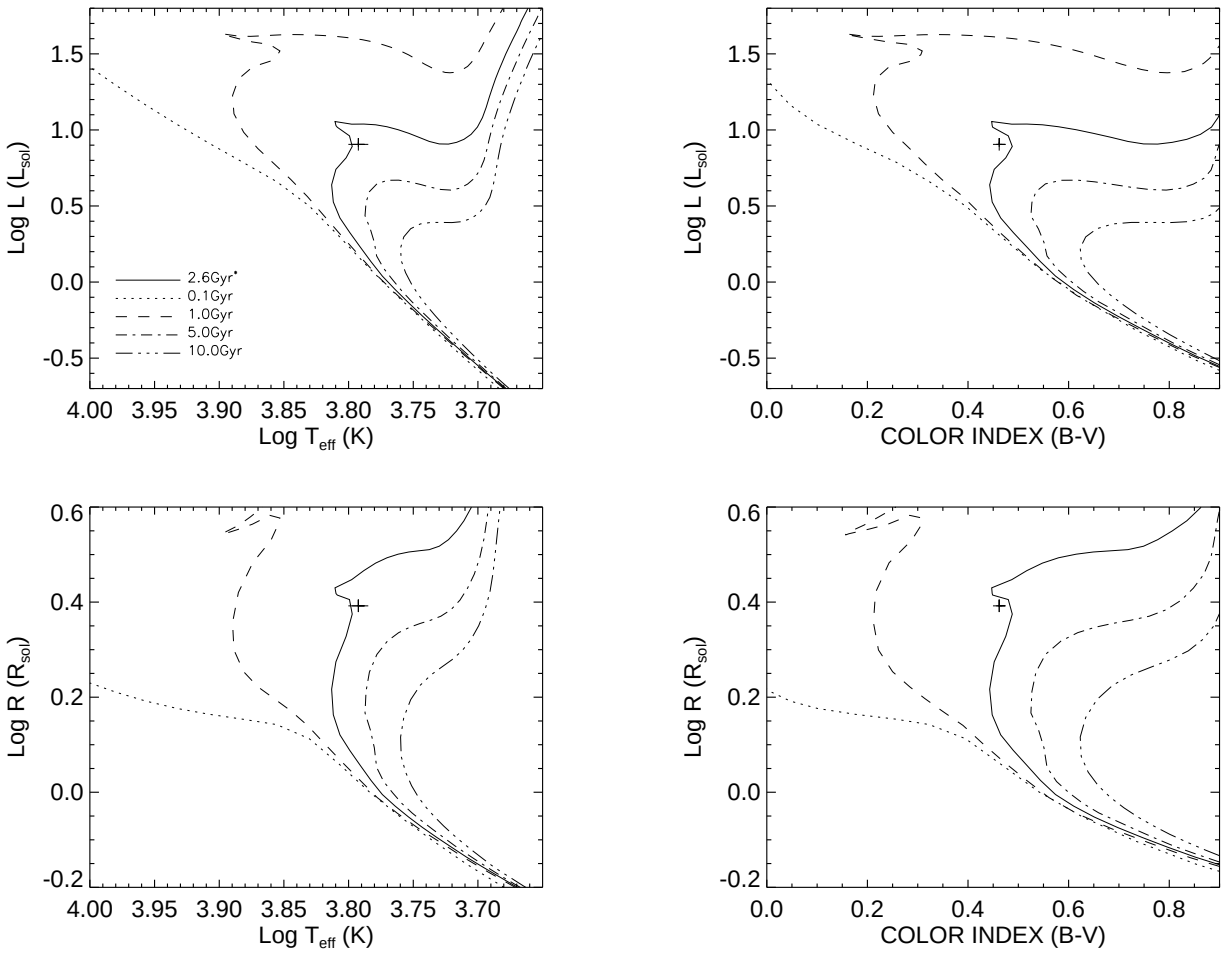

FIGURE C.34: **Y^2 Model Isochrones for HD 82328:** HD 82328 data (and 1-σ errors) plotted against Y^2 models isochrones ([α/Fe]=0.0, [Fe/H]=$-$0.12).

C.18 HD 82885

Table C.18: HD 82885 Visibilities

MJD	B (m)	ψ (°)	V	σV
54134.908	329.9	11.3	0.643	0.071
54134.921	329.7	8.2	0.530	0.065
54407.992	255.7	98.1	0.767	0.074
54408.004	265.9	95.4	0.734	0.064
54408.012	272.3	93.7	0.716	0.074
54408.020	278.8	91.8	0.725	0.062
54408.034	288.4	88.8	0.719	0.061
54408.042	293.2	87.2	0.756	0.066
54408.050	297.4	85.5	0.631	0.057
54411.935	289.8	48.3	0.655	0.064
54411.943	294.2	47.5	0.731	0.114
54411.951	298.5	46.6	0.748	0.136
54411.958	302.3	45.7	0.720	0.087
54411.966	305.9	44.7	0.726	0.075
54411.974	309.2	43.8	0.671	0.080
54411.981	312.3	42.7	0.685	0.080
54411.989	314.9	41.7	0.706	0.085
54412.009	321.1	38.6	0.610	0.091
54458.854	312.8	42.6	0.694	0.068
54458.866	316.9	40.8	0.704	0.060
54458.878	320.4	39.0	0.618	0.048
54458.889	323.1	37.3	0.611	0.058
54458.901	325.3	35.4	0.575	0.045

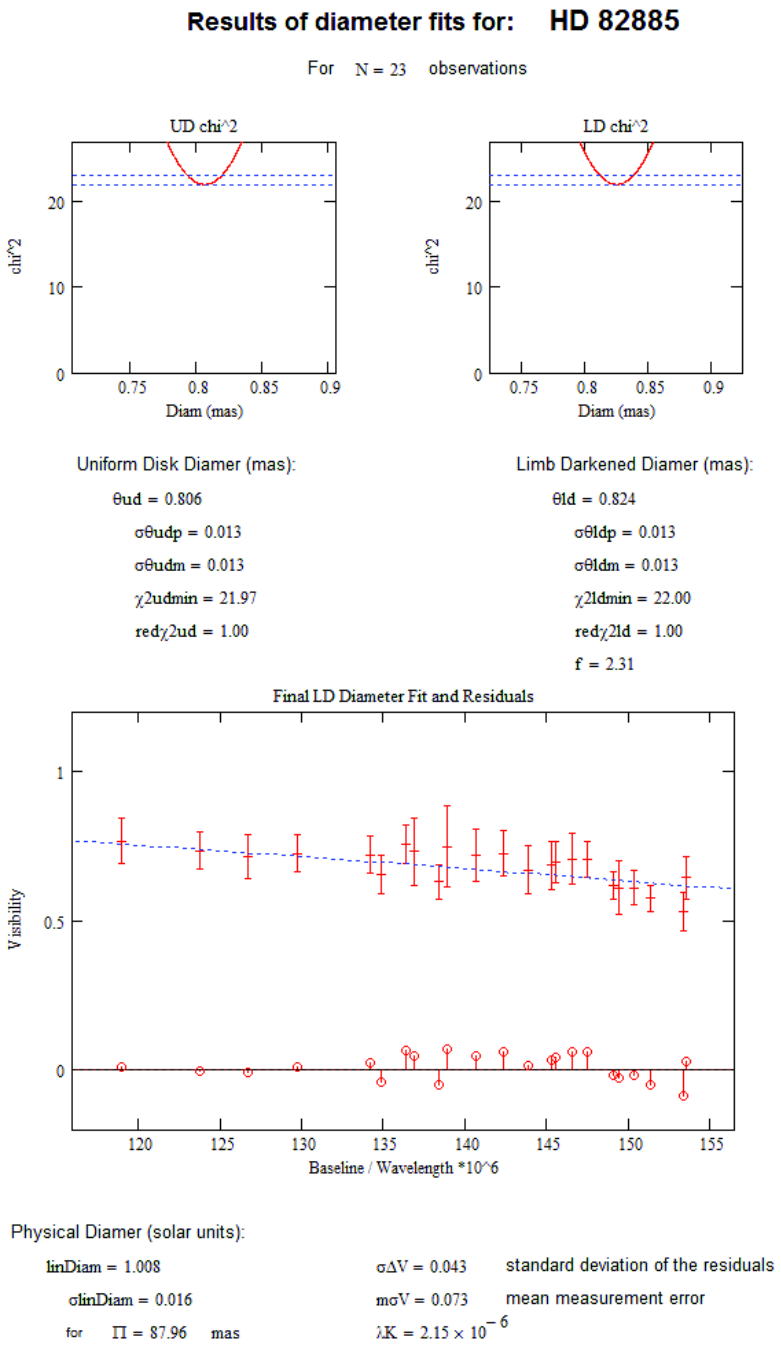

FIGURE C.35: **Diameter fit for HD 82885**

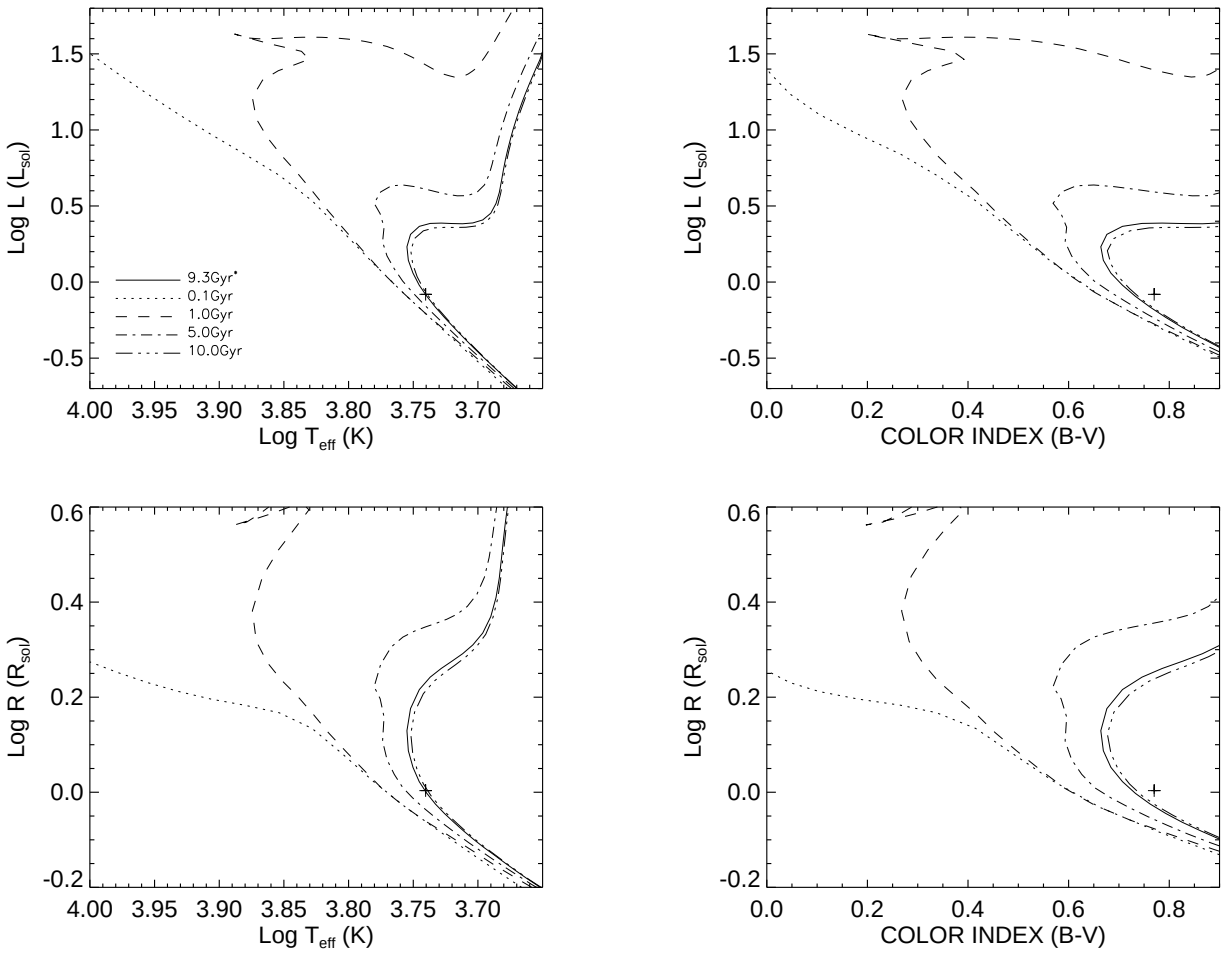

FIGURE C.36: **Y^2 Model Isochrones for HD 82885:** HD 82885 data (and 1-σ errors) plotted against Y^2 models isochrones ([α/Fe]=0.0, [Fe/H]=0.06).

C.19 HD 86728

TABLE C.19: HD 86728 Visibilities

MJD	B (m)	ψ (°)	V	σV
54419.878	259.1	50.1	0.727	0.076
54419.889	268.6	49.6	0.697	0.067
54419.901	277.0	49.0	0.704	0.096
54419.912	285.1	48.3	0.801	0.087
54419.924	292.6	47.4	0.722	0.084
54419.944	303.5	45.6	0.693	0.060
54419.955	308.7	44.5	0.705	0.069
54419.968	314.2	43.0	0.658	0.077
54419.976	316.9	42.1	0.640	0.083
54419.984	319.5	41.1	0.598	0.069
54420.889	270.1	49.5	0.710	0.087
54420.895	275.0	49.2	0.586	0.081
54458.846	307.9	44.7	0.684	0.035
54458.863	314.6	42.9	0.727	0.044
54458.875	318.7	41.4	0.612	0.052
54458.886	321.9	39.9	0.647	0.048
54458.897	324.5	38.4	0.668	0.050
54458.908	326.6	36.7	0.714	0.047
54786.948	307.8	44.7	0.660	0.059
54786.957	311.6	43.7	0.643	0.064
54786.965	314.7	42.8	0.682	0.068
54786.983	320.5	40.6	0.764	0.065
54786.991	322.7	39.5	0.655	0.053
54787.007	326.0	37.3	0.704	0.055
54787.029	329.0	33.7	0.706	0.046
54787.042	330.0	31.6	0.648	0.056
54787.051	330.4	30.0	0.767	0.068

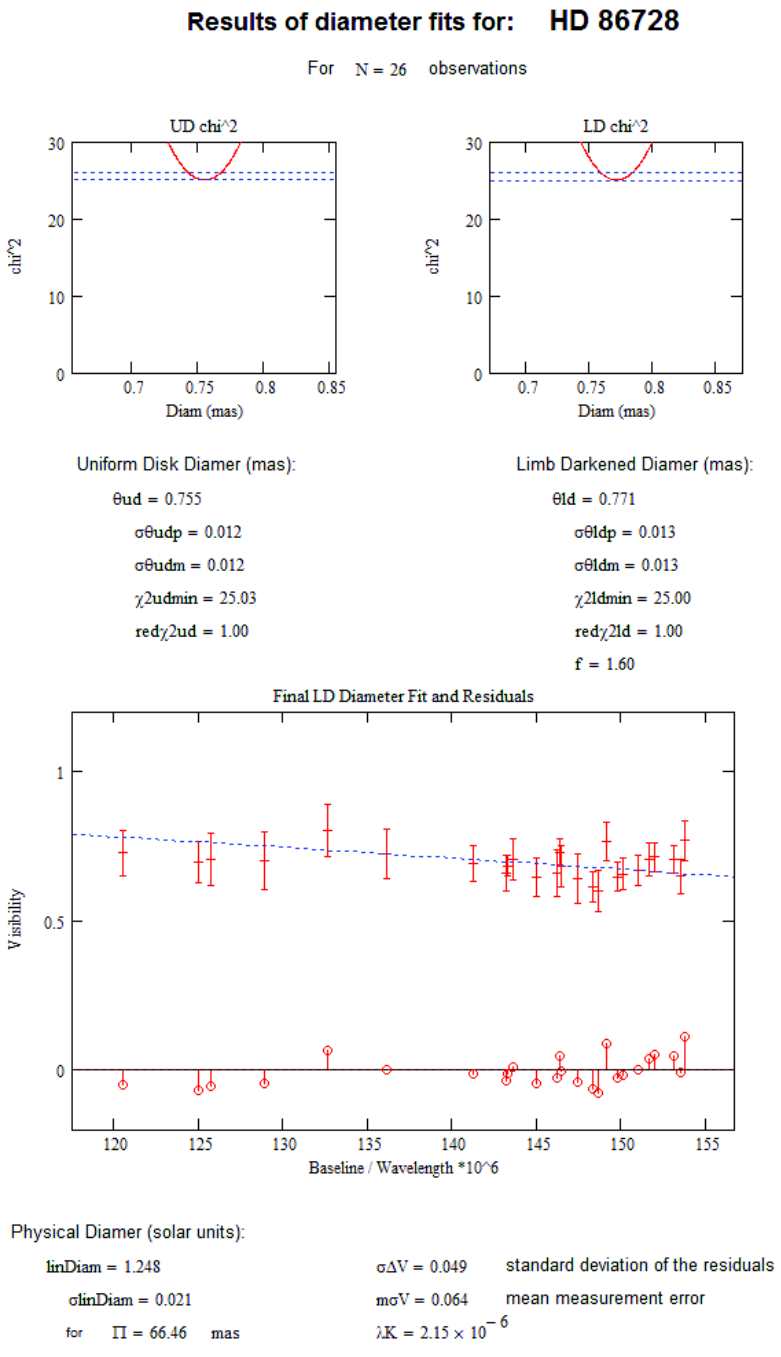

FIGURE C.37: **Diameter fit for HD 86728**

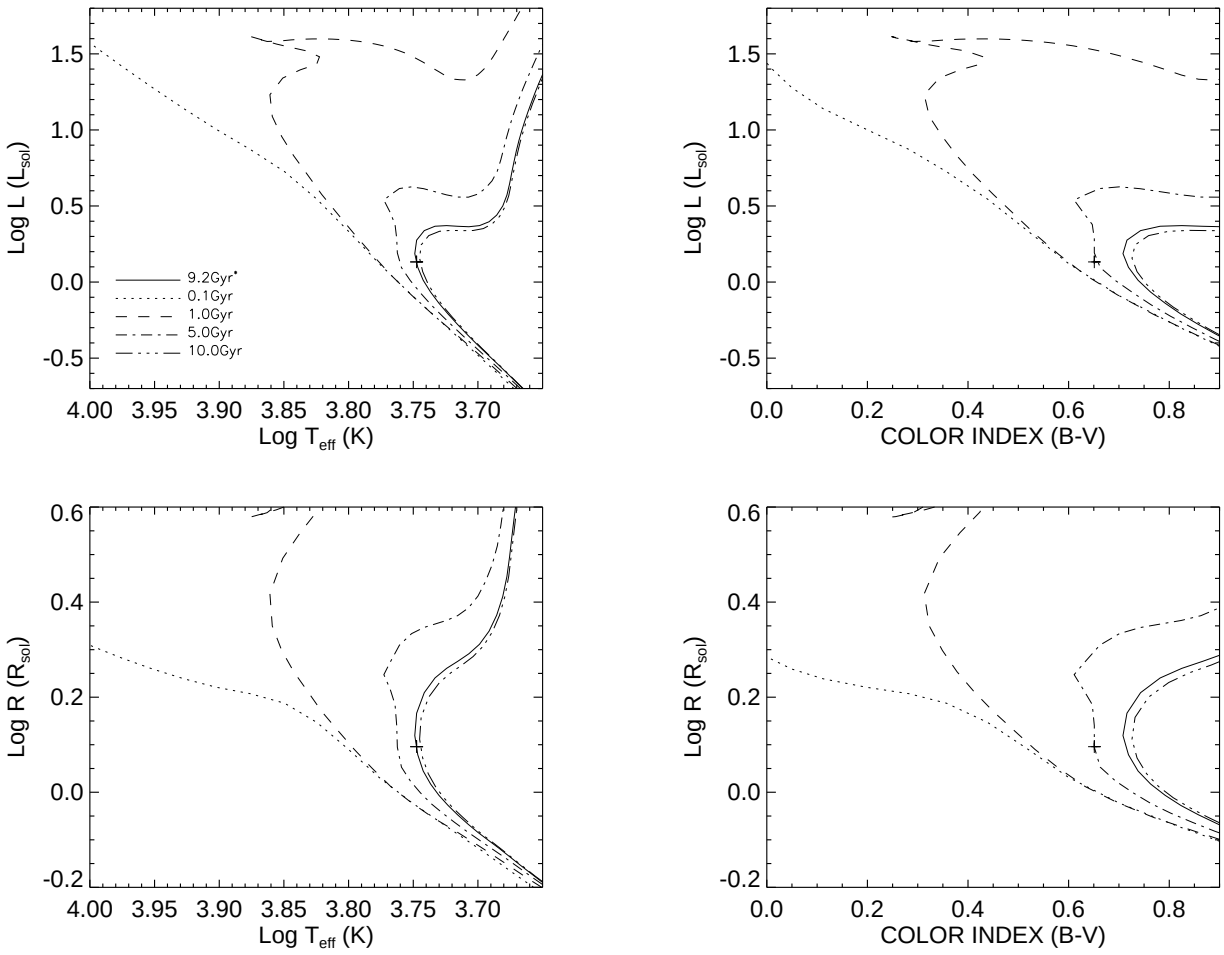

FIGURE C.38: **Y^2 Model Isochrones for HD 86728:** HD 86728 data (and 1-σ errors) plotted against Y^2 models isochrones ([α/Fe]=0.0, [Fe/H]=0.2).

C.20 HD 90839

Table C.20: HD 90839 Visibilities

MJD	B (m)	ψ (°)	V	σV
54420.922	231.2	65.5	0.732	0.069
54420.928	235.6	64.2	0.819	0.050
54420.935	240.8	62.7	0.820	0.069
54420.951	251.7	59.3	0.710	0.054
54420.957	255.4	58.1	0.721	0.045
54420.968	262.5	55.6	0.784	0.046
54420.975	266.1	54.3	0.786	0.047
54420.980	269.2	53.1	0.759	0.052
54420.987	272.5	51.8	0.734	0.049
54420.993	275.8	50.4	0.727	0.039
54573.688	311.4	25.3	0.718	0.097
54573.688	311.4	25.3	0.639	0.138
54573.710	314.6	20.1	0.690	0.119
54573.710	314.6	20.1	0.667	0.140
54573.741	317.6	12.6	0.714	0.064
54573.741	317.6	12.6	0.808	0.178
54573.760	318.7	8.2	0.662	0.064
54573.760	318.7	8.2	0.656	0.095
54573.777	319.2	3.8	0.714	0.085
54573.777	319.2	3.8	0.625	0.066

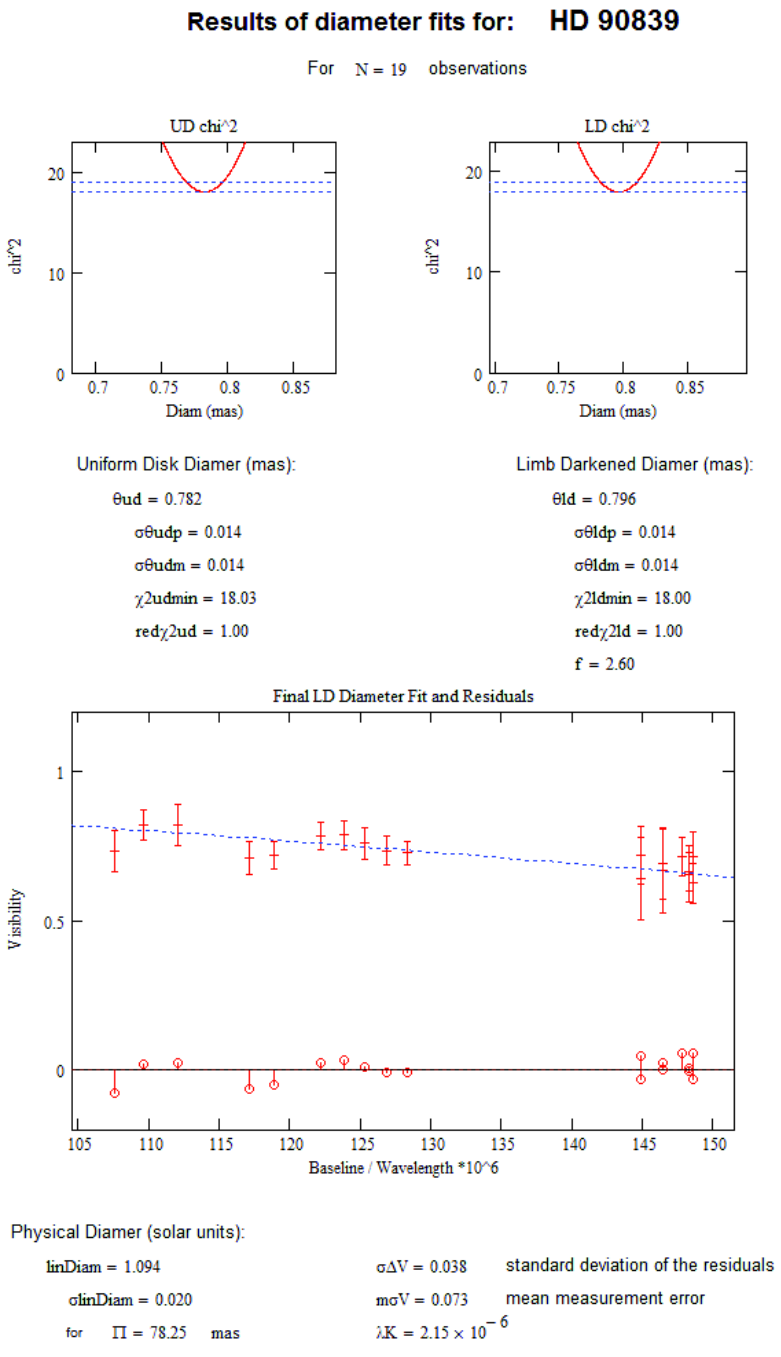

FIGURE C.39: **Diameter fit for HD 90839**

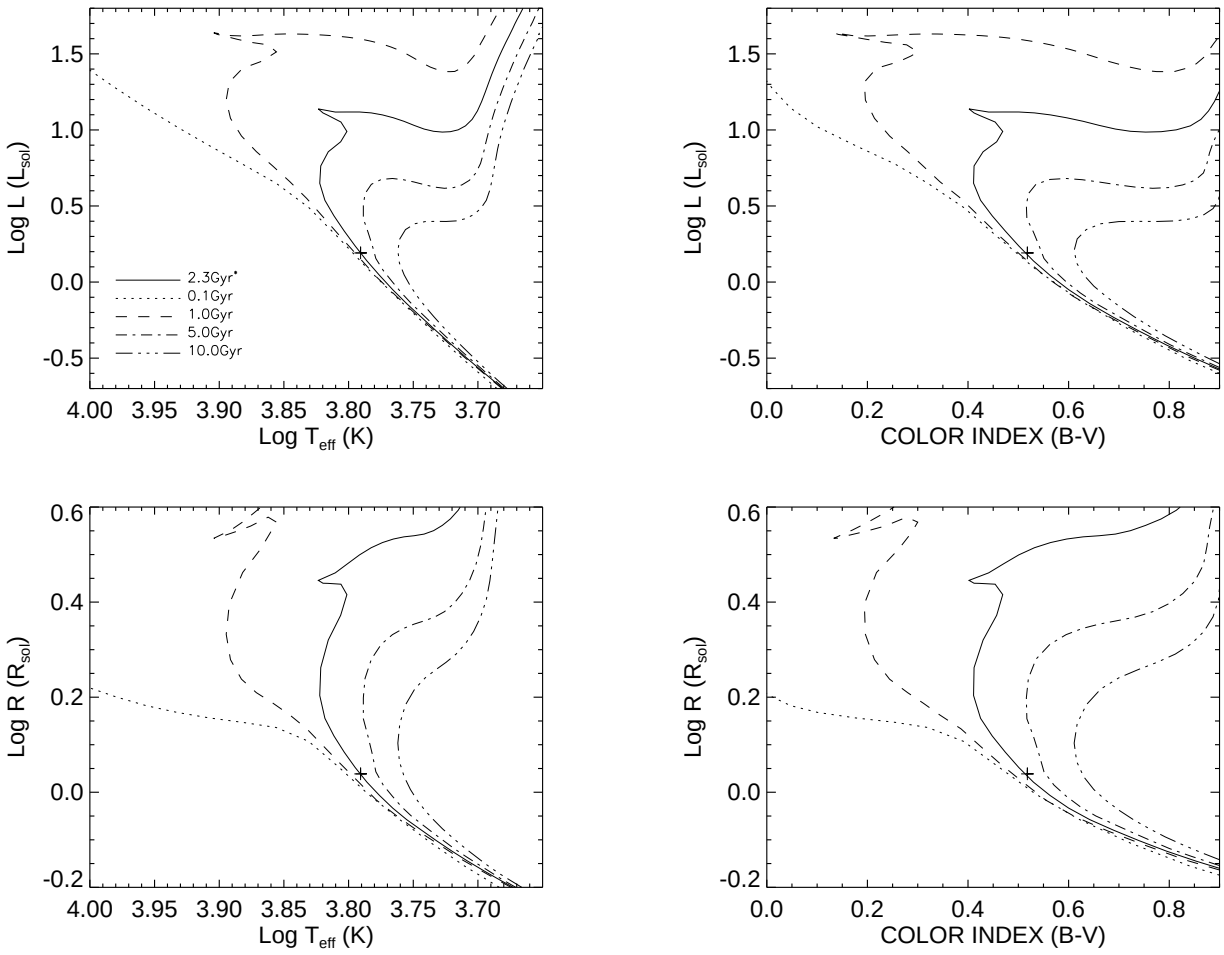

FIGURE C.40: **Y^2 Model Isochrones for HD 90839:** HD 90839 data (and 1-σ errors) plotted against Y^2 models isochrones ([α/Fe]=0.0, [Fe/H]=−0.16).

C.21 HD 97603

TABLE C.21: HD 97603 Visibilities

MJD	B (m)	ψ (°)	V	σV
54152.901	316.7	72.6	0.303	0.025
54152.912	315.0	74.9	0.323	0.025
54152.923	313.4	77.6	0.275	0.029
54152.934	312.0	80.3	0.278	0.020
54152.945	311.0	82.8	0.263	0.016
54152.958	310.2	86.2	0.252	0.012
54152.970	309.8	89.3	0.258	0.012
54152.981	309.9	−88.1	0.231	0.020
54152.992	310.4	−85.2	0.255	0.014
54153.003	311.1	−82.5	0.246	0.020
54169.825	322.0	66.2	0.268	0.038
54170.864	314.8	75.3	0.284	0.038
54170.876	313.2	78.0	0.270	0.023
54170.887	304.6	78.4	0.291	0.024
54170.901	310.6	84.4	0.284	0.034
54170.915	310.0	87.7	0.272	0.037

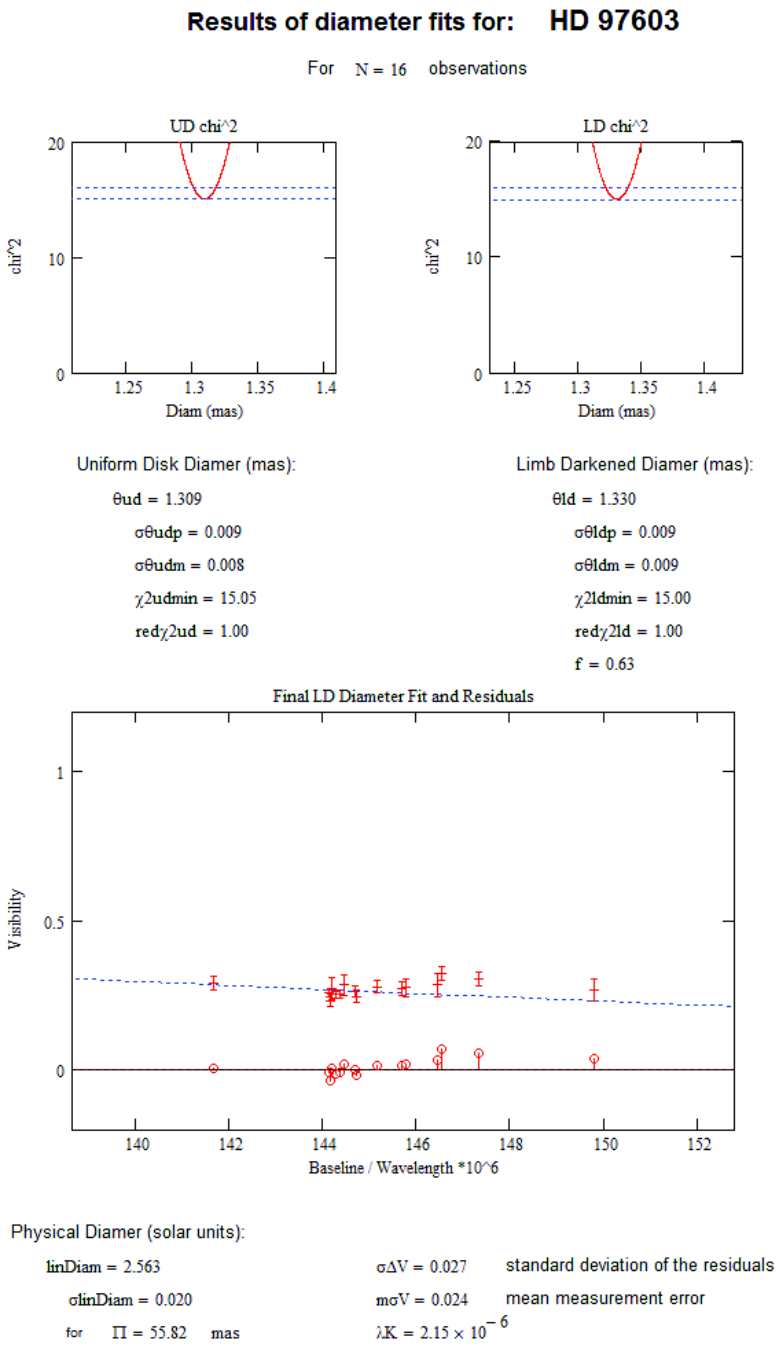

FIGURE C.41: **Diameter fit for HD 97603**

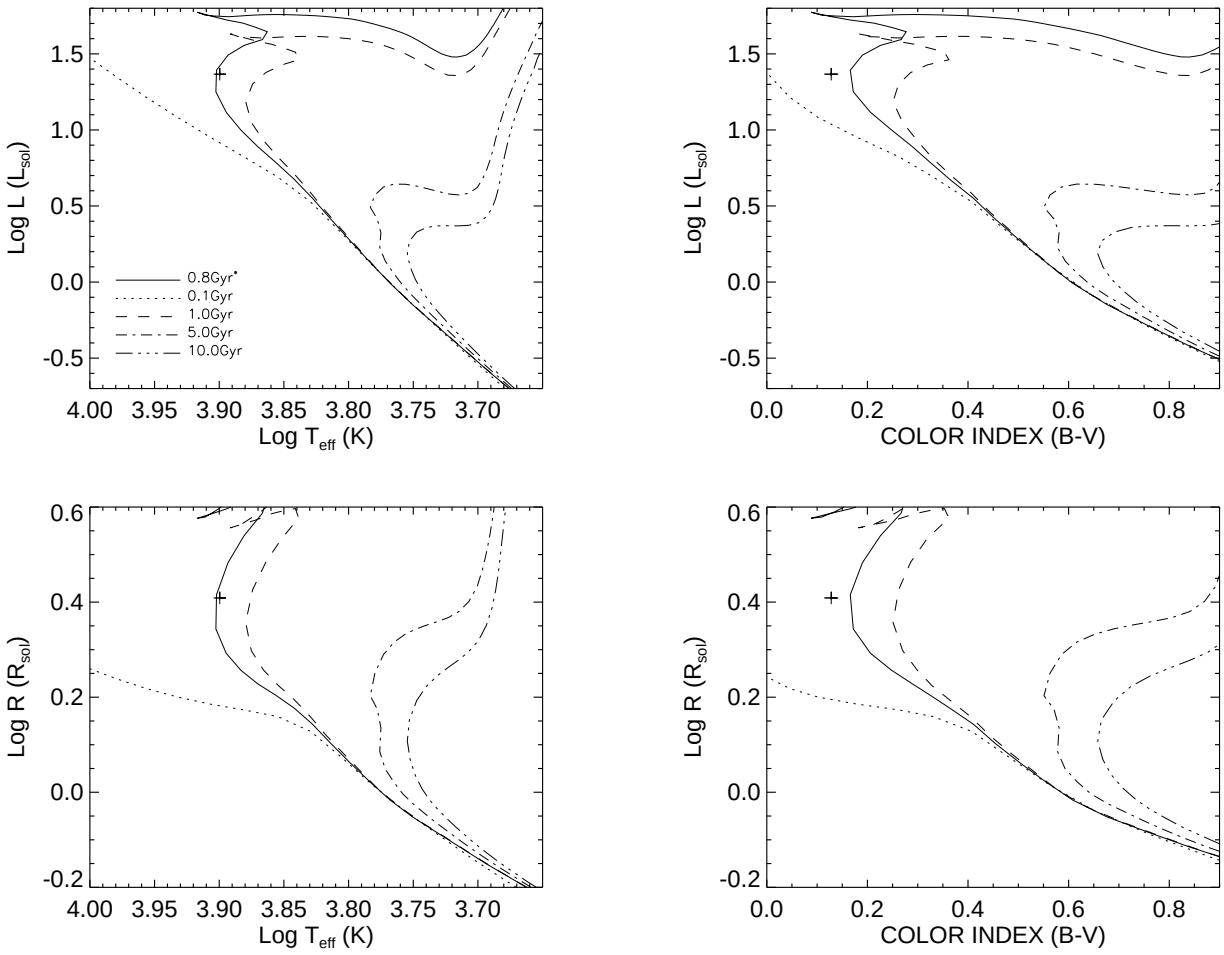

FIGURE C.42: **Y^2 Model Isochrones for HD 97603:** HD 97603 data (and 1-σ errors) plotted against Y^2 models isochrones ([α/Fe]=0.0, [Fe/H]=0.0).

C.22 HD 101501

Table C.22: HD 101501 Visibilities

MJD	B (m)	ψ (°)	V	σV
54420.003	294.4	47.3	0.620	0.054
54420.014	300.4	46.2	0.645	0.068
54420.023	304.9	45.2	0.605	0.045
54420.040	312.1	43.2	0.612	0.056
54420.050	315.6	41.9	0.594	0.068
54420.059	318.6	40.7	0.559	0.050
54420.071	321.9	38.9	0.571	0.043
54458.940	314.5	42.4	0.555	0.045
54458.963	321.5	39.1	0.539	0.040
54458.992	327.2	34.6	0.586	0.041

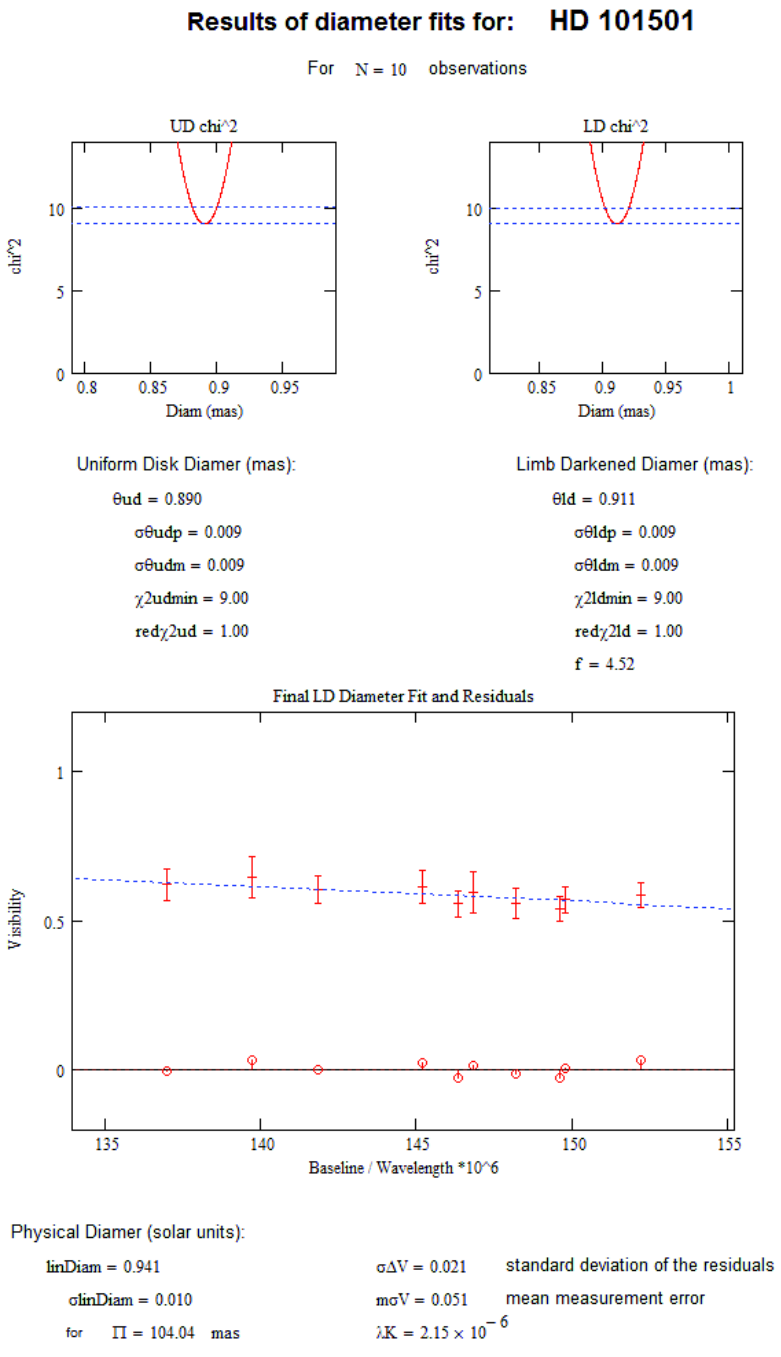

FIGURE C.43: **Diameter fit for HD 101501**

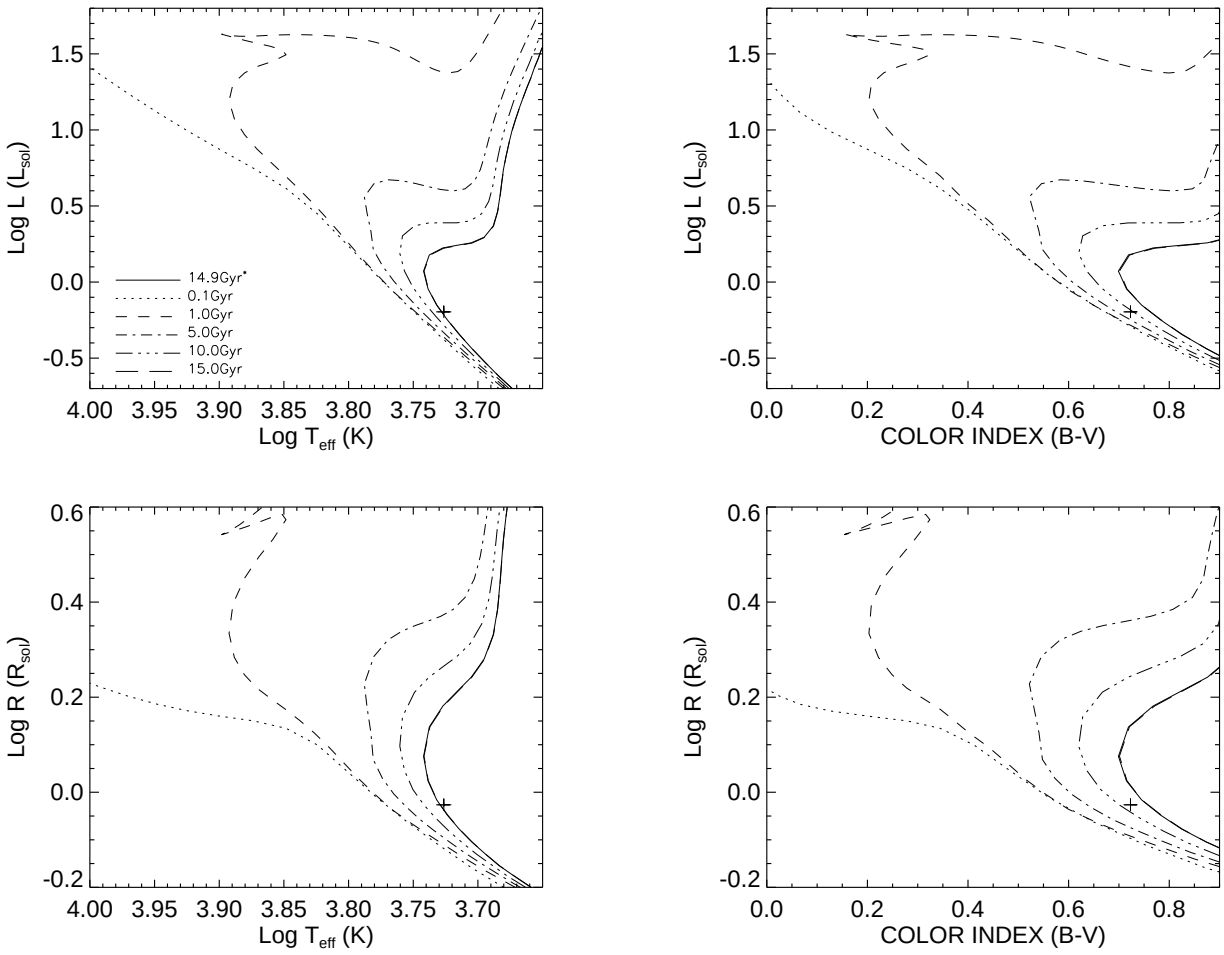

FIGURE C.44: **Y^2 Model Isochrones for HD 101501:** HD 101501 data (and 1-σ errors) plotted against Y^2 models isochrones ([α/Fe]=0.0, [Fe/H]=−0.12).

C.23 HD 102870

Table C.23: HD 102870 Visibilities

MJD	B (m)	ψ (°)	V	σV
54168.947	256.5	87.5	0.370	0.040
54168.959	256.3	−88.9	0.342	0.024
54168.970	257.0	−85.5	0.326	0.037
54168.982	258.7	−81.9	0.325	0.026
54168.994	261.4	−78.4	0.327	0.033
54169.017	268.6	−72.2	0.277	0.034
54458.001	314.0	36.3	0.207	0.019
54458.010	310.3	35.3	0.205	0.018
54458.026	303.5	33.3	0.208	0.024
54458.034	299.6	32.0	0.259	0.024
54575.660	197.9	154.7	0.329	0.177
54575.673	205.1	150.6	0.629	0.058
54575.681	209.8	148.3	0.568	0.072
54575.690	215.2	146.0	0.520	0.067
54575.697	219.8	144.2	0.510	0.066
54575.707	225.9	142.0	0.529	0.090
54575.715	230.7	140.4	0.478	0.062
54575.722	235.4	138.9	0.433	0.062
54578.665	316.0	36.9	0.186	0.034
54578.674	312.9	36.0	0.211	0.028
54578.682	309.6	35.1	0.223	0.031
54578.691	305.5	33.9	0.245	0.026
54578.699	302.0	32.8	0.235	0.021
54578.707	298.2	31.5	0.248	0.030
54578.722	290.9	28.9	0.287	0.034
54578.730	287.1	27.4	0.278	0.025
54578.738	283.4	25.9	0.295	0.031
54579.653	319.5	37.8	0.170	0.029
54579.674	311.8	35.7	0.186	0.032
54579.683	308.0	34.6	0.194	0.031
54579.690	304.7	33.6	0.221	0.029
54579.706	297.3	31.2	0.234	0.033
54579.714	293.7	30.0	0.247	0.025
54579.722	289.8	28.5	0.262	0.028

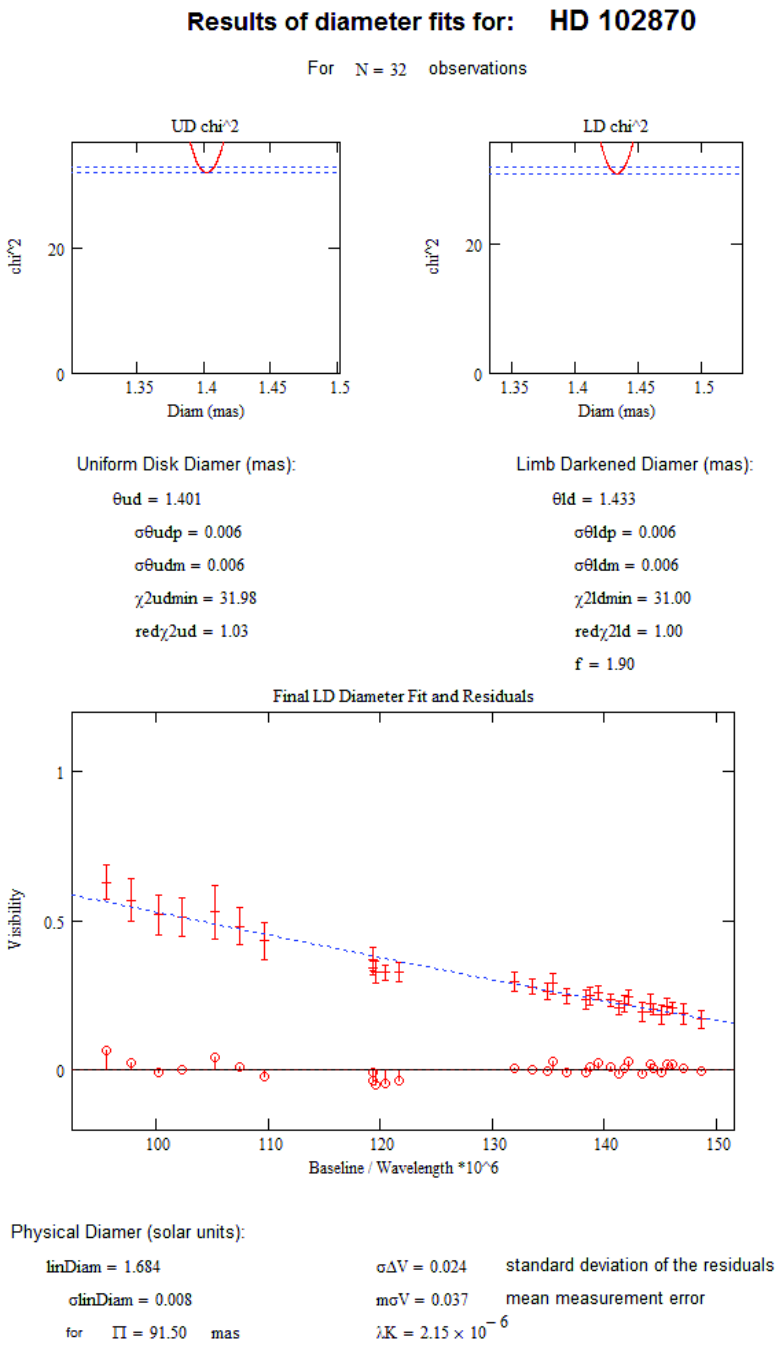

FIGURE C.45: **Diameter fit for HD 102870**

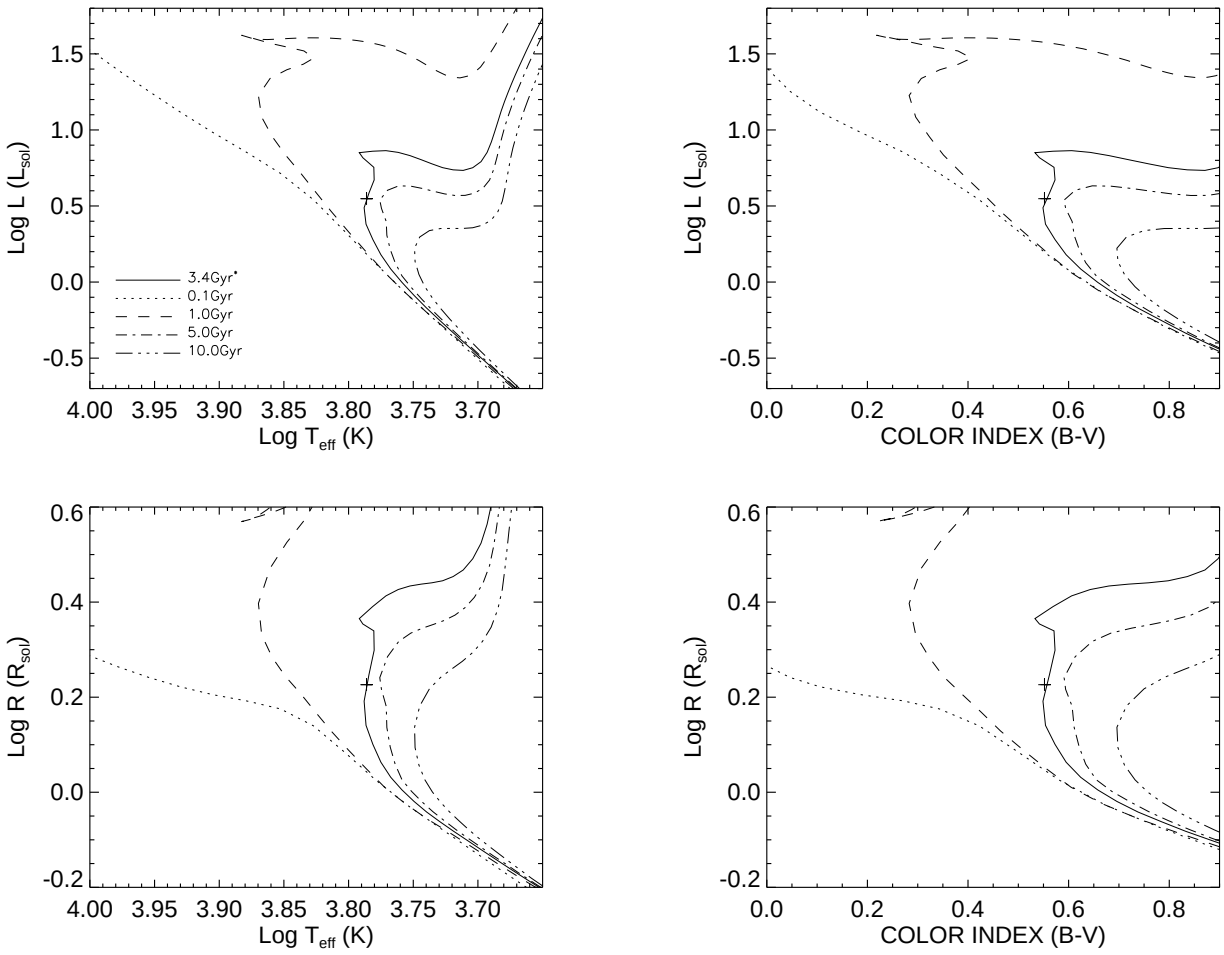

FIGURE C.46: **Y^2 Model Isochrones for HD 102870:** HD 102870 data (and 1-σ errors) plotted against Y^2 models isochrones ([α/Fe]=0.0, [Fe/H]=0.11).

C.24 HD 103095

Table C.24: HD 103095 Visibilities

MJD	B (m)	ψ (°)	V	σV
54421.009	288.2	48.7	0.773	0.090
54421.018	293.6	47.6	0.776	0.056
54421.032	300.7	45.9	0.769	0.066
54421.040	304.7	44.8	0.761	0.064
54421.047	307.5	43.9	0.755	0.057
54421.053	310.1	43.0	0.756	0.064
54421.060	312.5	42.1	0.752	0.073
54458.927	299.9	46.1	0.757	0.036
54458.935	304.1	45.0	0.759	0.043
54458.950	310.3	42.9	0.734	0.055
54458.959	313.5	41.7	0.714	0.053
54458.978	319.5	38.6	0.748	0.042
54458.996	323.7	35.6	0.733	0.031
54459.005	325.2	34.1	0.691	0.051
54459.013	326.5	32.6	0.724	0.047
54459.022	327.5	31.1	0.696	0.053
54459.030	328.5	29.4	0.820	0.071

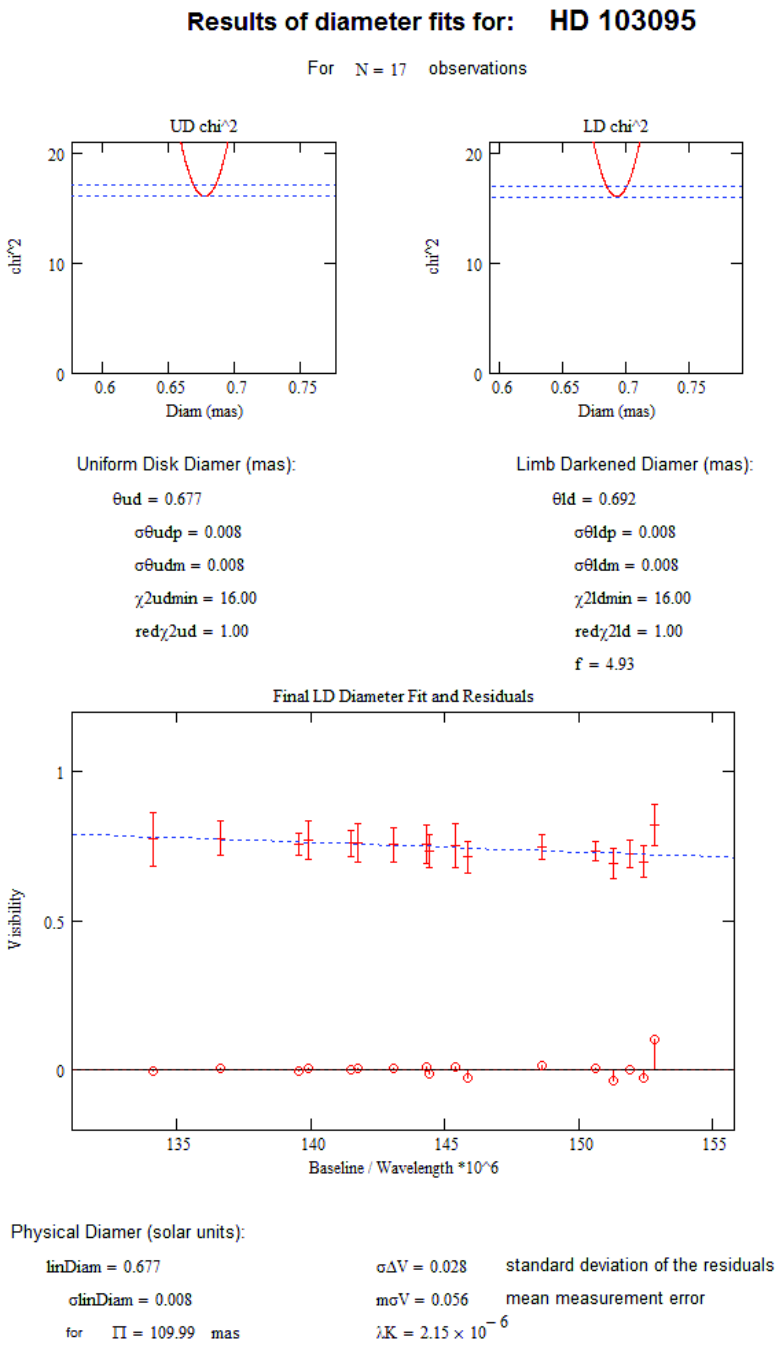

FIGURE C.47: **Diameter fit for HD 103095**

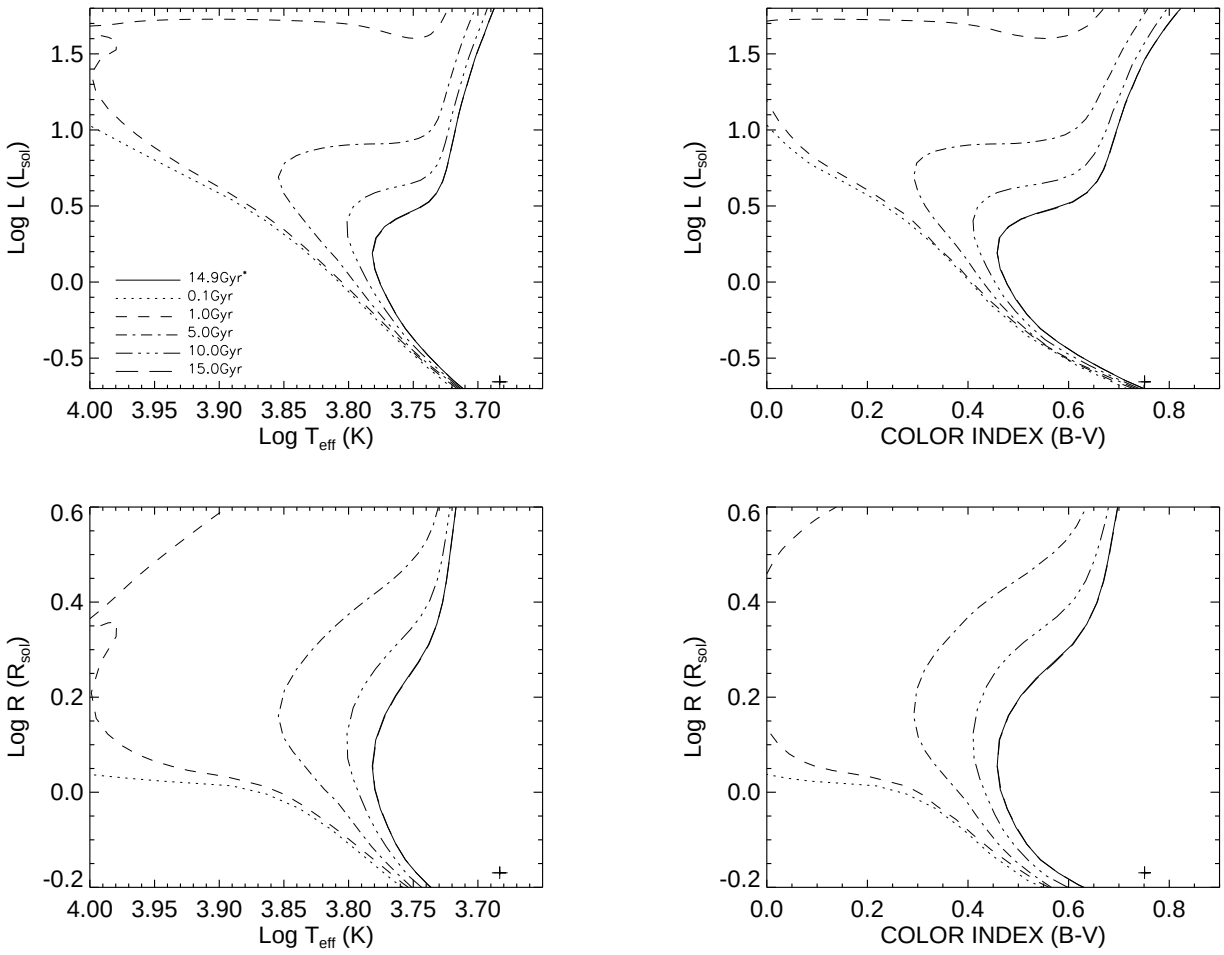

FIGURE C.48: **Y^2 Model Isochrones for HD 103095:** HD 103095 data (and 1-σ errors) plotted against Y^2 models isochrones ([α/Fe]=0.0, [Fe/H]=−1.36).

C.25 HD 109358

Table C.25: HD 109358 Visibilities

MJD	B (m)	ψ (°)	V	σV
54246.844	275.2	-68.4	0.469	0.033
54246.858	274.0	-65.7	0.537	0.046
54246.869	272.7	-63.5	0.498	0.042
54574.650	274.3	174.1	0.478	0.086
54574.666	274.8	169.6	0.424	0.049
54574.677	275.3	166.4	0.592	0.081
54574.688	275.8	163.5	0.452	0.066
54574.699	276.4	160.6	0.536	0.100
54574.666	274.8	169.6	0.332	0.040
54574.677	275.3	166.4	0.430	0.058
54574.688	275.8	163.5	0.353	0.048
54574.699	276.4	160.6	0.434	0.074

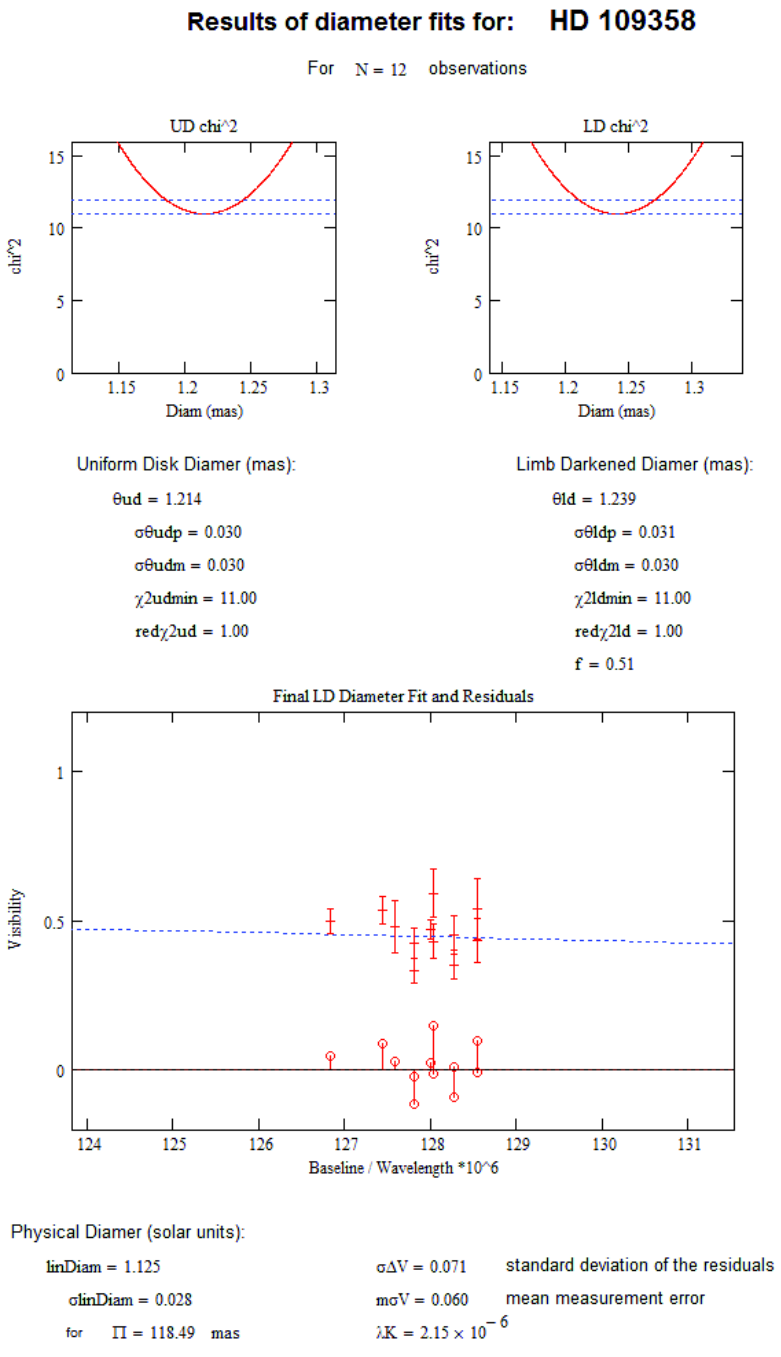

FIGURE C.49: **Diameter fit for HD 109358**

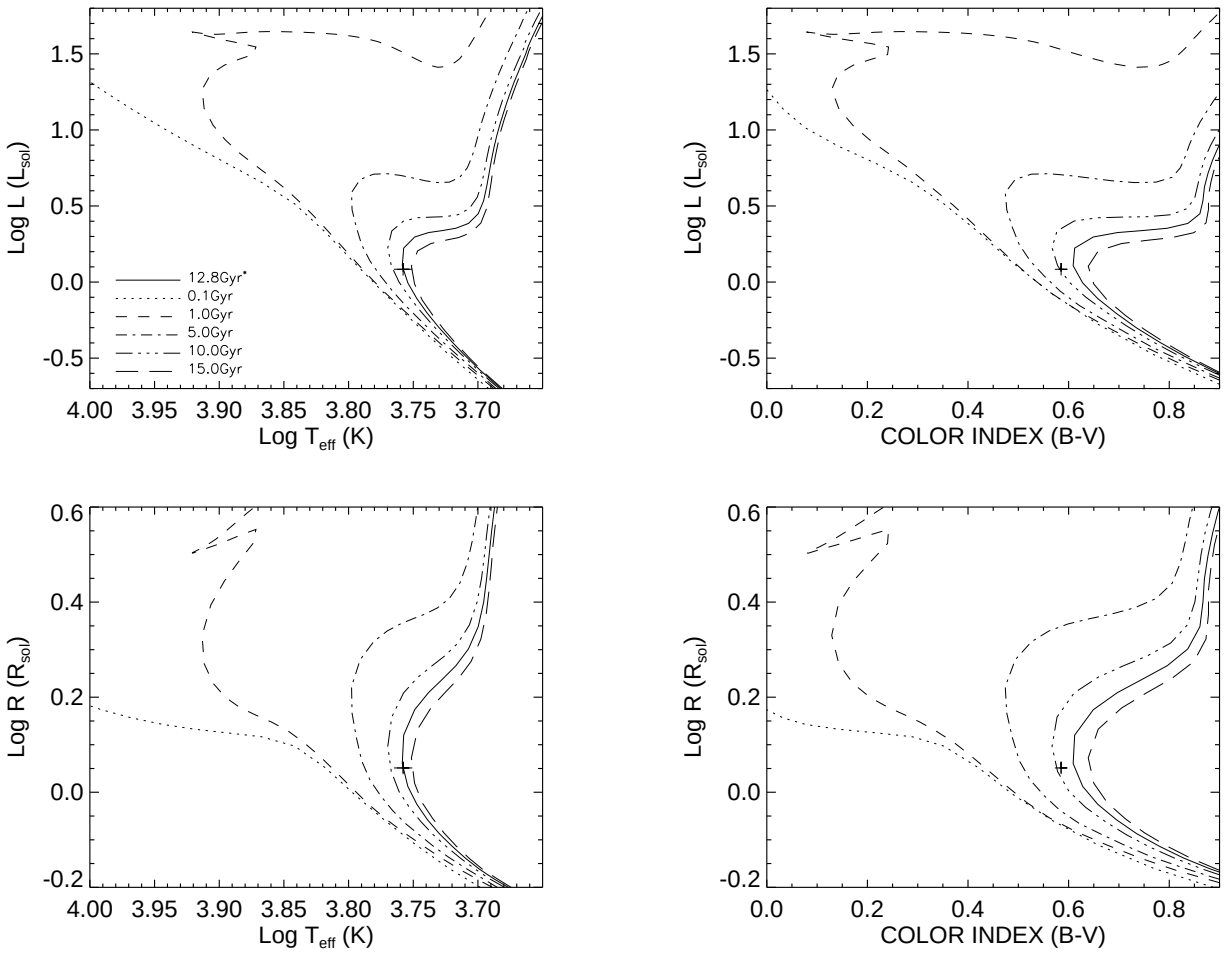

FIGURE C.50: **Y^2 Model Isochrones for HD 109358:** HD 109358 data (and 1-σ errors) plotted against Y^2 models isochrones ([α/Fe]=0.0, [Fe/H]=$-$0.3).

C.26 HD 114710

TABLE C.26: HD 114710 Visibilities

MJD	B (m)	ψ (°)	V	σV
54644.693	322.3	4.2	0.370	0.035
54644.700	322.1	2.4	0.378	0.034
54644.707	322.1	0.8	0.400	0.044
54644.713	322.1	179.3	0.444	0.040
54644.721	322.2	177.3	0.420	0.034
54644.727	322.3	175.9	0.362	0.043
54577.646	254.9	0.5	0.659	0.134
54577.664	255.2	175.4	0.560	0.084
54577.675	256.1	171.8	0.501	0.071
54577.688	257.3	168.1	0.578	0.114
54577.701	259.2	164.2	0.542	0.105
54577.714	261.4	160.5	0.548	0.104
54577.734	265.3	154.9	0.515	0.079
54577.743	267.1	152.6	0.484	0.076
54577.751	268.8	150.6	0.537	0.054
54577.760	270.5	148.5	0.565	0.072

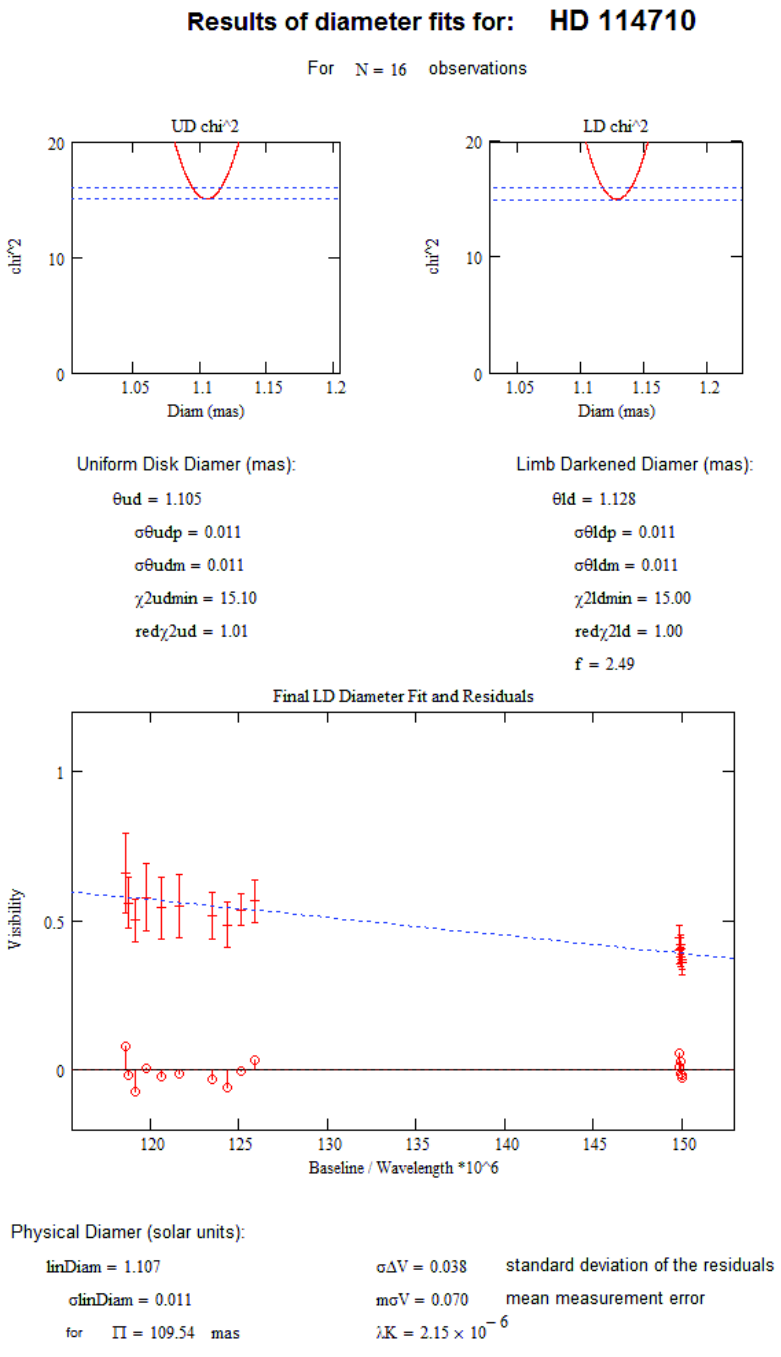

FIGURE C.51: **Diameter fit for HD 114710**

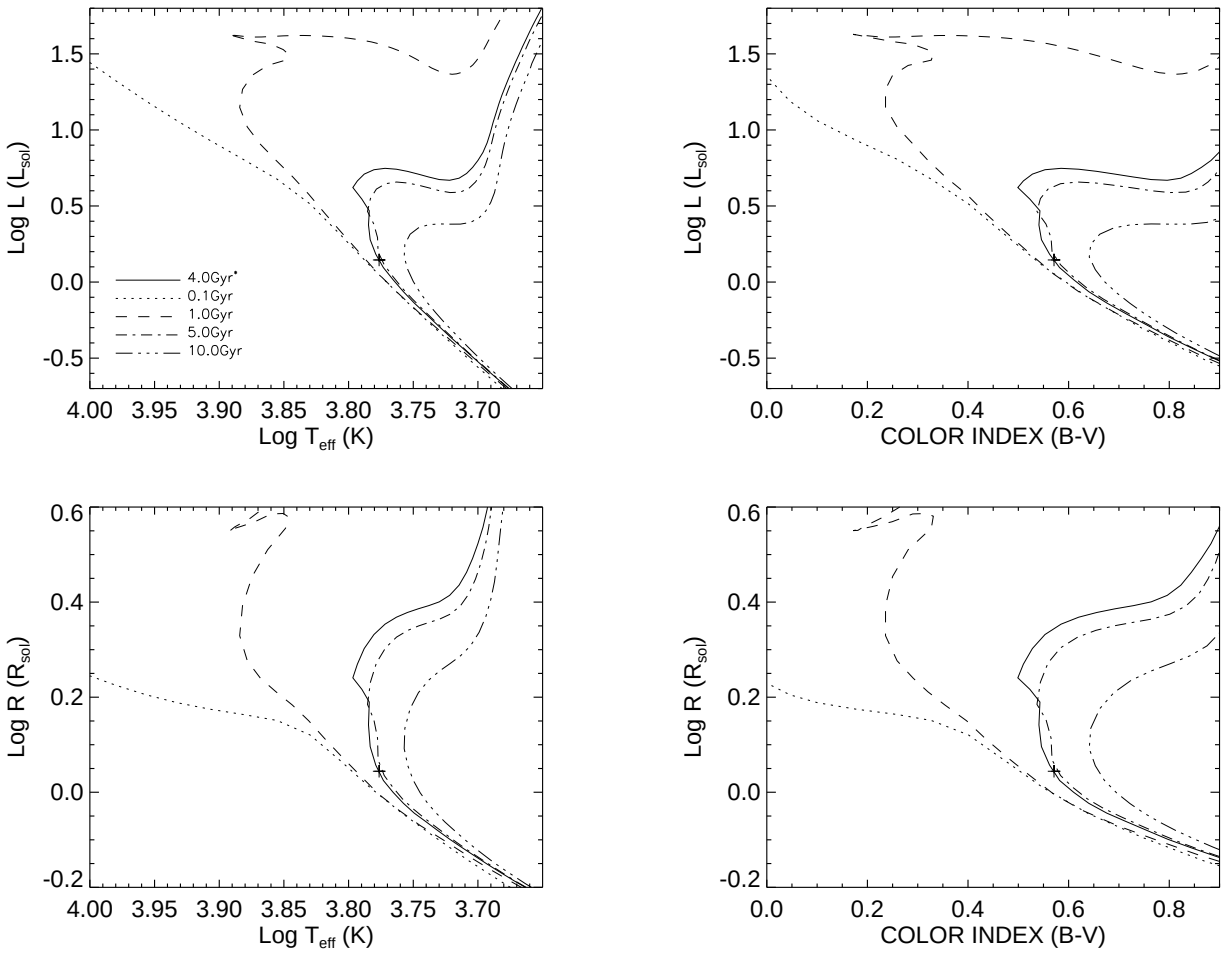

FIGURE C.52: **Y^2 Model Isochrones for HD 114710:** HD 114710 data (and 1-σ errors) plotted against Y^2 models isochrones ([α/Fe]=0.0, [Fe/H]=−0.06).

C.27 HD 118098

TABLE C.27: HD 118098 Visibilities

MJD	B (m)	ψ (°)	V	σV
54169.888	298.3	33.7	0.644	0.064
54169.903	290.6	31.4	0.678	0.097
54169.922	280.6	28.0	0.718	0.105
54169.937	273.2	24.9	0.670	0.097
54169.952	265.9	21.4	0.647	0.091
54169.970	258.4	16.7	0.599	0.117
54189.808	310.0	36.7	0.582	0.058
54189.819	305.1	35.5	0.635	0.055
54189.831	299.3	34.0	0.627	0.073
54189.843	293.2	32.2	0.671	0.071
54189.854	287.6	30.5	0.745	0.086
54458.058	316.3	38.2	0.596	0.064
54458.071	311.2	37.0	0.691	0.102

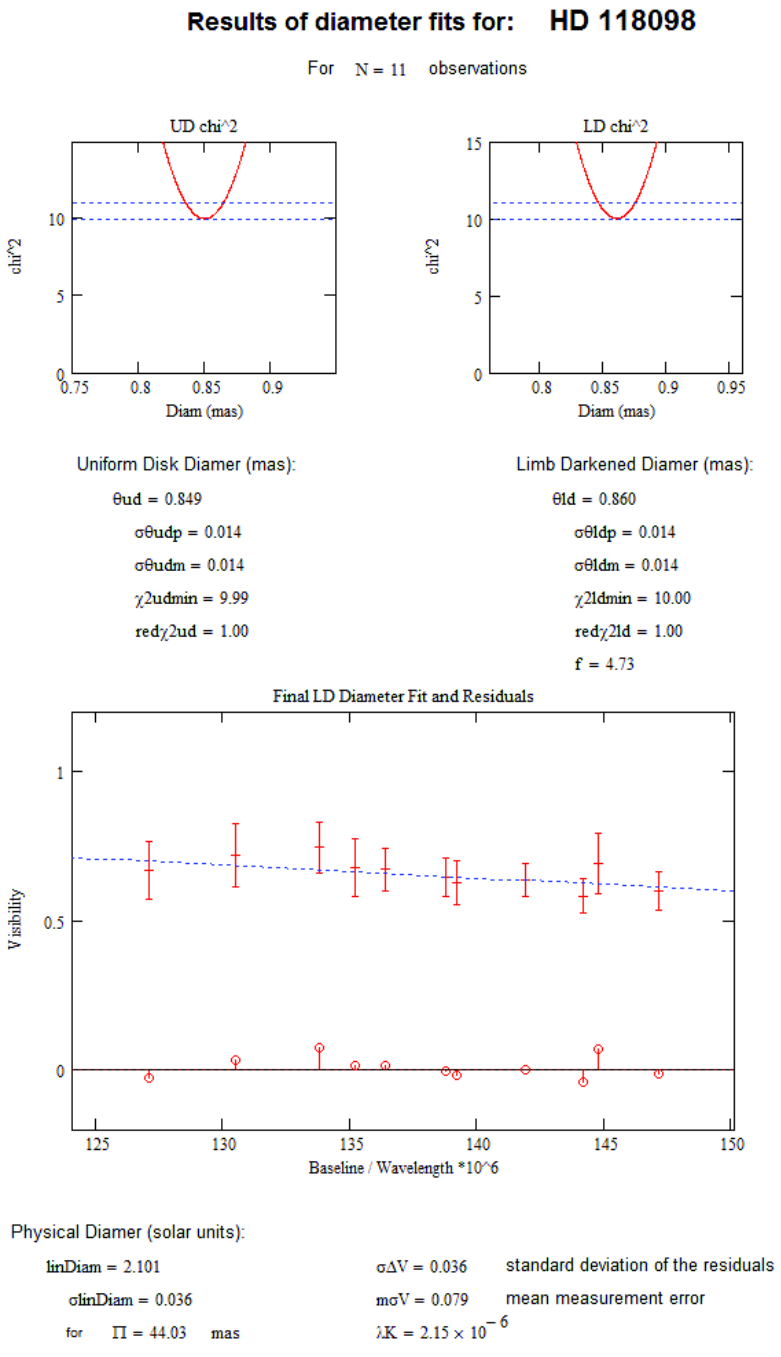

FIGURE C.53: **Diameter fit for HD 118098**

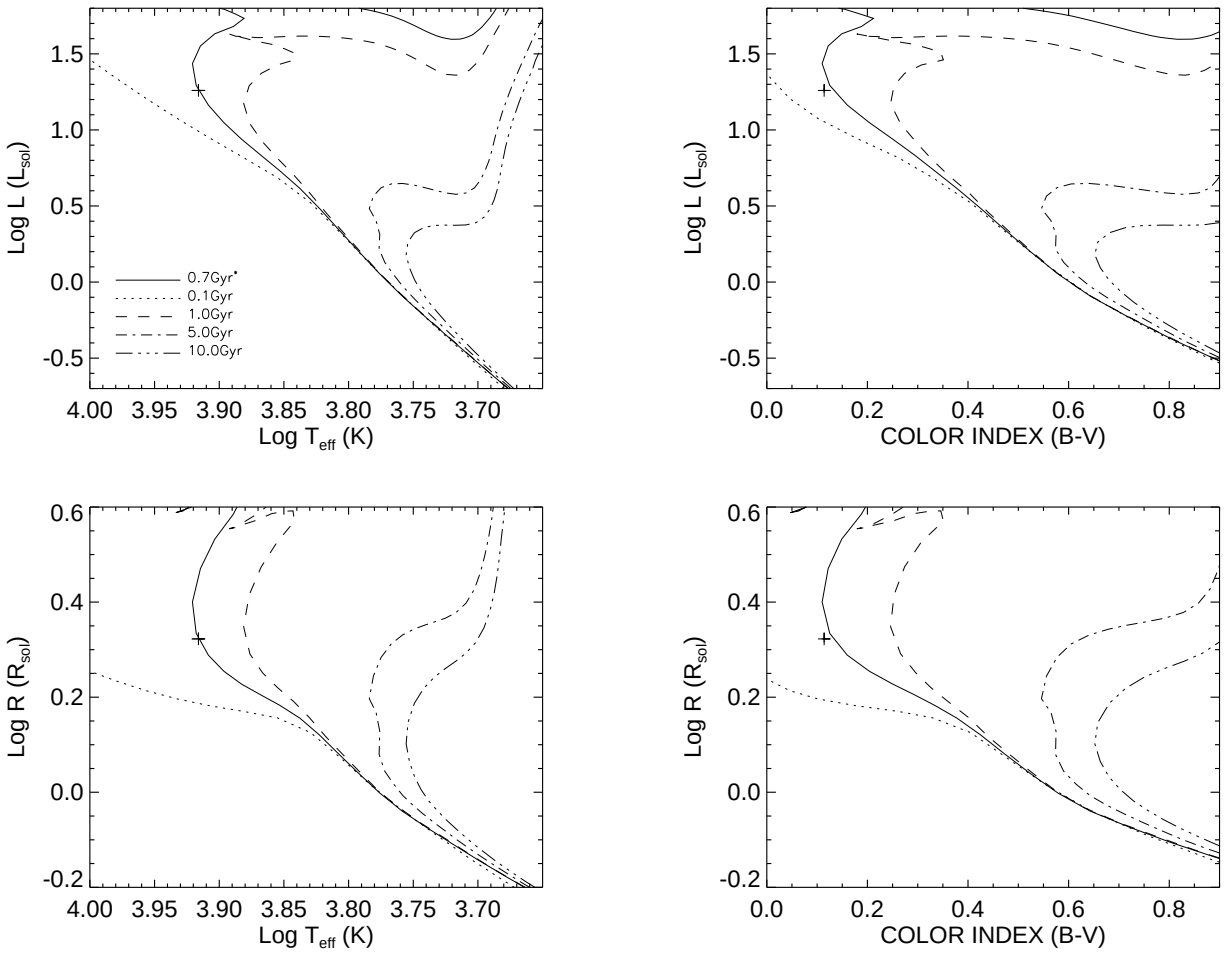

FIGURE C.54: **Y^2 Model Isochrones for HD 118098:** HD 118098 data (and 1-σ errors) plotted against Y^2 models isochrones ([α/Fe]=0.0, [Fe/H]=−0.02).

C.28 HD 126660

Table C.28: HD 126660 Visibilities

MJD	B (m)	ψ (°)	V	σV
54244.833	254.0	−31.9	0.572	0.030
54244.847	248.1	−28.6	0.561	0.029
54244.860	242.0	−25.5	0.623	0.030
54244.873	235.6	−22.6	0.598	0.045
54244.884	229.6	−20.1	0.677	0.044
54297.681	324.3	7.3	0.423	0.040
54297.711	324.7	90.0	0.396	0.026
54297.721	324.7	177.5	0.377	0.027
54297.747	324.2	172.1	0.415	0.019
54297.771	323.7	169.4	0.404	0.024
54297.795	323.1	166.8	0.397	0.022
54672.774	320.0	158.7	0.411	0.042
54672.781	319.2	157.1	0.444	0.053
54672.788	318.2	155.6	0.409	0.051
54672.795	317.2	154.0	0.422	0.053

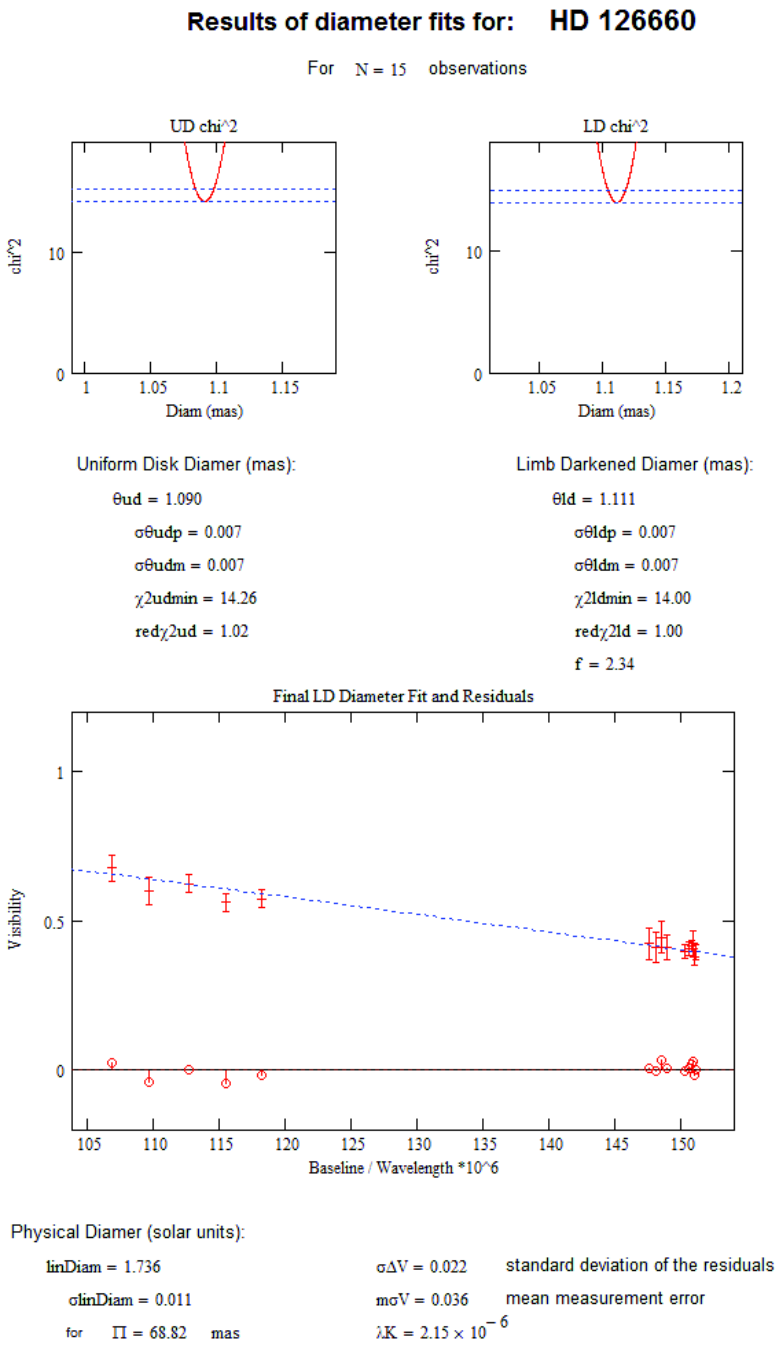

FIGURE C.55: **Diameter fit for HD 126660**

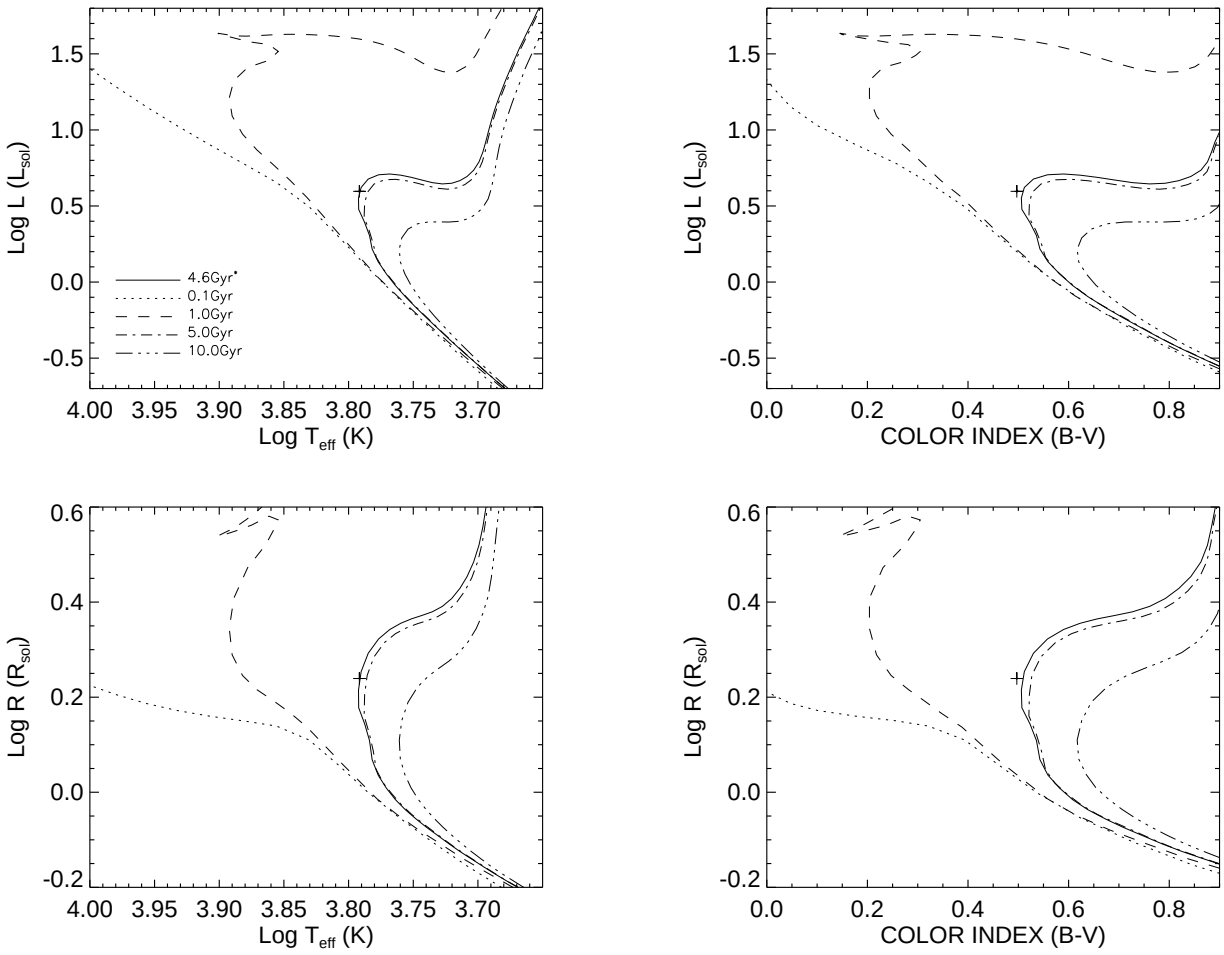

FIGURE C.56: **Y^2 Model Isochrones for HD 126660:** HD 126660 data (and 1-σ errors) plotted against Y^2 models isochrones ([α/Fe]=0.0, [Fe/H]=−0.14).

C.29 HD 128167

TABLE C.29: HD 128167 Visibilities

MJD	B (m)	ψ (°)	V	σV
54645.762	324.3	0.8	0.602	0.068
54645.767	324.3	179.4	0.610	0.068
54645.774	324.4	177.9	0.558	0.069
54645.780	324.5	176.3	0.676	0.075
54645.787	324.7	174.7	0.632	0.079
54653.703	325.4	9.5	0.575	0.109
54653.710	325.1	8.0	0.541	0.062
54653.717	324.8	6.3	0.596	0.080
54653.723	324.6	4.8	0.602	0.080
54653.730	324.5	3.2	0.634	0.073
54653.736	324.4	1.7	0.673	0.100
54653.743	324.3	90.2	0.644	0.104
54653.756	324.4	176.8	0.638	0.059
54653.762	324.6	175.5	0.630	0.053
54653.768	324.8	174.1	0.659	0.078
54653.774	325.0	172.6	0.633	0.076
54653.780	325.3	171.1	0.584	0.052
54671.674	276.3	177.9	0.710	0.072
54671.680	276.4	176.4	0.698	0.100
54671.686	276.5	175.1	0.633	0.128
54671.693	276.6	173.8	0.851	0.137
54671.706	276.9	171.0	0.709	0.120
54671.713	277.1	169.3	0.814	0.127
54671.720	277.3	167.8	0.659	0.081
54671.737	277.9	164.4	0.586	0.124
54671.749	278.3	161.9	0.677	0.151

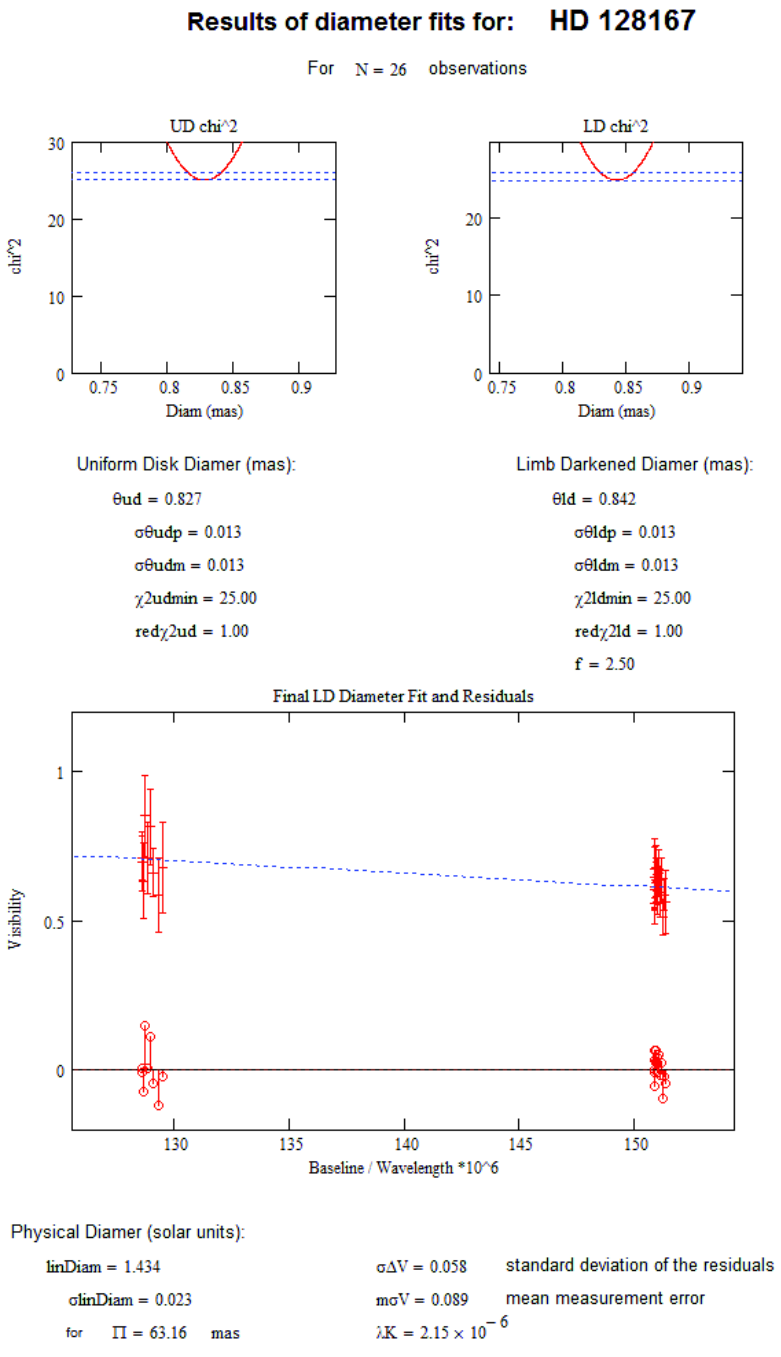

FIGURE C.57: **Diameter fit for HD 128167**

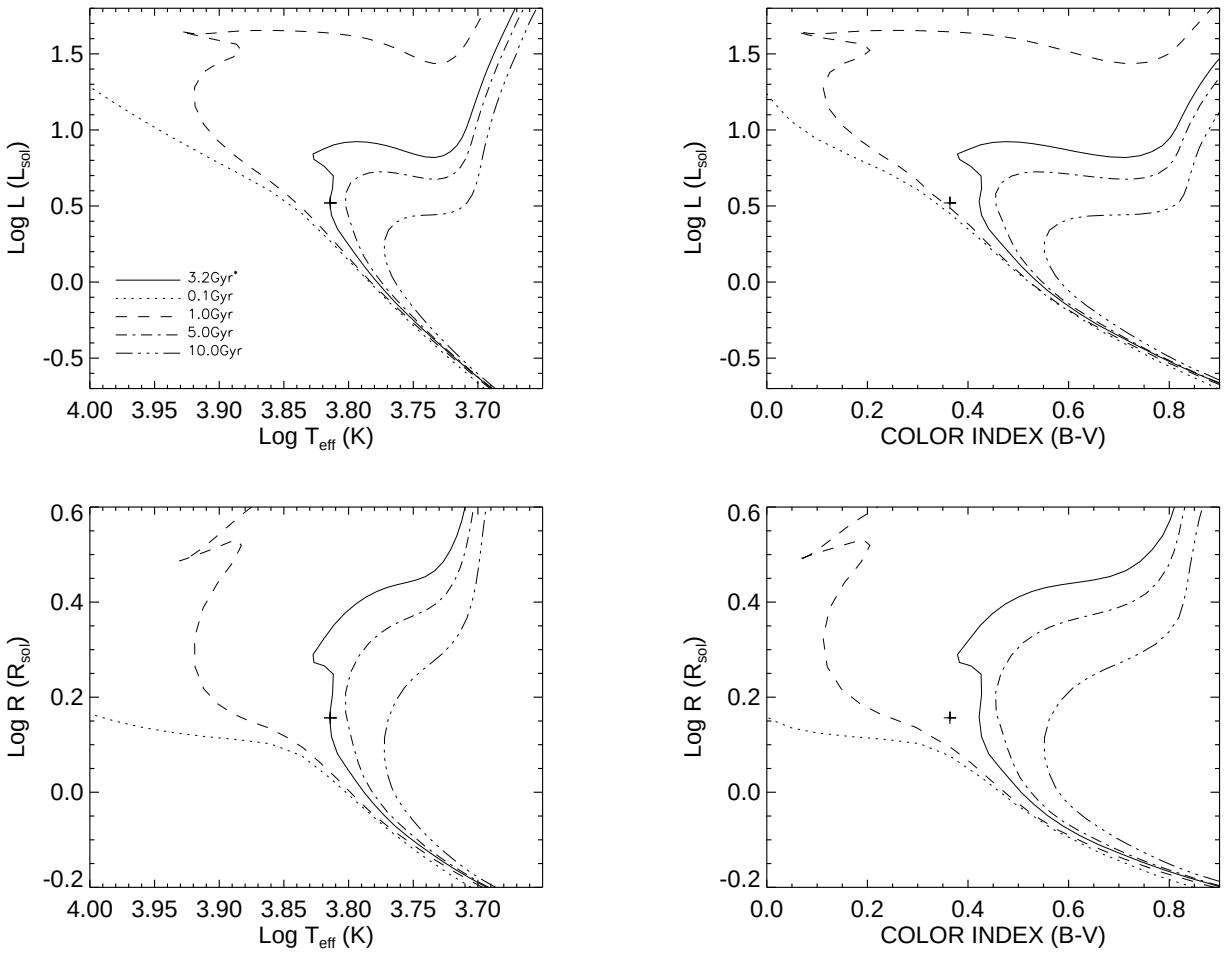

FIGURE C.58: **Y^2 Model Isochrones for HD 128167:** HD 128167 data (and 1-σ errors) plotted against Y^2 models isochrones ([α/Fe]=0.0, [Fe/H]=$-$0.36).

C.30 HD 131156

Table C.30: HD 131156 Visibilities

MJD	B (m)	ψ (°)	V	σV
54171.968	320.6	65.8	0.406	0.044
54171.983	317.6	68.8	0.425	0.044
54171.997	315.0	71.7	0.392	0.035
54172.011	312.5	74.9	0.417	0.040
54172.024	310.4	78.1	0.428	0.036
54574.861	267.1	141.9	0.466	0.051
54574.874	270.7	139.4	0.414	0.059
54574.914	277.8	133.1	0.417	0.023
54574.925	278.4	131.7	0.347	0.027
54574.943	278.0	129.6	0.466	0.021
54574.874	270.7	139.4	0.453	0.050
54574.914	277.8	133.1	0.499	0.029
54574.925	278.4	131.7	0.443	0.033
54574.943	278.0	129.6	0.472	0.024
54575.779	242.6	161.7	0.599	0.072
54575.792	246.2	157.9	0.538	0.059
54575.802	249.1	155.1	0.525	0.060
54575.817	254.0	151.2	0.531	0.083
54575.826	256.9	149.0	0.496	0.069
54575.842	262.0	145.4	0.503	0.050
54575.806	250.5	153.9	0.564	0.063
54644.751	308.1	7.2	0.521	0.078
54644.757	307.6	5.6	0.519	0.055
54644.764	307.2	4.0	0.465	0.055
54644.769	307.0	2.5	0.388	0.057
54644.775	306.9	1.1	0.445	0.044
54644.782	306.9	179.4	0.403	0.049
54644.796	307.3	175.8	0.408	0.041
54644.803	307.7	174.1	0.374	0.055
54644.810	308.4	172.2	0.350	0.050

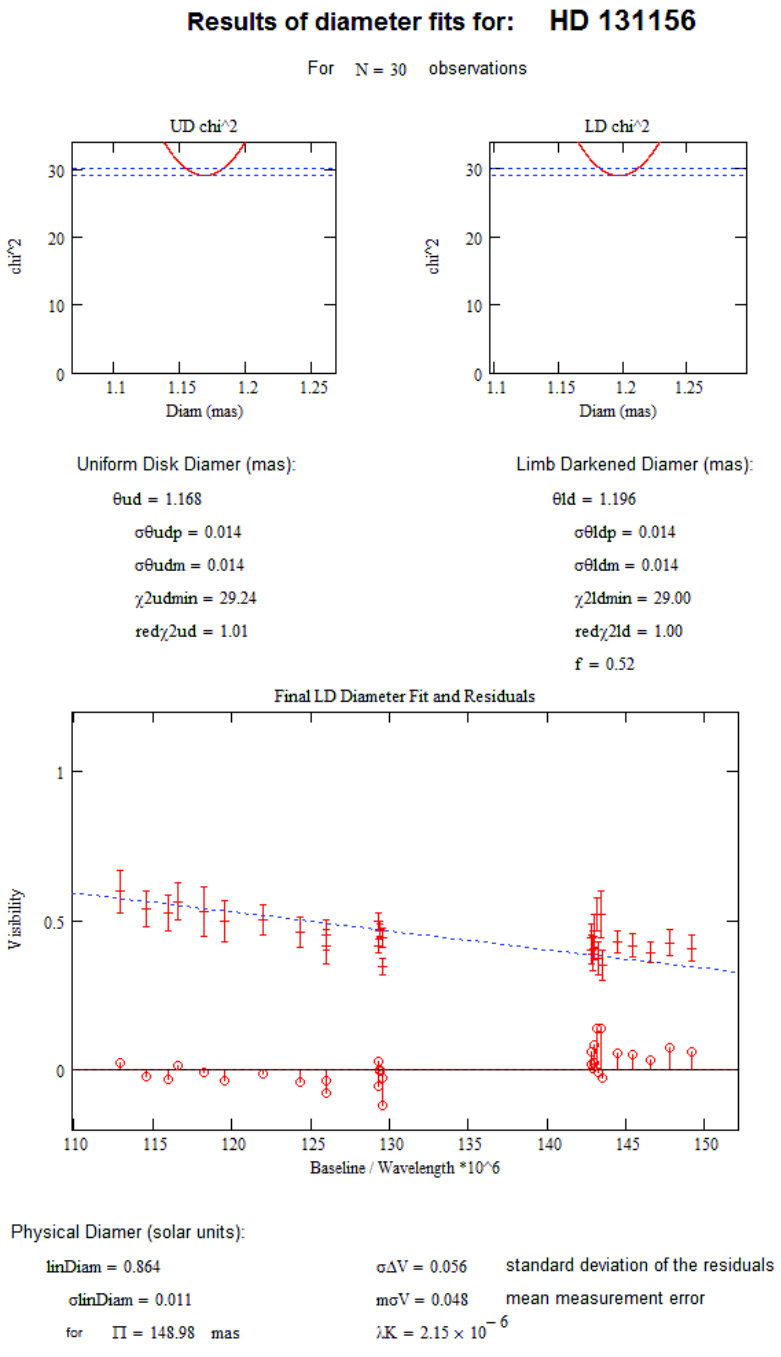

FIGURE C.59: **Diameter fit for HD 131156**

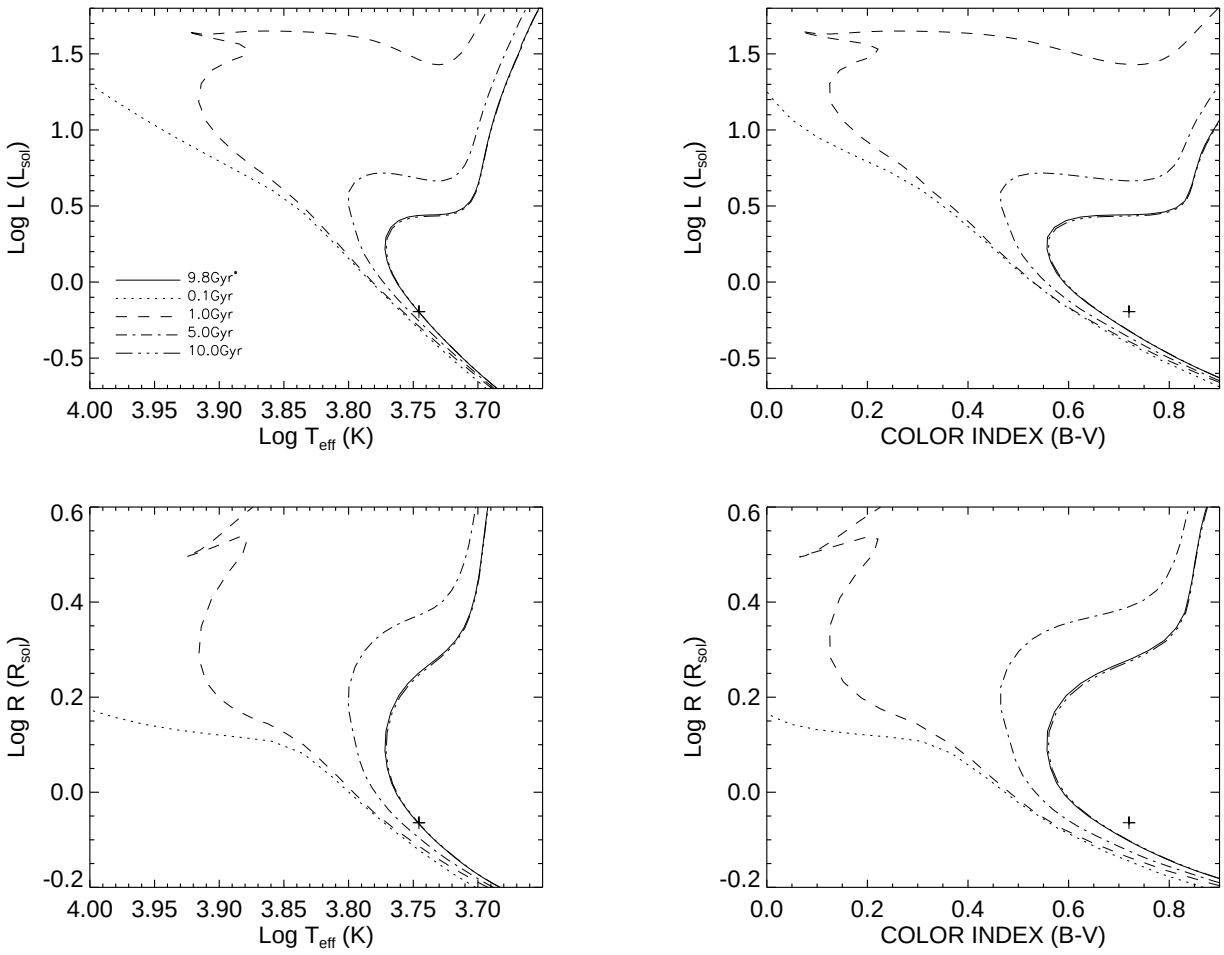

FIGURE C.60: **Y^2 Model Isochrones for HD 131156:** HD 131156 data (and 1-σ errors) plotted against Y^2 models isochrones ([α/Fe]=0.0, [Fe/H]=−0.33).

C.31 HD 141795

TABLE C.31: HD 141795 Visibilities

MJD	B (m)	ψ (°)	V	σV
54669.677	282.0	20.6	0.750	0.094
54669.684	279.1	18.8	0.753	0.097
54669.692	276.4	16.8	0.795	0.119
54669.701	273.8	14.7	0.701	0.081
54669.713	270.5	11.2	0.786	0.094
54669.722	268.7	8.9	0.752	0.079
54669.729	267.4	6.7	0.762	0.083
54669.738	266.4	4.2	0.768	0.083

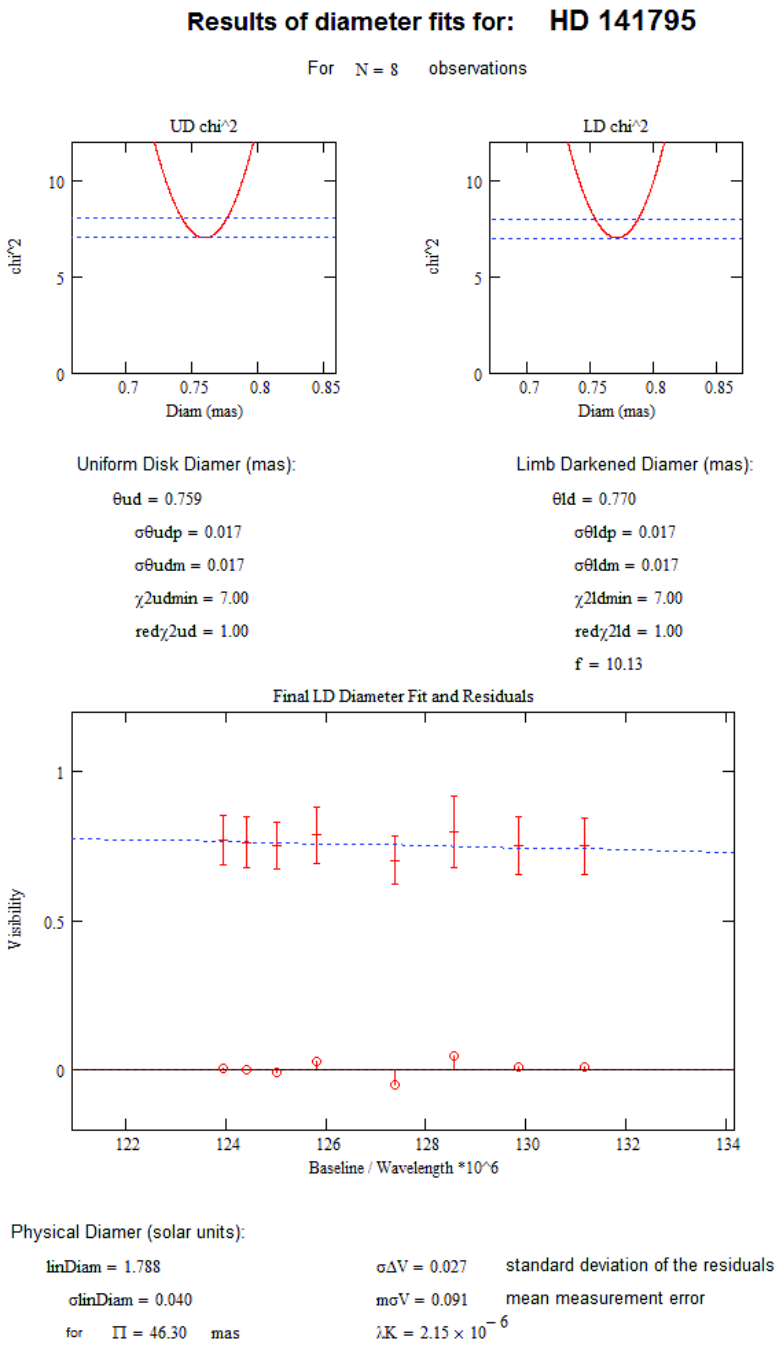

FIGURE C.61: **Diameter fit for HD 141795**

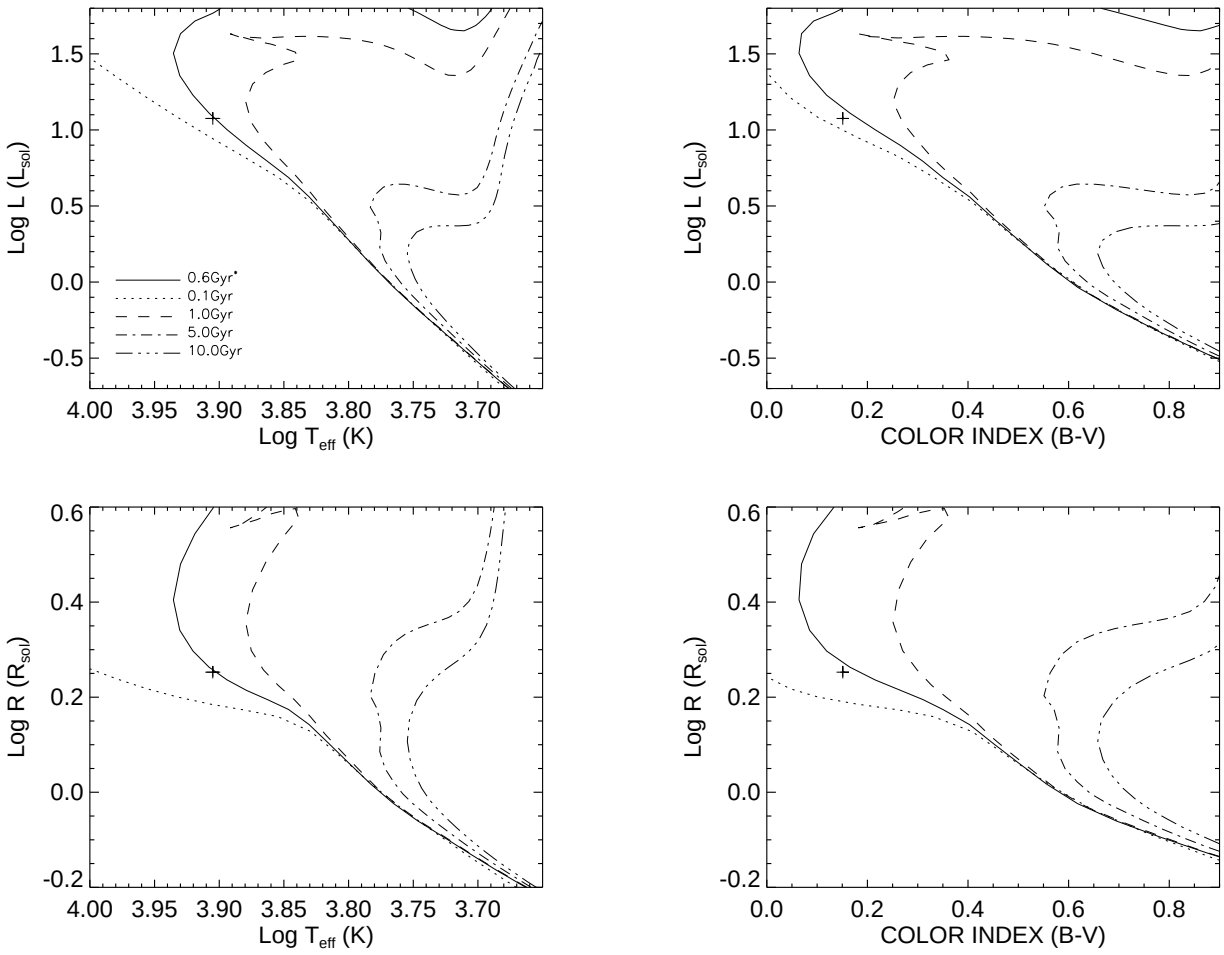

FIGURE C.62: **Y^2 Model Isochrones for HD 141795:** HD 141795 data (and 1-σ errors) plotted against Y^2 models isochrones ([α/Fe]=0.0, [Fe/H]=0.0).

C.32 HD 142860

TABLE C.32: HD 142860 Visibilities

MJD	B (m)	ψ (°)	V	σV
54301.760	298.9	89.4	0.379	0.036
54301.770	299.0	−87.9	0.396	0.034
54301.781	299.7	−84.9	0.349	0.042
54302.690	307.7	72.4	0.344	0.044
54302.696	306.3	73.9	0.353	0.030
54302.711	303.3	77.5	0.390	0.029
54302.718	302.2	79.3	0.381	0.026
54302.725	301.2	81.0	0.385	0.035
54302.734	300.2	83.3	0.385	0.041
54577.781	226.5	173.2	0.617	0.089
54577.789	227.6	170.5	0.575	0.120
54577.798	229.1	167.8	0.611	0.099
54577.805	230.7	165.3	0.603	0.057
54577.814	233.0	162.5	0.577	0.067
54577.822	235.3	160.1	0.570	0.066
54577.834	239.3	156.5	0.571	0.084
54577.842	242.1	154.2	0.590	0.065
54577.850	245.3	151.9	0.533	0.072
54577.859	248.6	149.7	0.562	0.084

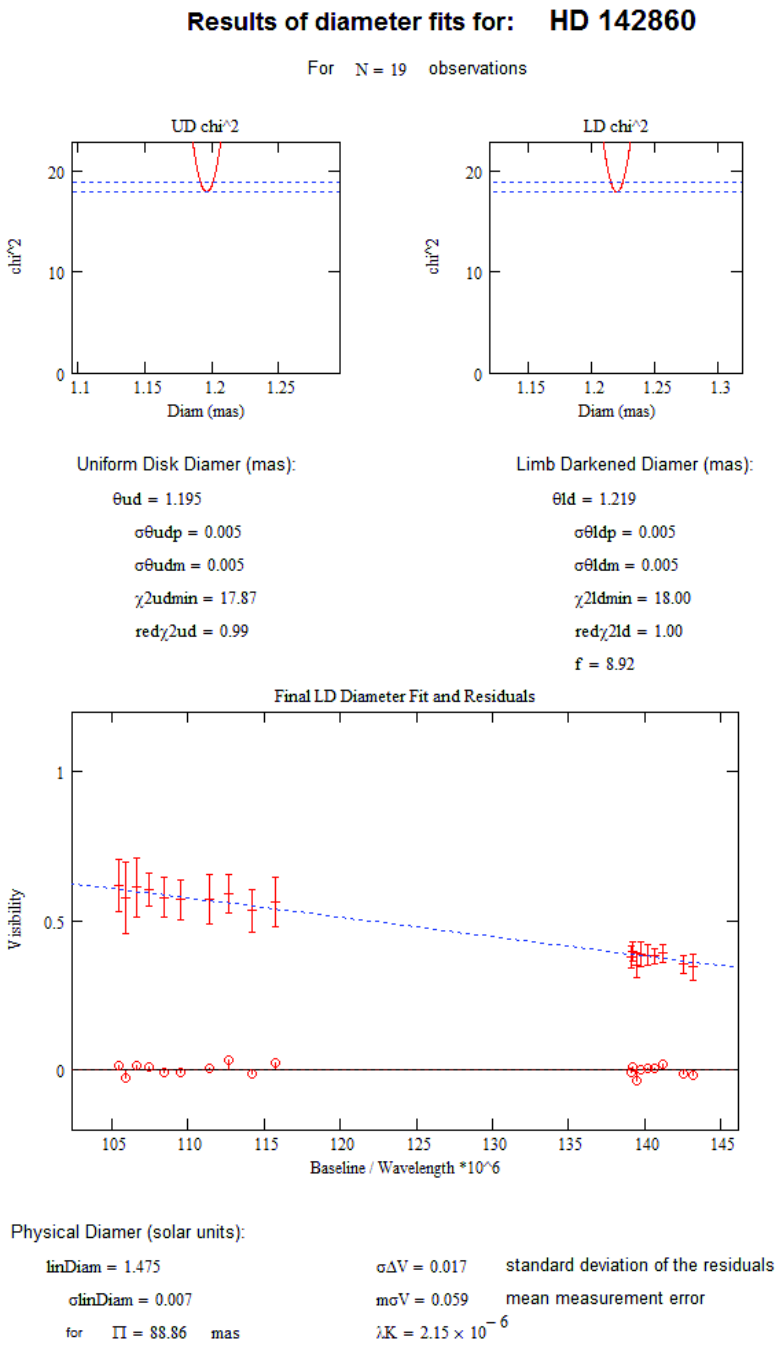

FIGURE C.63: **Diameter fit for HD 142860**

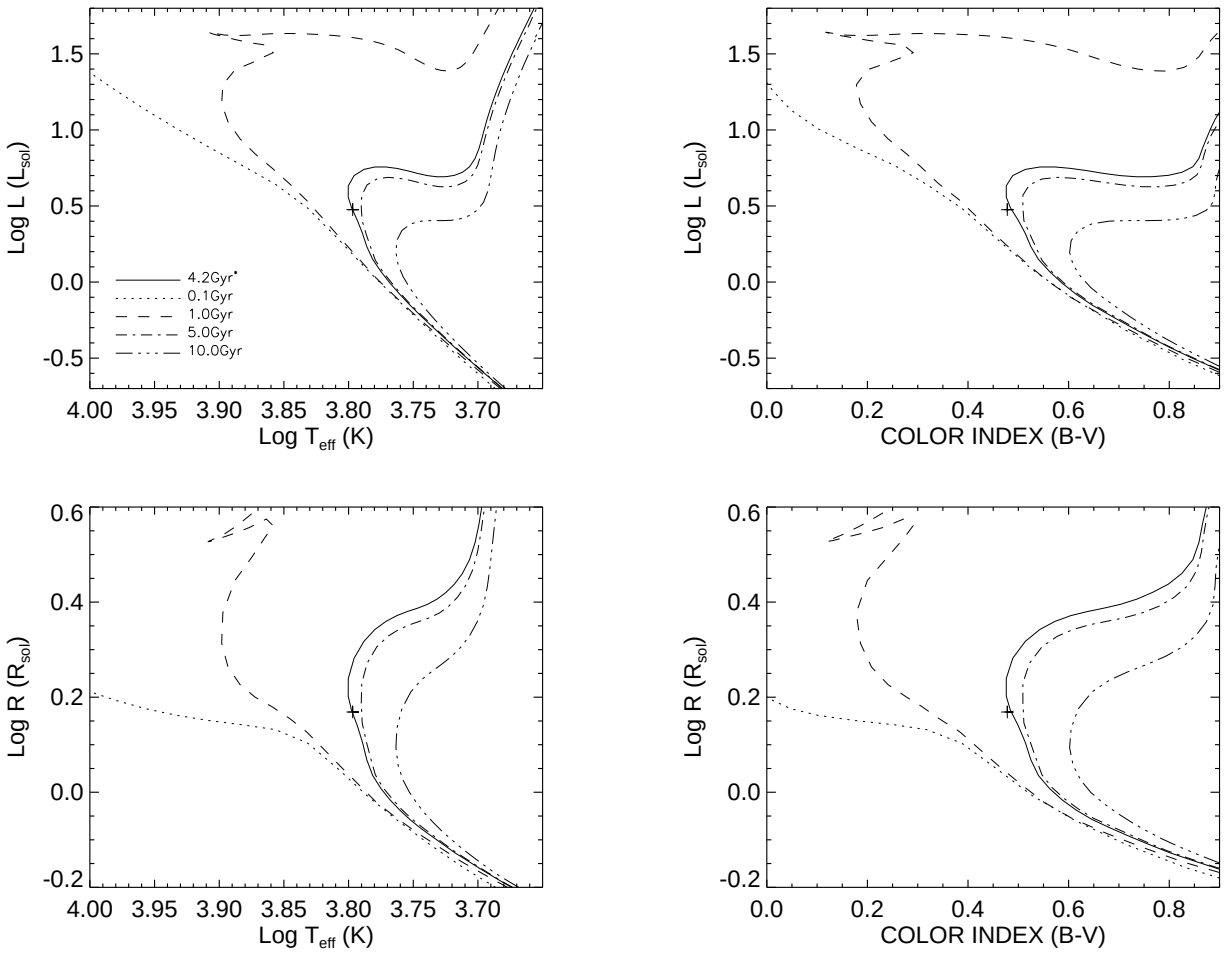

FIGURE C.64: **Y^2 Model Isochrones for HD 142860:** HD 142860 data (and 1-σ errors) plotted against Y^2 models isochrones ([α/Fe]=0.0, [Fe/H]=−0.19).

C.33 HD 146233

Table C.33: HD 146233 Visibilities

MJD	B (m)	ψ (°)	V	σV
54578.901	267.1	236.9	0.819	0.069
54578.923	252.2	241.1	0.786	0.085
54577.877	195.8	132.0	0.849	0.076
54577.903	216.5	136.6	0.823	0.107
54578.829	309.5	229.5	0.733	0.069
54578.837	305.9	229.9	0.715	0.075
54578.890	274.4	235.2	0.720	0.052
54578.912	259.7	238.8	0.815	0.059
54579.828	308.8	229.5	0.660	0.105
54579.856	293.6	231.6	0.748	0.099
54579.881	278.0	234.4	0.827	0.088
54577.891	206.7	134.6	0.823	0.086
54577.950	249.5	141.2	0.687	0.107
54575.877	190.8	130.6	0.837	0.064
54575.926	230.0	138.8	0.787	0.041
54575.954	248.8	141.1	0.790	0.033
54575.980	262.7	142.2	0.753	0.068
54575.863	179.3	126.9	0.894	0.066
54575.889	200.6	133.2	0.811	0.042
54575.914	221.0	137.4	0.802	0.047
54575.941	240.7	140.2	0.833	0.047
54575.966	255.7	141.7	0.833	0.059
54575.996	269.4	142.4	0.779	0.080
54602.945	196.3	187.6	0.741	0.076
54602.961	180.4	187.5	0.855	0.094

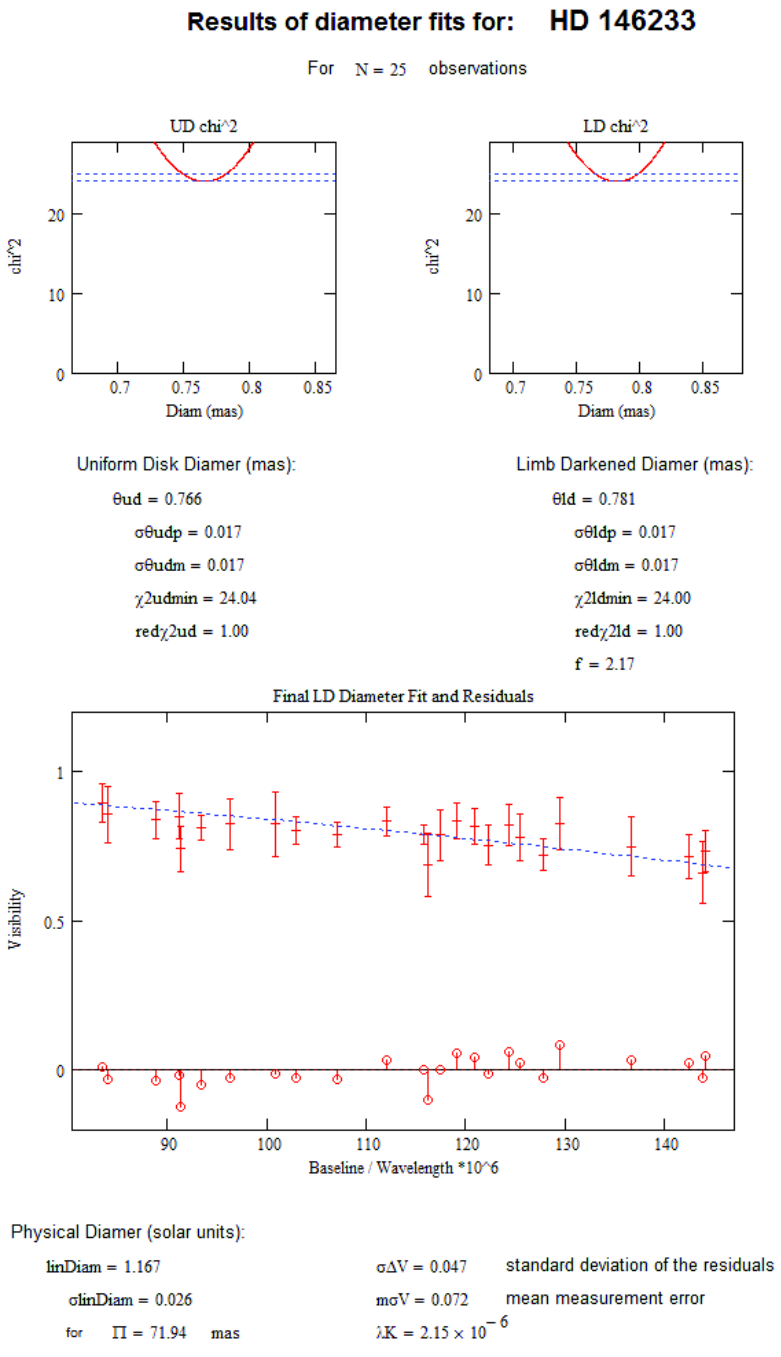

FIGURE C.65: **Diameter fit for HD 146233**

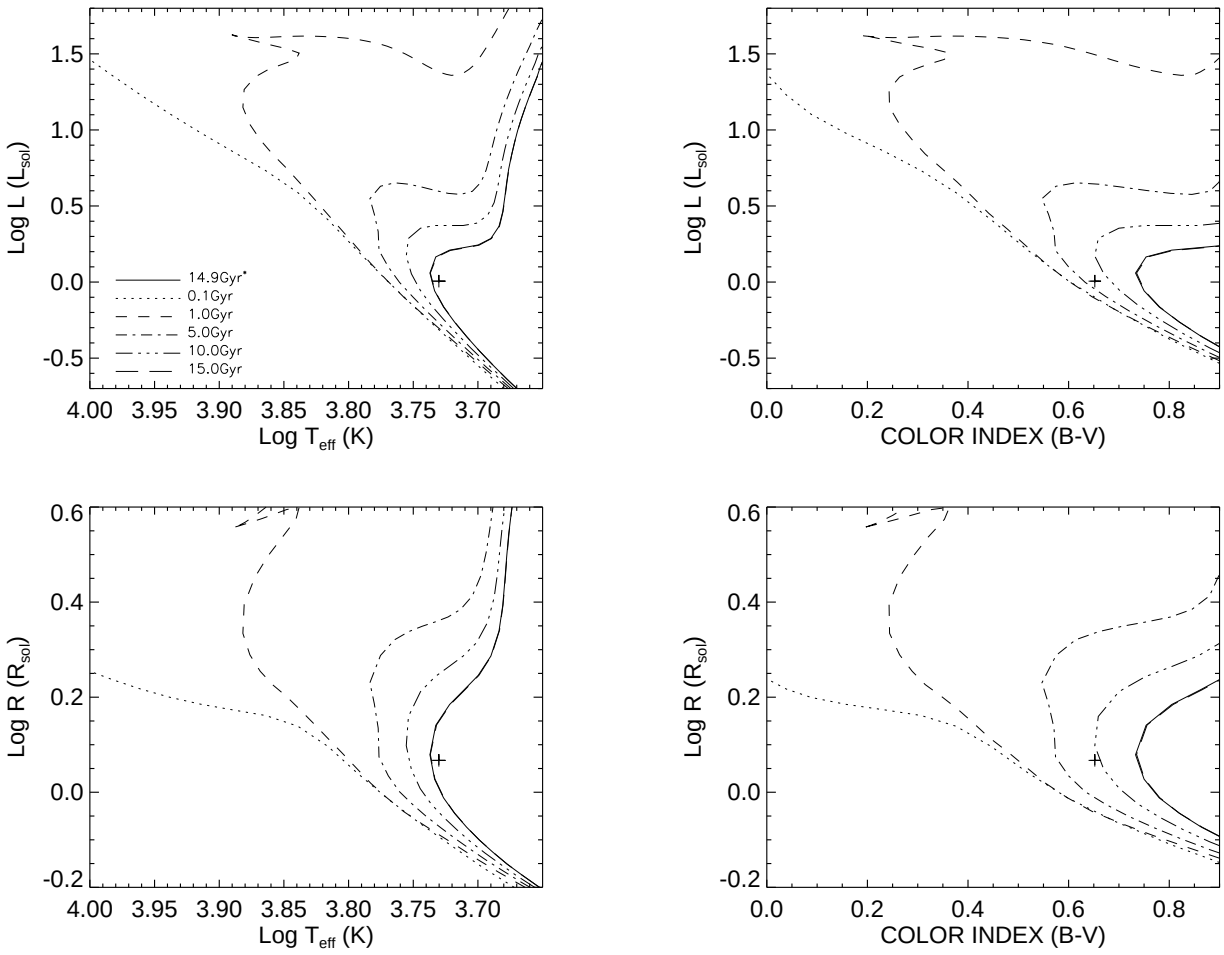

FIGURE C.66: **Y^2 Model Isochrones for HD 146233:** HD 146233 data (and 1-σ errors) plotted against Y^2 models isochrones ([α/Fe]=0.0, [Fe/H]=−0.02).

C.34 HD 162003

Table C.34: HD 162003 Visibilities

MJD	B (m)	ψ (°)	V	σV
54300.844	282.9	179.4	0.586	0.044
54300.854	282.8	176.6	0.687	0.055
54383.728	312.9	265.8	0.637	0.080
54383.742	312.9	90.9	0.734	0.064
54383.751	312.9	94.1	0.592	0.056
54383.763	312.9	98.3	0.591	0.087
54383.775	313.0	102.2	0.763	0.070
54383.786	313.1	106.4	0.641	0.074
54421.599	276.3	115.0	0.590	0.083
54421.609	274.8	117.8	0.602	0.099
54421.622	272.5	121.3	0.659	0.072
54421.632	270.5	124.1	0.663	0.090
54643.850	281.0	256.2	0.713	0.080
54643.859	281.6	258.5	0.780	0.072
54643.867	282.0	260.7	0.727	0.067
54643.874	282.4	262.8	0.675	0.096
54643.843	280.3	254.3	0.528	0.081

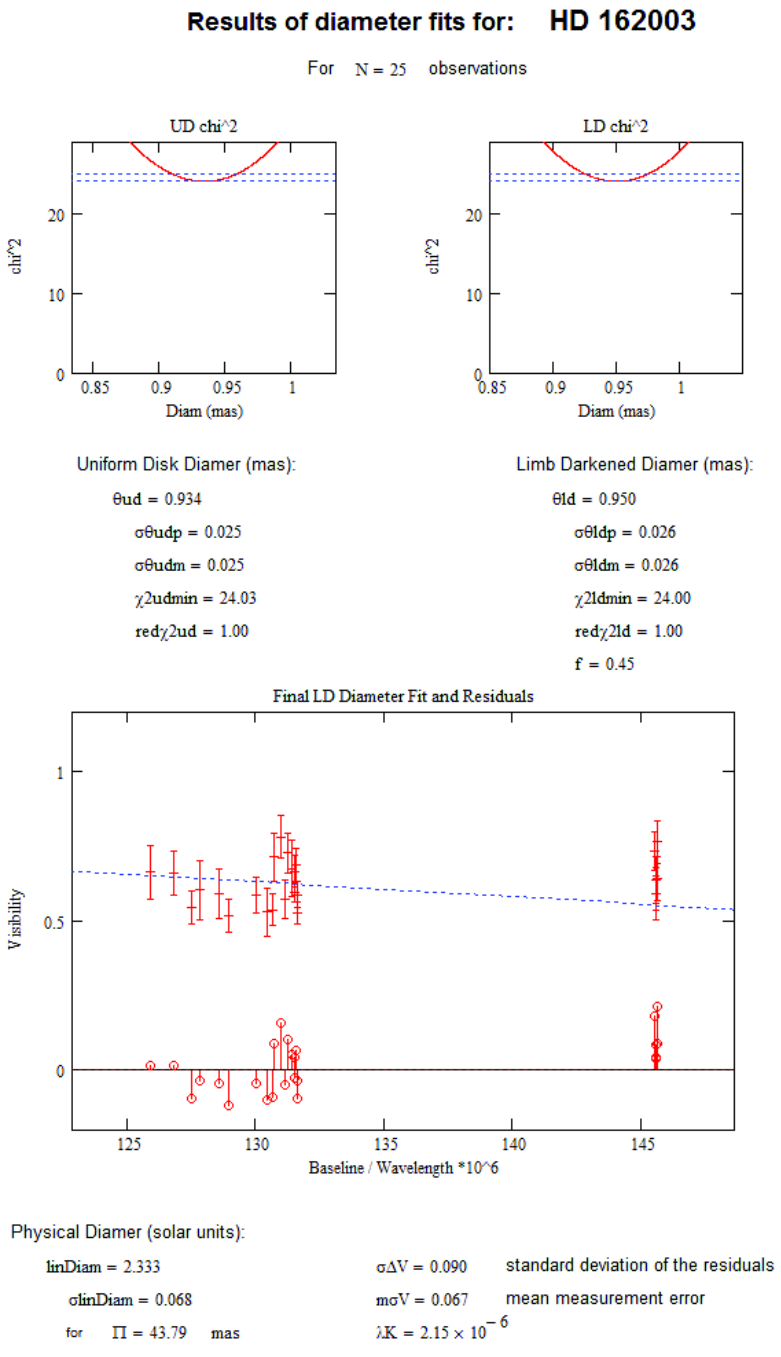

FIGURE C.67: **Diameter fit for HD 162003**

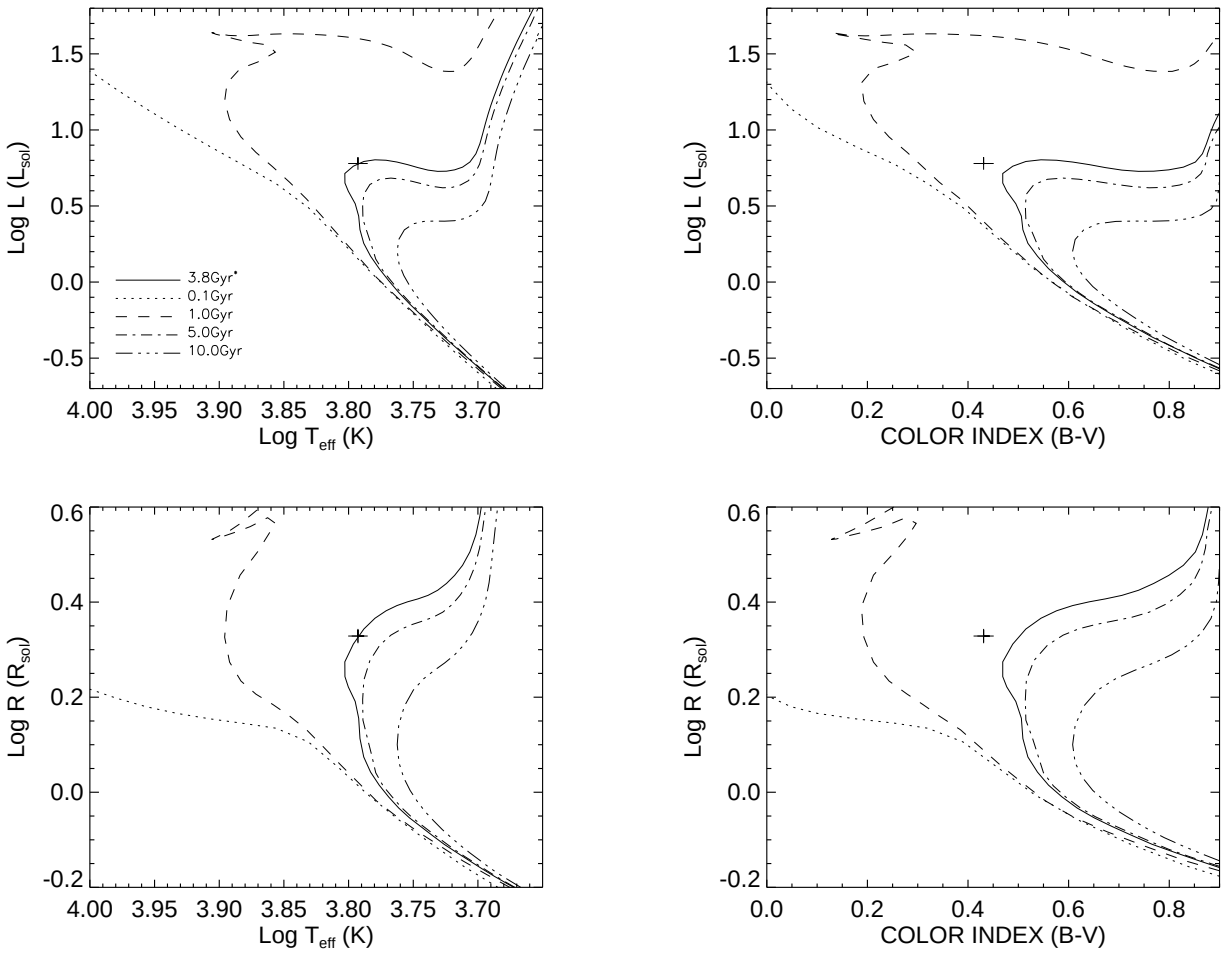

FIGURE C.68: **Y^2 Model Isochrones for HD 162003:** HD 162003 data (and 1-σ errors) plotted against Y^2 models isochrones ([α/Fe]=0.0, [Fe/H]=−0.17).

C.35 HD 164259

Table C.35: HD 164259 Visibilities

MJD	B (m)	ψ (°)	V	σV
54579.938	298.0	233.9	0.693	0.118
54578.954	290.6	235.7	0.636	0.062
54578.979	276.8	239.5	0.766	0.084
54578.940	298.4	233.8	0.847	0.134
54578.954	290.6	235.7	0.841	0.093
54578.965	284.4	237.3	0.890	0.102
54578.990	270.3	241.6	0.765	0.102
54578.997	266.4	243.1	0.806	0.085
54645.714	317.9	230.2	0.691	0.101
54645.721	315.2	230.6	0.625	0.078
54645.728	312.3	231.1	0.664	0.112
54645.735	309.5	231.6	0.663	0.135
54645.744	305.3	232.4	0.617	0.124
54673.681	202.7	127.5	0.789	0.102
54673.689	208.6	129.4	0.826	0.075
54673.697	214.5	131.1	0.849	0.092
54673.705	220.2	132.6	0.833	0.120
54673.713	226.1	134.0	0.935	0.116
54673.722	232.5	135.4	0.782	0.064

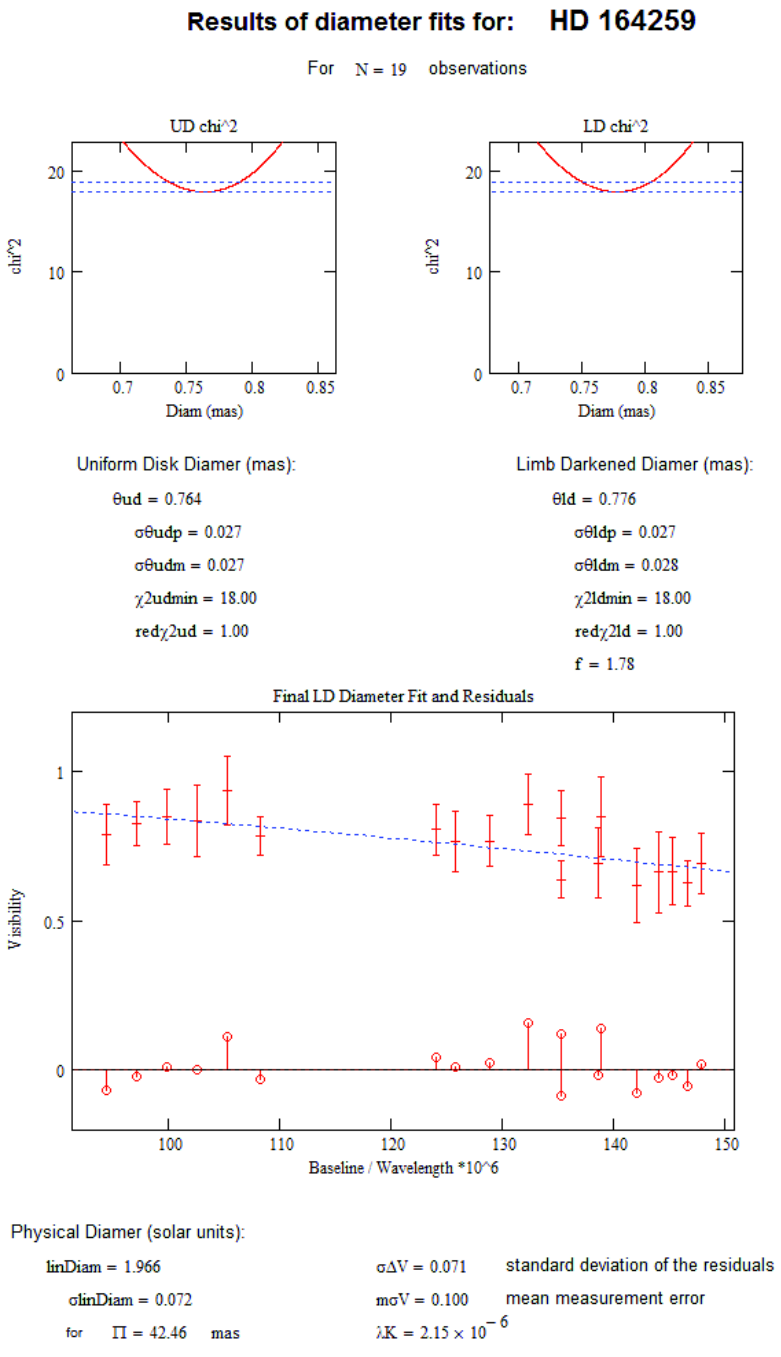

FIGURE C.69: **Diameter fit for HD 164259**

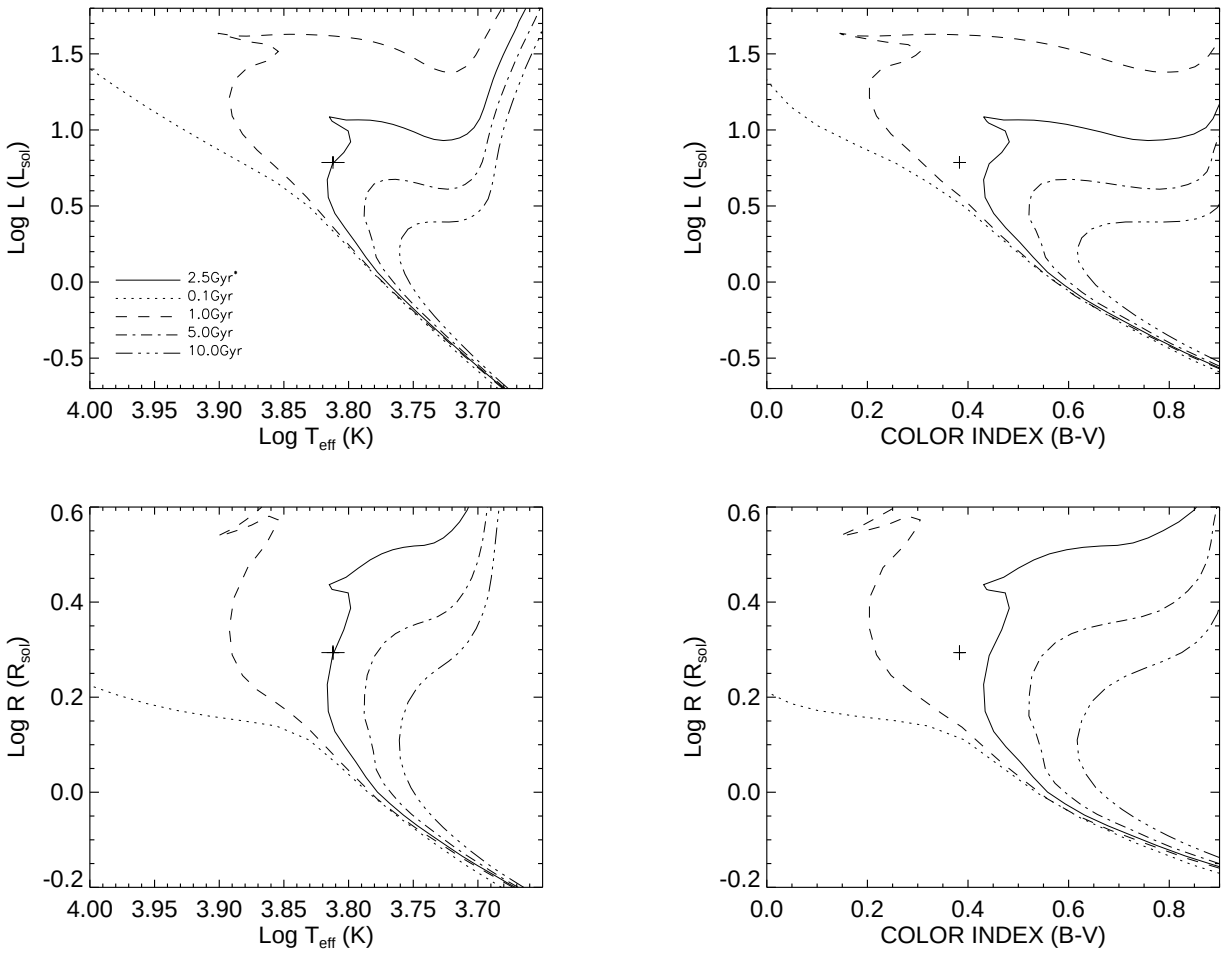

FIGURE C.70: **Y^2 Model Isochrones for HD 164259:** HD 164259 data (and 1-σ errors) plotted against Y^2 models isochrones ([α/Fe]=0.0, [Fe/H]=−0.14).

C.36 HD 173667

Table C.36: HD 173667 Visibilities

MJD	B (m)	ψ (°)	V	σV
54301.827	313.8	193.1	0.537	0.032
54301.838	312.5	190.7	0.482	0.026
54301.848	311.4	188.1	0.507	0.033
54302.755	325.4	207.5	0.467	0.047
54302.765	323.9	205.8	0.486	0.052
54302.773	322.5	204.2	0.506	0.059
54302.781	321.1	202.7	0.521	0.030
54302.789	319.7	201.1	0.433	0.029
54302.796	318.3	199.4	0.458	0.034
54302.805	316.8	197.6	0.484	0.035
54302.813	315.5	195.6	0.494	0.040
54302.821	314.3	193.8	0.506	0.031
54577.971	255.6	117.8	0.606	0.115
54577.987	260.5	121.8	0.566	0.170
54577.998	263.8	124.3	0.697	0.312
54645.817	325.4	242.5	0.556	0.102
54645.827	323.8	244.2	0.684	0.130
54645.836	322.2	246.1	0.550	0.081
54645.848	320.1	248.4	0.519	0.043
54645.857	318.4	250.5	0.493	0.098
54645.881	314.5	255.8	0.512	0.058
54645.891	313.1	258.2	0.595	0.093
54645.905	311.5	261.5	0.576	0.093
54654.777	260.5	121.8	0.490	0.043
54668.833	278.5	138.6	0.569	0.059
54670.718	302.6	189.8	0.648	0.042
54670.730	307.6	191.1	0.610	0.063
54670.740	310.7	192.3	0.561	0.061
54670.759	313.4	194.7	0.505	0.028
54670.769	313.4	195.9	0.522	0.038
54670.776	312.7	196.8	0.532	0.044
54669.807	315.9	253.8	0.472	0.062
54669.821	313.7	257.1	0.563	0.098
54669.833	312.2	260.0	0.655	0.102
54669.852	310.5	264.6	0.492	0.072
54669.864	310.0	267.6	0.494	0.065
54669.875	309.9	90.4	0.565	0.081

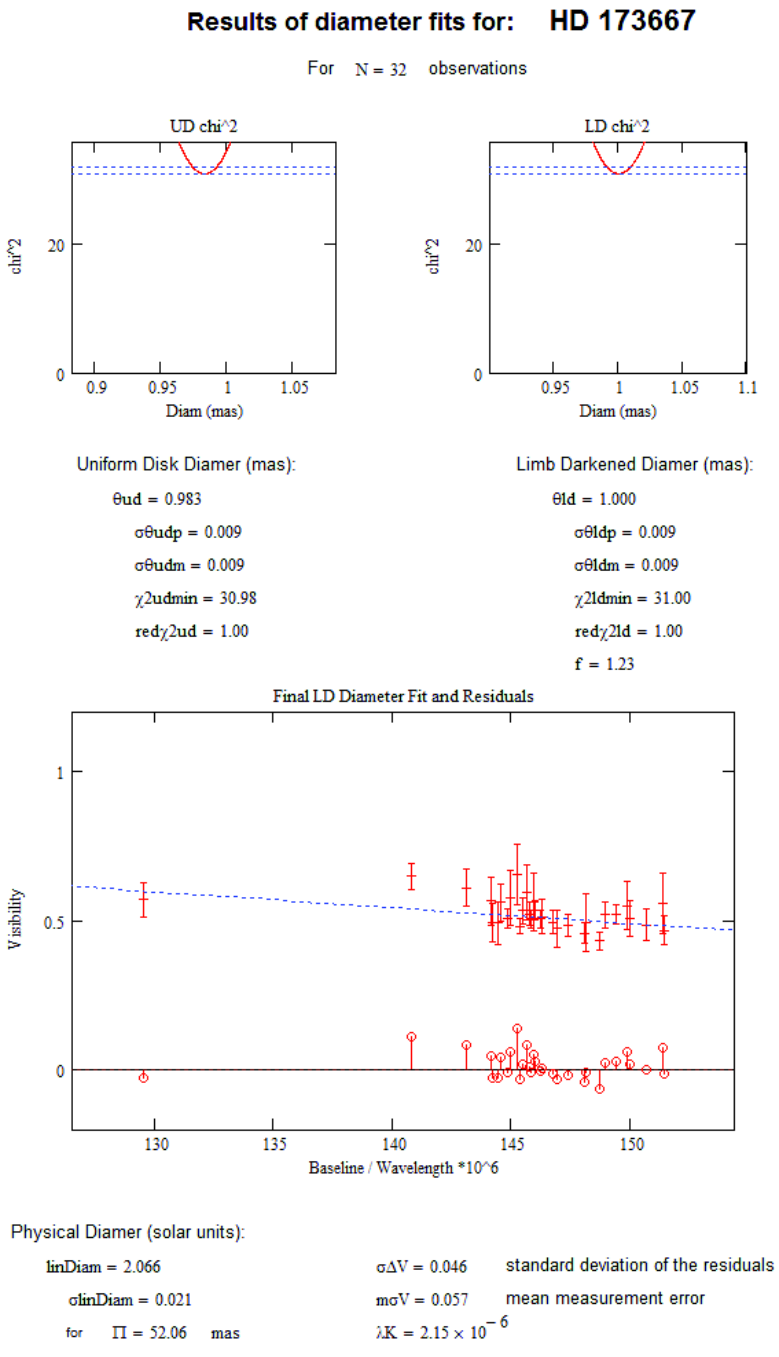

FIGURE C.71: **Diameter fit for HD 173667**

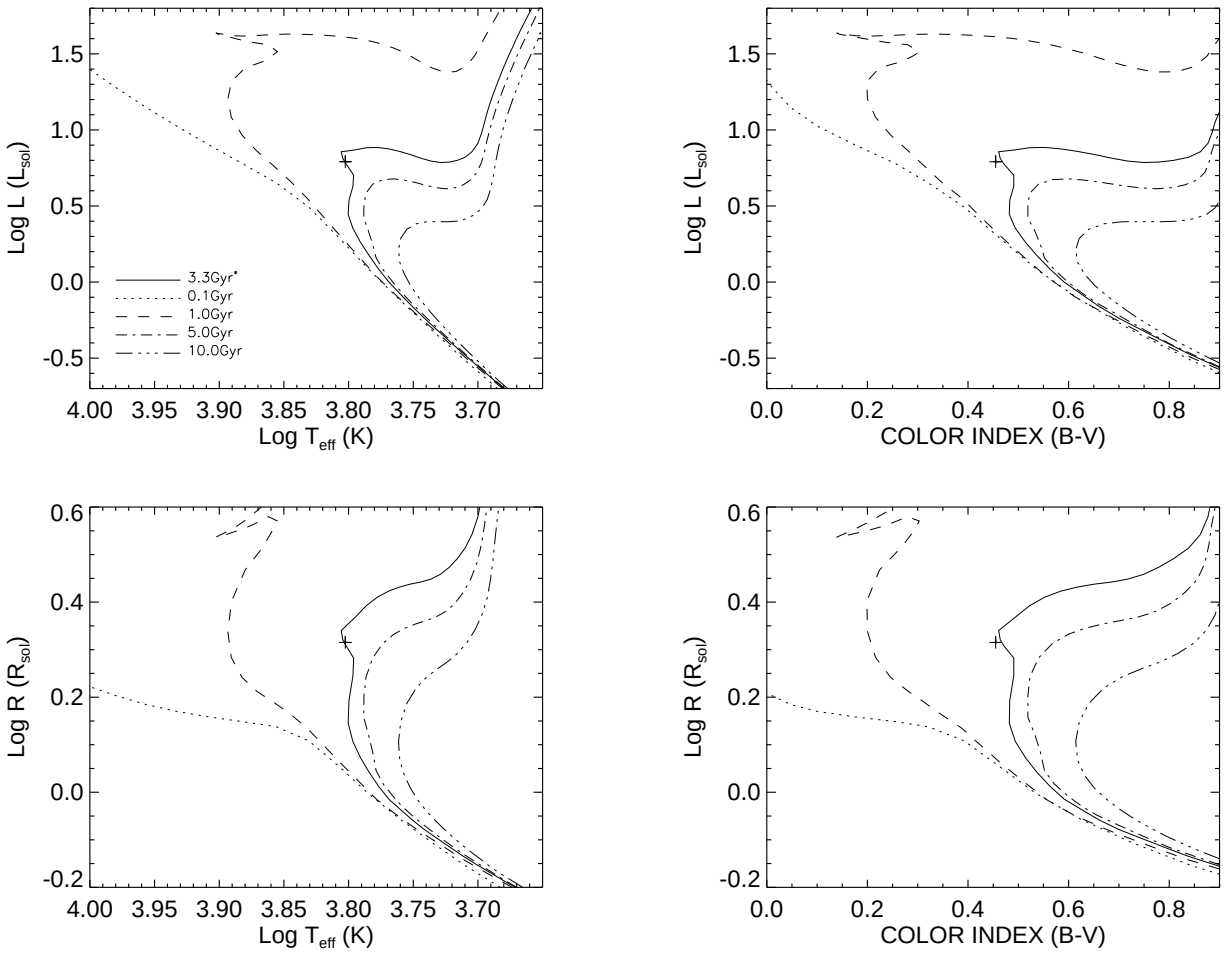

FIGURE C.72: **Y^2 Model Isochrones for HD 173667:** HD 173667 data (and 1-σ errors) plotted against Y^2 models isochrones ([α/Fe]=0.0, [Fe/H]=$-$0.15).

C.37 HD 177724

Table C.37: HD 177724 Visibilities

MJD	B (m)	ψ (°)	V	σV
54645.803	324.3	32.7	0.534	0.092
54645.810	322.8	31.6	0.606	0.132
54645.823	319.6	29.6	0.557	0.084
54645.833	317.1	27.9	0.499	0.066
54645.844	314.1	25.9	0.529	0.055
54645.854	311.3	23.9	0.595	0.074
54645.871	306.6	20.2	0.551	0.077
54645.877	305.0	18.9	0.519	0.081
54645.887	302.7	16.6	0.557	0.075
54645.901	299.6	13.3	0.551	0.078
54654.772	242.2	151.1	0.753	0.066
54654.784	247.0	148.1	0.756	0.060
54654.790	249.5	146.7	0.748	0.056
54654.797	252.4	145.1	0.757	0.059
54654.803	254.9	143.8	0.687	0.077
54668.827	274.9	133.4	0.689	0.080
54668.845	277.6	131.4	0.629	0.102
54668.857	278.4	130.2	0.588	0.047
54668.864	278.5	129.6	0.719	0.072
54670.713	294.3	79.7	0.602	0.056
54670.726	301.6	78.9	0.633	0.071
54670.736	306.5	78.2	0.718	0.052
54670.756	312.1	76.7	0.656	0.035
54670.766	313.3	75.9	0.639	0.044
54670.780	313.1	74.6	0.628	0.051
54669.801	307.8	21.2	0.587	0.079
54669.817	303.7	17.7	0.619	0.105
54669.829	301.1	15.0	0.670	0.089
54669.848	297.5	10.3	0.638	0.088
54669.859	295.9	7.3	0.631	0.067
54669.871	294.9	4.3	0.457	0.053

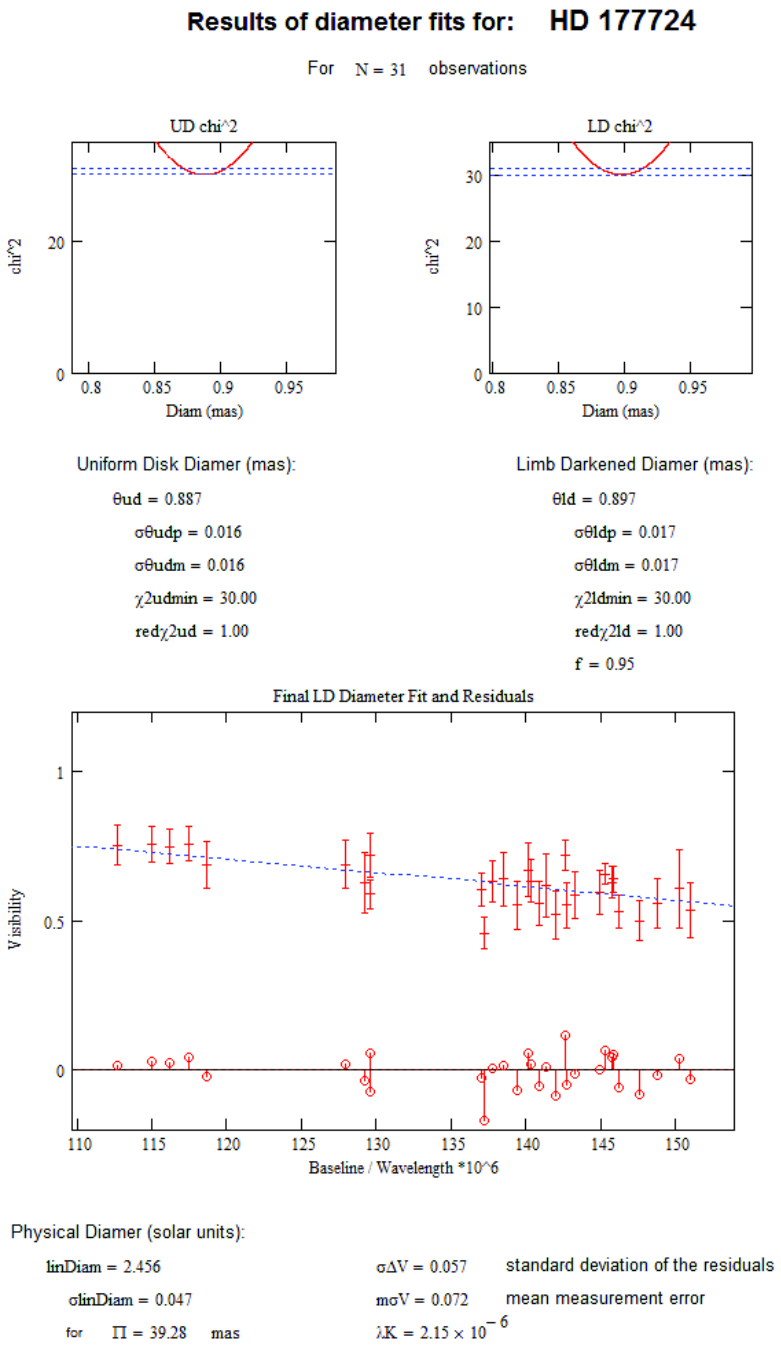

FIGURE C.73: **Diameter fit for HD 177724**

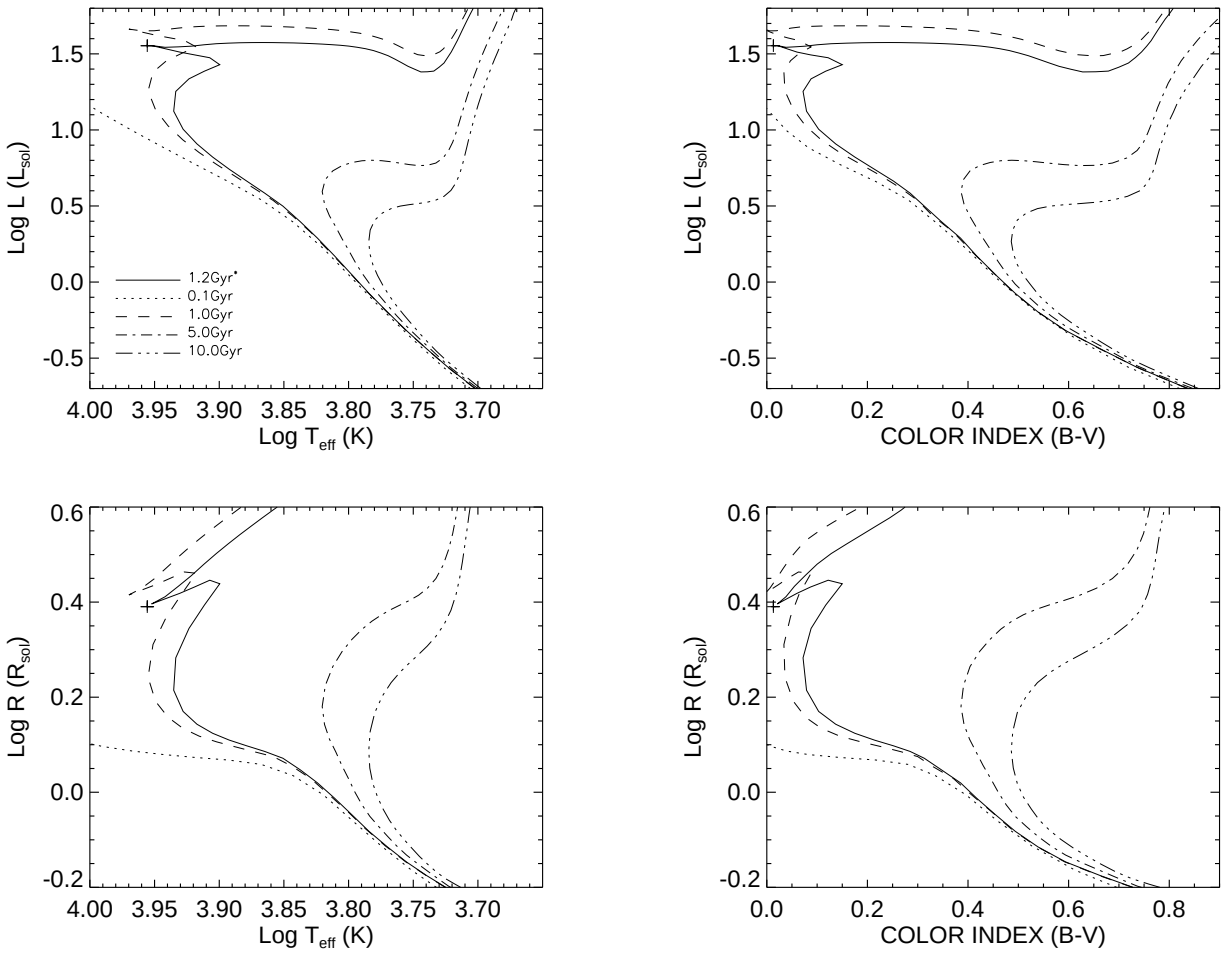

FIGURE C.74: **Y^2 Model Isochrones for HD 177724:** HD 177724 data (and 1-σ errors) plotted against Y^2 models isochrones ([α/Fe]=0.0, [Fe/H]=$-$0.68).

C.38 HD 182572

Table C.38: HD 182572 Visibilities

MJD	B (m)	ψ (°)	V	σV
54302.840	298.0	73.4	0.613	0.042
54302.847	296.3	75.0	0.678	0.052
54302.854	294.8	76.7	0.742	0.061
54302.862	293.2	78.7	0.756	0.065
54302.869	292.0	80.5	0.703	0.063
54302.875	291.0	82.2	0.719	0.047
54352.663	309.8	25.5	0.644	0.054
54352.670	307.7	24.2	0.654	0.093
54352.677	305.6	22.8	0.727	0.095
54352.684	303.6	21.3	0.615	0.087
54352.690	301.8	19.9	0.598	0.066
54352.697	300.0	18.4	0.596	0.068
54352.706	297.6	16.3	0.627	0.073
54352.712	296.1	14.8	0.646	0.060
54352.719	294.7	13.2	0.653	0.060
54352.726	293.2	11.3	0.737	0.068
54669.763	319.4	31.2	0.771	0.154
54669.769	317.5	30.1	0.586	0.080
54669.776	315.7	29.1	0.747	0.141
54669.782	313.8	27.9	0.657	0.090
54669.789	311.8	26.7	0.701	0.119
54671.787	260.2	17.9	0.602	0.081
54671.793	259.0	16.6	0.448	0.062
54671.800	257.8	15.2	0.536	0.066
54671.807	256.6	13.6	0.717	0.110
54671.814	255.6	12.2	0.630	0.093
54739.637	300.1	18.6	0.782	0.067
54739.644	298.3	16.9	0.789	0.072
54739.655	296.4	9.5	0.710	0.068
54739.671	294.5	5.3	0.762	0.101
54739.680	291.1	7.9	0.775	0.122
54739.686	290.3	6.3	0.685	0.108
54739.693	289.7	4.4	0.724	0.099
54739.700	289.3	2.5	0.846	0.080
54739.707	289.1	0.7	0.846	0.098

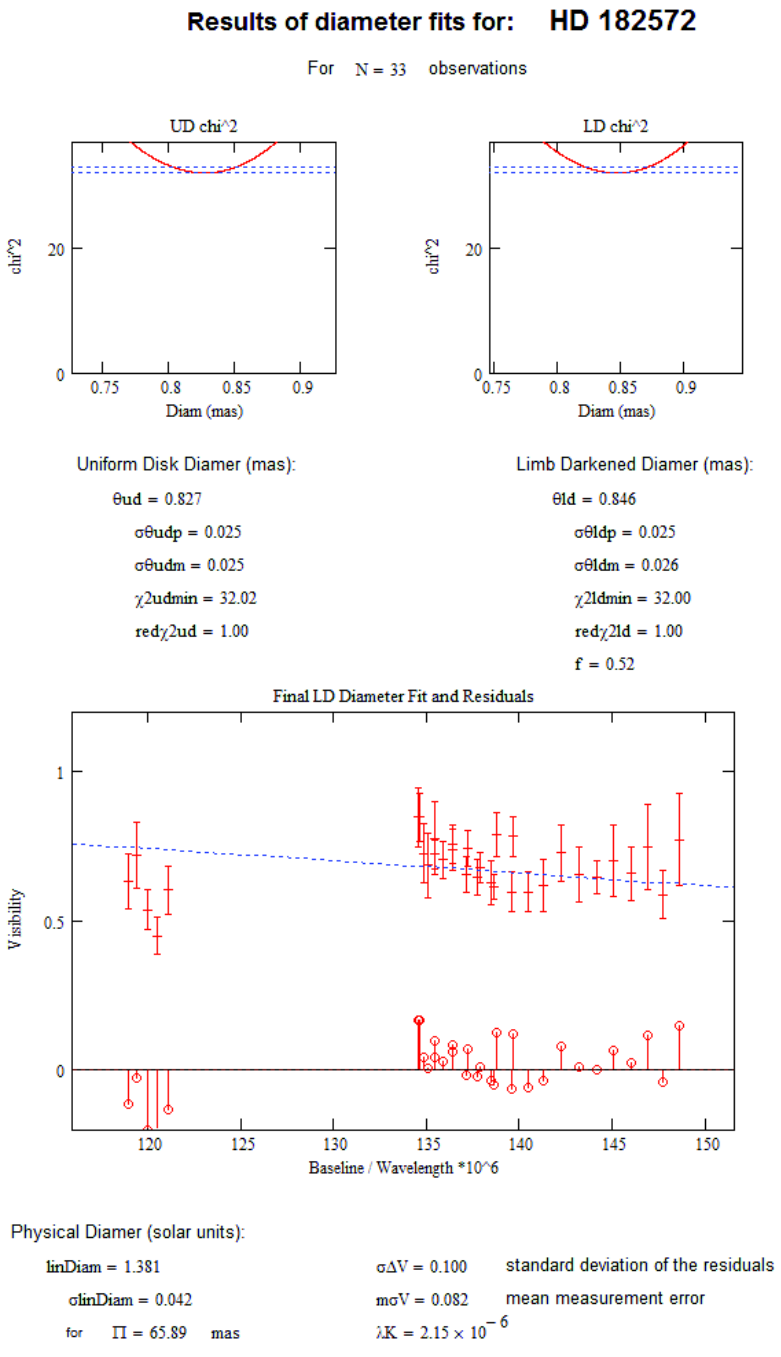

FIGURE C.75: **Diameter fit for HD 182572**

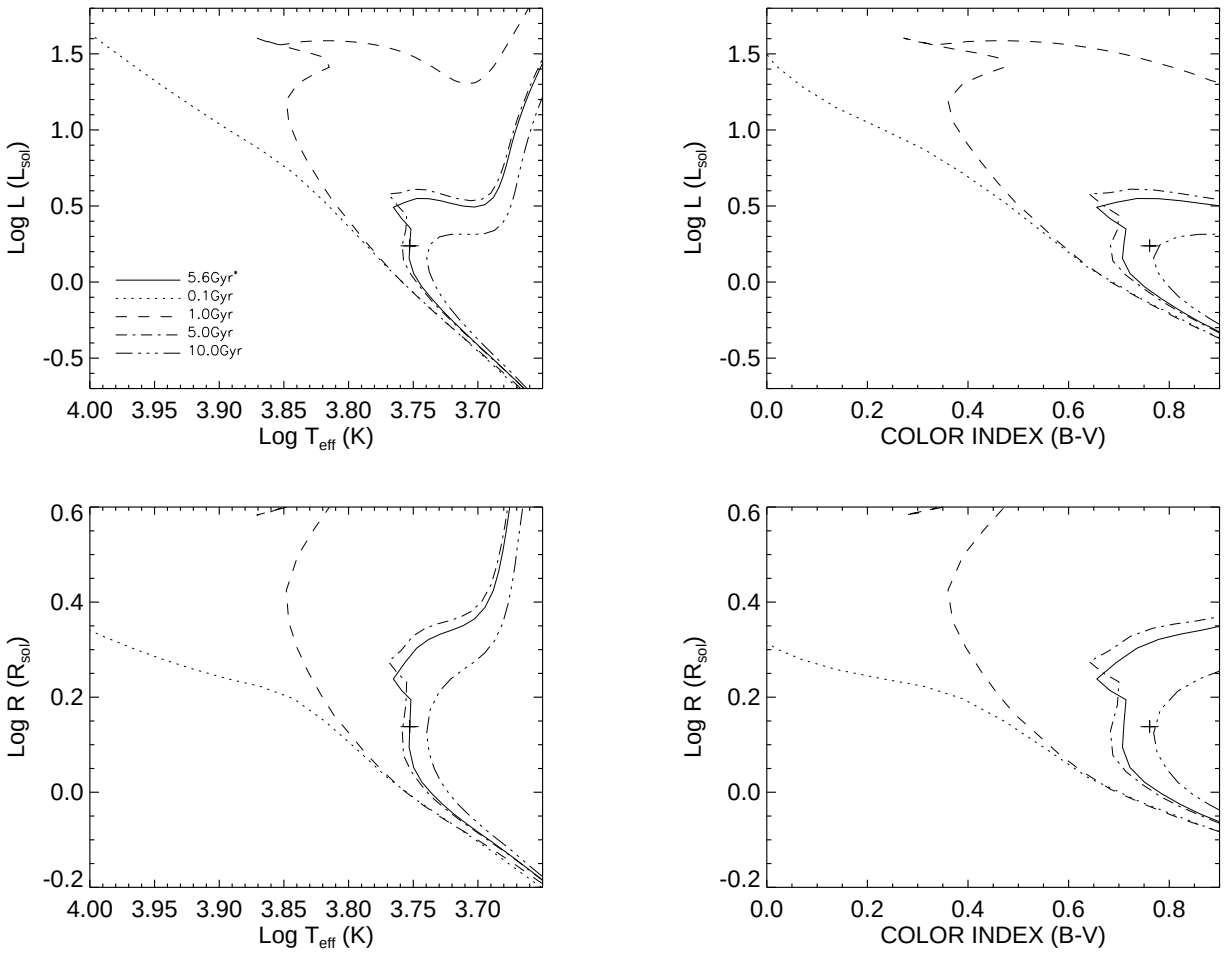

FIGURE C.76: **Y^2 Model Isochrones for HD 182572:** HD 182572 data (and 1-σ errors) plotted against Y^2 models isochrones ([α/Fe]=0.0, [Fe/H]=0.33).

C.39 HD 185144

Results on this star have been published in Boyajian et al. (2008). To re-iterate the important information, we give the calibrated visibilities and Diameter fit below.

TABLE C.39: HD 185144 Visibilities

MJD	**B** **(m)**	ψ (°)	**V**	σ**V**
54244.974	252.1	134.9	0.532	0.097
54244.984	250.1	131.7	0.575	0.051
54244.997	247.3	127.8	0.528	0.044
54245.971	252.0	134.7	0.522	0.050
54245.984	249.6	131.0	0.550	0.051
54245.995	247.2	127.7	0.520	0.053
54246.007	244.6	124.3	0.564	0.059
54279.838	303.2	268.9	0.380	0.016
54280.715	275.4	131.8	0.492	0.036
54280.860	307.1	260.5	0.346	0.034
54280.872	308.6	256.6	0.293	0.022
54280.884	309.9	252.5	0.307	0.020
54281.725	278.4	127.1	0.394	0.034
54282.675	267.4	145.5	0.472	0.056
54282.687	270.1	140.5	0.434	0.048

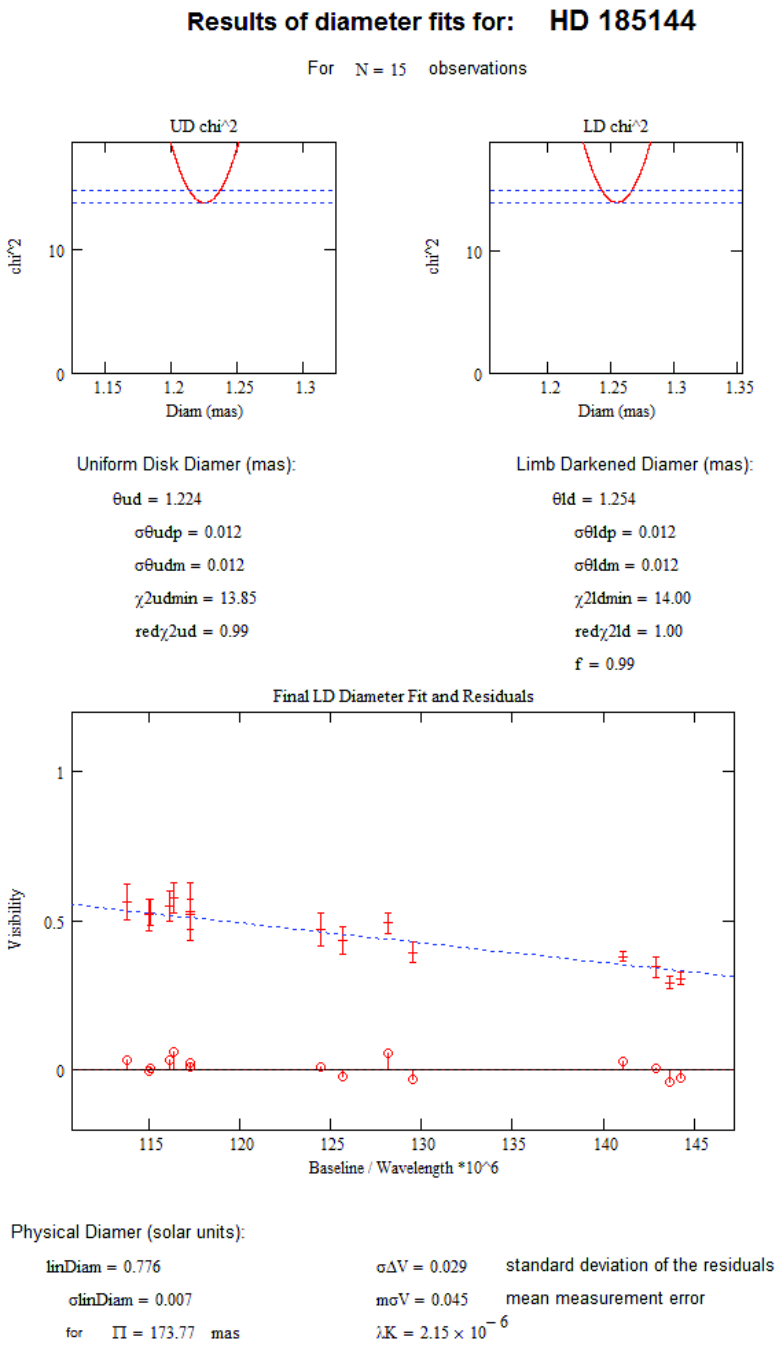

FIGURE C.77: **Diameter fit for HD 185144**

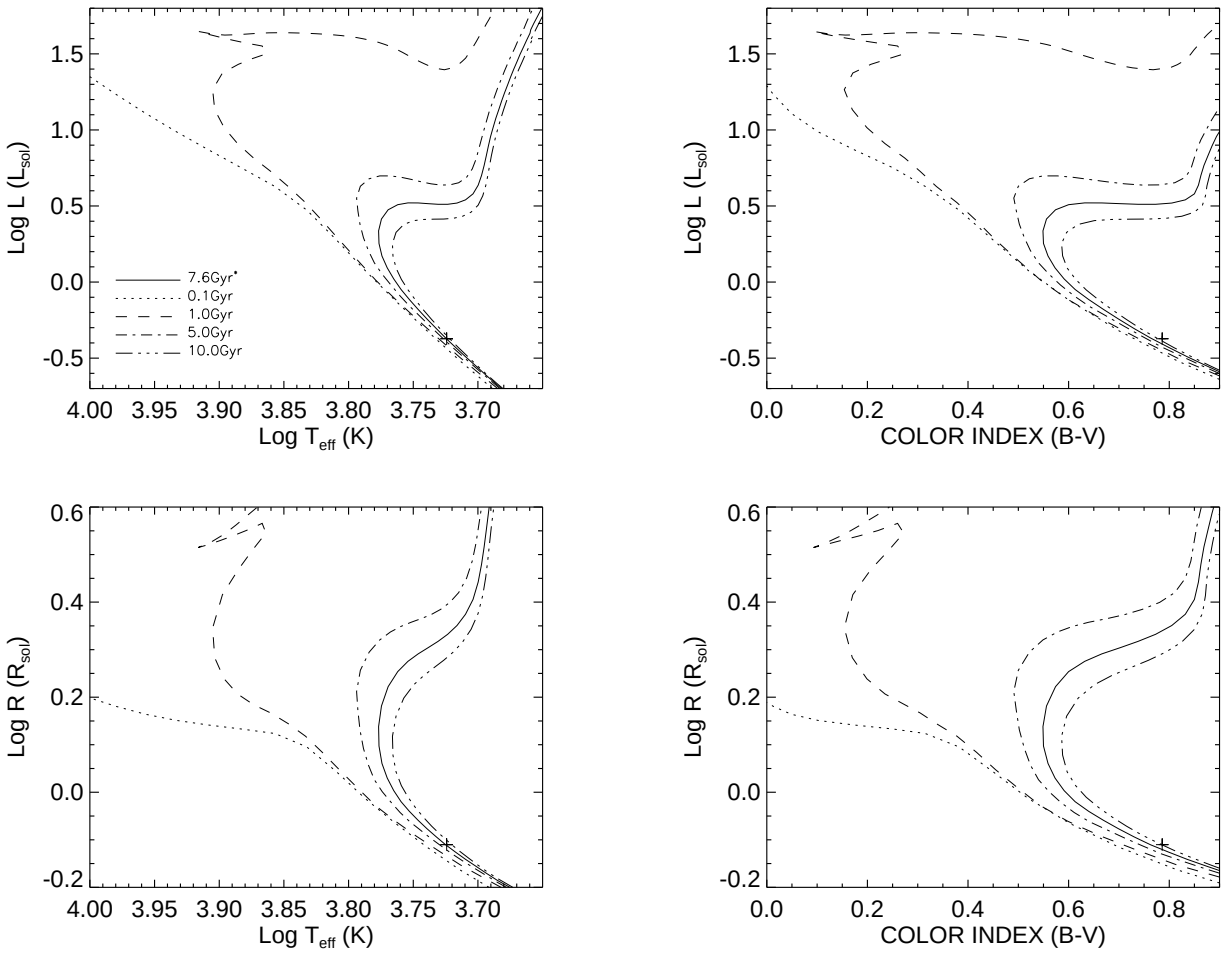

FIGURE C.78: **Y^2 Model Isochrones for HD 185144:** HD 185144 data (and 1-σ errors) plotted against Y^2 models isochrones ([α/Fe]=0.0, [Fe/H]=−0.24).

C.40 HD 185395

Table C.40: HD 185395 Visibilities

MJD	B (m)	ψ (°)	V	σV
54246.951	268.1	198.5	0.779	0.062
54301.708	290.5	226.4	0.738	0.047
54301.720	295.6	224.1	0.579	0.045
54301.736	301.7	221.0	0.563	0.067
54301.748	305.8	218.6	0.668	0.098
54301.760	309.3	216.2	0.609	0.070
54301.772	312.6	213.5	0.588	0.050
54301.784	315.2	211.0	0.598	0.059
54301.801	318.3	207.4	0.637	0.063
54301.811	319.8	205.2	0.720	0.077
54301.825	321.7	201.9	0.696	0.082
54301.836	322.8	199.5	0.667	0.050
54406.670	233.7	233.2	0.734	0.078
54406.677	232.1	235.8	0.737	0.079
54406.686	230.1	239.2	0.712	0.085
54406.693	228.6	241.7	0.737	0.091
54406.700	227.3	244.4	0.754	0.080
54672.812	322.3	249.2	0.612	0.051
54672.819	323.0	250.7	0.625	0.056
54672.826	323.6	252.3	0.646	0.044
54672.833	324.1	254.0	0.560	0.061
54672.840	324.6	255.6	0.550	0.053
54672.846	325.0	257.2	0.582	0.048
54672.853	325.3	258.7	0.535	0.053
54672.860	325.6	260.3	0.528	0.069

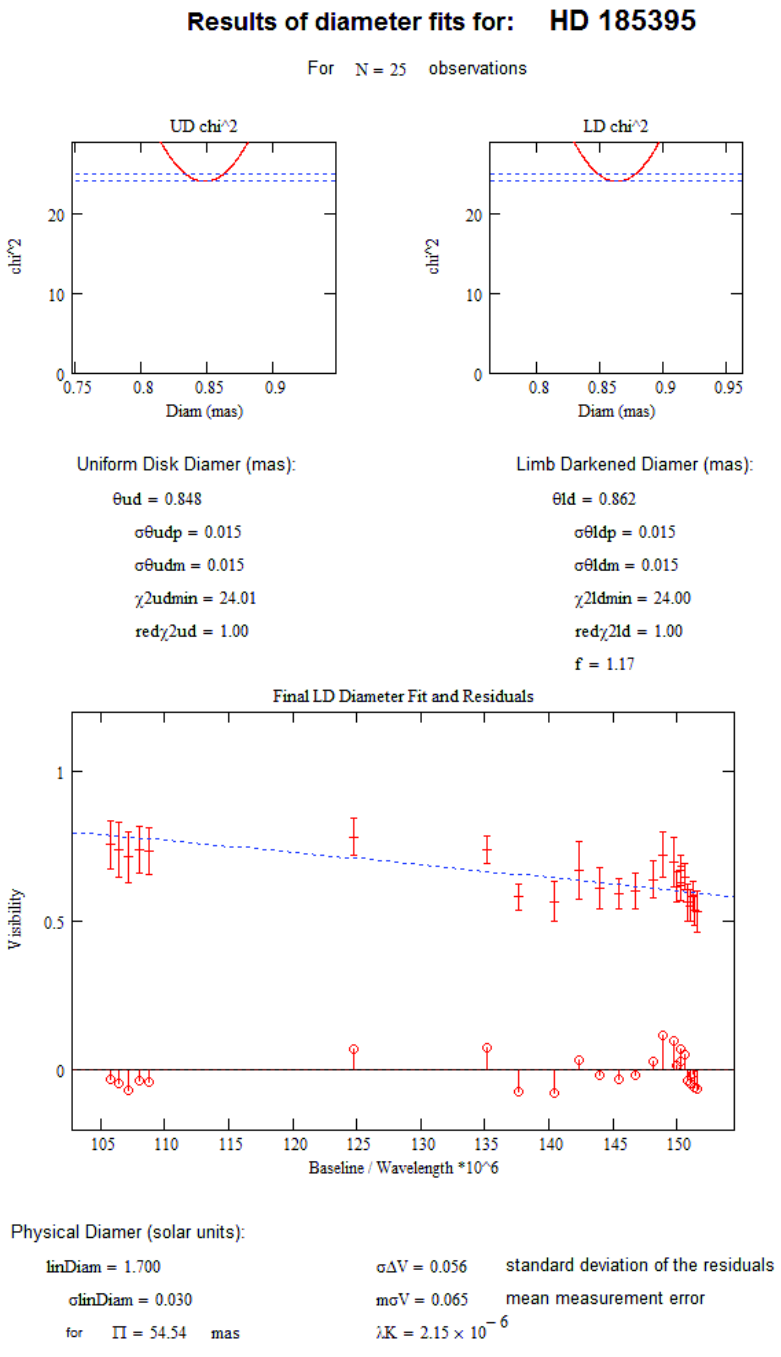

FIGURE C.79: **Diameter fit for HD 185395**

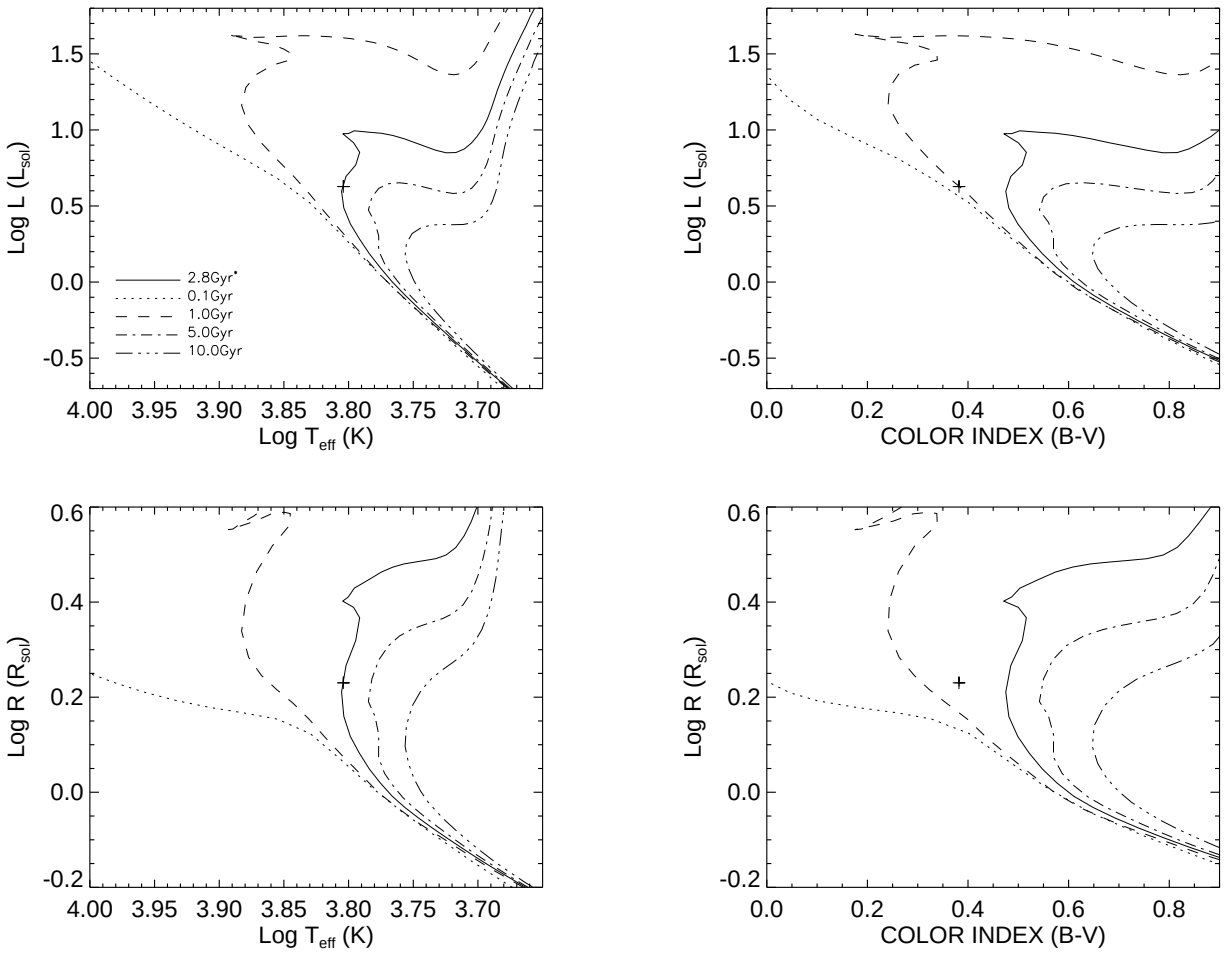

FIGURE C.80: **Y^2 Model Isochrones for HD 185395:** HD 185395 data (and 1-σ errors) plotted against Y^2 models isochrones ([α/Fe]=0.0, [Fe/H]=−0.04).

C.41 HD 210418

TABLE C.41: HD 210418 Visibilities

MJD	B (m)	ψ (°)	V	σV
54645.929	316.1	34.1	0.704	0.096
54645.938	312.8	32.9	0.723	0.159
54645.954	306.7	30.4	0.599	0.129
54645.966	301.9	28.3	0.824	0.130
54645.975	298.6	26.8	0.648	0.099
54645.983	295.2	25.1	0.591	0.066
54669.935	288.2	21.2	0.634	0.077
54669.948	283.8	18.2	0.611	0.094
54669.955	281.5	16.5	0.706	0.126
54669.962	279.6	14.8	0.650	0.125
54669.968	277.8	13.1	0.662	0.123
54669.979	275.4	10.3	0.717	0.071
54669.985	274.2	8.6	0.644	0.080
54669.991	273.2	6.8	0.647	0.090
54669.997	272.5	5.0	0.724	0.096
54671.846	264.6	28.6	0.677	0.094
54671.856	262.0	27.2	0.729	0.094
54671.865	259.5	25.7	0.688	0.105
54671.877	256.1	23.6	0.817	0.120
54740.683	311.0	32.2	0.674	0.075
54740.691	307.9	30.9	0.703	0.095

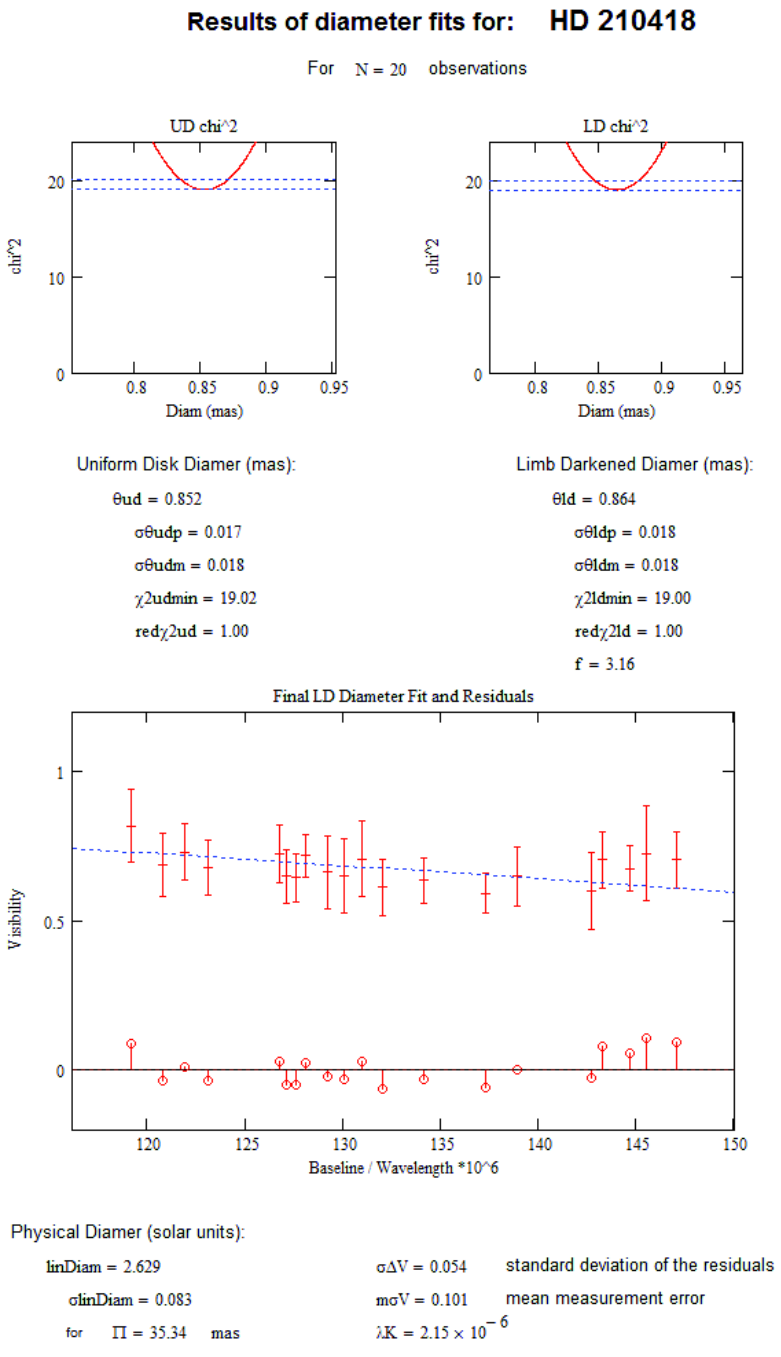

FIGURE C.81: **Diameter fit for HD 210418**

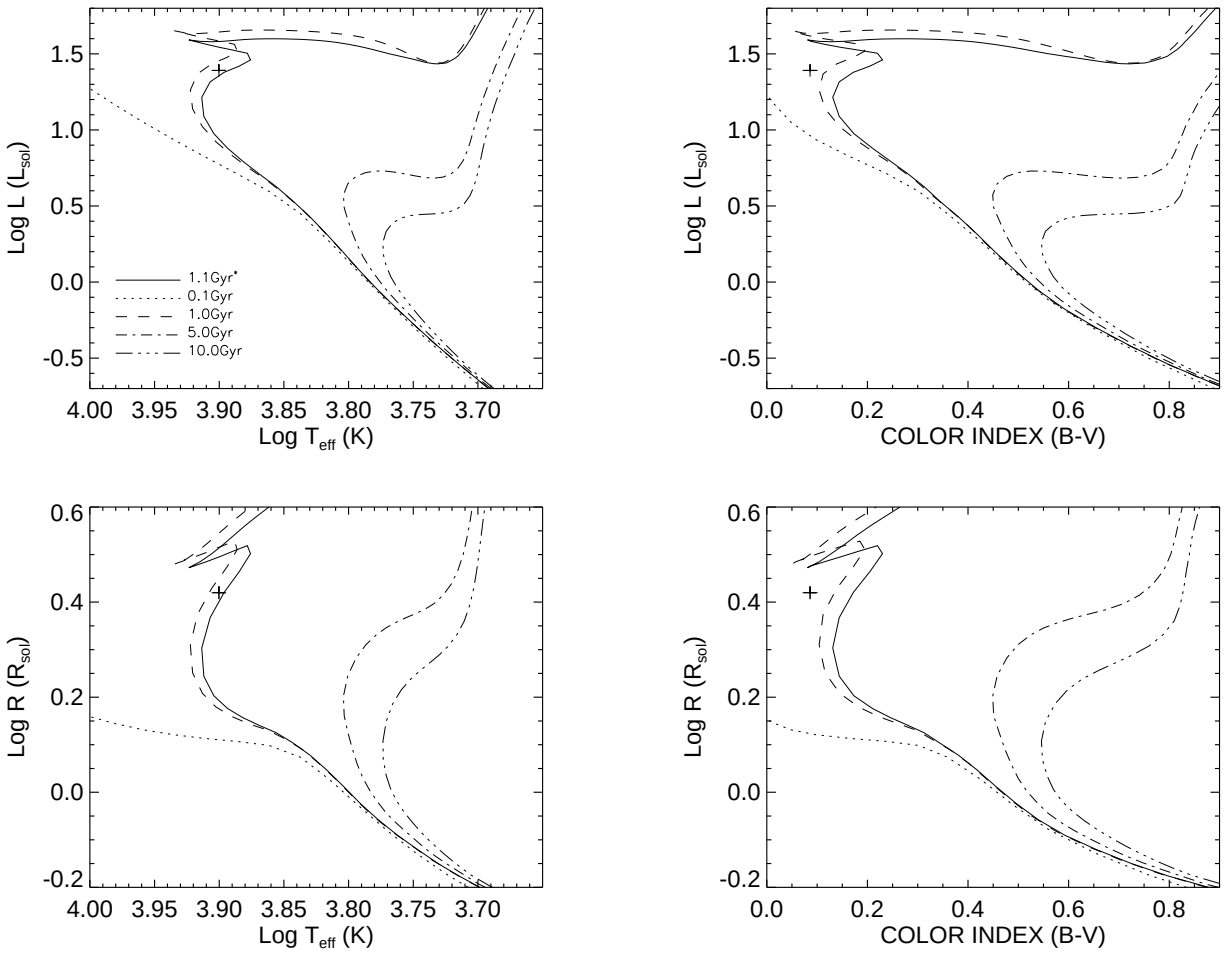

FIGURE C.82: **Y^2 Model Isochrones for HD 210418:** HD 210418 data (and 1-σ errors) plotted against Y^2 models isochrones ([α/Fe]=0.0, [Fe/H]=−0.38).

C.42 HD 213558

TABLE C.42: HD 213558 Visibilities

MJD	B (m)	ψ (°)	V	σV
54351.681	285.8	48.2	0.900	0.090
54351.717	301.3	41.2	0.833	0.066
54351.723	303.6	39.9	0.851	0.081
54351.731	306.0	38.4	0.807	0.104
54351.749	311.1	34.7	0.922	0.089
54383.812	304.4	46.3	0.826	0.052
54383.819	302.8	44.0	0.859	0.077
54383.825	301.4	41.9	0.771	0.079
54383.834	299.4	39.2	0.781	0.091
54383.840	297.9	37.1	0.786	0.084
54383.850	295.6	33.6	0.866	0.096
54383.856	294.2	31.6	0.835	0.070
54383.862	292.8	29.4	0.864	0.066
54383.879	289.2	23.2	0.742	0.092
54383.886	288.0	20.8	0.746	0.073
54383.872	290.6	25.7	0.841	0.086
54458.614	326.3	178.7	0.835	0.146
54458.625	326.2	175.9	0.722	0.096
54458.636	326.0	173.3	0.837	0.122
54458.648	325.6	170.5	0.837	0.079
54458.659	325.1	167.8	0.748	0.074
54458.672	324.3	164.8	0.823	0.086
54668.972	324.6	14.3	0.666	0.067
54668.979	325.0	12.7	0.626	0.078
54668.986	325.3	11.1	0.652	0.064
54668.993	325.6	9.5	0.712	0.066
54668.999	325.8	7.9	0.634	0.074

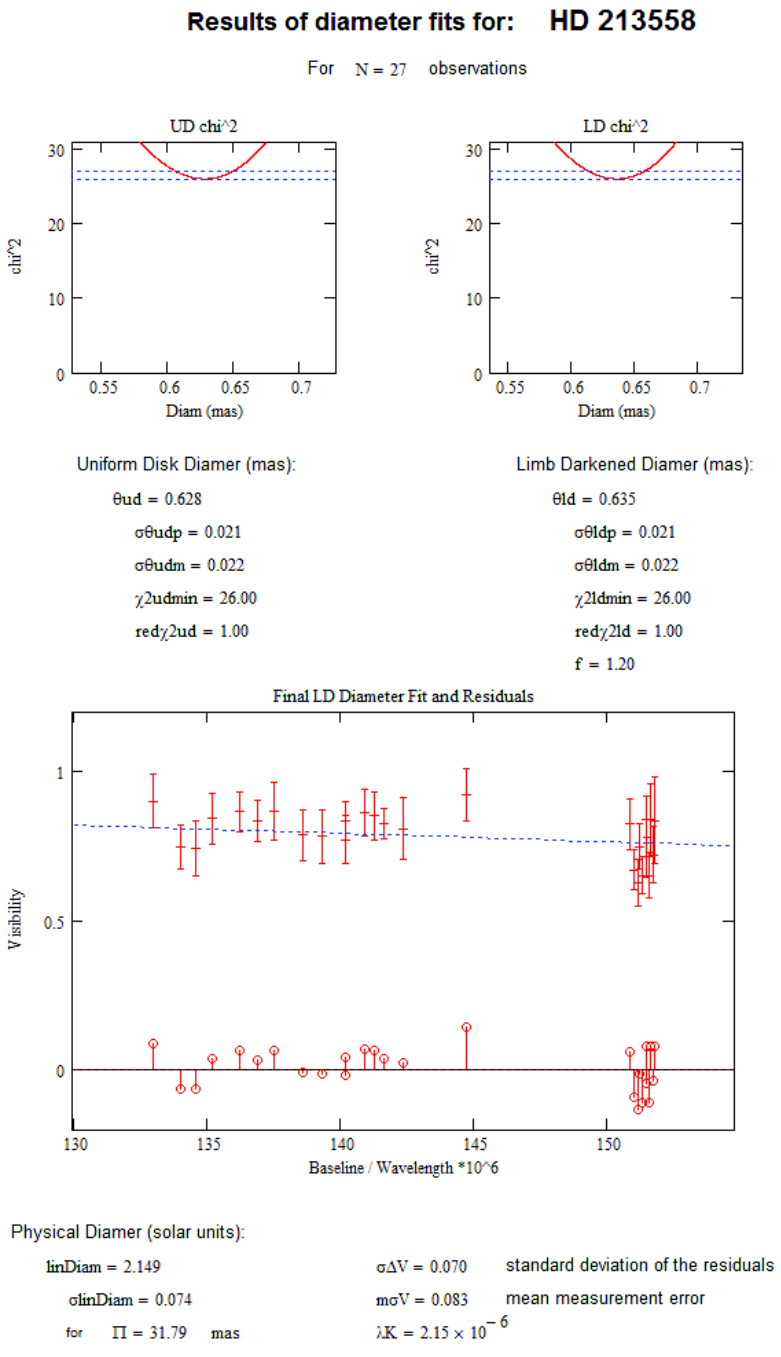

FIGURE C.83: **Diameter fit for HD 213558**

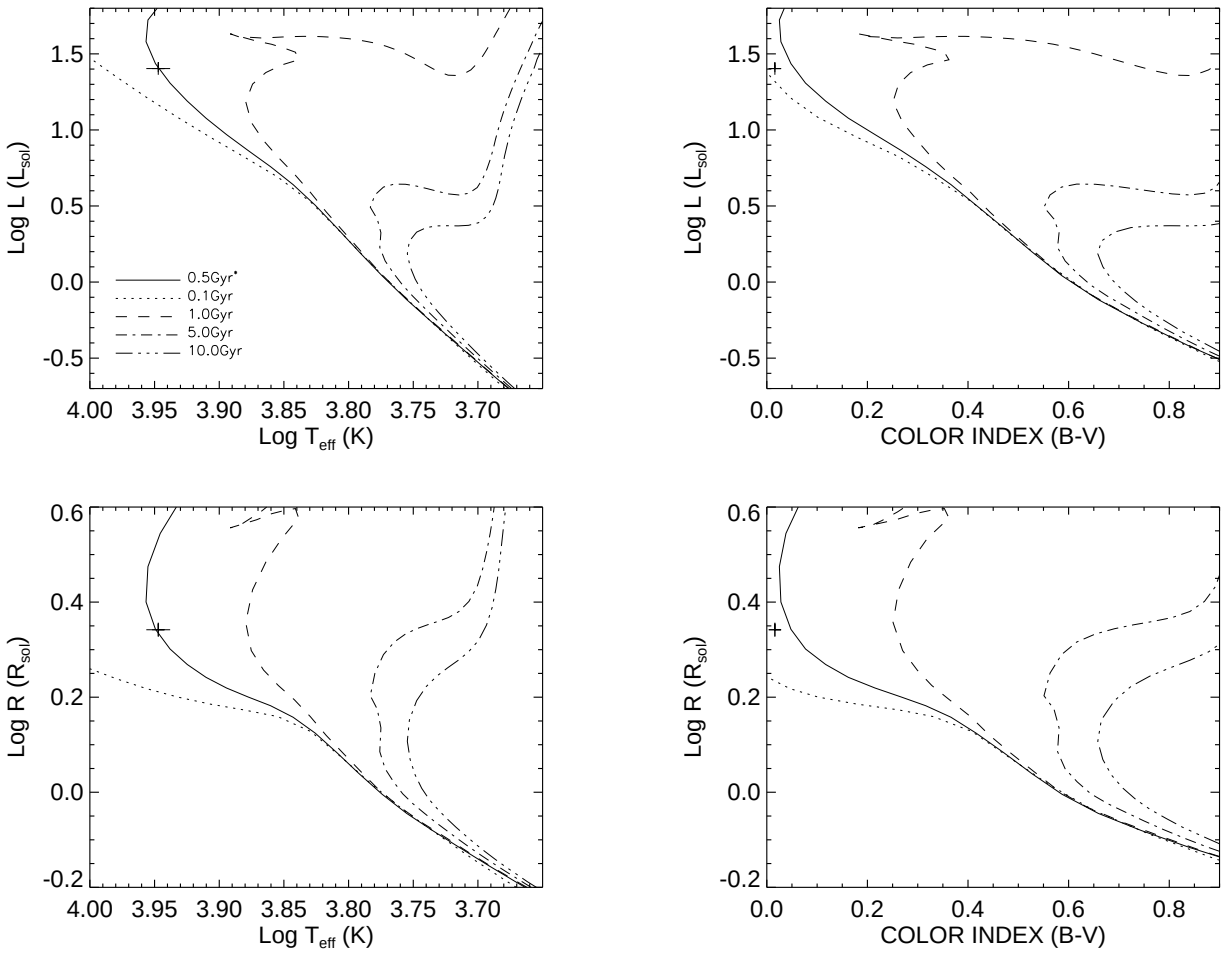

FIGURE C.84: **Y^2 Model Isochrones for HD 213558:** HD 213558 data (and 1-σ errors) plotted against Y^2 models isochrones ([α/Fe]=0.0, [Fe/H]=0.0).

C.43 HD 215648

Table C.43: HD 215648 Visibilities

MJD	B (m)	ψ (°)	V	σV
54298.116	326.3	228.4	0.414	0.028
54298.140	328.5	228.8	0.322	0.027
54298.166	330.0	229.5	0.329	0.029
54298.192	330.6	230.4	0.340	0.038
54302.910	318.8	210.6	0.442	0.025
54302.919	316.3	209.1	0.446	0.028
54302.925	314.4	208.0	0.435	0.027
54302.932	312.3	206.8	0.465	0.027
54302.944	308.7	204.5	0.461	0.020
54302.953	306.1	202.7	0.475	0.024
54302.961	303.6	200.9	0.479	0.034
54302.969	301.4	199.1	0.500	0.028
54302.978	299.0	197.1	0.541	0.030
54302.984	297.5	195.6	0.510	0.047
54302.991	296.0	194.0	0.569	0.049
54302.997	294.6	192.4	0.532	0.068
54303.004	293.3	190.6	0.523	0.055
54303.011	292.3	189.0	0.455	0.041
54671.891	267.7	245.4	0.597	0.097
54671.897	266.3	246.5	0.536	0.067
54671.903	265.1	247.6	0.538	0.071
54671.910	263.9	248.7	0.603	0.090
54671.916	262.7	249.9	0.510	0.051
54740.748	308.2	245.8	0.506	0.064
54740.773	300.8	251.4	0.402	0.055
54740.791	296.4	255.6	0.472	0.043
54740.801	294.2	258.1	0.521	0.045
54740.817	291.7	262.1	0.467	0.056
54740.699	322.2	237.4	0.411	0.050
54740.707	320.2	238.6	0.404	0.053
54740.714	318.2	239.7	0.431	0.049
54739.840	289.9	267.5	0.573	0.059
54739.849	289.7	180.0	0.519	0.054
54739.857	289.9	92.1	0.484	0.048

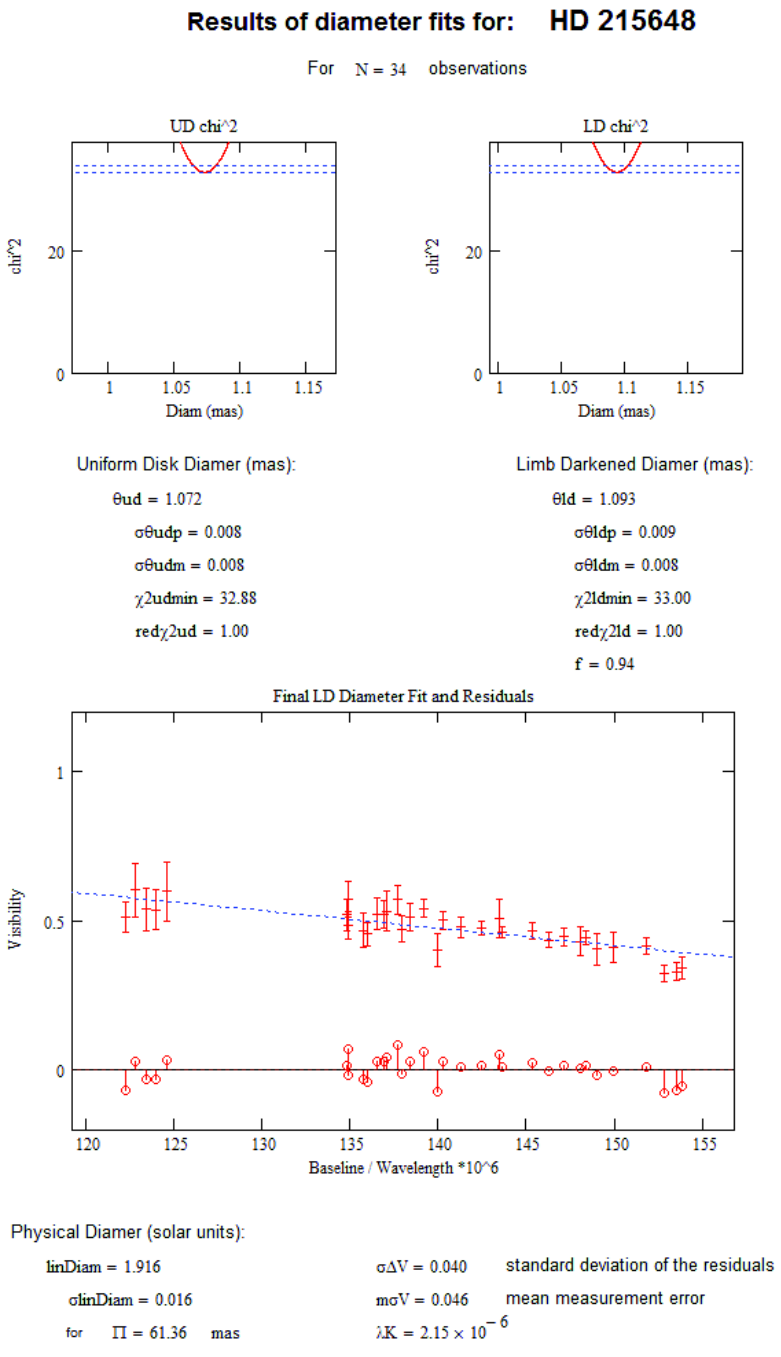

FIGURE C.85: **Diameter fit for HD 215648**

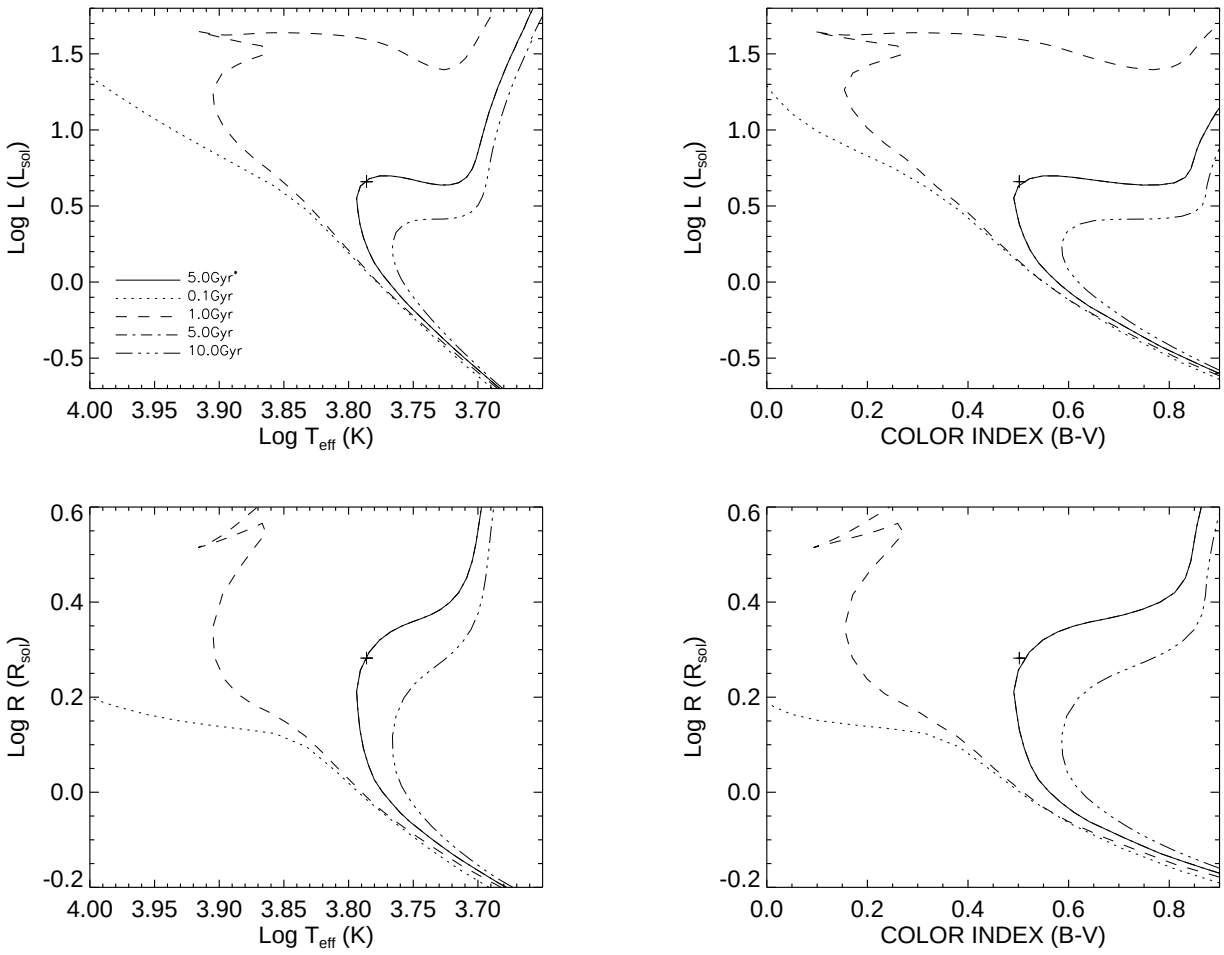

FIGURE C.86: **Y^2 Model Isochrones for HD 215648:** HD 215648 data (and 1-σ errors) plotted against Y^2 models isochrones ([α/Fe]=0.0, [Fe/H]=−0.24).

C.44 HD 222368

TABLE C.44: HD 222368 Visibilities

MJD	B (m)	ψ (°)	V	σV
54076.624	285.5	200.6	0.518	0.078
54076.635	281.5	197.8	0.446	0.065
54076.646	278.1	195.1	0.467	0.074
54076.658	275.0	192.0	0.678	0.095
54301.904	323.7	217.3	0.437	0.030
54301.914	320.9	216.3	0.454	0.030
54301.927	316.7	214.8	0.478	0.035
54301.942	311.5	212.8	0.447	0.023
54301.956	306.0	210.7	0.489	0.025
54301.971	300.0	208.1	0.496	0.028
54301.978	297.0	206.7	0.494	0.027
54301.986	293.6	205.1	0.488	0.035
54301.994	290.6	203.6	0.509	0.032
54302.001	287.9	202.0	0.557	0.042
54302.007	285.6	200.6	0.602	0.051
54352.768	323.0	233.0	0.355	0.053
54352.775	321.3	233.6	0.351	0.053
54352.781	319.4	234.3	0.429	0.050
54352.787	317.4	235.0	0.480	0.094
54352.793	315.2	235.8	0.495	0.067
54739.753	308.0	238.5	0.389	0.054
54739.763	304.1	240.1	0.429	0.073
54739.771	300.9	241.5	0.414	0.068
54739.778	298.0	242.8	0.417	0.037
54739.788	294.0	244.7	0.454	0.066
54739.795	291.2	246.1	0.457	0.084
54739.803	287.9	248.0	0.614	0.104
54739.726	317.8	234.8	0.452	0.048
54739.734	315.3	235.8	0.459	0.080
54739.741	312.9	236.7	0.390	0.056
54740.727	316.7	235.3	0.453	0.040
54740.740	312.2	236.9	0.467	0.066
54740.752	307.6	238.7	0.561	0.069
54740.781	295.8	243.8	0.548	0.059
54740.794	290.2	246.6	0.459	0.056
54740.805	286.2	249.0	0.452	0.058

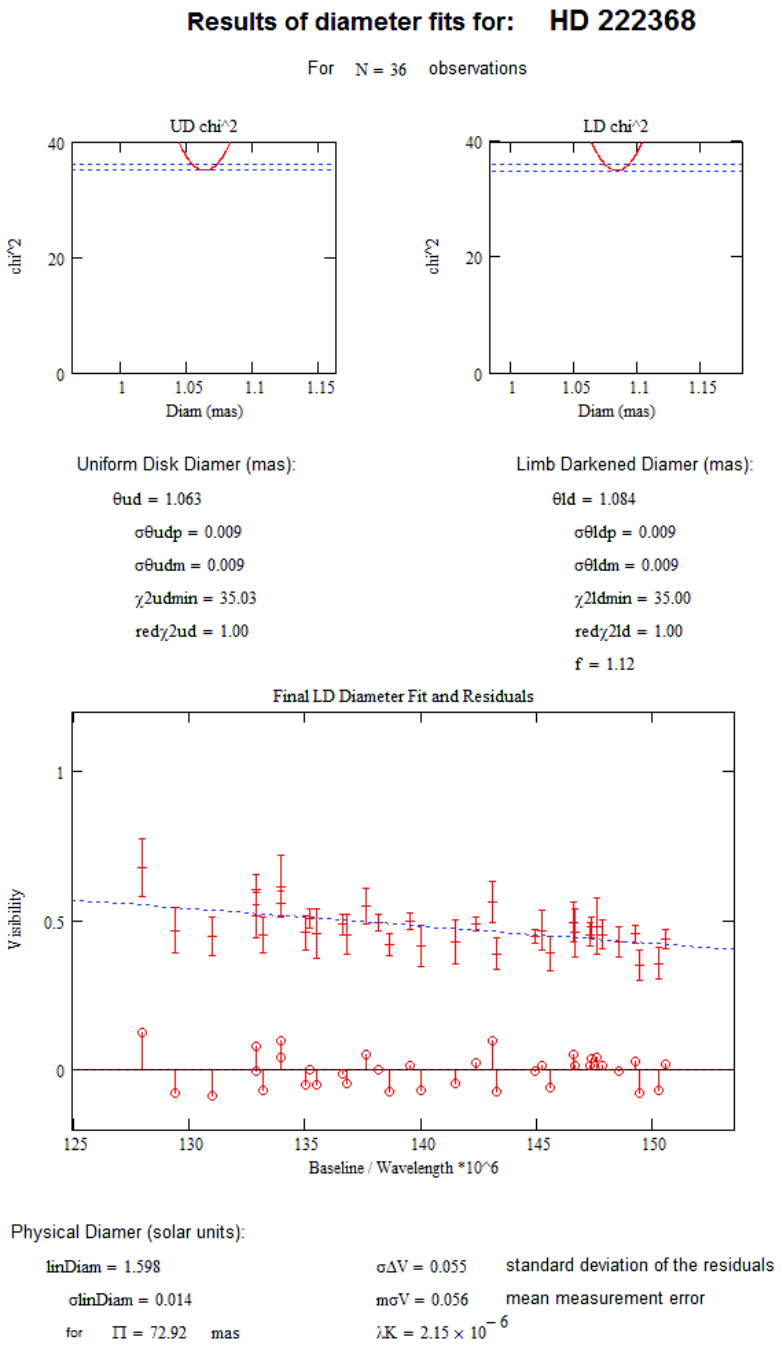

FIGURE C.87: **Diameter fit for HD 222368**

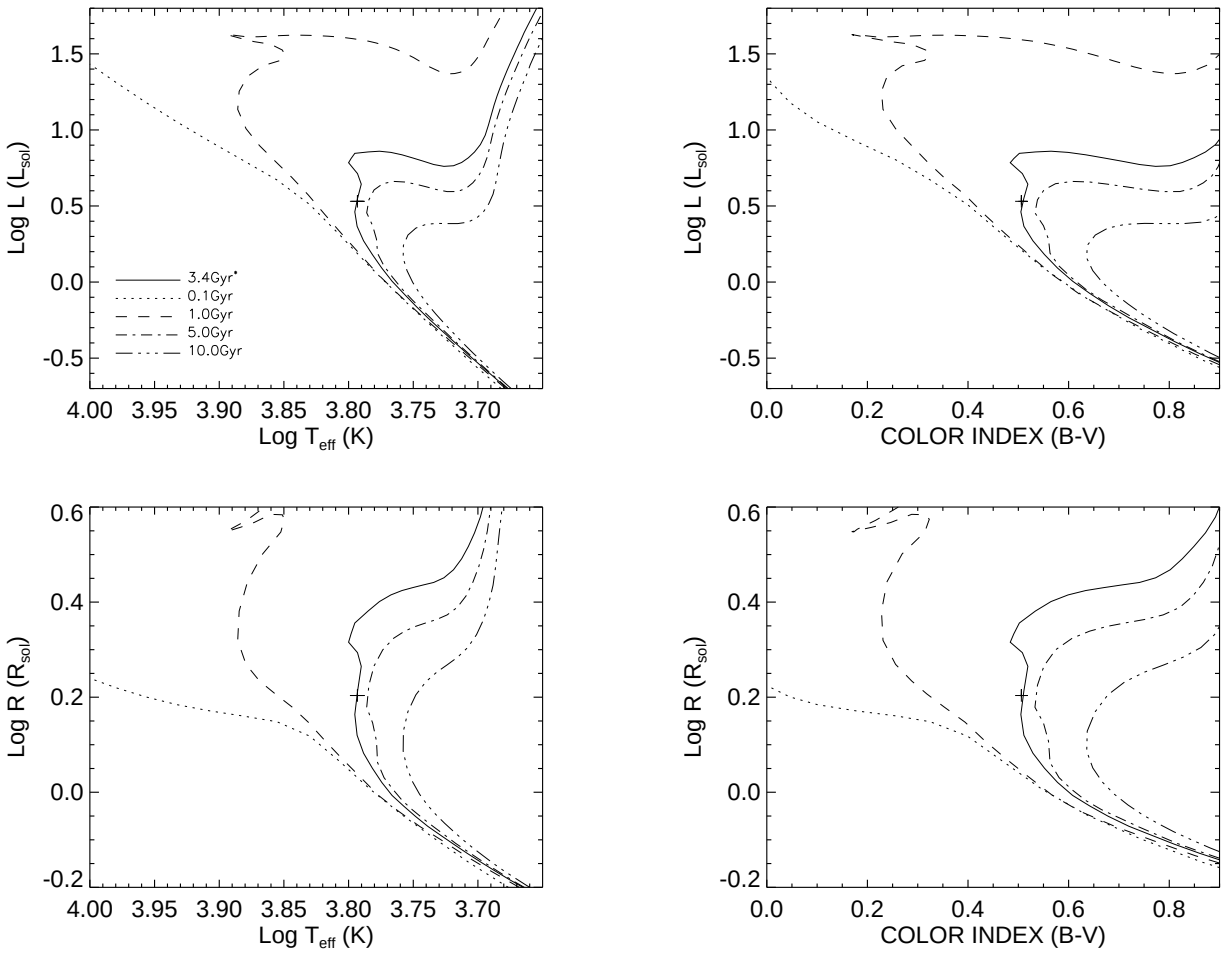

FIGURE C.88: **Y^2 Model Isochrones for HD 222368:** HD 222368 data (and 1-σ errors) plotted against Y^2 models isochrones ([α/Fe]=0.0, [Fe/H]=−0.08).

– D –

Appendix D: Published Work in the Field of Stellar Interferometry

This appendix includes published work in the general topic of stellar interferometry with the CHARA Array.

The Astrophysical Journal, 683:424–432, 2008 August 10

ANGULAR DIAMETERS OF THE G SUBDWARF μ CASSIOPEIAE A AND THE K DWARFS σ DRACONIS AND HR 511 FROM INTERFEROMETRIC MEASUREMENTS WITH THE CHARA ARRAY

Tabetha S. Boyajian, Harold A. McAlister, Ellyn K. Baines, Douglas R. Gies, Todd Henry, Wei-Chun Jao, David O'Brien, Deepak Raghavan, and Yamina Touhami
Center for High Angular Resolution Astronomy, Georgia State University, P.O. Box 3969, Atlanta, GA 30302-3969; tabetha@chara.gsu.edu, hal@chara.gsu.edu, baines@chara.gsu.edu, gies@chara.gsu.edu, thenry@chara.gsu.edu, jao@chara.gsu.edu, obrien@chara.gsu.edu, raghavan@chara.gsu.edu, yamina@chara.gsu.edu

Theo A. ten Brummelaar, Chris Farrington, P. J. Goldfinger, Laszlo Sturmann, Judit Sturmann, and Nils H. Turner
CHARA Array, Mount Wilson Observatory, Mount Wilson, CA 91023; theo@chara-array.org, farrington@chara-array.org, pj@chara-array.org, sturmann@chara-array.org, judit@chara-array.org, nils@chara-array.org

and

Stephen Ridgway
National Optical Astronomy Observatory, P.O. Box 26732, Tucson, AZ 85726-6732; sridgway@noao.edu
Received 2007 November 26; accepted 2008 April 16

ABSTRACT

Using the longest baselines of the CHARA Array, we have measured the angular diameter of the G5 V subdwarf μ Cas A, the first such determination for a halo population star. We compare this result to new diameters for the higher metallicity K0 V stars, σ Dra and HR 511, and find that the metal-poor star, μ Cas A, has an effective temperature ($T_{\rm eff} = 5297 \pm 32$ K), radius ($R = 0.791 \pm 0.008\ R_{\odot}$), and absolute luminosity ($L = 0.442 \pm 0.014\ L_{\odot}$) comparable to those of the other two stars with later spectral types. We show that stellar models show a discrepancy in the predicted temperature and radius for μ Cas A, and we discuss these results and how they provide a key to understanding the fundamental relationships for stars with low metallicity.

Subject headings: infrared: stars — stars: fundamental parameters (temperatures, diameters — stars: individual (HD 6582, HD 185144, HR 511, μ Cassiopeiae) — subdwarfs — techniques: interferometric

Online material: machine-readable table

1. INTRODUCTION

Direct measurements of stellar angular diameters offer a crucial means of providing accurate fundamental information for stars. Advances in long-baseline optical/infrared interferometry (LBOI) now enable us to probe the realm of cooler main-sequence stars to better define their characteristics. In their pioneering program at the Narrabri Intensity Interferometer, Hanbury Brown et al. (1974a) produced the first modern interferometric survey of stars by measuring the diameters of 32 bright stars in the spectral type range O5–F8 with seven stars lying on the main sequence. The current generation of interferometers possess sufficiently long baselines to expand the main-sequence diameter sensitivity to include even later spectral types, as exemplified by Lane et al. (2001), Ségransan et al. (2003), and Berger et al. (2006), who determined diameters of K–M stars, and Baines et al. (2008), who measured the radii of exoplanet host stars with types between F7 and K0.

In this work, we focus primarily on the fundamental parameters of the well-known population II star μ Cassiopeiae (μ Cas, HR 321, HD 6582, GJ 53 A), an astrometric binary with a period of ~22 yr consisting of a G5 + M5 pair of main-sequence stars with low metallicity (Drummond et al. 1995 and references therein). With the CHARA Array (Center for High Angular Resolution Astronomy), we have measured the angular diameter of μ Cas A to <1% accuracy, thereby yielding the effective temperature, linear radius, absolute luminosity, and gravity (with accuracies of 0.6%, 1.0%, 3.2%, and 9.0%, respectively). We compare these newly determined fundamental stellar parameters for μ Cas A to those of two K0 V stars, HR 511 (HD 10780, GJ 75) and σ Draconis (σ Dra, HR 7462, HD 185144, GJ 764), which we also observed with the CHARA Array (§ 4.1). These fundamental parameters are then compared to model isochrones (§ 4.2).

2. INTERFEROMETRIC OBSERVATIONS

Observations were taken using the CHARA Array, located on Mount Wilson, CA, and remotely operated from the Georgia State University AROC (Arrington Remote Operations Center) facility in Atlanta, GA. The data were acquired over several nights using a combination of the longest projected baselines (ranging from 230 to 320 m) and the CHARA Classic beam combiner in the K' band (ten Brummelaar et al. 2005). The data were collected in the usual calibrator-object-calibrator sequence (brackets), yielding a total of 26, 15, and 22 bracketed observations for μ Cas, σ Dra, and HR 511, respectively.

For both μ Cas A and HR 511, we used the same calibrator star, HD 6210, which is a relatively close, unresolved, bright star with no known companions. Under the same criteria, we selected HD 193664 as the calibrator star for σ Dra. For each star, a collection of magnitudes (Johnson *UBV*, Johnson et al. 1966; Strömgren *uvby*, Hauck & Mermilliod 1998; 2MASS *JHK*, Skrutskie et al. 2006) were transformed into calibrated flux measurements using the methods described in Colina et al. (1996), Gray (1998), and Cohen et al. (2003). We then fit a model spectral energy distribution[1] (SED) to the observed flux-calibrated photometry to

[1] The model fluxes were interpolated from the grid of models from R. L. Kurucz, available at http://kurucz.cfa.harvard.edu.

determine the limb-darkened angular diameters $\theta_{SED}(T_{eff}, \log g)$ for these stars. We find $\theta_{SED}(6100, 3.8) = 0.519 \pm 0.012$ mas for HD 6210 and $\theta_{SED}(6100, 4.5) = 0.494 \pm 0.019$ mas for HD 193664. These angular diameters translate to absolute visibilities of 0.87 and 0.89 for the mean baselines used for the observations, or $\pm 0.8\%$ and $\pm 1.2\%$ errors, where these errors are propagated through to the final visibility measurements for our stars during the calibration process. An additional independent source of error is the uncertainty in the effective wavelength of the observed spectral bandpass. As described by McAlister et al. (2005) the effective wavelength of the K' filter employed for these observations has been adjusted to incorporate estimates of the transmission and reflection efficiencies of the surfaces and mediums the light encounters on its way to the detector, as well as for the effective temperature of the star. This calculation yields an effective wavelength for these observations of 2.15 ± 0.01 μm, which leads to a contribution at the 0.4% level to the angular diameter error budget. Due to the fact that flux distribution in the K' band for all of our stars is in the Rayleigh-Jeans tail, we find that there are no object-to-object differences in this calculation of effective wavelength due each star having a different effective temperature.

3. DATA REDUCTION AND DIAMETER FITS

The data were reduced and calibrated using the standard data processing routines employed for CHARA Classic data (see ten Brummelaar et al. 2005 and McAlister et al. 2005 for details). For each calibrated observation, Table 1 lists the time of midexposure, the projected baseline B, the orientation of the baseline on the sky ψ, the visibility V, and the 1 σ error to the visibility σV.

We did not detect the secondary star in μ Cas as a separated fringe packet (SFP) in any of our observations (see Farrington & McAlister 2006 for discussion on interferometric detections of SFP binaries). However, for close binaries, the measured instrumental visibility is affected by the flux of two stars, so in addition to our analysis of μ Cas A, we must account for incoherent light from the secondary star affecting our measurements. By calculating the ephemeris positions of the binary at the time of our observations, we get the separation ρ_{AB} of the binary during each observation. Although the most recent published orbital parameters are from Drummond et al. (1995), G. Schaefer and collaborators (private communication) have provided us with their updated orbital elements for the binary based on *Hubble Space Telescope* observations (H. E. Bond, PI) taken every six months over the last decade. We use these separations (ranging from 1.380″ to 1.396″) in combination with $\Delta M_K = 3.5$ for the binary (McCarthy 1984; assuming $K \approx K'$) and seeing measurements at the time of each observation to calculate the amount of light the secondary contributes within our detector's field of view (details described in the Appendix). Fortunately our correction factors to the visibilities of μ Cas A are small (0.4%–1.4%), so even high uncertainties in this correction factor have minimal impact on the final corrected measurement.

In order to obtain limb-darkening coefficients for our target stars, SED fits were made to estimate T_{eff} and $\log g$. We used a bilinear interpolation in the Claret et al. (1995) grid of linear limb-darkening coefficients in the K band (μ_K) with our best-fit SED parameters to get μ_K for each star. Because limb darkening has minimal influence in the infrared (here we also assume $K \approx K'$), as well as minimal dependence on temperature, gravity, and abundance for these spectral types, we feel that this method is appropriate and at most will contribute an additional one-tenth of one percent error to our limb-darkened diameters. We calculate the uniform-disk θ_{UD} (eq. [1]) and limb-darkened θ_{LD} (eq. [2]) angular diameters from the calibrated visibilities by χ^2 minimization of the following relations (Hanbury Brown et al. 1974b):

TABLE 1
INTERFEROMETRIC MEASUREMENTS

Star	JD (−2,400,000)	B (m)	ψ (deg)	V[a]	σV
μ Cas A.....	54,282.917	233.2	135.0	0.739	0.093
	54,282.929	239.8	130.0	0.692	0.071
	54,282.954	253.8	120.4	0.652	0.065
	54,298.915	266.4	234.3	0.682	0.038
	54,298.929	274.0	231.4	0.672	0.023

NOTE.—Table 1 is published in its entirety in the electronic edition of the *Astrophysical Journal*. A portion is shown here for guidance regarding its form and content.
[a] Corrected for light from secondary for μ Cas A; see § 3.

$$V = \frac{2J_1(x)}{x}, \tag{1}$$

$$V = \left(\frac{1-\mu_\lambda}{2} + \frac{\mu_\lambda}{3}\right)^{-1}\left[(1-\mu_\lambda)\frac{J_1(x)}{x} + \mu_\lambda\left(\frac{\pi}{2}\right)^{1/2}\frac{J_{3/2}(x)}{x^{3/2}}\right], \tag{2}$$

$$x = \pi B\theta\lambda^{-1}, \tag{3}$$

where J_n is the nth-order Bessel function, and μ_λ is the linear limb darkening coefficient at the wavelength of observation. In equation (3), we define B as the projected baseline in the sky, θ as the uniform-disk angular diameter of the star when applied to equation (1) and the limb-darkened angular diameter when used in equation (2), and λ as the central wavelength of the observational bandpass.

The error to the diameter fit is based on the values on either side of the minimum for which $\chi^2 = \chi^2_{min} + 1$ (Press et al. 1992; Wall & Jenkins 2003). A summary of these results is presented in Table 2, and Figures 1 and 2 show the best fits to our calibrated visibilities along with the 1 σ errors.

4. DISCUSSION

The linear radii, temperatures, and absolute luminosities are calculated through fundamental relationships when the stellar distance, total flux received at Earth, and angular diameter are known. The linear radius of each star can be directly determined by combining our measured angular diameter with the *Hipparcos* parallax. Next, the fundamental relation between a star's total flux F_{BOL} and angular diameter (eq. [4]) is used to calculate the effective temperature T_{eff} and the absolute luminosity:

$$F_{BOL} = \frac{1}{4}\theta^2_{LD}\sigma T^4_{eff}, \tag{4}$$

where σ is the Stefan-Boltzmann constant. For μ Cas A, σ Dra, and HR 511, we calculate radii, effective temperatures, and luminosities purely from direct measurements (Table 2). For these calculations, the F_{BOL} for μ Cas A has been corrected for light contributed by the secondary by adopting the luminosity ratio of the two components from Drummond et al. (1995), effectively reducing its F_{BOL} by 1.3%.

Table 2 lists our derived temperatures for μ Cas A, σ Dra, and HR 511 ($T_{eff} = 5297 \pm 32$, 5299 ± 32, and 5350 ± 76 K, respectively). Our temperatures agree well with the numerous indirect techniques used to estimate T_{eff} with spectroscopic or photometric relationships. Temperatures of μ Cas A derived using these methods range from 5091 to 5387 K (5143–5344 K

TABLE 2
STELLAR PARAMETERS

Element	μ Cas A	σ Dra	HR 511
Spectral type	G5 Vp	K0 V	K0 V
V (mag)	5.17	4.70	5.63
$B-V$	0.69	0.79	0.81
π_{Hip} (mas)	132.42 ± 0.60	173.40 ± 0.46	100.24 ± 0.68
θ_{UD} (mas)	0.951 ± 0.009	1.224 ± 0.011	0.747 ± 0.021
Reduced χ^2_{UD}	0.96	1.00	0.78
θ_{LD} (mas)	0.973 ± 0.009	1.254 ± 0.012	0.763 ± 0.021
Reduced χ^2_{LD}	0.96	1.01	0.79
Radius ($R_\odot$)	0.791 ± 0.008	0.778 ± 0.008	0.819 ± 0.024
F_{BOL}[a] (erg s^{-1} cm^{-2})	2.482E−7[b]	4.130E−7[c]	1.588E−7[d]
[Fe/H][e]	−0.682[f] (−0.71)	−0.199[g] (−0.20)	0.005[g] (0.00)
T_{eff} (K)	5297 ± 32	5299 ± 32	5350 ± 76
Luminosity ($L_\odot$)	0.442 ± 0.014	0.428 ± 0.013	0.49 ± 0.04
log g (cgs)	4.52 ± 0.04	...	...

[a] Adopted 1.5% error.
[b] Average from Blackwell & Lynas-Gray (1998) and Alonso et al. (1996).
[c] Average from Bell & Gustafsson (1989) and Alonso et al. (1996).
[d] Alonso et al. (1995).
[e] Number in parenthesis is metallicity value used in models.
[f] Taylor (2005) +0.14 dex NLTE correction from Thévenin & Idiart (1999).
[g] Taylor (2005).

for σ Dra and 5250–5419 K for HR 511), and while the internal error is low in each reference, the apparent discrepancy among the various methods shows that there is some systematic offset for each temperature scale, as might be expected if atmospheric line opacities are not correctly represented in the models.

4.1. *Comparative Analysis to Observations of μ Cas A, σ Dra, and HR 511*

It can be seen in Table 2 that the temperature, radius, and luminosity of μ Cas A are quite similar to those of σ Dra and HR 511 despite the large difference in spectral types and $B-V$ color indices associated with the classical characteristics of metal-poor stars. These results support the conclusions in Drummond et al. (1995), where their model analysis predicts μ Cas A to have the characteristic radius, temperature, and luminosity of a typical K0 V star. In Figure 3, we compare our new linear radii versus $B-V$ color index to values measured from eclipsing binaries (EBs) and other LBOI measurements, as well as the position of the Sun and a theoretical zero-age main sequence (ZAMS) for solar metallicity stars. The gray scale indicates metallicity estimates for the LBOI points, showing μ Cas A is currently the lowest metallicity star observed in this region of the H-R diagram. The initial characteristics of evolution off the ZAMS is toward the upper-left region of the plot (larger and bluer), which is the main reason for the dispersion of the stellar radii for stars in this region. ZAMS lines for subsolar metallicities lie below this line, and are shifted to bluer colors.

Drummond et al. (1995) determined the mass of μ Cas A from the system's astrometric orbital solution. Lebreton et al. (1999) updated this mass utilizing the more accurate *Hipparcos* distance, yielding a mass of $0.757 \pm 0.060\ M_\odot$. We use this mass with our new radius, to derive a directly measured surface gravity of $\log g = 4.52 \pm 0.04$. This value is comparable to the nominal values for solar metallicity ZAMS G5 V and K0 V stars, $\log g = 4.49$ (Cox 2000).

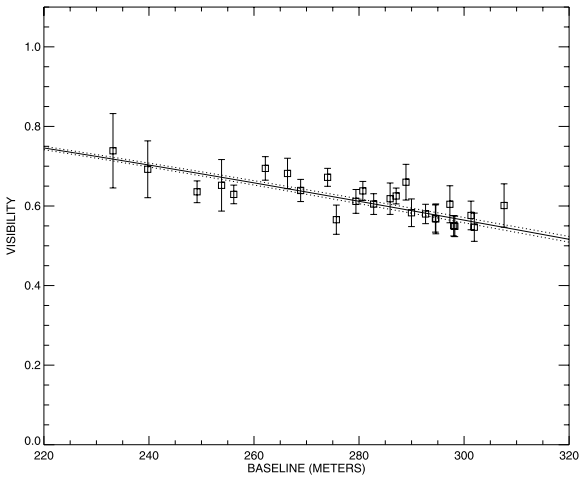

FIG. 1.—Limb-darkened angular diameter fit to μ Cas A.

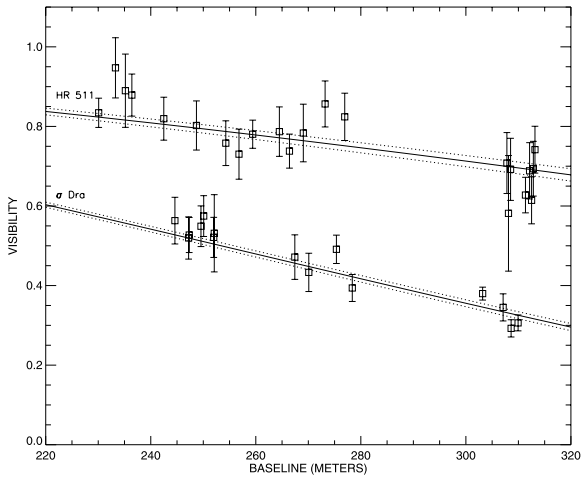

FIG. 2.—Limb-darkened angular diameter fit to σ Dra (*bottom curve*) and HR 511 (*top curve*).

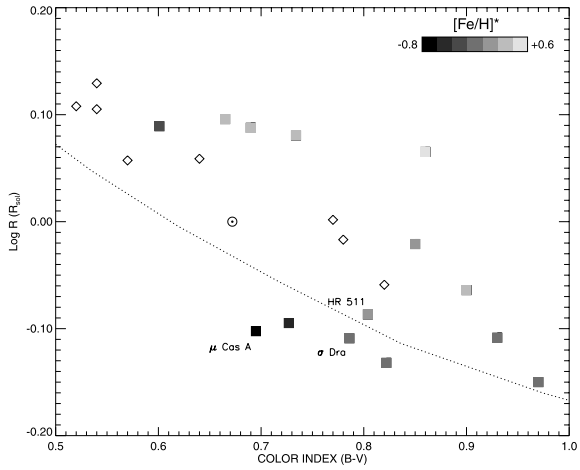

FIG. 3.—Plot of radius vs. $B-V$ color index for G- to mid-K-type stars, including our results for μ Cas A, σ Dra, and HR 511. Additional data plotted are from EBs (*diamonds*; Andersen 1991), LBOI (*squares*; Baines et al. 2008; Kervella et al. 2004; Lane et al. 2001), and the Sun (*solar symbol*). The gray-scale legend indicates the metallicity estimates for LBOI points from Taylor (2005; EB metallicity estimates are unreliable due to their duplicity). The dotted line represents a theoretical ZAMS line for solar metallicity ($Y = 0.275$, $Z = 0.02$) from the Dartmouth Stellar Evolution Models (Guenther et al. 1992; Chaboyer et al. 2001; available online at http://stellar.dartmouth.edu).

We believe that the position of μ Cas A on Figure 3 does not come from underestimated errors in our data, or in the archival data. For instance, the uncertainty in the stellar radius can arise from the angular diameter we measure of the star (discussed in § 3) and the *Hipparcos* parallax (Table 2). Because of their nearness to the Sun, the parallaxes of all three of our stars are well determined by *Hipparcos*, and with the combined accuracy of our angular diameters, the uncertainty on these radii are all less than 3%. The more pronounced discrepancy in the position of μ Cas A on Figure 3 is the large offset in the $B-V$ color index for μ Cas A with respect to the other two stars with the same effective temperatures, σ Dra and HR 511. However, according to the ranking system of Nicolet (1978) all three stars we analyze have the highest quality index of photometry, with a probable error in $B-V$ of ± 0.006. In this catalog, the worst-case scenario in photometry errors appears for characteristically dim stars with $V \gtrsim 10$, where the lowest rank quality index has an error in $B-V$ of ± 0.02, still not providing the desired effects to make the data agree within errors. With regards to the binarity of μ Cas A, the effect of the much cooler secondary star on the measured $B-V$ for the system as a whole would be less than 1 mmag (Casagrande et al. 2007), thus allowing us to ignore its contribution to these measurements as well. In other words, the position of μ Cas A on Figure 3 is simply a result of its lower metal abundance causing a reduction of opacity in its atmosphere, observationally making the star appear bluer in color than the other two stars with higher abundances with the same radius, effective temperature, and luminosity.

We would like to make it clear that for μ Cas A, a comparison of reduced opacities based solely on its iron abundance is a simplified approach, and complications arise in the determination of its true helium abundance (Haywood et al. 1992) as well as enhanced α-elements (Chieffi et al. 1991). In this respect, reducing the helium abundance, or increasing the α-element abundance, mimics the effect of increasing the metal abundance on a star's effective temperature and luminosity. In addition, over timescales of 10 Gyr, microscopic diffusion must also be considered in abundance analyses of subdwarfs (Morel & Baglin 1999). Here we do not wish to misrepresent the impact of these issues on various stellar parameters and modeling, but instead present a purely observational comparison to fundamentally observed properties of these three stars. These topics will be discussed further in § 4.2.

4.2. *Stellar Models*

While we can achieve a substantial amount of information from eclipsing binaries such as mass and radius, there still exists great uncertainty in the effective temperatures and luminosities of these systems (for example, see the discussion in §§ 3.4 and 3.5 in Andersen 1991). On the other hand, while observing single stars with LBOI is quite effective in determining effective temperatures and luminosities of stars, it lacks the means of directly measuring stellar masses. For μ Cas A, the results of this work combined with our knowledge of the binary from previous orbital analysis provides us the best of both worlds. Unfortunately, the current uncertainty in mass for μ Cas A is $\sim$10%, too great to produce useful information about the star when running model evolutionary tracks (see discussion below and Fig. 7). However, our newly determined physical parameters of μ Cas A provide us with a handy way to test the accuracy of stellar models for metal-poor stars.

To model μ Cas A, σ Dra, and HR 511, we use both the Y^2 (Yonsei-Yale) stellar isochrones by Yi et al. (2001, 2003), Kim et al. (2002), and Demarque et al. (2004), which apply the color table from Lejeune et al. (1998), and the Victoria-Regina (VR) stellar isochrones by VandenBerg et al. (2006) with *BVRI* color-$T_{\rm eff}$ relations as described by VandenBerg & Clem (2003). To run either of these model isochrones, input estimates are required for the abundance of iron [Fe/H] and α-elements [α/Fe], both of which contribute to the overall heavy-metal mass fraction Z.

The subdwarf μ Cas is considered to be metal-poor; there exist numerous abundance estimates ranging from $[{\rm Fe/H}] = -0.98$ (Fulbright 2000) to $[{\rm Fe/H}] = -0.55$ (Clegg 1977), and over time these estimates tend to favor lower and lower metallicity values. Overall, this large range in metallicities suggests an error of $\sim$0.2 dex. Systematic offsets aside, there exist a few additional variables which appear to create trouble in determining accurate metallicity estimates for this star. Torres et al. (2002) argue that abundance estimates for a binary are affected by the presence of the secondary in both photometric and spectroscopic measurement techniques. However, Wickes & Dicke (1974) measured the system's $\Delta m = 5.5 \pm 0.7$ at $\lambda = 0.55$ μm, limiting the secondary's influence of these estimates to no more than $\sim$0.05 dex, basically undetectable. Second, the abundance analysis by Thévenin & Idiart (1999) provides substantial evidence that it is imperative to use non-LTE (NLTE) treatment when measuring stars with subsolar abundances. In the case of μ Cas A, this correction factor is 0.14 dex, resulting in $[{\rm Fe/H}]_{\rm NLTE} = -0.56$ from their measurements. Applying this correction factor brings the range of abundance estimates cited above to $-0.84 < [{\rm Fe/H}] < -0.41$.

In this work, we use the averaged metallicity values from the Taylor (2005) catalog for all three stars (Table 2). We caution the reader that this average value of [Fe/H] for μ Cas A, corrected for NLTE effects described above, still lies below the value from Thévenin & Idiart (1999) by about 0.12 dex; however, both of these estimates are within the range listed above. Lebreton et al. (1999) show that indeed these corrections are needed to remove a large part of the discrepancy on model fits to match observations. NLTE corrections for the iron abundance estimates of σ Dra and HR 511 are not needed.

HR 511 and σ Dra show no sign of α-enhanced elements with respect to the Sun (i.e., $[\alpha/{\rm Fe}] = 0$), which is not a surprise

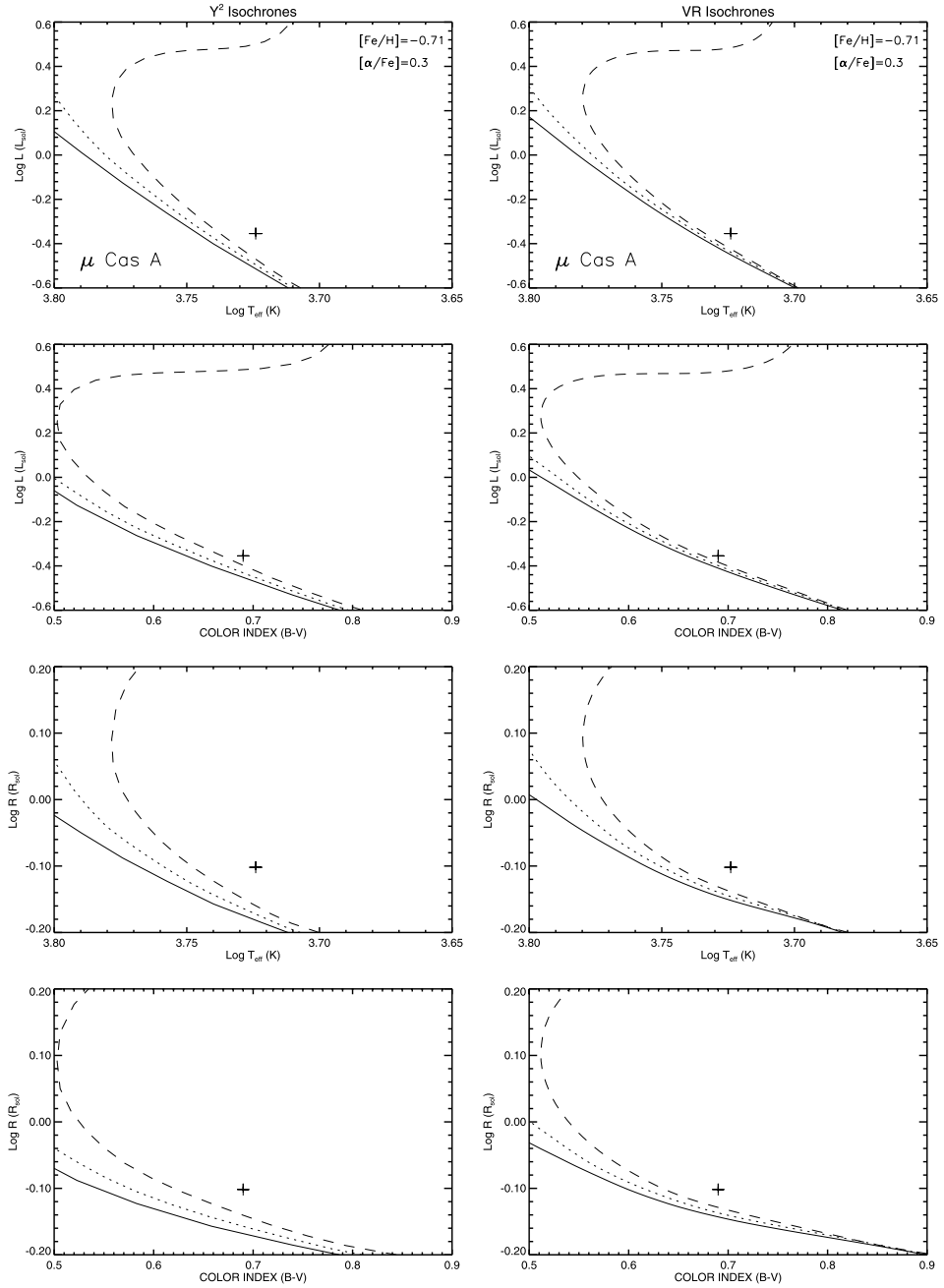

FIG. 4.—Data for μ Cas A (along with 1 σ errors) plotted against Y^2 and VR isochrones ([α/Fe] = 0.3, [Fe/H] = −0.71) for 1, 5, and 10 Gyr (*solid, dotted, and dashed lines, respectively*).

because they have near-solar iron abundances (Mishenina et al. 2004; Soubiran & Girard 2005; Fulbright 2000). However, these studies do detect the presence of α-enhanced elements such as Ca, Mg, Si, and Ti in μ Cas A, and we adopt an average value from these three sources to be $[\alpha/\mathrm{Fe}] = 0.36 \pm 0.06$.

To run models for each star, we round the average [Fe/H] value to the nearest [Fe/H] value in the VR models' grids (Table 2) and adopt $[\alpha/\mathrm{Fe}] = 0.3$ for μ Cas A and $[\alpha/\mathrm{Fe}] = 0.0$ for σ Dra and HR 511. This approximation allows us to use identical input parameters in each of the models in order to compare the similarity of the models to each other (Fig. 4). To justify this approximation, we ran the Y^2 models (using the interpolating routine available) for both the exact and rounded input parameters for μ Cas A, and we were not able to see any substantial differences in comparing the two.

We show our results compared to the Y^2 (*left column*) and VR (*right column*) stellar isochrones in Figures 4, 5, and 6 in both

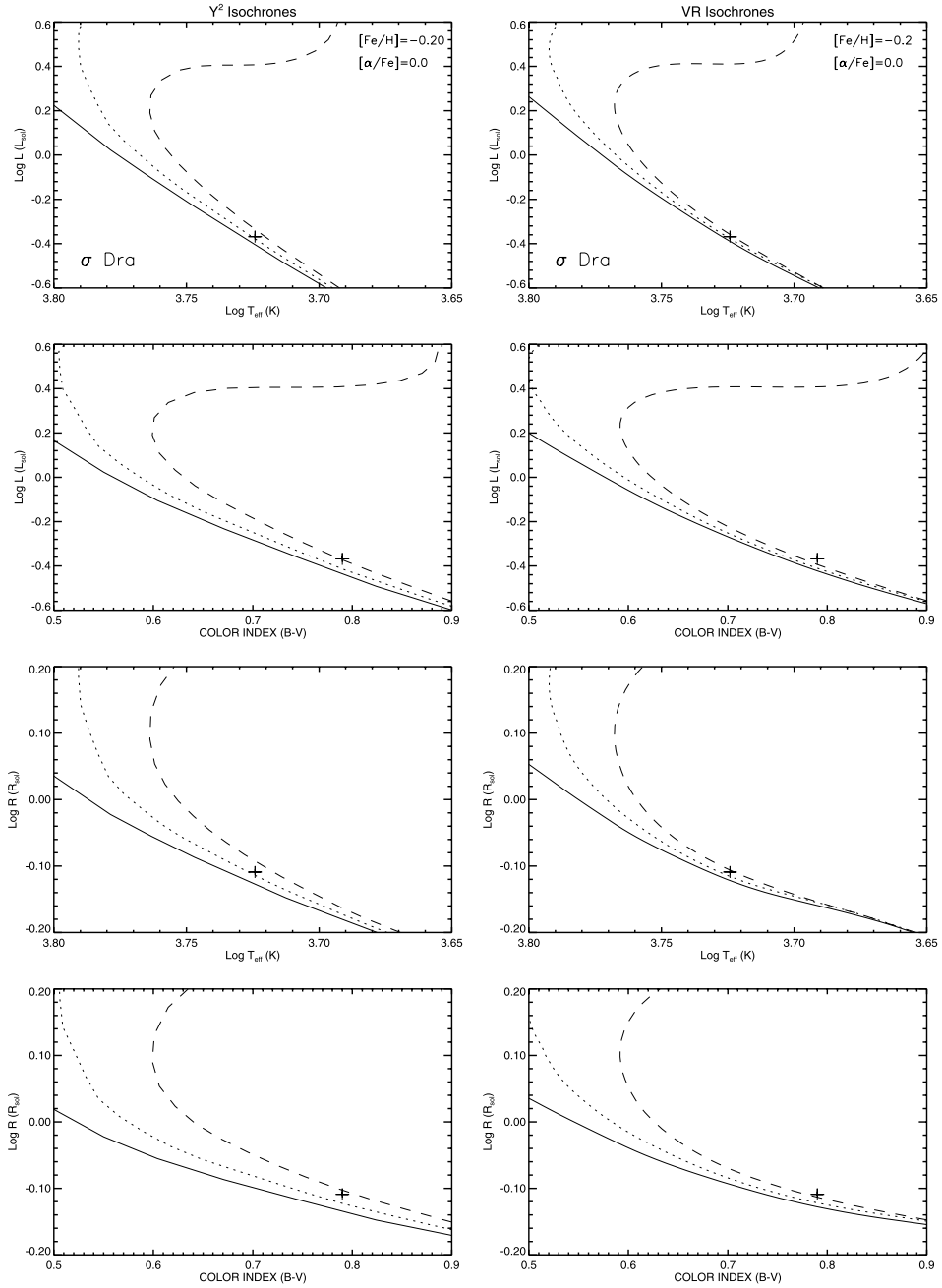

FIG. 5.—Data for σ Dra (along with 1 σ errors) plotted against Y^2 and VR isochrones ([α/Fe] = 0.0, [Fe/H] = −0.20) for 1, 5, and 10 Gyr (*solid, dotted, and dashed lines, respectively*).

the temperature- and color-dependent planes. The sensitivity to age in this region is minimal, but for reference, we plotted 1, 5, and 10 Gyr isochrones for each model, as well as the positions of μ Cas A, σ Dra, and HR 511. When comparing the model isochrones for μ Cas A in Figure 4, no significant differences are seen between the Y^2 and VR models. However, for both models these results show that there exist discrepancies with observations in the $T_{\rm eff}$ plane. Both of the models overpredict the temperature for μ Cas A for a given luminosity and radius. On the other hand, on the color-dependent plane, the models appear to do an adequate job fitting the observations in terms of luminosity (for a typical age of a halo star of $\sim$10 Gyr), but an offset is still seen in the model radii versus color index. In regards to model isochrones run for σ Dra and HR 511 (Figs. 5 and 6), both of which have abundances more similar to the Sun, we find that the models and our observations agree quite well.

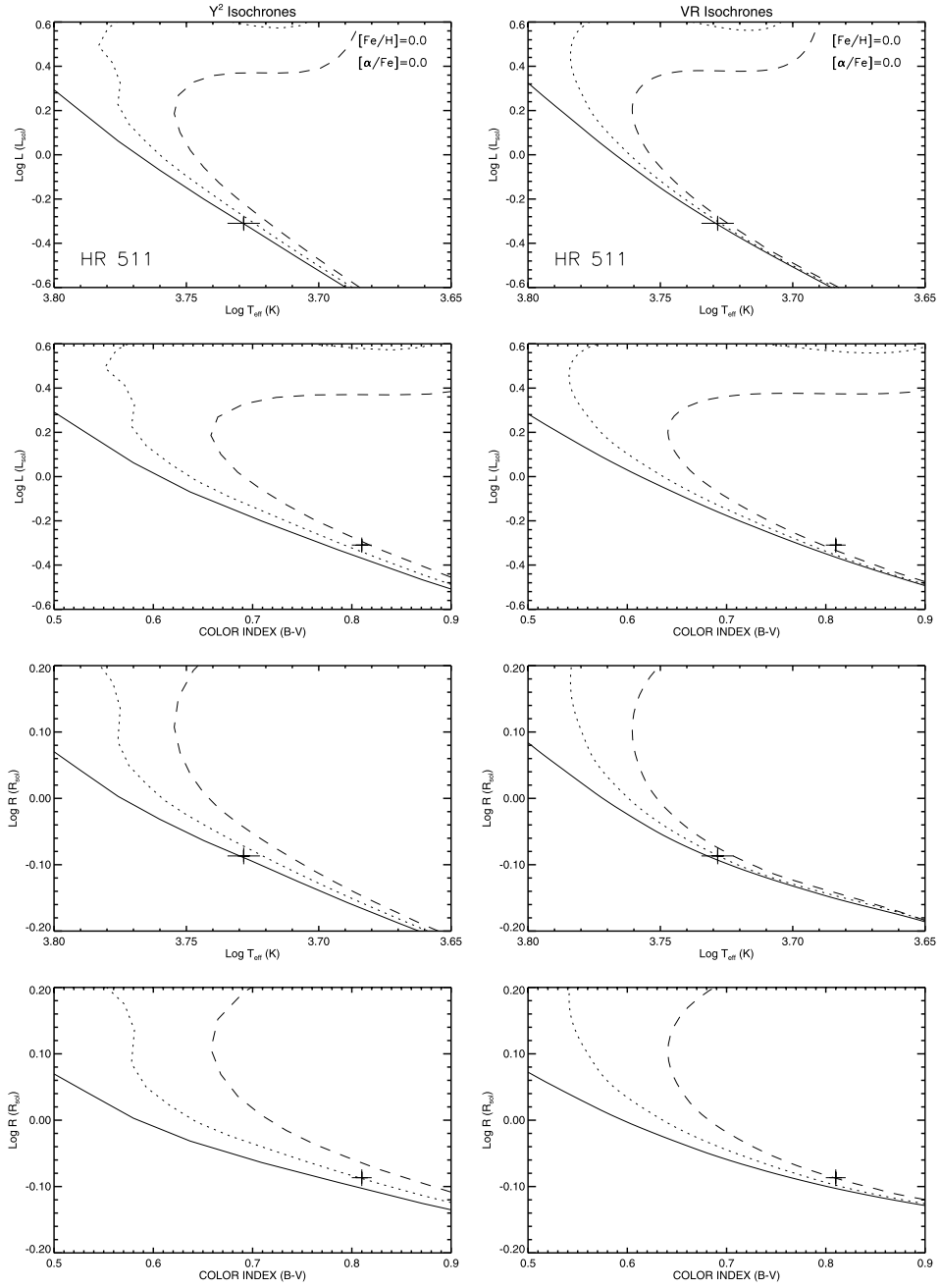

FIG. 6.—Data for HR 511 (along with 1 σ errors) plotted against Y^2 and VR isochrones ([α/Fe] = 0.0, [Fe/H] = 0.00) for 1, 5, and 10 Gyr (*solid, dotted, and dashed lines, respectively*).

It is apparent in Figure 4 that although both of the models are fairly consistent with each other, the methods used to transform $B - V$ color index to $T_{\rm eff}$ for metal-poor stars is not calibrated correctly. Likewise, as described by Popper (1997) as being a "serious dilemma," several recent works (utilizing all the current measurements of stellar radii measured) show that models are infamous in predicting temperatures that are too high and radii that are too small, while still being able to correctly reproduce the stellar luminosity (e.g., Morales et al. 2008; Ribas et al. 2007; López-Morales 2007). Explanations for these discrepancies are understood to be a consequence of the stellar metallicity, magnetic activity, and/or duplicity.

In Figure 7, we show our observations dependent on stellar mass compared to the model Y^2 isochrones for μ Cas A (VR models

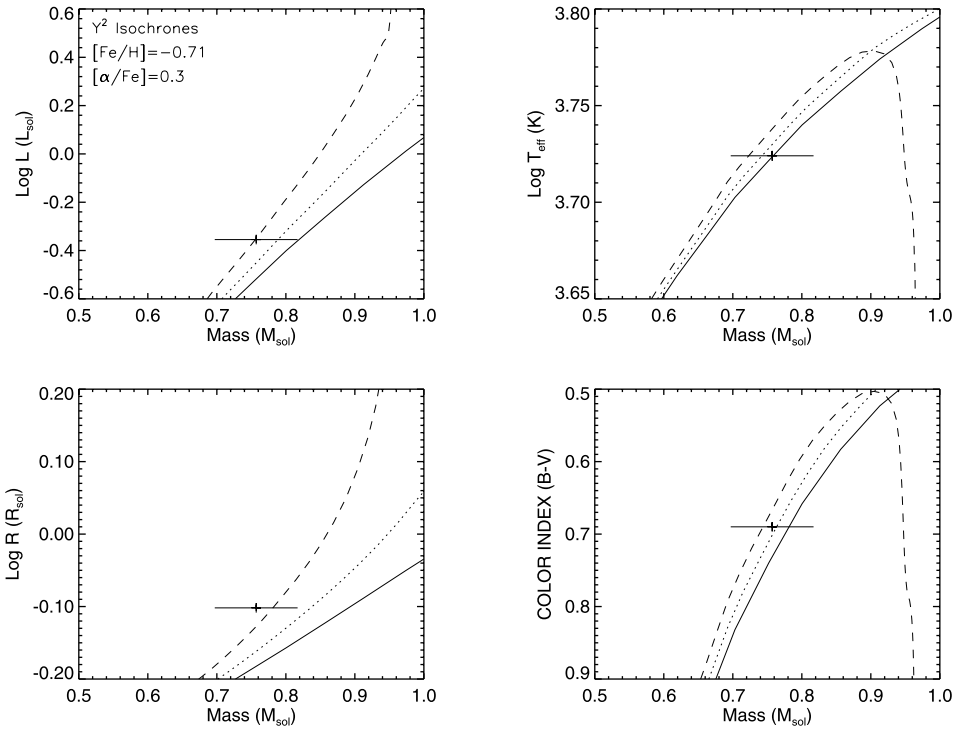

FIG. 7.—Mass relationships (along with 1 σ errors) for μ Cas A compared to Y^2 isochrones for 1, 5, and 10 Gyr (*solid, dotted, and dashed lines, respectively*).

are not shown for clarity, but display approximately the same relations). Here it is clear that the current errors in the measured mass for μ Cas A are not sufficiently constrained to conclude anything useful from the models. Fundamental properties of the secondary star are also an important constraint within these parameters, especially with respect to coevolution of the binary, but unfortunately both the Y^2 and VR models do not extend to masses low enough to test these issues.

5. CONCLUSION

In this first direct measurement of the diameter of a subdwarf, we find that although μ Cas A is classified as a G5 V star, its subsolar abundance leads it to resemble a K0 V star in terms of temperature, radius, and luminosity, whereas its surface gravity reflects the value for G5–K0 ZAMS stars with solar abundances. We find that while both the Y^2 and VR isochrones agree with our observations of σ Dra and HR 511, a discrepancy is seen in temperature and radius when comparing these models to our observations of μ Cas A.

We are currently working on modeling this star and other subdwarfs with hopes to better constrain stellar ages and composition. Future plans to observe more stars of similar spectral types to determine angular diameters for main-sequence stars are planned by T. S. B. This work will accurately determine the fundamental characteristics of temperature, radius, and absolute luminosity of a large sample of stars and thereby contribute to a broad range of astronomical interests.

We would like to thank Gail Schaefer for sharing her preliminary results with us for the orbit of μ Cas. We would also like to thank Gerard T. van Belle and David H. Berger for advice on the preparation of the project, as well as Andrew Boden for advice on analyzing the data. The CHARA Array is funded by the National Science Foundation through NSF grant AST 06-06958 and by Georgia State University through the College of Arts and Sciences. This research has made use of the SIMBAD literature database, operated at CDS, Strasbourg, France, and of NASA's Astrophysics Data System. This publication makes use of data products from the Two Micron All Sky Survey (2MASS), which is a joint project of the University of Massachusetts and the Infrared Processing and Analysis Center/California Institute of Technology, funded by the National Aeronautics and Space Administration and the National Science Foundation.

APPENDIX

We translate our measurement of r_0 into the astronomical seeing disk $\theta_{\rm Seeing}$ by

$$r_0 = 1.009D\left(\frac{\lambda}{\theta_{\rm Seeing}D}\right)^{6/5}, \quad \text{(A1)}$$

where D is the telescope aperture size, and λ is the wavelength of observation (ten Brummelaar 1993). To first order, an adequate representation of the intensity distribution of light from a star is a Gaussian (King 1971; Racine 1996), where $\theta_{\rm Seeing}$ is modeled as the full width at half-maximum of the Gaussian. Thus, we can write the normalized intensity distribution of light for a star as

$$I(x,x_0,y,y_0) = \frac{1}{2\pi\sigma^2}\,\exp\left\{-\frac{1}{2\sigma^2}\left[(x-x_0)^2+(y-y_0)^2\right]\right\}, \tag{A2}$$

where $\sigma \equiv 2.355^{-1}\theta_{\rm Seeing}$, and the coordinates (x_0, y_0) determine the central position of the star on the chip. Assuming the primary star is at the center of our 2×2 pixel array $(0, 0)$ and the secondary is offset by its separation in arcseconds $(0, \rho_{\rm AB})$, we then have the amount of light contributed by each star:

$$I_A = Q\int_{-1}^{1}\int_{-1}^{1} I(x,0,y,0)\,dx\,dy, \tag{A3}$$

$$I_B = \int_{-1}^{1}\int_{-1}^{1} I(x,0,y,\rho_{\rm AB})\,dx\,dy, \tag{A4}$$

where Q is the intensity ratio of the two stars, $Q = 10^{\Delta M_K/2.5}$. Hence, the conversion of the measured visibility V to the true visibility for the primary star V_A is

$$V_A = V(1 + I_B/I_A). \tag{A5}$$

REFERENCES

Alonso, A., Arribas, S., & Martinez-Roger, C. 1995, A&A, 297, 197
———. 1996, A&AS, 117, 227
Andersen, J. 1991, A&A Rev., 3, 91
Baines, E. K., McAlister, H. A., ten Brummelaar, T. A., Turner, N. H., Sturmann, J., Sturmann, L., Goldfinger, P. J., & Ridgway, S. T. 2008, preprint (arXiv: 0803.4131)
Bell, R. A., & Gustafsson, B. 1989, MNRAS, 236, 653
Berger, D. H., et al. 2006, ApJ, 644, 475
Blackwell, D. E., & Lynas-Gray, A. E. 1998, A&AS, 129, 505
Casagrande, L., Flynn, C., Portinari, L., Girardi, L., & Jimenez, R. 2007, MNRAS, 382, 1516
Chaboyer, B., Fenton, W. H., Nelan, J. E., Patnaude, D. J., & Simon, F. E. 2001, ApJ, 562, 521
Chieffi, A., Straniero, O., & Salaris, M. 1991, in ASP Conf. Ser. 13, The Formation and Evolution of Star Clusters, ed. K. Janes (San Francisco: ASP), 219
Claret, A., Diaz-Cordoves, J., & Gimenez, A. 1995, A&AS, 114, 247
Clegg, R. E. S. 1977, MNRAS, 181, 1
Cohen, M., Wheaton, W. A., & Megeath, S. T. 2003, AJ, 126, 1090
Colina, L., Bohlin, R., & Castelli, F. 1996, *HST* Instrument Science Report CAL/SCS-008 (Baltimore: STScI)
Cox, A. N. 2000, Allen's Astrophysical Quantities (4th ed.; New York: AIP)
Demarque, P., Woo, J.-H., Kim, Y.-C., & Yi, S. K. 2004, ApJS, 155, 667
Drummond, J. D., Christou, J. C., & Fugate, R. Q. 1995, ApJ, 450, 380
Farrington, C. D., & McAlister, H. A. 2006, Proc. SPIE, 6268, 90
Fulbright, J. P. 2000, AJ, 120, 1841
Gray, R. O. 1998, AJ, 116, 482
Guenther, D. B., Demarque, P., Kim, Y.-C., & Pinsonneault, M. H. 1992, ApJ, 387, 372
Hanbury Brown, R., Davis, J., & Allen, L. R. 1974a, MNRAS, 167, 121
Hanbury Brown, R., Davis, J., Lake, R. J. W., & Thompson, R. J. 1974b, MNRAS, 167, 475
Hauck, B., & Mermilliod, M. 1998, A&AS, 129, 431
Haywood, J. W., Hegyi, D. J., & Gudehus, D. H. 1992, ApJ, 392, 172
Johnson, H. L., Iriarte, B., Mitchell, R. I., & Wisniewskj, W. Z. 1966, Comm. Lunar Planet. Lab., 4, 99
Kervella, P., et al. 2004, in IAU Symp. 219, Stars as Suns: Activity, Evolution and Planets, ed. A. K. Dupree & A. O. Benz (San Francisco: ASP), 80
Kim, Y.-C., Demarque, P., Yi, S. K., & Alexander, D. R. 2002, ApJS, 143, 499
King, I. R. 1971, PASP, 83, 199
Lane, B. F., Boden, A. F., & Kulkarni, S. R. 2001, ApJ, 551, L81
Lebreton, Y., Perrin, M.-N., Cayrel, R., Baglin, A., & Fernandes, J. 1999, A&A, 350, 587
Lejeune, T., Cuisinier, F., & Buser, R. 1998, A&AS, 130, 65
López-Morales, M. 2007, ApJ, 660, 732
McAlister, H. A., et al. 2005, ApJ, 628, 439
McCarthy, Jr., D. W. 1984, AJ, 89, 433
Mishenina, T. V., Soubiran, C., Kovtyukh, V. V., & Korotin, S. A. 2004, A&A, 418, 551
Morales, J. C., Ribas, I., & Jordi, C. 2008, A&A, 478, 507
Morel, P., & Baglin, A. 1999, A&A, 345, 156
Nicolet, B. 1978, A&AS, 34, 1
Popper, D. M. 1997, AJ, 114, 1195
Press, W. H., Teukolsky, S. A., Vetterling, W. T., & Flannery, B. P. 1992, Numerical Recipes in C: The Art of Scientific Computing (2nd ed.; Cambridge: Cambridge Univ. Press)
Racine, R. 1996, PASP, 108, 699
Ribas, I., Morales, J., Jordi, C., Baraffe, I., Chabrier, G., & Gallardo, J. 2007, preprint (arXiv:0711.4451)
Ségransan, D., Kervella, P., Forveille, T., & Queloz, D. 2003, A&A, 397, L5
Skrutskie, M. F., et al. 2006, AJ, 131, 1163
Soubiran, C., & Girard, P. 2005, A&A, 438, 139
Taylor, B. J. 2005, ApJS, 161, 444
ten Brummelaar, T. 1993, Ph.D. thesis, Univ. Sydney
ten Brummelaar, T. A., et al. 2005, ApJ, 628, 453
Thévenin, F., & Idiart, T. P. 1999, ApJ, 521, 753
Torres, G., Boden, A. F., Latham, D. W., Pan, M., & Stefanik, R. P. 2002, AJ, 124, 1716
VandenBerg, D. A., Bergbusch, P. A., & Dowler, P. D. 2006, ApJS, 162, 375
VandenBerg, D. A., & Clem, J. L. 2003, AJ, 126, 778
Wall, J. V., & Jenkins, C. R. 2003, Practical Statistics for Astronomers (Cambridge: Cambridge Univ. Press)
Wickes, W. C., & Dicke, R. H. 1974, AJ, 79, 1433
Yi, S., Demarque, P., Kim, Y.-C., Lee, Y.-W., Ree, C. H., Lejeune, T., & Barnes, S. 2001, ApJS, 136, 417
Yi, S. K., Kim, Y.-C., & Demarque, P. 2003, ApJS, 144, 259

The Astrophysical Journal, 691:1243–1247, 2009 February 1 doi:10.1088/0004-637X/691/2/1243

ANGULAR DIAMETERS OF THE HYADES GIANTS MEASURED WITH THE CHARA ARRAY

Tabetha S. Boyajian[1], Harold A. McAlister[1], Justin R. Cantrell[1], Douglas R. Gies[1], Theo A. ten Brummelaar[2], Chris Farrington[2], P. J. Goldfinger[2], Laszlo Sturmann[2], Judit Sturmann[2], Nils H. Turner[2], and Stephen Ridgway[3]
[1] Center for High Angular Resolution Astronomy and Department of Physics and Astronomy, Georgia State University, P.O. Box 4106, Atlanta, GA 30302-4106, USA; tabetha@chara.gsu.edu, hal@chara.gsu.edu, cantrell@chara.gsu.edu, gies@chara.gsu.edu
[2] The CHARA Array, Mount Wilson Observatory, Mount Wilson, CA 91023, USA; theo@chara-array.org, farrington@chara-array.org, pj@chara-array.org, sturmann@chara-array.org, judit@chara-array.org, nils@chara-array.org
[3] National Optical Astronomy Observatory, P.O. Box 26732, Tucson, AZ 85726-6732, USA; sridgway@noao.edu
Received 2008 June 30; accepted 2008 October 5; published 2009 February 2

ABSTRACT

We present angular diameters of the Hyades giants, γ, δ^1, ϵ, and θ^1 Tau from interferometric measurements with the CHARA Array. Our errors in the limb-darkened angular diameters for these stars are all less than 2%, and in combination with additional observable quantities, we determine the effective temperatures, linear radii, and absolute luminosities for each of these stars. Additionally, stellar masses are inferred from model isochrones to determine the surface gravities. These data show that a new calibration of effective temperatures with errors well under 100 K is now possible from interferometric angular diameters of stars.

Key words: infrared: stars – stars: fundamental parameters – techniques: interferometric

1. INTRODUCTION

Because of its close proximity to the Sun, the Hyades cluster has served as a benchmark in studies ranging from stellar evolutionary modeling to calibrating the cosmic distance scale. In the context of evolutionary theory, *Hipparcos* distances and resolved binaries in the cluster have enabled us to test extensively those models (for example, see Perryman et al. 1998; Lastennet et al. 1999) using fundamental stellar properties such as effective temperature. The only direct way to determine the effective temperature of a star is to measure the star's angular diameter and integrated flux. While the dwarf stars in the Hyades are too small to resolve their angular diameters with current tools and methods, the four Hyades giants have been observed over the past few decades, beginning with lunar occultation (LO) measurements (see Table 1 for references and timeline of publications of this topic). Presently, long-baseline optical interferometry (LBOI) has trumped LO techniques in accurately measuring the angular diameters of such stars. In fact, for the Hyades giants in particular, the accuracy in the angular diameter measurements has improved by almost an order of magnitude over the past few decades.

In this work, we present the first uniform analysis of all four of the Hyades giants, γ Tau (HR 1346, HD 27371, HIP 20205), δ^1 Tau (HR 1373, HD 27697, HIP 20455), ϵ Tau (HR 1409, HD 28305, HIP 20889), and θ^1 Tau (HR 1411, HD 28307, HIP 20885). We observed these stars with the CHARA Array to obtain their angular diameters to better than 2% accuracy. In combination with the bolometric flux of each star, we derive their effective temperatures to 1% accuracy (Section 3). In this paper, we describe our observational results and then compare them to model isochrones for the Hyades, which demonstrate remarkable agreement within the temperature–luminosity plane for the cluster turnoff age and metallicity (Section 4).

2. OBSERVATIONS AND DATA REDUCTION

We observed these stars with the CHARA Array, located on the grounds of Mount Wilson Observatory, using the CHARA Classic beam combiner in K' band (ten Brummelaar et al. 2005) with the W2-E2 baseline (maximum baseline of 156.3 m) on 2007 November 2 from the Georgia State University Arrington Remote Operations Center (AROC) facility in Atlanta, GA. The chosen calibrator star, δ^2 Tau (HR 1380, HD 27819), an A7V with $v \sin i = 42$ km s^{-1} (Royer et al. 2007), is separated by less than 2 deg on the sky for all of the targets. It was observed in bracketed sequences, with each of the target stars yielding a total of nine bracketed observations for γ, δ^1, and ϵ Tau, and eight bracketed observations for θ^1 Tau. The angular diameter $\theta_{\rm SED}$ of the calibrator star was calculated by fitting observed photometry (see Boyajian et al. 2008 for details) to a model spectral energy distribution (SED).[4] The close proximity of the Hyades members to us ($\sim$ 47 parsecs; van Leeuwen 2007) introduces no effects on the SED fit due to interstellar reddening ($E(B-V) \leqslant 0.001$ mmag, Taylor 2006, and references therein). The SED model fit for the calibrator star yields $\theta_{\rm SED} = 0.457 \pm 0.020$ mas, for an effective temperature of $T_{\rm eff} = 8100$ K and $\log g = 4.1$. This corresponds to an absolute calibrated visibility for the calibrator star of $\sim$ 0.97 at these baselines. Data reduction and calibration follow the standard processing routines for CHARA Classic data (as described in ten Brummelaar et al. 2005 and McAlister et al. 2005).

For each calibrated observation, Table 2 lists the time of mid-exposure, the projected baseline B, the orientation of the baseline on the sky ψ, the visibility V, and the 1σ error to the visibility σV for each star.

The duplicity of these stars is not expected to affect our diameter measurements. The secondary stars in these systems are all high contrast in the K band, and our objects are considered as Hyades speckle singles in the infrared K band according to Patience et al. (1998). These nondetections are not surprising. For instance, δ^1 Tau is an SB1 with an M-dwarf companion (Griffin & Gunn 1977) and ϵ Tau is an exoplanet host star (Sato et al. 2007). γ Tau was resolved a single time as a speckle binary (with a large delta magnitude at 5000 Å) by Morgan et al. (1982), having a system separation of 0.395 arcsec. Since this measurement, it has remained undetected as a binary by other programs (McAlister 1978; Mason et al. 1993; Patience

[4] The model fluxes were interpolated from the grid of models from R. L. Kurucz available at http://kurucz.cfa.harvard.edu/.

Table 1
Comparison of Angular Diameter Measurements of the Hyades Giants

γ Tau		δ^1 Tau		ϵ Tau		θ^1 Tau		Method,
$\theta_{LD} \pm \sigma$	$\Delta\theta_{LD}/\sigma_C$[a]	$\theta_{LD} \pm \sigma$	$\Delta\theta_{LD}/\sigma_C$[a]	$\theta_{LD} \pm \sigma$	$\Delta\theta_{LD}/\sigma_C$[a]	$\theta_{LD} \pm \sigma$	$\Delta\theta_{LD}/\sigma_C$[a]	Reference
2.91 ± 0.16	-2.4	...	...	...	...	...	...	LO, 1
2.75 ± 0.18	-1.3	...	...	...	...	...	...	LO, 2
...	...	2.97 ± 0.7	-0.8	...	...	...	...	LO, 3
...	...	2.76 ± 0.7	-0.5	...	...	...	...	LO, 4
...	...	...	...	...	...	2.74 ± 0.12	-3.4	LO, 5
...	...	...	...	...	...	1.56 ± 0.45	1.6	LO, 6
...	...	...	...	...	...	3.4 ± 1.2	-0.9	LO, 7
...	...	...	...	...	...	2.0 ± 0.2	1.5	LO, 8
...	...	...	...	...	...	2.8 ± 0.3	-1.6	LO, 9
...	...	2.338 ± 0.033	1.4	2.671 ± 0.032	1.4	...	...	Mark III, 10
...	...	2.21 ± 0.08	2.2	2.41 ± 0.11	2.8	...	...	NPOI, 11
...	...	...	...	2.57 ± 0.06	2.4	...	...	PTI, 12
2.517 ± 0.034	0.0	2.408 ± 0.038	0.0	2.733 ± 0.031	0.0	2.305 ± 0.043	0.0	CHARA, This work

Notes.
[a] Here, we define the combined error, $\sigma_C = [\sigma^2_{CHARA} + \sigma^2_{Ref}]^{0.5}$, where σ_{Ref} is the error to the referenced measurement for each particular star entry. $\Delta\theta_{LD}$ is the difference between our angular diameter and the measurement for each reference.
References. (1) Ridgway et al. 1980; (2) Richichi et al. 1998; (3) Kornilov et al. 1984; (4) Trunkovskij 1987; (5) Ridgway et al. 1982; (6) Radick & Lien 1980; (7) Beavers et al. 1982; (8) Evans & Edwards 1981; (9) White 1979; (10) Mozurkewich et al. 2003; (11) Nordgren et al. 2001; (12) van Belle et al. 1999.

Table 2
Interferometric Measurements of Hyades Giants

Star Name	JD (−2,400,000)	B (m)	ψ (°)	V	σV
γ Tau	54406.745	120.8	194.8	0.495	0.060
γ Tau	54406.770	133.9	195.6	0.393	0.049
γ Tau	54406.784	140.1	196.2	0.391	0.034
γ Tau	54406.799	145.4	197.0	0.382	0.031
γ Tau	54406.822	151.7	198.5	0.413	0.046
γ Tau	54406.842	155.1	200.0	0.321	0.037
γ Tau	54406.861	156.2	201.7	0.350	0.041
γ Tau	54406.884	155.3	204.1	0.377	0.042
γ Tau	54406.913	150.7	207.7	0.355	0.024
δ^1 Tau	54406.752	122.7	193.4	0.504	0.041
δ^1 Tau	54406.776	134.8	194.7	0.507	0.032
δ^1 Tau	54406.793	142.0	195.7	0.447	0.043
δ^1 Tau	54406.819	150.1	197.6	0.410	0.042
δ^1 Tau	54406.846	155.0	199.9	0.368	0.047
δ^1 Tau	54406.865	156.2	201.8	0.395	0.059
δ^1 Tau	54406.874	156.2	202.8	0.356	0.038
δ^1 Tau	54406.897	154.4	205.6	0.380	0.033
δ^1 Tau	54406.925	149.0	209.8	0.403	0.051
ϵ Tau	54406.738	111.5	191.2	0.488	0.058
ϵ Tau	54406.764	126.6	192.7	0.406	0.041
ϵ Tau	54406.781	135.1	193.9	0.330	0.039
ϵ Tau	54406.790	138.8	194.5	0.326	0.038
ϵ Tau	54406.809	145.9	196.0	0.296	0.032
ϵ Tau	54406.833	152.0	198.1	0.246	0.044
ϵ Tau	54406.852	155.0	199.9	0.266	0.031
ϵ Tau	54406.888	155.8	204.1	0.239	0.035
ϵ Tau	54406.909	153.6	207.0	0.260	0.017
θ^1 Tau	54406.758	124.7	194.7	0.546	0.046
θ^1 Tau	54406.802	144.2	196.7	0.462	0.050
θ^1 Tau	54406.812	147.7	197.3	0.414	0.063
θ^1 Tau	54406.836	153.3	199.0	0.439	0.045
θ^1 Tau	54406.855	155.7	200.6	0.438	0.075
θ^1 Tau	54406.871	156.3	202.1	0.382	0.044
θ^1 Tau	54406.900	154.2	205.3	0.430	0.036
θ^1 Tau	54406.919	150.7	207.9	0.444	0.033

et al. 1998). In their infrared speckle program, Patience et al. (1998) did not detect a speckle companion for γ Tau, but placed a limit to the K-band magnitude difference of $\Delta K = 1.04$ for the system. We did not detect a separated fringe packet for the star in any of our observations, and hence we suggest that the detection from Morgan et al. (1982) may be spurious. The speckle binary, θ^1 Tau, is also an SB1 (Torres et al. 1997, and references therein). The companion to θ^1 Tau, is a late F main sequence star (Peterson et al. 1981b), which is supported by the nondetection in Patience et al. (1998), where they list the limiting $\Delta K = 4.6$ magnitudes. As described in Boyajian et al. (2008), our analysis of the binary μ Cas ($\Delta K = 3.5$) shows that the interferometric diameter measured of the primary star of μ Cas is affected by $\sim 1\%$ from the presence of the secondary. Since the magnitude difference in θ^1 Tau is at least one magnitude larger than this system, we neglect any possible influence the secondary star might have on our visibility measurements of the primary star.

3. ANGULAR DIAMETERS AND STELLAR PARAMETERS

The uniform-disk θ_{UD} and limb-darkened θ_{LD} angular diameters are expressed as the following relations:

$$V = \frac{2J_1(x)}{x}, \tag{1}$$

$$V = \left(\frac{1-\mu_\lambda}{2} + \frac{\mu_\lambda}{3}\right)^{-1} \times \left[(1-\mu_\lambda)\frac{J_1(x)}{x} + \mu_\lambda\left(\frac{\pi}{2}\right)^{1/2}\frac{J_{3/2}(x)}{x^{3/2}}\right], \tag{2}$$

and

$$x = \pi B \theta \lambda^{-1}, \tag{3}$$

where J_n is the $n$thorder Bessel function, and μ_λ is the linear limb-darkening coefficient at the wavelength of observation.[5] In

[5] In this work, we use $\mu_K = 0.301$ for all Hyades giants (Claret et al. 1995).

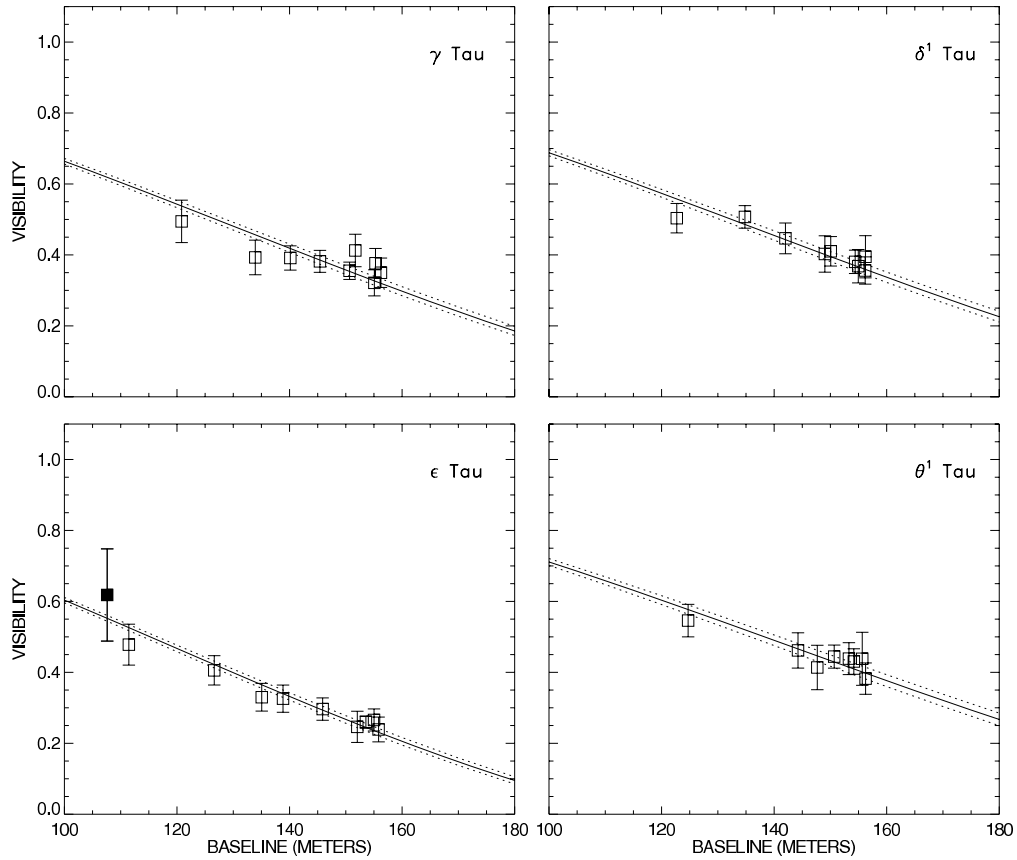

Figure 1. Limb-darkened diameter fits to our data on the Hyades giants. The plot for ϵ Tau also shows the data point from van Belle et al. (1999, filled square).

Table 3
Angular Diameters of Hyades Giants

Star Name	HR	Spectral Type	θ_{UD} (mas)	Reduced χ^2_{UD}	θ_{LD} (mas)	Reduced χ^2_{LD}
γ Tau	HR 1346	K0 III	2.452 ± 0.033	0.88	2.517 ± 0.034	0.86
δ^1 Tau	HR 1373	K0 III	2.347 ± 0.037	0.34	2.408 ± 0.038	0.34
ϵ Tau	HR 1409	G9.5 III	2.660 ± 0.030	0.36	2.734 ± 0.031	0.33
ϵ Tau[a]	HR 1409	G9.5 III	2.659 ± 0.030	0.33	2.733 ± 0.031	0.32
θ^1 Tau	HR 1411	K0 IIIb	2.247 ± 0.042	0.27	2.305 ± 0.043	0.27

Note. [a] Including van Belle et al. (1999) data point.

Table 4
Stellar Properties of Hyades Giants

Star Name	Radius ($R_\odot$)	log g[a] (cgs)	F_{BOL}[b] (erg s^{-1} cm^{-2})	T_{eff} (K)	Range of T_{eff} from Spectroscopy (K)	Range of T_{eff} from Direct Techniques[c] (K)
γ Tau	13.4 ± 0.2	2.58–2.61	116 ± 3	4844 ± 47	4800–4963	4508–4632
δ^1 Tau	12.3 ± 0.4	2.65–2.69	105 ± 3	4826 ± 51	4750–5000	4335–5038
ϵ Tau	13.4 ± 0.2	2.59–2.63	135 ± 4	4827 ± 44	4656–4929	4883–5141
θ^1 Tau	11.7 ± 0.2	2.69–2.73	95 ± 2	4811 ± 50	4874–5000	3962–5842

Notes.
[a] Based upon mass range of 2.48–2.70 $M_\odot$.
[b] Expressed in $F_{BOL}/1E-8$. To correct for the light from the secondary component of θ^1 Tau, a 3% reduction to F_{BOL} was applied (Torres et al. 1997; Peterson et al. 1981a, 1981b).
[c] Includes the LO- and the LBOI-measured angular diameters, when available (see Table 1).

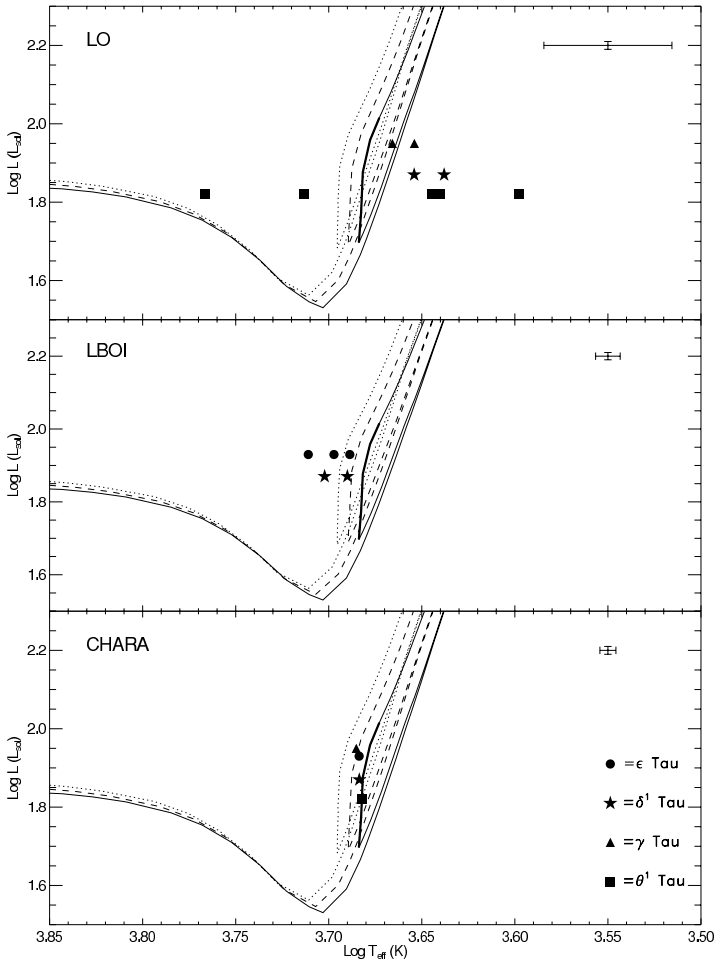

Figure 2. Effective temperatures derived from published angular diameter data from LO (top panel), previous LBOI (middle panel), and this work (bottom panel). The symbols denoting the objects are consistent within all three panels, and the references for each measurements can be found in Table 1. The typical 1σ error for each method is shown in the top right portion of each panel. Padova model isochrones for 625 Myr are plotted for solar metallicity $Z_{\odot} = 0.019$ (dotted line) and metallicities $Z = 0.024$ and $Z = 0.028$ (dashed line and solid line, respectively). The thick region of the Hyades isochrone for $Z = 0.028$ identifies the region of the helium burning RC.

Equation (3), B is the projected baseline in the sky, θ is the UD angular diameter of the star when applied to Equation (1) and the LD angular diameter when used in Equation (2), and λ is the central wavelength of the observational bandpass (Hanbury Brown et al. 1974).

We calculate the UD and LD diameters for each star from the calibrated visibilities by χ^2 minimization of Equations (1) and (2), where the error to the diameter fit is based upon the values on either side of the minimum for which $\chi^2 = \chi^2_{\rm min} + 1$ (Press et al. 1992; Wall & Jenkins 2003). Table 3 shows our results along with the reduced χ^2 values for these diameter fits. Note that our values for reduced χ^2 are less than 1, meaning we have overestimated the errors of the measured visibilities used in the diameter fits (σV in Table 2). The best fits for the limb-darkened angular diameters to our calibrated visibilities and the 1σ errors are shown in Figure 1. In our final analysis of ϵ Tau, we include the data point from van Belle et al. (1999), which was taken at the same wavelength as our observations, in the fit.

The angular diameters of these stars are then transformed into linear radii R using the van Leeuwen (2007) *Hipparcos* parallaxes. In addition to these quantities, we calculate the effective temperature $T_{\rm eff}$ using the relation

$$F_{\rm BOL} = \tfrac{1}{4}\theta^2_{\rm LD}\sigma T^4_{\rm eff}, \quad (4)$$

where σ is the Stefan–Boltzmann constant.

The bolometric flux $F_{\rm BOL}$ for each star was determined by applying the bolometric corrections of each star from Allende Prieto & Lambert (1999), assuming $M_{\rm BOL,\odot} = 4.74$. The results for the radius, bolometric flux, and effective temperature for each star are shown in Table 4. The significance of the luminosity subclass IIIb for θ^1 Tau (Table 3) is directly detected here in the smaller radius and $F_{\rm BOL}$ compared to the other giants.

4. DISCUSSION

Historically, each of these stars has been observed by LO and/or LBOI to obtain angular diameters (Table 1). Diameters of three of the four giants have been measured by LO, and somewhat surprisingly, only two of the four giants had been

measured by LBOI prior to this work. While the LO measurements show a considerable scatter and large errors, the LBOI points also vary considerably within their errors with respect to each other. Indeed, this is primarily an artifact of the relatively small size of these four stars creating quite a challenge for them to be sufficiently resolved with interferometers of modest baselines. The advantages of observing stellar diameters with the long baselines of the CHARA Array are apparent, allowing us to obtain optimal sampling of the visibility curve. For example, our measured diameter of ϵ Tau here includes the single PTI data point (Table 3 and Figure 1), clearly improving the diameter fit from van Belle et al. (1999; see Table 1). Secondly, the sensitivity of our beam combiner allows us to observe calibrator stars that are very unresolved, closing the gap for systematic errors that may arise in the calibration process. Additionally, these observations were made in the infrared, and are less subject to stellar limb darkening, making the transformations from the observed $\theta_{\rm UD}$ to the actual $\theta_{\rm LD}$ less model-dependent.

For all existing angular diameter measurements from LO and LBOI (Table 1), we use Equation (1) to calculate the effective temperatures of these stars (Table 4, Direct Techniques). For comparison, we show the range in effective temperature determinations when estimated via photometric and spectroscopic methods (Ochsenbein et al. 2000), also in Table 4. Our temperatures tend to lie on the low side of these ranges, which probably results from differences in model opacities and varying metallicity determinations of the models used in each reference. In the case of θ^1 Tau, the temperatures from spectroscopic techniques are higher than our derived temperature, which is likely to be an artifact of the duplicity of the star.

Figure 2 displays these available measurements on an H–R diagram for all stars, separated by the method of measurement. To model these stars, we use the Padova database of stellar evolutionary tracks and isochrones[6] (Marigo et al. 2008), using a cluster turnoff age of 625 Myr (Perryman et al. 1998). In Figure 2, we show isochrones for solar metallicity $Z_{\odot} = 0.019$ and two different metallicities of the Hyades $Z_{\rm Hyades} = 0.024$, 0.028 (Perryman et al. 1998; Thevenin 1998). The model isochrone for both Hyades metallicities ($Z_{\rm Hyades} = 0.028$, 0.024) are in excellent agreement with our observations. To identify which part of this isochrone our stars were likely to lie, we investigated a single-star evolutionary track for a mass of 2.5 $M_{\odot}$ to determine which part of the isochrone a star would spend most of its lifetime (Girardi et al. 2000). We find that from the beginning of the core helium burning stage, up until the time helium is exhausted from the core, corresponds to $\sim$ 20% of the stars' total lifetime, second only to the time spent on the main sequence, $\sim$ 75% of its total lifetime. The stars' placement on Figure 2 clearly mark all four giants as residing on the helium burning red clump (RC), and this region is indicated as the thicker part of the Hyades metallicity isochrone of $Z_{\rm Hyades} = 0.028$.

Within this region of the RC, we look back to the model isochrones in order to determine a range of masses that these stars may have. The model stellar mass for the lowest point of the RC is 2.48 $M_{\odot}$, and following this track up the end of the helium burning stage extends this model mass to 2.70 $M_{\odot}$. These masses are consistent with the Torres et al. (1997) giant masses for the Hyades. Assuming that these stars may fall anywhere between these masses, we predict a $\log g$ using the radii that we measure for each star (Table 4). These values are in excellent agreement with spectroscopically determined gravities found in the literature which have a large spread of values from $\log g = 2.2$ to $\log g = 3.17$, although for most estimates the gravity agrees with ours within 0.1 dex.

We thank Gerard T. van Belle for his advice on the data analysis. The CHARA Array is funded by the National Science Foundation through NSF grant AST-0606958 and by Georgia State University through the College of Arts and Sciences. This research has made use of the SIMBAD literature database, operated at CDS, Strasbourg, France, and of NASA's Astrophysics Data System. This publication makes use of data products from the Two Micron All Sky Survey (2MASS), which is a joint project of the University of Massachusetts and the Infrared Processing and Analysis Center/California Institute of Technology, funded by the National Aeronautics and Space Administration and the National Science Foundation.

[6] http://stev.oapd.inaf.it/cmd

REFERENCES

Allende Prieto, C., & Lambert, D. L. 1999, A&A, 352, 555
Beavers, W. I., Cadmus, R. R., & Eitter, J. J. 1982, AJ, 87, 818
Boyajian, T. S., et al. 2008, ApJ, 683, 424
Claret, A., Diaz-Cordoves, J., & Gimenez, A. 1995, A&AS, 114, 247
Evans, D. S., & Edwards, D. A. 1981, AJ, 86, 1277
Girardi, L., Bressan, A., Bertelli, G., & Chiosi, C. 2000, A&AS, 141, 371
Griffin, R. F., & Gunn, J. E. 1977, AJ, 82, 176
Hanbury Brown, R. H., Davis, J., Lake, R. J. W., & Thompson, R. J. 1974, MNRAS, 167, 475
Kornilov, V. G., Mironov, A. V., Trunkovskii, E. M., Khaliullin, K. F., & Cherepashchuk, A. M. 1984, Sov. Astron., 28, 431
Lastennet, E., Valls-Gabaud, D., Lejeune, T., & Oblak, E. 1999, A&A, 349, 485
Marigo, P., Girardi, L., Bressan, A., Groenewegen, M. A. T., Silva, L., & Granato, G. L. 2008, A&A, 482, 883
Mason, B. D., McAlister, H. A., Hartkopf, W. I., & Bagnuolo, Jr., W. G. 1993, AJ, 105, 220
McAlister, H. A. 1978, PASP, 90, 288
McAlister, H. A., et al. 2005, ApJ, 628, 439
Morgan, B. L., Beckmann, G. K., Scaddan, R. J., & Vine, H. A. 1982, MNRAS, 198, 817
Mozurkewich, D., et al. 2003, AJ, 126, 2502
Nordgren, T. E., Sudol, J. J., & Mozurkewich, D. 2001, AJ, 122, 2707
Ochsenbein, F., Bauer, P., & Marcout, J. 2000, A&AS, 143, 23
Patience, J., Ghez, A. M., Reid, I. N., Weinberger, A. J., & Matthews, K. 1998, AJ, 115, 1972
Perryman, M. A. C., et al. 1998, A&A, 331, 81
Peterson, D. M., Baron, R. L., Dunham, E., & Mink, D. 1981a, AJ, 86, 1090
Peterson, D. M., Baron, R. L., Dunham, E., Mink, D., Elliot, J. L., & Weekes, T. C. 1981b, AJ, 86, 280
Press, W. H., Teukolsky, S. A., Vetterling, W. T., & Flannery, B. P. 1992, Numerical Recipes in C. The Art of Scientific Computing, (2nd ed.; Cambridge: Cambridge Univ. Press)
Radick, R., & Lien, D. 1980, AJ, 85, 1053
Richichi, A., Ragland, S., Stecklum, B., & Leinert, C. 1998, A&A, 338, 527
Ridgway, S. T., Jacoby, G. H., Joyce, R. R., Siegel, M. J., & Wells, D. C. 1982, AJ, 87, 808
Ridgway, S. T., Jacoby, G. H., Joyce, R. R., & Wells, D. C. 1980, AJ, 85, 1496
Royer, F., Zorec, J., & Gómez, A. E. 2007, A&A, 463, 671
Sato, B., et al. 2007, ApJ, 661, 527
Taylor, B. J. 2006, AJ, 132, 2453
ten Brummelaar, T. A., et al. 2005, ApJ, 628, 453
Thevenin, F. 1998, VizieR Online Data Catalog, 3193, 0
Torres, G., Stefanik, R. P., & Latham, D. W. 1997, ApJ, 485, 167
Trunkovskij, E. M. 1987, Sov. Astron. Lett., 13, 379
van Belle, G. T., et al. 1999, AJ, 117, 521
van Leeuwen, F. 2007, Hipparcos, the New Reduction of the Raw Data, Cambridge Univ. Series: Astrophysics and Space Science Library 350 (Cambridge, UK: Institute of Astronomy), 20
Wall, J. V., & Jenkins, C. R. 2003, Practical Statistics for Astronomers (Princeton Series in Astrophysics)
White, N. M. 1979, AJ, 84, 872

– E –

Appendix E: Published Work in the Field of Optical Spectroscopy

This appendix includes published work in the general topic of optical spectroscopy of early-type stars.

THE ASTROPHYSICAL JOURNAL, 621:978–984, 2005 March 10

THE MASSIVE RUNAWAY STARS HD 14633 AND HD 15137[1]

T. S. BOYAJIAN, T. D. BEAULIEU, D. R. GIES,[2] E. GRUNDSTROM,[2] W. HUANG,[2]
M. V. MCSWAIN,[2,3,4] R. L. RIDDLE,[2,5] AND D. W. WINGERT[2]
Center for High Angular Resolution Astronomy; and Department of Physics and Astronomy, Georgia State University, P.O. Box 4106, Atlanta, GA 30302-4106; boyajian@chara.gsu.edu, beaulieu@chara.gsu.edu, gies@chara.gsu.edu, erika@chara.gsu.edu, huang@chara.gsu.edu, mcswain@astro.yale.edu, riddle@astro.caltech.edu, wingert@chara.gsu.edu

AND

M. DE BECKER
Institut d'Astrophysique et de Géophysique, Université de Liège, 17, Allée du 6 Août, B5c, 4000 Sart Tilman, Belgium; debecker@astro.ulg.ac.be
Received 2004 October 29; accepted 2004 November 21

ABSTRACT

We present results from a radial velocity study of two runaway O-type stars, HD 14633 (ON8.5 V) and HD 15137 [O9.5 III(n)]. We find that HD 14633 is a single-lined spectroscopic binary with an orbital period of 15.4083 days. The second target, HD 15137, is a radial velocity variable and a possible single-lined spectroscopic binary with a period close to 1 month. Both binaries have large eccentricity, small semiamplitude, and a small mass function. We show the trajectories of the stars in the sky based on an integration of motion in the Galactic potential, and we suggest that both stars were ejected from the vicinity of the open cluster NGC 654 in the Perseus spiral arm. The binary orbital parameters and runaway velocities are consistent with the idea that both these stars were ejected by supernova explosions in binaries and that they host neutron star companions. We find that the time of flight since ejection is longer than the predicted evolutionary timescales for the stars. This discrepancy may indicate that the stars have a lower mass than normally associated with their spectral classifications, that they were rejuvenated by mass transfer prior to the supernova, or that their lives have been extended through rapid rotation.

Subject headings: binaries: spectroscopic — open clusters and associations: individual (NGC 654) — stars: early-type — stars: individual (HD 14633, HD 15137) — supernovae: general

1. INTRODUCTION

There are two competing theories to explain the origin of the massive OB runaway stars. The model first suggested by Zwicky (1957) and Blaauw (1961) proposes that these stars were originally the binary companions of a star that exploded in a supernova and that the linear momentum of a runaway star balances the momentum lost in the explosion. Since mass ratio reversal probably occurs prior to the explosion, many runaways should still be binaries with a neutron star or black hole companion, unless the system was disrupted by an asymmetric kick velocity imparted to the remnant during the supernova (Brandt & Podsiadlowski 1995). A second model proposes that close gravitational encounters during the young, high stellar number density epoch after cluster formation can lead to ejections through encounters with hard binaries (Poveda et al. 1967; Leonard & Duncan 1988). This model predicts that most runaways will be single stars, although some close binaries can be ejected in exceptional circumstances. Gies & Bolton (1986) made a radial velocity survey of bright, northern sky runaway stars and found that most were indeed radial velocity constant, implying that they were not members of binary systems. More recently Hoogerwerf et al. (2000) explored the motions and origins of runaways using proper-motion data from *Hipparcos* (Perryman 1997), and they found examples of ejection by both mechanisms.

Here we present new radial velocity measurements for two northern sky runaway stars, HD 14633 and HD 15137. HD 14633 is classified as a nitrogen-strong ON 8V star (Walborn 1972). It appears at Galactic coordinates $l = 140\overset{\circ}{.}78$ and $b = -18\overset{\circ}{.}20$, and with a spectroscopic parallax distance of 2.15 kpc (van Steenberg & Shull 1988), it is located approximately 670 pc below the Galactic plane. The weighted means of the proper motions from *Hipparcos* (Perryman 1997) and Tycho 2 (Høg et al. 2000) are $\mu_\alpha \cos\delta = 0.08 \pm 0.65$ and $\mu_\delta = -6.94 \pm 0.57$ mas yr^{-1}. The spectral lines have a moderate projected rotational velocity with $V \sin i$ estimates of 111 km s^{-1} (Conti & Ebbets 1977), 110 km s^{-1} (Schönberner et al. 1988), and 134 km s^{-1} (Howarth et al. 1997). Rogers (1974) found that the star is a single-lined spectroscopic binary with a period of 15.335 days and an orbital eccentricity of $e = 0.68$. However, subsequent analysis by Bolton & Rogers (1978) did not confirm the initial orbital parameters, and Bolton & Rogers (1978) suggested that the binary might have a nearby third star that modulates the velocity curve. There is no known visual companion to HD 14633 (Mason et al. 1998). Additional spectroscopic observations by Stone (1982) showed little evidence of velocity variability.

The second target is the star HD 15137, which Gies (1987) categorized as a field O star, but we show below (§ 4) that its

[1] Based in part on observations made at the Observatoire de Haute Provence (CNRS), France.
[2] Visiting Astronomer, Kitt Peak National Observatory, National Optical Astronomy Observatory, which is operated by the Association of Universities for Research in Astronomy, Inc., under contract with the National Science Foundation.
[3] Current address: Astronomy Department, Yale University, New Haven, CT 06520-8101.
[4] NSF Astronomy and Astrophysics Postdoctoral Fellow.
[5] Current address: California Institute of Technology, TMT Project, 1200 East California Boulevard, Mail Code 102-8, Pasadena, CA 91125.

peculiar velocity is large enough that the star should also be grouped with the runaway stars. It appears in a similar part of the sky as HD 14633 at $l = 137.^{\circ}46$ and $b = -7.^{\circ}58$, and it has a spectroscopic parallax distance of 2.65 kpc (van Steenberg & Shull 1988), placing it approximately 350 pc below the Galactic plane. The weighted means of the proper motions from *Hipparcos* and Tycho 2 are $\mu_\alpha \cos\delta = 0.56 \pm 0.54$ and $\mu_\delta = -4.60 \pm 0.62$ mas yr^{-1}. Walborn (1973) classified HD 15137 as O9.5 II–III(n), where the suffix (n) indicates broad lines. Conti & Ebbets (1977) reported observing partially resolved double lines in their spectrum. However, Howarth et al. (1997) analyzed a single high-dispersion spectrum from *International Ultraviolet Explorer* (*IUE*) and used a cross-correlation method to find the projected rotational velocity, $V \sin i = 336$ km s^{-1}. They caution that the cross-correlation function is broad, asymmetric, and difficult to measure. We show below that the star is indeed broad-lined, and it may display rapid line-profile variability normally associated with nonradial pulsation (Howarth & Reid 1993; Kambe et al. 1997). Conti et al. (1977) suggest that the stellar radial velocity is variable. There is no evidence of a nascent cluster nearby (de Wit et al. 2004).

Here we present new radial velocities (§ 2) based on high signal-to-noise ratio (S/N) CCD spectroscopy of these two runaways. We give new orbital elements for HD 14633 (§ 3.1) and a tentative binary interpretation for HD 15137 (§ 3.2). We use radial velocity and proper-motion data to calculate the Galactic trajectories of both stars, and we suggest that both originated in or near the open cluster NGC 654 (§ 4). We argue that both stars were probably ejected by a supernova in a binary and that their unseen companions are probably neutron stars (§ 5).

2. OBSERVATIONS AND RADIAL VELOCITIES

Most of the optical spectra were obtained with the Kitt Peak National Observatory 0.9 m coudé feed telescope during observing runs from 2000 September 30 to 2000 October 13 and from 2000 December 10 to 2000 December 23. The spectra have a resolving power of $R = \lambda/\delta\lambda = 9500$. They were made using the long collimator, grating B (in second order with order sorting filter OG 550), camera 5, and the F3KB CCD, a Ford Aerospace 3072×1024 device. This arrangement produced a spectral coverage of 6440–7105 Å. Exposure times varied between 20 and 30 minutes, and usually two spectra were taken only a few hours apart each night. The spectra generally have S/N ≈ 200 pixel^{-1}. We also observed the rapidly rotating A-type star, ζ Aql, which we used for removal of atmospheric water vapor and O_2 bands. Each set of observations was accompanied by numerous bias, flat-field, and Th-Ar comparison lamp calibration frames. One earlier red spectrum of HD 14633 was made with the coudé feed telescope on 1999 November 13, but this spectrum was obtained with the short collimator and grating RC 181 (in first order with a GG 495 filter to block higher orders), which yielded a lower resolving power, $R = \lambda/\delta\lambda = 4000$. Two additional red spectra of HD 14633 were obtained with the coudé feed on 2004 October 12 and 14, and one final red spectrum of HD 15137 was made on 2004 October 12. These three spectra are similar to the main group, but they were made with the T2KB CCD (2048×2048 pixels). The dates of observation are given in Tables 1 and 2. The spectra were extracted and calibrated using standard routines in IRAF.[6] All the spectra were rectified to a unit continuum by fitting line-free regions. The removal of atmospheric lines was done by creating a library of ζ Aql spectra from each run, removing the broad stellar features from these, and then dividing each target spectrum by the modified atmospheric spectrum that most closely matched the target spectrum in a selected region dominated by atmospheric absorptions. The spectra from each run were then transformed to a common heliocentric wavelength grid.

Two spectra of HD 14633 in the blue domain (4550–4900 Å) were obtained at the Observatoire de Haute-Provence (OHP) in 2003 October. These observations were carried out with the Aurélie spectrograph fed by the 1.52 m telescope (Gillet et al. 1994). The detector was a 2048×1024 CCD (EEV 42-20 No. 3), with a pixel size of $13.5\ \mu\text{m} \times 13.5\ \mu\text{m}$. We used a 600 line mm^{-1} grating, offering a resolving power of about 8000 in the blue with a reciprocal dispersion of 16 Å mm^{-1}. The exposure times were 45 and 30 minutes, and the spectra have S/N = 350 and 480 pixel^{-1}. The spectra were wavelength-calibrated using a Th-Ar spectrum taken just after the observation of the star. The data were reduced using the MIDAS software package developed at ESO and were normalized to a unit continuum.

We measured radial velocities for the red spectra of both HD 14633 and HD 15137 by cross-correlating the line profiles of each spectrum with those in one spectrum selected for optimum S/N properties. We measured individually the deepest and best defined absorption lines in this spectral region: Hα, the blend of He I λ6678 and He II λ6683, and He I λ7065. There was no

TABLE 1
HD 14633 Radial Velocity Measurements

HJD (−2,400,000)	Orbital Phase	V_r (km s^{-1})	$O-C$ (km s^{-1})
51495.903	0.741	−31.6	−1.8
51818.807	0.698	−29.3	1.0
51819.741	0.758	−29.4	0.2
51820.786	0.826	−28.5	0.6
51821.746	0.888	−29.6	0.1
51822.797	0.957	−35.6	1.6
51822.963	0.967	−41.0	0.1
51823.738	0.018	−66.5	0.5
51823.899	0.028	−66.1	−0.9
51824.732	0.082	−51.8	1.4
51824.928	0.095	−50.3	1.1
51830.758	0.473	−31.4	2.6
51830.889	0.482	−34.5	−0.6
51889.828	0.307	−39.5	−1.4
51890.749	0.367	−36.2	0.3
51892.727	0.495	−32.9	0.8
51893.753	0.562	−32.2	0.2
51895.688	0.687	−29.9	0.6
51895.777	0.693	−30.0	0.4
51896.617	0.748	−30.8	−1.0
51896.750	0.756	−28.7	0.9
51897.613	0.812	−28.1	1.1
51897.751	0.821	−29.6	−0.4
51898.620	0.878	−30.8	−1.4
51898.754	0.886	−29.7	0.0
51899.624	0.943	−34.8	−0.8
51899.757	0.951	−35.9	−0.2
51900.619	0.007	−67.7	−1.6
51900.751	0.016	−65.2	2.0
51901.604	0.071	−58.7	−3.6
51901.737	0.080	−52.4	1.3
52930.558	0.851	−30.3	−1.1
52934.413	0.101	−50.4	0.2
53290.840	0.233	−41.5	−0.6
53292.825	0.362	−38.2	−1.6

[6] IRAF is distributed by the National Optical Astronomy Observatory.

TABLE 2
HD 15137 Radial Velocity Measurements

HJD (−2,400,000)	Orbital Phase	V_r (km s^{-1})	$O-C$ (km s^{-1})
51817.788	0.985	−59.6	−3.4
51818.797	0.021	−58.5	5.6
51819.758	0.054	−70.8	−5.3
51820.793	0.090	−63.7	−0.2
51821.762	0.124	−59.7	1.3
51822.805	0.161	−57.5	0.9
51822.970	0.167	−54.8	3.3
51823.746	0.194	−60.6	−4.1
51823.907	0.199	−54.6	1.6
51824.739	0.228	−54.3	0.3
51824.935	0.235	−55.3	−1.0
51830.770	0.439	−46.8	0.3
51830.897	0.444	−46.4	0.5
51889.849	0.505	−47.4	−2.0
51890.769	0.537	−41.4	3.2
51892.761	0.606	−46.4	−3.3
51893.788	0.642	−40.7	1.6
51894.790	0.677	−44.2	−2.5
51895.699	0.709	−40.3	0.8
51895.788	0.712	−36.7	4.4
51896.628	0.742	−47.9	−7.3
51896.762	0.746	−42.8	−2.3
51897.627	0.776	−41.4	−1.2
51897.762	0.781	−38.8	1.3
51898.633	0.812	−31.9	8.1
51898.766	0.816	−34.9	5.1
51899.635	0.847	−45.8	−5.7
51899.768	0.851	−43.7	−3.6
51900.630	0.881	−38.9	2.0
51900.762	0.886	−44.1	−3.1
51901.615	0.916	−38.3	4.6
51901.748	0.921	−43.9	−0.5
53290.849	0.482	−45.3	0.6

evidence of Hα emission in either star's spectrum. We then formed the mean difference between the velocity for each line and that of He I λ7065, and we applied these differences to each line's velocities to place them on the same velocity system as that for He I λ7065 in the reference spectrum. Finally, we made a Gaussian fit of the He I λ7065 profile in the reference spectrum and added this to the mean velocity from all three lines to transform the results from relative to absolute radial velocity. We relied on the Gaussian fit of He I λ7065 alone, because both of the other features are blends with weaker components of He II and simple Gaussian fits of these will be biased by line blending. These two stars were observed in conjunction with a program on eight other O star targets, and we used measurements of the interstellar lines in those spectra to make small corrections (on the order of 1 km s^{-1}) to the velocity measurements from each night.

We determined radial velocities for the two blue spectra of HD 14633 by parabolic fitting of the line cores of He I $\lambda\lambda$4471, 4713 and He II $\lambda\lambda$4541, 4686. Many O stars exhibit line-to-line radial velocity differences due to subtle blends and atmospheric expansion (Hutchings 1976; Bohannan & Garmany 1978; Gies & Bolton 1986), but we found that the average radial velocity for these He lines matched those based on the red He I λ7065 line quite well (§ 3.1). Our final radial velocities are presented in Table 1 (HD 14633) and Table 2 (HD 15137).

3. ORBITAL ELEMENTS

3.1. *HD 14633*

Rogers (1974) found that HD 14633 is a single-lined spectroscopic binary with a period of 15.335 days, a small semiamplitude ($K = 31.3$ km s^{-1}), and a large eccentricity ($e = 0.68$). However, additional spectroscopic analysis by Bolton & Rogers (1978) cast some doubt on the original solution. Our 2000 December run was long enough to cover an almost complete cycle of variations, and the velocities do indeed suggest an orbital period close to the 15 day period found by Rogers (1974).

We made an initial period search using the "phase dispersion minimization" technique of Stellingwerf (1978), which is especially useful for finding nonsinusoidal signals in time series data. We combined our radial velocities (Table 1) with measurements from Bolton & Rogers (1978) and Stone (1982) (for a total of 89 measurements spanning nearly 83 yr). We omitted from this sample three velocities from *IUE* (Stickland & Lloyd 2001) and two velocities from Conti et al. (1977) that appeared to be systematically shifted to more positive and more negative velocities, respectively, compared to the rest. We found one strong signal at a period of 15.409 days (with one weaker alias at a period of 15.433 days), and we used this period as the starting value in the nonlinear least-squares fitting program of Morbey & Brosterhus (1974) to establish the orbital elements of HD 14633. The results are presented in Table 3 together with the original estimates from Rogers (1974). The two sets of elements are comparable, but the new period is larger and the semiamplitude is smaller than that obtained by Rogers (1974). We suspect that Rogers found an alias period that failed to fit the additional data reported later by Bolton & Rogers (1978).

The full sample of historical and new radial velocity data forms a very heterogeneous collection based on different lines,

TABLE 3
Orbital Elements for HD 14633

Element	Rogers (1974)	Bolton & Rogers (1978) + Stone (1982) + New	New
P (days)	15.335	15.4083 ± 0.0004	15.4083[a]
T (HJD −2,400,000)	42007.3	44227.26 ± 0.21	51854.28 ± 0.05
e	0.68	0.63 ± 0.05	0.698 ± 0.010
ω (deg)	166.3	142 ± 10	140.3 ± 2.2
K (km s^{-1})	31.3	15.9 ± 1.4	19.0 ± 0.4
γ (km s^{-1})	−46.0	−38.8 ± 0.8	−37.9 ± 0.3
$f(m)$ ($M_\odot$)	0.019	0.0030 ± 0.0009	0.0040 ± 0.0003
$a_1 \sin i$ ($R_\odot$)	6.95	3.8 ± 0.4	4.14 ± 0.10
rms (km s^{-1})	...	7.4	1.3

[a] Fixed.

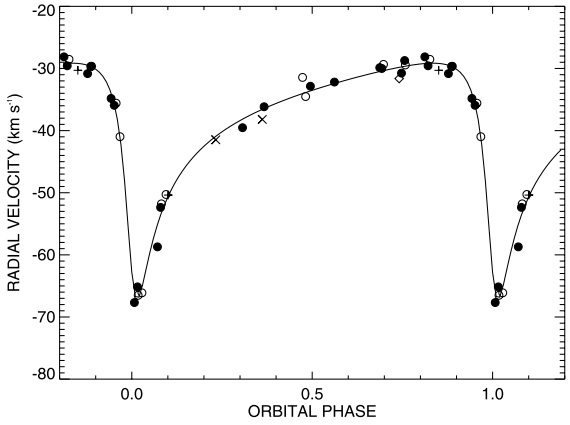

FIG. 1.—Calculated radial velocity curve (*solid line*) for HD 14633. The different symbols indicate observations from 1999 November (*diamond*), 2000 October (*open circles*), 2000 December (*filled circles*), 2003 October (*plus signs*), and 2004 October (*crosses*).

spectroscopic dispersions, and S/N in the spectra. Consequently, we repeated the orbital element fitting procedure with the more homogeneous set of velocities from Table 1, this time fixing the period to the value derived from the full, many-year sample. These elements appear in the final column of Table 3, and indeed the rms residuals from the fit are now much smaller and comparable to our measurement errors. The final fit and observed velocities are illustrated in Figure 1.

3.2. *HD 15137*

The photospheric lines in HD 15137 are much more rotationally broadened and shallower than those of HD 14633. The half-width near the continuum of the two He I lines is 309 ± 4 km s^{-1}, which is comparable to the projected rotational velocity of $V \sin i = 336$ km s^{-1} found by Howarth et al. (1997). The He I profiles show significant night-to-night variations in shape that are similar to those observed in the nonradial pulsators HD 93521 (Howarth & Reid 1993) and ζ Oph (Kambe et al. 1997), which are also rapidly rotating, late O-type stars. The profiles appear with a central inversion on a few occasions, giving the impression of a partially resolved, double-lined binary (as claimed by Conti & Ebbets 1977). An investigation with a finer time resolution would clearly be rewarding, but the rapid and complex changes observed in the spectra available indicate that the profile variations are probably due to photospheric modulations rather than the blending of components of a short-period binary. These variations do, unfortunately, introduce an additional component of scatter into our radial velocity measurements. Nevertheless, there is a clear indication that the velocity is variable on timescales of a month or so. The mean velocity from the 2000 October run was −57.1 ± 1.9 km s^{-1}, compared with −41.6 ± 1.0 km s^{-1} for the 2000 December run (where the errors are the standard deviation of the mean). We again used the phase dispersion minimization technique to search for possible periods, and we found candidate periods of 21.2, 28.6, and 43.4 days (with acceptable periods in a large range surrounding the latter two). This target has unfortunately been largely ignored by observers, and the only two measurements made in the last 40 years are single velocities from *IUE* (Stickland & Lloyd 2001) and from Conti et al. (1977). Once again, the *IUE* measurement appears to be much more positive than any of the other observations, while the measurement from Conti et al. (1977) is lower than any of ours.

TABLE 4

PRELIMINARY ORBITAL ELEMENTS FOR HD 15137

Element	Value
P (days)	28.61 ± 0.09
T (HJD −2,400,000)	51904.0 ± 0.7
e	0.52 ± 0.07
ω (deg)	125 ± 11
K (km s^{-1})	12.9 ± 1.3
γ (km s^{-1})	−49.0 ± 0.7
$f(m)$ ($M_\odot$)	0.0039 ± 0.0013
$a_1 \sin i$ ($R_\odot$)	6.2 ± 0.7
rms (km s^{-1})	3.8

The best-fit period for our data is 28.61 days, but there are numerous and almost equally good alias periods at intervals of +0.62n days (where n is an integer) spanning the range from 28.6 to 31.1 days in addition to the other periods mentioned above. We caution that the current data set samples essentially only the velocity extrema at two epochs, so the periodic nature of the variations remains to be verified. Nevertheless, the velocity variations are consistent with those expected for a long-period and small-semiamplitude binary.

The limited time span of the available data rules out the determination of an accurate period, but we used the candidate period to find a preliminary set of orbital elements. These elements are presented in Table 4, and the radial velocity curve is illustrated in Figure 2. Although the period is poorly known, tests with other trial periods showed that the resulting semiamplitude and eccentricity were not too different from the values reported in Table 4. Thus, the current set of velocities suggests that the star is a spectroscopic binary with a low semiamplitude and an eccentric orbit.

4. EJECTION FROM THE GALACTIC PLANE

Both HD 14633 and HD 15137 are found well outside the plane of the Galaxy, and *Hipparcos* proper motions (Perryman 1997) indicate that both stars are moving away from the plane. Here we present numerical integrations of their motion in the Galaxy made in order to estimate their possible site of origin and their time of flight since ejection.

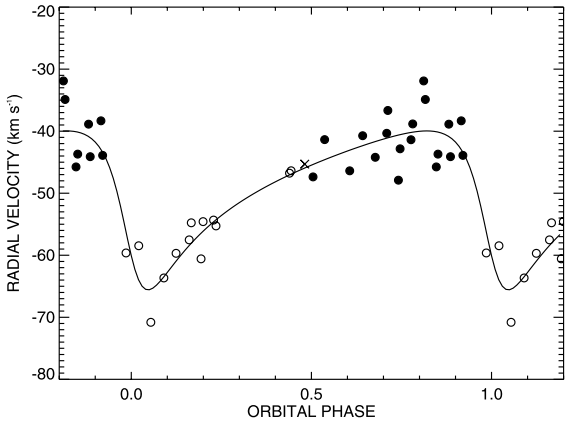

FIG. 2.—Preliminary radial velocity curve (*solid line*) for HD 15137. The different symbols indicate observations from 2000 October (*open circles*), 2000 December (*filled circles*), and 2004 October (*cross*).

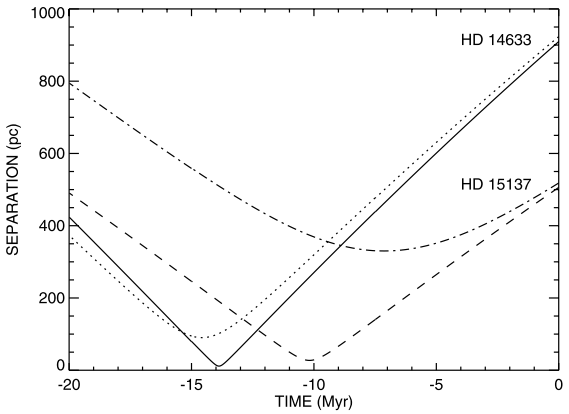

FIG. 3.—Separation between HD 14633 and NGC 654, and between HD 15137 and NGC 654, plotted against time in millions of years relative to the present. The dotted line shows the separation for the nominal current distance to HD 14633 of 2.15 kpc, while the solid line shows the separation for a trajectory calculated using a current distance of 2.24 kpc. Likewise the dot-dashed line shows the separation for the nominal distance to HD 15137 of 2.65 kpc, while the dashed line shows the same for a current distance of 2.29 kpc.

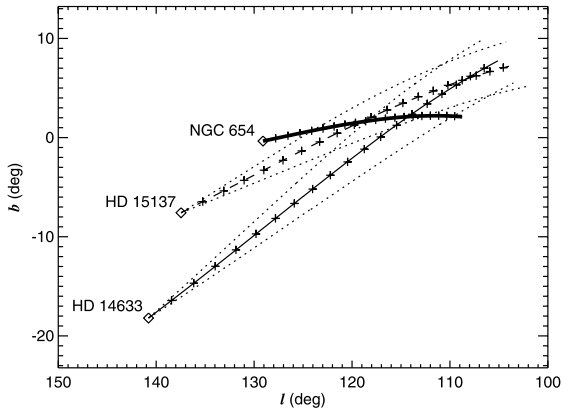

FIG. 4.—Past trajectories of HD 14633 (*thin solid line*), HD 15137 (*thin dashed line*), and NGC 654 (*thick solid line*) in Galactic longitude and latitude. The diamonds mark the current positions, and tick marks are placed at 1 Myr intervals along each track. The dotted lines show the tracks for $\pm 1\ \sigma$ errors in proper motion for the runaway stars.

The integration of motion was made using a cylindrical coordinate system (r, ϕ, z). We first determined the position and resolved velocity components of the star in this system using the Galactic coordinates (l, b), proper motion, distance estimate, radial velocity, velocity of the Sun with respect to the local standard of rest (LSR; Dehnen & Binney 1998a), and the Sun's position relative to the plane (Holmberg et al. 1997). We then performed integrations backward in time using a fourth-order Runge-Kutta method and a model for the Galactic potential from Dehnen & Binney (1998b). We adopted model 2 from Dehnen & Binney (1998b), which uses a Galactocentric distance of 8.0 kpc and a disk density exponential scale length of 2.4 kpc. We used time steps of 0.01 Myr over a time span of 20 Myr. The procedure compared the Sun's and the star's position to find the distance and Galactic coordinates l and b for each time step. We determined when and where the star's trajectory crossed the Galactic plane, and we then integrated forward in time to find the current position and distance of the LSR of the intersection site. We then inspected a list of Galactic open clusters (Leisawitz 1988) to search for candidate birthplace clusters.

We calculated a trajectory for HD 14633 using an adopted current distance of 2.15 kpc (van Steenberg & Shull 1988), the weighted mean of the proper motions from *Hipparcos* (Perryman 1997) and from Tycho 2 (Høg et al. 2000), and the systemic radial velocity from Table 3. According to this model, the star crossed the plane of the Galaxy about 13 Myr ago, in agreement with prior estimates (Hobbs 1983). We found that the closest cluster to this trajectory was NGC 654, an open cluster in the Cas OB8 association in the Perseus spiral arm. We calculated the trajectory of NGC 654 based on proper motions of $\mu_\alpha \cos\delta = -1.34 \pm 0.51$ and $\mu_\delta = -0.72 \pm 0.64$ mas yr^{-1} from Baumgardt et al. (2000), a mean radial velocity of $V_r = -33.8 \pm 1.4$ km s^{-1} from Rastorguev et al. (1999), and a distance of $d = 2.50 \pm 0.30$ kpc from Huestamendia et al. (1993); and the spatial separation between HD 14633 and NGC 654 is plotted as a function of time in Figure 3. This shows that the closest approach occurred about 14.6 Myr ago. The greatest uncertainty in the calculation comes from the errors in spectroscopic parallax for HD 14633 (approximately ±28%), so we also calculated the closest separations for a grid of current distances to find the minimum separation possible with all the other parameters fixed. We found that the minimum separation was 11 pc for a test value of current distance of 2.24 kpc (well within the error range), and Figure 3 also shows the temporal variation in cluster-star separation for this case. This minimum occurred 13.9 Myr ago, when the relative velocity of the cluster and star was 69 km s^{-1}. If the star was actually ejected at this time from this cluster, then this relative velocity is the ejection velocity.

We illustrate the trajectories of the star and cluster as viewed from the Sun in Figure 4. Tick marks along each trajectory mark intervals of 1 Myr before the current time (*diamonds*). We also show the trajectories for the $\pm 1\ \sigma$ errors in the proper motions (*dotted lines*). The errors in proper motion probably introduce a ±2 Myr error in the estimated time of closest approach.

We performed the same kind of calculation for HD 15137 using a nominal distance estimate of 2.65 kpc (van Steenberg & Shull 1988), the weighted mean of the *Hipparcos* and Tycho 2 proper motions, and the systemic radial velocity from Table 4. We found that the star crossed the plane of the Galaxy some 8 Myr ago for this assumed distance. We searched for possible clusters of origin, and we were surprised to find that NGC 654 once again presented the closest approach of trajectories. The separation between HD 15137 and NGC 654 is plotted in Figure 3, and we found that the smallest separation was 328 pc for the nominal distance estimate. However, we tested a grid of trajectories for different values of the assumed current distance, and the minimum star-cluster separation occurred for an assumed current distance of 2.29 kpc (again within the errors associated with the spectroscopic parallax). The minimum separation was 27 pc at a time 10.2 Myr ago, when the relative velocity was 50 km s^{-1} (Fig. 3). The paths of the star and cluster for the past 20 Myr are illustrated in Figure 4, where we see that errors in the proper motion contribute an uncertainty of ±2 Myr in the estimate of the ejection time.

5. DISCUSSION

OB runaway stars are probably ejected by one of two mechanisms, sudden mass loss during a supernova explosion in a binary or a close gravitational encounter involving binaries

(Gies & Bolton 1986; Hoogerwerf et al. 2000). The supernova theory predicts that runaways will either be single stars (in which the binary was disrupted because of a large, asymmetric kick velocity imparted during the supernova) or binaries with neutron star or black hole companions (such as high-mass X-ray binaries). On the other hand, the gravitational encounter theory suggests that most runaways will be single objects, although in rare cases hard binaries of mass ratio near unity are ejected.

Our radial velocity study has demonstrated that HD 14633 and possibly HD 15137 are binary stars with low-mass companions. If we suppose that the masses of the primary are 23 $M_\odot$ for HD 14633 (Keenan & Dufton 1984) and 24 $M_\odot$ for HD 15137 (Vacca et al. 1996), then the minimum masses of the companion derived from the orbital mass function (Tables 3 and 4) will be 1.3 and 1.5 $M_\odot$, respectively (for an orbital inclination of 90°). These masses are close to the 1.35 $M_\odot$ value found for most neutron stars in binaries (Thorsett & Chakrabarty 1999). These runaways may be the first examples of the long-sought "quiet" massive X-ray binaries, i.e., those with wide separations in which wind accretion is too weak to power an accretion disk X-ray source (van den Heuvel 1976). We searched for evidence of a companion spectrum in both cases using a Doppler tomography algorithm (Bagnuolo et al. 1994), but no spectral features were found. A faint, low-mass, main-sequence star could easily remain hidden in the glare of an O star (for example, the magnitude difference is $\triangle V \approx 8$ between such O stars and a F3 V companion of mass 1.4 $M_\odot$). Nevertheless, we doubt that these systems are extreme mass ratio binaries containing an O- and an F-type star, since no such systems are known among the O stars and since such systems would probably be disrupted in close gravitational encounters leading to ejection.

Both HD 14633 and HD 15137 have many characteristics in common with the massive X-ray binary and microquasar LS 5039 (McSwain et al. 2004). All are runaway objects with very eccentric orbits and small orbital mass functions. LS 5039 has a much shorter period (4.4267 days), and the smaller semimajor axis results in a modestly dense wind in the vicinity of the orbiting neutron star, so that LS 5039 is a weak X-ray source. In contrast, the longer period systems HD 14633 and HD 15137 will have very rarefied winds close to their neutron star companions, and consequently their accretion fluxes are expected to be extremely faint (perhaps also as the result of centrifugal inhibition of accretion; Stella et al. 1986). Neither system is listed in the *ROSAT* All-Sky Survey Faint Source Catalogue (Voges et al. 2000). Furthermore, neither system appears to be associated with an EGRET γ-ray source (Hartman et al. 1999), nor are they known radio sources (Vallee & Moffat 1985; Wendker 1995; Sayer et al. 1996). Thus, wind accretion onto a neutron star in these systems must be too feeble to produce the high-energy phenomena associated with other massive X-ray binaries.

McSwain et al. (2004) found that the supernova mass-loss prediction for LS 5039 was different depending on whether the calculation was based on orbital eccentricity or runaway velocity, and they argued that both the eccentricity and runaway velocity can be explained if a significant asymmetric kick velocity was imparted to the neutron star during formation. A similar conclusion can be derived for HD 14633 and HD 15137. If we use the expressions for supernova mass loss given by Nelemans et al. (1999) and adopt the primary masses given above and secondary masses of 1.4 $M_\odot$, then the predicted supernova mass loss is 17 and 13 $M_\odot$ for HD 14633 and HD 15137, respectively, based on their observed eccentricities. On the other hand, the supernova mass-loss estimates are 6.9 and 6.4 $M_\odot$, respectively, based on the relative runaway velocities between star and cluster from the models given in § 4. These significant differences suggest that both systems suffered kick velocities at birth that substantially altered the eccentricity. The supernova mass-loss estimates from the runaway velocities should be more reliable, since the runaway velocities are less affected by kicks (Brandt & Podsiadlowski 1995).

Two other features of these stars also link them to supernova ejections. First, HD 14633 is a well-known, nitrogen-rich ON star (Walborn 1972; Schönberner et al. 1988), and McSwain et al. (2004) have shown that massive X-ray binary LS 5039 also shares this trait. McSwain et al. (2004) suggest that the nitrogen enrichment is the result of mass transfer of CNO-processed gas from the supernova progenitor prior to the explosion, although rotationally induced mixing may also play a role. Second, HD 15137 is a very rapid rotator, a characteristic shared with many other OB runaway stars (Blaauw 1993). Mass transfer prior to the supernova may lead to a spin-up of the mass gainer, and this process may be responsible for the largest class of massive X-ray sources, the rapidly rotating, Be X-ray binaries (Coe 2000).

Both runaways appear to have been ejected from the Perseus spiral arm, and our analysis of their motions in the Galaxy (§ 4) indicates a probable origin in the open cluster NGC 654 in the Cas OB8 association. The cluster's age is 14 ± 4 Myr (Huestamendia et al. 1993), and the cluster contains a number of early B-type stars and two massive supergiants (HD 10494, F5 Ia, and BD +61°315, A2 Ib). Garmany & Stencel (1992) include the nearby O star BD +60°261 [O7.5 III(n)((f)); Walborn 1973] as a cluster member. The Cas OB8 association has a diameter of approximately 85 pc and contains several other clusters, including NGC 581, 659, and 663 (Garmany & Stencel 1992), which have slightly greater ages of 22, 35, and 16 Myr, respectively, according to the WEBDA database (Mermilliod & Paunzen 2003).[7] The time of flight for HD 15137 (10 Myr) suggests that the star was ejected from NGC 654 when the cluster was approximately 4 Myr old, which may be consistent with the evolutionary timescale required for a supernova progenitor. However, the main-sequence lifetime of a star of 24 $M_\odot$ is approximately 6.7 Myr (Schaller et al. 1992), which is less than the time of flight for HD 15137. The situation is even more discrepant for HD 14633, which has a time of flight of at least 12 Myr (see also the extreme case of the runaway star HD 93521; Howarth & Reid 1993). It is difficult to reconcile these long travel times with the expected short lifetimes of O stars. There are several possible explanations. First, the runaways may have been rejuvenated by mass transfer just prior to the supernova explosion, which would reset their effective zero-age times to an epoch just prior to ejection. Second, at least HD 15137 is a rapid rotator, and fast rotation may help to mix gas and extend the main-sequence lifetime of massive stars (Heger & Langer 2000; Meynet & Maeder 2000). Third, these stars may be overluminous for their mass in same way as some massive X-ray binaries (Kaper 2001), so that their masses are lower and their evolutionary lifetimes are longer than simple estimates suggest.

The orbital properties of these two runaway binaries, their small-mass functions, and their probable origin in a cluster containing evolved, massive stars all indicate that these stars

[7] Maintained by J.-C. Mermilliod at http://obswww.unige.ch/webda/webda.html.

were ejected during a supernova explosion in a binary. They are not known X-ray sources, presumably because of their large semimajor axes and low wind accretion rates, but it is possible that they exhibit transient X-ray emission when their neutron stars pass through the densest stellar wind regions near the periastron orbital phase. It is important to pursue radial velocity studies of other OB runaway stars to search for additional instances of such low-amplitude binary systems. Only then will we determine the relative importance of the supernova and close encounter ejection processes for the kinematics of massive runaway stars.

We thank the staff of KPNO for their assistance in making these observations possible. We also thank Walter Dehnen for sending us his code describing the Galactic gravitational potential. Financial support was provided by the National Science Foundation through grant AST 02-05297 (D. R. G.). Institutional support has been provided from the GSU College of Arts and Sciences and from the Research Program Enhancement fund of the Board of Regents of the University System of Georgia, administered through the GSU Office of the Vice President for Research. M. D. acknowledges financial support through the PRODEX XMM-OM Project.

REFERENCES

Bagnuolo, W. G., Jr., Gies, D. R., Hahula, M. E., Wiemker, R., & Wiggs, M. S. 1994, ApJ, 423, 446
Baumgardt, H., Dettbarn, C., & Wielen, R. 2000, A&AS, 146, 251
Blaauw, A. 1961, Bull. Astron. Inst. Netherlands, 15, 265
———. 1993, in ASP Conf. Ser. 35, Massive Stars: Their Lives in the Interstellar Medium, ed. J. P. Cassinelli & E. B. Churchwell (San Francisco: ASP), 207
Bohannan, B., & Garmany, C. D. 1978, ApJ, 223, 908
Bolton, C. T., & Rogers, G. L. 1978, ApJ, 222, 234
Brandt, N., & Podsiadlowski, Ph. 1995, MNRAS, 274, 461
Coe, M. J. 2000, in IAU Colloq. 175, The Be Phenomenon in Early-Type Stars, ed. M. A. Smith, H. F. Henrichs, & J. Fabregat (ASP Conf. Ser. 214; San Francisco: ASP), 656
Conti, P. S., & Ebbets, D. 1977, ApJ, 213, 438
Conti, P. S., Leep, E. M., & Lorre, J. J. 1977, ApJ, 214, 759
Dehnen, W., & Binney, J. J. 1998a, MNRAS, 298, 387
———. 1998b, MNRAS, 294, 429
de Wit, W. J., Testi, L., Palla, F., Vanzi, L., & Zinnecker, H. 2004, A&A, 425, 937
Garmany, C. D., & Stencel, R. E. 1992, A&AS, 94, 211
Gies, D. R. 1987, ApJS, 64, 545
Gies, D. R., & Bolton, C. T. 1986, ApJS, 61, 419
Gillet, D., et al. 1994, A&AS, 108, 181
Hartman, R. C., et al. 1999, ApJS, 123, 79
Heger, A., & Langer, N. 2000, ApJ, 544, 1016
Hobbs, L. M. 1983, ApJ, 265, 817
Høg, E., et al. 2000, A&A, 355, L27
Holmberg, J., Flynn, C., & Lindegren, L. 1997, in *Hipparcos*, Venice '97, ed. B. Battrick (ESA SP-402; Noordwijk: ESA), 721
Hoogerwerf, R., de Bruijne, J. H. J., & de Zeeuw, P. T. 2000, ApJ, 544, L133
Howarth, I. D., & Reid, A. H. N. 1993, A&A, 279, 148
Howarth, I. D., Siebert, K. W., Hussain, G. A. J., & Prinja, R. K. 1997, MNRAS, 284, 265
Huestamendia, G., del Rio, G., & Mermilliod, J.-C. 1993, A&AS, 100, 25
Hutchings, J. B. 1976, ApJ, 203, 438
Kambe, E., et al. 1997, ApJ, 481, 406
Kaper, L. 2001, in The Influence of Binaries on Stellar Population Studies ed. D. Vanbeveren (Dordrecht: Kluwer), 125
Keenan, F. P., & Dufton, P. L. 1984, A&A, 139, 227
Leisawitz, D. 1988, Catalog of Open Clusters and Associated Interstellar Matter (NASA RP-1202; Washington, DC; NASA)
Leonard, P. J. T., & Duncan, M. J. 1988, AJ, 96, 222
Mason, B. D., Gies, D. R., Hartkopf, W. I., Bagnuolo, W. G., Jr., ten Brummelaar, T., & McAlister, H. A. 1998, AJ, 115, 821
McSwain, M. V., Gies, D. R., Huang, W., Wiita, P. J., Wingert, D. W., & Kaper, L. 2004, ApJ, 600, 927
Mermilliod, J.-C., & Paunzen, E. 2003, A&A, 410, 511
Meynet, G., & Maeder, A. 2000, A&A, 361, 101
Morbey, C., & Brosterhus, E. B. 1974, PASP, 86, 455
Nelemans, G., Tauris, T. M., & van den Heuvel, E. P. J. 1999, A&A, 352, L87
Perryman, M. A. C. 1997, The *Hipparcos* and Tycho Catalogues (ESA SP-1200; Noordwijk: ESA)
Poveda, A., Ruiz, J., & Allen, C. 1967, Bol. Obs. Tonantzintla Tacubaya, 4, 86
Rastorguev, A. S., Glushkova, E. V., Dambis, A. K., & Zabolotskikh, M. V. 1999, AZh Pis'ma, 25, 689 (English transl. in Astron. Lett., 25, 595)
Rogers, G. L. 1974, M.S. thesis, Univ. Toronto
Sayer, R. W., Nice, D. J., & Kaspi, V. M. 1996, ApJ, 461, 357
Schaller, G., Schaerer, D., Meynet, G., & Maeder, A. 1992, A&AS, 96, 269
Schönberner, D., Herrero, A., Becker, S., Eber, F., Butler, K., Kudritzki, R. P., & Simon, K. P. 1988, A&A, 197, 209
Stella, L., White, N. E., & Rosner, R. 1986, ApJ, 308, 669
Stellingwerf, R. F. 1978, ApJ, 224, 953
Stickland, D. J., & Lloyd, C. 2001, Observatory, 121, 1
Stone, R. C. 1982, ApJ, 261, 208
Thorsett, S. E., & Chakrabarty, D. 1999, ApJ, 512, 288
Vacca, W. D., Garmany, C. D., & Shull, J. M. 1996, ApJ, 460, 914
Vallee, J. P., & Moffat, A. F. J. 1985, AJ, 90, 315
van den Heuvel, E. P. J. 1976, in IAU Symp. 73, Structure and Evolution of Close Binary Systems, ed. P. Eggleton (Dordrecht: Reidel), 35
van Steenberg, M. E., & Shull, J. M. 1988, ApJS, 67, 225
Voges, W., et al. 2000, IAU Circ., 7432, 1
Walborn, N. R. 1972, AJ, 77, 312
———. 1973, AJ, 78, 1067
Wendker, H. J. 1995, A&AS, 109, 177
Zwicky, F. 1957, Morphological Astronomy (Berlin: Springer)

The Astrophysical Journal, 646:1209–1214, 2006 August 1

THE B SUPERGIANT COMPONENTS OF THE DOUBLE-LINED BINARY HD 1383

T. S. Boyajian, D. R. Gies,[1] M. E. Helsel,[2] A. B. Kaye,[1] M. V. McSwain,[1,3,4] R. L. Riddle,[1,5] and D. W. Wingert[1]
Center for High Angular Resolution Astronomy and Department of Physics and Astronomy, Georgia State University, P.O. Box 4106, Atlanta, GA 30302-4106; tabetha@chara.gsu.edu, gies@chara.gsu.edu, marian.helsel@furman.edu, anthony.kaye@itt.com, mcswain@astro.yale.edu, riddle@astro.caltech.edu, wingert@chara.gsu.edu
Received 2005 December 20; accepted 2006 April 8

ABSTRACT

We present new results from a study of high-quality red spectra of the massive binary star system HD 1383 (B0.5 Ib + B0.5 Ib). We determined radial velocities and revised orbital elements ($P = 20.28184 \pm 0.0002$ days) and made Doppler tomographic reconstructions of the component spectra. A comparison of these with model spectra from non-LTE, line-blanketed atmospheres indicates that the two stars have almost identical masses ($M_2/M_1 = 1.020 \pm 0.014$), temperatures ($T_{\rm eff} = 28{,}000 \pm 1000$ K), gravities ($\log g = 3.25 \pm 0.25$), and projected rotational velocities ($V \sin i \lesssim 30$ km s^{-1}). We investigate a number of constraints on the radii and masses of the stars based on the absence of eclipses, surface gravity, stellar wind terminal velocity, and probable location in the Perseus spiral arm of the Galaxy, and these indicate a range in probable radius and mass of $R/R_\odot = 14$–20 and $M/M_\odot = 16$–35, respectively. These values are consistent with model evolutionary masses for single stars of this temperature and gravity. Both stars are much smaller than their respective Roche radii, so the system is probably in a precontact stage of evolution. A fit of the system's spectral energy distribution yields a reddening of $E(B-V) = 0.55 \pm 0.05$ and a ratio of total-to-selective extinction of $R = 2.97 \pm 0.15$. We find no evidence of Hα emission from colliding stellar winds, which is probably the consequence of the low gas densities in the colliding winds zone.

Subject headings: binaries: spectroscopic — stars: early-type — stars: evolution — stars: individual (HD 1383) — stars: winds, outflows — supergiants

1. INTRODUCTION

The evolutionary paths of massive binaries depend critically on processes related to mass transfer and mass loss at the time when the initially more massive star begins to fill its Roche volume (Langer et al. 2004; Petrovic et al. 2005). On the one hand, mass from the donor star may end up entirely in a rejuvenated mass gainer, but on the other hand a high mass transfer rate may cause the gainer to swell and bring the system into a common-envelope phase, in which most of the donor's mass is lost from the system entirely. Evidence of both outcomes is found among post–Roche lobe overflow systems (Langer et al. 2004; Petrovic et al. 2005). We can better constrain the problem of the probable results of the interaction by studying binaries in an advanced evolutionary state just prior to Roche filling. Those binaries of nearly identical masses are particularly interesting because we can usually observe the spectra of both components.

Close pairs of nearly identical, evolved massive stars are quite rare. The HD 1383 system is the only such system found in *Ninth Catalogue of Spectroscopic Binary Orbits* (Pourbaix et al. 2004; with identical components of types B0.5 Ib + B0.5 Ib; Hill & Fisher 1986). Another similar massive stellar system, HD 152248, was previously classified as a O7 I + O7 I (Penny et al. 1999), although a more thorough analysis by Sana et al. (2001) revised the classifications to O7.5 III + O7 III, deviating from the exact match of types found in HD 1383. The HD 152248 system is eclipsing, and the mass determinations made by Penny et al. (1999) and Sana et al. (2001) indicate that both stars are undermassive (by factors of 2 and 1.4, respectively, in the two studies) relative to the predicted evolutionary masses for single stars. Here we focus our attention on HD 1383 (BD +60 25, HIP 1466). The system was identified as a double-lined binary early on (Sanford & Merrill 1938; Slettebak 1956), but the first orbital elements were determined later by Hill & Fisher (1986) who found that the system consists of two nearly identical stars with an orbital period of 20.3 days. Morgan et al. (1955) originally adopted the system as a spectral standard for the B1 II type, but Hill & Fisher (1986) revised the types slightly based on detailed measurements of line equivalent widths of both components. The system is located in the sky in the vicinity of the Cas OB4 association (Humphreys 1978), which is located in the Perseus arm of the Galaxy. The star has played an important role in studies of the interstellar medium in this direction (see Cartledge et al. 2004). Various distances have been estimated based on the assumption that HD 1383 is a single, B1 II star. Wakker et al. (1998) found a distance of 1.7 kpc, which agrees well with Humphreys (1978) value of 1.68 kpc. Humphreys (1978) noted that HD 1383 might not be a member of the Cas OB4 association, because the latter has a greater distance of 2.88 kpc. However, the fact that HD 1383 is a binary consisting of two stars with approximately equal brightness implies that it is farther away from us than these previous estimates indicate and that it is closer to Cas OB4 (Hill & Fisher [1986] offer a distance of 3.0 kpc for HD 1383).

Here we present a study of a set of red spectra of HD 1383 that we obtained (§ 2) to reanalyze the orbital elements (§ 3) and to search for evidence of Hα emission related to colliding winds (Thaller 1997; Sana et al. 2001). We discuss the physical parameters of the stars from an analysis of their individual spectra obtained from a Doppler tomography reconstruction (§ 4). We then present a number of constraints on the radii and masses of the stars (§ 5) that lead us to conclude that both stars have radii

[1] Visiting Astronomer, Kitt Peak National Observatory, National Optical Astronomy Observatory, operated by the Association of Universities for Research in Astronomy, Inc., under contract with the National Science Foundation.
[2] Current address: Department of Chemistry, Furman University, 3300 Poinsett Highway, Greenville, SC 29613.
[3] Current address: Astronomy Department, Yale University, New Haven, CT 06520-8101.
[4] NSF Astronomy and Astrophysics Postdoctoral Fellow.
[5] Current address: Department of Astronomy, California Institute of Technology, 305 South Hill Avenue, MC 102-8, Pasadena, CA 91125.

smaller than their Roche radii and luminosities that are too small to power strong winds (explaining the lack of Hα emission from colliding winds).

2. OBSERVATIONS AND RADIAL VELOCITIES

The optical spectra of HD 1383 were obtained with the Kitt Peak National Observatory 0.9 m coudé feed telescope during four observing runs between 1999 August and December. Most of these spectra were obtained with the short collimator and grating RC181 (316 grooves mm^{-1} with a blaze wavelength of 7500 Å; made in first order with a GG495 filter to block higher orders), which yielded an average resolving power of $R = \lambda/\delta\lambda = 4000$ (see Gies et al. [2002a] for details of each observing run). The last four spectra were made with grating A (632 grooves mm^{-1} with a blaze wavelength of 6000 Å in second order), and these have a much higher resolving power, $R = \lambda/\delta\lambda = 21{,}300$. Exposure times varied from 20 to 30 minutes. These spectra all cover a common spectral range between 6456 and 6728 Å, and they generally have a S/N $\approx$ 340 pixel^{-1} in the continuum. The spectra were extracted and calibrated using standard routines in IRAF,[6] and then each continuum rectified spectrum was transformed onto a uniform heliocentric wavelength grid for analysis. Atmospheric telluric lines were removed by division of modified versions of spectra of the rapidly rotating A-star ζ Aql that we also observed (Gies et al. 2002a).

We measured radial velocities for HD 1383 using a template fitting method (Gies et al. 2002b). The red spectrum of HD 1383 has few lines in the region observed. Hα was not used in the radial velocity analysis because it is too broad and the components are generally blended. The lines of C II $\lambda\lambda$6578, 6582 and O II $\lambda\lambda$6641, 6721 are very weak and difficult to measure in individual spectra. Thus, we focused on the remaining, problem-free line of He I λ6678 for this radial velocity study. The individual component lines are quite narrow, symmetric, and comparable in shape to the instrumental broadening function, so we chose to represent each component's profile as a Gaussian function. We selected appropriate shape parameters by fitting Gaussians to the best separated profiles of He I λ6678, and we used the average values of the parameters to create separate Gaussian absorption line profiles to represent both the primary and secondary stars. We also obtained preliminary orbital velocity curves based on the Gaussian fits of the well-separated spectra, and these were used to estimate the approximate velocities for all the times of observation. We then determined radial velocities for both components in all of our spectra by a nonlinear, least-squares fit of the composite profiles, and our results are collected in Table 1, which lists the heliocentric Julian date of midexposure, orbital phase from the solution for the primary component, and the observed velocity plus the residual from the fit (observed minus calculated) for both components.

TABLE 1
HD 1383 Radial Velocity Measurements

HJD (−2,451,000)	Primary Orbital Phase[a]	V_1 (km s^{-1})	$(O-C)_1$ (km s^{-1})	V_2 (km s^{-1})	$(O-C)_2$ (km s^{-1})
419.951[b]	0.253	−19.9	1.9	−65.0	−20.7
420.950	0.302	14.0	3.7	−77.4	1.7
421.869	0.347	36.3	2.0	−102.3	3.7
421.891	0.348	37.1	2.3	−101.0	5.5
423.865	0.445	69.0	2.7	−143.6	−2.4
425.851	0.543	71.7	2.2	−144.4	−2.5
425.875	0.545	70.1	0.7	−143.6	−2.0
426.827	0.591	59.6	−0.9	−126.4	3.6
427.806	0.640	45.7	1.2	−105.2	5.8
427.856	0.642	44.6	1.1	−104.9	4.9
428.778	0.688	21.9	0.1	−84.3	1.5
428.816	0.690	19.8	−0.9	−84.3	0.4
429.792	0.738	9.0	17.8	−49.3	4.9
429.813	0.739	−5.6	3.9	−62.4	−8.9
464.737	0.461	71.1	2.5	−144.6	−1.0
465.774	0.512	62.7	−8.9	−154.4	−9.0
465.788	0.512	71.1	−0.5	−146.2	−0.9
466.756	0.560	64.7	−2.4	−139.6	−1.0
467.822	0.613	51.1	−3.2	−122.4	0.0
467.836	0.613	53.3	−0.7	−119.1	3.1
468.773	0.660	35.9	0.0	−95.5	5.8
469.799	0.710	0.5	−8.3	−80.7	−8.5
469.813	0.711	8.8	0.4	−72.3	−0.6
491.730[b]	0.792	−57.9	−10.0	−9.1	7.4
492.693	0.839	−94.4	−9.2	16.9	−0.2
493.677	0.888	−125.2	−3.6	46.8	−1.7
494.689	0.937	−150.1	0.9	73.2	−0.2
495.747	0.990	−162.7	3.5	91.1	4.1
496.742	0.039	−161.3	1.0	87.4	1.8
497.700	0.086	−144.0	−1.2	68.4	−2.2
516.645	0.020	−162.3	3.5	89.6	1.8
517.641	0.069	−153.8	−2.6	74.8	−2.6
520.601	0.215	−53.9	−4.4	−19.6	−4.1
522.644	0.316	16.5	−1.8	−88.2	−0.1

[a] Secondary phase = primary phase − 0.051.
[b] Primary-secondary swapped velocities are given and assigned zero weight.

3. ORBITAL ELEMENTS OF HD 1383

Hill & Fisher (1986) found that HD 1383 is a double-lined spectroscopic binary with a period of 20.2819 days. We combined our radial velocities (Table 1) with the compilation of radial velocity measurements from Hill & Fisher (1986) for a total of 101 and 77 radial velocity measurements (spanning 75 yr) of the primary and secondary components, respectively. Using a "dirty" discrete Fourier transform and CLEAN deconvolution algorithm (Roberts et al. 1987), we constructed power spectra for both the primary and secondary using the time series of radial velocity measurements for each. The strongest signal in the power spectra occurs at $P = 20.3$ days, which we then used as a starting value for the following orbital solutions.

We used the nonlinear, least-squares fitting program from Morbey & Brosterhus (1974) to determine orbital elements. We found that our derived velocities were swapped between the primary and secondary for two observations when the components were thoroughly blended, and we assigned zero weight to these measurements in our orbital fit. First, we determined the period of the primary and secondary independently using all the data available, and then we determined a mean value of $P = 20.28184 \pm 0.00020$ days, which we fixed for both stars in the subsequent orbital solutions for HD 1383. Then only the new radial velocity data presented in this paper were used to calculate independent orbital elements for the primary and secondary stars. The separate results for the primary and secondary are presented in Table 2, together with the original results from Hill & Fisher (1986), and the radial velocity curves and observations are plotted in Figure 1. We find that the orbital elements for the primary and secondary are mainly consistent with each other and with the original determinations by Hill & Fisher (1986), with two interesting exceptions. First, the star identified as the "primary" by Hill & Fisher (1986) turns out to be the lower mass object in

[6] IRAF is distributed by the National Optical Astronomy Observatory, which is operated by the Association of Universities for Research in Astronomy, Inc., under cooperative agreement with the National Science Foundation.

TABLE 2
ORBITAL ELEMENTS FOR HD 1383

Element	Hill & Fisher (1986)	This Work
P (days)	20.2819[a]	20.28184[a]
T_1 (HJD − 2,400,000)	...	51414.8 ± 0.4
T_2 (HJD − 2,400,000)	...	51415.9 ± 0.6
e_1	0.076 ± 0.024	0.116 ± 0.012
e_2	0.027 ± 0.028	0.069 ± 0.009
ω_1 (deg)	181 ± 10	178 ± 6
ω_2 (deg)	355 ± 29	17 ± 10
K_1 (km s^{-1})	113 ± 1	119 ± 1
K_2 (km s^{-1})	117 ± 2	117 ± 1
γ_1 (km s^{-1})	−35.1 ± 1.8	−33.8 ± 1.0
γ_2 (km s^{-1})	−34.7 ± 2.1	−36.5 ± 0.8
q (M_2/M_1)	0.968 ± 0.018	1.02 ± 0.01
$M_1 \sin^3 i$ ($M_\odot$)	12.7 ± 0.2	13.7 ± 0.2
$M_2 \sin^3 i$ ($M_\odot$)	12.4 ± 0.2	13.7 ± 0.2
$a \sin i$ ($R_\odot$)	92.2 ± 0.8	94.2 ± 0.6
σ_1 (km s^{-1})	8.0	5.1
σ_2 (km s^{-1})	9.6	4.3

[a] Fixed.

our solution because of a slight revision in the semiamplitudes. Rather than introducing more confusion about the stars' identities, we retain the labels of primary and secondary given by Hill & Fisher (1986). Second, we find that the eccentricity derived for the primary is approximately 3 σ different from that obtained for the secondary. Furthermore, the longitude of periastron values are suspiciously close to 0° and 180°, which suggests that the velocity curves may be distorted by subtle emission effects from circumstellar gas (the possible origin of the nonuniform distribution of longitude of periastron among massive binaries known as the Barr Effect; Batten & Ovenden 1968; Fracastoro 1979; Howarth 1993). Given these difficulties, we decided not to force a joint solution with a common geometry and systemic velocity.

4. TOMOGRAPHIC RECONSTRUCTION AND STELLAR PARAMETERS

Once the orbital solution was found for HD 1383, we used a tomographic reconstruction technique (Bagnuolo et al. 1994) to separate the two individual spectra of the system. The method of

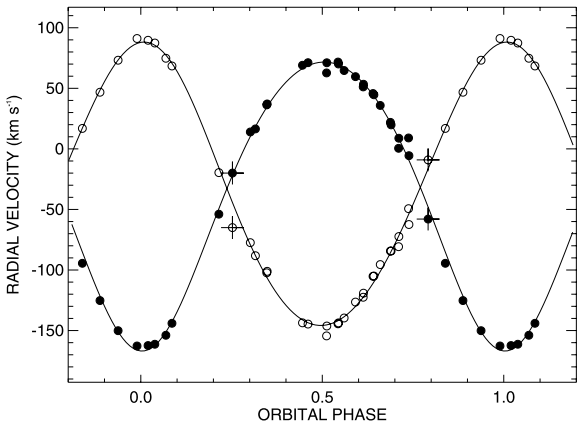

FIG. 1.—Calculated radial velocity curves (*solid lines*) for HD 1383. The errors in the measured radial velocities of the primary star (*filled circles*) and the secondary star (*open circles*) are comparable to the symbol sizes. Plus signs mark the measurements from two blended phases that were assigned zero weight.

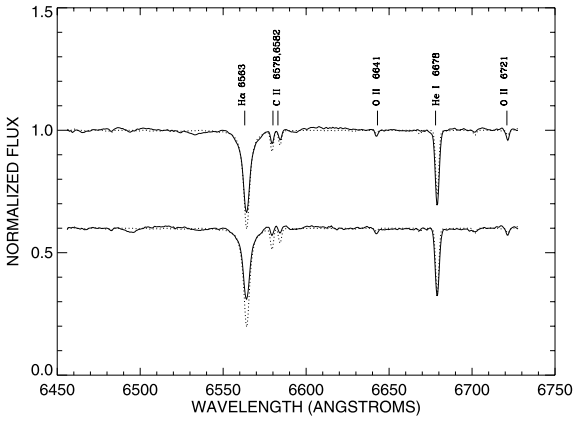

FIG. 2.—Tomographically reconstructed spectra (*solid lines*) of the (slightly more massive) secondary (*top*) and primary star (*bottom*) together with model spectra (*dotted lines*) for $T_{\rm eff} = 28{,}000$ K, $\log g = 3.25$, and $V \sin i = 70$ km s^{-1} (a rotational broadening appropriate for He I λ6678).

tomographic reconstruction uses all the combined spectra and their associated radial velocities to determine the appearance of each star's spectrum. The monochromatic flux ratio of the primary to the secondary was assumed to be 1.0 (Hill & Fisher 1986). The ISM lines were removed from each spectrum prior to reconstruction to avoid spurious reconstructed features in their vicinity. Figure 2 shows a plot of the reconstructed spectra with identifications of the principal lines. The two spectra are remarkably similar in the red spectral region.

We made estimates of the effective temperatures, gravities, and projected rotational velocities through a comparison with model spectra from the codes TLUSTY and SYNSPEC (Hubeny 1988; Hubeny & Lanz 1995; Hubeny et al. 1998). Lanz & Hubeny (2003) presented a grid of model spectra for O-type stars that use line-blanketed, non–local thermodynamic equilibrium, plane-parallel, hydrostatic atmospheres, and fortunately, these models extend to cool enough temperatures (27500 K) to be applicable to the stars in HD 1383. These models adopt a fixed microturbulent velocity of 10 km s^{-1}, a value that is appropriate for B-supergiants (Gies & Lambert 1992). These models were also used by Dufton et al. (2005) in their spectral analysis of B-supergiants in the SMC.

The projected rotational velocity, $V \sin i$, for each star was measured by comparing the observed FWHM of an absorption line with that for model profiles for a range in assumed $V \sin i$. The rotationally broadened profiles were calculated by a simple convolution of the zero-rotation model profiles with a rotational broadening function (Gray 1992) using a linear limb-darkening coefficient $\epsilon = 0.220$ (from the tabulated value for $T_{\rm eff} = 30{,}000$ K, $\log g = 3.0$, and $\lambda = 6975$ Å from Wade & Rucinski 1985). The derived projected rotational velocities based on the He I λ6678 profile are $V \sin i = 76 \pm 6$ and 72 ± 6 km s^{-1} for the primary and secondary, respectively, in good agreement with the estimate of 75 ± 5 km s^{-1} for both stars from measurements of blue spectral lines by Hill & Fisher (1986). However, the weaker C II $\lambda\lambda$6578, 6582 lines are distinctly narrower, and their mean projected rotational velocities are $V \sin i = 32 \pm 18$ and 26 ± 18 km s^{-1} for the primary and secondary, respectively (almost unresolved at our spectral resolution). Ryans et al. (2002) argue that the line broadening of B-supergiants is probably dominated by macroturbulence, so that the measured broadening only provides an upper limit on the actual rotational velocity.

They also find a trend for stronger lines (such as He I λ6678) to display greater broadening than weaker lines (such as C II $\lambda\lambda$6578, 6582), perhaps because of an increase in turbulent broadening with height in the atmosphere. Thus, the true projected rotational velocities of the components of HD 1383 are probably less than $\approx$30 km s^{-1}.

We then compared rotationally broadened versions of the model solar abundance spectra from Lanz & Hubeny (2003) directly with the reconstructed spectra to estimate temperatures and gravities. The best matches were found with $T_{\rm eff} = 28{,}000 \pm 1000$ K and $\log g = 3.25 \pm 0.25$ for both stars, and the model spectra for these parameters are shown in Figure 2 as dotted lines. This spectral region contains a number of features that are particularly sensitive to temperature and gravity. For example, at hotter temperatures the C II, O II, and He I lines weaken, while new lines of Si IV $\lambda\lambda$6667, 6701 and He II λ6683 appear that are clearly absent in the reconstructed spectra of HD 1383. On the other hand, at cooler temperatures the C II doublet increases greatly in strength and the N II λ6610 line first appears (again absent in the reconstructed spectra). The wings of the Hα line provide a diagnostic of the gravity (wider due to greater linear Stark broadening in higher gravity models). We caution that the core of Hα appears to be filled in with residual emission from the stellar wind, and the TLUSTY models we used are based on static atmospheres that do not account for wind outflow. However, we expect that the wind effects will be mainly confined to the higher opacity line core in relatively weak-wind stars like those in HD 1383 and that the gravity derived from the pressure-broadened line wings will be close to (or slightly less) than the actual gravity (see the discussion about the Hγ line wings in Puls et al. 1996). The observed C II lines appear to be somewhat weaker than predicted in the best matching model spectrum, which may reflect an underabundance of C caused by mixing of CNO-processed gas into the atmosphere. McErlean et al. (1999) also observed this effect in other B-supergiants. They give model fitting results for two galactic B0.5 Ib stars, HD 192422 and HD 213087, and their derived temperatures and gravities are in reasonable agreement with our adopted values for HD 1383. We found that the generally good match between the model and observed spectra indicates that the monochromatic flux ratio is 1.0 ± 0.1.

5. DISCUSSION

We can use our results to place some general constraints on the evolutionary status of the binary system. These various limits are summarized in a radius-mass diagram for the secondary star shown in Figure 3 (the corresponding diagram for the primary would appear almost the same). The system is not a known eclipsing binary, and we confirmed the lack of eclipses (or any other orbital phase-related variations) by plotting the available photometry from *Hipparcos* (Perryman 1997) as a function of orbital phase. If we assume that the stars have the same radius R (as indicated by their temperatures and the observed flux ratio), then the upper limit on the orbital inclination i set by the lack of eclipses is found from

$$\tan i = \frac{a \sin i}{2R} \frac{1 - e^2}{1 + e \cos \nu}. \quad (1)$$

We considered both conjunctions, $\nu = 90^\circ - \omega$ and $270^\circ - \omega_2$, with the derived eccentricities for the primary and secondary to find the maximum inclination for a given radius and hence a lower limit on the mass of the secondary from $M_2 \sin^3 i$ (Table 2), and the resulting radius-mass relationships are plotted as dashed lines in Figure 3. The acceptable solution space is restricted to the region above these lines (at lower i). The next constraint comes from the gravity determination found by fitting the Hα line wings, and the solid lines in Figure 3 show the relations for $\log g = 3.25 \pm 0.25$. If weak stellar wind emission is biasing this measurement, then the actual $\log g$ may be somewhat larger than our estimate.

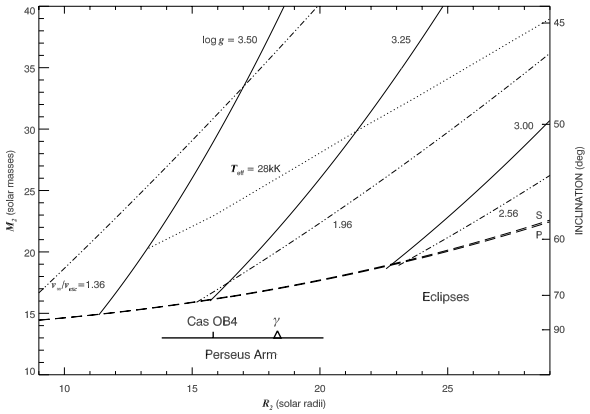

FIG. 3.—Plot of the possible range in secondary mass and radius. The system inclination for $M_2 \sin^3 i = 13.7$ is given on the right axis. The dashed lines mark the lower mass limit set by the absence of eclipses and based on the parameters from the primary (*P*) and secondary (*S*) orbital solutions. The three solid lines show the relations for the range in gravity set by the Hα line wings (indicated by values of $\log g$). The three double-dot–dashed lines show the relations set by the span of values for the $v_\infty/v_{\rm esc}$ ratio (with the constant of proportionality labeled in each case). The dotted line indicates the single star evolutionary mass for a temperature of $T_{\rm eff} = 28{,}000$ K (Schaller et al. 1992). The bar at the bottom shows the corresponding radii for distances spanning a cut through the Perseus arm, the location of the Cas OB4 association, and the location where differential Galactic rotation matches the binary systemic velocity (γ).

We can use the stellar wind properties to find additional limitations. Theoretical and observational studies of the winds of massive stars show that the wind terminal velocity v_∞ is generally proportional to the escape velocity $v_{\rm esc}$ among stars of comparable temperature (Prinja et al. 1990; Lamers et al. 1995; Kudritzki & Puls 2000; Evans et al. 2004; Crowther et al. 2006). Prinja et al. (1990) have made the most complete study of this relationship among the B-supergiants, and they find that $v_\infty = (1.96 \pm 0.60) v_{\rm esc}$ for B0-B3 I stars. We measured the terminal velocity to be $v_\infty = 1100 \pm 120$ km s^{-1} according to the short-wavelength absorption minimum point in the profile of the C IV λ1550 P Cygni line in a high dispersion spectrum of HD 1383 from the archive of the *International Ultraviolet Explorer* satellite (made at orbital phase $\phi = 0.21$, near conjunction). This terminal velocity is somewhat lower than the mean for the B0.5 supergiants of 1405 km s^{-1} but it is well within the range of terminal velocities for this group (Prinja et al. 1990). We show the resulting radius-mass functions from the mean and ± 1 σ limits of the $v_\infty/v_{\rm esc}$ relation in Figure 3 (*double-dot–dashed line*). Note that the larger values of this ratio found in recent studies (Evans et al. 2004; Crowther et al. 2006) are probably more appropriate for much more luminous stars and would lead to unrealistically large radii in the case of HD 1383.

Finally, we can obtain one more constraint by considering the radius-distance relationship that is established from fits of the reddened stellar flux distribution. We show in Figure 4 the observed spectral energy distribution for HD 1383 based on low-dispersion UV spectroscopy from *IUE*, Johnson *U*, *B*, *V* magnitudes (Haug 1970; Colina et al. 1996), and 2MASS *J*, *H*, *K* infrared magnitudes (Cohen et al. 2003; Cutri et al. 2003). We

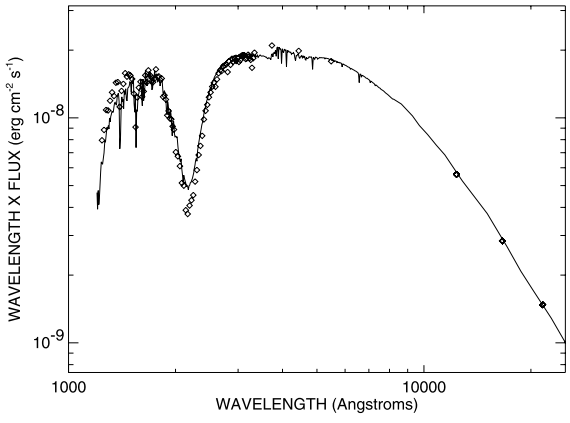

FIG. 4.—Spectral flux distribution and fit for the combined light of the HD 1383 components. The fitting parameters are $T_{\rm eff} = 28{,}000$ K, $\log g = 3.25$, $E(B-V) = 0.55$ mag, $R = 2.97$, and $\theta_{\rm LD} = 54$ μas for each star.

fit this flux distribution using a model spectrum from Lanz & Hubeny (2003) for two identical stars of $T_{\rm eff} = 28{,}000$ K and $\log g = 3.25$, which we transformed using the Galactic extinction curve from Fitzpatrick (1999). The best-fit parameters for the extinction curve are a reddening of $E(B-V) = 0.55 \pm 0.05$ and a ratio of total-to-selective extinction of $R = 2.97 \pm 0.15$. The normalization of the model spectrum yields the limb darkened angular diameter of one star, $\theta_{\rm LD} = 54 \pm 7$ μas, and therefore the stellar radius is related to the distance d (measured in kpc) by

$$R/R_\odot = (5.8 \pm 0.8)d. \qquad (2)$$

The binary is too distant to obtain a reliable parallax from *Hipparcos* measurements (Schröder et al. 2004). Our view through the plane of the Galaxy in the direction of HD 1383 ($l = 119\overset{\circ}{.}02$, $b = -0\overset{\circ}{.}89$) traverses first the nearer Perseus arm ($d = 2.4$–3.5 kpc) and then the more distant Cygnus arm ($d \gtrsim 3.9$ kpc) (Kimeswenger & Weinberger 1989; Negueruela & Marco 2003). We suspect that HD 1383 resides in the closer Perseus arm. It is very close in the sky to BD +60 39 (spectral classification of O9 V), which has an identical reddening and which Garmany & Stencel (1992) assign to the Cas OB4 association (at a distance of 2.8 kpc). There is a considerable amount of differential Galactic rotation along this line of sight, and we can estimate at what distance the systemic velocity of the binary matches the expected radial velocity difference between the Sun and the remote local standard of rest. We used the procedure described by Berger & Gies (2001) to find the distance–radial velocity relation along this line of sight, and the binary's systemic velocity places it at a distance of 3.2 kpc (although if we allow a ± 10 km s^{-1} deviation in motion from the local standard of rest, then the acceptable range is between 2.3 and 4.2 kpc). Both lines of evidence are consistent with a location in the Perseus arm, and we have plotted the corresponding stellar radius range as a solid line in the bottom of Figure 3.

The combination of all these constraints indicates that the parameter ranges are probably $R/R_\odot = 14$–20 and $M/M_\odot = 16$–35. This range is consistent with the masses predicted by single-star evolutionary tracks for the temperature and gravity of the components in HD 1383 (illustrated in Fig. 3 as a dotted line, from the evolutionary tracks for nonrotating, solar metallicity stars of

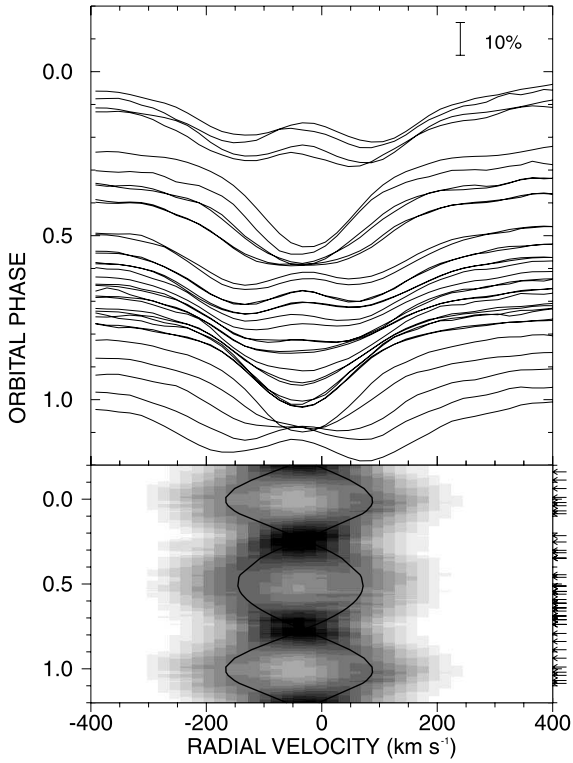

FIG. 5.—*Top:* Hα line profiles plotted against heliocentric radial velocity. The continuum of each observation is normalized so that the y-ordinate equals the primary star phase at the time of observation. *Bottom:* A gray-scale plot that shows the phase and velocity variations of the Hα line profiles shown above. Specific times of individual measurements are indicated by arrows on the right hand side. There are 16 gray levels that are determined by the difference in intensities between the minimum to maximum observed values for all spectra. The phase has been wrapped to enhance the sense of phase continuity, and the calculated radial velocity curves from the orbital solution are displayed as thick black lines.

$T_{\rm eff} = 28{,}000$ K; Schaller et al. 1992). The radii are much smaller than the Roche lobe radii (approximately 44 $R_\odot$ for masses of 25 $M_\odot$), so the system is probably still observed in a precontact phase in which both stars have evolved like single objects.

We originally selected HD 1383 as a possible target for exhibiting Hα emission from colliding winds (Thaller 1997). However, our spectra show no obvious signs of such Hα emission. We show in Figure 5 the Hα profiles arranged as a function of orbital phase, and the variations appear to be entirely consistent with the motion of the photospheric Hα lines of both components. Sana et al. (2001) found evidence of a weak, broad, and stationary Hα emission feature in their spectra of the similar colliding winds binary HD 152248, and they argue that the emission forms in a planar collision zone between the stars. The lack of Hα colliding winds emission in the spectrum of HD 1383 is probably due to three significant differences between these binary systems. First, the mass-loss rates are lower in HD 1383 than in HD 152248. We can estimate approximately the mass-loss rates using the wind momentum relation for hot stars,

$$\log [\dot{M} v_\infty (R/R_\odot)^{1/2}] = \log D_0 + x \log (L/L_\odot), \qquad (3)$$

where D_0 and x are constants and L is the stellar luminosity (Kudritzki & Puls 2000; Vink et al. 2000). If we adopt $T_{\rm eff} = 28{,}000$ K, $R/R_\odot = 14$–20, and $v_\infty = 1100$ km s^{-1}, then the predicted mass loss rate is $\log \dot{M} = -6.3 \pm 0.4$ (units of $M_\odot$ yr^{-1}) according to the model of Vink et al. (2000), which is about 6 times lower than the mass-loss rates of the stars in HD 152248 (Sana et al. 2004). Second, the binary separation is about twice as large in HD 1383 as in HD 152248 (Sana et al. 2004), and hence the wind density in the regions near the collision zone will be much lower. Third, the collision zone itself may cool less efficiently and may avoid the formation of high-density gas fragments that are predicted to occur according to hydrodyanmical simulations of the winds of HD 152248 (Sana et al. 2004). Stevens et al. (1992) show how the gas dynamics of the colliding winds zone depend on the ratio of the cooling timescale to the gas flow timescale, $\chi \approx v_8^4 d_{12}/\dot{M}_{-7}$, where v_8 is the wind velocity in units of 1000 km s^{-1}, d_{12} is the distance from the star to the contact surface in units of 10^7 km, and $\dot{M}_{-7}$ is the mass loss rate in units of 10^{-7} $M_\odot$ yr^{-1}. This ratio is about 1.1 for HD 1383, indicating that the collision zone remains hot over dimensions comparable to those of the binary system (an adiabatic wind zone), but the ratio is much smaller (0.1) in the case of HD 152248 where efficient cooling (in a radiative colliding wind) leads to the fragmentation of the shock front into knots of cool gas (Sana et al. 2004). Since Hα emission is a recombination process that depends on the square of the gas density and since the colliding wind density will be much lower in HD 1383 than in HD 152248 for all of the reasons outlined above, the apparent lack of Hα emission in the spectrum of HD 1383 is not surprising.

Our results indicate that HD 1383 is a wide enough system that the components have avoided direct interaction or mass exchange. According to the models of Schaller et al. (1992), this state may last for another 0.5 Myr (for masses of 25 $M_\odot$). However, after that time both stars will quickly grow in radius and reach contact within the last 10^4 yr before they explode as supernovae. Their brief interaction phase then may result in a common-envelope stage leading to a shorter period system containing an O supergiant and a neutron star (like the massive X-ray binary system HD 153919/4U 1700–37; Ankay et al. 2001) or in a wider binary consisting of a rapidly evolving B-A supergiant transferring mass at a tremendous rate to a collapsed companion surrounded by a super-Eddington accretion disk (like SS 433; Hillwig et al. 2004). Either way, HD 1383 is destined to become an extraordinarily energetic interacting binary for a brief instant in the Galaxy's future.

We thank Daryl Willmarth and the staff of KPNO for their assistance in making these observations possible. We are also grateful to the referee, Hugues Sana, for his insight and helpful comments on this study. This work was supported by the National Science Foundation under grant AST 02-05297. Institutional support has been provided from the GSU College of Arts and Sciences and from the Research Program Enhancement fund of the Board of Regents of the University System of Georgia, administered through the GSU Office of the Vice President for Research.

REFERENCES

Ankay, A., Kaper, L., de Bruijne, J. H. J., Dewi, J., Hoogerwerf, R., & Savonije, G. J. 2001, A&A, 370, 170
Bagnuolo, W. G., Jr., Gies, D. R., Hahula, M. E., Wiemker, R., & Wiggs, M. S. 1994, ApJ, 423, 446
Batten, A. H., & Ovenden, M. W. 1968, PASP, 80, 85
Berger, D. H., & Gies, D. R. 2001, ApJ, 555, 364
Cartledge, S. I. B., Lauroesch, J. T., Meyer, D. M., & Sofia, U. J. 2004, ApJ, 613, 1037
Cohen, M., Wheaton, W. A., & Megeath, S. T. 2003, AJ, 126, 1090
Colina, L., Bohlin, R., & Castelli, F. 1996, Huble Space Telescope Instrument Science Report CAL/SCS-008 (Baltimore: STScI)
Crowther, P. A., Lennon, D. J., & Walborn, N. R. 2006, A&A, 446, 279
Cutri, R. M., et al. 2003, The 2MASS All-Sky Catalog of Point Sources (Pasadena: IPAC/Caltech)
Dufton, P. L., Ryans, R. S. I., Trundle, C., Lennon, D. J., Hubeny, I., Lanz, T., & Allende Prieto, C. 2005, A&A, 434, 1125
Evans, C. J., Lennon, D. J., Trundle, C., Heap, S. R., & Lindler, D. J. 2004, ApJ, 607, 451
Fitzpatrick, E. L. 1999, PASP, 111, 63
Fracastoro, M. G. 1979, A&A, 78, 112
Garmany, C. D., & Stencel, R. E. 1992, A&AS, 94, 211
Gies, D. R., & Lambert, D. L. 1992, ApJ, 387, 673
Gies, D. R., McSwain, M. V., Riddle, R. L., Wang, Z., Wiita, P. J., & Wingert, D. W. 2002a, ApJ, 566, 1069
Gies, D. R., Penny, L. R., Mayer, P., Drechsel, H., & Lorenz, R. 2002b, ApJ, 574, 957
Gray, D. F. 1992, The Observation and Analysis of Stellar Photospheres (2nd ed.; Cambridge: Cambridge Univ. Press)
Haug, U. 1970, A&AS, 1, 35
Hill, G., & Fisher, W. A. 1986, Publ. Dominion Astrophys. Obs., 16, 193
Hillwig, T. C., Gies, D. R., Huang, W., McSwain, M. V., Stark, M. A., van der Meer, A., & Kaper, L. 2004, ApJ, 615, 422
Howarth, I. D. 1993, Observatory, 113, 75
Hubeny, I. 1988, Comput. Phys. Commun., 52, 103
Hubeny, I., Heap, S. R., & Lanz, T. 1998, in ASP Conf. Ser. 131, Properties of Hot, Luminous Stars, ed. I. D. Howarth (San Francisco: ASP), 108
Hubeny, I., & Lanz, T. 1995, ApJ, 439, 875
Humphreys, R. M. 1978, ApJS, 38, 309
Kimeswenger, S., & Weinberger, R. 1989, A&A, 209, 51
Kudritzki, R., -P., & Puls, J. 2000, ARA&A, 38, 613
Lamers, H. J. G. L. M., Snow, T. P., & Lindholm, D. M. 1995, ApJ, 455, 269
Langer, N., Yoon, S.-C., Petrovic, J., & Heger, A. 2004, in Proc. IAU Symp. 215, Stellar Rotation, ed. A. Maeder & P. Eenens (San Francisco: ASP), 535
Lanz, T., & Hubeny, I. 2003, ApJS, 146, 417
McErlean, N. D., Lennon, D. J., & Dufton, P. L. 1999, A&A, 349, 553
Morbey, C., & Brosterhus, E. B. 1974, PASP, 86, 455
Morgan, W. W., Code, A. D., & Whitford, A. E. 1955, ApJS, 2, 41
Negueruela, I., & Marco, A. 2003, A&A, 406, 119
Penny, L. R., Gies, D. R., & Bagnuolo, W. G., Jr. 1999, ApJ, 518, 450
Perryman, M. A. C. 1997, The *Hipparcos* and Tycho Catalogues (ESA SP-1200; Noordwijk: ESA)
Petrovic, J., Langer, N., & van der Hucht, K. A. 2005, A&A, 435, 1013
Pourbaix, D., et al. 2004, A&A, 424, 727
Prinja, R. K., Barlow, M. J., & Howarth, I. D. 1990, ApJ, 361, 607
Puls, J., et al. 1996, A&A, 305, 171
Roberts, D. H., Lehár, J., & Dreher, J. W. 1987, AJ, 93, 968
Ryans, R. S. I., Dufton, P. L., Rolleston, W. R. J., Lennon, D. J., Keenan, F. P., Smoker, J. V., & Lambert, D. L. 2002, MNRAS, 336, 577
Sana, H., Rauw, G., & Gosset, E. 2001, A&A, 370, 121
Sana, H., Stevens, I. R., Gosset, E., Rauw, G., & Vreux, J.-M. 2004, MNRAS, 350, 809
Sanford, R. F., & Merrill, P. W. 1938, ApJ, 87, 517
Schaller, G., Schaerer, D., Meynet, G., & Maeder, A. 1992, A&AS, 96, 269
Schröder, S. E., Kaper, L., Lamers, H. J. G. L. M., & Brown, A. G. A. 2004, A&A, 428, 149
Slettebak, A. 1956, ApJ, 124, 173
Stevens, I. R., Blondin, J. M., & Pollock, A. M. T. 1992, ApJ, 386, 265
Thaller, M. L. 1997, ApJ, 487, 380
Vink, J. S., de Koter, A., & Lamers, H. J. G. L. M. 2000, A&A, 362, 295
Wade, R. A., & Rucinski, S. M. 1985, A&AS, 60, 471
Wakker, B., van Woerden, H., de Boer, K. S., & Kalberla, P. 1998, ApJ, 493, 762

The Astrophysical Journal, 664:1121–1129, 2007 August 1

THE LONG-PERIOD, MASSIVE BINARIES HD 37366 AND HD 54662: POTENTIAL TARGETS FOR LONG-BASELINE OPTICAL INTERFEROMETRY[1]

T. S. Boyajian,[2] D. R. Gies,[2] J. P. Dunn, C. D. Farrington, E. D. Grundstrom,[2] W. Huang,[3]
M. V. McSwain,[2,4,5] S. J. Williams,[2] and D. W. Wingert[2]
Center for High Angular Resolution Astronomy and Department of Physics and Astronomy, Georgia State University, Atlanta, GA 30302-4106;
tabetha@chara.gsu.edu, gies@chara.gsu.edu, dunn@chara.gsu.edu, farrington@chara.gsu.edu, erika@chara.gsu.edu,
wenjin@astro.caltech.edu, mcswain@astro.yale.edu, swilliams@chara.gsu.edu, wingert@chara.gsu.edu

A. W. Fullerton
Space Telescope Science Institute, Baltimore, MD 21218; fullerton@stsci.edu

and

C. T. Bolton
David Dunlap Observatory, University of Toronto, Richmond Hill, ON L4C 4Y6, Canada; bolton@astro.utoronto.ca
Received 2006 December 12; accepted 2007 April 22

ABSTRACT

We present the results from an optical spectroscopic analysis of the massive stars HD 37366 and HD 54662. We find that HD 37366 is a double-lined spectroscopic binary with a period of 31.8187 ± 0.0004 days, and HD 54662 is also a double-lined binary with a much longer period of 557.8 ± 0.3 days. The primary of HD 37366 is classified as O9.5 V, and it contributes approximately two-thirds of the optical flux. The less luminous secondary is a broad-lined, early B-type main-sequence star. Tomographic reconstruction of the individual spectra of HD 37366 reveals absorption lines present in each component, enabling us to constrain the nature of the secondary and physical characteristics of both stars. Tomographic reconstruction was not possible for HD 54662; however, we do present mean spectra from our observations that show that the secondary component is approximately half as bright as the primary. The observed spectral energy distributions (SEDs) were fit with model SEDs and galactic reddening curves to determine the angular sizes of the stars. By assuming radii appropriate for their classifications, we determine distance ranges of 1.4–1.9 and 1.2–1.5 kpc for HD 37366 and HD 54662, respectively.

Subject headings: binaries: spectroscopic — stars: early-type — stars: individual (HD 37366, HD 54662)

1. INTRODUCTION

There remains considerable uncertainty about the masses of the most massive stars because of the relatively small number of known binary systems for which accurate masses can be determined (Gies 2003). Spectroscopic measurements alone yield mass functions dependent on the unknown orbital inclination, and the determination of inclination requires either the good fortune of finding eclipsing binaries or the angular resolution of the orbit on the sky. The angular semimajor axis of a binary (in units of milliarcseconds) is given by

$$a(\mathrm{mas}) = 0.28\,\frac{[P/(10\ \mathrm{days})]^{2/3}[M_{\mathrm{total}}/(30\ M_{\odot})]^{1/3}}{[d/(1\ \mathrm{kpc})]}, \quad (1)$$

where P is the orbital period, M_{total} is the combined mass of the stars, and d is the distance. The denominators of each unit give typical values for these parameters among OB binaries, and the leading coefficient of 0.28 mas indicates that most massive systems are probably too closely separated for direct resolution with optical long-baseline interferometers, where the limits are currently above 1 mas. The key objective here is to find double-lined spectroscopic binaries with long orbital periods. Such binaries are difficult to detect because their orbital semiamplitudes are small, the component lines are often blended, and a long-term observational program is required to obtain adequate phase coverage. The best candidates for direct resolution are 15 Mon ($P \approx 25$ yr; Gies et al. 1997), HD 15558 ($P = 442$ days; Garmany & Massey 1981; De Becker et al. 2006), and HD 193322 ($P = 311$ days; McKibben et al. 1998).

Here we report on new orbits for two such long-period massive binaries, HD 37366 and HD 54662. The star HD 37366 (BD +30 968, HIP 26611, O9.5 V; Walborn 1973) is a member of the Aur OB1 association at a distance of approximately 1.3 kpc (Humphreys 1978). This association has many bright early-type giants and supergiants, but HD 37366 has the earliest spectral type among the member stars that still reside on the main sequence. The *Hipparcos* mission (Perryman et al. 1997) detected a visual companion to HD 37366 with $\Delta H_p = 3.5$, a separation of 0.58″, and a period of approximately 1300 yr (Mason et al. 1998). The brighter component of these two stars ($H_p = 7.7$) is a radial velocity variable (Petrie & Pearce 1961; Young 1942), and it is known to show asymmetry in its spectral lines (Grigsby et al. 1992). Observations with the *International Ultraviolet Explorer* (*IUE*) confirm that the spectrum displays double lines (Stickland & Lloyd 2001).

[1] Based on observations obtained at the Canada-France-Hawaii Telescope (CFHT), which is operated by the National Research Council of Canada, the Institut National des Sciences de l'Univers of the Centre National de la Recherche Scientifique of France, and the University of Hawaii.
[2] Visiting Astronomer, Kitt Peak National Observatory, National Optical Astronomy Observatory.
[3] Current address: Department of Astronomy, California Institute of Technology, Pasadena, CA 91125.
[4] Current address: Astronomy Department, Yale University, New Haven, CT 06520-8101.
[5] NSF Astronomy and Astrophysics Postdoctoral Fellow.

The second target, HD 54662 (BD −10 1892, HIP 34536, LS 197, O6.5 V; Walborn 1972), is also the brightest and earliest member of its resident association, CMa OB1, at a distance of 1.3 kpc (Humphreys 1978). Radial velocity measurements for HD 54662 extend back many decades (Plaskett 1924; Conti et al. 1977; Garmany et al. 1980), and these display only modest variability. However, Fullerton (1990) noted the presence of blue extensions to the spectral lines that probably indicate the presence of a companion in a long-period orbit. The scatter in the *IUE* velocities also indicates that the star is a binary (Stickland & Lloyd 2001).

Here we present an analysis of the radial velocities and spectra of both stars from spectroscopic observations that we have obtained over the past few years (§ 2). We discuss each system's orbital velocity solution (§ 3) and the spectral and physical properties of each component star in these binaries (§§ 4 and 5). We conclude with a consideration of the prospects for the angular resolution of the orbits using optical long-baseline interferometry (§ 6).

2. OBSERVATIONS

We observed HD 37366 and HD 54662 with the Kitt Peak National Observatory (KPNO) 0.9 m coudé feed telescope during two separate observing runs in 2000 October and December. The spectra were made using the long collimator, grating B (in second order with order sorting filter OG 550), camera 5, and the F3KB CCD, a Ford Aerospace 3072 × 1024 device with 15 μm square pixels. The setup yielded a resolving power of $R = \lambda/\delta\lambda = 9500$, with a spectral coverage of 6440–7105 Å. Exposure times were usually 10 minutes or less, and we generally obtained two spectra (taken a few hours apart) each night. For HD 37366, we made two more red spectral observations in 2004 October using a similar arrangement but with a different detector, the T2KB CCD (2048 × 2048 24 μm square pixels). In 2006 October, both HD 37366 and HD 54662 were observed in the red region again using this same instrumental setup. We also observed the rapidly rotating A-type star, ζ Aql, which we used for removal of atmospheric water vapor and O_2 bands. Each set of observations was accompanied by numerous bias, flat-field, and Th-Ar comparison lamp calibration frames.

We also obtained a small set of blue spectra of these targets. For HD 37366, the first group of four spectra were made in 2005 October with the KPNO 2.1 m telescope and GoldCam spectrometer. We used the No. 47 grating in second order, recording the spectral region from 4050 to 4950 Å with a resolving power of $R = \lambda/\delta\lambda \approx 3000$. Then in 2005 November and 2006 October we obtained higher resolution observations in the blue with the KPNO coudé feed 0.9 m telescope. HD 37366 was observed on both occasions, whereas HD 54662 was only included during the 2006 observing run. We used grating A in second order with order sorting filter 4-96, camera 5, and the T2KB CCD. This setup gave us a resolving power of $R = \lambda/\delta\lambda \approx 12{,}100$ and a wavelength coverage of 4240–4585 Å.

The spectra were extracted and calibrated using standard routines in IRAF.[6] All the spectra were rectified to a unit continuum by fitting line-free regions. The removal of atmospheric lines from the red spectra was done by creating a library of ζ Aql spectra from each run, removing the broad stellar features from these, and then dividing each target spectrum by the modified atmospheric spectrum that most closely matched the target spectrum in a selected region dominated by atmospheric absorptions. The spectra from each run were then transformed to a common heliocentric wavelength grid.

[6] IRAF is distributed by the National Optical Astronomy Observatory, which is operated by the Association of Universities for Research in Astronomy, Inc., under cooperative agreement with the National Science Foundation.

3. RADIAL VELOCITIES AND ORBITAL ELEMENTS

3.1. *HD 37366*

We measured radial velocities of the high-resolution red spectra collected in 2000 and 2006 using a template fitting scheme (Gies et al. 2002) for the He I λ6678 line. We decided not to measure the other strong lines in this region because the binary components are badly blended in the Hα profile, and the He I λ7065 line was marred by residual features left behind by the telluric cleaning procedure. This radial velocity measurement scheme assigns template spectra that are approximate matches for the primary (hotter and more massive star) and secondary spectra, and then makes a nonlinear least-squares fit of the shifts for each component that best matches the observed line profile. We need to make assumptions at the outset about the temperature, gravity, projected rotational velocity, and flux contribution of each star, but these can be checked after completion of the velocity analysis by studying the properties of tomographically reconstructed spectra of the components (§ 4).

The matching template spectra for the primary and secondary components were constructed from the grid of O-type star model spectra from Lanz & Hubeny (2003) that are based on the line-blanketed, non-LTE, plane-parallel, hydrostatic atmosphere code TLUSTY and the radiative transfer code SYNSPEC (Hubeny 1988; Hubeny & Lanz 1995; Hubeny et al. 1998). We selected the spectrum taken on HJD 2,451,901.92, which shows well-separated, individual components of each star, as a reference to determine the approximate spectral parameters for both stars.

The template fitting procedure also requires preliminary estimates of the primary and secondary stars' radial velocities. We estimated these for each spectrum with well-separated lines using the IRAF `splot` routine and deblend option to fit two Gaussians to each composite profile. We also measured relative radial velocity shifts of the strong interstellar lines in all the spectra referenced to the first spectrum in the stack. We then used these relative shifts in the interstellar lines (which should remain motionless) to make additional small corrections for the wavelength calibrations (all these corrections were <2 km s^{-1}).

The final radial velocities from this template fitting procedure (the majority of the observations) are listed in Table 1 along with the heliocentric Julian date of mid-observation, the corresponding orbital phase, and the residual from the orbital fit (observed minus calculated) for both the primary and the secondary. The typical errors in these velocities are also listed in Table 1. We measure only one line for this data set, so we list the characteristic errors (not individual errors), which are based on the scatter in closely spaced pairs of observations. These errors are 1.3 and 2.2 km s^{-1} for the primary and secondary, respectively.

This template fitting routine was also used in determining radial velocities for the high-resolution blue spectra (collected in 2005 November and 2006 October), using the four lines O II λ4349, He I $\lambda\lambda$4387, 4471, and Mg II λ4481. We followed the same procedure in obtaining the spectral templates and the preliminary radial velocity estimates as described above. Since no strong interstellar features are apparent in this region, no additional radial velocity correction was applied. The line-to-line

TABLE 1
HD 37366 Radial Velocity Measurements

HJD (−2,400,000)	Telescope/Band	Orbital Phase	V_1 (km s^{-1})	σ_1 (km s^{-1})	$(O-C)_1$ (km s^{-1})	V_2 (km s^{-1})	σ_2 (km s^{-1})	$(O-C)_2$ (km s^{-1})
46,821.612	*IUE*/UV	0.303	76.9	5.0	0.7	−57.3	10.0	4.3
46,866.116	*IUE*/UV	0.702	13.2	5.0	−0.5	...	...	...
51,817.934	CF/red	0.327	75.9	1.3	−1.3	−64.5	2.2	−1.5
51,818.938	CF/red	0.358	76.2	1.3	−1.0	−67.1	2.2	−4.1
51,819.929	CF/red	0.389	75.5	1.3	−0.6	−53.2	2.2	8.3
51,820.922	CF/red	0.420	74.7	1.3	0.8	−63.8	2.2	−5.2
51,821.918	CF/red	0.452	71.2	1.3	0.4	−51.9	2.2	2.5
51,822.918	CF/red	0.483	64.1	1.3	−2.7	−49.4	2.2	−0.3
51,823.853	CF/red	0.513	62.2	1.3	−0.1	−38.1	2.2	4.9
51,823.980	CF/red	0.517	60.1	1.3	−1.5	−41.7	2.2	0.4
51,824.881	CF/red	0.545	55.8	1.3	−0.7	−38.8	2.2	−3.6
51,824.997	CF/red	0.549	57.1	1.3	1.3	−36.9	2.2	−2.6
51,830.904	CF/red	0.734	0.2	1.3	−1.1	45.9	2.2	7.4
51,889.881	CF/red	0.588	47.9	1.3	0.5	−26.0	2.2	−3.0
51,890.819	CF/red	0.617	42.0	1.3	2.0	−20.9	2.2	−7.6
51,892.787	CF/red	0.679	20.9	1.3	−0.8	17.9	2.2	6.7
51,893.855	CF/red	0.713	9.6	1.3	−0.2	26.5	2.2	−0.7
51,894.780	CF/red	0.742	−1.6	1.3	0.3	53.6	2.2	10.9
51,894.856	CF/red	0.744	−3.3	1.3	−0.5	47.2	2.2	3.2
51,895.874	CF/red	0.776	−19.6	1.3	−2.4	58.7	2.2	−4.5
51,896.802	CF/red	0.805	−32.7	1.3	−1.0	78.4	2.2	−4.2
51,896.914	CF/red	0.809	−34.6	1.3	−1.0	78.8	2.2	−6.1
51,897.802	CF/red	0.837	−46.9	1.3	1.7	100.7	2.2	−4.4
51,897.910	CF/red	0.840	−51.4	1.3	−0.8	96.0	2.2	−11.6
51,898.811	CF/red	0.868	−66.2	1.3	0.3	128.1	2.2	−0.8
51,898.922	CF/red	0.872	−68.7	1.3	−0.2	133.2	2.2	1.6
51,899.809	CF/red	0.900	−83.5	1.3	−0.1	153.0	2.2	1.7
51,899.915	CF/red	0.903	−84.4	1.3	0.5	154.2	2.2	0.7
51,900.802	CF/red	0.931	−95.5	1.3	0.6	171.8	2.2	3.5
51,900.908	CF/red	0.934	−96.3	1.3	0.7	172.6	2.2	3.1
51,901.788	CF/red	0.962	−99.8	1.3	0.3	173.7	2.2	0.2
51,901.917	CF/red	0.966	−100.5	1.3	−0.7	177.2	2.2	4.1
53,291.928	CF/red	0.651	30.8	2.6	0.2	...	...	...
53,292.984	CF/red	0.684	20.6	0.4	0.6	...	...	...
53,658.997[a]	2.1 m/blue	0.187	52.6	6.7	−0.8	...	...	...
53,659.000[a]	2.1 m/blue	0.187	51.5	1.4	−2.0	...	...	...
53,663.010[a]	2.1 m/blue	0.313	71.6	0.4	−5.0	...	...	...
53,663.989[a]	2.1 m/blue	0.344	89.0	4.2	11.7	...	...	...
53,684.903	CF/blue	0.001	−85.7	1.3	0.8	155.4	4.2	0.1
53,686.902	CF/blue	0.064	−30.1	0.7	0.9	76.3	9.8	−4.9
53,688.846	CF/blue	0.125	21.9	0.9	0.9	13.1	5.2	1.3
54,020.972	CF/red	0.564	51.2	1.8	−1.1	−25.8	2.2	4.1
54,024.926	CF/red	0.688	17.4	2.8	−1.0	13.9	3.4	−1.1
54,030.021	CF/blue	0.848	−56.0	2.0	−0.8	103.2	2.4	−9.3
54,031.999	CF/blue	0.911	−90.1	2.9	−1.7	144.4	3.5	−12.0

[a] Zero weight.

1 σ errors in these V_R measurements are <1 km s^{-1} for the primary and 4–9 km s^{-1} for the secondary (Table 1). These final V_R measurements are also presented in Table 1.

The four observations made in the blue during 2005 October had a much lower resolution, thus making it difficult to apply this method of template fitting. To avoid possible errors from unseen line blending in the two components, we chose to measure only radial velocities of the He II $\lambda\lambda$4541, 4686 lines present, since these lines are found only in the spectrum of the much hotter, primary star (§ 4). We used a parabolic fitting routine to determine the mean velocities of these lines (Table 1). The line-to-line 1 σ errors associated with these measurements are <6 km s^{-1} (Table 1).

The two red observations made in 2004 showed no indication of double-lined profiles. In this case, we measured velocities only for the primary star by parabolic fitting of the line cores of He I $\lambda\lambda$6678, 7065 in order to minimize the influence of the secondary on the line profile. The line-to-line 1 σ error associated with these fits are <2 km s^{-1} (exclusive of blending errors). These velocities are also presented in Table 1.

The final two spectra of HD 37366 were collected and downloaded from the archive of the *IUE* satellite.[7] We measured radial velocities for these two high-dispersion, short-wavelength, prime camera spectra using a cross-correlation method (Penny et al. 1999) with the spectrum of HD 34078 as the reference template. The spectrum was double-lined in the first spectrum, SWP 30165. The errors are approximately 5 km s^{-1} for the

[7] See http://archive.stsci.edu/iue/.

TABLE 2
ORBITAL ELEMENTS FOR HD 37366

Element (1)	Primary (2)	Secondary (3)	Joint Solution (4)
P (days)	31.8187 ± 0.0004	31.822 ± 0.002	31.8188[a]
T_1 (HJD −2,400,000)	53653.013 ± 0.04	...	53653.02[a]
T_2 (HJD −2,400,000)	...	53653.15 ± 0.19	53653.02[a]
e_1	0.329 ± 0.003	...	0.330[a]
e_2	...	0.35 ± 0.012	0.330[a]
ω_1 (deg)	211.4 ± 0.6	...	211.6[a]
ω_2 (deg)	...	212 ± 2	211.6[a]
K_1 (km s^{-1})	88.6 ± 0.3	...	88.7 ± 0.2
K_2 (km s^{-1})	...	118.4 ± 1.6	117.4 ± 1.2
γ_1 (km s^{-1})	13.3 ± 0.2	...	13.3 ± 0.2
γ_2 (km s^{-1})	...	20.6 ± 1.3	21.6 ± 0.9
$M_1 \sin^3 i$ ($M_\odot$)	13.8 ± 0.3	...	13.9 ± 0.3
$M_2 \sin^3 i$ ($M_\odot$)	...	10.5 ± 0.1	10.42 ± 0.08
$a_1 \sin i$ ($R_\odot$)	52.6 ± 0.2	...	52.62 ± 0.13
$a_2 \sin i$ ($R_\odot$)	...	69.7 ± 1.0	69.7 ± 0.7
σ_1 (km s^{-1})	1.1	...	1.0
σ_2 (km s^{-1})	...	5.3	5.4

[a] Fixed.

primary and 10 km s^{-1} for the secondary. These final velocities are also presented in Table 1.

The radial velocities from all the data sets (six total) span 20 yr with 45 radial velocity measurements for the primary and 38 radial velocity measurements for the secondary (Table 1). We first constructed a power spectrum using all the primary star's radial velocity measurements, being more reliable and plentiful, to identify possible orbital periods for the binary. We used the discrete Fourier transform and CLEAN deconvolution algorithm (Roberts et al. 1987), which shows that the strongest signal occurs near $P = 31.7$ days. We then used this estimate as a starting value for the period in fits of the orbital elements.

We determined the orbital elements of the binary using the nonlinear, least-squares, orbital fitting program from Morbey & Brosterhus (1974). We began with a fit of the primary's velocities that is given in column (2) of Table 2 done with equal weighting except for the low-resolution blue spectra, which have a weight set to zero. This solution has a period of 31.8187 ± 0.0004 days. The independent orbital solution for the secondary has a period of 31.822 ± 0.002 days, given in column (3) of Table 2. Since the independent solutions agree well with each other, we derive a joint solution by fixing the weighted means of the shared orbital parameters (P, T, e, ω) found in the independent solutions for the binary in order to make fits of the systemic velocity, $\gamma_{1,2}$, and the semiamplitude, $K_{1,2}$, for each component (col. [4] of Table 2). In the case of massive binaries, the systemic velocities of the components may not agree exactly because of differences in their expanding atmospheres and/or, in our case, differences in the shapes of the template spectra for the He I λ6678, He II λ6683 blend. The radial velocity curves for the joint solution are plotted together with the observations in Figure 1. We also made similar fits weighting each point by the normalized, inverse square of its associated error; these results matched within errors of those from the equal weighting fits given in Table 2.

3.2. *HD 54662*

We obtained relative radial velocities for the primary (hotter, more massive) star in HD 54662 by cross-correlation with a single spectrum of the star that had good signal-to-noise ratio (S/N) properties. These relative velocities were transformed to an absolute velocity scale by adding the mean velocity measured through parabolic fits to the cores of the absorption lines in this reference spectrum. All the strong lines were included in the cross-correlation measurements, namely, Hα, He I λ6678 + He II λ6683, and He I λ7065. We excluded He II λλ6527, 6890 because their measurements deviated from the set listed above, as well as compared to each other. We suspect that the residual telluric lines in the spectra, which are very prominent in these regions, are the cause of this disagreement. The velocities for the primary star are presented in Table 3, along with the average velocity and σ (line-to-line) from the C IV λλ5801, 5812 and He I λ5876 lines presented by Fullerton (1990). We were unable to measure velocities for the secondary star in individual

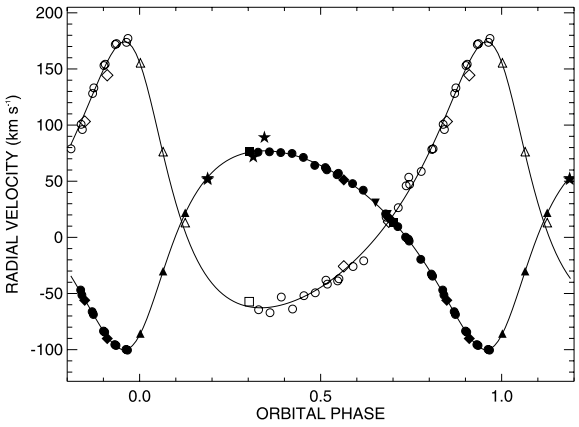

FIG. 1.—Calculated radial velocity curves (*solid lines*) for HD 37366. The primary and secondary stars' measured radial velocities are indicated by circles (2000), inverted triangles (2004 October), stars (2005 October), triangles (2005 November), diamonds (2006 October), and squares (*IUE* 1987). The filled symbols correspond to the primary, and the open symbols correspond to the secondary. The uncertainties in individual measurements are generally smaller than the size of the symbols.

TABLE 3
HD 54662 Primary Radial Velocity Measurements

HJD (−2,400,000)	Telescope/Band	Orbital Phase	V_r (km s^{-1})	σ(line-line) (km s^{-1})	$O-C$ (km s^{-1})
46,426.830	CFHT/yellow	0.191	62.2	2.0	−0.3
46,426.904	CFHT/yellow	0.191	61.3	1.6	−1.1
46,426.980	CFHT/yellow	0.191	61.8	1.6	−0.6
46,427.802	CFHT/yellow	0.192	61.3	1.7	−1.2
46,427.869	CFHT/yellow	0.192	61.6	2.2	−0.9
46,427.925	CFHT/yellow	0.193	61.1	2.0	−1.4
46,427.973	CFHT/yellow	0.193	61.5	1.6	−1.0
46,428.036	CFHT/yellow	0.193	61.6	1.4	−0.9
46,428.132	CFHT/yellow	0.193	62.0	2.1	−0.5
46,428.805	CFHT/yellow	0.194	62.2	2.0	−0.3
46,429.021	CFHT/yellow	0.194	61.4	1.9	−1.2
46,429.814	CFHT/yellow	0.196	61.8	1.7	−0.8
46,429.883	CFHT/yellow	0.196	61.5	2.1	−1.1
46,432.853	CFHT/yellow	0.201	61.4	2.1	−1.3
46,432.897	CFHT/yellow	0.201	60.9	1.4	−1.8
46,432.999	CFHT/yellow	0.202	62.2	2.0	−0.5
46,433.093	CFHT/yellow	0.202	61.2	1.5	−1.6
51,817.967	CF/red	0.855	33.2	0.6	0.0
51,818.962	CF/red	0.857	33.5	2.5	0.4
51,819.962	CF/red	0.859	33.7	1.1	0.7
51,820.990	CF/red	0.860	33.0	2.1	0.1
51,821.968	CF/red	0.862	33.0	0.9	0.2
51,822.941	CF/red	0.864	34.6	3.7	1.9
51,823.957	CF/red	0.866	34.5	3.4	1.8
51,824.903	CF/red	0.867	35.2	1.2	2.6
51,889.990	CF/red	0.984	37.5	2.6	0.7
51,890.923	CF/red	0.986	37.1	1.2	0.0
51,892.899	CF/red	0.989	35.0	2.0	−2.6
51,893.926	CF/red	0.991	37.5	1.9	−0.3
51,894.882	CF/red	0.993	37.5	1.5	−0.6
51,894.956	CF/red	0.993	39.0	2.3	0.9
51,895.934	CF/red	0.995	37.6	1.3	−0.8
51,896.033	CF/red	0.995	39.0	1.6	0.6
51,896.881	CF/red	0.996	39.4	0.6	0.8
51,896.952	CF/red	0.997	37.0	1.6	−1.7
51,897.879	CF/red	0.998	37.9	1.7	−1.0
51,897.943	CF/red	0.998	37.1	1.6	−1.8
51,898.891	CF/red	0.000	39.1	2.5	−0.1
51,898.953	CF/red	0.000	38.3	2.0	−0.9
51,899.885	CF/red	0.002	37.4	0.8	−2.1
51,899.947	CF/red	0.002	38.3	0.5	−1.2
51,900.878	CF/red	0.004	39.0	2.9	−0.8
51,900.940	CF/red	0.004	38.7	3.1	−1.1
51,901.885	CF/red	0.005	39.5	2.9	−0.6
51901.949	CF/red	0.006	39.1	2.8	−1.0
54,020.025	CF/red	0.802	33.9	7.5	−2.5
54,024.964	CF/red	0.811	31.8	5.6	−4.0
54,027.025	CF/blue	0.815	35.8	5.0	0.2
54,028.964	CF/blue	0.819	34.4	6.4	−0.9
54,030.961	CF/blue	0.822	37.4	4.4	2.3
54,032.012	CF/blue	0.824	35.2	4.3	0.2

spectra due to severe line blending with profiles of the primary star (see § 5).

Published velocities for HD 54662 (§ 1) do not show significant variations. Table 3 shows that our measurements change only slightly over our observation period. However, Fullerton (1990) found convincing evidence that this system is a double-lined binary with either a long period or high eccentricity, since he observed a blueshifted secondary component (suspected O7 spectral type) in the profiles of C IV $\lambda\lambda$5801, 5812 and He I λ5876.

Here we present a preliminary orbital solution for the primary component that was determined using our measurements combined with published measurements (Plaskett 1924; Garmany et al. 1980; Fullerton 1990; Stickland & Lloyd 2001) for a total of 67 radial velocities spanning 85 yr. Stickland & Lloyd (2001) proposed a possible period of ≈92 days; however, their orbit was determined excluding selected data points. We reinvestigated the possible period by power-spectrum analysis of all the available data. We examined all the peaks in the CLEANed spectrum using the nonlinear, least-squares, orbital fitting routine,

TABLE 4
PRELIMINARY ORBITAL ELEMENTS FOR HD 54662

Element	Value
P (days)	557.8 ± 0.3
T (HJD −2,400,000)	22333 ± 5
e	0.28 ± 0.04
ω (deg)	238 ± 5
K (km s^{-1})[a]	15.9 ± 0.5
γ (km s^{-1})	49.9 ± 0.6
$f(m)$ ($M_\odot$)[a]	0.20 ± 0.02
$a_1 \sin i$ ($R_\odot$)[a]	168 ± 6
rms (km s^{-1})	3.3

[a] Lower limit due to line blending.

and among the periods limited by the timescales sampled in our two long runs, we find that the best solution occurs at a period of ≈558 days. This confirms the suggestion from Fullerton (1990) that HD 54662 is in fact a long-period binary. Table 4 lists the preliminary orbital elements for HD 54662 assuming equal weighting for all velocities, and this solution is plotted in Figure 2. We show below (§ 5) that these results are affected by line blending, and the derived semiamplitude, for example, is a lower limit to the actual value. It is also possible that the results collected in the literature have systematic differences related to the specific lines and measurement techniques used. These systematic offsets are likely much smaller than the system semiamplitude, and since this system has such a long orbital period, we include all available measurements for this preliminary orbital solution.

4. TOMOGRAPHIC SPECTRAL RECONSTRUCTION AND STELLAR PARAMETERS FOR HD 37366

We used a Doppler tomography algorithm (Bagnuolo et al. 1994) to separate the primary and secondary spectra of HD

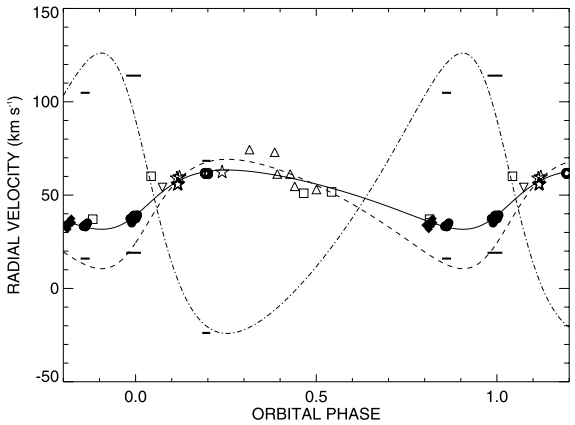

FIG. 2.—Tentative radial velocity curve (*solid line*) for HD 54662 for a period of 558 days. The measured radial velocities are indicated by filled circles (2000), filled diamonds (2006), squares (Stickland & Lloyd 2001), open circles (Fullerton 1990), stars (Garmany et al. 1980), inverted triangles (Conti et al. 1977), and triangles (Plaskett 1924). Expanded horizontal bars are plotted to show the radial velocities derived from fitting the composite line profile from the average spectra for three observational epochs (§ 5). The dashed and dot-dashed lines are the radial velocity curves to these time-averaged points for the primary and secondary star, respectively. The uncertainties in individual measurements are generally smaller than the size of the symbols.

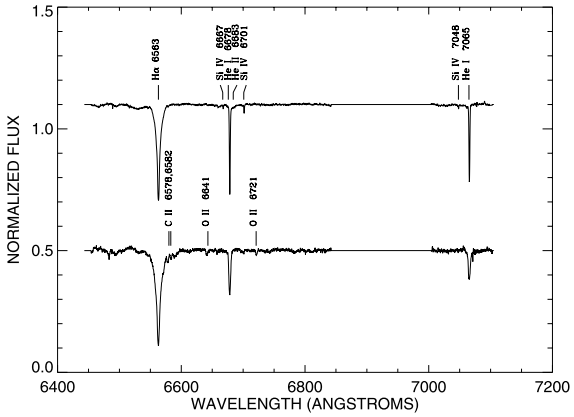

FIG. 3.—Tomographic reconstruction of the spectra of HD 37366 based on the 30 red spectra obtained in 2000. This plot shows the primary (*top*) and the secondary (*bottom*) spectrum, as well as absorption-line identifications (*vertical marks*). The atmospheric lines in the region of 6850–7000 Å are replaced with the continuum.

37366. We applied tomographic reconstruction to the red spectra collected in 2000 (30 total) and to the high-dispersion blue spectra collected in 2005 and 2006 (five total). Figure 3 shows the reconstructed red spectra for the primary (*top*) and the secondary (*bottom*). The region affected by the atmospheric band from ≈6850 to 7000 Å was set to unity. The secondary spectrum shows the weak lines of O II λλ6641, 6721 and C II λλ6578, 6582. These lines are absent in the primary spectrum, which shows instead features such as He II λ6683 that are found in O-type spectra. To determine a monochromatic flux ratio, F_2/F_1, we used the equivalent width of He I λ6678, since it does not change significantly with spectral type for late-O to early-B stars (Conti 1974). These equivalent widths in the primary and secondary reconstructed spectra are equal for a flux ratio of $F_2/F_1 = 0.35 \pm 0.05$.

We fit these reconstructed spectra with the TLUSTY/SYNSPEC model synthetic spectra (see § 3) to estimate the projected rotational velocity $V \sin i$, effective temperature $T_{\rm eff}$, and gravity $\log g$. These values are listed for both components of HD 37366 in Table 5 (where subscript 1 identifies the primary and 2 the secondary). For stars like these, the disappearance of the C II and O II lines and the emergence of the He II and Si IV lines with increasing temperature provide a useful temperature estimate, while the width of the Hα wings is sensitive to the adopted gravity. The $V \sin i$ was measured using a rotational broadening function applied to the model spectra to fit the two He I absorption lines. The red spectra were first used in the determination of these

TABLE 5
STELLAR PARAMETERS FOR HD 37366

Parameter	Value
$V_1 \sin i$ (km s^{-1})	30 ± 10
$V_2 \sin i$ (km s^{-1})	100 ± 10
$T_{\rm eff,1}$ (kK)	33 ± 1
$T_{\rm eff,2}$ (kK)	30 ± 1
$\log g_1$ (cgs)	4.0 ± 0.1
$\log g_2$ (cgs)	4.5 ± 0.2
F_2/F_1	0.35 ± 0.05
ΔM_V	1.1 ± 0.1

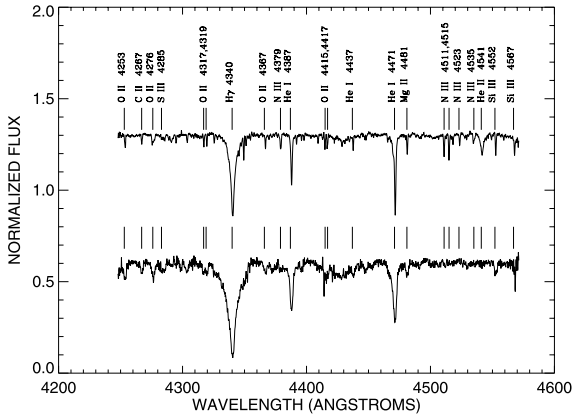

FIG. 4.—Tomographic reconstruction of the spectra of HD 37366 based on five blue spectra from runs in 2005 and 2006. Plot same as in Fig. 3.

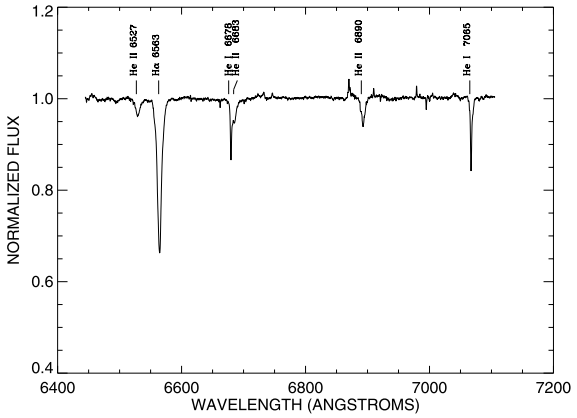

FIG. 5.—Mean spectrum of HD 54662 from our observations. Line identifications are marked by vertical lines.

parameters, and the results were later checked with the reconstructed blue spectra, which include Hγ as well as other lines from heavier elements. The small $V \sin i$ estimate we derive for the primary agrees with the *IUE* measurements from Howarth et al. (1997) and Stickland & Lloyd (2001), and is much smaller than the value for the broader lined secondary. The primary's temperature is somewhat larger than the $T_{\rm eff} = 29.0 \pm 1.8$ kK estimate by Grigsby et al. (1992), but the gravities agree exactly. Our results for $T_{\rm eff}$ and $\log g$ using the TLUSTY code are expected to be more reliable than the previous models used in Grigsby et al. (1992), which used the PAM code (Anderson 1985) that only includes nine elements and many fewer metal lines than does TLUSTY.

The reconstructions from the five high-resolution blue spectra are presented in Figure 4 along with identifications of absorption lines. The secondary spectrum (*bottom*) has lower S/N, but even with only five spectra the tomography algorithm was able extract its spectrum. It is again apparent that the lines of the secondary are much broader than those of the primary. Note also the absence of the He II λ4541 line in the secondary's spectrum, reinforcing our conclusion that the secondary is the cooler of the two stars. Based on the secondary's cooler temperature and high surface gravity, we estimate that it is a B0–1 V star. Note that the magnitude difference we derive is larger than expected for main-sequence stars separated by only a subtype or so (Martins et al. 2005), so it is possible that the primary is a somewhat evolved, more luminous star, and/or the companion is a very young star close to the zero-age main sequence (ZAMS). It is interesting to note that the high $M_1 \sin^3 i$ and $M_2 \sin^3 i$ values from the orbital solution suggest that the inclination is large, $i = 60°$–$90°$. However, *Hipparcos* photometry plotted with the period from our spectroscopic orbital solution shows no evidence of eclipses.

5. STELLAR PARAMETERS FOR HD 54662 FROM COMPOSITE PROFILE FITS

Radial velocities measured for HD 54662 were used to create mean spectra for our observations made in 2000 (Fig. 5) and for those made by Fullerton (1990) in 1986. Figure 6 shows an expanded view of the regions surrounding the He I profiles for two epochs of observation. We see that the secondary component appeared blueshifted during the 1986 run (*left*) and redshifted in recent spectra (*right*).

We made preliminary two-component fits of the blended He I lines (λ5876 for the spectra obtained by Fullerton 1990 and λ7065 for this work) using TLUSTY/SYNSPEC models. We used the temperature and gravity calibrations of Martins et al. (2005) to select parameters for the composite model profiles to fit our observations. Our model spectra for the primary star are based on an assumed type of O6.5 V (Walborn 1972). We constructed model spectra for the secondary for spectral subtypes of O7 V–O9.5 V. Next, we compared our observed mean line profiles to these models applying the appropriate flux ratio (from ΔM_V in Martins et al. 2005) for each spectral component in the shifted, combined line profiles. In each trial for a given secondary spectral type, the only variables were the component radial velocities and the secondary's projected rotational velocity $V_2 \sin i$ (we assumed $V_1 \sin i = 70$ km s^{-1}; Conti & Ebbets 1977). Our best match for the secondary was made with an O9 V subtype and $V_2 \sin i = 110 \pm 10$ km s^{-1}, which yields a flux ratio of $F_2/F_1 = 0.51$. Our fits of He I λ7065 required us to make small and equal adjustments to the model line depths. The resulting fits are shown in Figure 6. We caution that an uncertainty in $V_2 \sin i$ has a large effect on the best-fit line shifts and flux ratio results.

The wavelength shifts made to fit these composite line profiles provide us with average velocities for the primary and secondary components for each observing run. Assuming that the true anomaly ν and the longitude of periastron ω are known from the preliminary orbital fit (Table 4), we may estimate the systematic velocity γ and semiamplitude K by making a least-squares, linear fit of these three velocities using

$$V_r = \gamma_{1,2} \pm K_{1,2}[\cos(\nu + \omega) + e \cos \omega]. \quad (2)$$

This solution gives semiamplitudes of $K_1 = 29 \pm 4$ and $K_2 = 75 \pm 7$ km s^{-1} and systemic velocities of $\gamma_1 = 45 \pm 3$ and $\gamma_2 = 40 \pm 6$ km s^{-1}. This estimate of the secondary radial velocity curve also allows us to compute the component minimum masses of the system, $M_1 \sin^3 i \approx 41.5 \pm 7.6\ M_\odot$ and $M_2 \sin^3 i \approx 16.0 \pm 3.4\ M_\odot$. The radial velocity curves for these solutions for the primary (*dashed line*) and secondary (*dot-dashed line*) are also plotted in Figure 2, along with the time-averaged radial velocities from the two-component fits. This analysis of the line blending problem clearly illustrates how the presence of the blended secondary spectrum skews the velocity measurements

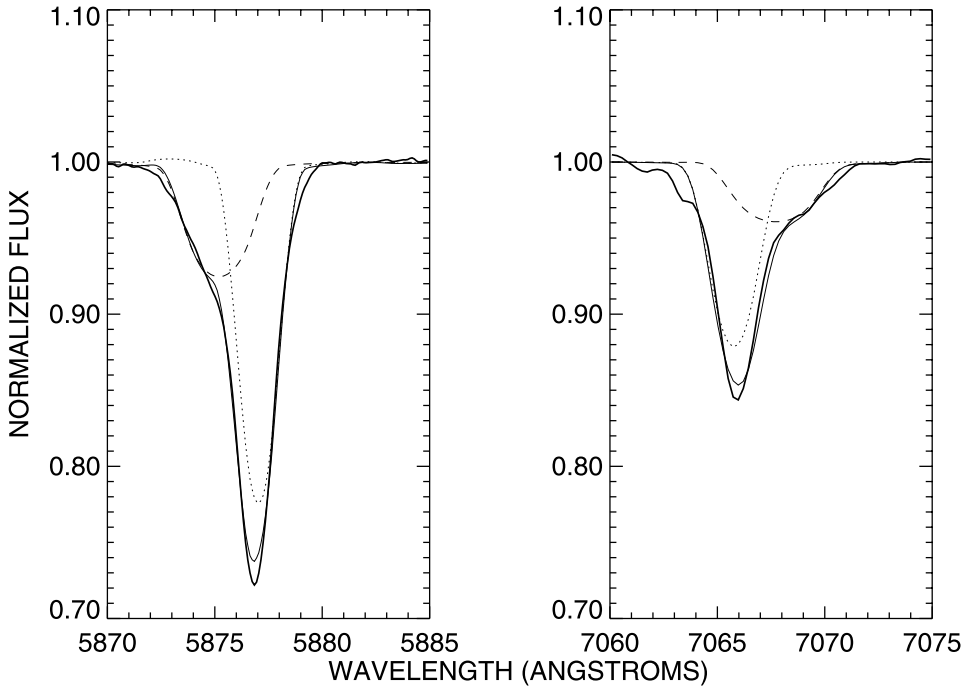

FIG. 6.—Mean line profiles of HD 54662 for He I λ5876 (*left*; Fullerton 1990) and He I λ7065 (*right*; this work). The observations are plotted as thick lines, the combined model fit as thin lines, and the individual component profiles as dotted and dashed lines for the primary and secondary, respectively.

for the primary (Table 3) toward the system's center of mass, resulting in a semiamplitude (Table 4) that is approximately a factor of 2 smaller than the actual value.

6. DISCUSSION

One of the motivations for this study was to find long-period binaries that may be resolved by optical long-baseline interferometry. The CHARA Array, for example, can resolve binaries with angular separations as small as 1 mas (ten Brummelaar et al. 2005). To determine the angular separation of the binaries' components, we reestimated their distances by fitting their observed spectral energy distribution (SED) with a model SED to find the angular stellar diameters that we then compared with stellar radii estimates for their spectral classifications. For each binary, the model temperatures, gravities, and flux ratios were applied to create a combined model flux distribution over a range of 1200–30000 Å. The galactic extinction curve from Fitzpatrick (1999) was then applied to the model SED to fit the observed photometry for each target. The observed SED includes ultraviolet fluxes (*IUE*; TD-1; Thompson et al. 1978) and *UBV* (Neckel et al. 1980), *uvby* (Hauck & Mermilliod 1998), and 2MASS (Two Micron All Sky Survey) *JHK* infrared magnitudes (Skrutskie et al. 2006; Cutri et al. 2003), all of which were transformed into calibrated flux measurements (Colina et al. 1996; Gray 1998; Cohen et al. 2003). The best-fit parameters for reddening $E(B-V)$, ratio of total-to-selective extinction R, and the limb-darkened angular diameter for the primary θ_{LD} (from the flux normalization) are listed in Table 6. Figures 7 and 8 show the SED plots of these best fits for HD 37366 and HD 54662, respectively.

TABLE 6
SED PARAMETERS

Parameter	HD 37366	HD 54662
Primary type	O9.5 V[a]	O6.5 V[a]
Secondary type	B0–1 V	O9 V
$E(B-V)$ (mag)	0.39 ± 0.01	0.32 ± 0.01
R_V (mag)	3.59 ± 0.01	2.82 ± 0.01
θ_{LD} (μas)[b]	48.4 ± 3.0	72.7 ± 3.4
d (kpc)	1.38–1.92	1.23–1.53
ρ_{max} (mas)	0.4–0.5	3.7–4.7

[a] Walborn (1972, 1973).
[b] Primary.

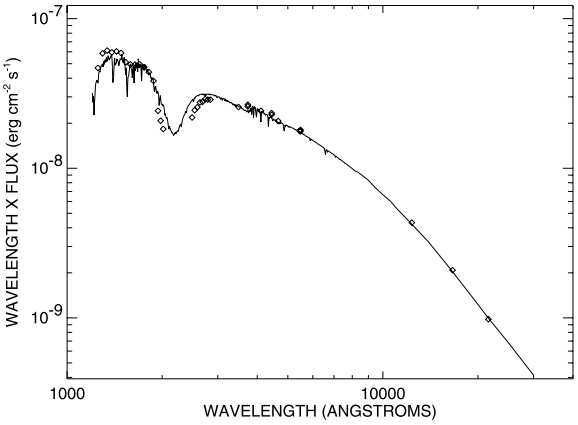

FIG. 7.—Best-fit SED for HD 37366. The solid line indicates the combined model flux for the binary, and the diamonds represent the photometric observations (described in the text).

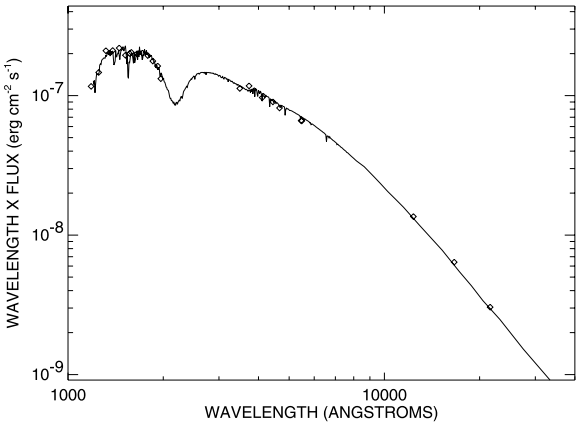

FIG. 8.—Same as Fig. 7, but for HD 54662.

We then compared the expected theoretical radii for the primary stars, based on their spectral classifications as main-sequence stars (Martins et al. 2005), with the angular sizes to obtain distances of 1.38 and 1.23 kpc for HD 37366 and HD 54662, respectively (Table 6). These estimates are consistent with the accepted distances to their home associations (Humphreys 1978). The distance ranges given in Table 6 reflect the change in stellar radius between ZAMS luminosity class V and giant luminosity class III. The midpoint increase in size is $\triangle R \approx 3\ R_{\odot}$ for our stars, and we adopted this difference to estimate the associated range in distance. Errors will also result from the spread in radius for each spectral subtype bin, but this is quite small ($\pm 0.4\ R_{\odot}$) compared to the luminosity range. The error in θ_{LD} from the SED fit contributes only $\approx$1% in the distance error budget.

The binary semimajor axis a was found using Kepler's third law, the derived orbital period, and the stellar mass calibrations from Martins et al. (2005; for O stars) and Harmanec (1988; for B stars). The results for the maximum angular separation $\rho_{\max}$ for the projected elliptical orbit are also presented in Table 6, where we give the range in $\rho_{\max}$ associated with the range in distance. These separations are too small for speckle resolution ($\rho > 0.035''$ for $\triangle m < 3.0$), but they are close to or above the limits of long-baseline interferometry. The HD 54662 binary system in particular may prove to be an important target for mass determination by interferometry.

We thank Daryl Willmarth, Paul Rybski, Eric Phillips, Travis Fischer, and the KPNO staff for their assistance in making these observations possible. This material is based on work supported by the National Science Foundation (NSF) under grants AST 05-06573 and AST 06-06861. C. T. B.'s research is partially supported by a Natural Sciences and Engineering Research Council of Canada (NSERC) Discovery Grant. A. W. F. held an NSERC Post graduate scholarship during the course of this work. Some of the data presented in this paper were obtained from the Multimission Archive at the Space Telescope Science Institute (MAST). STScI is operated by the Association of Universities for Research in Astronomy, Inc., under National Aeronautics and Space Administration (NASA) contract NAS5-26555. Support for MAST for non-*HST* data is provided by the NASA Office of Space Science via grant NAG5-7584 and by other grants and contracts. This publication makes use of data products from the Two Micron All Sky Survey (2MASS), which is a joint project of the University of Massachusetts and the Infrared Processing and Analysis Center/California Institute of Technology, funded by NASA and NSF.

REFERENCES

Anderson, L. S. 1985, ApJ, 298, 848
Bagnuolo, W. G., Jr., Gies, D. R., Hahula, M. E., Wiemker, R., & Wiggs, M. S. 1994, ApJ, 423, 446
Cohen, M., Wheaton, W. A., & Megeath, S. T. 2003, AJ, 126, 1090
Colina, L., Bohlin, R., & Castelli, F. 1996, *HST* Instrument Science Report CAL/SCS-008 (Baltimore: STScI)
Conti, P. S. 1974, ApJ, 187, 539
Conti, P. S., & Ebbets, D. 1977, ApJ, 213, 438
Conti, P. S., Leep, E. M., & Lorre, J. J. 1977, ApJ, 214, 759
Cutri, R. M., et al. 2003, The 2MASS All Sky Catalog of Point Sources (Pasadena: IPAC)
De Becker, M., Rauw, G., Manfroid, J., & Eenens, P. 2006, A&A, 456, 1121
Fitzpatrick, E. L. 1999, PASP, 111, 63
Fullerton, A. W. 1990, Ph.D. thesis, Univ. Toronto
Garmany, C. D., Conti, P. S., & Massey, P. 1980, ApJ, 242, 1063
Garmany, C. D., & Massey, P. 1981, PASP, 93, 500
Gies, D. R. 2003, in IAU Symp. 212, A Massive Star Odyssey: From Main Sequence to Supernova, ed. K. van der Hucht, A. Herrero, & C. Esteban (San Francisco: ASP), 91
Gies, D. R., Penny, L. R., Mayer, P., Drechsel, H., & Lorenz, R. 2002, ApJ, 574, 957
Gies, D. R., et al. 1997, ApJ, 475, L49
Gray, R. O. 1998, AJ, 116, 482
Grigsby, J. A., Morrison, N. D., & Anderson, L. S. 1992, ApJS, 78, 205
Harmanec, P. 1988, Bull. Astron. Inst. Czechoslovakia, 39, 329
Hauck, B., & Mermilliod, M. 1998, A&AS, 129, 431
Howarth, I. D., Siebert, K. W., Hussain, G. A. J., & Prinja, R. K. 1997, MNRAS, 284, 265
Hubeny, I. 1988, Comput. Phys. Commun., 52, 103
Hubeny, I., Heap, S. R., & Lanz, T. 1998, in ASP Conf. Ser. 131, Boulder-Munich II: Properties of Hot Luminous Stars, ed. I. D. Howarth (San Francisco: ASP), 108
Hubeny, I., & Lanz, T. 1995, ApJ, 439, 875
Humphreys, R. M. 1978, ApJS, 38, 309
Lanz, T., & Hubeny, I. 2003, ApJS, 146, 417
Martins, F., Schaerer, D., & Hillier, D. J. 2005, A&A, 436, 1049
Mason, B. D., Gies, D. R., Hartkopf, W. I., Bagnuolo, W. G., Jr., ten Brummelaar, T., & McAlister, H. A. 1998, AJ, 115, 821
McKibben, W. P., et al. 1998, PASP, 110, 900
Morbey, C. L., & Brosterhus, E. B. 1974, PASP, 86, 455
Neckel, T., Klare, G., & Sarcander, M. 1980, A&AS, 42, 251
Penny, L. R., Gies, D. R., & Bagnuolo, W. G., Jr. 1999, ApJ, 518, 450
Perryman, M. A. C., et al. 1997, The *Hipparcos* and Tycho Catalogues (ESA SP-1200; Noordwijk: ESA)
Petrie, R. M., & Pearce, J. A. 1961, Publ. Dom. Astrophys. Obs. Victoria, 12, 1
Plaskett, J. S. 1924, Publ. Dom. Astrophys. Obs. Victoria, 2, 285
Roberts, D. H., Lehár, J., & Dreher, J. W. 1987, AJ, 93, 968
Skrutskie, M. F., et al. 2006, AJ, 131, 1163
Stickland, D. J., & Lloyd, C. 2001, Observatory, 121, 1
ten Brummelaar, T. A., et al. 2005, ApJ, 628, 453
Thompson, G. I., Nandy, K., Jamar, C., Monfils, A., Houziaux, L., Carnochan, D. J., & Wilson, R. 1978, Catalogue of Stellar Ultraviolet Fluxes: A Compilation of Absolute Stellar Fluxes Measured by the Sky Survey Telescope (S2/68) aboard the ESRO Satellite TD-1 (London: Science Research Council)
Walborn, N. R. 1972, AJ, 77, 312
———. 1973, AJ, 78, 1067
Young, R. K. 1942, Publ. David Dunlap Obs., 1, 251

Publications of the Astronomical Society of the Pacific, **119**: 742–746, 2007 July

Radial Velocities of Six OB Stars

T. S. Boyajian,[1] D. R. Gies,[1] E. K. Baines, P. Barai,[2] E. D. Grundstrom,[1] M. V. McSwain,[1,3,4] J. R. Parks, R. L. Riddle,[1,5] W. T. Ryle, and D. W. Wingert[1]

Center for High Angular Resolution Astronomy, and Department of Physics and Astronomy, Georgia State University, Atlanta, GA; tabetha@chara.gsu.edu, gies@chara.gsu.edu, baines@chara.gsu.edu, pabar56@phy.ulaval.ca, erika@chara.gsu.edu, mcswain@astro.yale.edu, parksj@physics.emory.edu, riddle@astro.caltech.edu, ryle@chara.gsu.edu, wingert@chara.gsu.edu

Received 2007 May 21; accepted 2007 June 7; published 2007 July 24

ABSTRACT. We present new results from a radial velocity study of six bright OB stars with little or no prior measurements. One of these, HD 45314, may be a long-period binary, but the velocity variations of this Be star may be related to changes in its circumstellar disk. Significant velocity variations were also found for HD 60848 (possibly related to nonradial pulsations) and HD 61827 (related to wind variations). The other three targets, HD 46150, HD 54879, and HD 206183, are constant-velocity objects, but we note that HD 54879 has Hα emission that may originate from a binary companion. We illustrate the average red spectrum of each target.

Online material: extended table

1. INTRODUCTION

Radial velocity measurements exist for many of the bright OB stars because of their usefulness for binary mass determination and cluster dynamics. However, of the 227 stars listed by Mason et al. (1998) in a survey of the multiplicity of bright O stars, 17 lacked sufficient radial velocity data to determine whether or not they were members of spectroscopic binaries. We observed six of these targets with unknown spectroscopic duplicity in two extended observing runs of high dispersion and high signal-to-noise ratio (S/N) spectroscopy at the Kitt Peak National Observatory (KPNO) coudé feed telescope in 2000. We have already reported on discoveries made during these runs, of new single-lined spectroscopic binaries (HD 14633, HD 15137; Boyajian et al. 2005) and double-lined spectroscopic binaries (HD 37366, HD 54662; Boyajian et al. 2007). Here we present our results on the six stars with mainly "unknown" spectroscopic binary status from the list of Mason et al. (1998). We describe the observations, measurements, and analysis in § 2 and then discuss the individual targets in detail in § 3. Our results are summarized in Table 2 of § 2.

2. OBSERVATIONS AND RADIAL VELOCITIES

Red spectra were collected with the KPNO 0.9 m coudé feed telescope during two observing runs in 2000 October and December. The spectra were made using the long collimator, grating B (in second order, with order-sorting filter OG 550), camera 5, and the F3KB CCD, a Ford Aerospace 3072 × 1024 device. The setup yielded a resolving power of $R = \lambda/\delta\lambda \approx 9500$, with a spectral coverage of 6440–7105 Å. The exposure times were less than 30 minutes, yielding a S/N ≈ 200 pixel^{-1}. We obtained between 22 and 62 spectra of each star.

The spectra were extracted and calibrated using standard routines in *IRAF*,[6] and then each continuum-rectified spectrum was transformed onto a uniform heliocentric wavelength grid for analysis. We removed atmospheric lines by creating a library of spectra from each run of the rapidly rotating A star ζ Aql, removing the broad stellar features from these, and then dividing each target spectrum by the modified atmospheric spectrum that most closely matched the target spectrum in a selected region dominated by atmospheric absorptions.

We measured radial velocities in two ways. For targets with absorption lines, we formed a cross-correlation function (CCF) between a given spectrum and a single reference spectrum of the star (usually the first observation). These relative velocities were then transformed to an absolute velocity scale by adding a mean velocity measured by parabolic fits to the lower halves of the absorption lines in the reference spectrum. Two of the targets have spectra dominated by emission lines, and in these cases we measured bisector velocities for the extreme line

[1] Visiting Astronomer, Kitt Peak National Observatory, National Optical Astronomy Observatory, operated by the Association of Universities for Research in Astronomy, Inc., under contract with the National Science Foundation.

[2] Current address: Departement de Physique, de Genie Physique et d'Optique, Université Laval, Québec, QC, Canada.

[3] Current address: Astronomy Department, Yale University, New Haven, CT.

[4] NSF Astronomy and Astrophysics Postdoctoral Fellow.

[5] Current address: Thirty Meter Telescope, Pasadena, CA.

[6] IRAF is distributed by the National Optical Astronomy Observatory, which is operated by the Association of Universities for Research in Astronomy, Inc., under cooperative agreement with the National Science Foundation.

TABLE 1
RADIAL VELOCITY MEASUREMENTS

Star Name	Date (HJD −2,450,000)	V_r (km s^{-1})	σ (km s^{-1})
HD 45314	1817.942	−31.3	...
HD 45314	1818.945	−32.2	...
HD 45314	1819.936	−31.2	...
HD 45314	1820.931	−32.0	...
HD 45314	1821.931	−32.2	...
HD 45314	1822.926	−31.9	...
HD 45314	1823.866	−32.0	...
HD 45314	1823.987	−32.5	...
HD 45314	1824.888	−31.4	...
HD 45314	1825.004	−30.6	...
HD 45314	1830.956	−34.2	...

NOTE.—Table 1 is published in its entirety in the electronic edition of the *PASP*. A portion is shown here for guidance regarding its form and content.

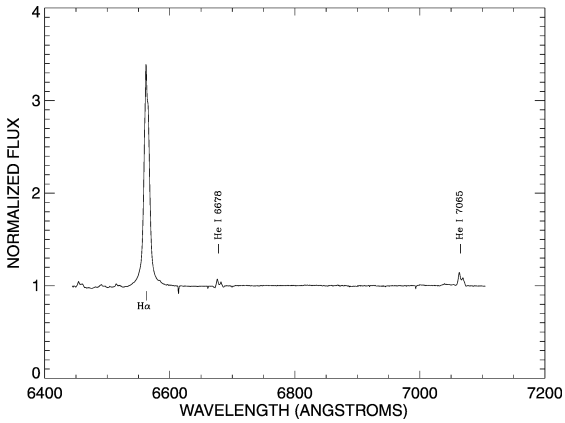

FIG. 1.—Mean red spectrum of HD 45314 in the rest frame. Line identifications are marked by vertical lines.

wings, using the method of Shafter et al. (1986). All these velocities are shown in Table 1, which lists the star name, Heliocentric Julian Date of midexposure, radial velocity, and the line-to-line standard deviation σ (where multiple lines were measured). In § 3, we give a more detailed description of the radial velocity analysis performed on the individual stars.

We checked for evidence of temporal variations in the velocity data by comparing the external scatter between observations E (equal to the standard deviation of the individual velocities in Table 1) with an estimate of the internal error I. The internal error is the average of the line-to-line standard deviation σ for all but the cases of HD 45314 and HD 60848, where only one spectral feature was measured. For these two cases, we estimated I by the average of $|V_i - V_{i+1}|/\sqrt{2}$ for observations closely spaced in time. We then computed the F-statistic to determine the probability that the observed scatter is due to random noise (Conti et al. 1977a). We assume that the variations are significant if this probability is below 1% (Conti et al. 1977a). The results are summarized in Table 2, which lists the star name, number of observations, the mean velocity, E and I, the derived probability, and a short description of the probable source of the variations if present. Details for each target follow in the next section.

3. NOTES ON INDIVIDUAL STARS

3.1. HD 45314

The star HD 45314 (O9 pe, Conti 1974; B0 IVe, Negueruela et al. 2004) has a speckle interferometric companion at a separation of 50 mas (corresponding to a period of ≈30 yr; Mason et al. 1998). The average red spectrum illustrated in Figure 1 shows that Hα and He I $\lambda\lambda$6678, 7065 are double-peaked emission lines. This suggests that the emission forms in a disk and that the line wings form in the gas closest to the star. Thus, we can use measurements of the Hα wings as a proxy for the motion of the underlying star. We measured radial velocities using the wing bisector method of Shafter et al. (1986).

Our results indicate that there was a significant change in velocity from -32.0 ± 0.9 to -21.6 ± 1.9 km s^{-1} between the runs. This may indicate that the Be star is a spectroscopic binary with a period of months. However, the emission profiles changed in shape between the runs (see Fig. 2 for the Hα averages from each run), so it is also possible that the changes in bisector velocity result from physical changes in the gas distribution in the disk rather than orbital motion. We rec-

TABLE 2
RADIAL VELOCITY SUMMARY

Star Name	N	$\langle V_r \rangle$ (km s^{-1})	E (km s^{-1})	I (km s^{-1})	Prob. (%)	Status
HD 45314	33	−25.1	5.2	0.4	0	Long-period SB or disk variation
HD 46150	30	33.8	3.8	1.3	0.6	Constant
HD 54879	26	35.4	1.4	0.6	3.1	Constant
HD 60848	62	5.5	3.2	1.0	0.3	Short-period variation
HD 61827	25	70.2	5.4	0.5	0	Wind-related variation
HD 206183	22	−7.8	1.4	0.6	3.4	Constant

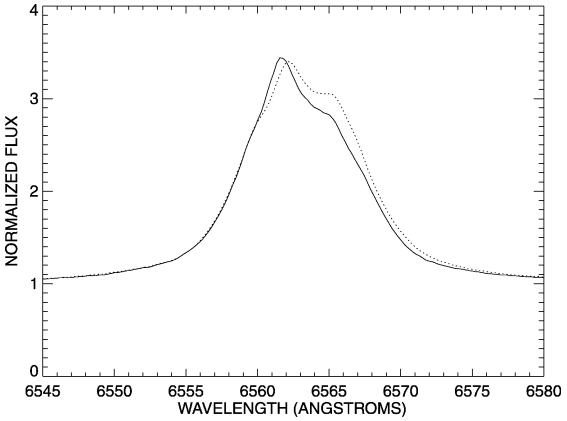

FIG. 2.—HD 45314 mean Hα line profiles observed during the first (*solid line*) and second (*dotted line*) observing runs.

ommend a program of blue spectroscopy of this star to distinguish between the binary and disk variation explanations.

3.2. HD 46150

The spectroscopic binary status of HD 46150 (O5 V((f)); Underhill & Gilroy 1990) remains inconclusive, even though it has a history of radial velocity measurements spanning eight decades (Plaskett 1924; Abt 1970; Conti et al. 1977b; Garmany et al. 1980; Liu et al. 1989, 1991; Underhill & Gilroy 1990; Fullerton 1990; Stickland & Lloyd 2001). The measured radial velocities fall in the range of $V_r = 14$–51 km s^{-1}. Stickland & Lloyd (2001) suggest that this range is significantly larger than expected for diverse measurements of a single star. The most extensive analysis of this star by Garmany et al. (1980) covered four observing seasons, with a mean of $V_r = 39$ km s^{-1} and a range of 26 km s^{-1}. They conclude that the scatter results from atmospheric rather than orbital variations (see also Underhill & Gilroy 1990).

The mean red spectrum in Figure 3 shows a strong He II spectrum associated with a very early type star. We measured CCF velocities of the Hα, He I $\lambda\lambda$6678, 7065, and He II $\lambda\lambda$6683, 6890 features. The error in the mean velocity from closely spaced pairs is $I = 1.3$ km s^{-1}, while the standard deviation among the mean velocities is $E = 3.8$ km s^{-1}. A standard F-test (Conti et al. 1977a) indicates that a temporal variation this large is expected from random variations with a probability of 0.6%; i.e., the observed variation is probably significant. However, most of the variance comes from the first run, in which there appear to be relatively large night-to-night variations that are absent in the second run. This may indicate that the observational errors were larger in the first run compared to our estimate of I from the scatter in measurements from the second run (also consistent with the larger line-to-

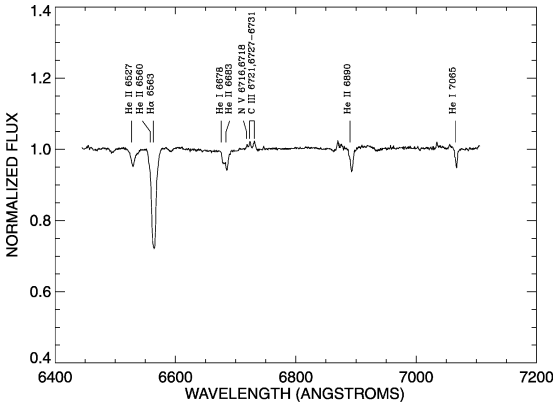

FIG. 3.—Mean spectrum of HD 46150.

line scatter in σ for the first run). Thus, the velocity variations are probably not significant and are consistent with constant radial velocity over the interval of our observations.

3.3. HD 54879

The target HD 54879 (B3 V, Neubauer 1943; O9.5 V, Morgan et al. 1955; B0 V, Claria 1974) has only a few spectroscopic measurements over the past century. The mean spectrum shown in Figure 4 indicates that it has Hα emission and is thus a Be star, which has historically never been observed in emission until now. We made CCF velocity measurements using the lines He I $\lambda\lambda$6678, 7065, C II $\lambda\lambda$6578, 6583, and Si IV $\lambda\lambda$6667, 6701.

Our V_r measurements show no evidence of Doppler shifts in the absorption lines over both short and long timescales. The external error $E = 1.4$ km s^{-1} is somewhat larger than the

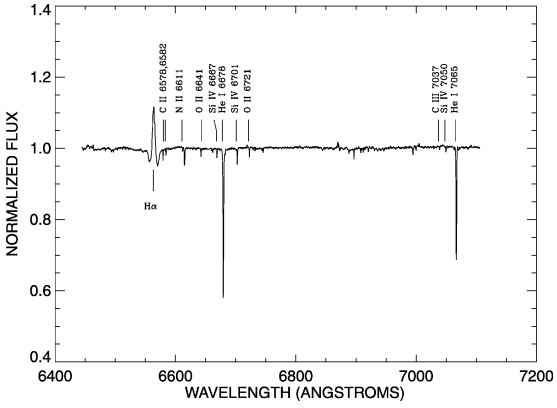

FIG. 4.—Mean spectrum of HD 54879.

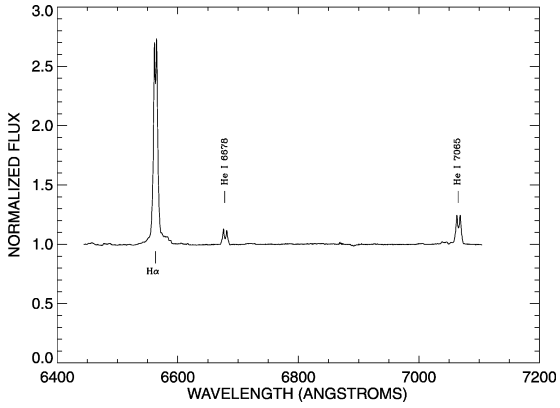

FIG. 5.—Mean spectrum of HD 60848.

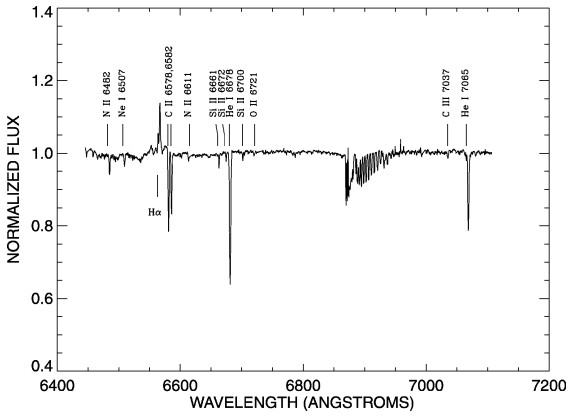

FIG. 6.—Mean spectrum of HD 61827. Features in the 6830–6870 Å region are incompletely removed atmospheric lines.

internal error $I = 0.6$ km s^{-1}. The F-test indicates that a scatter between observations of this size is expected with a probability of 3.1%, so this star is radial velocity constant over the duration of the runs. The only other radial velocity measurement on record, $V_r = 15.6 \pm 1.4$ km s^{-1}, from Neubauer (1943), is smaller than our mean of $V_r = 35.4 \pm 1.4$ km s^{-1}. We caution that this discrepancy may be caused by measuring different lines in the blue part of the spectrum, or by long-term changes in the spectrum.

The mean spectrum has very narrow lines of He I, C II, N II, O II, and Si IV. These apparently sharp absorption lines are unexpected in Be stars that are normally rapid rotators with broad lines. One possibility is that HD 54879 is a rare Be star that is seen almost pole-on, so that the rotation is tangential to the line of sight and the lines do not suffer rotational broadening. Another possibility is that HD 54879 is a Be shell star in which the narrow absorptions form in a circumstellar disk that is projected against the star. The star might have a strong magnetic field that controls the gas outflow and has spun down the star. Finally, the spectrum may be that of a long-period binary consisting of a bright, narrow-lined B star and a fainter Be star (although no companion was found in the speckle survey by Mason et al. 1998). This explanation is supported by the fact that the Hα emission does vary in strength and shape on short and long timescales in our observations, while the absorption lines are constant.

3.4. HD 60848

The star HD 60848 is another Be-type object (O9.5 IVe; Negueruela et al. 2004) that may be a runaway star because of its position well out of the Galactic plane (de Wit et al. 2005). It was recently observed with moderate-dispersion blue spectra by McSwain et al. (2007), who found no evidence of velocity variability. We observed this star only during the second run, but with a higher sampling rate (as frequent as 15 minute intervals during some nights). The mean red spectrum (Fig. 5) shows that Hα and He I $\lambda\lambda$6678,7065 all display double-peaked emission.

We measured relative radial velocities by determining CCF offsets from the first spectrum for the He I λ6678 region, and these were then placed on an absolute scale by finding the bisector velocity of the profile in the first spectrum, using the method from Shafter et al. (1986). The external error of $E = 3.2$ km s^{-1} is larger than the internal error of $I = 1.0$ km s^{-1}, and the F-test indicates that this scatter has a probability of 0.3% for an origin in random variations. Furthermore, there is clear evidence of systematic trends within some nights. We used the CLEAN algorithm from Roberts et al. (1987) to find evidence of two periodic signals with periods of 3.51 ± 0.03 and 3.74 ± 0.03 hr (both with peak power far above the 1% false-alarm probability defined by Scargle 1982). These periods are much too small to be related to binary motion. They may be due to changes in disk density or illumination caused by nonradial pulsations in the underlying star (Rivinius et al. 2003).

3.5. HD 61827

The star HD 61827 (O8–9 Ib, Houk 1982; B3 Iab, Garrison et al. 1977; B3 Ia, Turner 1977) is a luminous object in an association surrounding the cluster NGC 2439 (Turner 1977). We found no evidence of a prior radial velocity measurement in the literature. The star's red spectrum (Fig. 6) shows Hα in emission, as is often the case for B supergiants. The lack of He II λ6683 and the relative strength of C II $\lambda\lambda$6578, 6583 support the later subtype adopted by Garrison et al. (1977) and Turner (1977). We used the C II $\lambda\lambda$6578, 6583 and He I $\lambda\lambda$6678, 7065 absorption lines in the CCF to determine radial velocities

for this star. The ratio of the external to the internal error indicates that the star is a velocity variable.

Our spectra show dynamic Hα emission changes, with variable red and blue peaks appearing to vary on a timescale of 5–10 days. We suspect that these variations are related to structures in the stellar wind that are modulated by rotation and temporal changes in the outflow. These emission variations in Hα appear to affect the velocities measured for the absorption lines of C II and He I through subtle effects of emission filling that are not apparent to the eye. For example, during the first run, we observed the emergence of a strong redshifted Hα peak during the time when the absorption velocities attained their minimum value, and the appearance of a strongly blueshifted Hα peak occurred at the time when the absorption velocities reached a maximum. This correlation indicates that the absorption lines we measured (C II and He I) are probably also partially filled in by weak emission that shifts the line center away from the location of the emission. Thus, we suggest that the apparent velocity variations in HD 61827 are due to the effects of variations in the star's wind.

3.6. HD 206183

HD 206183 (O9.5 V; Daflon et al. 2003) resides in the Tr 37 cluster in the Cep OB2 association. Mason et al. (1998) list two visual companions but assign the star to the "unknown" status as a spectroscopic binary, since only one other velocity measurement exists (Sanford & Merrill 1938). The average red spectrum (Fig. 7) shows that the lines are narrow ($V \sin i = 19.2 \pm 1.9$ km s^{-1}; Daflon et al. 2003). We measured CCF radial velocities for HD 206183 using Hα and He I $\lambda\lambda$6678, 7065. The mean velocities show no evidence for velocity variability over the two runs.

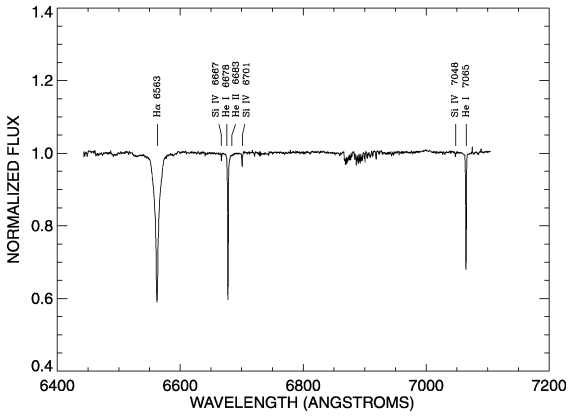

FIG. 7.—Mean spectrum of HD 206183.

We thank Daryl Willmarth and the staff of KPNO for their assistance in making these observations possible. This work was supported by the National Science Foundation under grants AST 02-05297, AST 05-06573, and AST 06-06861. Institutional support has been provided from the GSU College of Arts and Sciences and from the Research Program Enhancement fund of the Board of Regents of the University System of Georgia, administered through the GSU Office of the Vice President for Research.

REFERENCES

Abt, H. A. 1970, ApJS, 19, 387
Boyajian, T. S., et al. 2005, ApJ, 621, 978
———. 2007, ApJ, 664, 1121
Claria, J. J. 1974, A&A, 37, 229
Conti, P. S. 1974, ApJ, 187, 539
Conti, P. S., Garmany, C. D., & Hutchings, J. B. 1977a, ApJ, 215, 561
Conti, P. S., Leep, E. M., & Lorre, J. J. 1977b, ApJ, 214, 759
Daflon, S., Cunha, K., Smith, V. V., & Butler, K. 2003, A&A, 399, 525
de Wit, W. J., Testi, L., Palla, F., & Zinnecker, H. 2005, A&A, 437, 247
Fullerton, A. W. 1990, Ph.D. thesis, Univ. Toronto
Garmany, C. D., Conti, P. S., & Massey, P. 1980, ApJ, 242, 1063
Garrison, R. F., Hiltner, W. A., & Schild, R. E. 1977, ApJS, 35, 111
Houk, N. 1982, Catalogue of Two-Dimensional Spectral Types for the HD Stars, Vol. 3 (Ann Arbor: Univ. Michigan)
Liu, T., Janes, K. A., & Bania, T. M. 1989, AJ, 98, 626
Liu, T., Janes, K. A., & Bania, T. M. 1991, AJ, 102, 1103
Mason, B. D., Gies, D. R., Hartkopf, W. I., Bagnuolo, Jr., W. G., ten Brummelaar, T., & McAlister, H. A. 1998, AJ, 115, 821
McSwain, M. V., Boyajian, T. S., Grundstrom, E. D., & Gies, D. R. 2007, ApJ, 655, 473
Morgan, W. W., Code, A. D., & Whitford, A. E. 1955, ApJS, 2, 41
Negueruela, I., Steele, I. A., & Bernabeu, G. 2004, Astron. Nachr., 325, 749
Neubauer, F. J. 1943, ApJ, 97, 300
Plaskett, J. S. 1924, Publ. Dom. Astrophys. Obs., 2, 285
Rivinius, T., Baade, D., & Štefl, S. 2003, A&A, 411, 229
Roberts, D. H., Lehár, J., & Dreher, J. W. 1987, AJ, 93, 968
Sanford, R. F., & Merrill, P. W. 1938, ApJ, 87, 517
Scargle, J. D. 1982, ApJ, 263, 835
Shafter, A. W., Szkody, P., & Thorstensen, J. R. 1986, ApJ, 308, 765
Stickland, D. J., & Lloyd, C. 2001, Observatory, 121, 1
Turner, D. G. 1977, AJ, 82, 805
Underhill, A. B., & Gilroy, K. K. 1990, ApJ, 364, 626